Synthesis and Characterisation of *N*-substituted Pyrrole Monomers and Polypyrrole Films

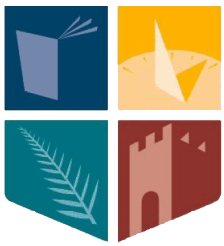

NUI MAYNOOTH

Ollscoil na hÉireann Má Nuad

Niall B. McGuinness BSc

Thesis Submitted to the National University of Ireland in Fulfilment of the Requirements for the Degree of

Doctor of Philosophy

Department of Chemistry

National University of Ireland Maynooth

2013

Research Supervisor: Dr A. Denise Rooney

Head of Department: Dr John C. Stephens

Contents

Author Declaration

I hereby certify that this thesis, which I submit to the National University of Ireland for examination in consideration for the award of Doctor of Philosophy, is entirely my own personal effort and has not been previously submitted, in whole or in part, to NUIM or elsewhere for the procurement of said degree. Where applicable, any content contributed from collaborative research is accordingly accredited and to the best of my knowledge, the work herein is completely original and does not breach copyright law, unless otherwise stated and therefore is cited or acknowledged.

Signed:

Student Number:

Date:

Acknowledgements

Firstly, I must thank my supervisor, Dr Denise Rooney, for her guidance and support during my research project. Her passion for chemistry, coupled with her unparalleled motivation and focus are what helped me to get to where I am. Working under your supervision has been one of the best experiences of my life, I owe you so much. To Dr Trinny Velasco-Torrijos, thank you for your supervision during my 4th year project and introducing me to organic synthesis; your help was greatly appreciated.

My sincere thanks to my Mum and Dad, Marie and Brendan, for their encouragement, advice and patience, I promise I will get a job now, and my sister, Sweet Dee, for being such a great person, if only more people were like you. I want to thank my gran, Brigie, for all the prayers over the years; I'll definitely have to buy you some new rosary beads.

Special thanks has to go out to Mairead, Barry and Nakita, Sage, Amro, Yuhang, Bod, Desy, Spud, Bloxham and everybody else who's put up with me over the years.

Thanks to Conor and Lynn for all the craic in the lab, John for the good times in 69 Silken Vale and Roisin, Michelle, Ruth, Ross, Chig and Barry, cheers for all the banter. Wayne, a big thank you for helping me deal with the many problems I encountered with MS Word and printing. Cheers to Gillian, Ursula, Conor and Adelaide; thanks so much for the proof reading and corrections, you all were a huge help.

I would like to thank Dr Mary Pryce from the Chemical Sciences in DCU, for the use of her OTTLE cell. Also, thank you to Dr Nikolay Petkov, Dr Patrick Carolan and Mr Vince Lodge in the Tyndall National Institute, Cork, for all the FESEM and TEM analyses. Also, to Dr Mircea Modreanu for the Raman spectroscopy and a big thank you to Mr Paul Roseingrave for all the help with the National Access Programme grant proposal.

A special thanks to Dr Anne Shanahan in the Focus Institute, DIT, Dublin, for being so accommodating, your expertise using Raman spectroscopy has been invaluable.

To Dr Fatima Laffir in the Materials and Surface Science Institute (MSSI), UL, Limerick, thanks for the XPS analysis. A big thank you to Ms Barbara Woods, thanks so much for running the mass specs, Mr Noel Williams for the computer/everything else and a thank you to all the other technicians who've helped.

To Prof. Peter Carr, thank you for all the insightful conversations, for taking the time to give your welcome advice.

I would like to thank Science Foundation Ireland for the opportunity to do my PhD at NUIM and a grateful acknowledgement to the heads of department, Prof. John Lowry and Dr John Stephens.

Abbreviations

$(PyPrNHCO)_2Bipy$	4,4’-bis-(*N*-propyl-3-pyrrole-carbamoyl)-2,2’-bipyridine
$[Py\text{-}Py]^{+\bullet}$	pyrrole radical cation dimer
$[Py\text{-}Py\text{-}Py]^{+\bullet}$	pyrrole radical cation trimer
1D	one-dimensional
2D	two-dimensional
3D	three-dimensional
AAO	anodic aluminium oxide
ADH	alcohol dehydrogenase
antiHAS	anti-human serum albumin
ASPO	spiro[azahomoadamantane-phenanthrolinoxazine]
ATP	adenosine triphosphate
ATR-FTIR	attenuated total reflectance-Fourier transform infrared spectroscopy
Bipy	2,2’-bipyridine
BipyPy	pyrrole substituted 2,2’-bipyridine
br	broad (FTIR)
Bz	benzyl
C	Chemical
CNT	carbon nanotubes

conc.	concentration
CORM	carbon monoxide releasing molecule
CORP	carbon monoxide releasing polymer
COSY	correlation spectroscopy
CP	conducting polymer
Cp	cyclopentadiene
CPA	constant potential amperometry
CuAAC	copper(I)catalysed azide-alkyne cycloaddition
CV	cyclic voltammetry
d	doublet (NMR)
DCM	dichloromethane
D-CSA	D-camphorsulfonic acid
dd	doublet of doublets (NMR)
De	decyl
DEPT	distortionless enhancement by polarization transfer
Dia.	diameter
DIPEA	diisopropylethylamine
DMF	dimethylformamide
DMSO	dimethylsulfoxide
DNA	deoxyribonucleic acid
DPV	differential pulse voltammetry
E	Electrochemical

ECH	electrocatalytic hydrogenation
ECL	electrochemiluminescene
ECR	electrocatalytic reduction
ED-FFT	electron diffraction-fast Fourier transform
EDOT	3,4-ethylenedioxythiophene
EDX	energy-dispersive X-ray spectroscopy
ee	enantiomeric excess
EIS	electrochemical impedance spectroscopy
en	ethylenediamine
eq.	equivalent
EQCM	electrochemical quartz crystal microbalance
Et	ethyl
Et_2O	diethyl ether
EtOAc	ethyl acetate
EtOH	ethanol
Fc	ferrocene
FcCCH	ethynylferrocene
FESEM	field emission scanning electron microscopy
FTIR	Fourier transform infrared spectroscopy
GCE	glassy carbon electrode

GOx	glucose oxidase
GRGDS	Gly-Arg-Gly-Asp-Ser
HMQC	heteronuclear multiple-quantum correlation
HOMO	highest occupied molecular orbital
ICP	inductively coupled plasma spectrometry
IN	instantaneous nucleation
IN2D	instantaneous nucleation and two dimensional growth
IN3D	instantaneous nucleation and three dimensional growth
ISPO	spiro[indoline-phenanthrolinoxazine]
ITO	indium tin oxide
L	ligand
LDV	Teflon-lined digestion vessel
LiTFSI	lithium bis(trifluoromethane)sulfonimide
LUMO	lowest unoccupied molecular orbital
M	metal
m	multiplet (NMR)
MAS	microwave-assisted synthesis
Me	methyl
MeCN	acetonitrile

MeOH	methanol
MOR	methanol oxidation reaction
ESI-MS	electronspray ionisation-mass spectrometry
MWCNT	multi-walled carbon nanotubes
N_4CBz	benzyl 5-tetrazolate
N_4CPh	phenyl 5-tetrazolate
N_4CR	tetrazolate
N_4CT	thiophene 5-tetrazolate
NaDS	sodium dodecyl sulfate
NCBz	benzyl cyanide
NCPh	benzonitrile
NCT	2-thiophenecarbonitrile
NG	nucleation and growth
NGM	nucleation and growth mechanism
NMR	nuclear magnetic resonance
OHDR	oligomeric high-density region
ORR	oxygen reduction reaction
OSWV	Osteryoung square wave voltammetry
OTTLe	optically transparent thin-layer electrochemistry
Ox	Oxidation
PA	polyacetylene
PANI	polyaniline

PBS	phosphate buffer solution
PC	polycarbonate
PEDOT	poly(3,4-ethylenedioxythiophene)
Ph	phenyl
pip	piperidine
PN	progressive nucleation
PN2D	progressive nucleation and two-dimensional growth
PN3D	progressive nucleation and three-dimensional growth
PPy	polypyrrole
PPyCl	polypyrrole chloride
PPyDeN$_3$	poly[*N*-(10-azidodecyl)pyrrole]
PPyEtCN	poly[*N*-(2-cyanoethyl)pyrrole]
PPyEtCO$_2$H	poly[*N*-(2-carboxyethyl)pyrrole]
PPyEtN$_3$	poly[*N*-(2-azidoethyl)pyrrole]
PPyMe	poly[*N*-(1-methyl)pyrrole]
PPyPrN$_3$	poly[*N*-(3-azidopropyl)pyrrole]
Pr	propyl
PT	polythiophene
pt	*pseudo* triplet (NMR)
Py	pyrrole
Py$^{+\bullet}$	pyrrole radical cation monomer
Py$^+$-Py$^+$	pyrrole dication dihydromer

PyDeN$_3$	*N*-(10-azidodecyl)pyrrole
PyDeTriazoleCholesterol	cholesterol functionalized triazole Py
PyEtN$_3$	*N*-(2-azidoethyl)pyrrole
PyPrN$_3$	*N*-(3-azidopropyl)pyrrole
PyPrNH$_2$	*N*-(3-aminopropyl)pyrrole
Py-Py	pyrrole aromatic dimer
Py-Py$^+$-Py$^+$	pyrrole dication trihydromer
Py-Py-Py	pyrrole aromatic trimer
q	quartet (NMR)
R.T.	room temperature
Red	Reduction
s	singlet (NMR)
s	strong (FTIR)
SA	self-assembly
SCE	saturated calomel electrode
SEM	scanning electron microscopy
SS	stainless steel
STEM	scanning transmission electron microscopy
Sub	Substitution
SWCNT	single-walled carbon nanotubes
T	thiophene
TBABF$_4$	tetrabutylammonium tetrafluoroborate

$TBAPF_6$	tetrabutylammonium hexafluorophosphate
$TBAClO_4$	tetrabutylammonium perchlorate
TEA	triethylamine
TEM	transmission electron microscopy
THF	tetrahydrofuran
TLC	thin-layer chromatography
TM	transition metal
TMANO	trimethylamine *N*-oxide
TMS	tetramethylsilane
UV	ultraviolet
UV-Vis	ultraviolet-visible spectroscopy
vs.	versus
w	weak (FTIR)
WNV	West Nile virus
XPS	X-ray photoelectron spectroscopy

Symbols

Ω	ohm
<	less than
>	greater than
≤	less or equal to
≥	greater or equal to
a	length of a 1D box

C	Celsius
C_{α}	alpha carbon
C_{β}	beta carbon
D	distance
e^-	electron
$E_{1/2}$	half-wave potential
E_{app}	applied potential
E_{FWHM}	energy of full width at half maximum
E_{ox}	oxidation potential
E_{p}	peak potential
E_{pa}	anodic peak potential
E_{pc}	cathodic peak potential
E_{pox}	peak oxidation potential
h	Plank's constant
H_{α}	alpha proton
H_{β}	beta proton
J	coupling
j	current density
j_a	anodic current density
j_c	cathodic current density
j_p	peak current density
j_{pa}	anodic peak current density
j_{pc}	anodic peak current density

j_{pox}	peak oxidation current density
j-t	current density-time
m	mass of an electron
N	large number of carbon atoms
^{o}	degree
q	charge density
q-t	charge density-time
q-τ	charge density-induction time
r^2	correlation coefficient
t_0,j_0	current density-time minimum
t_{max},j_{max}	current density-time maximum
$\nu^{1/2}$	square root of scan rate
α	alpha
β	beta
δ	chemical shift
Δ	heating to reflux temperature
ΔE	difference in energy
ΔE_p	peak potential separation
$\Delta\varepsilon^{bip}$	bipolaron mid-gap energy level
$\Delta\varepsilon^{pol}$	polaron mid-gap energy level
ε	dielectric constant
σ	degree of electrical conductivity
τ	induction time

Units

%	percent
Å	Angstrom
C cm^{-2}	coulombs per centimetre squared
cm	centimetre (10^{-2})
cm^{-1}	wavenumbers
cm^{2}	centimetre squared
cm^{3}	centimetre cubed
eV	electron volt
g 100 cm^{-3}	grams per one hundred centimetres cubed
g mol^{-1}	grams per mole
g	gram
h	hour
Hz	hertz
keV	kiloelectronvolt
kV	kilovolt
mA cm^{-2}	milliamps per centimetre squared
mC cm^{-2}	millicoulombs per centimetre squared
MHz	megahertz
min	minute
mm	millimetre (10^{-3})

mM	millimolar
mol%	mole percent
mV s^{-1}	millivolts per second
mW	milliwatt
nm	nanometre (10^{-9})
pm	picometre
ppb	parts per billion
ppm	parts per million
S m^{-1}	siemens per metre
s	second
V	volt
v/v	volume-volume percent
W	watt
µC cm^{-2}	microcoulombs per centimetre squared
µM mM^{-1}	micromole per millimole
µm	micrometre (10^{-6})

Abstract

In this body of work, the polymerisation of *N*-substituted pyrrole monomers and the functionalisation of the monomers or the resulting polymers, with transition metal complexes, were performed. Polymer deposition was executed, utilising the electrochemical deposition technique, due to its facile use and the unequivocal control attained during the experimental procedure. The pyrrole monomers employed, possessed either azide, 2,2'-bipyridine or nitrile moieties, as these species have been universally exploited in cycloaddition and coordination chemistry.

Firstly, *N*-(10-azidodecyl)pyrrole, *N*-(3-azidopropyl)pyrrole and *N*-(2-azidoethyl)pyrrole were electropolymerised in the bulk morphology and characterised. Then, employing copper(I)-catalysed azide-alkyne cycloaddition chemistry, the monomers, *N*-(10-azidodecyl)pyrrole and *N*-(2-azidoethyl)pyrrole, were reacted with the redox active molecule, ethynylferrocene, to yield the products, 1-[10-(4-ferrocenyl-1*H*-1,2,3-triazol-1yl)decyl]pyrrole and 1-[2-(4-ferrocenyl-1*H*-1,2,3-triazol-1yl)ethyl]pyrrole, which were subsequently electropolymerised and characterised.

Development of a novel, template-free, electrodeposition method yielded the facile fabrication of the nanostructured poly[*N*-(2-azidoethyl)pyrrole] film, shown using field emission scanning electron microscopy and transmission electron microscopy. The deposition mechanism, involving a bielectrolyte co-solvent system, was investigated using nucleation and growth mechanisms, while the roles of both the 'seed' ($LiClO_4$) and 'bulk' ($(NH_4)H_2PO_4$) electrolyte were determined. Chemical post-functionalisation of the nanowire film, *via* copper(I)-catalysed azide-alkyne cycloaddition chemistry, permitted the covalent attachment of ethynylferrocene, which created the possibility of a very effective, mediator-less (covalently bound), nanostructured biosensor.

A novel pyrrole monomer, 4,4'-bis-(*N*-propyl-3-pyrrole-carbamoyl)-2,2'-bipyridine was synthesised and coordinated with Group 6 metal carbonyls, producing 4,4'-bis-(*N*-propyl-3-pyrrole-carbamoyl)-2,2'-bipyridine tetracarbonyl chromium(0),

molybdenum(0) and tungsten(0). The electroactivity of 4,4'-bis-(*N*-propyl-3-pyrrole-carbamoyl)-2,2'-bipyridine tetracarbonyl molybdenum(0) was determined utilising cyclic voltammetry, while the controlled release of carbon monoxide was induced by introducing acetonitrile. The 4,4'-bis-(*N*-propyl-3-pyrrole-carbamoyl)-2,2'-bipyridine ligand was electropolymerised and post-functionalisation with Group 6 metal carbonyls was attempted, to possibly produce medically beneficial carbon monoxide releasing polymers.

Utilising the nitrile moiety, tricarbonyl cyclopentadienyl *N*-2-(5-tetrazolatephenyl) molybdenum(II), tricarbonyl cyclopentadienyl *N*-2-(5-tetrazolate-2-thiophene) molybdenum(II) and tricarbonyl cyclopentadienyl *N*-2-(5-tetrazolate-1-benzyl) molybdenum(II) were synthesised *via* cycloaddition chemistry employing sodium azide. *N*-(2-cyanoethyl)pyrrole, possessing the ability to be electrodeposited as a nanostructured film was employed, producing dicarbonyl cyclopentadienyl (*N*-2-(5-tetrazolate-2-ethylpyrrole) iron(II**)**.

Chapter 1 Introduction

1.1 Introduction

In this body of work, the general aim was the attainment of a polymer modified electrode, functionalised with transition metal (TM) complexes to facilitate their application in biosensing and drug delivery technologies. Our first objective was to electrodeposit novel, *N*-substituted polypyrrole (PPy) films, comprised of terminating azide[1] and 2,2'-bipyridine[2] moieties, by employing traditional methodologies. The incorporation of these groups yielded the employment of both cycloaddition[3] and coordination[4] chemistry, which could permit reaction between the polymer film and TM complexes, such as ethynylferrocene (FcCCH) and Group 6 metal carbonyls. These complexes were selected explicitly, as they have been reported to promote biosensor efficiency[5] and release beneficial carbon monoxide (CO) in an immunotherapeutic approach, respectively.[6]

The second objective was the template-free electrodeposition of a poly[*N*-(2-azidoethyl)pyrrole] ($PPyEtN_3$) nanowire film, by employing a bielectrolyte co-solvent system, a method adapted from the analogous deposition of PPy nanowire films.[7-9] Nanostructured polymer films retain many desirable attributes in comparison to their bulk counterparts, such as, owning a greater surface area, demonstrating a faster redox activity and displaying quantum effects.[10] We have already reported the deposition of poly[*N*-(2-cyanoethyl)pyrrole] (PPyEtCN) nanowire and microtube films,[11,12] therefore, we believed it rational to explore the possibility of coordinating metal carbonyls to *N*-(2-cyanoethyl)pyrrole (PyEtCN) and other coordinating nitrile ligands, with the goal of eventually binding these complexes to a nanostructured polymer modified electrode.

This introductory chapter discusses all of the important concepts and processes investigated during this study; the mechanism and also, the methods employed during deposition of both bulk and nanowire polypyrrole films, the deposition and use thereafter of *N*-substituted PPy films and finally, the cycloaddition and coordination of metal complexes with *N*-substituted pyrroles (Py).

1.2 Conducting polymers

Polymers have dramatically changed the way people live; they are necessary to support and elongate life, through their use in biological and medical applications, while they also enhance our lives, as they are employed within every instrument, which facilitates technological entertainment. They can be fabricated to possess many different properties, such as ion-exchange capabilities, redox activity, chemically resistance, lightness, conductivity and biocompatibility.[13-16]

The one greatly beneficial attribute belonging to certain polymers (Figure 1.1) is the possibility to possess electrical conductivity, which was first reported for polyacetylene in 1977 by Shirakawa, Heeger and MacDiarmid, for which in 2000, they received the Nobel prize.[17] This property is usually associated with metals, but most conducting polymers (CP) consist of repeating organic monomers. They can possess this property, as they are composed of conjugated sp^2 carbon double bonds, along the polymer backbone. Generally, in order to achieve electrical conductivity, the polymer backbone is oxidised, forming empty p-orbitals, which permit the increased mobility of electrons, thus facilitating the movement of charge along the polymer. In the oxidised state, electrolytic anions from solution ingress into the polymer, neutralising the charge and the polymer is said to be doped.

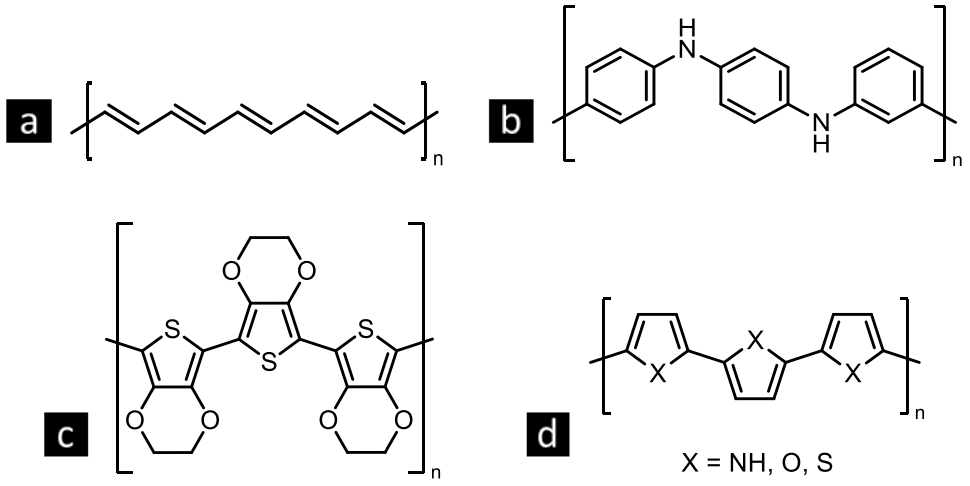

Figure 1.1: Structures of common CPs in their non-doped state. (a) Polyacetylene (PA), (b) Polyaniline (PANI), Poly(3,4-ethylenedioxythiophene) (PEDOT) and (d) Polypyrrole (PPy) X = NH, Polyfuran (PF) X = O, Polythiophene (PT) X = S.

1.3 Polypyrrole

PPy is probably the most thoroughly studied CP, as the Py monomer is oxidised with ease' it possesses reasonable water solubility and is commercially available. PPy possesses advantageous attributes, such as high electrical conductivity and good redox properties.[13,18] Therefore, as anticipated, PPy possesses the potential for employment in a vast array of applications, such as batteries,[19] supercapacitors,[20,21] electrochemical sensors,[22] textile/fabrics,[23] drug delivery systems[24] and protective coatings.[16]

1.3.1 Structural properties of polypyrrole

PPy is an amorphous material; insoluble in solvents and usually black or blue, but its colour may vary, due to the oxidation state of the polymer.[25] The polymer may exist in a fully oxidised (bipolaron), partially oxidised (polaron) or neutral state. The polymer may expand and contract during oxidation and reduction, due to the ingress and egress of counter and solvation ions.[26] The polymer is constituted of repeating Py monomer units, which are five-membered heterocyclic rings, with the nitrogen and four carbon atoms being sp^2 hybridised. Since the Py ring is diunsaturated, accompanied by a lone pair of electrons on the nitrogen atom in the $2p_z$ orbital, this produces a delocalised aromatic π-system. During polymerisation, the monomer units covalently bind, orientating in a near coplanar fashion (Figure 1.2), permitting electron delocalisation along the conjugated polymer backbone and providing the polymer with its electrical conductivity property.

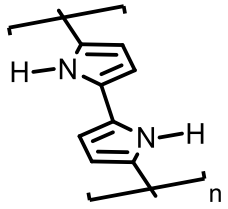

Figure 1.2: PPy displaying a coplanar polymer backbone.

The conductivity of PPy can be affected negatively by structural defects, which can occur during polymer propagation. The Py monomer (Figure 1.3) has four positions

on the ring (2, 3, 4, 5), which can facilitate propagation, but these sites are all susceptible to defect formation.

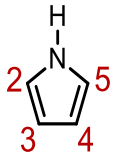

Figure 1.3: Structure of Py unit assigning position (2,5) and (3,4).

Propagation at the 2 and 5 positions are the most desired for good electrical conductivity of the polymer; referred to as α-coupling (Figure 1.4 (a)), but after initiation of polymerisation, there is a tendency for the Py trimers to propagate at the 3 and 4 position, which is referred to as β-coupling. This may occur at every third Py unit,[15,27] which may be already α-coupled, creating a branched β-coupling (Figure 1.4 (b)). This β-branching inflicts a decrease in coplanarity,[28,29] resulting with diminished conjugation[30] and increased resistivity of the polymer.[31]

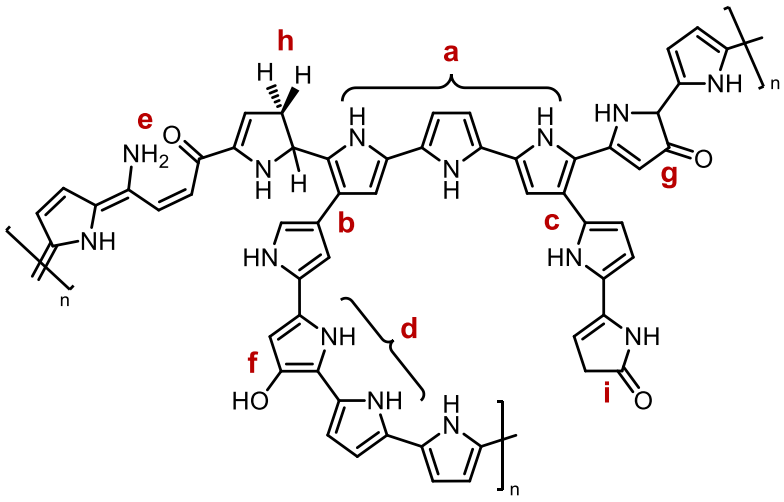

Figure 1.4: PPy chains structural possibilities. (a) α-coupling, (b) β-coupling at a polymer branch, (c) α-b coupling at a polymer branch and (d) unrotated α-coupling. Polymer defects instigated by nucleophilic attack of H_2O causing (e) ring opening of Py, (f) overoxidation, yielding a 3-hydroxypyrrole species and (g) overoxidation, yielding a pyrrolinone species. (h) Hydrogenation and (i) termination site.

Defects are also attributed to secondary reactions that transpire during propagation. At the α-position, H_2O, acting as a nucleophile, may attack a cationic site on the

polymer backbone, inducing the ring opening of a Py unit (Scheme 1.1), which disrupts the structure and thus the conjugation of the polymer.

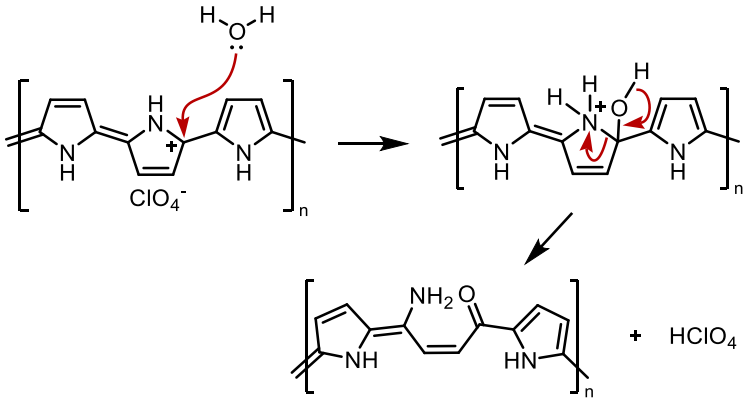

Scheme 1.1: Mechanism of nucleophilic attack by H_2O at the carbocation.

Polymer overoxidation can be instigated at the β-position by hydroxide nucleophilic attack at cationic sites, yielding 3-hydroxypyrrole species along the PPy backbone.

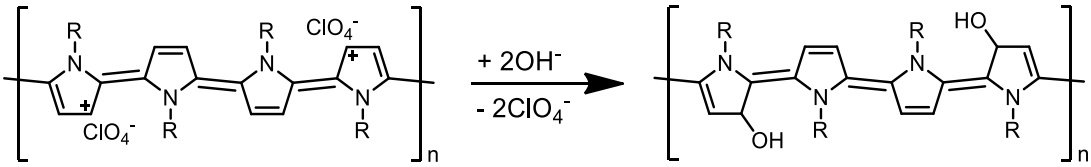

Scheme 1.2: Overoxidation of bipolaron to 3-hydroxypyrrole species.

Once the first overoxidation step has occurred; nucleophilic attack of hydroxide species at the bipolaron yields the 3-hydroxypyrrole species, then further β-position overoxidation can occur. Since an oxidant or oxidising potential is present during Py polymerisation, a 3-hydroxypyrrole species can be subject to a chemical or electrochemical 2-electron oxidation, producing a pyrrolinone species (Scheme 1.3).

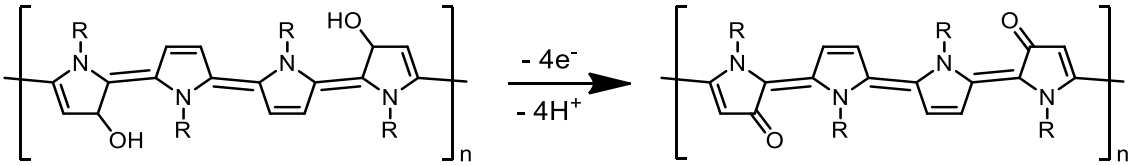

Scheme 1.3: Overoxidation of 3-hydroxypyrrole to pyrrolinone species.

1.3.2 Electronic properties of polypyrrole

The band theory of solids can be utilised to explain the electrical conductivity of CPs, by describing their extended π-conjugated system.[32,33] Using polyacetylene

(PA) as an example, since it is the structurally simplest CP, and employing quantum mechanics, the energy level distribution of the π-orbitals can be attained. The energy of the n^{th} level is

$$E_n = \frac{h^2 n^2}{8ma^2} \tag{1.1}$$

where h is Plank's constant, m is the mass of an electron and a is the length of a 1D box. The length of the 1D box can be equated to the length of the PA chain and since PA possesses a large number of carbon atoms, N, which are spaced apart at distance, d, therefore, the length of the 1D box can be approximated as

$$a = Nd \tag{1.2}$$

In the PA unit, each carbon atom contributes one electron each, so N carbon atoms will contribute N $2p_z$ π-electrons. Therefore, the Highest Occupied Molecular Orbital (HOMO) is the

$$n = \frac{N}{2} \tag{1.3}$$

energy level and the Lowest Unoccupied Molecular Orbital (LUMO) is the

$$n = \frac{N}{2} + 1 \tag{1.4}$$

energy level. The difference in energy between the LUMO and HOMO is

$$\Delta E = E_{LUMO} - E_{HOMO} \cong \frac{\left(h/d\right)^2}{8m} \cdot \frac{1}{N} \tag{1.5}$$

Equations 1.1 and 1.2 state that, as N increases, so will the number of energy levels. This produces a greater density of energy states, and the ΔE is seen to decrease.

When *N* is large, therefore, the densities of the states for the π-bonding and the π*-antibonding orbitals will be great, permitting the allocation of the terms, valence and conduction band, respectively. Therefore, Δ*E* (Figure 1.5) is equivalent to the band gap and it is this Δ*E*, which restricts the mobility of electrons along the PA backbone, as it is a forbidden energy area, but once energy, which is at least equal to the band gap is supplied, the electron is excited to the higher energy state, permitting movement along the chain. The width of this band gap is very important, as it is the determining factor, when examining the intrinsic electrical properties of a material.[32,33]

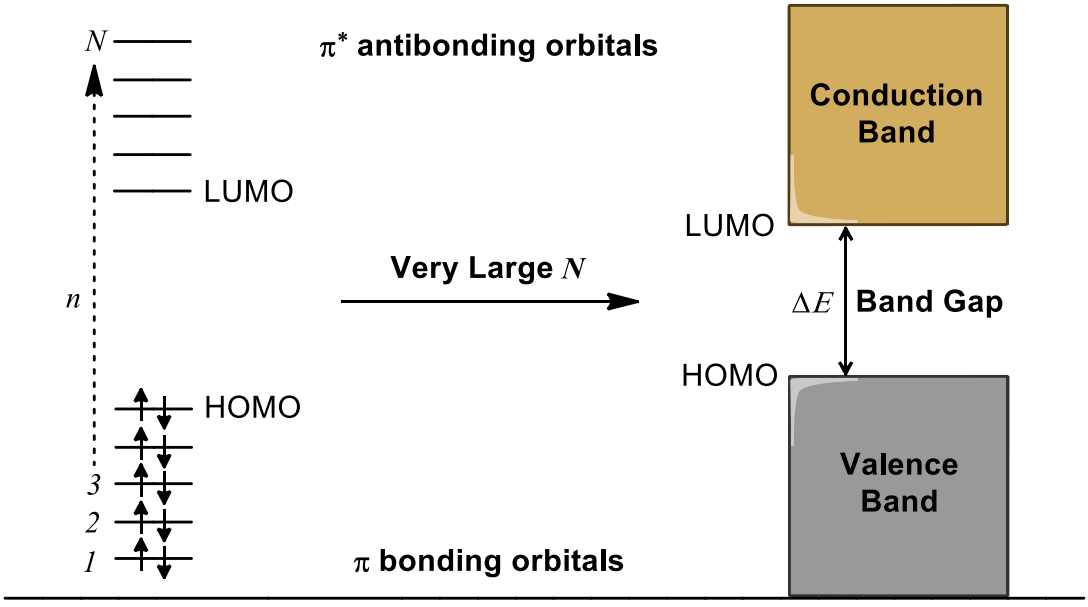

Figure 1.5: Energy level diagrams for PA.

All materials possess a degree of electrical conductivity (σ, S m^{-1}) and can be referred to as insulators, semiconductors or conductors (Figure 1.6). An electrical insulator, such as glass or paper, is a material, which does not possess freely flowing internal electric charges, and therefore, do not conduct, or conduct very little electric current ($\sigma = 10^{-6}$ S m^{-1}). This is due to the large band gap they possess, which restricts the excitation of electrons from the valence band to the conduction band, as the energy required is usually 10 eV.

An electrical conductor, such as metal, is a material, which possesses freely flowing internal electric charges ($\sigma = 10^{2}$ S m^{-1}). This occurs, as the valence and conduction band overlap, producing an electron cloud in the absence of a band gap.

An electrical semi-insulator, such as silicon, possesses electrical conductivity, which falls in the region, σ = 10^{-6} - 10^{2} S m^{-1}, and requires a band gap <4.0 eV, for excitation of an electron to occur. When PPy is in its reduced state, the band gap has been reported to be 3.16 eV.[34] Upon oxidation of the polymer, doping with counterions is induced, yielding a material, which could be classified as metallic in nature, due to the high conductivity (10^{2} - 10^{5} S m^{-1}) it possesses. Oxidation and subsequent doping of the polymer facilitates the formation of mid-band gap energy levels and the production of charge carrier species (polarons/bipolarons) in the CP.

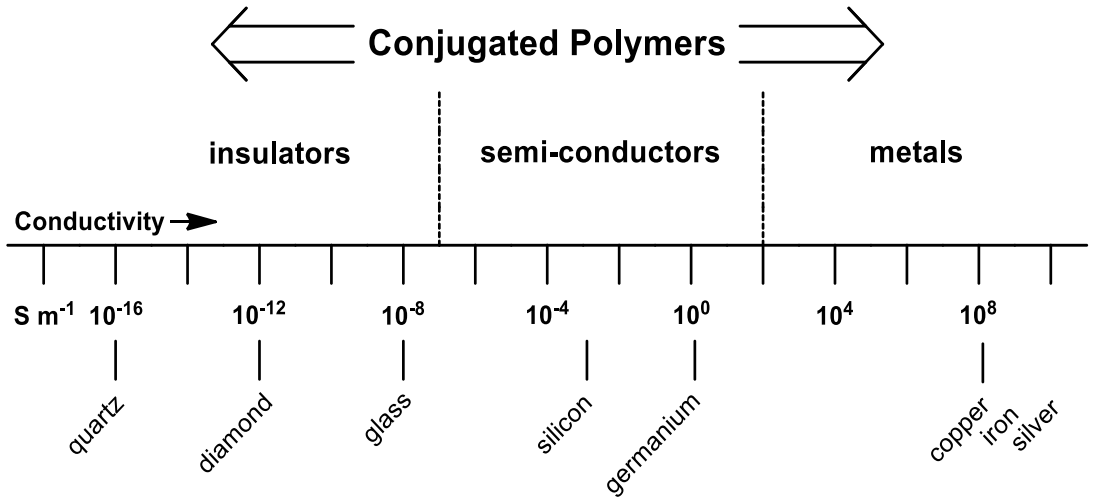

Figure 1.6: Classification of electrically conducting materials.

1.3.3 Redox properties of polypyrrole

CPs are 'doped' upon the incorporation of negatively or positively charged counterions into the polymer, which are necessary for neutralisation of polymer chains, grown by application of oxidative or reductive potentials, respectively. In general, PPy is oxidised during the propagation process, inducing the loss of an electron, producing a radical cation (polaron) on the polymer chain, which is separated by a finite number of Py units of a conjugation length, X_1 (Figure 1.7 (a)). As propagation continues, the additional oxidation of PPy promotes the loss of another electron, producing a dication (bipolaron) on the polymer chain (Figure 1.7 (b)),[32,33] accompanied by shortening of the conjugation length, X_2.[35]

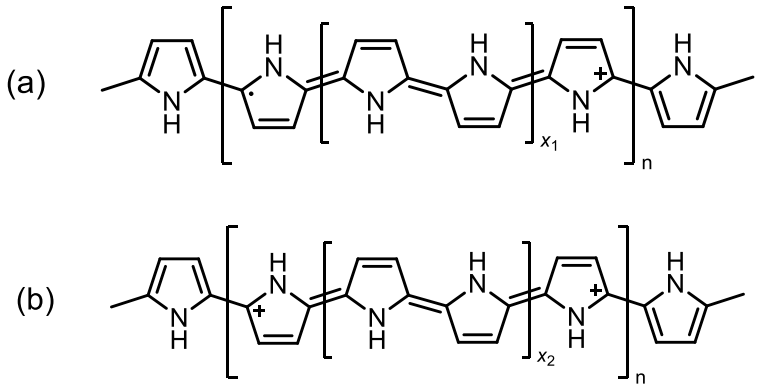

Figure 1.7: (a) Polaron and (b) bipolaron species within PPy chain structure.

During the oxidation of PPy, these polaron and bipolaron species form positive charges along the polymer chains, which must be stabilised by negatively charged counterions.[32,33] Once termination of polymerisation has taken place, an oxidative or reductive potential may be applied to the polymer, without seriously damaging the polymer structure or electrical conductivity, as these processes are reversible. Therefore, upon application of a reductive potential, the anions, which are responsible for neutralisation of the positively charged polymer chains, egress from the polymer to the bulk solution, causing the polymer to contract. Then, if an oxidative potential is applied, the anions can ingress from the bulk solution to the polymer, neutralising the polaron and bipolaron species (Figure 1.8 (a)). This is usually the case for anions, which are mobile and possess a small ionic radius, such as the chloride and tetrafluoroborate anion. Anions, which are bulky and possess low mobility, such as sulfated β-cyclodextrin or 4-sulfonic calix[6]arene,[36] are ensnared within the polymer matrix and have difficulty egressing from the polymer, upon application of a reductive potential. Therefore, to maintain polymer stability, cations from the bulk solution can ingress into the polymer, inducing formation of ion pairs (Figure 1.8 (b)), which can cause the polymer to swell, due to the presence of the ion pairs and solvation.

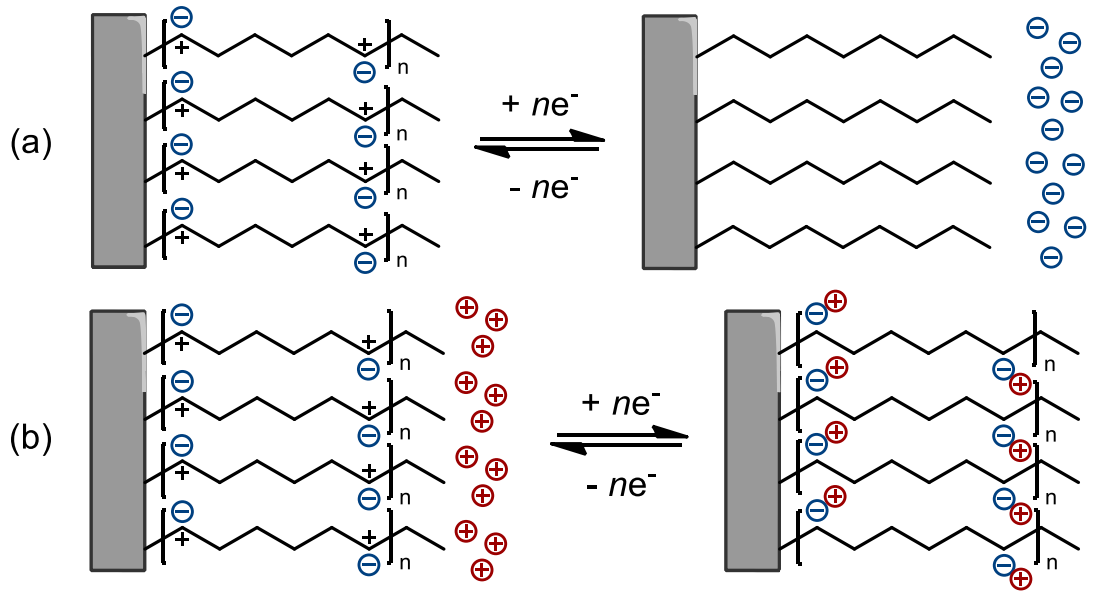

Figure 1.8: CP redox switching and ion exchange. (a) Anionic exchange and (b) cationic exchange.

1.3.4 Charge transport in polypyrrole

The manifestation of energy levels within the band gap has been reported to increase the conductivity of doped CPs. It is these polaron and bipolarons, which permit the flow of the internal electric charges within the polymer.[32,33] Upon oxidation of PPy, the charges are localised on the polymer chain, resulting in a local distortion and relaxation of the lattice. The distortion, due to the presence of the polaron, cause an increase in energy of the HOMO ($+\Delta\varepsilon^{pol}$) and a decrease in energy of the LUMO ($-\Delta\varepsilon^{pol}$). In this way, two new localised mid-gap states, corresponding to the energy levels of the polaron, are formed in the band gap (Figure 1.9 (a)). Further oxidation can occur, resulting in the removal of another electron from the HOMO (Figure 1.9 (b)). In this case, the distortion energy, due to the local excess of charge, is larger than that for a polaron, due to the effect of doubling the charge, $\Delta\varepsilon^{bip} > \Delta\varepsilon^{pol}$.

The formation of a bipolaron is possible when the stabilisation energy, gained by the interaction with the distorted lattice, is larger than the Coulomb repulsion between the two charges of the same sign, confined in the same location. Therefore, the amount of counterion, introduced into the polymer, plays a crucial role in the formation of polarons and bipolarons. At low doping levels, the conduction is

governed by polarons, whereas at moderate levels, bipolarons start appearing and finally, at high doping levels, bipolaron bands are formed inside the band gap.[32,33]

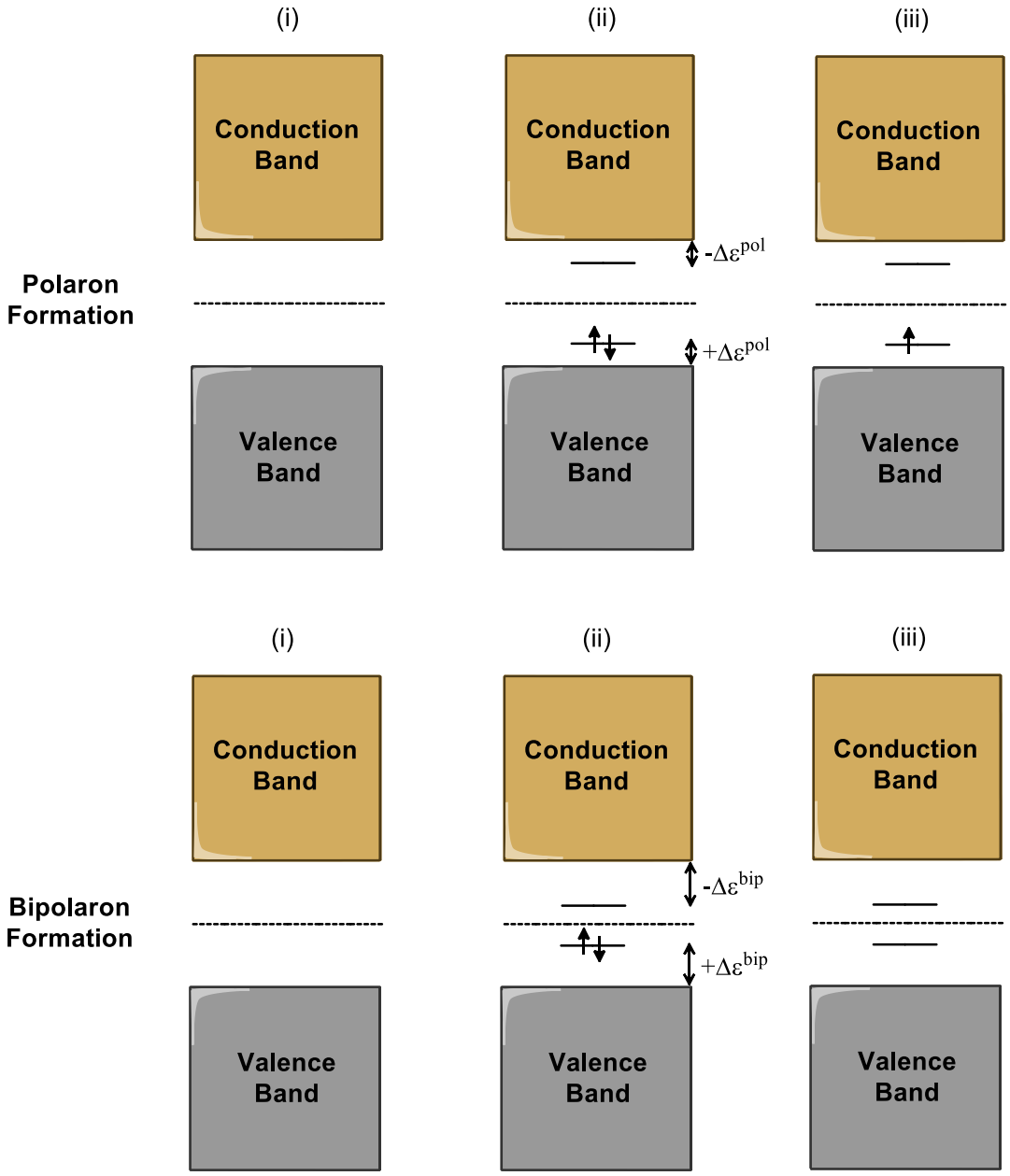

Figure 1.9: Polaron formation: (i) no E_{ox} applied, (ii) E_{ox} induces a local distortion of the polymer lattice, creating the increased HOMO and decreased LUMO mid gap energy levels, $+\Delta\varepsilon^{pol}$ and $-\Delta\varepsilon^{pol}$, respectively and (iii) an electron is removed from the mid gap level, yielding the spin +1/2 polaron species. Bipolaron formation: (i) no E_{ox} applied, (ii) E_{ox} induces a local distortion of the polymer lattice, creating the increased HOMO and decreased LUMO mid gap energy levels, $+\Delta\varepsilon^{bip}$ and $-\Delta\varepsilon^{bip}$, respectively and (iii) two electrons are removed from the mid gap level, yielding the spinless bipolaron species.

The charge carrier species of the CP, the polarons and bipolarons, are capable of both intrachain (along the chain) and interchain (chain to chain) transfer. Taking PA as an example, the intrachain transfer mechanism occurs, when there are two polaron species on a conjugated polymer chain (Figure 1.10 (a)). The two polaron radicals can travel along the chain and recombine (Figure 1.10 (b)), yielding two bipolaron species and a double bond, at the position where they recombine (Figure 1.10 (c)). When a sufficient distribution of anionic counterions are in close proximity of the conjugated chain, the bipolaron species may travel along the polymer backbone *via* double bond rearrangements (Figure 1.10 (d) - (f)). The anionic counterion not only permits the mobility of bipolaron species, but it also facilitates the interchain transfer mechanism, whereby the charge carriers move from chain to chain *via* the anionic tunnelling bridge.[37] Needless to say, as with PA, the conducting nature of PPy is greatly dependent on its ability to permit the doping of the polymer chains with anionic counterions, for the facilitation of charge carrier concentration and mobility.[32,38]

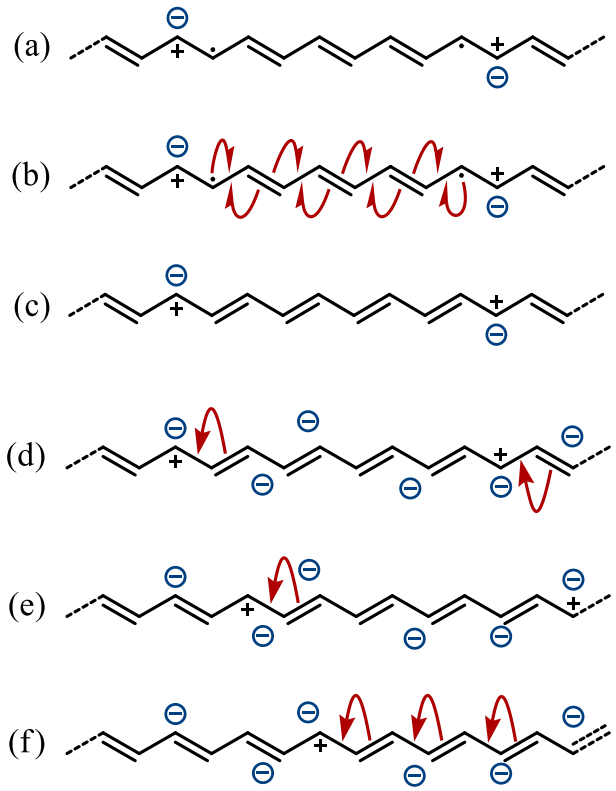

Figure 1.10: Mechanism of charge carrier intrachain mobility in PA.

1.3.5 Methods of preparation of polypyrrole

PPy can be produced *via* oxidation of the Py monomer, using both chemical and electrochemical methodologies.[39,40] To perform the chemical synthesis of PPy, a strong oxidising agent, such as iron(III) chloride,[41] is added to a solution containing Py monomer. During polymerisation, the oxidised Py species are neutralised by the anionic counterions of the oxidant (chloride) and the insoluble PPyCl precipitates out of solution. To perform the electrochemical synthesis of PPy, an anodic potential is applied to a solution of Py, which contains an electrolytic salt such as lithium perchlorate. This is used to reduce background current contributions (migration current)[34] and to provide the anionic counterion, for stabilisation of the oxidised PPy. The main benefit of electrochemically polymerising Py, in comparison to the chemical method, is that the process can be precisely controlled using various methods of deposition, such as the potentiostatic (constant potential amperometry, CPA) galvanostatic (constant current) and potentiodynamic (cyclic voltammetry, CV) techniques. The mechanism reported by Diaz and co-workers is the most widely accepted mechanism for the polymerisation of Py[42,43] (Scheme 1.4, 1.6, 1.8 and 1.10) and this process was confirmed by Waltman and Bargon using theoretical studies, which related the reactivity and the unpaired electron density of the radical cations.[44,45] In step 1a (Scheme 1.4), the oxidation, E_1, of the monomer, Py, occurs at the substrate, producing the radical cation monomer, $Py^{+\bullet}$. In step 1b, the radical cation, $Py^{+\bullet}$, dimerises with another radical cation monomer, yielding the dication dihydromer, Py^{+}-Py^{+}. In the stabilisation step, 1c, double deprotonation produces the aromatic dimer, Py-Py.

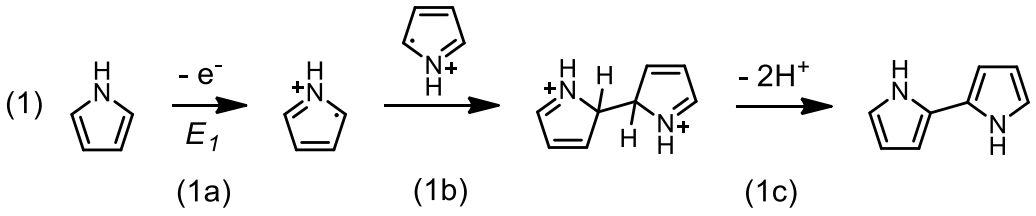

Scheme 1.4: Mechanism for the formation of the dimer, Py-Py.

The radical cation of the Py monomer, $Py^{+\bullet}$, produced upon oxidation of the monomer, exists in various forms (Scheme 1.5). The formation, which dominates the

dimerisation process, possesses its unpaired radical at the α-position, as this structure is the most stable.

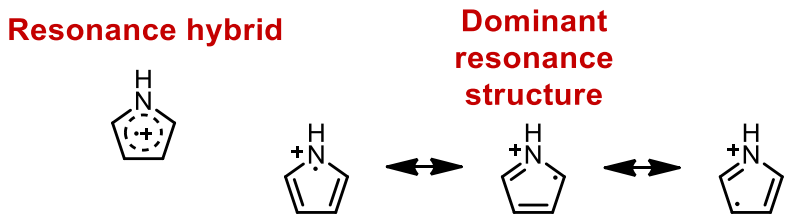

Scheme 1.5: Resonance structures of radical cation monomer, $Py^{+\bullet}$.

In step 2a (Scheme 1.6), the aromatic dimer, Py-Py, is oxidised, producing a radical cation dimer, $[Py\text{-}Py]^{+\bullet}$. Possessing an unpaired electron, which is delocalised over the dimer rings, causes the radical cation dimer, $[Py\text{-}Py]^{+\bullet}$, to be more easily oxidised, E_2, in comparison to the monomer, Py. In step 2b, the radical cation dimer, $[Py\text{-}Py]^{+\bullet}$, reacts with a radical cation monomer, $Py^{+\bullet}$, to produce the dication trihydromer, $Py\text{-}Py^{+}\text{-}Py^{+}$. In step 2c, double deprotonation produces the aromatic trimer, Py-Py-Py.

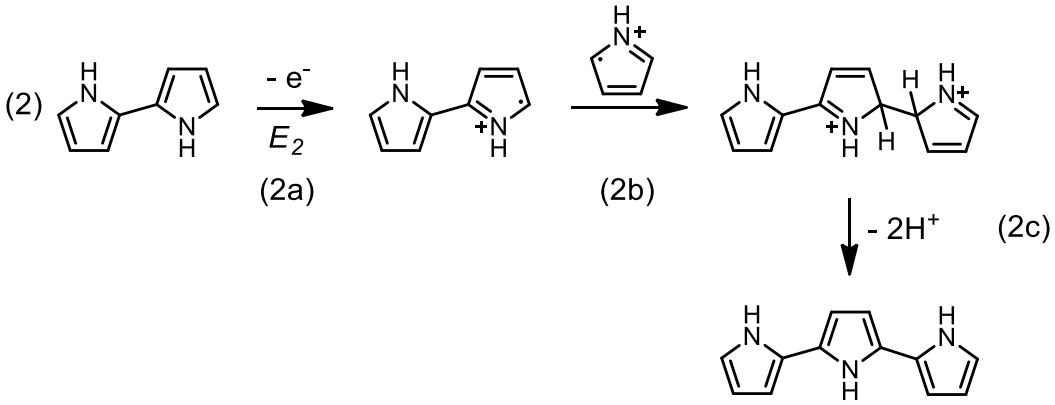

Scheme 1.6: Mechanism of trimer formation.

The radical cation of the Py dimer, $[Py\text{-}Py]^{+\bullet}$, can exist in various resonance formations (Scheme 1.7), but the resonance structure, possessing its unpaired electron at the more reactive α-position, dominates during the dimerisation process, as it is the most stable of all the resonance structures.

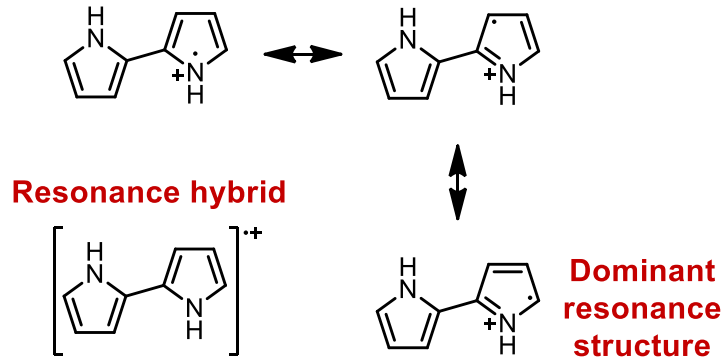

Scheme 1.7: Resonance structures of radical cation dimer, $[Py\text{-}Py]^{+\bullet}$.

In step ia (Scheme 1.8), the aromatic trimer, Py-Py-Py, is electro-oxidised, E_i, to produce the radical cation trimer, $[Py\text{-}Py\text{-}Py]^{+\bullet}$. Then in step ib, the radical cation trimer, $[Py\text{-}Py\text{-}Py]^{+\bullet}$, reacts with a radical cation monomer, $Py^{+\bullet}$, and propagation continues in the same sequence; oxidation, coupling and deprotonation, until attainment of the polymer.

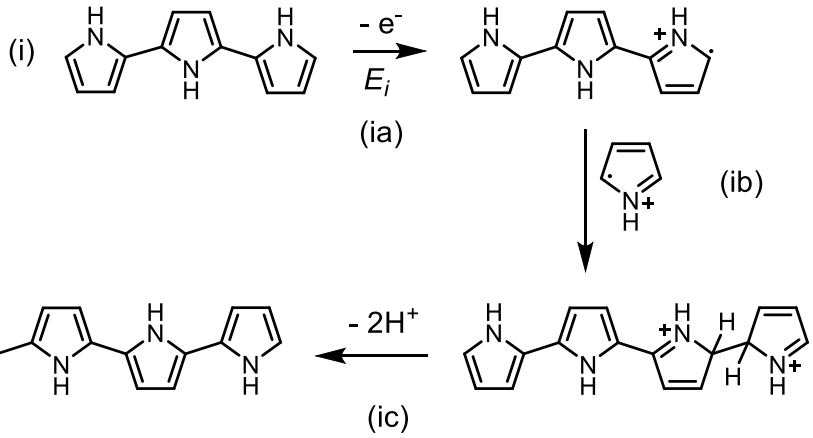

Scheme 1.8: Mechanism of chain propagation.

The radical cation of the Py trimer, $[Py\text{-}Py\text{-}Py]^{+\bullet}$, predominantly dimerises at the α position, but at this stage of oligmerisation the β-positions can also be subject to coupling, as Waltman and Bargon reported that the spin densities, at the α and β positions, are nearly equal.[45,46] Furthermore, as conjugation length increases during the polymerisation process, the difference in reactivity between the α-position and β position of the radical cation decreases.[10] This results in an increase in the proportion of β-coupling to α-coupling, yielding more chain defects[28,29] and a diminished electrical conductivity.[30,31]

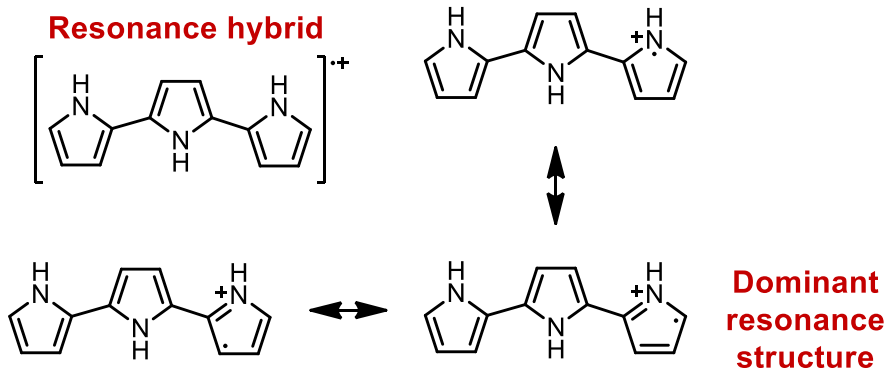

Scheme 1.9: Resonance structures of radical cation trimer, $[Py\text{-}Py\text{-}Py]^{+\bullet}$.

The attained polymer is not in a neutral state, but in an oxidised form, possessing a positive charge every three to four Py units, which is doped with the relevant anion. Therefore, the films usually consist of a ratio of 3:1 polymer/counterion. Termination of chain propagation occurs *via* stabilisation of the delocalised radical cation (nb) or by reaction with H_2O.[42]

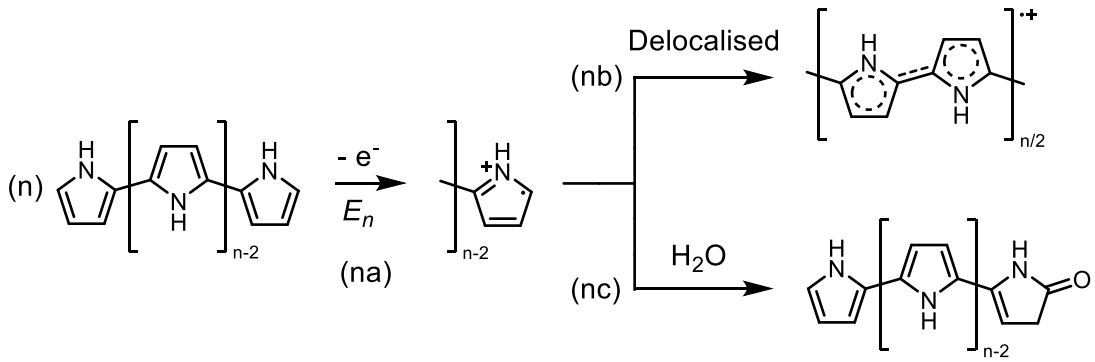

Scheme 1.10: Mechanism of chain termination, either by radical delocalisation or nucleophilic attack by water.

1.4 Conducting polymer in a nanowire morphology

Nanostructured CPs are desirable for use in technological applications, as they are anticipated to possess more advantageous properties, when compared to traditional bulk polymers. Such properties, which are a consequence of the nanoscale dimensions, are their large electrical conductivity,[47,48] the large specific surface area, short path lengths for ion transport[49] and improved cycle life, facilitated by electrochemical reaction strain accommodation.[50,51]

1.4.1 Electrochemical deposition of conducting polymer nanowires

CP nanowires can be deposited utilising three approaches; the hard template, the soft template and finally, the surfactant-less/template-free methods; basically a self-template process.[52,53] The hard template and the soft template methods both possess advantages and disadvantages. The hard template approach permits the preparation of highly ordered and oriented 1D CP nanostructures, but once they are fabricated, it is necessary to etch away the template,[54] which possibly damages the softer polymeric material,[55] or may induce the formation of polymer aggregates.[56] The soft template approach is a simpler technique to utilise, as a post-synthesis etching process is unnecessary and it is inexpensive in comparison to the hard template approach, as the employment of a solid template is eliminated. The surfactant-less/template-free method is usually covered under the umbrella of the soft template method, but deserves its own section, as it is a defined subset.

1.4.1.1 Hard template approach

The hard template approach was proposed by Martin and co-workers to involve CP synthesis utilising membrane pores/channels. They accomplished this by employing both track-etch polycarbonate (PC), or polyester membranes and anodic aluminium oxide (AAO) membranes.[57,58] Hard templates are generally used by initiating polymerisation in the presence of the template, followed by deposition of the polymer within the pores/channels of the template. Once polymerisation has been terminated and the employed template has been eliminated, the desired CP nanostructures are retrieved (Figure 1.11 (a)).[47,59] Nanowires can also be employed

as a hard template, yielding hollow nanotubes (Figure 1.11 (b)), by growing polymer on the nanowires and then dissolving the nanowires. Colloidal particles may be exploited as a hard template to fabricate nanoporous membranes (Figure 1.11 (c)), by growing polymer within the voids among the colloidal particles, which when removed produce a 3D nanoporous polymer structure. Selection of the appropriate template usually determines the dimensions and geometry of the CP nanostructures, but in 2011, Seferos and co-workers reported the electrochemical deposition of PT nanotubes using an AAO approach, where they were able to vary the thickness of PT nanotube walls within the membrane, by altering the electrolyte and organic solvent employed, thus controlling the rate of polymer growth.[60]

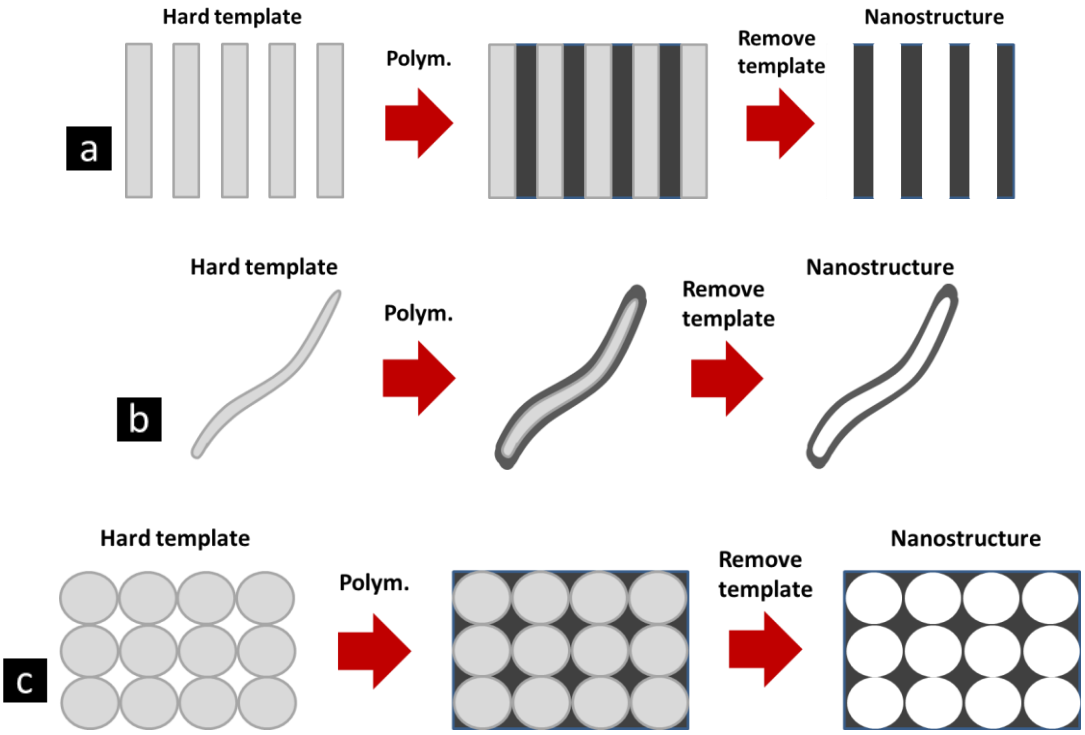

Figure 1.11: CP nanostructures: (a) nanowires, (b) nanotubes and a (c) nanoporous membrane synthesised using the hard template method.

1.4.1.2 Soft template approach

The soft template approach involves the presence of structure-directing reagents. Surfactants,[61-65] deoxyribonucleic acid (DNA),[66,67] lipid tubules,[68] liquid crystalline[69] and adsorbed thiolates[70] are just some, which may be employed, depending on the experimental constraints. Soft templates are usually formed by employing a

surfactant, to restrict the CP polymerisation process. More specifically, acting as soft templates, micelles can form by self-assembly, which is succeeded by monomer polymerisation on the micelle, producing nanotubes (Figure 1.12 (a)). Micelles may also produce nanowires, but in this case, polymerisation proceeds inside the micelle (Figure 1.12 (b)) Common soft template techniques, which are reported in the literature, include microemulsion (oil-in-water) polymerisation and reversed microemulsion (water-in-oil) polymerisation. The microemulsion technique involves the polymerisation of the monomer micelles in a polar solvent, due to the presence of a suitable surfactant,[71,72] while the reversed microemulsion technique involves the polymerisation of monomer on the outside of surfactant micelles in a non-polar solvent.[73,74] With regards to the electrochemical deposition of nanowires utilising a soft template, in 2007, Ge and co-workers employed the polysaccharide, starch, as a 'morphology directing agent', for the growth of PPy nanowires on an electrode and they suggested that the Py H-bonded to the starch in solution, directing growth of the nanowires.[75] Again, in 2011, they reported a similar electrodeposition process, employing gelatin.[76]

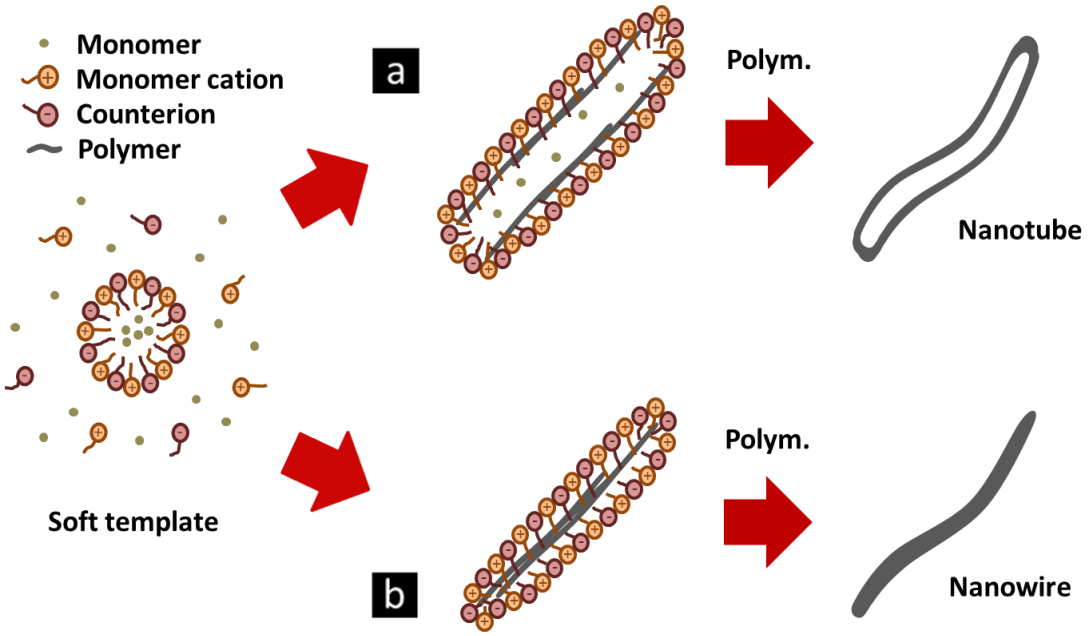

Figure 1.12: CP nanostructures synthesised using the soft template method.

1.4.1.3 Template-free approach

The surfactant-less/template-free approach is a process where the monomer, by itself, forms micelles and this acts as a 'template', permitting the fabrication of the desired nanostructures. The type of nanostructure attained, can be influenced by changing the polymer chain length, the polymerisation technique, the counterion and other reaction parameters.[78,79] More specifically, by varying the previously stated parameters, the template-free technique can yield nanowire films bound to a substrate. This occurs by first instigating a fast, instantaneous nucleation process, which deposits polymer across the substrate simultaneously. After this nucleation step, a slow growth process is initiated, which continues the propagation of polymer on the surface in a highly controlled manner, developing 1D nanowires, which grow away perpendicularly from a thin polymer film.

In 2002 and 2003, Liu and co-workers demonstrated the direct electrochemical synthesis of large arrays of uniform and oriented conducting PANI nanowires (<100 nm), on a variety of substrates *via* application of a three step electrochemical procedure. First, a high current density of 0.08 mA cm^{-2} was applied to the substrate, to induce instantaneous nucleation, succeeded by the application of lower current densities for longer periods of growth, but this methodology required a polymerisation time of 6.5 hours.[80,81] In 2006, Ge and co-workers reported the deposition of PPy nanowires in a phosphate and carbonate solution, without the use of the step-wise electrodeposition method and also reported that nanowire deposition would not occur in a solution containing oxalate.[8] In 2007, Li and Lin utilised a solution containing carbonate, to achieve PPy nanowire electrodeposition on a glassy carbon electrode (GCE). They dispersed Pt nanoclusters within the PPy nanowires and used this composite to reveal that the PPy-Pt/GCE had superior electrocatalytic activities toward both the oxygen reduction reaction (ORR) and the methanol oxidation reaction (MOR), when compared to that of the flat bare Pt electrode.[9] Then in 2008, Li and co-workers employed a phosphate buffer solution (PBS) to induce PPy nanowire deposition, but altered the pH of the PBS to successfully control the width of the polymer nanowires grown on the substrate. In this work, it was suggested that H-bonding contributed to the 1D growth observed.[7]

In 2010, Wei and co-workers employed a phosphate buffer to produce well defined PPy nanowire arrays, possessing short penetrating paths with low ion resistance for counter-ion diffusion, which also displayed superior capacitive properties, when compared to disordered nanowire networks, or the traditional thin polymer film.[82]

In 2007, Catherine Debiemme-Chouvy began investigating the influence of the phosphate and carbonate anion, with regard to thin PPy films and nanowire films, concluding that these anions control the rate of polymer deposition.[83-87] During polymerisation of Py, deprotonation of the PPy chain occurs, decreasing the local pH at the substrate. This decrease in pH, producing acidic conditions, has been reported to catalyse the polymerisation of Py.[88] She suggests that since the carbonate and phosphate anions incorporated were weakly basic, they became protonated, yielding a low anion concentration at the electrode. In a separate paper, she illustrated that by introducing dihydrogen phosphate, it is possible to slow down PPy polymerisation.[85]

1.5 *N*-substituted polypyrroles containing an organic functionality

An overwhelming expanse of work has been reported in the literature with regards to the deposition of the Py monomer. Accompanying these reports, there is a significant amount of research focussing on the deposition of *N*-substituted Py polymers, namely poly[*N*-(1-methyl)pyrrole] (PPyMe), PPyEtCN and poly[*N*-(2-carboxyethyl)pyrrole] (PPyEtCO_2H). To our knowledge, there has been very little investigation of the properties of *N*-substituted PPy monomers, which terminate their alkyl chain with an azide moiety. This is peculiar, due to the obvious benefits of the polymer possessing this functional group, as it is well known that the azide moiety can easily undergo cycloaddition, resulting in high yield with a varied range of reactants. One point to note is that substitution of PPy at the heteroatom incurs a decrease of coplanarity in the repeating PPy rings backbone (Figure 1.13). This loss of coplanarity, upon *N*-substitution, is induced by the steric effects, inflicted on the polymer backbone, by the bulkiness of the R group.[29] The steric hindrance reduces the length of conjugation within the polymer,[30] diminishing the polaron and bipolaron concentration,[89] thus increasing the resistivity of *N*-substituted PPy film. Herein, we discuss these *N*-substituted polymers and how the functional group at the substituted nitrogen position, has been reacted with an array of diverse compounds.

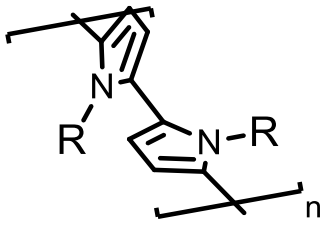

Figure 1.13: PPyR (R = alkyl), displaying a non-planar polymer backbone, due to steric hindrance from the alkyl substitution at the heteroatom.

1.5.1 *N*-(1-methyl)pyrrole

In 1996, Li and Ouyang investigated the electropolymerisation of PyMe (Figure 1.14) in aqueous media[90] and shortly afterwards, Farrington and Slater briefly investigated the effect the methyl moiety had on the polymer film.

They determined that its effect was negligible, as only a small amount of polymer backbone twisting was observed during molecular modelling. They also reported that the methyl substituted film was no different in sensitivity for target analytes, when compared to PPy.[91] In 2001, Garcia and co-workers investigated the effect of pH on PPyMe in aqueous media and concluded that decreasing pH induced degradation of the polymer, as increases in the C=O stretching bands were observed in the FTIR spectral data.[92] Shirsat and co-workers later reported that both the pH and the current density employed to deposit the PPyMe films, had a huge effect on film conductivity.[93]

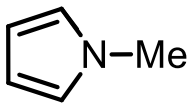

Figure 1.14: Structure of *N*-(1-methyl)pyrrole (PyMe).

Films of PPyMe have been used extensively in chemical and biosensor technology. In 2002, Fridman *et al.* electrochemically codeposited PPyMe and horseradish peroxidase, yielding individual nanosized composite particles on the surface, for the improved catalysis of hydrogen peroxide reduction.[94] To investigate the possibility of producing nanostructured PPyMe, Myung and co-workers fabricated PPyMe nanowires, approx. 100 nm in diameter, electrochemically, within the nanochannels between microfabricated Au electrodes, while employing chloride and *p*-toluene sulfonate counterions. This was performed in the presence of biotin quantum dots, which increased the conductivity of the film, when compared to that without.[95] Increased conductivity was also demonstrated, when electrodepositing a PPyMe/carbon nanotube composite, galvanostatically in an ionic liquid, resulting in a film more conducting than if only composed of PPyMe. Importantly, in 2010, Atta *et al.* electrodeposited PPyMe/palladium nanoclusters, which displayed strong electrocatalytic activity with regard to the oxidation of dopamine, ascorbic acid and uric acid. Significantly, oxidation peaks for the three analytes were well-resolved and well-separated, permitting simultaneous detection.[96]

A group that have performed a considerable amount of work, regarding the deposition of PPyMe, are Aleman and co-workers. Since 2010, the group has

constructed hollow PPyMe nanostructured particles, fabricated by the layer-by-layer templating technique, where the particles were approx. 30 nm in diameter and successfully detected dopamine.[97] Afterwards in 2011, they electrodeposited a nanosized PPyMe film on to Au and reported that it could detect low dopamine concentrations.[98] PPyMe has also been utilised as a chemo-sensor. Electrodeposited in the presence of single walled CNTs (SWCNTs), these PPyMe/CNT composites display improved, very low, NH_3 detection limits of 10 ppb, when compared to pristine SWCNTs.[99] It has also been employed as a protective coating for metals, but more recently, nanostructured composites have shown promising results. In 2011, Maumoudian *et al.* electrodeposited a PPyMe film in the absence and presence of ZnO nanoparticles, reporting that the ZnO nanoparticles increased the pore resistance of the coating, while improving the protectiveness of the film, due to the increase in surface area.[100] Then in 2012, Duran and Bereket reported the electrodeposition of PPyMe nanofilms using CV, which could protect copper from acid rain corrosive media for 12 days, due to self-healing behaviour exhibited by the polymer coating. This occurred due to the ejection of oxalate anions from the polymer, upon exposure to the corrosive media, inducing the reduction of the PPyMe film, thus thickening the copper oxalate passivation layer.[101] Copolymers of PPyMe with PPy have produced much interest, as these films have been recognised to detect NH_3,[102,103] cholesterol[104] and to protect metals,[105-107] while it has been reported that upon copolymerisation with PEDOT, overall film properties will improve.[108-112]

1.5.2 *N*-(2-cyanoethyl)pyrrole

Although it has already been stated that the substitution of Py at the N position with bulky groups, inflicts a loss of planarity between the Py units in the chain, there is a significant amount of work reported, regarding PyEtCN (Figure 1.15). Such work includes the brief investigation by Farrington and Slater in 1997, where they determined that the nitrile moiety could incur greater porosity in the film,[91] permitting better mobility of ions within the polymer. By this time, Thompson and co-workers had investigated the interaction of electrodeposited PPyEtCN films with MeCN and reported that dipole-dipole interactions were observed between the

respective nitrile moieties.[113] They had also investigated the morphology and properties, produced by the various redox states of PPyEtCN films and concluded that these different redox states could be used as a sensor to distinguish structurally similar gaseous organic vapours.[114] In 2003, Domb and co-workers investigated the hydrophobicity of PPyEtCN in relation to other *N*-substituted PPy monomers, reporting a water droplet hydrophobic contact angle measurement of 32°.[115] Tuzun *et al.* have reported an experimental and quantum mechanical study on the electrochemical properties of PyEtCN and reported that the HOMO and LUMO of PPyEtCN were lowered, when compared to PPy, due to the electron withdrawing nature of the nitrile moiety.[116]

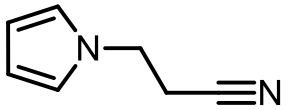

Figure 1.15: Structure of *N*-(2-cyanoethyl)pyrrole (PyEtCN).

An extensive amount of work has been reported, regarding the use of PPyEtCN within copolymerisation. In 2010, Aleman and co-workers investigated the block copolymerisation of PPyEtCN with PPy and PEDOT, reporting that the electrochemical behaviour of the film depended on the micrometric or nanometric thickness of the layers.[117] They also characterised and examined the properties of PPyEtCN, determining that trilayer copolymers of PPyEtCN/PEDOT/PPyEtCN and PEDOT/PPyEtCN/PEDOT possessed significantly greater electrochemical activity and stability. They also suggested that other copolymers, possessing PPyMe may be replaced with PPyEtCN, due to its beneficial properties.[118] After this, they investigated the electronic and structural properties of PyEtCN, revealing that the electronic properties of the film were greatly affected by C=O groups on the Py ring. These carbonyl groups were present due to the secondary oxidation reaction occurring during polymerisation and were also present as a terminating group on the end of small branches (Section 1.3.1).[119] They then performed chemical polymerisation of PyEtCN in iron(III) chloride, producing hollow core shell microparticle spheres using a layer-by-layer technique.[120]

The polymer has also been employed in a variety of applications. Films of PPyEtCN have been used to inhibit corrosion[121] and have also been used in sensor technology. In 2011, Kim and co-workers immobilised antibodies on to PPyEtCN films using CV. This was achieved *via* electrostatic interactions between the nitrile moieties on the film and hydroxyl groups of the antibodies, which resulted with enhanced antibody interaction (×4), when compared to antibodies immobilised *via* physisorption.[122] Also, Aleman and co-workers developed ultrathin films for which they could detect dopamine at a concentration of 100 μM.[98] In 2012, we developed the template-free electrochemical fabrication of PPyEtCN in the nanowire formation, using a novel bielectrolyte co-solvent system of ammonium dihydrogen phosphate and lithium perchlorate in EtOH/H_2O.[11] Then in 2013, we performed the novel electrochemical deposition of hollow PPyEtCN microtubes, which was facilitated by an acoustically formed emulsion of PyEtCN in toluene/EtOH/H_2O, with ammonium dihydrogen phosphate and lithium perchlorate.[12]

1.5.3 *N*-(2-carboxyethyl)pyrrole

There has been much interest in PyEtCO_2H (Figure 1.16); it has been examined thoroughly and applied to many areas of polymer chemistry. The basic properties of electrodeposited PPyEtCO_2H were examined by Dong *et al.* in 2009, using traditional characterisation techniques, which revealed that the film exhibited a hydrophilic nanoporous structure, an abundance of carboxylic acid groups in the polymer backbone and high fluorescent emission under laser excitation.[123]

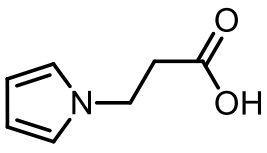

Figure 1.16: Structure of *N*-(2-carboxyethyl)pyrrole (PyEtCO_2H).

The utilisation of PPyEtCO_2H in the nanometre range has been extensively examined. PPyEtCO_2H has been shown to produce nanocomposites *via* an *in situ* polymerisation of PyEtCO_2H, in the presence of Fe_2O_3 nanoparticles.[124] It has also been utilised as an immuno-sensor, to detect rabbit IgG, by encapsulating anti-rabbit IgG biomolecules *via* electropolymerisation on TiO_2-nanowires.[125] The fabrication of

PPyEtCO$_2$H in the nanowire morphology, *via* a hard template method has been reported in the literature. This was performed by Wanekaya and co-workers on a gold sputtered film, electrochemically using AAO in 2008. The nanowires (~200 nm in diameter) were centrifuged, neutralised and the carboxylic acid group had anti-human serum albumin (antiHSA) bound, for the selective detection of HSA, when diagnosing incipient renal disease.[126] Again, in 2009, Wanekaya and co-workers modified the same nanowires with cysteine at the carboxylic acid. This moiety was capable of removing lead(II), arsenic(III) and cadmium(II) to undetectable limits, *via* chelation of the metals with the nitrogen, sulfur and oxygen atoms of the cysteine molecule.[127]

The presence of the carboxylate group on the PyEtCO$_2$H molecule enables the immobilisation of a range of biomolecules on to the polymer surface *via* condensation reactions (Scheme 1.11) and this versatility has been demonstrated in the literature. In 1999 and 2000, Cooper and Glidle demonstrated the chelation of nickel(II) at this moiety, which then provided a site for immobilisation of poly(histidine), but they also covalently reacted a 3-(aminopropyl)imidazole with the carboxylic acid, exploiting the free imidazole nitrogen, for coordination with the nickel(II). This work revealed that the film possessed sufficient porosity, which provides potential immobilisation sites throughout the film, for biosensor applications.[128,129] In 2006, Lee *et al.* chemically modified an electrodeposited PPyEtCO$_2$H film, by covalently immobilising a cell-adhesion-promoting-sequence, Gly-Arg-Gly-Asp-Ser (GRGDS), at the free carboxylic acid group. Human umbilical vascular endothelial cells were then seeded on the film and displayed an improved ability to attach to the surface and spread.[130]

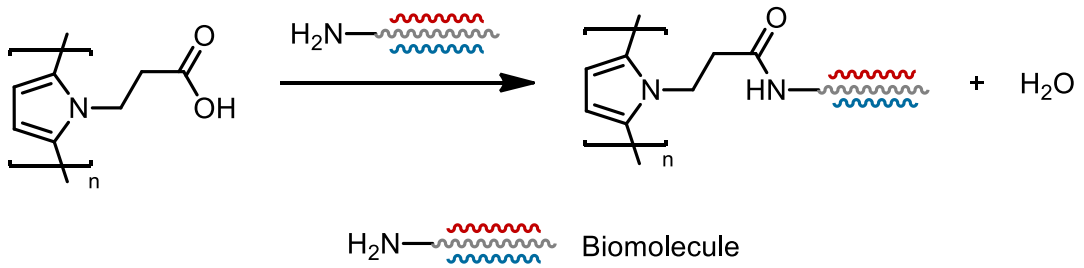

Scheme 1.11: Covalent immobilisation of various amine functionalised biomolecules on to PPyEtCO$_2$H film *via* a condensation reaction.

PPyEtCO_2H is very commonly used for the sensing of glucose. In 1998, Miyauchi and co-workers electrodeposited PPyEtCO_2H on a substrate. They then covalently immobilised glucose oxidase (GOx) on to the film using a dehydration reagent (carbodiimide) (Scheme 1.12) and this displayed an amperometric response to glucose, which increased linearly up to 80 mM.[131] Again, in 1999, they electrodeposited PPyEtCO_2H films and reported that the amperometric response of the PPy-GOx film was directly related to the immobilised enzymes activity, which was dependent on the optimum pH (7.0) and the temperature (40 ^oC).[132] In 2000, Yasuzawa *et al.* improved this technique by performing the *in situ* electropolymerisation of PyEtCO_2H with GOx, immobilising the enzyme during the polymerisation process. This was then treated with a carbodiimide, to covalently bind the GOx to the polymer, which displaying improved stability of the glucose response in this biosensor.[133]

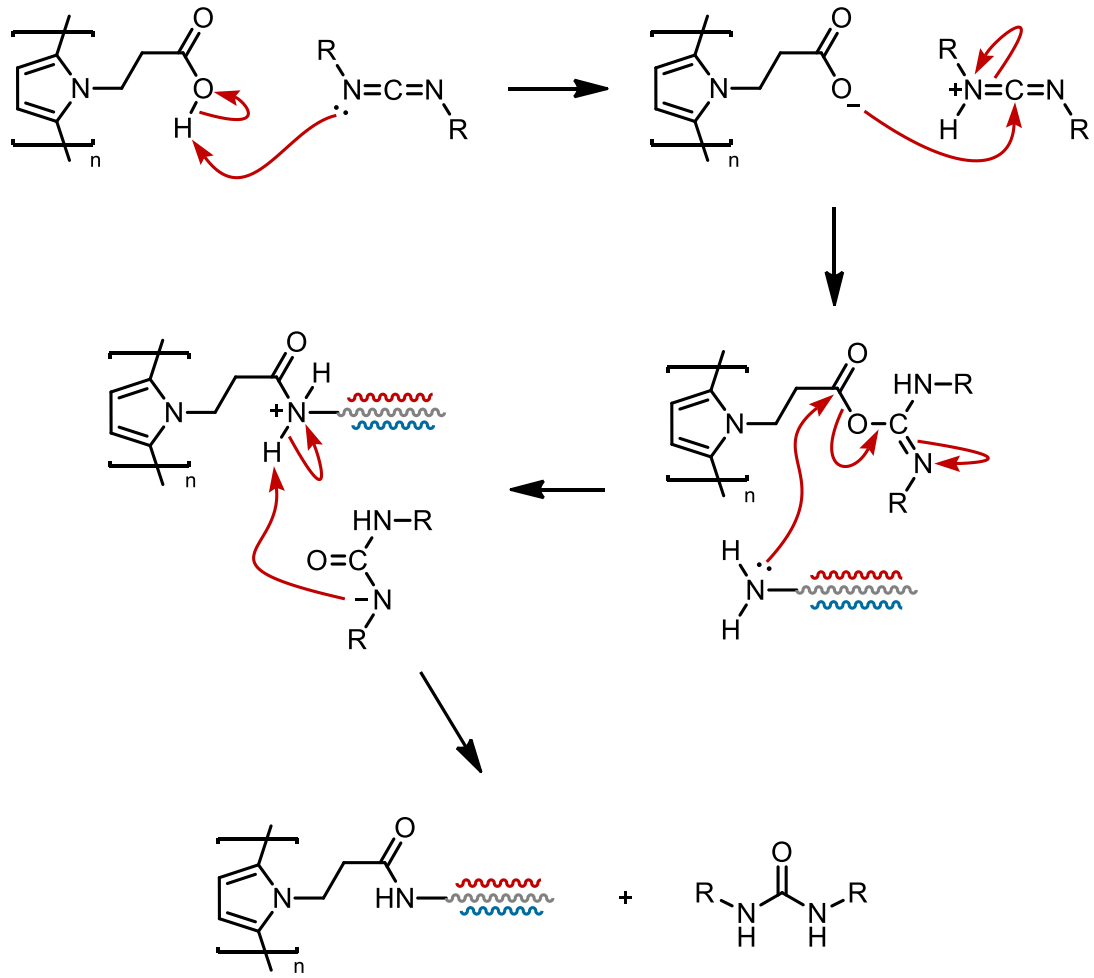

Scheme 1.12: General reaction mechanism for coupling reaction. The carboxylic acid is activated by the carbodiimide, for reaction with a primary amine to permit amide formation.

The next logical step in the evolution of $PyEtCO_2H$ was the fabrication of a nanowire based glucose sensor. This was completed by Shi and co-workers in 2012. They developed a glucose biosensor, created from a $PyEtCO_2H$ and Py composite, by using a two-step electrosynthesis process, consisting of the deposition of a PPy nanowire film from a phosphate buffer solution, with *p*-toluenesulfonate acid as the soft template and then electropolymerising $PyEtCO_2H$ on to the PPy nanowires, attached to the Au substrate.[134]

$PPyEtCO_2H$ has also been employed in the fabrication of various copolymers. In 2011, Zhang and Zhang fabricated large, free-standing poly[pyrrole-co-(*N*-(2-carboxyethyl)pyrrole)], which grew at an air/liquid interface, along the direction of an applied electrical field.[135] Zhang and co-workers synthesised electroactive

Py/PyEtCO_2H copolymer nanoparticles using an alcohol-assisted microemulsion polymerisation, which then had ruthenium bis(2,2′-bipyridine) (2,2′-bipyridine-4,4′-dicarboxylic acid)-ethylenediamine covalently coupled to the nanoparticle, for use as a chemiluminescence aptasensor in the detection of thrombin.[136] Mehmet Senel performed the electrodeposition of Py, PyEtCO_2H and *N*-(3-(1*H*-pyrrol-1-yl)ethyl)ferrocenecarboxate, to produce a copolymer electron mediator, which then had GOx covalently immobilised to it *via* the free carboxylic acid group, yielding a glucose biosensor.[137]

1.5.4 *N*-(2-azidoethyl)pyrrole

To our knowledge, there is no published work regarding the electrochemical deposition of short chained *N*-(azidoalkyl)pyrrole monomers, such as PyEtN_3 and *N*-(3-azidopropyl)pyrrole (PyPrN_3), on to a substrate. Longer chained analogues, namely *N*-(10-azidodecyl)pyrrole (PyDeN_3) have been reported in the literature, with varied applications demonstrated herein.

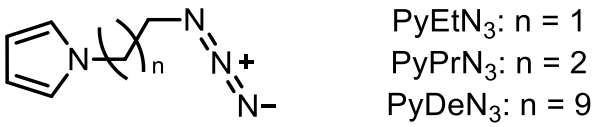

Figure 1.17: Structure of *N*-(azidoalkyl)pyrrole monomers.

Liebscher and co-workers have utilised PyDeN_3 and copper(I)-catalysed azide-alkyne cycloaddition chemistry (CuAAC) to bind biomolecules, such as biotin, cholesterol, monosaccharides and uridine. Utilising cholesterol, the authors produced a cholesterol functionalised triazole Py monomer, PyDeTriazoleCholesterol. They then copolymerised the PyDeTriazoleCholesterol monomer with Py *via* chemical oxidation, while encapsulating iron(II,III) oxide (Fe_3O_4) nanoparticles (core-shell particles). This encapsulation made the core-shell particles more tolerable to biological systems, when used in such systems for use as cancer therapeutics.[138]

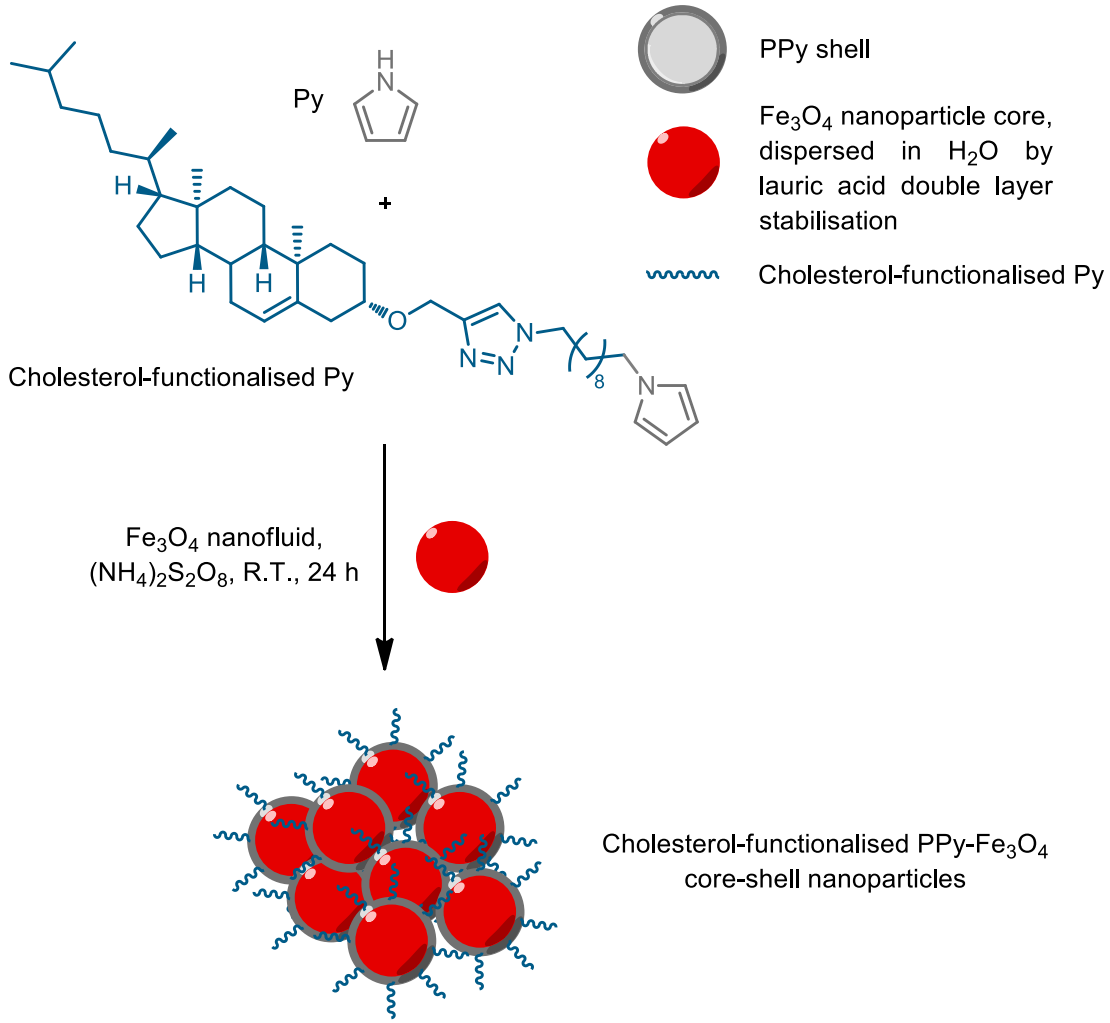

Scheme 1.13: Chemical copolymerisation of Py with PyDeTriazoleCholesterol in a Fe_3O_4 nanofluid producing magnetic core shell nanoparticles.

Storey and co-workers synthesised $PyEtN_3$ and $PyPrN_3$ terminated polyisobutylene *via* two methods, then employing CuAAC, bonded functional alkynes; propargyl alcohol, propargyl acrylate, glycidyl propargyl ether and 3-dimethylamino-1-propyne[139] and also alkyne-functional chain transfer agents.[140] Bedioui and co-workers have electrodeposited $PPyDeN_3$ on to self-assembled, 900 nm diameter, polystyrene nanospheres and used CuAAC to bind FcCCH to the modified electrode,[141] while Li and co-workers have electrodeposited $PPyDeN_3$ on to a substrate and utilised CuAAC to covalently bind quinone, cholic acid and thymidine to the substrate, without loss of electroactivity.[1]

In Chapter 3 of this work, bulk films of $PPyDeN_3$, $PPyPrN_3$ and $PPyEtN_3$ were deposited electrochemically on to Au substrates, while nanowire films of $PPyEtN_3$

were electrochemically deposited, by employing a template-free method. The polymer films were characterised using CV, SEM, FTIR spectroscopy and Raman spectroscopy. In Chapter 4, the nanowire films of $PPyEtN_3$ were examined further, by observing the development of the nanowire morphology over time and determining the nucleation and growth processes, which attributed to the nanowire morphology. The functions of the important electrolytic ions were also investigated and the nanowire films were characterised using FESEM, TEM, CV, FTIR spectroscopy, Raman spectroscopy and XPS.

1.5.5 *N*-substituted pyrrole iron(II) complexes

There has been a significant amount of research, focussing on the electrodeposition of *N*-substituted PPy films, which possess a terminating Fc moiety, as this compound is used as an electron mediator, within the deposited polymer. The employed FcPy monomers usually vary in regards to the linkage spacer, which tethers the Fc electron mediator, to the PPy backbone. This tether can vary from a simple alkyl chain, to a chain possessing various functional groups, or exist as a more complicated tether, which can interact with species, forming complexes, both during and after deposition of the film. One of the simplest Fc tethered Py monomers possesses an amide functional group. To our knowledge, this polymer, poly[$(PyPrNHCO)_2Fc$] (Figure 1.18 (a)), was first electrodeposited on an electrode in 1986, by Parker and co-workers.[142] Then in 1989, they electrodeposited the same monomer on GCE, Pt and indium tin oxide (ITO), but they observed that the films electroactivity decayed during cycling. They found that copolymerisation of the $(PyPrNHCO)_2Fc$ monomer with PyMe was sufficient to yield a stable Fc^{III}/Fc^{II} couple.[143] Also in 2003, Cretin and co-workers electropolymerised the mono-substituted monomer, PyPrNHCOFc (Figure 1.18 (b)), on Pt and stainless steel (SS) meshes and also found that copolymerisation with Py, produced films of improved electrostability.[144]

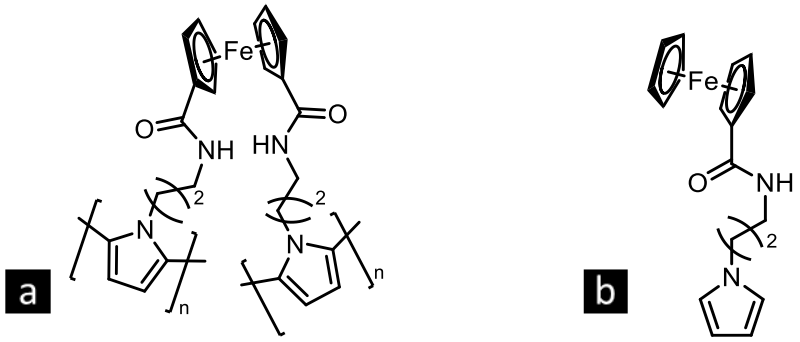

Figure 1.18: Structures of electrodeposited Fc N-substituted Py. (a) Di-substituted and (b) mono-substituted Fc amide Py polymer and monomer respectively

In 1996, Saint-Aman and co-workers altered the structure of the Fc tethered Py monomer, $(PyPrNHCO)_2Fc$, by changing it slightly to a tertiary amide, substituted with an ethyl group (Figure 1.19 (a)). They investigated the monomers electrochemical behaviour, using CV in both organic and aqueous solutions and reported that the electrolytic anion, largely affected the Fc formal potential in aqueous solution. It was also observed that the Li^+ cation, of the electrolytic salt, complexed to the di-substituted derivative, causing possible conformational changes and increased efficiency, during polymer deposition.[145] Again in 1997, from the same group, Visan and co-workers reported successful deposition of this monomer (Figure 1.19 (a)) and determined that increasing monomer concentration and film thickness, resulted with increases in current density, for the Fc redox couple.[146]

Work has also been conducted on Fc, tethered to Py *via* alkyl chains of varied length, with no functional groups present. In 1986, Haimeil and Merz reported that they could not electrodeposit poly[PyEtFc] (Figure 1.19 (b)), as a homopolymer on a substrate, but were capable of copolymerising the monomer with Py, in a 1:1 ratio on a Pt wire.[147] Afterwards, in 1995, Zotti *et al.* investigated the *in situ* conductivity of poly[$Py(CH_2)_6Fc$] in MeCN; reporting that the Fc redox conductivity was enhanced by electron hopping along the polymer backbone and noted also, that the hopping rate was increased by decreasing spacer length.[148] Again, in 1997, they reported the self-assembly (SA) and electropolymerisation of this monomer on a substrate at 0.200 V vs. Fc^{III}/Fc^{II} and determined that the Py moiety was assigned the role of the adsorbing head, during formation of the SA layer.[149]

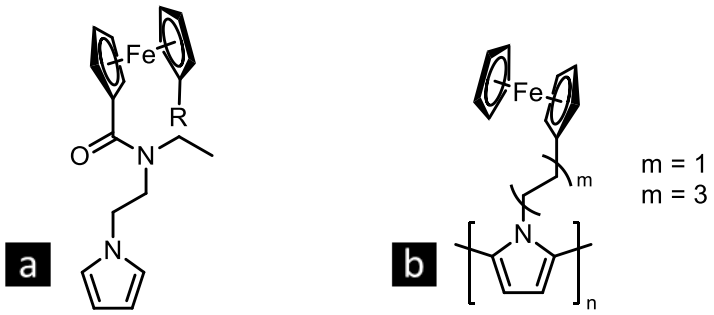

Figure 1.19: Structures of electrodeposited Fc *N*-substituted PPy. (a) di/mono-substituted Fc amide EtPy (R = H, PyEtN(Et)C(O)) and (b) $PPy(CH_2)_mFc$ (m = 1 and 3).

Since the first of the Fc *N*-substituted PPy films were fabricated, their use in a range of applications has been investigated. In 1988, Foulds and Lowe electrodeposited *N*-substituted PPy derivatives covalently bound to Fc (Figure 1.18 (a) and Figure 1.20 (a) variant), in the presence of GOx, producing a mediator-less glucose electrode, which circumvents toxicity issues, caused by leaching of the mediator.[150] As reports from Parker and co-workers and Cretin and co-workers have shown, copolymerisation of these monomer types with PyMe[143] and Py[144] improves stability and this technique has been employed with regard to the fabrication of sensors employing GOx.

In 2011, Singh and co-workers electro-copolymerised a Fc carboxylphenyl Py (Figure 1.20 (b)) with Py on ITO, while entrapping GOx, to produce a mediator-less electrochemical sensor with a detection limit of 0.17 mM and sensitivity of 19.21 μM mM^{-1}.[151] At the same time, Mehmet Senel electro-copolymerised Py, $PyEtCO_2H$ and $PyEtCO_2MeFc$ (Figure 1.20 (c)) together and covalently immobilised GOx to the CP film, *via* the free carboxylic acid group of $PyEtCO_2H$, which showed good stability, possibly attributed to the strong attachment of enzyme on the polymer backbone.[137]

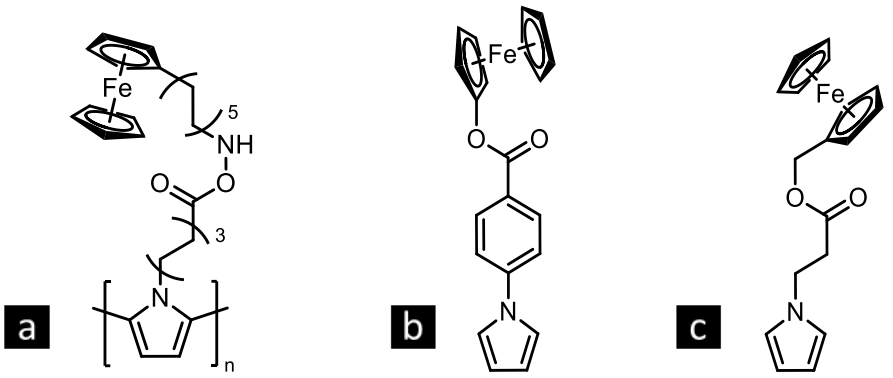

Figure 1.20: Structures of electrodeposited Fc *N*-substituted PPy. (a) PPy carboxylamide Fc, (b) $PyPhCO_2Fc$ and (c) $PyEtCO_2MeFc$.

Other beneficial properties, yielded by the Fc terminal moiety, have also been demonstrated, while exploiting copolymerisation methods. In 2007, Park *et al.* constructed an electrode material for use as a secondary battery, *via* electro-copolymerisation of Fc *N*-substituted Py monomer (Figure 1.18 (b)) with Py and found that Fc, covalently bound to the polymer, increased the specific capacity of the material.[152] Then in 2012, Camurlu and Gultekin, using the monomer, TPy(ANIMeFc)T (Figure 1.21 (a)), electrodeposited homopolymers and copolymers with Py, producing electrochromic devices, assembled in the form, glass/ITO/P(TPy(ANIMeFc)T)/PEDOT/ITO/glass. During this work, the group reported that the tethering of Fc, to the polymer backbone, enhanced the colouration efficiency of the polymer.[153]

Fc *N*-substituted PPy films have also been exploited to detect other target compounds such as $H_2PO_4^-$. This was accomplished by observing the redox activity of Fc using CV, as the Fc peak currents diminish in the presence of $H_2PO_4^-$. In 2003, Moutet and co-workers reported the electrodeposition of monomers, with an ammonium tetrafluoroborate tether (Figure 1.21 (b)). Utilised for the electrochemical sensing of $H_2PO_4^-$, the sensor showed good selectivity for $H_2PO_4^-$ over NO_3^-, HSO_4^-, ATP^{2-} and F^-.[154] Then, in 2005, Arrigan and co-workers electrodeposited the mono-substituted, Fc modified Py (Figure 1.18 (b)) on to a Pt microelectrode array, for the detection $H_2PO_4^-$ in nonaqueous media, while using differential pulse voltammetry (DPV).[155] Afterwards, in 2008, Casando and co-workers were able to electrodeposit an Fc *N*-substituted PPy, possessing a dendrimer structure (Figure 1.21 (c)), from

DCM/MeCN solutions, which adhered well to the electrode and while utilising Osteryoung square wave voltammetry (OSWV), sensed $H_2PO_4^-$ in aqueous solution.[156]

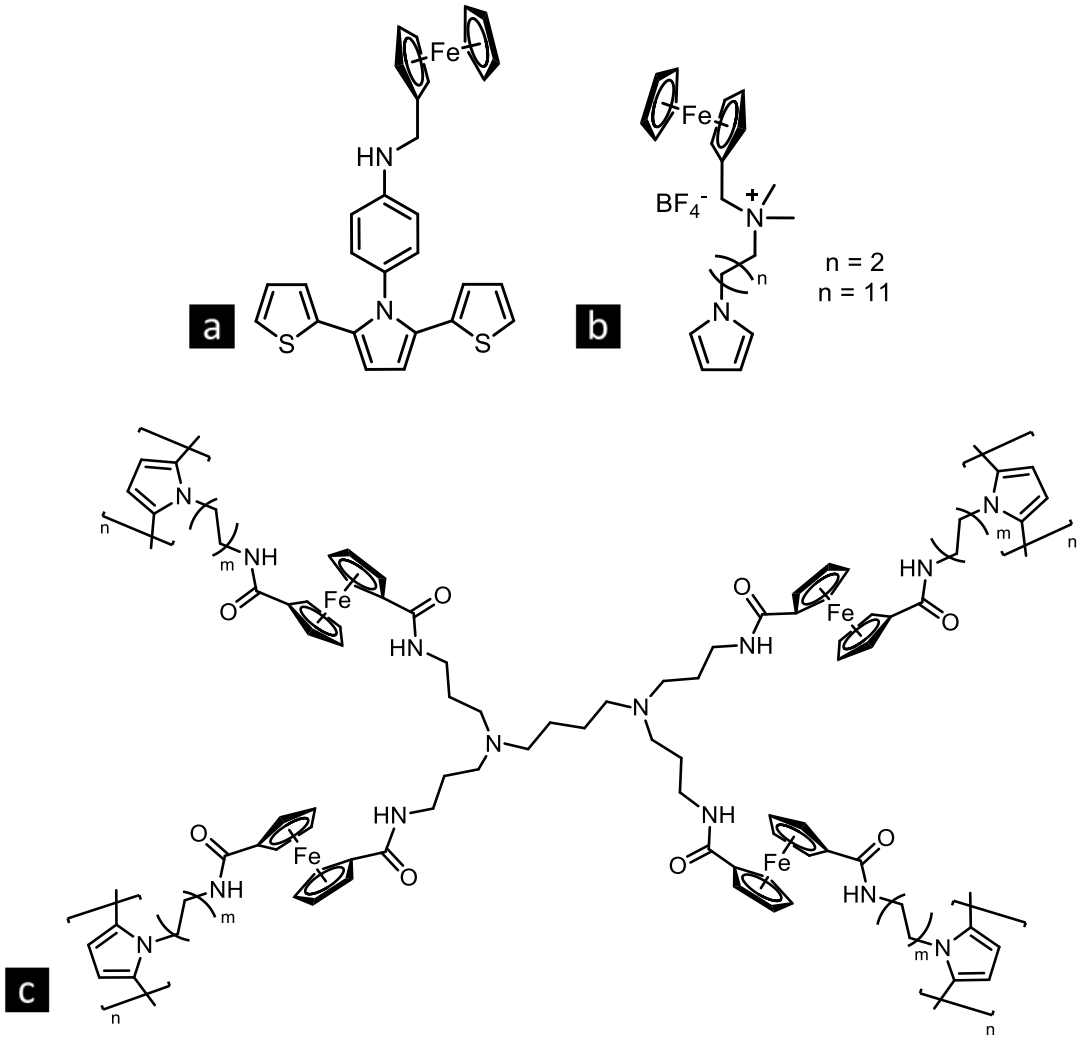

Figure 1.21: Structures of electrodeposited Fc *N*-substituted PPy. (a) TPy(ANIMeFc)T, (b) $[Py(CH_2)_mN(Me)_2Fc]BF_4$ (m =2 and 11) and (c) Fc *N*-substituted PPy dendrimer.

The Fc functionalised Py monomers have been developed further, by employing other moieties, so as to permit the deliberate complexation of metal ions with the polymer *via* modification of the tether. In 1997, Moutet and co-workers electropolymerised a monomer, composed of a crown ether tether, functionalised with terminal Py and Fc moieties (Figure 1.22 (a)). The crown ether site was used for the electrochemical recognition of Ba^{2+} and Ca^{2+} ions in organic media, while it was insensitive to other metals ions such as Li^+, Na^+, K^+ and Mg^{2+}.[157]

Afterwards, in 1999, the authors reported the electrochemical impedance spectroscopy (EIS) of the same compound, which further confirmed the complexation data.[158] Soon after this, in 2000, they also reported the incorporation of bis-2,2-bipyridine (bis-Bipy), within the tether (Figure 1.22 (b)), which in their work, was proposed to selectively coordinate with Cu^{I} and not Ni^{II}.[159]

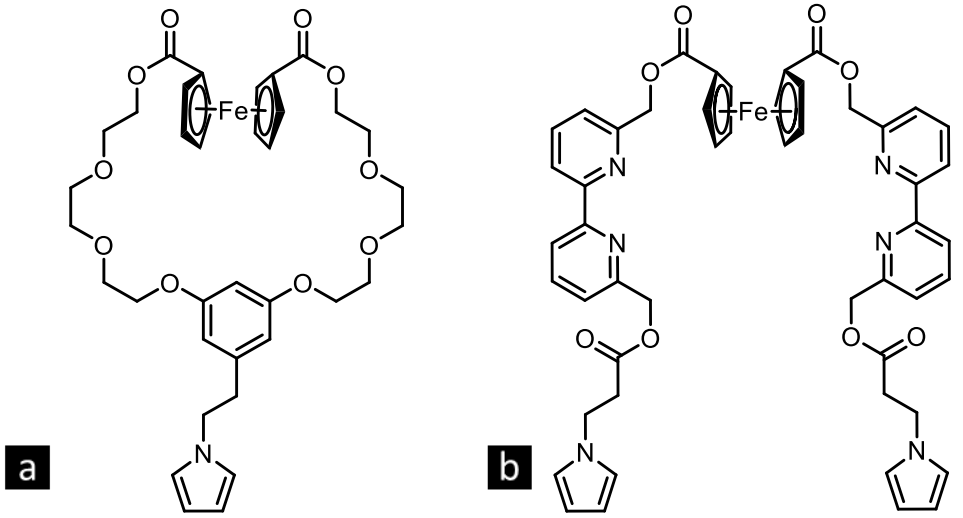

Figure 1.22: Structures of electrodeposited Fc *N*-substituted PPy. (a) Fc *N*-substituted Py crown ether and (b) Fc *N*-substituted Py bis-Bipy.

In our research, we are particularly interested with the possible post-polymerisation functionalisation of PPy and other CPs. This type of functionalisation enables the user, to electrodeposit a CP on the substrate and once the polymer is adhered, it can be modified with any desired unit, *via* covalent interaction with the CP backbone. In 2005, Billon and co-workers performed the post-functionalisation of *N*-substituted PPy with Fc (Figure 1.20 (a)), achieving an efficiency of 20-22% and this poor conversion value was not observed to change, upon lengthening of the space arm.[160] It has been observed in the literature that coupling, condensation and other reactions are inefficient at binding the desired component, to the modified electrode.[161] However, it has also been reported that CuAAC reactions can be exploited as a means to post-functionalisation CP films with high conversion[3,162] and 'Click' reactions have been utilised, to attach various compounds to *N*-substituted PPy films,[1] which are already bound to an electrode surface. Even so, to our knowledge, no investigations, specifically regarding CuAAC of FcCCH with short chain azide

functionalised PPy have been reported, but works, developing this analogous reactions with long chain azide functionalised PPy[141] and PEDOT[163] are present. In 2008 and 2011, Baurle and co-workers reported the post-functionalisation of electrodeposited PEDOT films with FcCCH, using CuAAC chemistry in anhydrous MeCN, with Cu^0 and $[Cu^I(MeCN)_4]PF_6$ (Figure 1.23)[3,162] and in 2009, Xian and co-workers replicated this reaction in aqueous conditions, using $Cu^{II}SO_4.5H_2O$ and sodium ascorbate, to facilitate cycloaddition. The polymer was characterised using SEM, FTIR spectroscopy and Raman spectroscopy, demonstrating high grafting of FcCCH. The polymer possessed a fast electron transfer rate and displayed electrochromic properties, upon variation of the E_{app}.[163]

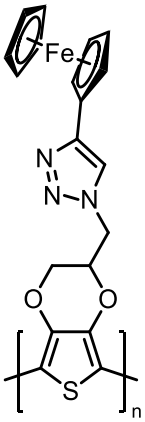

Figure 1.23: Structure of electrodeposited Fc functionalised PEDOT.

In Chapter 4 of this work, the CuAAC reactions of FcCCH with the $PyEtN_3$ monomer and also with films nanowire morphology $PPyEtN_3$ were examined. In Chapter 5 of this work, a range of nitrile terminating compounds, including PyEtCN, were coordinated to the carbonyl cyclopentadienyl TM complexes, $[CpMo^I(CO)_3]_2$ and $[CpFe^{II}(CO)_2THF]BF_4$, followed by a cycloaddition reaction, which was initiated using sodium azide, to produce neutral tetrazolate complexes. The monomer and polymer products of the cycloaddition reactions were characterised appropriately, using conventional methods and a range of surface analysis techniques, respectively.

1.5.6 *N*-(2,2'-bipyridine-alkyl)pyrrole transition metal complexes

A substantial amount of work has been performed, regarding the polymerisation of more complicated *N*-substituted Py monomers, by covalently attaching Bipy to the alkyl chain, at the Py nitrogen atom (BipyPy). The majority of research has been reported by Moutet, Cosnier and Deronzier, where they electropolymerised TM complexes, possessing the BipyPy ligand. Their investigations began in the 1980's, with ruthenium(II) complexes.

In 1985, Moutet and co-workers probed the electrochemical behaviour of an electrodeposited complex, possessing the ligand, L_a (Figure 1.24 (a)). It was composed of a mono-substituted Bipy, possessing a tether at the 4 position and terminating with a Py moiety. The complexes employed in their study, $[Ru^{II}(Bipy)_2(L_a)]^{2+}$ (Figure 1.24 (b)), $[Ru^{II}(Bipy)(L_a)_2]^{2+}$ (Figure 1.24 (c)) and $[Ru^{II}(L_a)_3]^{2+}$ (Figure 1.24 (d)), were electrodeposited and displayed both electroactive and photosensitive properties. The authors examined the influence of film thickness on the photoresponse of the deposited films, in terms of photocurrent intensities.[164] In 1986, they investigated the complex, *fac*-$Re^{I}(L_g)(CO)_3Cl$ (Figure 1.24 (e)), by electrodeposition of a polymer film and examined its use as an electrocatalyst, for the reduction of CO_2. In their work, they found that the stability of the catalyst was greatly enhanced within the polymer film (236 turnovers compared with 48 in homogeneous catalysis).[165]

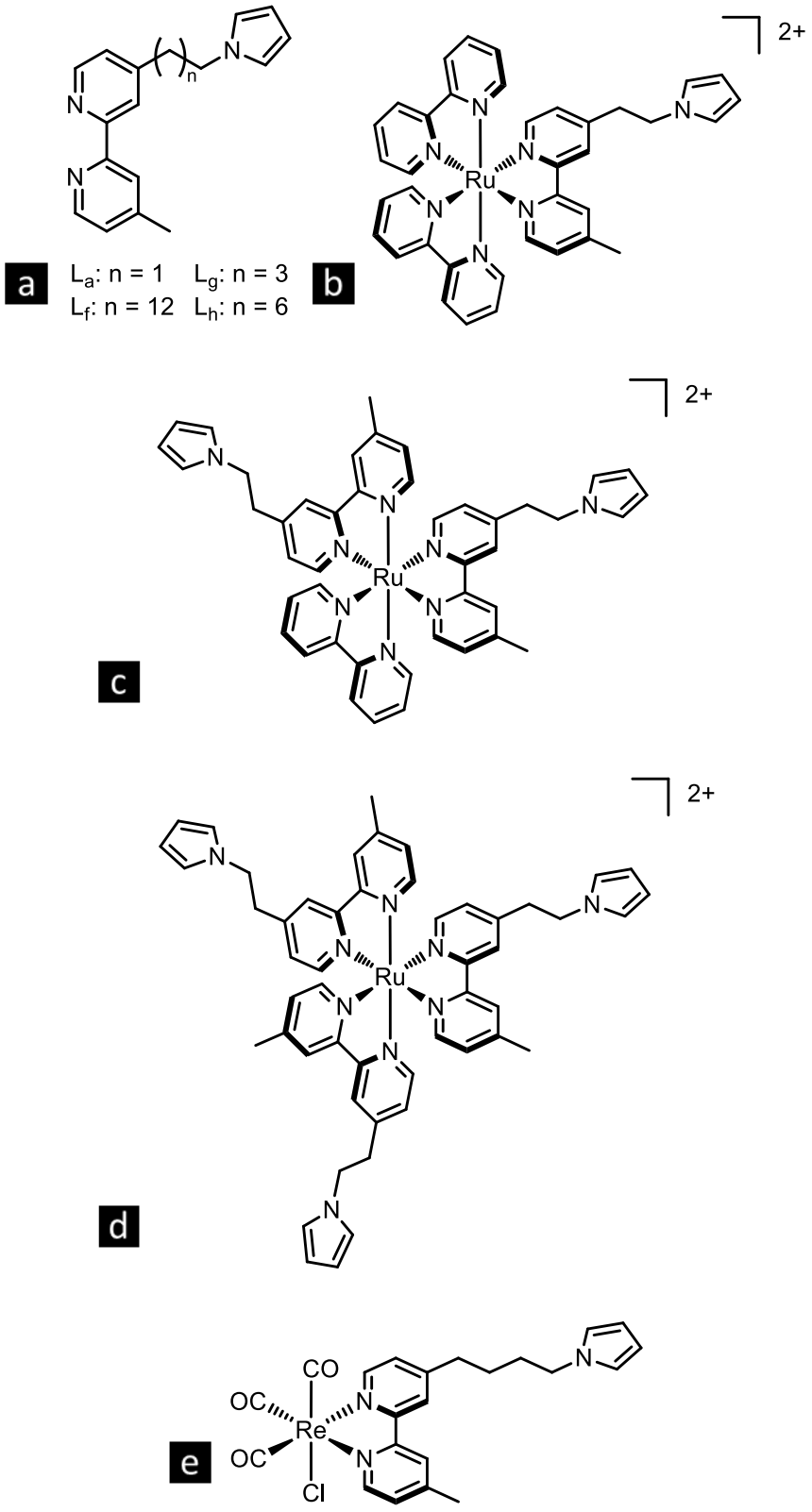

Figure 1.24: Structure of (a) ligand, L_a, Bipy, mono-substituted at the 4 position, capable of polymerisation *via* electrochemical oxidation of the Py moiety, and complexes (b) $[Ru^{II}(Bipy)_2(L_a)]^{2+}$, (c) $[Ru^{II}(Bipy)(L_a)_2]^{2+}$, (d) $[Ru^{II}(L_a)_3]^{2+}$ and (e) *fac*-$Re^{I}(L_g)(CO)_3Cl$.

During the late 1980's, Daire *et al.* began to expand the research outlined above, by encompassing other TMs, producing works regarding the electropolymerisation of poly[$Cu^{II}(L_a)_3]^{2+}$,[166] poly[$Co^{II}(L_a)_3]^{2+}$,[167] and poly[$Ni^{II}(L_a)_3]^{2+}$ films[168] on to Au substrates, for possible applications in catalysis. The authors observed that exchange occurred within the polymer film, between the polymerised ligand and compounds in solution, permitting catalytic reduction of the compounds in solution to occur at low potential values.[168]

Parker and co-workers altered the structure of the ligand, producing the variation, L_b (Figure 1.25 (a)), by substituting the Bipy moiety at the 5 position and employing one CH_2 unit in the tether, for attachment of the Py moiety. This enabled procurement of the complexes, $[M^{II}(L_b)_3]^{2+}$ (M = Fe, Ru, Cu) (Figure 1.25 (b)) and $[Ru^{II}(Bipy)(L_b)_2]^{2+}$ (Figure 1.25 (c)). Electropolymerisation of these complexes yielded films of poly$[Fe^{II}(L_b)_3]^{2+}$, poly$[Ru^{II}(L_b)_3]^{2+}$ and poly$[Ru^{II}(Bipy)(L_b)_2]^{2+}$. The electrodeposition of $[Cu^{II}(L_b)_2]^{2+}$ was also attempted in this study, but was unsuccessful, due to formation of an irreversible Cu^{III} state during polymerisation.[169] By 1989, research had yielded a significant amount of work regarding these complexes, so Deronzier and Moutet produced a review, illustrating the use of the TM complex based mono-substituted PPyBipy films, in electrocatalysis and other applications.[170]

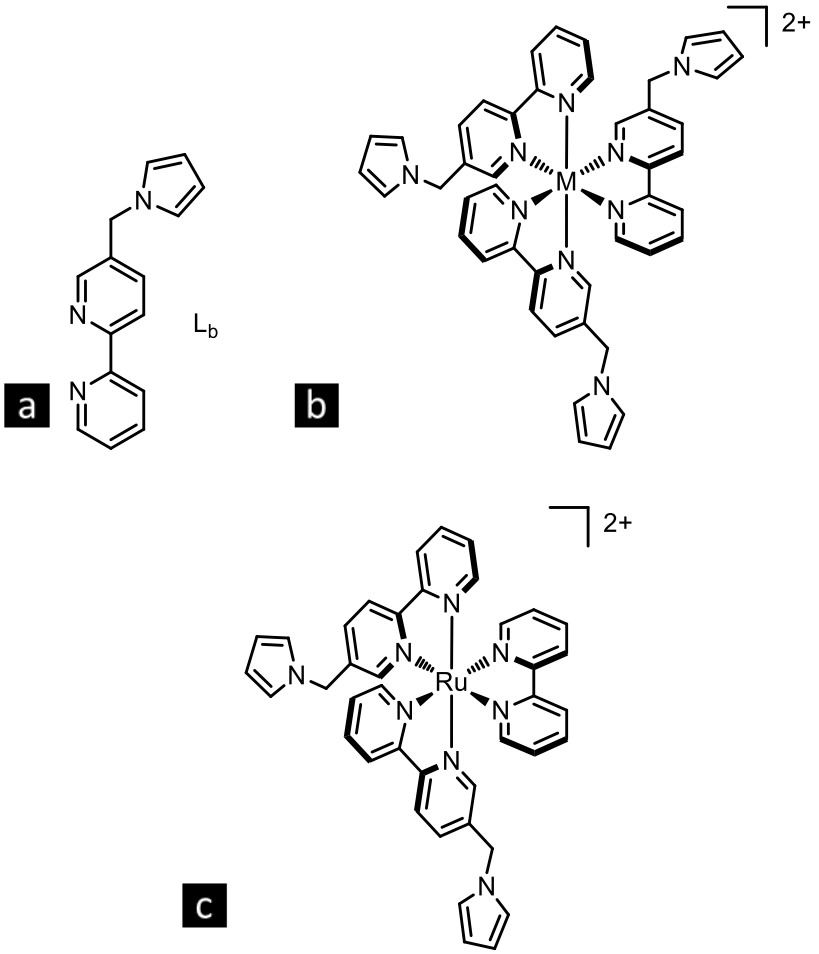

Figure 1.25: Structure of (a) ligand, L, Bipy, mono-substituted at the 5 position, capable of polymerisation, *via* electrochemical oxidation of the Py moiety and complexes (b) $[M^{II}(L_b)_3]^{2+}$ (M = Fe, Ru, Cu) and (c) $[Ru^{II}(Bipy)(L_b)_2]^{2+}$.

During the 1980's and 1990's, there was a considerable amount of work performed on these PPy bound TM complexes, focussing on the investigation of their use in electrocatalysis, but primarily on the oxidation of benzyl alcohol to benzaldehyde. In 1988, Moutet and co-workers modified electrodes with a poly$[Ru^{II}(L_a)_3]^{2+}$ film, dispersing RuO_2 particles in the film and demonstrated the formation of a strong oxidant, RuO_4^{2-}. This yielded an electrocatalytic electrode, which could oxidise benzyl alcohol, with a high current efficiency (96%) and high turnover (approx. 5000).[171] Then in 1992, Giovani and Deronzier demonstrated the electrodeposition of a poly$[Ru^{II}(L_g)_2Cl_2]$ film (Scheme 1.14 (a)), which converted to other ruthenium(II) complexes upon polymerisation (Scheme 1.14). It was shown that substitution of chloro by aqua ligands occurred (Scheme 1.14 (b), which were then substituted for

MeCN ligands (Scheme 1.14 (c)) and these substitutions were accompanied by isomerisation and dimerisation.[172] After this, in 1993, Meyer and co-workers electrodeposited thin, polymeric films of the poly-*cis*-$[Ru^{II}(L_a)_2(H_2O)_2]^{2+}$ type complexes[173] and in 1996, Deronzier and co-workers investigated the electro and spectroelectrochemistry of the poly-*cis*-$[Ru^{II}(L_a)_2(H_2O)_2]^{2+}$ films in non-coordinating solvent and found that the aqua ligands, slowly substituted for the electrolytic anion. Along with this, they investigated the electrocatalysis of benzyl alcohol and reported that a high stability for selectively obtaining benzaldehyde, was observed.[174] In 2003, they developed new ruthenium(II) complexes to be used as catalysts for the oxidation of benzyl alcohol and these possessed a high efficiency.[175]

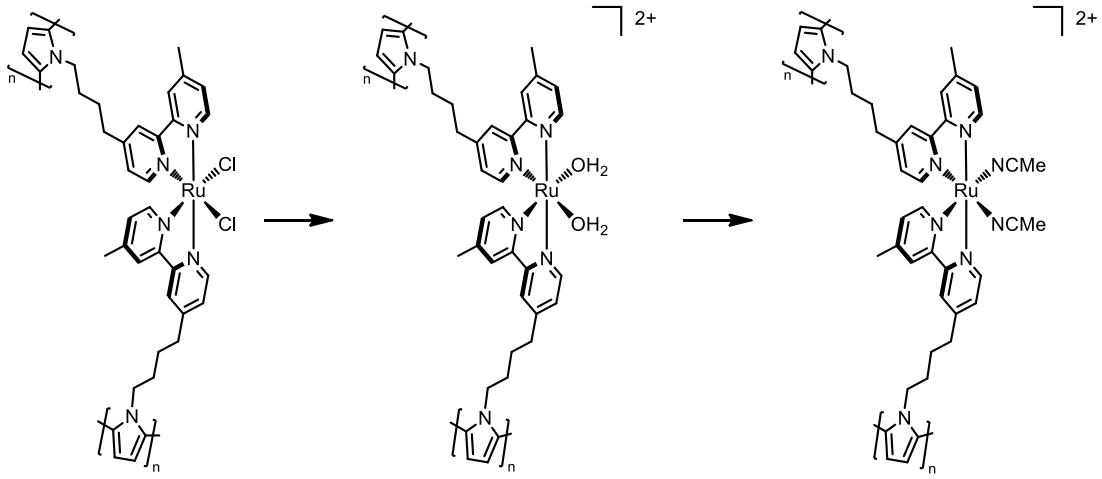

Scheme 1.14: Electrodeposition of (a) poly$[Ru^{II}(L_g)_2Cl_2]$, resulting with ligand substitution within the polymer, yielding (b) poly$[Ru^{II}(L_g)_2(H_2O)_2]^{2+}$, succeeded by (c) poly$[Ru^{II}(L_g)_2(MeCN)_2]^{2+}$.

While employing TM complexes within PPy films, the electrocatalytic reduction (ECR) and hydrogenation (ECH) of compounds were also probed. In 1990, Moutet and co-workers electrodeposited complexes possessing the ligand, L_a, (Figure 1.24 (a)) and also the ligand, $L_{c/d}$ (Figure 1.26 (a)), which were composed of a di-substituted Bipy, possessing tethers at the 4,4' position, containing carboxyl groups and terminated with Py moieties. The complexes employed in this work, were of the form $[Rh^{III}(L_a)_2Cl_2]^{2+}$ and $[Rh^{III}(L_c)_2Cl_2]^{2+}$ (Figure 1.26 (b)) and were electrodeposited as films, to be used as electrocatalysts, for the reduction of water to hydrogen and for the hydrogenation of cyclohexanone to cyclohexanol. They found that the films exhibited high and stable ECH of these organic

substrates.[176] Afterwards, in 1995, Moutet and co-workers reported the ECH of cyclohexanone, cryptone, dihydrocarvone and carvone, in aqueous electrolyte *via* electropolymerised poly$[Rh^{III}(L_a)_2(Cl)_2]^+$ and poly$[Rh^{III}(L_c)_2(Cl)_2]^+$ complexes, producing efficient turnovers of approx. 5000, but with a loss of electrocatalytic activity. The films possessing the $[Rh^{III}(L_c)_2(Cl)_2]^+$ complex were found to be less stable, due to hydrolysis, promoting loss of the complex molecules.[177] In 1997, the authors improved the synthesis and electrocatalytic activity of poly$[M^I(L_a)(diene)]^+$ and poly$[M^I(L_c)(diene)]^+$ (M = Rh, Ir) films in aqueous media and they described the hydrogenation of α,β-unsaturated ketones, along with water reduction, in this work.[178] They also electrodeposited polymer films, which possessed the complexes, $[(\eta^5\text{- }C_5Me_5)M^{III}(L_g)Cl]^+$ and $[(\eta^5\text{-}C_5Me_5)M^{III}(L_c)Cl]^+$ (M = Rh, Ir), that could produce an electrogenerated hydrido complex (Figure 1.26 (c) (i)), succeeded by insertion of 2-cyclohexen-1-one (**S**) in the metal-hydride bond (Figure 1.26 (c) (ii)). It was found in this work that the rhenium(I) complex was better than the iridium(I) complex as a catalyst and that the immobilisation of the catalyst on the electrode surface decreased the activity.[179] Afterwards, in 1999, they reported the ECH of acetophenone and 2-butanone in aqueous electrolyte using poly$[Rh^{III}(L_{c/d})_2Cl_2]^+$, where the ligand ($L_d$) was a mono-substituted Bipy, but a chiral variation, similar to that displayed in Figure 1.24 (a). The use of this chiral ligand yielded a high catalytic efficiency (4750 turnover) and asymmetric induction (up to 20% *ee*), which was improved, upon immobilisation of the complex on to the substrate as a polymeric film.[180]

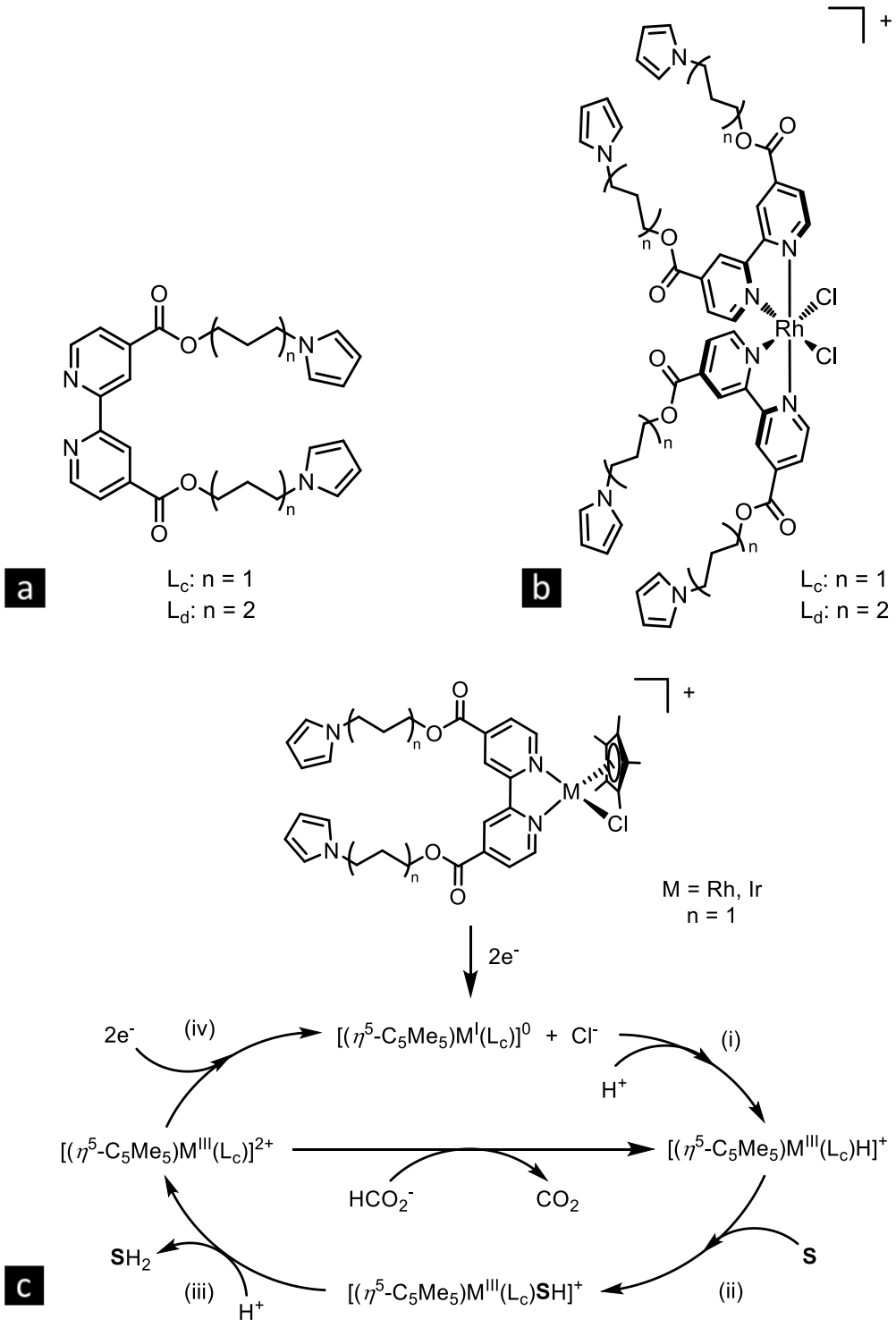

Figure 1.26: Structure of (a) ligand, $L_{c/d}$, Bipy, di-substituted at the 4,4' position, possessing carboxyl functional groups within the tethers, capable of polymerisation *via* electrochemical oxidation of the Py moieties, (b) complex $[Rh^{III}(L_{c/d})_2Cl_2]^+$ and (c) chemical/electrochemical pathways for the hydrogenation of 2-cyclohexen-1-one (**S**) catalysed by $[(\eta^5\text{-}C_5Me_5)M^{III}(L_c)Cl]^+$ (M = Rh, Ir) in the presence of formic acid.

Apart from the abundant work reported regarding electrocatalysis, these types of polymeric TM complexes have been developed in additional ways, for use in other applications. In 1996, Moutet and co-workers employed the $[Ru^{II}(L_a)_2$(Bipy-amidebenzaldehyde)$]^{2+}$ complex and electrodeposited it, demonstrating that the film could be used to electrochemically recognise certain halide anions, as it produced a shift in potential, with regard to the first one electron reduction of the redox-active species in the presence of Cl^-. It was found that I^- and Br^- had no detectable influence, while the electroactivity of the film was completely transformed in the presence of the F^- anion.[181] In 1997, they employed the complexes $[(L_a)_2Ru^{II}$(BipyCalix)$]^{2+}$ and $[(L_a)_2Ru^{II}((Bipy)_2Calix)Ru^{II}(L_a)_2]^{4+}$ (Figure 1.27) and reported the first electrodeposition of thin films, where the ligands were composed of either one or two Bipy moieties, substituted at the 5 position with a calix[4]arene, for their possible application as chemical and luminescent sensors.[182]

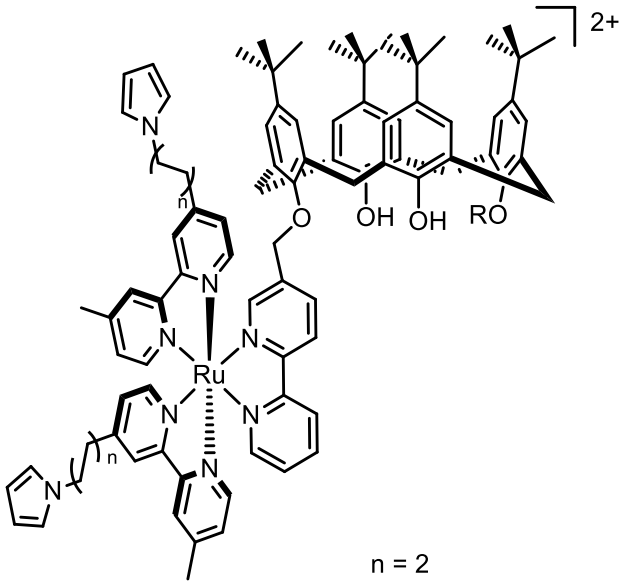

Figure 1.27: Structure of $[Ru^{II}(L_a)_2$(CalixBipyR)$]^{2+}$ (R = H (2+), ((4-Bipy)$Ru^{II}(L_a)_2$) (4+)).

Electrodeposited PPy films, containing TM complexes, have also been exploited for use in biosensor technology. In 2002 and 2007, Motonaka and co-workers developed glucose sensors, utilising the $[Os^{II}(Bipy)_2(L_a)]^{2+}$ complex for the deposition of homopolymer[183] and copolymer[184] films, respectively. In 2004, Cosnier and co-workers employed the use of another ligand, L_e (Figure 1.28 (a)), which was composed of a di-substituted Bipy, possessing alkyl chain tethers at the

4,4' positions. The authors incorporated this ligand into the complex, $[Ru^{II}(L_e)_2(BipyBiotin)]^{2+}$ (Figure 1.28 (b)), which was electrodeposited and reported to be a photosensitive polymer film, enabling its use as a photo-electrochemical immuno-sensor, for the determination of anti-cholera toxin antibody.[185,186] Also, in 2007, Cosnier and co-workers reported the electrodeposition of poly$[Ru^{II}(L_a)_3]^{2+}$ films, which then had T7 bacteriophages, displaying the West Nile virus (WNV) epitope, photochemically grafted on to the film and the electrode was used for amperometric detection of the WNV antibody.[187]

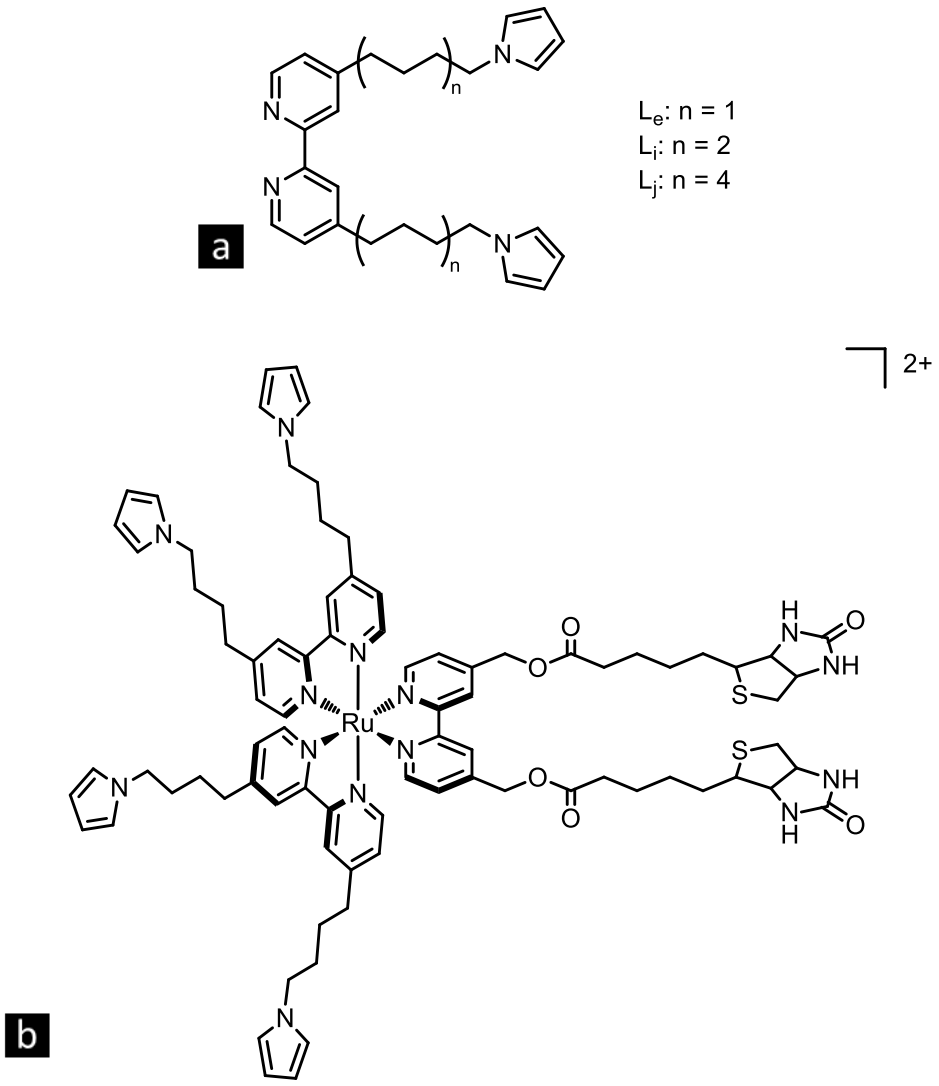

Figure 1.28: Structure of (a) ligand, $L_{e/i/j}$, Bipy, di-substituted at the 4,4' position, capable of polymerisation *via* electrochemical oxidation of the Py moiety and (b) complex $[Ru^{II}(L_e)_2(BipyBiotin)]^{2+}$.

Apart from the usual anodic electropolymerisation of TM functionalised Py monomers, modifications of this procedure, along with other methods, have been exploited to deposit films of this type. In 1994, Moutet and co-workers described the electroreductive film deposition, of amphiphilic poly$[Ru^{II}(Bipy)_2(L_f)]^{2+}$, poly$[Ru^{II}(Bipy)_2(L_e)]^{2+}$, poly$[Ru^{II}(Bipy)(L_f)_2]^{2+}$ and poly$[Ru^{II}(L_f)_3]^{2+}$, complexed *via* photo and electropolymerisation.[188] In 2000, Moutet and Cho investigated the post-functionalisation of poly($L_{g/c}$) films with $[Rh^{I}(Bipy)(diene)]^{+}$, interestingly producing films of poly$[Rh^{I}(L_{g/c})(diene)]^{+}$, which when subjected to further reductive cycling, yielded films of poly$[Rh^{I}(L_{g/c})_2]^{+}$.[4] In 2004, Deronzier and co-workers developed dispersed metal composite materials, by distributing Pd, Ru and Rh nanoparticles on to a electrodeposited film of poly$[Ru^{II}(L_g)(CO)_2(MeCN)_2]^{2+}$.[189] Then, in 2006, they electropolymerised the binuclear complexes, $[Ru^{I}(L_{a/c/e/g/h/i/j})(CO)_2(MeCN)]_2^{2+}$ (Figure 1.29), to form binuclear poly$[Ru^{I}(L_{a/c/e/g/h/i/j})(CO)_2(MeCN)]_2^{2+}$ films.[190]

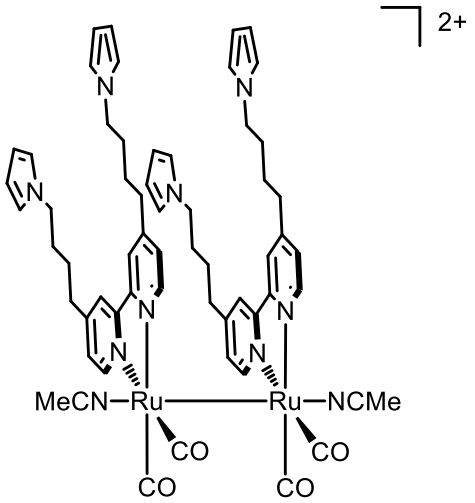

Figure 1.29: Structure of dinuclear ruthenium(I) complex, employing the di-substituted ligand, L_e.

The ligands, described previously and their variations, have been applied to many areas of chemistry, as these ligands possess many beneficial attributes and can be varied very easily, producing new TM complexes, evident in the literature. In 2010, Cosnier and co-workers employed the familiar complex, $[Ru^{II}(L_a)_2(Bipy)]^{2+}$ (Figure 1.24 (c)) and electropolymerised it as a film, from both aqueous and organic media, for the elucidation of its solid state electrochemiluminescene (ECL) mechanism.[191] Then, in 2013, they fabricated a novel EtOH biosensor, by casting a

composite of alcohol dehydrogenase (ADH) and laponite colloids on to poly[$Ru^{II}(L_a)_3$]/Pt, producing a biosensor exhibiting stable responses and a wide range for EtOH detection. The authors attributed these properties to the covalent linkage of the luminphor, $[Ru^{II}(Bipy)_3]^{2+}$, with the PPy backbone, which omitted leaching of luminescent reagent, accompanied by retention of ADH enzyme activity, facilitated by the biocompatibility of the laponite colloids. Also influential, the incorporation of the ADH into the laponite matrix covering the poly[$Ru^{II}(L_a)_3$] film, inhibited the binding of ADH with $[Ru^{II}(Bipy)_3]^{2+}$, circumventing diminished enzyme activity, while electrostatic interactions, between the negatively charged bio-organic gel and the positively charged poly[$Ru^{II}(L_a)_3$] film, yielded good stability.[192] As mentioned in Section 1.5.3, in 2011, Zhang and co-workers synthesised electroactive Py/PyEtCO_2H copolymer nanoparticles, using an alcohol-assisted microemulsion polymerisation. The authors then incorporated a ruthenium bis(2,2′-bipyridine) (2,2′-bipyridine-4,4′-dicarboxylic acid)-ethylenediamine complex, by covalently coupling it to the nanoparticle for use as a chemiluminescence aptasensor, in the detection of thrombin.[136] In 2011, Cosnier and co-workers employed another variation of the di-substituted BipyPy ligand, 4,4'-bishydroxy-2-2'-bipyridine, L_l (Figure 1.30 (a)) and constructed the two complexes, $[Ru^{II}(L_l)(Bipy)_2]^{2+}$ (Figure 1.30 (b)) and $[Ru^{II}(L_l)_3]^{2+}$ (Figure 1.30 (c)), electrodepositing them on both Pt and multi-walled carbon nanotube (MWCNT) functionalised electrodes. The electrodes, which were modified first with MWCNTs and then, further functionalised with electrodeposited films of poly$[Ru^{II}(L_l)(Bipy)_2]^{2+}$ and poly$[Ru^{II}(L_l)_3]^{2+}$, possessed an increase in surface area due to the MWCNT. This induced an increase in the permeability, accompanied by a decrease in the charge trapping phenomenon, which occurs during the redox of the PPy backbone possessed by the poly$[Ru^{II}]^{2+}$ films.[193]

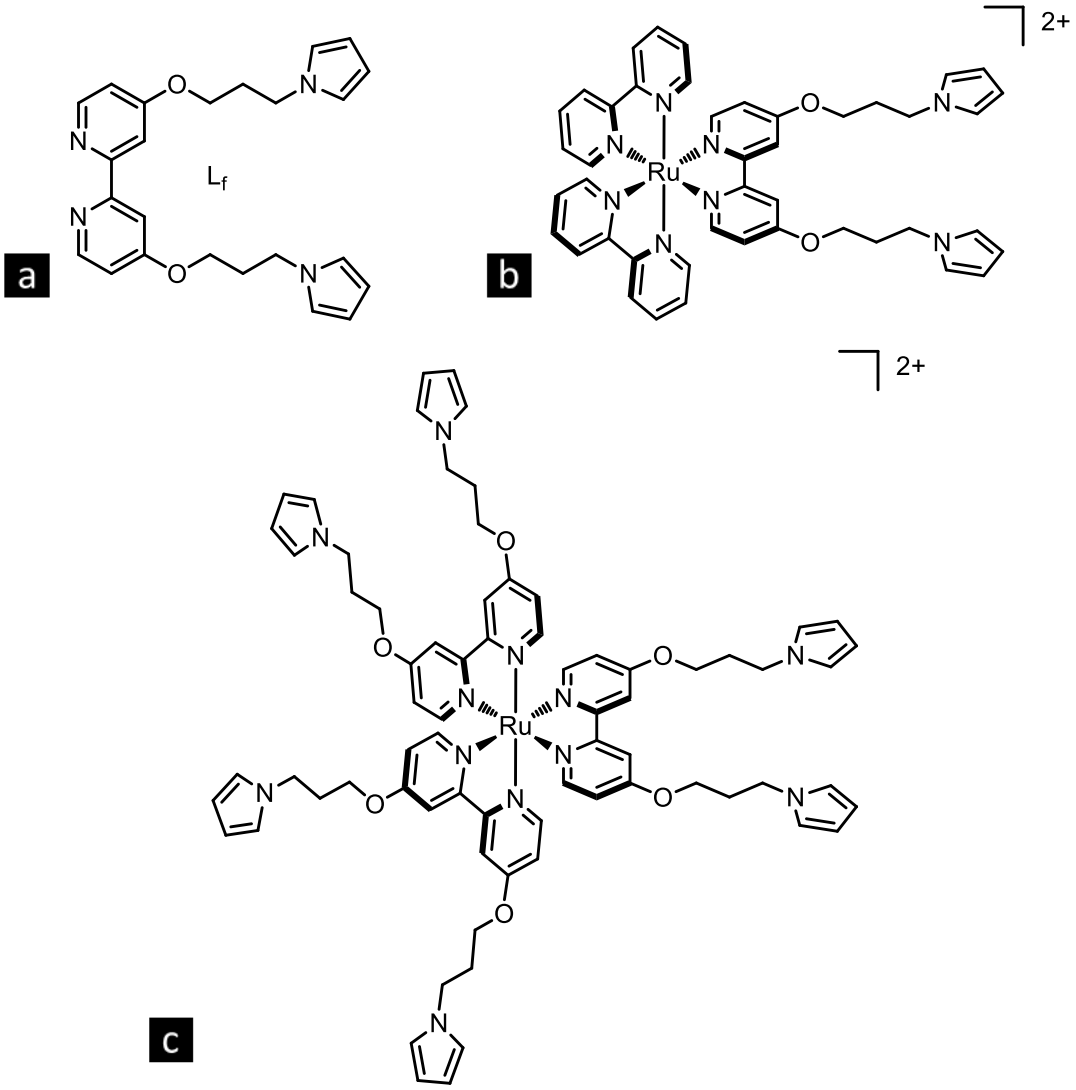

Figure 1.30: Structure of (a) ligand L_l, Bipy, di-substituted at the 4,4' position, possessing ether functional groups within the tethers, capable of polymerisation *via* electrochemical oxidation of the Py moiety. Complexes (b) $[Ru^{II}(L_l)(Bipy)2]^{2+}$and (c) $[Ru^{II}(Ll)_3]^{2+}$.

Ligands, possessing a variation of the chelating Bipy moiety, have also been electrodeposited as films, on to the electrode surface. The ligand, (*N*-(3-*N*,*N*'-bis(2-pyridyl)propylamino)pyrrole, L_k (Figure 1.31 (a)), was employed by Wong and co-workers in 2009 to electropolymerise the complex, $Re^{I}(CO)_3(L_k)Cl$ (Figure 1.31 (b)) on to a GCE, as the complex exhibited electrocatalytic activity for the reduction of CO_2 to CO.[194] Then, in 2011, the authors described the direct electropolymerisation of the complex, $[Ru^{II}(L_k)(Tpy)X]^{n+}$ ($X = Cl^-$, H_2O, MeCN) (Figure 1.31 (c)), in aqueous medium and this permitted the observation of high valent Ru^{IV}=O species,

which has been demonstrated previously, as a reactive electrocatalyst, for the multielectron oxidation of substrates.[195]

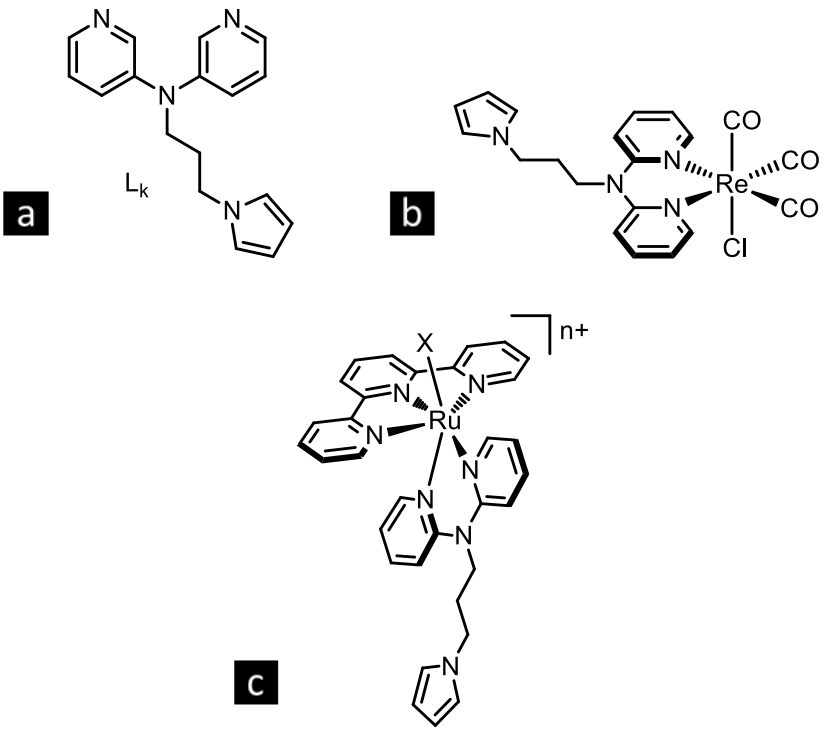

Figure 1.31: (a) Structure of monomer ligand, L_k (b) $Re^{I}(L_k)(CO)_3Cl$ and (c) $[Ru(L_k)(Ter)X]^{n+}$ ($X = Cl^-$, H_2O, MeCN).

In Chapter 5 of this work, the synthesis and characterisation of TM complexes of tetracarbonyl Group 6 metals, which possess a novel di-substituted BipyPy ligand, are described. The electrochemical polymerisation of the BipyPy ligand and that of the respective complexes were investigated, utilising various conditions and the possible post-functionalisation of the novel poly(BipyPy) films was also probed. This work was performed specifically, to attempt the formation of a polymeric material, possessing the capability of controlled CO release, upon stimulation *via* electrochemical means.

1.6 References

1. Li, Y.; Zhang, W.; Chang, J.; Chen, J.; Li, G.; Ju, Y. *Macromol. Chem. Phys.* **2008**, *209*, 322-329.
2. Bidan, G.; Deronzier, A.; Moutet, J. C. *Nouv. J. Chim.* **1984**, *8*, 501-503.
3. Bu, H.-B.; Götz, G.; Reinold, E.; Vogt, A.; Schmid, S.; Segura, J. L.; Blanco, R.; Gómez, R.; Bäuerle, P. *Tetrahedron* **2011**, *67*, 1114-1125.
4. Moutet, J. C.; Cho, L. Y. *Inorg. Chem. Commun.* **2000**, *3*, 620-623.
5. Amer, W. A.; Wang, L.; Amin, A. M.; Ma, L. A.; Yu, H. J. *J. Inorg. Organomet. Polym. Mater.* **2010**, *20*, 605-615.
6. Mann, B. E. *Organometallics* **2012**, *31*, 5728-5735.
7. Zang, J. F.; Li, C. M.; Bao, S. J.; Cui, X. Q.; Bao, Q. L.; Sun, C. Q. *Macromolecules* **2008**, *41*, 7053-7057.
8. Wang, J. X.; Mo, X. P.; Ge, D. T.; Tian, Y.; Wang, Z.; Wang, S. C. *Synth. Met.* **2006**, *156*, 514-518.
9. Li, J.; Lin, X. Q. *J. Electrochem. Soc.* **2007**, *154*, 1074-1079.
10. Wanekaya, A. K.; Chen, W.; Myung, N. V.; Mulchandani, A. *Electroanal.* **2006**, *18*, 533-550.
11. McCarthy, C. P.; McGuinness, N. B.; Alcock-Earley, B. E.; Breslin, C. B.; Rooney, A. D. *Electrochem. Commun.* **2012**, *20*, 79-82.
12. McCarthy, C. P.; McGuinness, N. B.; Carolan, P. B.; Fox, C. M.; Alcock-Earley, B. E.; Breslin, C. B.; Rooney, A. D. *Macromolecules* **2013**, *46*, 1008-1016.
13. Johanson, U.; Marandi, A.; Tamm, T.; Tamm, J. *Electrochim. Acta* **2005**, *50*, 1523-1528.
14. Dziewonski, P. M.; Grzeszczuk, M. *J. Phys. Chem. B* **2010**, *114*, 7158-7171.
15. George, P. M.; Lyckman, A. W.; LaVan, D. A.; Hegde, A.; Leung, Y.; Avasare, R.; Testa, C.; Alexander, P. M.; Langer, R.; Sur, M. *Biomaterials* **2005**, *26*, 3511-3519.
16. Annibaldi, V.; Rooney, A. D.; Breslin, C. B. *Corros. Sci.* **2012**, *59*, 179-185.
17. Shirakawa, H.; Louis, E. J.; Macdiarmid, A. G.; Chiang, C. K.; Heeger, A. J. *Chem. Commun.* **1977**, *0*, 578-580.
18. Mathad, J. K.; Rao, R. M. V. G. K. *Polym. Compos.* **2011**, *32*, 1416-1422.
19. Wang, J.; Too, C. O.; Zhou, D.; Wallace, G. G. *J. Power Sources* **2005**, *140*, 162-167.
20. Dubal, D. P.; Lee, S. H.; Kim, J. G.; Kim, W. B.; Lokhande, C. D. *J. Mater. Chem.* **2012**, *22*, 3044-3052.
21. Kathuroju, P. K.; Nagaraju, J. *Micro Nano Lett.* **2011**, *6*, 1002-1006.
22. Kathuroju, P. K.; Jampana, N. *IEEE T. Instrum. Meas.* **2012**, *61*, 2339-2345.
23. Zhao, F.; Liu, L.; Yang, F.; Ren, N. *Chem. Eng. J.* **2013**, *230*, 491-498.
24. Kępińska, D.; Budniak, A.; Kijewska, K.; Blanchard, G. J.; Mazur, M. *Polymer* **2013**, *54*, 4538-4544.
25. Chiu, H. T.; Lin, J. S.; Shiau, J. N. *J. Appl. Electrochem.* **1992**, *22*, 522-527.
26. Kim, L. T. T.; Gabrielli, C.; Pailleret, A.; Perrot, H. *Electrochim. Acta* **2011**, *56*, 3516-3525.
27. Pfluger, P.; Street, G. B. *J. Chem. Phys.* **1984**, *80*, 544-553.
28. Waltman, R. J.; Diaz, A. F.; Bargon, J. *J. Phys. Chem.* **1984**, *88*, 4343-4346.

29. Ferraris, J. P.; Andrus, R. G.; Hrncir, D. C. *Chem. Commun.* **1989**, 1318-1320.
30. Liu, J.; Zhang, R.; Sauve, G.; Kowalewski, T.; McCullough, R. D. *J. Am. Chem. Soc.* **2008**, *130*, 13167-13176.
31. West, R.; Josowicz, M.; Janata, J.; Minet, I.; Hevesi, L. *J. Electrochem. Soc.* **2009**, *156*, 55-59.
32. Brédas, J. L.; Scott, J. C.; Yakushi, K.; Street, G. B. *Phys. Rev. B* **1984**, *30*, 1023-1025.
33. Bredas, J. L.; Street, G. B. *Acc. Chem. Res.* **1985**, *18*, 309-315.
34. Chandrasekhar, P. *Conducting Polymers, Fundamental and Applications.*; Kluwer Academic Publishers, 1999.
35. Cabala, R.; Skarda, J.; Potje-Kamloth, K. *Phys. Chem. Chem. Phys.* **2000**, *2*, 3283-3291.
36. Latonen, R. M.; Akieh, M. N.; Vavra, K.; Bobacka, J.; Ivaska, A. *Electroanal.* **2013**, *25*, 991-1004.
37. Zuppiroli, L.; Bussac, M. N.; Paschen, S.; Chauvet, O.; Forro, L. *Phys. Rev. B* **1994**, *50*, 5196-5203.
38. Otero, T. F.; Tejada, R.; Elola, A. S. *Polymer* **1987**, *28*, 651-658.
39. Feast, W. J.; Tsibouklis, J.; Pouwer, K. L.; Groenendaal, L.; Meijer, E. W. *Polymer* **1996**, *37*, 5017-5047.
40. Toshima, N.; Hara, S. *Prog. Polym. Sci.* **1995**, *20*, 155-183.
41. Chitte, H. K. *J. Sens. Tech.* **2011**, *01*, 47-56.
42. Sadki, S.; Schottland, P.; Brodie, N.; Sabouraud, G. *Chem. Soc. Rev.* **2000**, *29*, 283-293.
43. Genies, E. M.; Bidan, G.; Diaz, A. F. *J. Electroanal. Chem.* **1983**, *149*, 101-113.
44. Waltman, R. J.; Bargon, J. *Can. J. Chem.* **1986**, *64*, 76-95.
45. Waltman, R. J.; Bargon, J. *Tetrahedron* **1984**, *40*, 3963-3970.
46. Jang, J.; Oh, J. H.; Li, X. L. *J. Mater. Chem.* **2004**, *14*, 2872-2880.
47. Wu, C. G.; Bein, T. *Science* **1994**, *264*, 1757-1759.
48. Yin, Z. H.; Long, Y. Z.; Gu, C. Z.; Wan, M. X.; Duvail, J. L. *Nanoscale Res. Lett.* **2009**, *4*, 63-69.
49. Yang, J. L.; Wang, J. J.; Tang, Y. J.; Wang, D. N.; Xiao, B. W.; Li, X. F.; Li, R. Y.; Liang, G. X.; Sham, T. K.; Sun, X. L. *J. Mater. Chem.* **2013**, *1*, 7306-7311.
50. Pei, Q. B.; Inganas, O. *J. Phys. Chem.* **1992**, *96*, 10507-10514.
51. Pei, Q.; Inganaes, O. *J. Phys. Chem.* **1993**, *97*, 6034-6041.
52. Wan, M. X. *Adv. Mater.* **2008**, *20*, 2926-2932.
53. Wan, M. *Macromol. Rapid Commun.* **2009**, *30*, 963-975.
54. Cai, Z. H.; Martin, C. R. *J. Am. Chem. Soc.* **1989**, *111*, 4138-4139.
55. Duchet, J.; Legras, R.; Demoustier-Champagne, S. *Synth. Met.* **1998**, *98*, 113-122.
56. Wei, Z.; Zhang, Z.; Wan, M. *Langmuir* **2002**, *18*, 917-921.
57. Martin, C. R. *Science* **1994**, *266*, 1961-1966.
58. C. Hulteen, J.; Martin, C. R. *J. Mater. Chem.* **1997**, *7*, 1075-1087.
59. Wang, Z.; Chen, M. A.; Li, H. L. *Mat. Sci. Eng. A* **2002**, *328*, 33-38.
60. DiCarmine, P. M.; Fokina, A.; Seferos, D. S. *Chem. Mater.* **2011**, *23*, 3787-3794.

61. John, V. T.; Simmons, B.; McPherson, G. L.; Bose, A. *Curr. Opin. Colloid Interface Sci.* **2002**, *7*, 288-295.
62. Carswell, A. D.; O'Rear, E. A.; Grady, B. P. *J. Am. Chem. Soc.* **2003**, *125*, 14793-14800.
63. Yang, C. H.; Chih, Y. K.; Cheng, H. E.; Chen, C. H. *Polymer* **2005**, *46*, 10688-10698.
64. Sarno, D. M.; Manohar, S. K.; MacDiarmid, A. G. *Synth. Met.* **2005**, *148*, 237-243.
65. Wang, H. X.; Lin, T.; Kaynak, A. *Synth. Met.* **2005**, *151*, 136-140.
66. Shao, Y.; Jin, Y. D.; Dong, S. J. *Electrochem. Commun.* **2002**, *4*, 773-779.
67. Zhu, N. N.; Chang, Z.; He, P. G.; Fang, Y. Z. *Electrochim. Acta* **2006**, *51*, 3758-3762.
68. Goren, M.; Qi, Z. G.; Lennox, R. B. *Chem. Mater.* **2000**, *12*, 1222-1228.
69. Huang, L. M.; Wang, Z. B.; Wang, H. T.; Cheng, X. L.; Mitra, A.; Yan, Y. S. *J. Mater. Chem.* **2002**, *12*, 388-391.
70. Tagowska, M.; Mazur, M.; Krysinski, P. *Synth. Met.* **2004**, *140*, 29-35.
71. Zhou, C.; Han, J.; Guo, R. *Macromol. Rapid Commun.* **2009**, *30*, 182-187.
72. Jang, J.; Oh, J. H.; Stucky, G. D. *Angew. Chem., Int. Ed.* **2002**, *41*, 4016-4019.
73. Jang, J.; Yoon, H. *Langmuir* **2005**, *21*, 11484-11489.
74. Zhang, X. Y.; Lee, J. S.; Lee, G. S.; Cha, D. K.; Kim, M. J.; Yang, D. J.; Manohar, S. K. *Macromolecules* **2006**, *39*, 470-472.
75. Shi, W.; Liang, P.; Ge, D.; Wang, J.; Zhang, Q. *Chem. Commun.* **2007**, *0*, 2414-2416.
76. Ge, D. T.; Mu, J.; Huang, S. Q.; Liang, P. F.; Gcilitshana, O. U.; Ji, S.; Linkov, V.; Shi, W. *Synth. Met.* **2011**, *161*, 166-172.
77. Xia, L.; Wei, Z.; Wan, M. *J. Colloid Interface Sci.* **2010**, *341*, 1-11.
78. Qiu, H.; Wan, M.; Matthews, B.; Dai, L. *Macromolecules* **2001**, *34*, 675-677.
79. Zhang, L.; Wan, M. *Adv. Funct. Mater.* **2003**, *13*, 815-820.
80. Liang, L.; Liu, J.; Windisch Jr, C. F.; Exarhos, G. J.; Lin, Y. *Angew. Chem., Int. Ed.* **2002**, *41*, 3665-3668, 3520.
81. Liu, J.; Lin, Y.; Liang, L.; Voigt, J. A.; Huber, D. L.; Tian, Z. R.; Coker, E.; McKenzie, B.; McDermott, M. J. *Chemistry* **2003**, *9*, 604-611.
82. Huang, J. Y.; Wang, K.; Wei, Z. X. *J. Mater. Chem.* **2010**, *20*, 1117-1121.
83. Debiemme-Chouvy, C. *Electrochem. Commun.* **2009**, *11*, 298-301.
84. Al-Mashat, L.; Debiemme-Chouvy, C.; Borensztajn, S.; Wlodarski, W. *J. Phys. Chem. C* **2012**, *116*, 13388-13394.
85. Debiemme-Chouvy, C. *Electrochem. Solid St.* **2007**, *10*, 24-26.
86. Debiemme-Chouvy, C.; Tran, T. T. M. *Electrochem. Commun.* **2008**, *10*, 947-950.
87. Debiemme-Chouvy, C. *Biosens. Bioelectron.* **2010**, *25*, 2454-2457.
88. Zhou, M.; Heinze, J. *Journal of Physical Chemistry B* **1999**, *103*, 8443-8450.
89. Street, G. B. *J. Phys. Colloques* **1983**, *186*, 599-606.
90. Ouyang, J. Y.; Li, Y. F. *J. Appl. Polym. Sci.* **1996**, *61*, 1487-1491.
91. Farrington, A. M.; Slater, J. M. *Electroanal.* **1997**, *9*, 843-847.
92. Larraz, E.; Redondo, M. I.; Gonzalez-Tejera, M. J.; Raso, M. A.; Tortajada, J.; de la Blanca, E. S.; Garcia, M. V. *Synth. Met.* **2001**, *122*, 413-423.

93. Shirale, D. J.; Gade, V. K.; Gaikwad, P. D.; Kharat, H. J.; Kakde, K. P.; Savale, P. A.; Hussaini, S. S.; Dhumane, N. R.; Shirsat, M. D. *Mater. Lett.* **2006**, *60*, 1407-1411.
94. Fridman, V. A.; Bogdanovskaya, V. A.; Tarasevich, M. R. *Russ. J. Electrochem.* **2002**, *38*, 539-543.
95. Ramanathan, K.; Bangar, M. A.; Yun, M.; Chen, W.; Mulchandani, A.; Myung, N. V. *Electroanal.* **2007**, *19*, 793-797.
96. Atta, N. F.; El-Kady, M. F.; Galal, A. *Anal. Biochem.* **2010**, *400*, 78-88.
97. Marti, M.; Fabregat, G.; Estrany, F.; Aleman, C.; Armelin, E. *J. Mater. Chem.* **2010**, *20*, 10652-10660.
98. Fabregat, G.; Cordova-Mateo, E.; Armelin, E.; Bertran, O.; Aleman, C. *J. Phys. Chem. C* **2011**, *115*, 14933-14941.
99. Datta, K.; Ghosh, P.; More, M. A.; Shirsat, M. D.; Mulchandani, A. *J. Phys. D: Appl. Phys.* **2012**, *45*, 1-8.
100. Mahmoudian, M. R.; Basirun, W. J.; Alias, Y.; Zak, A. K. *Thin Solid Films* **2011**, *520*, 258-265.
101. Duran, B.; Bereket, G. *Ind. Eng. Chem. Res.* **2012**, *51*, 5246-5255.
102. Lahdesmaki, I.; Kubiak, W. W.; Lewenstam, A.; Ivaska, A. *Talanta* **2000**, *52*, 269-275.
103. Kadam, S. B.; Datta, K.; Ghosh, P.; Kadam, A. B.; Khirade, P. W.; Kumar, V.; Sonkawade, R. G.; Gambhire, A. B.; Lande, M. K.; Shirsat, M. D. *Appl. Phys. A* **2010**, *100*, 1083-1088.
104. Singh, K.; Basu, T.; Solanki, P. R.; Malhotra, B. D. *J. Mater. Sci.* **2009**, *44*, 954-961.
105. Ashrafi, A.; Golozar, M. A.; Mallakpour, S. *Iran. Polym. J.* **2003**, *12*, 485-490.
106. Tüken, T.; Tansuğ, G.; Yazıcı, B.; Erbil, M. *Surf. Coat. Technol.* **2007**, *202*, 146-154.
107. Su, W. C.; Iroh, J. O. *Synth. Met.* **2000**, *114*, 225-234.
108. Estrany, F.; Aradilla, D.; Oliver, R.; Aleman, C. *Eur. Polym. J.* **2007**, *43*, 1876-1882.
109. Alemán, C.; Estrany, F.; Armelin, E.; Oliver, R.; Casanovas, J. *Polymer* **2007**, *48*, 6162-6169.
110. Estrany, F.; Aradilla, D.; Oliver, R.; Armelin, E.; Aleman, C. *Eur. Polym. J.* **2008**, *44*, 1323-1330.
111. Aradilla, D.; Estrany, F.; Armelin, E.; Aleman, C. *Thin Solid Films* **2010**, *518*, 4203-4210.
112. Aradilla, D.; Ocampo, C.; Armelin, E.; Aleman, C.; Oliver, R.; Estrany, F. *Mater. Corros.* **2007**, *58*, 867-872.
113. Deng, Z. P.; Stone, D. C.; Thompson, M. *Can. J. Chem.* **1995**, *73*, 1427-1435.
114. Deng, Z. P.; Stone, D. C.; Thompson, M. *Analyst* **1996**, *121*, 1341-1348.
115. Weiss, Z.; Mandler, D.; Shustak, G.; Domb, A. J. *J. Polym. Sci., Part A: Polym. Chem.* **2004**, *42*, 1658-1667.
116. Tuzun, N. S.; Bayata, F.; Sarac, A. S. *J. Mol. Struct. Theochem* **2008**, *857*, 95-104.
117. Aradilla, D.; Estrany, F.; Oliver, R.; Aleman, C. *Eur. Polym. J.* **2010**, *46*, 2222-2228.

118. Aradilla, D.; Estrany, F.; Armelin, E.; Oliver, R.; Iribarren, J. I.; Aleman, C. *Macromol. Chem. Phys.* **2010**, *211*, 1663-1672.
119. Aradilla, D.; Torras, J.; Aleman, C. *J. Phys. Chem. B.* **2011**, *115*, 2882-2889.
120. Fabregat, G.; Aleman, C.; Casas, M. T.; Armelin, E. *J. Phys. Chem. B* **2012**, *116*, 5064-5070.
121. Haase, V.; Beck, F. *Electrochim. Acta* **1994**, *39*, 1195-1205.
122. Um, H. J.; Kim, M.; Lee, S. H.; Min, J.; Kim, H.; Choi, Y. W.; Kim, Y. H. *Talanta* **2011**, *84*, 330-334.
123. Dong, H.; Cao, X.; Li, C. M. *ACS Appl. Mater. Interfaces* **2009**, *1*, 1599-1606.
124. Karaoğlu, E.; Baykal, A.; Deligöz, H.; Şenel, M.; Sözeri, H.; Toprak, M. S. *J. Alloys Compd.* **2011**, *509*, 8460-8468.
125. Chu, Y. M.; Lin, C. C.; Chang, H. C.; Li, C.; Guo, C. *Biosens. Bioelectron.* **2011**, *26*, 2334-2340.
126. Tolani, S. B.; Craig, M.; DeLong, R. K.; Ghosh, K.; Wanekaya, A. K. *Anal. Bioanal. Chem.* **2009**, *393*, 1225-1231.
127. Tolani, S.; Mugweru, A.; Craig, M.; Wanekaya, A. K. *J. Appl. Polym. Sci.* **2010**, *116*, 308-313.
128. Davis, J.; Glidle, A.; Cass, A. E. G.; Zhang, J. K.; Cooper, J. M. *J. Am. Chem. Soc.* **1999**, *121*, 4302-4303.
129. Glidle, A.; Hadyoon, C. S.; Cass, A. E. G.; Cooper, J. M. *Electrochim. Acta* **2000**, *45*, 3823-3831.
130. Lee, J. W.; Serna, F.; Nickels, J.; Schmidt, C. E. *Biomacromolecules* **2006**, *7*, 1692-1695.
131. Kojima, K.; Yamauchi, T.; Shimomura, M.; Miyauchi, S. *Polymer* **1998**, *39*, 2079-2082.
132. Yamauchi, T.; Kojima, K.; Oshima, K.; Shimomura, M.; Miyauchi, S. *Synth. Met.* **1999**, *102*, 1320.
133. Yasuzawa, M.; Nieda, T.; Hirano, T.; Kunugi, A. *Sens. Actuators, B* **2000**, *66*, 77-79.
134. Jiang, H. R.; Zhang, A. F.; Sun, Y. A.; Ru, X. N.; Ge, D. T.; Shi, W. *Electrochim. Acta* **2012**, *70*, 278-285.
135. Zhang, L.; Zhang, Z. *Synth. Met.* **2011**, *161*, 724-730.
136. Ma, F.; Jia, L. J.; Zhang, Y.; Sun, B.; Qi, H. L.; Gao, Q.; Zhang, C. X. *Sci. China, Ser. B* **2011**, *54*, 1357-1364.
137. Şenel, M. *Synth. Met.* **2011**, *161*, 1861-1868.
138. Karsten, S.; Ameen, M. A.; Kallane, S. I.; Nan, A.; Turcu, R.; Liebscher, J. *Synthesis* **2010**, 3021-3028.
139. Martinez-Castro, N.; Magenau, A. J. D.; Storey, R. F. *J. Polym. Sci., Part A: Polym. Chem.* **2010**, *48*, 2533-2545.
140. Magenau, A. J. D.; Martinez-Castro, N.; Savin, D. A.; Storey, R. F. *Macromolecules* **2009**, *42*, 8044-8051.
141. Cernat, A.; Griveau, S.; Martin, P.; Lacroix, J. C.; Farcau, C.; Sandulescu, R.; Bedioui, F. *Electrochem. Commun.* **2012**, *23*, 141-144.
142. Eaves, J. G.; Munro, H. S.; Parker, D. *Synth. Met.* **1986**, *16*, 123-125.
143. Eaves, J. G.; Mirrazaei, R.; Parker, D.; Munro, H. S. *J. Chem. Soc., Perk. T. 2* **1989**, *0*, 373-376.

144. Naji, A.; Cretin, M.; Persin, M.; Sarrazin, J. *J. Appl. Polym. Sci.* **2004**, *91*, 3947-3958.
145. Moutet, J. C.; SaintAman, E.; Ungureanu, M.; Visan, T. *J. Electroanal. Chem.* **1996**, *410*, 79-85.
146. Saint-Aman, E.; Ungureanu, M.; Visan, T.; Moutet, J. C. *Electrochim. Acta* **1997**, *42*, 1829-1837.
147. Haimerl, A.; Merz, A. *Angew. Chem., Int. Ed.* **1986**, *98*, 179-181.
148. Zotti, G.; Zecchin, S.; Schiavon, G.; Berlin, A.; Pagani, G.; Canavesi, A. *Chem. Mater.* **1995**, *7*, 2309-2315.
149. Zotti, G.; Schiavon, G.; Zecchin, S.; Berlin, A.; Canavesi, A.; Pagani, G. *Synth. Met.* **1997**, *84*, 239-240.
150. Foulds, N. C.; Lowe, C. R. *Anal. Chem.* **1988**, *60*, 2473-2478.
151. Palomera, N.; Vera, J. L.; Melendez, E.; Ramirez-Vick, J. E.; Tomar, M. S.; Arya, S. K.; Singh, S. P. *J. Electroanal. Chem.* **2011**, *658*, 33-37.
152. Park, K. S.; Schougaard, S. B.; Goodenough, J. B. *Adv. Mater.* **2007**, *19*, 848-851.
153. Camurlu, P.; Gultekin, C. *Sol. Energy Mater. Sol. Cells* **2012**, *107*, 142-147.
154. Reynes, O.; Royal, G.; Chainet, E.; Moutet, J. C.; Saint-Aman, E. *Electroanal.* **2003**, *15*, 65-69.
155. Berduque, A.; Herzog, G.; Watson, Y. E.; Arrigan, D. W. M.; Moutet, J. C.; Reynes, O.; Royal, G.; Saint-Aman, E. *Electroanal.* **2005**, *17*, 392-399.
156. Martinez, F. J.; Gonzalez, B.; Alonso, B.; Losada, J.; Garcia-Armada, M. P.; Casado, C. M. *J. Inorg. Organomet. Polym. Mater.* **2008**, *18*, 51-58.
157. Ion, A.; Ion, I.; Popescu, A.; Ungureanu, M.; Moutet, J.-C.; Saint-Aman, E. *Adv. Mater.* **1997**, *9*, 711-713.
158. Ion, A. C.; Moutet, J. C.; Pailleret, A.; Popescu, A.; St Aman, E.; Siebert, E.; Ungureanu, E. M. *J. Electroanal. Chem.* **1999**, *464*, 24-30.
159. Buda, M.; Moutet, J.-C.; Pailleret, A.; Saint-Aman, E.; Ziessel, R. *J. Electroanal. Chem.* **2000**, *484*, 164-171.
160. Calvo-Muñoz, M. L.; Bile, B. E.-A.; Billon, M.; Bidan, G. *J. Electroanal. Chem.* **2005**, *578*, 301-313.
161. Decreau, R. A.; Collman, J. P.; Hosseini, A. *Chem. Soc. Rev.* **2010**, *39*, 1291-1301.
162. Bu, H. B.; Gotz, G.; Reinold, E.; Vogt, A.; Schmid, S.; Blanco, R.; Segura, J. L.; Bauerle, P. *Chem. Commun.* **2008**, 1320-1322.
163. Xu, J. J.; Tian, Y.; Peng, R.; Xian, Y. Z.; Ran, Q.; Jin, L. T. *Electrochem. Commun.* **2009**, *11*, 1972-1975.
164. Cosnier, S.; Deronzier, A.; Moutet, J. C. *J. Phys. Chem.* **1985**, *89*, 4895-4897.
165. Cosnier, S.; Deronzier, A.; Moutet, J.-C. *J. Electroanal. Chem. Interfacial Electrochem.* **1986**, *207*, 315-321.
166. Daire, F.; Bedioui, F.; Devynck, J.; Bied-Charreton, C. *J. Electroanal. Chem. Interfacial Electrochem.* **1986**, *205*, 309-318.
167. Daire, F.; Bedioui, F.; Devynck, J.; Biedcharreton, C. *J. Electroanal. Chem.* **1987**, *224*, 95-110.
168. Daire, F.; Bedioui, F.; Devynck, J.; Bied-Charreton, C. *Electrochim. Acta* **1988**, *33*, 567-571.
169. Eaves, J. G.; Munro, H. S.; Parker, D. *Inorg. Chem.* **1987**, *26*, 644-650.
170. Deronzier, A.; Moutet, J. C. *Acc. Chem. Res.* **1989**, *22*, 249-255.

171. Cosnier, S.; Deronzier, A.; Moutet, J. C. *Inorg. Chem.* **1988**, *27*, 2389-2390.
172. De Giovani, W. F.; Deronzier, A. *Chem. Commun.* **1992**, *0*, 1461-1463.
173. Guadalupe, A. R.; Chen, X. H.; Sullivan, B. P.; Meyer, T. J. *Inorg. Chem.* **1993**, *32*, 5502-5512.
174. Collomb-Dunand-Sauthier, M.-N.; Deronzier, A.; Bozec, H. L.; Navarro, M. *J. Electroanal. Chem.* **1996**, *410*, 21-29.
175. Rodríguez, M.; Romero, I.; Sens, C.; Llobet, A.; Deronzier, A. *Electrochim. Acta* **2003**, *48*, 1047-1054.
176. De Oliveira, I. M. F.; Moutet, J.-C.; Vlachopoulos, N. *J. Electroanal. Chem. Interfacial Electrochem.* **1990**, *291*, 243-249.
177. Chardon-Noblat, S. *J. Mol. Catal. A: Chem.* **1995**, *99*, 13-21.
178. Hamar-Thibault, S.; Moutet, J.-C.; Tingry, S. *J. Organomet. Chem.* **1997**, *532*, 31-37.
179. Caix, C.; ChardonNoblat, S.; Deronzier, A.; Moutet, J. C.; Tingry, S. *J. Organomet. Chem.* **1997**, *540*, 105-111.
180. Moutet, J. C.; Cho, L. Y.; Duboc-Toia, C.; Menage, S.; Riesgo, E. C.; Thummel, R. P. *Nouv. J. Chim.* **1999**, *23*, 939-944.
181. Lopez, C.; Moutet, J.-C.; Saint-Aman, E. *J. Chem. Soc., Faraday Trans.* **1996**, *92*, 1527.
182. Bettega, H. C. Y.; Hissler, M.; Moutet, J. C.; Ziessel, R. *Chem. Mater.* **1997**, *9*, 3-5.
183. Motonaka, J.; Yabutani, T.; Maruyama, K.; Shiomi, T.; Tateishi, N.; Mishima, Y. *Bunseki Kagaku* **2002**, *51*, 1165-1170.
184. Tsujimoto, M.; Yabutani, T.; Sano, A.; Tani, Y.; Murotani, H.; Mishima, Y.; Maruyama, K.; Yasuzawa, M.; Motonaka, J. *Anal. Sci.* **2007**, *23*, 59-63.
185. Haddour, N.; Cosnier, S.; Gondran, C. *Chem. Commun.* **2004**, 2472-2473.
186. Haddour, N.; Chauvin, J.; Gondran, C.; Cosnier, S. *J. Am. Chem. Soc.* **2006**, *128*, 9693-9698.
187. Ionescu, R. E.; Cosnier, S.; Herzog, G.; Gorgy, K.; Leshem, B.; Herrmann, S.; Marks, R. S. *Enzyme Microb. Technol.* **2007**, *40*, 403-408.
188. Deronzier, A.; Moutet, J.-C.; Zsoldos, D. *J. Phys. Chem.* **1994**, *98*, 3086-3089.
189. Sigaud, M.; Li, M.; Chardon-Noblat, S.; Aires, F. J. C. S.; Soldo-Olivier, Y.; Simon, J. P.; Renouprez, A.; Deronzier, A. *J. Mater. Chem.* **2004**, *14*, 2606-2608.
190. Chardon-Noblat, S.; Pellissier, A.; Cripps, G.; Deronzier, A. *J. Electroanal. Chem.* **2006**, *597*, 28-38.
191. Ding, S.-N.; Cosnier, S.; Shan, D.; Sun, Y.-M.; Wang, Y. *Electrochem. Commun.* **2010**, *12*, 905-908.
192. Gao, B.-H.; Ding, S.-N.; Wang, Y.-H.; Dai, Y.; Xia, J.; Sun, Y.-M.; Cosnier, S. *Electroanal.* **2013**, *25*, 697-702.
193. Le Goff, A.; Holzinger, M.; Cosnier, S. *Electrochim. Acta* **2011**, *56*, 3633-3640.
194. Cheung, K. C.; Guo, P.; So, M. H.; Lee, L. Y. S.; Ho, K. P.; Wong, W. L.; Lee, K. H.; Wong, W. T.; Zhou, Z. Y.; Wong, K. Y. *J. Organomet. Chem.* **2009**, *694*, 2842-2845.
195. Cheung, K. C.; Guo, P.; So, M. H.; Zhou, Z. Y.; Lee, L. Y.; Wong, K. Y. *Inorg. Chem.* **2012**, *51*, 6468-6475.

Chapter 2 Experimental

2.1 Introduction

The research performed in this work, primarily focused on the fabrication and characterisation of polymer films. Firstly, the monomer component of these films needed to be synthesised, before electrochemical polymerisation of the monomer could be performed.

The polymers examined in this work were polypyrrole (PPy), poly[*N*-2-azidoethyl)pyrrole] ($PPyEtN_3$), poly[*N*-ferrocenyl-(ethylpyrrole)-1*H*-[1,2,3]triazole] ($PPyEtN_3C_2HFc$), and poly[4,4'-bis-(*N*-propyl-3-pyrrole-carbamoyl)-2,2'-bipyridine] ($poly[(PyPrNHCO)_2Bipy]$). These materials were deposited on to Au and Pt substrates as either bulk or nanowire morphologies. A mono-electrolytic system usually consisting of either lithium perchlorate, tetrabutylammonium perchlorate or tetrabutylammonium hexafluorophosphate in MeCN was utilised when depositing bulk films, while a bielectrolytic co-solvent system, comprised of lithium perchlorate and ammonium dihydrogen phosphate in ethanol and water, was required for the deposition of nanowire films. The electroactivity of the films was investigated using CV, while surface analyses were performed using SEM, TEM and FESEM. The chemical structure, degree of oxidation and doping levels were examined by employing Raman spectroscopy, FTIR spectroscopy, EDX spectroscopy and XPS. Various tetrazolate and 2,2'-bipyridine TM carbonyl containing compounds were also synthesised, using microwave assisted and conventional methods, while employing air-sensitive techniques. Characterisation of these compounds was performed utilising NMR spectroscopy, FTIR spectroscopy and mass spectrometry.

Specific details regarding the synthesis and characterisation of all compounds and polymer films are presented in the ensuing sections.

2.2 Common chemicals

Solvents were dried and degassed as described in the literature. Toluene, hexane Et_2O, THF and heptane were refluxed over sodium wire/benzophenone and stored under nitrogen or argon gas. DCM and $CHCl_3$ were pre-dried by overnight stirring in calcium hydride and then refluxed and stored under nitrogen or argon gas. NMR spectroscopy solvents, $CDCl_3$ and $(CD_3)_2SO$ were supplied by Sigma Aldrich and used without further purification but 5 cycles of freeze-pump-thaw were applied under certain circumstances. Magnesium sulfate anhydrous (98%), Millipore H_2O, MeOH, EtOH, acetone and anhydrous DMF were supplied by Sigma Aldrich and used without further purification. Gases were supplied by BOC.

2.3 Common instrumentation

2.3.1 Spectroscopy

EDX spectroscopy was performed using a Hitachi S-3200-N with a tungsten filament, which possessed a maximum magnification of ×200,000 with a resolution of 3.5 nm. It was equipped with an Oxford Instruments INCAx-act EDX system with silicon drift detector. The X-ray detector was extended to it maximum distance within the chamber. The voltage was maintained at 8 kV along with a beam current of 30 μA. The stage was tilted to 45º at a working distance of 15-17 mm and the largest aperture (0) was utilised. The spectra were analysed using Oxford Instruments INCA software.

FTIR spectra were recorded on a Perkin Elmer Precisely Spectrum 100 FTIR spectrometer. Solid samples were finely ground with an excess of dry KBr, which had been kept in the oven at 250ºC, then pressed into a disc using a stainless steel die, under a pressure of 9 tonnes. Liquid samples were dissolved in solvent and injected between two potassium bromide windows held within a metal cell. They were also mixed with Nujol oil and pipetted in between two NaCl plates, which were kept in a desiccator, then compressed together by a metal casing for analyses. The spectra were processed using Perkin Elmer Spectrum software version 6.3.1.0132.

ATR-FTIR spectra were recorded on a Perkin Elmer Precisely Spectrum 100 FTIR spectrometer. Liquid samples were analysed on a trough 45^{o} ZnSe crystal and solid samples were analysed on a flat-plate 45^{o} ZnSe crystal, both positioned on top of a Pike Technologies ATR Max II. The spectra were processed using Perkin Elmer Spectrum software version 6.3.1.0132.

OTTLe cell measurements were performed using an Omni-Cell Specac P/N 1800, provided by Dr Mary Pryce, Dublin City University (DCU), Dublin. OTTLe cell spectra were recorded on a Perkin Elmer Precisely Spectrum 100 FTIR spectrometer and processed using Perkin Elmer Spectrum software version 6.3.1.0132. The OTLLE cell consists of an air tight solution cell, composed of two calcium fluoride windows held inside a metal casing. The liquid sample (approx. 0.3 cm^3) was injected between the two calcium fluoride windows, where the cell was modified with a bare Ag wire *pseudo*-reference electrode and two 1 cm^2 Pt mesh electrodes (working and counter) for the performance of spectroelectrochemistry.

NMR spectra were recorded on a Bruker Avance spectrometer that operated at 300 MHz for ^{1}H and 75.5 MHz for ^{13}C. The probe temperature was 30 ^{o}C. Internal standards used for ^{1}H and ^{13}C NMR spectroscopy were tetramethylsilane and residual protonated solvent. The spectra were processed using Bruker Biospin 2005 Topspin software version 1.3 and ICON NMR 4.0.7 Build 1.

UV-Vis spectroscopy was performed using a UNICAM UV 500 UV-Visible spectrometer, while employing quartz (1 cm path length) cuvettes and the spectra were analysed using UNICAM Ltd Vision software version 3.40 with Maths software version 19.00.

Raman spectroscopy measurements were performed at the Focas Institute in Dublin Institute of Technology (DIT), Dublin by Dr Anne Shanahan, using a Horiba Jobin-Yvon LabRAM 1B confocal Raman microscope spectrometer, while employing a solid state diode laser (100 mW) at a laser line of 660 nm. The samples were analysed using a KBr pellet containing polymer, which had been scrapped from the electrode surface. The spectra were analysed using Bruker OPUS software version 5.5.

XPS was performed at the Materials and Surface Science Institute (MSSI) in University of Limerick (UL), Limerick by Dr Fathima Laffir, using a Kratos Analytical AXIS 165 X-ray photoelectron spectrometer. The sample energy was kept between 20-30 °C. A mono Al K_α 1486.58 eV X-ray gun was used at a power of 150 W (10 mA, 15 kV). The pass energy was set to 160 eV for the survey spectra and 20 eV for the narrow regions. The C 1s line at 284.8 eV was used as charge reference. Construction and peak fitting of the synthetic peaks in the narrow region spectra used a Shirely type background and the synthetic peaks were of a mixed Gaussian-Lorentzian type. The relative sensitivity factors used were from CasaXPS library, containing Scofield cross-sections.

2.3.2 Microscopy

SEM was performed using a Hitachi S-3200-N with a tungsten filament, which possessed a maximum magnification of ×200,000 with a resolution of 3.5 nm. It was equipped with an Oxford Instruments INCAx-act EDX system with silicon drift detector.

FESEM was performed at the Tyndall National Institute, Cork by Mr Vincent Lodge, using a Hitachi S-4000 with a cold cathode field emission electron source, which possessed a maximum magnification of ×300,000 with a resolution of 1.5 nm. It was equipped with a Princeton Gamma Technology Avalon 8000 EDX system with liquid nitrogen cooled Li(Si) detector. Also utilised at the Tyndall National Institute, Cork, was a FEI Nova NanoSEM 630 ultra-high resolution SEM with a field emission gun (FEG), which possessed a maximum magnification of ×1,000,000 with a resolution of 1 nm. It was equipped with an Oxford Instrument X-MAX 80 large area Si diffused detector. Before the analyses of electrode samples were performed, the electrodes were dried *in vacuo* and then placed in the sputter-coater for 30 minutes *in vacuo*. The chamber was pumped until 0.1 mB was attained. Employing a thickness monitor, the Au/Pd target deposited a coating of 10-15 nm under argon gas.

TEM was performed at the Tyndall National Institute, Cork by Dr Patrick Carolan, using a JEOL 2010 with a LaB_6 filament operating at 200 kV. Samples were prepared by removing the polymer from the substrate using a surgical blade and then

sonicated in EtOH for 10 minutes. Several drops of the polymer/EtOH mixture were pipetted into the TEM grid and allowed to evaporate for analysis. Data processing was performed using Oxford Instruments INCA software and ImageJ software version 1.46r.

Light microscopy was performed using an Olympus BX161 optical microscope and images were analysed using Cell^F software and ImageJ software version 1.46r.

2.3.3 Electrochemistry

CV, CPA and spectroelectrochemical measurements were performed using Scribner Associates Corrware software version 3.0. CV, CPA and spectroelectrochemical analyses were performed using Scribner Associates Corrview software version 3.3c and Bio-Logic Science Instruments EC-lab version 10.23. OTTLe cell measurements were performed using an Omni-Cell Specac P/N 1800, applying potentials *via* a Solartron potentiostat model 1285 coupled with Scribner Associates Corrware software version 3.0.

2.3.4 Spectrometry

Mass spectrometry was performed by Ms Barbara Woods, using a liquid chromatographer (LC) model 1200 Series (Agilent Corp, Santa Clara, CA). The injection volume was 10 mm^3 and the column was an Agilent Eclipse XBD-C18 (Agilent), 5-micron with a mobile phase of A = acetonitrile with 0.1 % formic acid and B = 0.1 % formic acid in water. The gradient was 5% A to 100% over 15 minutes at a flow rate of 0.5 cm^3 min^{-1}. The liquid chromatographer/time-of-flight mass spectrometer (TOF-MS) was a model 6210 TOF LC/MS (Agilent Corp, Santa Clara, CA) with an electrospray source positive and negative (ESI+/-), capillary 3,500 V, nebuliser spray 30 psig, drying gas 5 dm^3 min^{-1}, source temperature 325 ^oC. The fragmentor was used at 175 V. Reference masses (Agilent Solution) were 121.050873, 149.02332, 322.048121, 922.009798, 1221.990633, 1521.971475 and 2421.91399 m/z. LC-MS grade acetonitrile and water were obtained from Sigma Aldrich, while formic acid was obtained from Agilent.

2.4 Synthesis

All syntheses were performed under nitrogen or argon using normal Schlenk conditions unless stated otherwise. All apparatus was oxygen and moisture free, being evacuated and filled with nitrogen or argon gas for three cycles before initiation of reaction. In certain cases anhydrous solvents were degassed using 5 cycles of freeze-pump-thaw. Microwave assisted synthesis was performed using a CEM Corporation Discovery microwave coupled with an Explorer arm and experimental methods were programed utilising Synergy software version 1.5.8.

2.4.1 Chemicals

1*H*-pyrrole (≥98%, distilled using a Kugelrohr and stored in absence of light at -40 °C), 1,10-dibromodecane (97%), sodium hydride (60% dispersion in mineral oil), sodium azide (99.5%), *N*-(2-bromoethyl)pyrrole (>97%), *N*-(3-bromopropyl)pyrrole (>95%) and *N*-(2-chloroethyl)pyrrole (>98%), ammonium dihydrogen phosphate (99.999%), lithium perchlorate (99%), sodium perchlorate (≥99%), potassium perchlorate (≥99%), lithium nitrate (99.99%), lithium sulfate (99.99%), lithium tetrafluoroborate (98%), lithium bis(trifluoromethane)sulfonimide (99.95%), ferrocene (98%), tetrabutylammonium perchlorate (99%), tetrabutylammonium tetrafluoroborate (99%), tetrabutylammonium hexafluorophosphate (99%), ethynylferrocene (97%, was kept in the fridge at 4 °C), copper(0) powder (99.999%, washed with dilute nitric acid, water and acetone, then dried *in vacuo* before use), diisopropylethylamine (≥90%), 2,6-lutidine (98%), *N*-(2-cyanoethyl)pyrrole (>99%), lithium aluminium hydride powder (95%), 4,4’-dimethyl-2,2’-bipyridine (99%), sulphuric acid (95%), sodium dichromate hexahydrate (99%), thionyl chloride (99%), triethylamine (99%), hexacarbonyl chromium (98%), hexacarbonyl molybdenum (98%), hexacarbonyl tungsten (97%), 2,2’-bipyridine (≥99%), sodium dodecyl sulfate (≥99%), cyclopentadienylmolybdenum(II) tricarbonyl, dimer (98%), benzonitrile anhydrous (99%), 2-thiophenecarbonitrile (99%), benzyl cyanide (98%), cyclopentadienyldicarbonyl(tetrahydrofuran)iron(II) tetrafluoroborate silver hexafluorophosphate (99.99%) were purchased from Sigma Aldrich or TCIEurope. All chemicals were used as received.

2.4.2 Synthesis of *N*-(azidoalkyl)pyrroles

The monomer *N*-(10-azidodecyl)pyrrole was prepared by adapting methods reported by Janata and co-workers, Urya and co-workers and using a method reported by Li and co-workers in the literature.[1-3] The monomers *N*-(2-azidoethyl)pyrrole and *N*-(3-azidopropyl)pyrrole were prepared *via* a method reported by Storey and co-workers in the literature.[4]

2.4.2.1 Synthesis of *N*-(10-azidodecyl)pyrrole ($PyDeN_3$)

2.4.2.1a Synthesis of *N*-(10-bromodecyl)pyrrole (PyDeBr)

1*H*-Pyrrole (0.91 cm^3, 13 mmol) was injected into anhydrous THF (20 cm^3) and stirred. Sodium hydride, 60% in mineral oil (0.786 g, 20 mmol, 1.5 eq.) was added to this and the reaction mixture was stirred for 2 h resulting with the evolution of hydrogen gas and the precipitation of pyrrole sodium salt. The THF was removed *in vacuo* and anhydrous DMSO (20 cm^3) was added for dissolution of the white precipitate. 1,10-Dibromodecane (9.8 g, 33 mmol, 2.5 eq.) was stirred in anhydrous THF (50 cm^3) while the pyrrole sodium salt/DMSO solution was added slowly *via* dropping funnel over 4 h. The reaction mixture was left to stir for 12 h at R.T.. The mixture was then added to water (50 cm^3) and the crude product was extracted with Et_2O (5 × 25 cm^3), dried over $MgSO_4$, filtered and dried *in vacuo*. This was purified *via* column chromatography on silica gel utilising *n*-hexane/DCM (10:1), yielding a yellow oil (0.800 g, 22%).

^{1}H-NMR: ($CDCl_3$) δ = 6.84 (t, 2H, *J* = 2.1 Hz, Py-H_α), 6.34 (t, 2H, *J* = 2.1 Hz, Py-H_β), 4.05 (t, 2H, *J* = 6.9 Hz, Py-CH_2), 3.59 (t, 2H, *J* = 6.9 Hz, Br-CH_2), 2.06 (m, 2H, CH_2), 1.97 (m, 2H, CH_2), 1.65 (m, 2H, CH_2), 1.53 (m, 10H, (CH_2)$_5$) ppm.

ESI-MS: Calc. $(M+H)^+$ = 286.1165 g mol^{-1}; found $(M+H)^+$ = 286.1165 g mol^{-1} (0.05 ppm).

2.4.2.1b Synthesis of *N*-(10-azidodecyl)pyrrole (PyDeN$_3$)

N-(10-bromodecyl)pyrrole (0.200 g, 0.7 mmol) was added to anhydrous DMF (3 cm^3). Sodium azide (0.230 g, 3.5 mmol, 5 eq.) was added to the stirred solution and the reaction mixture was heated at reflux temperature for 12 hours under nitrogen in the absence of light. The mixture was permitted to cool to R.T. and filtered on a Buchner funnel to remove excess sodium azide. The filtrate was dissolved in DCM (25 cm^3) and washed with water (5 × 20 cm^3), dried over $MgSO_4$, filtered and then dried *in vacuo* to produce a brown oil (0.172 g, 99%).

^{1}H-NMR: ($CDCl_3$) δ = 6.66 (t, 2H, *J* = 2.1 Hz, Py-H_α), 6.14 (t, 2H, *J* = 2.1 Hz, Py-H_β), 3.87 (t, 2H, *J* = 7.2 Hz, Py-CH_2), 3.26 (t, 2H, *J* = 5.7 Hz, N_3-CH_2), 1.77 (m, 2H, CH_2), 1.61 (m, 2H, CH_2), 1.36 (m, 2H, CH_2), 1.31 (m, 10 H, (CH_2)$_5$) ppm.

FTIR: (KBr) 3101 ν(CH), 2929 $\nu_{as}(CH_2)$, 2855 $\nu_s(CH_2)$, 2095 $\nu_{as}(N_3)$, 1258 $\nu_s(N_3)$, 1088 ν(C–C)/ν(C–N), 814 (C–H_β), 721 γ(C–H_α)/(CH_2 rock) cm^{-1}.

ESI-MS: Calc. $(M+NH_4)^+$ = 266.2339 g mol^{-1}; found $(M+NH_4)^+$ = 266.2343 g mol^{-1} (1.42 ppm).

2.4.2.2 Synthesis of *N*-(2-azidoethyl)pyrrole (PyEtN$_3$)

N-(2-chloroethyl)pyrrole (1.68 cm^3, 15 mmol) was added to anhydrous DMF (3 cm^3). Sodium azide (1.500 g, 23 mmol, 1.5 eq.) was added to the stirred solution and the reaction mixture was heated at reflux temperature for 12 h under N_2 gas in the absence of light. The mixture was permitted to cool to R.T. and filtered on a Buchner funnel to remove excess sodium azide. The filtrate was dissolved in DCM (50 cm^3) and washed with water (5 × 40 cm^3), dried over $MgSO_4$, filtered and then dried *in vacuo* to produce a brown oil (1.980 g, 99%).

^{1}H-NMR: ($CDCl_3$) δ = 6.72 (t, 2H, *J* = 2.1 Hz, Py-H_α), 6.23 (t, 2H, *J* = 2.1 Hz, Py-H_β), 4.06 (t, 2H, *J* = 5.7 Hz, Py-CH_2), 3.59 (t, 2H, *J* = 5.7 Hz, N_3-CH_2) ppm.

^{13}C-NMR: ($CDCl_3$) δ = 120.7 (2C, Py-C_α), 109.0 (2C, Py-C_β), 52.4 (2C, N_3-CH_2), 48.7 (2C, Py-CH_2) ppm.

FTIR: (KBr) 3100 ν(CH), 2929 $\nu_{as}(CH_2)$, 2870 $\nu_s(CH_2)$, 2099 $\nu_{as}(N_3)$, 1258 $\nu_s(N_3)$, 1090 ν(C–C)/ν(C–N), 826 $\gamma(C–H_\beta)$, 728 $\gamma(C–H_\alpha)$ cm^{-1}.

2.4.2.3 Synthesis of *N*-(3-azidopropyl)pyrrole (PyPrN$_3$)

The reaction was performed according to the procedure described for the *N*-(2-azidoethyl)pyrrole monomer. *N*-(3-bromopropyl)pyrrole (1.000 g, 5.3 mM) was utilised during the synthesis, which produced a brown oil (0.791 g, 99%).

^{1}H-NMR: ($CDCl_3$) δ = 6.67 (t, 2H, *J* = 2.1 Hz, Py-H_α), 6.18 (t, 2H, *J* = 2.1 Hz, Py-H_β), 3.41 (t, 2H, *J* = 6.6 Hz, Py-CH_2), 3.27 (t, 2H, *J* = 6.6 Hz, N_3-CH_2), 2.02 (m, 2H, $CH_2CH_2CH_2$) ppm.

FTIR: (KBr) 3100 ν(CH), 2933 $\nu_{as}(CH_2)$, 2876 $\nu_s(CH_2)$, 2100 $\nu_{as}(N_3)$, 1258 $\nu_s(N_3)$, 1089 ν(C–C)/ν(C–N), 727 $\gamma(C–H_\alpha)$ cm^{-1}.

2.4.3 Synthesis of ferrocene substituted triazole alkyl pyrroles

$PyDeN_3C_2H_3Fc$ and $PyEtN_3C_2H_3Fc$ were prepared by a adaption of a method outlined by Bauerle and co-workers.[5] Tetrakis(acetonitrile)copper(I) hexafluorophosphate had been previously prepared by a method reported by Kubas and co-workers and stored under N_2 gas.[6]

2.4.3.1 Synthesis of ferrocene substituted triazole decyl pyrrole (PyDeN$_3$C$_2$HFc) [1]

N-(10-azidodecyl)pyrrole (0.315 g, 1.3 mmol), ethynylferrocene (0.275 g, 1.27 mmol) and tetrakis(acetonitrile)copper(I) hexafluorophosphate (0.024 g, 0.06 mmol, 5 mol%) were dissolved in degassed anhydrous. Copper(0) powder (0.081 g, 1.27 mmol) was washed with 30% aqueous HNO_3, H_2O and acetone, dried under vacuum and then added to the solution. The mixture was stirred at ambient temperature for 3 days. Progression of the reaction was followed by TLC and upon completion the mixture was diluted with DCM. The copper metal was removed by filtration and solvent was removed *in vacuo* to yield the crude product. This was purified *via* column chromatography on silica gel utilising DCM:EtOAc (9.25:0.75), which produced an orange oil (0.383 g, 66 %).

^{1}H-NMR: ($CDCl_3$) δ = 7.43 (s, 1H, triazole-*H*), 6.59 (t, 2H, *J* = 2.1 Hz, Py-H_α), 6.08 (t, 2H, *J* = 2.1 Hz, Py-H_β), 4.68 (t, 2H, *J* = 1.5 Hz, Cp-H_α), 4.30 (t, 2H, *J* = 7.2 Hz, triazole-CH_2), 4.25 (t, 2H, *J* = 1.5 Hz, Cp-H_β), 4.03 (s, 5H, Cp-*H*), 3.80 (t, 2H, *J* = 7.2 Hz, Py-CH_2), 1.88 (m, 2H, CH_2), 1.69 (m, 2H, CH_2), 1.25 (m, 12H, (CH_2)$_6$) ppm.

^{13}C-NMR: ($CDCl_3$) δ = 146.5 (1C, vinyl-C_{quat}), 120.3 (2C, Py-C_α), 118.7 (1C, triazole-*C*H), 107.6 (2C, Py-C_β), 75.5 (1C, Cp-C_{quat}), 69.5 (5C, Cp-*C*), 68.5 (2C, Cp-C_α), 66.5 (2C, Cp-C_β), 50.1 (2C, triazole-*C*H_2), 49.5 (2C, Py-*C*H_2), 31.4 (2C, *C*H_2), 30.1 (2C, *C*H_2), 29.2 (2C, *C*H_2), 29.2 (2C, *C*H_2), 29.0 (2C, *C*H_2), 28.8 (2C, *C*H_2), 26.6 (2C, *C*H_2), 26.3 (2C, *C*H_2) ppm.

FTIR: (KBr) 3117 ν(Cp-H), 3078 ν(CH), 2929 $\nu_{as}(CH_2)$, 2854 $\nu_s(CH_2)$, 1106 ν_{as}(C-C), 1000 γ(C–H), 819 γ(C–H), 720 γ(C–H_α)/(CH_2 rock), 506 ν_{as}(Fe–Cp), 488 δ_{as}(ring tilt) cm^{-1}.

ESI-MS: Calc. $(M+H)^+$ = 459.2206 g mol^{-1}; found $(M+H)^+$ = 459.2216 g mol^{-1} (2.26 ppm).

R_f: 0.55 (silica gel, DCM/EtOAc:9.25/0.75).

2.4.3.2 Synthesis of ferrocene substituted triazole ethyl pyrrole (PyEtN_3C_2HFc) [2]

N-(2-azidoethyl)pyrrole (0.191 g, 1.4 mM) and ethynylferrocene (0.300 g, 1.4 mmol) were dissolved in degassed anhydrous MeCN (10 cm^3). Base (2,6-lutidine or diisopropylethylamine (DIPEA)) (1.62 cm^3 or 2.43 cm^3, 14 mmol, 10 eq.) was injected into the stirred solution. Copper(0) powder (0.089 g, 14 mmol) was washed with 30% aqueous HNO_3, H_2O and acetone, dried under vacuum and then added to the solution. Tetrakis(acetonitrile)copper(I) hexafluorophosphate (0.026 g, 0.07 mmol, 5 mol%) was added and the mixture was stirred at ambient temperature for 8 h. Progression of the reaction was followed by TLC and upon completion the mixture was diluted with DCM (50 cm^3). The copper metal was removed by filtration, solvent was evaporated *in vacuo* and the remaining residue was purified by column chromatography on silica gel using DCM/EtOAc (9.5:1.0) to produce a

yellow/orange solid (0.315 g, 65%) and (0.478 g, 99%) for the reactions employing 2,6-lutidine and DIPEA respectively.

^{1}H-NMR: ($CDCl_3$) δ = 6.74 (s, 1H, triazole-H), 6.50 (t, 2H, *J* = 2.1 Hz, Py-H_α), 6.18 (t, 2H, *J* = 2.1 Hz, Py-H_β), 4.65 (s, 2H, Fc), 4.63 (t, 2H, *J* = 5.7 Hz, Py-CH_2), 4.37 (t, 2H, *J* = 5.7 Hz, triazole-CH_2), 4.28 (t, 2H, Fc), 4.06 (s, 5H, Fc) ppm.

^{13}C-NMR: ($CDCl_3$) δ = 146.9 (1C, C_{quat}), 120.6 (2C, Py-C_α), 119.9 (1C, triazole-CH), 109.6 (2C, Py-C_β), 75.3 (1C, C_{quat}), 69.7 (5C, Fc), 68.8 (2C, Fc), 66.7 (2C, Fc), 51.6 (2C, Py-CH_2), 49.6 (2C, triazole-CH_2) ppm.

FTIR: (KBr) 3109 ν(Cp–H), 3095 ν(CH), 2928 $\nu_{as}(CH_2)$, 2860 $\nu_s(CH_2)$, 1430 ν(C–C), 1103 ν(C–C), 1000 γ(C–H), 815 γ(C–H_β), 730 (C–H_α), 513 ν_{as}(Fe–Cp) 486 δ_{as}(ring tilt) cm^{-1}.

ESI-MS: Calc. $(M+H)^+$ = 347.0954 g mol^{-1}; found $(M+H)^+$ = 347.0945 g mol^{-1} (-2.48 ppm).

R_f: 0.27 (silica gel, DCM/EtOAc:9.5/1.0).

2.4.4 Synthesis of ferrocene substituted triazole ethyl polypyrrole films

$PPyEtN_3C_2H_3Fc$ was prepared by a adaption of a method outlined by Bauerle and co-workers.[5] Tetrakis(acetonitrile)copper(I) hexafluorophosphate had been previously prepared by a method reported by Kubas and co-workers and stored under N_2 gas.[6]

2.4.4.1 Synthesis of ferrocene substituted triazole ethyl polypyrrole films *via* CuAAC chemistry of $PPyEtN_3$ with FcCCH ($PPyEtN_3C_2HFc$) [4]

Electrodes modified with a $PPyEtN_3$ film were submerged in a solution of degassed anhydrous MeCN containing FcCCH (5 mM), $[Cu^I(MeCN)_4]PF_6$ (10 mol%) and DIPEA or 2,6-lutidine (100 mM). Copper(0) powder (5 mM) was added to the solution and this was left at ambient temperature for 30 h with constant stirring. The coated electrodes were steeped and rinsed with acetonitrile several times, washed with methanol and diethyl ether and dried for 12 h *in vacuo*.

2.4.5 Synthesis of 2,2'-bipyridine and dipiperidine tetracarbonyl Group 6 metal complexes

The Group 6 metal complexes, 2,2'-bipyridine tetracarbonyl chromium(0), molybdenum(0) and tungsten(0) were prepared by a method reported by Green and co-workers and Paz and co-workers.[7,8] Tetracarbonyl dipiperidine molybdenum(0) was prepared by a method reported by Darensbourg and Kump.[9]

2.4.5.1 Synthesis of 2,2'-bipyridine tetracarbonyl chromium(0) ($Cr^0(CO)_4$(Bipy))

Hexacarbonyl chromium(0) (0.200 g, 0.91 mmol) and 2,2'-bipyridine (0.142 g, 0.91 mmol) was suspended in anhydrous toluene (3 cm^3) and anhydrous diglyme (1.5 cm^3) inside a Teflon-lined digestion vessel (LDV) and heated to 180 °C for 10 min at 300 W. The reaction mixture was cooled to R.T. and precipitation was completed with the addition of anhydrous hexane (3 × 6 cm^3). The solid was collected by filtration and dried *in vacuo* to give the title compound as a red solid (0.175 g, 60%).

FTIR: (DCM) 2010 ν(C≡O), 1901 ν(C≡O), 1880 ν(C≡O), 1829 ν(C≡O) cm^{-1}.

2.4.5.2 Synthesis of 2,2'-bipyridine tetracarbonyl molybdenum(0) ($Mo^0(CO)_4$(Bipy))

Hexacarbonyl molybdenum (0.200 g, 0.75 mmol) and 2,2'-bipyridine (0.118 g, 0.75 mmol) was suspended in anhydrous toluene (3 cm^3) and diglyme (1.5 cm^3) inside a Teflon LDV and heated to 180 °C for 1 min at 300 W. The reaction mixture was cooled to R.T. and precipitation was completed with the addition of anhydrous hexane (3 × 6 cm^3). The solid was collected by filtration and dried *in vacuo* to give the title compound as a red solid (0.277 g, 90%).

FTIR: (KBr) 2009 ν(C≡O), 1916 ν(C≡O), 1869 ν(C≡O), 1812 ν(C≡O) cm^{-1}.

2.4.5.3 Synthesis of ($Mo^0(CO)_4$(Bipy)) from tetracarbonyl dipiperidine molybdenum(0) ($Mo^0(CO)_4(pip)_2$)

2.4.5.3a Synthesis of tetracarbonyl dipiperidine molybdenum(0) ($Mo^0(CO)_4(pip)_2$)

Hexacarbonyl molybdenum (1.020 g, 3.8 mmol) and piperidine (2.521 cm^3, 25 mmol) were refluxed in degassed anhydrous heptane (25 cm^3) for 4 h under argon from which a yellow solid precipitated. The solution was filtered hot to remove any heptane soluble $Mo(CO)_5$(pip). The precipitate was washed with cold heptane and dried *in vacuo* to give the title compound as a yellow solid (0.681 g, 70%).

FTIR: (KBr) 2012 ν(C≡O), 1914 ν(C≡O), 1888 ν(C≡O), 1839 ν(C≡O) cm^{-1}.

2.4.5.3b Synthesis of ($Mo^0(CO)_4$(Bipy)) from tetracarbonyl dipiperidine molybdenum(0) ($Mo^0(CO)_4(pip)_2$)

Tetracarbonyl dipiperidine molybdenum(0) (0.200 g, 0.54 mmol) and 2,2'-bipyridine (0.084 g, 0.54 mmol) were refluxed in degassed anhydrous DCM (15 cm^3) overnight under nitrogen in the absence of light. This produced a pink reaction mixture, which was allowed to cool and it was dried *in vacuo*.

FTIR: (KBr) 2010 ν(C≡O), 1917 ν(C≡O), 1871 ν(C≡O), 1814 ν(C≡O) cm^{-1}.

A synonymous procedure was performed at ambient temperature, which failed to produce the tetracarbonyl dipiperidine molybdenum(0) complex, confirmed using FTIR spectroscopy. Also, an analogous procedure, employing a poly[4,4'-bis-(*N*-propyl-3-pyrrole-carbamoyl)-2,2'-bipyridine] film, submerged in the reaction mixture was performed at room temperature, failed to produce a TM carbonyl functionalised poly[4,4'-bis-(*N*-propyl-3-pyrrole-carbamoyl)-2,2'-bipyridine] film, which was confirmed using FTIR spectroscopy.

2.4.6 Synthesis of 4,4'-bis-(*N*-propyl-3-pyrrole-carbamoyl)-2,2'-bipyridine ((PyPrNHCO)$_2$Bipy) [5]

N-(3-aminopropyl)pyrrole was prepared by a method reported by Marks and co-workers.[10] 2,2'-bipyridine-4,4'-dicarboxylic acid was prepared by method reported by Meyer and co-workers.[11] 2,2'-bipyridine-4,4'-diacyl chloride was prepared by method reported by Hupp and co-workers.[12] 4,4'-bis-(*N*-propyl-3-pyrrole-carbamoyl)-2,2'-bipyridine was prepared by adaptation of the method outlined by Beer and co-workers.[13]

2.4.6.1 Synthesis of *N*-(3-aminopropyl)pyrrole (PyPyNH$_2$)

N-(2-cyanoethyl)pyrrole (7.66 cm^3, 67 mmol) in Et_2O (50 cm^3) was added dropwise to a suspension of lithium aluminium hydride (6.325 g, 167 mmol) in Et_2O (150 cm^3), and the mixture was refluxed for 10 h under N_2. After cooling, the excess hydride was destroyed by successive addition of water (6.1 cm^3), a solution of 15% (w/v) NaOH (18.2 cm^3), and water (6.1 cm^3). The solution was heated to 40 °C for 2 h and filtered on Celite before drying *in vacuo*, which produced the title compound as yellow oil (7.800 g, 94%).

^{1}H-NMR: ($CDCl_3$) δ = 6.66 (t, *J* = 1.8 Hz, 2H, Py-H$_\alpha$), 6.14 (t, *J* = 1.8 Hz, 2H, Py-H$_\beta$), 3.97 (t, 2H, Py-C*H*$_2$), 2.70 (m, 2H, $CH_2CH_2CH_2$), 1.90 (m, 2H, C*H*$_2$NH$_2$) ppm.

FTIR: (Nujol) 3368 ν_{as}(N–H), 3298 ν_s(N–H), 3097 ν(C–H), 726 γ(C–H$_\alpha$) cm^{-1}.

2.4.6.2 Synthesis of 2,2'-bipyridine-4,4'-dicarboxylic acid ((HOCO)$_2$Bipy)

4,4'-dimethyl-2,2'-bipyridine (25 g, 136 mmol) in heated conc. H_2SO_4 (300 cm^3, 70-80 °C) had sodium dichromate hexahydrate (80.337 g, 307 mmol) added to it slowly and the temperature (70-80 °C) was kept constant during the transfer. The dark green mixture was poured over ice/H_2O (700 cm^3), producing a bright yellow precipitate. This was isolated by vacuum filtration and washed with H_2O. The solid was refluxed in 50% HNO_3 (300 cm^3) for 4 h. The cooled solution was then poured

over ice and diluted with H_2O (800 cm^3). Vacuum filtration and washing with H_2O (800 cm^3) produced the title compound as a white solid (29.823 g, 90%).

FTIR: (KBr) 3430 ν(O–H), 1718 ν(C=O) cm^{-1}.

M.P.: 320 - 325 ^oC.

2.4.6.3 Synthesis of 2,2'-bipyridine-4,4'-diacyl chloride ((ClCO)$_2$Bipy)

2,2'-bipyridine-4,4'-dicarboxylic acid (1.752 g, 7.17 mmol) was refluxed in thionyl chloride (30 cm^3) for 5 h. The thionyl chloride was eliminated by rotary evaporation in excess toluene (40 cm^3), which produced the title compound as a yellow solid. (1.996 g, 99%)

^{1}H-NMR: ($CDCl_3$) δ = 9.08 (d, *J* = 0.6 Hz, *J* = 1.8 Hz, 2H, Bipy-*H*), 8.97 (dd, *J* = 0.6 Hz, *J* = 5.1Hz, 2H, Bipy-*H*), 7.97 (dd, *J* = 1.8 Hz, *J* = 5.1Hz, 2H, Bipy-*H*) ppm.

FTIR: (KBr) 3067 ν(C–H), 1754 ν(C=O), 1550 ν(C=N) cm^{-1}.

2.4.6.4 Synthesis of 4,4'-bis-(*N*-propyl-3-pyrrole-carbamoyl)-2,2'-bipyridine ((PyPrNHCO)$_2$Bipy) [5]

N-(3-aminopropyl)pyrrole (0.885 g, 7.1 mmol) and triethylamine (0.993 cm^3, 7.1 mmol) stirred in DCM (60 cm^3), had a solution of 2,2'-bipyridine-4,4'-diacyl chloride (1.001 g, 3.56 mmol) in DCM (60 cm^3) added to it dropwise, over 5 min. The solution was stirred for 24 h and H_2O (60 cm^3) was added. The resultant bi-phasic solution was stirred for 15 min. The solution was filtered under vacuum, washed with DCM (2 × 60 cm^3), then H_2O, MeOH and Et_2O and dried to produce the title compound as a pink solid (1.006 g, 62%).

^{1}H-NMR: ($(CD_3)_2SO$) δ = 8.95 (t, *J* = 5.1 Hz, 2H, CON*H*), 8.87 (d, *J* = 4.8 Hz, 2H, Bipy 6,6'), 8.80 (s, 2H, Bipy 3,3'), 7.85 (dd, *J* = 0.9 Hz, *J* = 4.8 Hz, 2H, Bipy 5,5'), 6.79 (pt, *J* = 1.8 Hz, 4H, Py-H$_\alpha$), 5.99 (pt, *J* = 1.8 Hz, 4H, Py-H$_\beta$), 3.96 (pt, *J* = 6.9 Hz, 4H, Py-C*H*$_2$), 3.29 (pt, *J* = 6.0 Hz, 4H, CONHC*H*$_2$), 1.99 (m, 4H, $CH_2CH_2CH_2$) ppm.

^{13}C-NMR: ($(CD_3)_2SO$) δ = 164.7 (R*C*ONH), 155.5 (Bipy 2,2'), 150.0 (Bipy 6,6'), 142.9 (Bipy 4,4'), 121.9 (Bipy 5,5'), 120.5 (Py-C_α), 118.2 (Bipy 3,3'), 107.5 (Py-C_β), 46.4 (Py-*C*H_2), 37.0 (CONH*C*H_2), 31.0 (CH_2*C*$H_2$$CH_2$) ppm.

FTIR: (KBr) 3297(s) ν_s(N–H), 1638(s) ν(C=O), 1555 ν(C=N), 1535(s) δ(N–H)/ν(C–N), 1501 ν(Py ring), 1284 ν(C–N), 727 γ(C–H_α) cm^{-1}.

ESI-MS: Calc. $(M+H)^+$ = 457.2347 g mol^{-1}; found $(M+H)^+$ = 457.2326 g mol^{-1} (-4.48 ppm).

2.4.7 Synthesis of tetracarbonyl (4,4'-bis-(*N*-propyl-3-pyrrole-carbamoyl)-2,2'-bipyridine) Group 6 metal complexes

The Group 6 metal complexes, tetracarbonyl (4,4'-bis(*N*-propyl-3-pyrrole-carbamoyl)-2,2'-bipyridine) chromium(0), molybdenum(0) and tungsten(0) were prepared by adaptation of the method outlined by Green and co-workers and Paz and co-workers.[7,8]

2.4.7.1 Synthesis of tetracarbonyl (4,4'-bis-(*N*-propyl-3-pyrrole-carbamoyl)-2,2'-bipyridine) chromium(0) ($Cr^0(CO)_4((PyPrNHCO)_2Bipy)$) [6]

Hexacarbonyl chromium(0) (0.089 g, 0.34 mmol) and 4,4'-bis-(*N*-propyl-3-pyrrole-carbamoyl)-2,2'-bipyridine (0.184 g, 0.40 mmol) were suspended in toluene (3 cm^3) and diglyme (1.5 cm^3) in a Teflon LDV and heated to 180 °C for 10 min at 300 W. The reaction mixture was cooled to R.T. and precipitation was completed with the addition of hexane (3 × 6 cm^3). The solid was collected by filtration and dried *in vacuo* to give the title compound as a red solid (0.159 g, 64%).

^{1}H-NMR: ($(CD_3)_2SO$) δ = 8.96 (d, *J* = 5.1 Hz, 2H, Bipy 6,6'), 8.94 (t, *J* = 5.1 Hz, 2H, CON*H*), 8.86 (s, 2H, Bipy 3,3'), 7.95 (dd, *J* = 1.2 Hz, *J* = 4.8 Hz, 2H, Bipy 5,5'), 6.79 (t, *J* = 1.8 Hz, 4H, Py-H_α), 5.99 (t, *J* = 1.8 Hz, 4H, Py-H_β), 3.96 (t, *J* = 7.5 Hz, 4H, Py-C*H*$_2$), 3.34 (q, 4H, CONHC*H*$_2$), 1.98 (m, 4H, CH_2C*H*$_2$$CH_2$) ppm.

^{13}C-NMR: ($(CD_3)_2SO$) δ = 206.5 (*C*≡O), 165.0 (R*C*ONH), 155.9 (Bipy 2,2'), 150.9 (Bipy 6,6'), 142.9 (Bipy 4,4'), 123.4 (Bipy 5,5'), 120.5 (Py-C_β), 119.3 (Bipy 3,3'), 107.6 (Py-C_α), 46.4 (Py-*C*H_2), 37.0 (CONH*C*H_2), 31.0 ($CH_2CH_2CH_2$) ppm.

FTIR: (KBr) 2006, 1899, 1878, 1826 ν(C≡O) cm^{-1}.

ESI-MS: Calc. M-($Cr(CO)_4$+H)$^+$ = 457.2347 g mol^{-1}; found M-($Cr(CO)_4$+H)$^+$ = 457.2355 g mol^{-1} (1.86 ppm).

2.4.7.2 Synthesis of tetracarbonyl (4,4'-bis-(*N*-propyl-3-pyrrole-carbamoyl)-2,2'-bipyridine) molybdenum(0) ($Mo^0(CO)_4$((PyPrNHCO)$_2$Bipy)) [7]

Hexacarbonyl molybdenum(0) (0.200 g, 0.76 mmol) and 4,4'-bis-(*N*-propyl-3-pyrrole-carbamoyl)-2,2'-bipyridine (0.346 g, 0.76 mmol) was suspended in toluene (3 cm^3) and diglyme (1.5 cm^3) in a LDV and heated at 180 °C for 1 min at 300 W. The reaction mixture was cooled to R.T. and precipitation was completed with the addition of hexane (3 × 6 cm^3). The solid was recrystallised from acetone with water, collected by filtration, and dried *in vacuo* to give the title compound as a red solid (0.480 g, 95%).

^{1}H-NMR: ($(CD_3)_2SO$) δ = 9.13 (d, *J* = 5.1 Hz, 2H, Bipy 6,6'), 9.08 (t, *J* = 5.1 Hz, 2H, CON*H*), 8.96 (s, 2H, Bipy 3,3'), 7.95 (dd, *J* = 1.2 Hz, *J* = 5.1 Hz, 2H, Bipy 5,5'), 6.79 (t, *J* = 1.8 Hz, 4H, Py-H_α), 5.99 (t, *J* = 1.8 Hz, 4H, Py-H_β), 3.98 (t, *J* = 6.9 Hz, 4H, Py-C*H*$_2$), 3.36 (q, 4H, CONHC*H*$_2$), 2.00 (m, 4H, $CH_2CH_2CH_2$) ppm.

^{13}C-NMR: ($(CD_3)_2SO$) δ = 204.8 (*C*≡O), 163.5 (R*C*ONH), 154.7 (Bipy 2,2'), 153.1 (Bipy 6,6'), 143.5 (Bipy 4,4'), 123.9 (Bipy 5,5'), 120.6 (Py-C_α), 118.2 (Bipy 3,3'), 107.6 (Py-C_β), 46.4 (Py-*C*H_2), 37.1 (CONH*C*H_2), 31.0 ($CH_2CH_2CH_2$) ppm.

FTIR: (KBr) 2011, 1902, 1878, 1830 ν(C≡O) cm^{-1}.

ESI-MS: Calc. (M+H-($Mo(CO)_4$))$^+$ = 457.2347g mol^{-1}; found (M+H-($Mo(CO)_4$))$^+$ = 457.2383 g mol^{-1} (7.99 ppm).

2.4.7.3 Synthesis of tetracarbonyl (4,4'-bis-(*N*-propyl-3-pyrrole-carbamoyl)-2,2'-bipyridine) tungsten(0) ($W^0(CO)_4((PyPrNHCO)_2Bipy)$) [8]

Hexacarbonyl tungsten(0) (0.032 g, 0.09 mmol) and 4,4'-bis-(*N*-propyl-3-pyrrole-carbamoyl)-2,2'-bipyridine (0.041 g, 0.09 mmol) were suspended in toluene (3 cm^3) and diglyme (1.5 cm^3) in a LDV and heated to 180 °C for 20 min at 300 W. The reaction mixture was cooled to R.T. and precipitation was completed with the addition of hexane (3 × 6 cm^3). The solid was collected by filtration and dried *in vacuo* to give the title compound as a red solid (0.037 g, 55%).

^{1}H-NMR: ($(CD_3)_2SO$) δ = 9.23 (d, *J* = 5.1 Hz, 2H, Bipy 6,6'), 9.11 (t, *J* = 5.1 Hz, 2H, CON*H*), 9.02 (s, 2H, Bipy 3,3'), 7.99 (dd, *J* = 1.2 Hz, *J* = 5.7 Hz, 2H, Bipy 5,5'), 6.79 (t, *J* = 1.8 Hz, 4H, Py-H_α), 6.05 (t, *J* = 1.8 Hz, 4H, Py-H_β), 3.99 (t, *J* = 6.9 Hz, 4H, Py-CH_2), 3.38 (q, 4H, CONHCH_2), 2.00 (m, 4H, $CH_2CH_2CH_2$) ppm.

^{13}C-NMR: ($(CD_3)_2SO$) δ = 201.4 (*C*≡O), 163.5 (R*C*ONH), 156.8 (Bipy 6,6'), 151.0 (Bipy 2,2'), 143.3 (Bipy 4,4'), 124.9 (Bipy 5,5'), 122.0 (Bipy 3,3'), 120.5 (Py-C_α), 107.6 (Py-C_β), 46.3 (Py-*C*H_2), 37.2 (CONH*C*H_2), 31.0 ($CH_2CH_2CH_2$) ppm.

FTIR: (KBr) 2005, 1890, 1872, 1825 ν(C≡O) cm^{-1}.

ESI-MS: Calc. $(M)^+$ = 752.1574 g mol^{-1}; found $(M)^+$ = 752.1577 g mol^{-1} (-0.38 ppm).

2.4.8 Synthesis of *N*-2-tetrazolate substituted tricarbonyl cyclopentadienyl molybdenum(II) complexes

Benzonitrile tricarbonyl cyclopentadienyl molybdenum(II) tetrafluoroborate, tricarbonyl cyclopentadienyl 2-thiophencarbonitrile molybdenum(II) tetrafluoroborate and benzyl cyanide tricarbonyl cyclopentadienyl molybdenum(II) tetrafluoroborate were prepared by adaptation of the method outlined by Louattani and Suades[14] and reported by a previously member of our research group, Dr Ciara O'Brien.[15] Tricarbonyl cyclopentadienyl *N*-2-(5-tetrazolatephenyl) molybdenum(II), tricarbonyl cyclopentadienyl *N*-2-(5-tetrazolate-2-thiophene) molybdenum(II) and

tricarbonyl cyclopentadienyl *N*-2-(5-tetrazolate-1-benzyl) molybdenum(II) were prepared by adaptation of the method outlined by Palazzi *et al.*.[16]

2.4.8.1 Synthesis of tricarbonyl cyclopentadienyl *N*-2-(5-tetrazolatephenyl) molybdenum(II) [9]

2.4.8.1a Synthesis of benzonitrile tricarbonyl cyclopentadienyl molybdenum(II) tetrafluoroborate ($[CpMo^{II}(CO)_3NCPh]BF_4$)

Benzonitrile (0.211 cm^3, 2.1 mmol) in DCM (5 cm^3) was added to a solution of cyclopentadienyl molybdenum(II) tricarbonyl, dimer (0.5 g, 1.05 mmol) in DCM (5 cm^3). Silver tetrafluoroborate (0.408 g, 2.1 mmol) was added to the solution and the reaction mixture was stirred at R.T. for 7 days under N_2. The silver precipitate was filtered off on Celite and the solution was evaporated to dryness. The residue was washed in Et_2O and dried *in vacuo* to give the title compound as an orange solid (0.336 g, 76%).

^{1}H-NMR: ($CDCl_3$) δ = 7.95 (dt, *J* = 1.2 Hz, *J* = 7.2 Hz, 2H, phenyl-CH_{orto}), 7.72 (tt, *J* = 1.2 Hz, *J* = 7.5 Hz, 1H, phenyl-CH_{para}), 7.54 (t, *J* = 7.5 Hz, 2H, phenyl-CH_{meta}), 6.06 (s, 5H, Cp-*H*) ppm.

^{13}C-NMR: ($CDCl_3$) δ = 233.8 ($C{\equiv}O_{trans}$), 223.7 ($C{\equiv}O_{cis}$), 143.7 ($C{\equiv}N$), 135.7 (phenyl-C_{para}), 134.1 (phenyl-C_{orto}), 129.7 (phenyl-C_{meta}), 109.3 (phenyl-C_{quart}), 96.6 (Cp-*C*) ppm.

FTIR: (KBr) 2272 ν(C≡N), 2075 ν(C≡O), 2044 ν(C≡O), 1975 ν(C≡O) cm^{-1}.

2.4.8.1b Synthesis of tricarbonyl cyclopentadienyl *N*-2-(5-tetrazolatephenyl) molybdenum(II) ($CpMo^{II}(CO)_3N_4CPh$) [9]

To a solution of benzonitrile tricarbonyl cyclopentadienyl molybdenum(II) tetrafluoroborate (0.070 g, 0.16 mmol) in DCM (10 cm^3) at R.T. was added an excess of sodium azide (0.052 g, 0.81 mmol). The resulting suspension was stirred at R.T. for 70 h. The mixture was filtered on Celite, which was washed with DCM (3 × 10 cm^3) and evaporated to dryness. Column chromatography of the residue on Al_2O_3 with DCM as eluent yielded cyclopentadienyl molybdenum(II) tricarbonyl,

dimer as a purple fraction. Further elution with a mixture DCM/MeCN (9.5:0.5, v/v) and removal of solvent *in vacuo* produced the title compound as a yellow solid. (0.046 g, 74%)

^{1}H-NMR: ($CDCl_3$) δ = 8.10 (dt, *J* = 1.8 Hz, *J* = 6.6 Hz, 2H, phenyl-CH_{orto}), 7.43 (tt, *J* = 1.8 Hz, *J* = 6.9 Hz, 2H, phenyl-CH_{para}), 7.40 (m, 2H, phenyl-CH_{meta}), 5.70 (s, 5H, Cp-*H*) ppm.

^{13}C-NMR: ($CDCl_3$) δ = 237.4 ($C{\equiv}O_{trans}$), 224.4 ($C{\equiv}O_{cis}$), 164.8 (tetrazolate-C_5), 128.2 (phenyl-C_{quart}), 128.1 (phenyl-C_{para}), 127.5 (phenyl-C_{orto}), 125.6 (phenyl-C_{meta}), 94.4 (Cp-*C*) ppm.

FTIR: (KBr) 2052 ν(C≡O), 1971 ν(C≡O), 1956 ν(C≡O), 1640 ν(C=N) cm^{-1}.

ESI-MS: Calc. $(M)^+$ = 391.9802 g mol^{-1}; found $(M)^+$ = 391.9819 g mol^{-1} (4.47 ppm).

R_f: 0.52 (Al_2O_3, DCM/MeCN:9.5/0.5).

2.4.8.2 Synthesis of tricarbonyl cyclopentadienyl *N*-2-(5-tetrazolate-2-thiophene molybdenum(II) [10]

2.4.8.2a Synthesis of tricarbonyl cyclopentadienyl 2-thiophenecarbonitrile molybdenum(II) tetrafluoroborate ($[CpMo^{II}(CO)_3NCT]BF_4$)

2-Thiophenecarbonitrile (0.077 cm^3, 0.82 mM) in DCM (5 cm^3) was added to a solution of cyclopentadienyl molybdenum(II) tricarbonyl, dimer (0.2 g, 0.41 mM) in DCM (5 cm^3). Silver tetrafluoroborate (0.163 g, 0.82 mM) was added to the solution and the reaction mixture was stirred at R.T. for 7 days under N_2. The silver precipitate was filtered off on Celite and the solution was evaporated to dryness. The residue was washed in Et_2O and dried *in vacuo* to give the title compound as an orange solid (0.111 g, 62%).

^{1}H-NMR: ($CDCl_3$) δ = 8.24 (dd, *J* = 1.2 Hz, *J* = 3.9 Hz, 1H, thiophene-C*H*), 7.84 (dd, *J* = 1.2 Hz, *J* = 5.1 Hz, 1H, thiophene-C*H*), 7.23 (dd, 1H, *J* = 3.9 Hz, *J* = 5.1 Hz, thiophene-C*H*), 6.05 (s, 5H, Cp-H) ppm.

^{13}C-NMR: ($CDCl_3$) δ = 233.8 (*C*≡O_{trans}), 223.4 (*C*≡O_{cis}), 144.0 (thiophene-*C*H), 137.7 (thiophene-*C*H), 129.0 (thiophene-*C*H), 106.1 (thiophene-C_{quart}), 96.6 (Cp-*C*) ppm.

FTIR: (KBr) 2253 ν(C≡N), 2073 ν(C≡O), 2040(w) ν(C≡O), 1973 ν(C≡O) cm^{-1}.

2.4.8.2b Synthesis of tricarbonyl cyclopentadienyl *N*-2-(5-tetrazolate-2-thiophene) molybdenum(II) ($CpMo^{II}(CO)_3N_4CT$) [10]

To a solution of tricarbonyl cyclopentadienyl 2-thiophenecarbonitrile molybdenum(II) tetrafluoroborate (0.100 g, 0.23 mmol) in degassed anhydrous DCM (10 cm^3) at R.T. was added an excess of sodium azide (0.737 g, 1.13 mmol). The resulting suspension was stirred at R.T. for 15 h. The mixture was filtered on Celite and evaporated to dryness. Column chromatography of the residue on Al_2O_3 with DCM as eluent gave cyclopentadienyl molybdenum(II) tricarbonyl, dimer as a purple fraction. Further elution with a mixture DCM/MeCN (9.5:0.5, v/v) and removal of solvent *in vacuo* produced the title compound as a yellow solid. (0.060 g, 67%)

^{1}H-NMR: ($CDCl_3$) δ = 7.68 (dd, *J* = 1.2 Hz, *J* = 3.6 Hz, 1H, 3-thiophene-C*H*), 7.34 (dd, *J* = 1.2 Hz, *J* = 5.1 Hz, 1H, 5-thiophene-C*H*), 7.09 (dd, *J* = 3.6 Hz, *J* = 5.1 Hz, 1H, 4-thiophene-C*H*), 5.71 (s, 5H, Cp-*H*) ppm.

^{13}C-NMR: ($CDCl_3$) δ = 237.3 (*C*≡O_{trans}), 224.2 (*C*≡O_{cis}), 160.7 (tetrazolate-C_5), 130.3 (thiophene-C_{quart}), 126.5 (4-thiophene-*C*), 125.1 (thiophene-*C*), 125.0 (thiophene-*C*), 94.4 (Cp-*C*) ppm.

FTIR: (KBr) 2058 ν(C≡O), 1951 ν(C≡O) cm^{-1}, 1632 (C=N) cm^{-1}.

ESI-MS: Calc. $(M+H)^+$ = 398.9444 g mol^{-1}; found $(M+H)^+$ = 397.9409 g mol^{-1} (-8.76 ppm).

R_f: 0.51 (Al_2O_3, DCM/MeCN:9.5/0.5).

2.4.8.3 Synthesis of tricarbonyl cyclopentadienyl *N*-2-(5-tetrazolate-1-benzyl) molybdenum(II) [11]

2.4.8.3a Synthesis of benzyl cyanide tricarbonyl cyclopentadienyl molybdenum(II) tetrafluoroborate ($[CpMo^{II}(CO)_3NCBz]BF_4$)

Benzyl cyanide (0.168 g, 1.46 mmol) in DCM (5 cm^3) was added to a solution of cyclopentadienyl molybdenum(II) tricarbonyl, dimer (0.036 g, 0.73 mmol) in DCM (5 cm^3). Silver tetrafluoroborate (0.288 g, 1.46 mmol) was added to the solution and the reaction mixture was stirred at R.T. for 7 days under N_2. The silver precipitate was filtered off on Celite and the solution was evaporated to dryness. The residue was washed in Et_2O and dried *in vacuo* to give the title compound as an orange solid. (0.480 g, 73%)

^{1}H-NMR: ($CDCl_3$) δ = 7.37 (m, 4H, benzyl-C$H_{orto,meta}$), 7.29 (m, 1H, benzyl-CH_{para}), 6.00 (s, 5H, Cp-*H*), 4.33 (s, 2H, benzyl-CH_2) ppm.

^{13}C-NMR: ($CDCl_3$) δ = 224.3 (*C*≡O$_{trans}$), 215.6 (*C*≡O$_{cis}$), 129.7 (benzyl-*C*), 129.3 (*C*≡N), 128.8 (benzyl-*C*), 128.6 (benzyl-*C*), 128.1 (benzyl-*C*$_{quart}$), 96.4 (Cp-*C*), 26.5 (benzyl-*C*H_2) ppm.

FTIR: (KBr) 2280 ν(C≡N), 2067(br) ν(C≡O), 1972 ν(C≡O) cm^{-1}.

2.4.8.3b Synthesis of tricarbonyl cyclopentadienyl *N*-2-(5-tetrazolate-1-benzyl) molybdenum(II) ($CpMo(CO)_3N_4CBz$) [11]

To a solution of benzyl cyanide tricarbonyl cyclopentadienyl molybdenum(II) tetrafluoroborate (0.027 g, 0.06 mmol) in DCM (8 cm^3) at R.T. was added an excess of sodium azide (0.020 g, 0.3 mmol). The resulting suspension was stirred at R.T. for 70 h. The mixture was filtered on Celite and evaporated to dryness. Column chromatography of the residue on Al_2O_3 with DCM as eluent yielded cyclopentadienyl molybdenum(II) tricarbonyl, dimer as a purple fraction. Further elution with a mixture DCM/MeCN (9.5:0.5, v/v) and removal of solvent *in vacuo* produced the title compound as a yellow solid. (0.020 g, 82 %)

^{1}H-NMR: ($CDCl_3$) δ = 7.28 (m, 3H, benzyl-C$H_{meta,para}$), 7.20 (m, 2H, benzyl-CH_{orto}), 5.65 (s, 5H, Cp-*H*), 4.18 (s, 2H, benzyl-CH_2) ppm.

^{13}C-NMR: ($CDCl_3$) δ = 238.6 (*C*≡O$_{trans}$), 225.5 (*C*≡O$_{cis}$), 165.7 (tetrazolate-C_5), 138.5 (benzyl-C_{quart}), 129.0 (benzyl-*C*), 128.5 (benzyl-*C*), 126.4 (benzyl-C_{para}), 94.4 (Cp-*C*), 31.8 (benzyl-*C*H_2) ppm.

FTIR: (KBr) 2060 ν(C≡O), 1972(br) ν(C≡O), 1632 ν(C=N) cm^{-1}.

ESI-MS: Calc. $(M)^+$ = 407.0036 g mol^{-1}; found $(M)^+$ = 407.0053 g mol^{-1} (4.12 ppm). Calc. $(M+Na)^+$ = 428.9856 g mol^{-1}; found $(M+Na)^+$ = 428.9864 g mol^{-1} (1.94 ppm).

R_f: 0.52 (Al_2O_3, DCM/MeCN:9.5/0.5).

2.4.9 Synthesis of *N*-2-(tetrazolate-2-ethylpyrrole) substituted dicarbonyl cyclopentadienyl iron(II) complex [13]

Dicarbonyl *N*-(2-cyanoethyl)pyrrole cyclopentadienyl iron(II) tetrafluoroborate and dicarbonyl cyclopentadienyl *N*-2-(5-tetrazolate-2-ethylpyrrole) iron(II) were prepared by adaptation of the method reported by Palazzi *et al.* and Catheline and Astruc in the literature.[16,17]

2.4.9.1 Synthesis of dicarbonyl *N*-(2-cyanoethyl)pyrrole cyclopentadienyl iron(II) tetrafluoroborate ([CpFe^{II}(CO)$_2$NCEtPy]BF_4) [12]

N-(2-cyanoethyl)pyrrole (0.012 cm^3, 0.11 mmol) was injected into a solution of dicarbonyl cyclopentadienyl tetrahydrofuran iron(II) tetrafluoroborate (0.034 g, 0.1 mmol) in degassed anhydrous DCM (3 cm^3). The reaction mixture was stirred for 17 h at R.T. under N_2 in the absence of light. After 17 h the reaction mixture had changed from a red to an orange mixture. The DCM was removed *in vacuo* and the crude product was employed in the next step of the synthesis.

2.4.9.2 Synthesis of dicarbonyl cyclopentadienyl *N*-2-(5-tetrazolate-2-ethylpyrrole) iron(II) (CpFe^{II}(CO)$_2$N$_4$CEtPy) [13]

Sodium azide (0.020 g, 0.3 mmol) was added to a solution of dicarbonyl *N*-(2-cyanoethyl)pyrrole cyclopentadienyl iron(II) tetrafluoroborate (0.039 g, 0.1 mmol) in

DCM (3 cm^3). The reaction mixture was stirred at R.T. under N_2 in the absence of light. After 24 h the suspension had changed from an orange to a yellow mixture. The sodium tetrafluoroborate side-product and excess sodium azide were filtered off on Celite, washed with DCM (3 × 5 cm^3) and the solvent was then removed *in vacuo*. ^1H and ^{13}C NMR spectroscopy and mass spectrometry were performed on the crude product. Preparative TLC of the yellow residue was conducted on Al_2O_3 using a mixture of DCM/MeCN (4:1 v/v). Isolation of the product was not possible at this stage due to complications after separation, so characterisation from the crude material was reported but it was estimated that a 28% conversion to the title compound occurred.

^{1}H-NMR: ($CDCl_3$) δ = 6.56 (s, 2H, Py-$H_{\beta a}$), 6.08 (s, 2H, Py-H_α), 4.86 (s, 5H, Cp-*H*), 4.49 (s, 2H, Py-CH_2), 3.20 (s, 2H, N_4C-CH_2) ppm.

^{13}C-NMR: ($CDCl_3$) δ = 211.1 (*C*≡O), 120.8 (Py-C_β), 108.7 (Py-C_α), 86.0 (Cp-*C*), 48.5 (Py-*C*H_2), 29.5 (N_4C-*C*H_2) ppm.

ESI-MS: Calc. $(M+H)^+$ = 340.0491 g mol^{-1}; found $(M+H)^+$ = 340.0492 g mol^{-1} (0.18 ppm).

2.5 Electrochemical techniques

2.5.1 Electrochemical cell set-up

The electrochemical cell set-up that was employed during experiments consisted of a cylindrical glass vial with dimensions of approx. 50 mm high × 25 mm wide. During air-sensitive electrochemical analyses an air-tight lid was employed. A three electrode set-up was employed connected to a potentiostat, controlled *via* computer. A Pt mesh or Pt wire was used as a counter electrode. A saturated calomel electrode (SCE) or a Ag/AgCl was used as a reference electrode for aqueous electrochemical analyses, while a $Ag/AgNO_3$, a bare silver wire *pseudo*-reference or a SCE incorporating a salt bridge were used as a reference electrode during nonaqueous electrochemical analyses. The salt bridge if employed during nonaqueous electrochemical analyses was composed of a glass U-tube containing 1000 mM electrolytic salt in degassed anhydrous solvent (experiment dependent) retained within by glass wool.

2.5.1.1 Preparation of working electrode

The working electrodes were fabricated on site and consisted of GCE, Au or Pt substrate. This substrate was wired within a protective Teflon casing and held within this by an epoxy resin. These electrodes once constructed were ground down to a flat finish and the resistance from substrate to the exposed wire connection was tested (0.0 Ω). Prior to experimentation the substrate was ground down using a Buehler METASERV grinder polisher with Buehler SiC grinding paper (Grit P 2500). The substrate was then hand polished employing Buehler MetaDI monocrystalline diamond suspension and a Buehler polishing microcloth until a mirror finish was obtained. This was executed using successively finer diamond grades (30-1 micron), while the substrate was rinsed with distilled water and sonicated for 5 min in EtOH followed by H_2O.

2.5.1.2 Electrochemical materials

The monomers, 1*H*-pyrrole and *N*-(2-cyanoethyl)pyrrole) were purchased from Sigma Aldrich and distilled by vacuum distillation using a Kugelrohr before use. The monomers, *N*-(10-azidodecyl)pyrrole, *N*-(3-azidopropyl)pyrrole and *N*-(2-azidoethyl)pyrrole were synthesised using methods reported in the literature,[1-4] which have been described in Section 2.4.2. $PyDeN_3C_2HFc$ and $PyEtN_3C_2HFc$ were synthesised from a method adapted from the literature[5] described in 2.4.3.1. All of these monomers were stored under inert gas in the absence of light at approx. -40 ^oC.

2.5.2 Electrochemistry of metal carbonyls

$Cr^0(CO)_4$(Bipy) and $Mo^0(CO)_4$(Bipy) were prepared by the method outlined by Green and co-workers and Paz and co-workers,[7,8] as shown previously in Section 2.4.5. $Mo^0(CO)_4$((PyPrNHCO)$_2$Bipy) was prepared by adaptation of the method outlined by Green and co-workers and Paz and co-workers as shown previously in Section 2.4.7.[7,8]

2.5.2.1 Polypyrrole deposition in the presence of metal carbonyls

PPy was deposited on to a polished Au substrate from a solution containing Py (100 mM) with $LiClO_4$ (200 mM) and $Cr^0(CO)_4$(Bipy) (50 mM) in MeCN at 0.850 V vs. SCE, until a q of 0.80 C cm^{-2} was attained.

PPy was deposited on a polished Au substrate from a solution containing Py (100 mM) with NaDS (100 mM) and $Cr^0(CO)_4$(Bipy) or $Mo^0(CO)_4$(Bipy) (7 mM) in H_2O at 0.500 V vs. SCE, until a charge density of 0.10 C cm^{-2} was attained.

2.5.2.2 Cyclic voltammetry of the complexes $Mo^0(CO)_4$(Bipy) and $Mo^0(CO)_4$((PyPrNHCO)$_2$Bipy)

$Mo^0(CO)_4$(Bipy) (2 mM) or $Mo^0(CO)_4$((PyPrNHCO)$_2$Bipy) (2 mM) and $TBAPF_6$ (200 mM) were transferred to an argon containing electrochemical cell, which had been dried in the oven overnight, then flushed with gas for 5 min. Degassed anhydrous DCM (8 cm^3) was syringed into the cell and activated molecular sieves (4 Å) were added under a positive pressure of argon, which was

present at all times. A cold temperature slush of CO_2/acetone was placed around the cell and CV was performed between approx. -1.300-1.300 V vs. Ag/Ag^+ at 250 mV s^{-1}. Degassed anhydrous MeCN (6 mM) was added to the cell *via* syringe and cycling was continued.

2.5.2.3 Spectroelectrochemistry of the complex $Mo^0(CO)_4$(Bipy)

$Mo^0(CO)_4$(Bipy) (2 mM) and $TBAPF_6$ (200 mM) were transferred to an argon containing electrochemical cell, which had been dried in the oven overnight, then flushed with gas for 5 minutes. Degassed anhydrous DCM (8 cm^3) was syringed into the cell and activated molecular sieves (4 Å) were added under a positive pressure of argon, which was present at all times. A synonymous cell containing no $Mo^0(CO)_4$(Bipy) was also prepared, to be employed as a background solution for FTIR spectroscopy, when utilising the OTTLE cell. The OTTLE cell was flushed with anhydrous DCM and dried with argon before every experiment. The background scan was performed at 2 cm^{-1} resolution from 2200-1800 cm^{-1}. Once a scan of the background solution was performed the metal carbonyl solution was syringed into the OTTLE cell, making sure there were no bubbles present within the cell. An FTIR spectrum of the solution was attained at a resting potential. A spectrum was then attained every minute, while applying a constant potential of 0.500 V vs. Ag/Ag^+ for 15 minutes. A new solution was added to the cell after cleaning and drying was performed. Then a synonymous solution, which contained degassed anhydrous MeCN (6 mM) was added to the OTTLE cell. A scan at resting potential was obtained and then a constant potential of 0.500 V vs. Ag/Ag^+ was applied for 8 min during which successive scanning was performed.

2.5.3 Co-polymerisation of Py and $(PyPrNHCO)_2$Bipy

2.5.3.1 Chemical polymerisation of $(PyPrNHCO)_2$Bipy

Polymerisation was performed on a glass substrate, which had been roughened with sand paper (400 grit) to increase surface area and improve adhesion. Once the substrate had been cleaned, $(PyPrNHCO)_2$Bipy (15 mM) was applied to the surface as a thin layer. The glass substrate modified with the monomer was submerged in

DCM containing iron(III) trichloride hexahydrate (25 mM) as oxidant/dopant, and 60% perchloric acid ($HClO_4$) (100 mM) in a Teflon beaker. Upon addition of $(PyPrNHCO)_2Bipy$ to the reaction mixture, polymerisation proceeded and a black film was formed on the glass substrate. After 18 h, the slide was removed from the mixture and extensively washed with DCM, H_2O, MeOH and DCM and dried *in vacuo*.

2.5.3.2 Electrochemical polymerisation of $(PyPrNHCO)_2Bipy$

$(PyPrNHCO)_2Bipy$ (100 mM) was deposited on to the Au substrate from a solution of MeCN containing $LiClO_4$ (200 mM) and $HClO_4$ (550 mM) between 1.000 - 1.150 V vs. SCE in 0.050 V increments. The film was washed with MeCN, H_2O and MeCN, then dried *in vacuo*.

Electrochemical characterisation of the poly[$(PyPrNHCO)_2Bipy$] film was performed in monomer free MeCN containing $LiClO_4$ (200 mM), between 0.000 - 0.900 V vs. Ag/Ag^+ over 20 cycles at 100 mV s^{-1}.

2.5.3.3 Electrochemical diblock co-polymerisation of Py and $(PyPrNHCO)_2Bipy$

Py (100 mM) monomer was deposited from a solution of H_2O containing $LiClO_4$ (200 mM) by applying a potential of 0.650 V vs. SCE, until a q of 0.80 C cm^{-2} was attained. The polymer was then removed from the solution and washed with MeCN. The PPy modified substrate was transferred to a solution containing $(PyPrNHCO)_2Bipy$ (55 mM), $LiClO_4$ (200 mM) and $HClO_4$ (550 mM) in MeCN. Potentials between 0.650 - 0.900 V vs. SCE (50 mV increments) were applied until the desired charge density was attained.

2.5.4 Electrochemistry of ferrocene functionalised PPy films

2.5.4.1 Synthesis of azide substituted decyl/propyl/ethyl polypyrrole films *via* electrodeposition of bulk $PPyDeN_3$/$PPyPrN_3$/$PPyEtN_3$ films

Bulk films of $PPyDeN_3$, $PPyPrN_3$ and $PPyEtN_3$ were deposited on to Au and Pt substrates employing a solution of the respective monomer (5-35 mM) in anhydrous

degassed MeCN (3-10 cm^3) with lithium perchlorate (100 mM) present. A potential window of approx. 0.000 - 1.500 V vs. $Ag/AgNO_3$ was applied to the electrochemical cell until approx. 10 cycles had been performed. Bulk films were also deposited from using CPA by applying a constant potential of 0.850 V vs. SCE until charge densities of either 1.9 mC cm^{-2}, 4.4 mC cm^{-2}, 6.3 mC cm^{-2} and 12.6 mC cm^{-2} were obtained.

The films were characterised using CV, submerged in an electrolytic solution of $LiClO_4$ (100 mM) in anhydrous MeCN, which had been purged with argon gas for 15 minutes. Scanning was performed between 0.000 - 1.250 V vs. Ag/AgCl, at non-consecutive scan rates of 25, 50, 75, 100 and 125 mV s^{-1}.

2.5.4.2 Synthesis of azide substituted ethyl polypyrrole films *via* electrodeposition of nanowire PPyEtN$_3$ films

Nanowire films of $PPyEtN_3$ were deposited on to Au and Pt substrates employing a solution of the respective monomer (20-65 mM) in a bi-electrolytic co-solvent system consisting of $EtOH/H_2O$ (3:4) (10 cm^3) with lithium perchlorate (20 mM) and sodium dihydrogen phosphate (250-300 mM) present. An oxidising potential of between 0.700 - 0.950 V vs. SCE was applied to the electrochemical cell until the desired charge density was obtained.

The films were characterised using CV, submerged in an electrolytic solution of $LiClO_4$ (100 mM) in anhydrous MeCN, which had been purged with argon gas for 15 minutes. Scanning was performed between -0.500 - 1.000 V vs. $Ag/AgNO_3$, at non-consecutive scan rates of 25, 50, 75, 100 and 125 mV s^{-1}.

2.5.4.3 Synthesis of ferrocene substituted triazole ethyl polypyrrole films *via* electrodeposition of bulk PPyEtN$_3$C$_2$HFc film

The electroactivity of $PyEtN_3C_2HFc$ was investigated using Au substrates, while employing a solution of the respective monomer (5-50 mM) in anhydrous degassed MeCN (3-10 cm^3) with tetrabutylammonium hexafluorophosphate (100 mM) present. Potential windows within -0.500 - 1.600 V vs. $Ag/AgNO_3$ were applied to the electrochemical cell at 200 mV s^{-1}.

Bulk films of $PPyEtN_3C_2HFc$ were deposited on to the Au substrates by employing a solution of the respective monomer (50 mM) in anhydrous degassed MeCN (3-10 cm^3) with tetrabutylammonium hexafluorophosphate (100 mM). A constant potential of 1.250 V vs. $Ag/AgNO_3$ was applied to the system for 5 min until a charge density of 1.19 C cm^{-2} was attained.

The films were characterised using CV, submerged in an electrolytic solution of $TBAPF_6$ (100 mM) in anhydrous MeCN, which had been purged with argon gas for 15 min. Scanning was performed between -0.500 - 0.800 V vs. $Ag/AgNO_3$ at non-consecutive scan rates of 25, 50, 75 and 100 mV s^{-1}.

2.6 References

1. Li, Y.; Zhang, W.; Chang, J.; Chen, J.; Li, G.; Ju, Y. *Macromol. Chem. Phys.* **2008**, *209*, 322-329.
2. West, R.; Josowicz, M.; Janata, J.; Minet, I.; Hevesi, L. *J. Electrochem. Soc.* **2009**, *156*, 55-59.
3. Kim, K. S.; Kato, T.; Uryu, T. *J. Polym. Sci., Part A: Polym. Chem.* **1999**, *37*, 3877-3887.
4. Martinez-Castro, N.; Magenau, A. J. D.; Storey, R. F. *J. Polym. Sci., Part A: Polym. Chem.* **2010**, *48*, 2533-2545.
5. Bu, H. B.; Gotz, G.; Reinold, E.; Vogt, A.; Schmid, S.; Blanco, R.; Segura, J. L.; Bauerle, P. *Chem. Commun.* **2008**, 1320-1322.
6. Kubas, G. J.; Monzyk, B.; Crumblis, A. L. In *Inorg. Synth.*; John Wiley & Sons, Inc.: 2007, pp 68-70.
7. VanAtta, S. L.; Duclos, B. A.; Green, D. B. *Organometallics* **2000**, *19*, 2397-2399.
8. Braga, S. S.; Coelho, A. C.; Gonçalves, I. S.; Almeida Paz, F. A. *Acta Crystallogr. E* **2007**, *63*, 780-782.
9. Darensbourg, D. J.; Kump, R. L. *Inorg. Chem.* **1978**, *17*, 2680-2682.
10. Abu-Rabeah, K.; Polyak, B.; Ionescu, R. E.; Cosnier, S.; Marks, R. S. *Biomacromolecules* **2005**, *6*, 3313-3318.
11. Hoertz, P. G.; Staniszewski, A.; Marton, A.; Higgins, G. T.; Incarvito, C. D.; Rheingold, A. L.; Meyer, G. J. *J. Am. Chem. Soc.* **2006**, *128*, 8234-8245.
12. Kim, Y.; Vanhelmont, F. W. M.; Stern, C. L.; Hupp, J. T. *Inorg. Chim. Acta* **2001**, *318*, 53-60.
13. Vickers, M. S.; Martindale, K. S.; Beer, P. D. *J. Mater. Chem.* **2005**, *15*, 2784-2790.
14. Louattani, E.; Suades, J. *J. Organomet. Chem.* **2000**, *604*, 234-240.
15. O'Brien, C. T., Ph.D. Thesis, National University of Ireland Maynooth (NUIM), Ireland, **2004**.
16. Palazzi, A.; Stagni, S.; Bordoni, S.; Monari, M.; Selva, S. *Organometallics* **2002**, *21*, 3774-3781.
17. Catheline, D.; Astruc, D. *Organometallics* **1984**, *3*, 1094-1100.

Chapter 3 Deposition of poly[N-(azidoalkyl)pyrrole] bulk and nanowire films

3.1 Introduction

The growth of *N*-functionalised azide polypyrrole films has attracted significant attention, as their azide moiety is capable of facilitating facile post-polymerisation functionalisation of the polymer with a vast array of compounds.[1-5] Also, an ever increasing substantial interest is manifesting itself, in regards to the deposition of polymer nanowire films.[6-9] More recently, there have been specific developments concerning the utilisation of a direct electrochemical deposition process, in the absence of a hard or soft template such as aluminium oxide or sodium dodecyl sulfate (NaDS) respectively.[10-14] Coined the 'template-free' or 'template-less' approach, this technique possesses a more environmentally friendly method, as it employs few hazardous chemicals and little procedural time is necessary. Requiring decreased labour investment, this procedure permits the completion of a greater number of experiments in a smaller time window, thus delivering more data for the analysis and optimisation of the fabricated nanowire films. These are all very important attributes, especially when pertaining to the production of conducting polymers in industry. The desirability of a polymer film possessing nanowire morphology stems from its greater specific surface area, compared to that of conventional bulk polypyrrole films. The greater specific surface area belonging to the nanowire morphology permits the faster ingress/egress of dopant counterions, yielding a faster electrochemical response. Furthermore, it retains an increased number of sites experiencing interaction with molecules/compounds, which is crucial in drug delivery and sensing.

3.2 Results and discussion

In this chapter, we engage in studies concerning the polymerisation of bulk *N*-substituted azide pyrrole (Py) monomers, *N*-(10-azidodecyl)pyrrole ($PyDeN_3$), *N*-(3-azidopropyl)pyrrole ($PyPrN_3$) and *N*-(2-azidoethyl)pyrrole) ($PyEtN_3$). Preliminary investigations were performed on poly[*N*-(10-azidodecyl)pyrrole] ($PPyDeN_3$) and poly[*N*-(3-azidopropyl)pyrrole] ($PPyPrN_3$), while more extensive work was executed on the ethyl analogue, poly[*N*-(2-azidoethyl)pyrrole] ($PPyEtN_3$). Concentration was focussed on this specifically selected monomer as it possesses attributes, in terms of solubility in polar solvents, deeming it the most viable candidate for successful polymerisation into a nanowire film. The following *N*-substituted Py monomers were synthesised using literature procedures.[2,5,15,16]

3.2.1 Deposition and characterisation of bulk poly[*N*-(azidoalkyl)pyrrole] films

3.2.1.1 Poly[*N*-(10-azidodecyl)pyrrole]

The $PyDeN_3$ monomer was synthesised by adapting methods reported by both Janata and co-workers and Urya and co-workers, while also using a method reported by Li and co-workers in the literature.[5,15,16] $PPyDeN_3$ films have been grown previously using similar conditions to those used in this research.[5] Before proceeding with the electrochemical polymerisation studies, the electrochemical activity and the peak oxidation potential (E_{pox}) of the monomer was determined, using a solution of $PyDeN_3$ (20 mM), in anhydrous acetonitrile (MeCN) with lithium perchlorate ($LiClO_4$) (100 mM) as the electrolyte. Polymerisation was achieved by scanning for 8 cycles in the appropriate potential window (0.000 - 1.400 V vs. Ag/AgCl) (Figure 3.1).

The oxidation of the monomer was depicted by the presence of an oxidation peak shoulder at approx. 1.200 V vs. Ag/AgCl, which was comparable to other *N*-alkyl Py monomers.[5] The first cycle exhibits the 'trace-crossing' or 'nucleation loop', observed due to polymer nucleation on the substrate.[17] From the literature, it is known that growth of polypyrrole (PPy) is indicated by the increase in the capacitance current and the formation of the *quasi*-reversible redox couple associated

with the doping/de-doping of the growing polymer, which moves to more positive potentials as the polymer thickness increases.[15] Polymer manifestation was evident after the first scan due to the appearance of a broad capacitance cathodic current (0.500 - 0.000 V vs. Ag/AgCl) in the reverse scan indicating reduction of the deposited film, while also corresponding to the visual development of a black polymer on the substrate surface. Further cycling up to approx. 8 scans resulted in increased currents for the redox process of polymer doping/de-doping, as is characteristic for the growth of polymer films. During cycling the anodic peak potential (E_{pa}) and the cathodic peak potential (E_{pc}) both shift to more positive potentials by approx. 0.200 and 0.050 V vs. Ag/AgCl respectively, representing an increase in resistance of the polymer film as it increases in thickness.[15,18] Shifts of this magnitude have been reported for other long chained CP, as the long alkyl chain has the ability to disturb the planarity of the polymer backbone,[4] which affects the conjugation of the bonded Py units and therefore, the global conductivity of the film.[15] It was observed that if the polymer was grown for more than 8 cycles at these conditions, the CVs displayed a peak capacitance current for the polymer that dropped gradually with each successive cycle, producing a resistive film. In addition, if the growth of the polymer was attempted using potentials greater than 1.500 V vs. Ag/AgCl, the capacitance current was observed to rapidly decrease after approx. 3 cycles. This was due to overoxidation of the polymer induced by application of an excessive anodic switching potential (E_{λ}).[15]

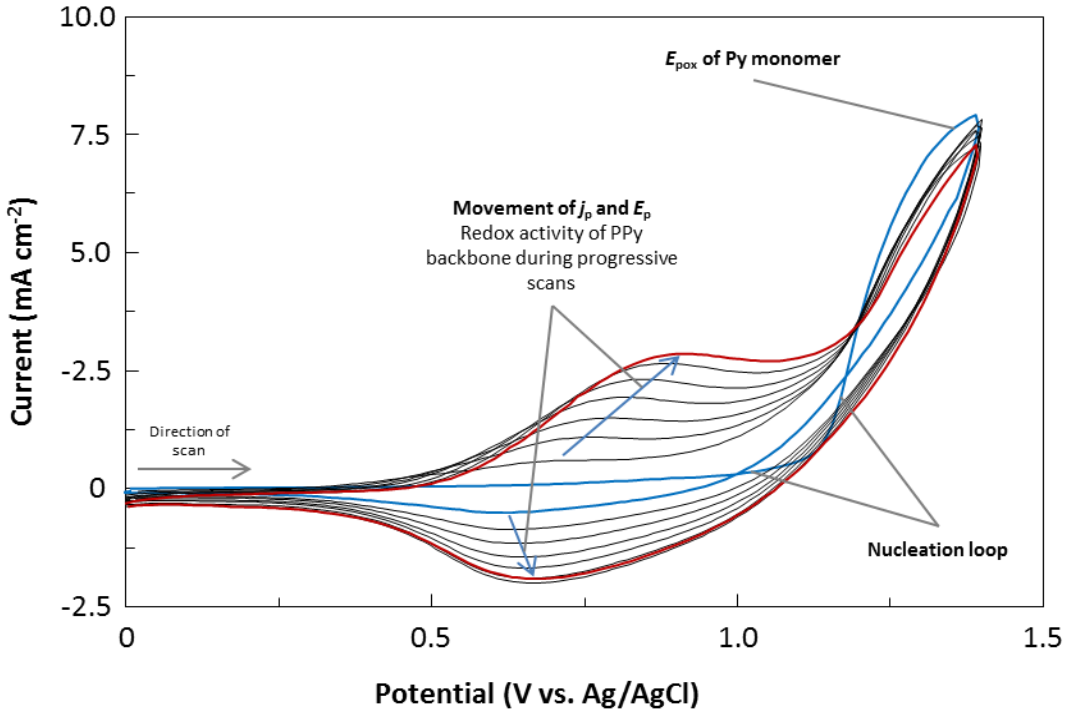

Figure 3.1: CVs recorded from a reaction medium involving $PyDeN_3$ (20 mM) and $LiClO_4$ (100 mM) in MeCN, utilising the Au substrate at a scan rate of 100 mV s^{-1}. The polymer was grown for 8 cycles (first (—) and last (—) cycle)).

$PPyDeN_3$ formed on the substrate as a thin black film, when grown using the conditions given in Figure 3.1. It was then washed with fresh MeCN and characterised using FTIR spectroscopy, SEM, EDX spectroscopy and CV. In order to determine that the polymer was formed with the azide moiety still intact, the film was scrapped of the electrode and ground into KBr, so that an FTIR spectrum could be recorded. The resulting spectrum (Figure 3.2 (b) (—)), along with that for the monomer (Figure 3.2 (a) (—)), were similar to that previously reported in the literature.[5] The bands at 2095 cm^{-1} and 2094 cm^{-1} corresponded to the azide ν_1 asymmetric stretch[5] for the monomer and polymer, respectively. Also, the band at 1258 cm^{-1} in both spectra were assigned to the ν_2 symmetric stretch of the azide.[19] The presence of these bands represented the intact azide moiety, attached to the Py backbone after polymerisation had concluded. The bands at 2929 cm^{-1} and 2854 cm^{-1} were assigned to the CH aliphatic stretching vibrations.[20] The broad band at approx. 1626 cm^{-1} was assigned to residual H_2O remaining within the polymer. This may be present due to the incorporation of solvated perchlorate anions during oxidation and

this has also been reported in the literature for PPyMe.[21] The modes for the polymer backbone were assigned to the less intense bands from 1600 - 1000 cm^{-1} and the ν_2 mode of the perchlorate anion[22,23] was represented by a sharp band at 1084 cm^{-1}. The spectrum of the monomer (Figure 3.2 (a) (—)) showed a sharp band at 721 cm^{-1}, which was assigned to the H_α on the heterocyclic ring. This band was produced by the CH out of plane bending vibration, documented for other *N*-substituted Py monomers.[24] This band was not present in the spectrum of the polymer (Figure 3.2 (b) (—)) due to propagation at these positions during polymerisation.

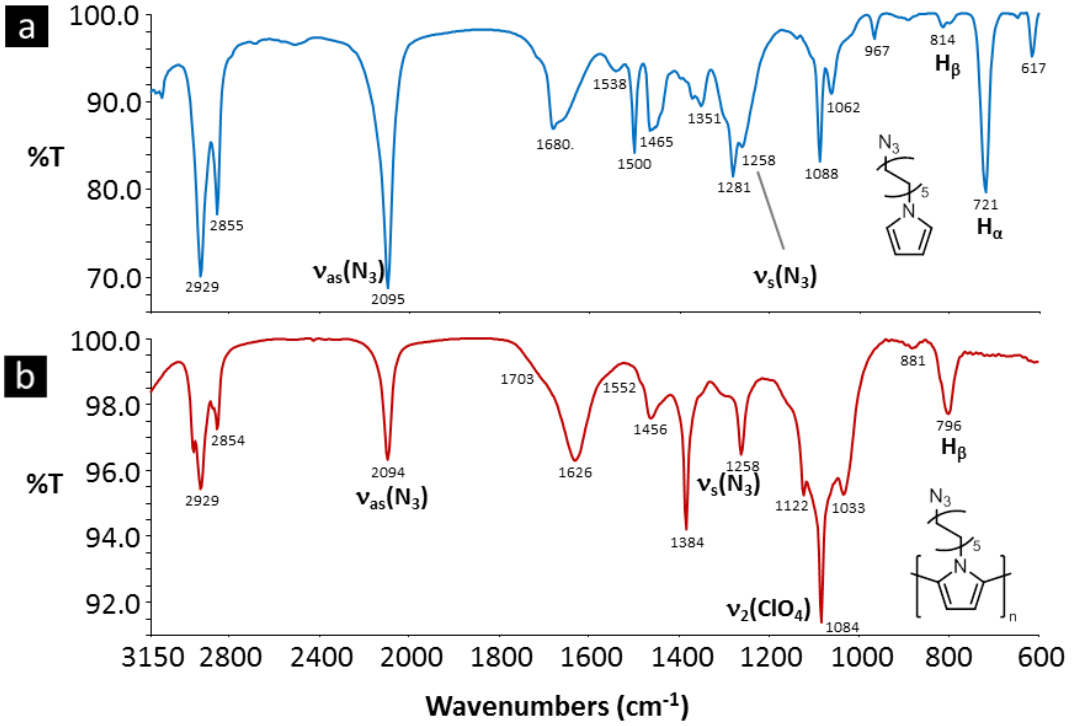

Figure 3.2: FTIR spectra of (a) $PyDeN_3$ (—) and (b) $PPyDeN_3$ grown in MeCN with $LiClO_4$ (100 mM) (—) performed at ±2 cm^{-1} resolution in KBr. The band at 1384 cm^{-1} observed in the polymer spectrum (Figure 3.19 (b) (—)) was due to an impurity present in the KBr powder.[25]

The deposited $PPyDeN_3$ film was investigated by SEM using a plan-view orientation (Figure 3.3) and as can be seen from the micrographs, the polymer forms a homogeneous layer across the electrode surface, possessing the typical 'cauliflower' morphology of PPy.[26,27] The overall linear configurations of growth (rows of polymer) easily recognisable in Figure 3.3 (b) and (c) were not a characteristic of the polymer. This undesired linear configuration of polymer growth was due to

mechanical grinding on the gold substrate, but was necessary to replenish the electrode surface between each experiment. The linear growth of the polymer was induced by scratch marks, remaining on the electrode surface after this grinding process was complete and these scratch marks acted as a template for growth. It is known that defect sites are localities of high energy on the surface, which promote faster growth during polymerisation.[28,29]

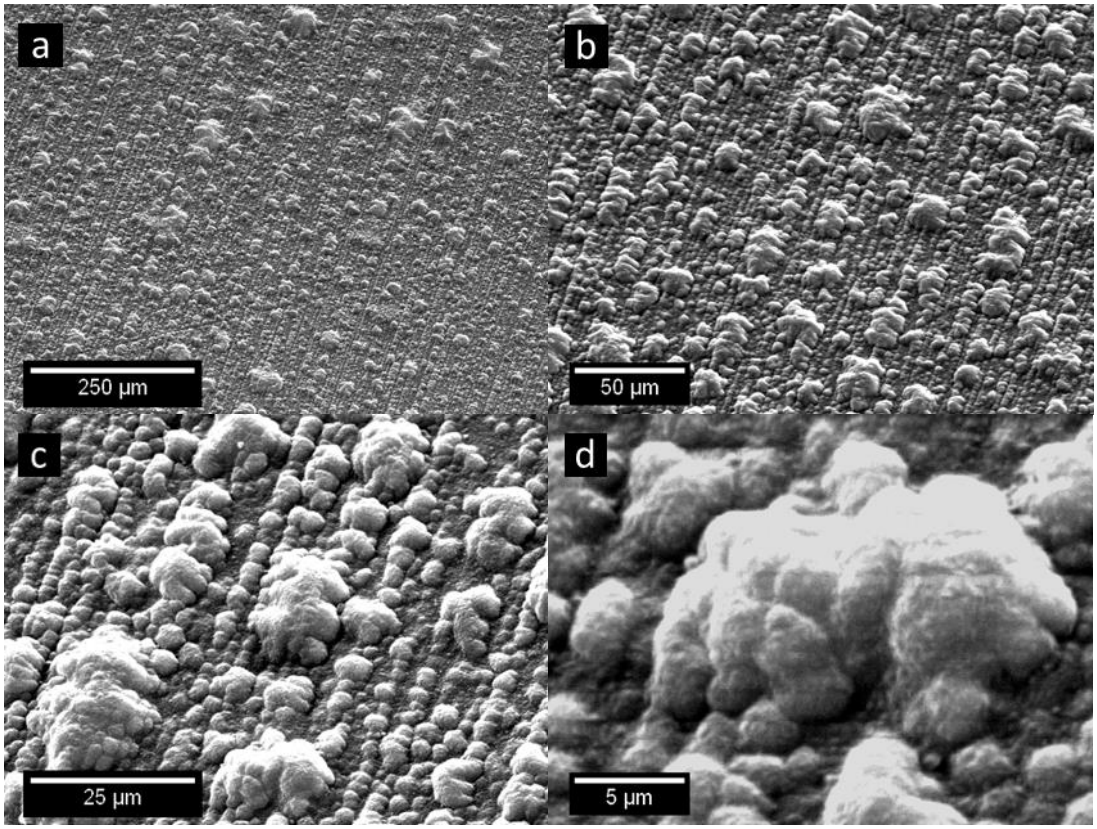

Figure 3.3: SEM micrographs of $PPyDeN_3$ grown in MeCN with $LiClO_4$ (100 mM) displaying the 'cauliflower' morphology.

The EDX spectrum of the $PPyDeN_3$ film (Figure 3.4) possessed carbon and nitrogen signals which appeared at 0.277 and 0.392 keV respectively. These signals appeared due to the PPy backbone which consisted of the heterocyclic ring substituted at the nitrogen heteroatom. The substitution consisted of an alkyl chain terminating with an azide moiety, which also attribute to these signals. There were chlorine signals present at 0.182, 2.622 and 2.816 keV, accompanied by an oxygen signal positioned at 0.525 keV. These peaks were a consequence of doping of the polymer during electrochemical deposition, as perchlorate anions stabilise the cationic charges

created on the polymer backbone during the application of oxidative potentials.[30] As the polymer film was grown by CV and cycling finished at a reductive potential, 0.000 V vs. Ag/AgCl, lithium cations may also be present within the film. We could not confirm this using EDX spectroscopy, as the technique does not recognise elements of light mass such as hydrogen, helium or lithium.[31,32] In relation to un-substituted PPy films, it has been reported in the literature that during CV, perchlorate anions become trapped due to hydrogen bonding with the Py secondary amine proton. When observing the relevant FTIR spectrum, the H-bonding interaction has been reported to induce a shift of the NH stretch vibration to lower wavenumbers.[33] As reductive potentials are applied neutralising the PPy backbone, lithium (0.68 Å) cations must diffuse into a polymer to stabilise the trapped perchlorate (2.88 Å) anions.[30,34] This cationic mechanism has been recorded for PPy in MeCN.[34] Since the Py unit utilised here is substituted with an alkyl chain at the nitrogen position, it does not acquire a perchlorate anion through H-bonding.[33] As this is so, it must be considered that the diffusion of ions may be purely an anionic mechanism, as this has been recorded for the structurally similar PPyMe[21] and other *N*-substituted Py polymers.[33] The cationic and anionic mechanisms are displayed in Scheme 3.1 for PPy and $PPyDeN_3$ respectively.

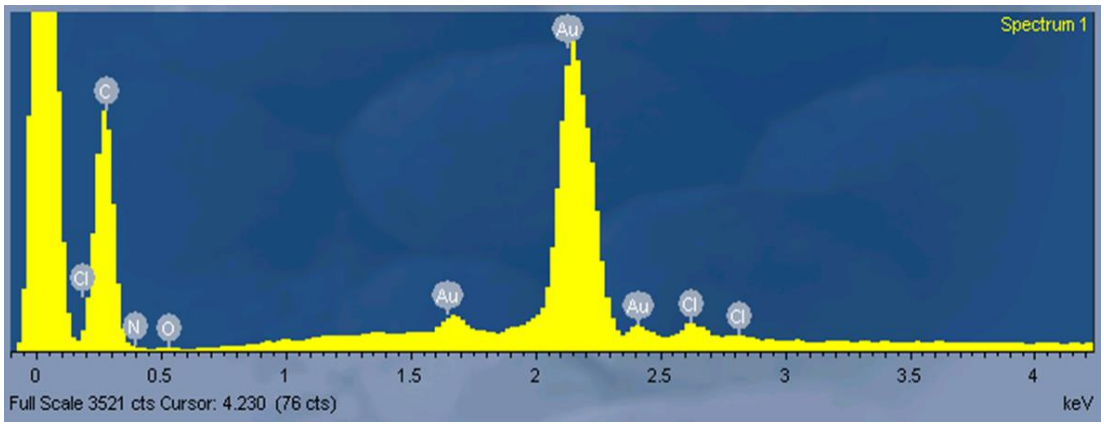

Figure 3.4: EDX spectrum of $PPyDeN_3$ grown in MeCN doped with $LiClO_4$. Intense Au peaks were a consequence of the gold substrate utilised for electrodeposition.

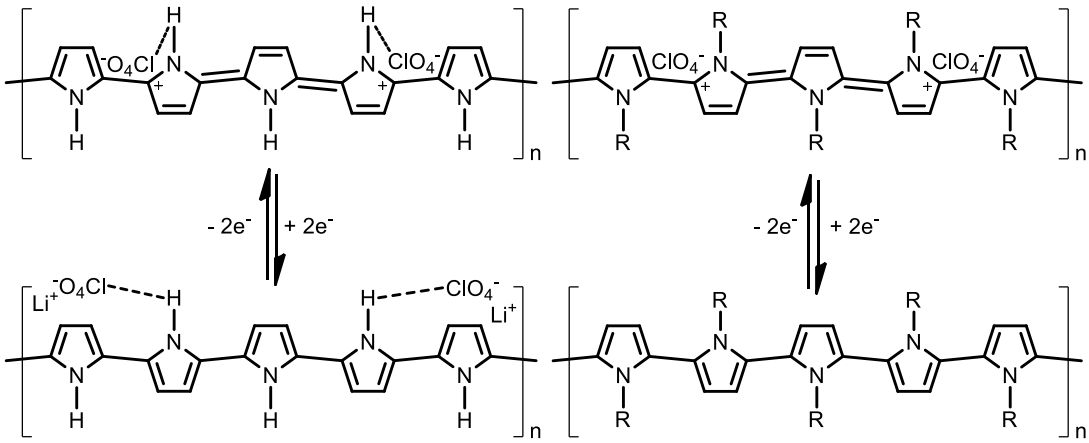

Scheme 3.1: (Left) The electrochemical redox behaviour of PPy depicting H-bonding with perchlorate anions, neutralising bipolaron charges during oxidation and the ingress of lithium cations for neutralisation of perchlorate anions, trapped during reduction. (Right) The electrochemical redox behaviour of PPyR (R = DeN_3) depicting neutralisation of bipolarons by perchlorate anions during oxidation and egress of perchlorate anions during reduction.

Electrochemical characterisation of the $PPyDeN_3$ film was performed utilising CV at 0.000 - 1.100 V vs. Ag/AgCl, with the polymer modified electrode submerged in a monomer free anhydrous MeCN solution containing $LiClO_4$ (100 mM). The CVs were recorded non-consecutively at five different scan rates between 25 - 125 mV s^{-1} (Figure 3.5). The reversible redox couple of the polymer was located between 0.690 - 0.900 V vs. Ag/AgCl and the ratio of cathodic peak current density to anodic peak current density, (j_c/j_a) varied from 1.02 to 1.07, over the range of applied scan rates. This result is very close to unity, which is required for representing the one-electron transfer mechanism.

The $PPyDeN_3$ film possesses good electrochemical stability during the redox transition, only a small loss of electrochemical activity occurred during the first few cycles and no discernible variations were observed in the successive scans. Cycling at a scan rate of 25 mV s^{-1} produced a peak potential separation (ΔE_p) of 31 mV, which upon increased scanning, shifted the E_{pa} and E_{pc} to progressively higher and lower potentials respectively, concluding with a ΔE_p of 205 mV for a scan rate of 125 mV s^{-1}. The shift in peak potentials was coupled with an increase in the magnitude of the peak currents with scan rate. When plotted the intensity of the peak currents densities, j_{pa} and j_{pc}, (with the background current density removed)

increased linearly with square root of scan rate, $v^{1/2}$, and possessed correlation coefficients (r^2) of 0.9759 and 0.9890 respectively, indicating that diffusion controlled processes dominate within this system.[35]

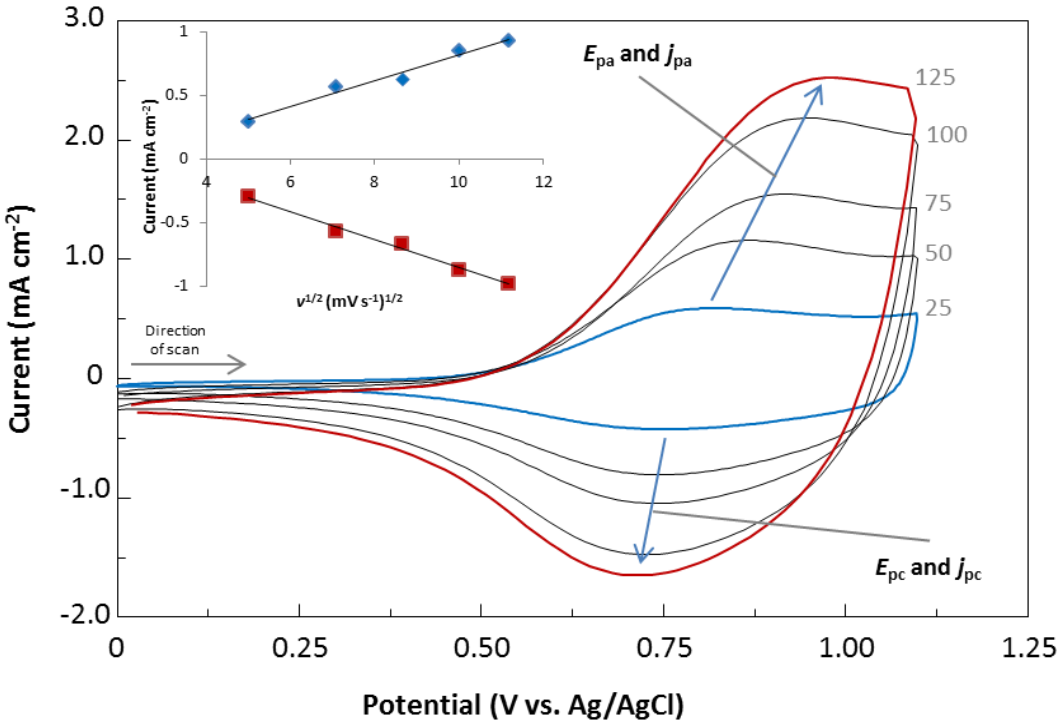

Figure 3.5: CVs of $PPyDeN_3$ grown in MeCN and doped with $LiClO_4$, showing the electroactivity of the polymer cycled in MeCN and $LiClO_4$ (100 mM) from 25 (—) to 125 (—) mV s^{-1} in 25 mV s^{-1} increments. (Inset) Plot of anodic and cathodic peak current, j_p vs. square root of potential scan rate, $v^{1/2}$.

3.2.1.2 Poly[*N*-(3-azidopropyl)pyrrole]

The $PyPrN_3$ monomer was synthesised using a method reported by Storey and co-workers in the literature.[2] $PyPrN_3$ (20 mM) was electrochemically deposited on to a polished Au substrate from a solution of $LiClO_4$ (100 mM) in anhydrous MeCN. Scanning was performed for 6 cycles in the appropriate potential window (0.000 - 1.400 V vs. Ag/AgCl) at 100 mV s^{-1} (Figure 3.6). For each cycle the onset of monomer oxidation was observed at approx. 1.200 V vs. Ag/AgCl and the current density continued to rise steeply to produce the presence of an oxidation peak shoulder at 1.400 V vs. Ag/AgCl. As stated previously for the $PPyDeN_3$ film and other *N*-alkyl Py monomers,[5] the monomer oxidation peak was expected to occur at

potentials greater than 1.000 V vs. Ag/AgCl and once again, the first cycle exhibited a 'nucleation loop' signifying polymer nucleation on the substrate.[17] The irreversible oxidation of the monomer was followed by development of a *quasi*-reversible redox couple due to doping/de-doping of the growing polymer. This redox couple for the PPy backbone was observed to possess a greater current density with every successive cycle; a polymer film growth characteristic, and also displayed a gradual shift to higher oxidative potentials during cycling as the polymer thickness increased,[15] signifying increased resistivity within the polymer.[18] As discussed previously for the $PPyDeN_3$ film, the same structural features apply to the $PPyPrN_3$ film; due to substitution at the heteroatom, coplanarity is lost between repeating monomer units,[4] affecting the polymer backbone conjugation and eventually decreasing overall conductivity of the film.[15]

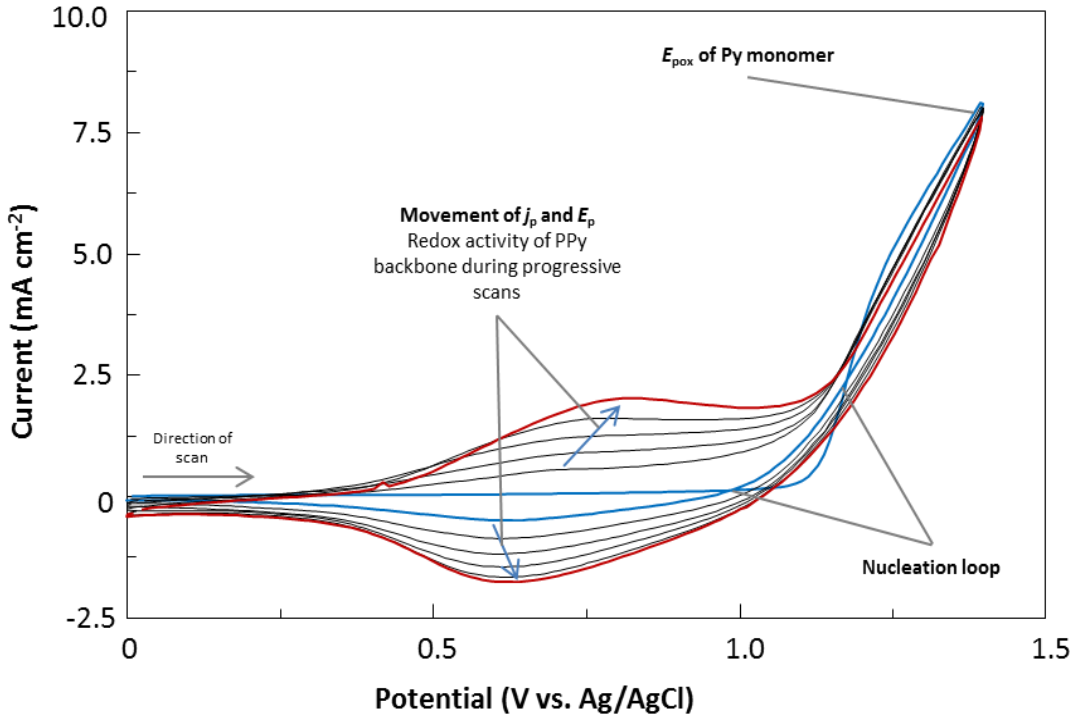

Figure 3.6: CVs recorded from a reaction medium involving $PyPrN_3$ (20 mM) and $LiClO_4$ (100 mM) in MeCN, utilising the Au substrate at a scan rate of 100 mV s^{-1}. The polymer was grown for 6 cycles (first (—) and last (—) cycle)).

$PPyPrN_3$ was deposited on the substrate in the form of a thin black film and was washed with MeCN to remove any residual monomer and electrolytic salt. The film

was characterised using FTIR spectroscopy, SEM, EDX spectroscopy and CV. The FTIR spectra of the monomer (Figure 3.7 (a) (—)) and the polymer film (Figure 3.7 (b) (—)) both possessed bands at approx. 2100 and 1259 cm^{-1}, which were assigned to the azide asymmetric[5] and symmetric stretch, respectively.[19] These bands were an indication that the azide moiety had remained intact and bound to the alkyl chain, which had bands attributed to it at 2923 and 2854 cm^{-1}; assigned to the CH aliphatic stretching vibrations.[20] The polymer backbone modes were assigned to the less intense bands within the 1600 - 1000 cm^{-1} region, while the most significant band in the region, at 1085 cm^{-1} was assigned to the ν_2 mode of the dopant perchlorate anion.[22,23] The broad band at approx. 1630 cm^{-1} was representative of the ν_1 mode of H_2O molecules in the film.[21] In the spectrum of the monomer (Figure 3.7 (a) (—)) there was a strong band at 727 cm^{-1}, which was attributed to the CH out of plane bending vibration for the H_α on the heterocyclic ring. This band had been reported in the literature for other *N*-substituted Py monomers[24] and was not present in the polymer film spectrum (Figure 3.7 (b) (—)). This feature was most probably attested to chain propagation at these positions during polymerisation.

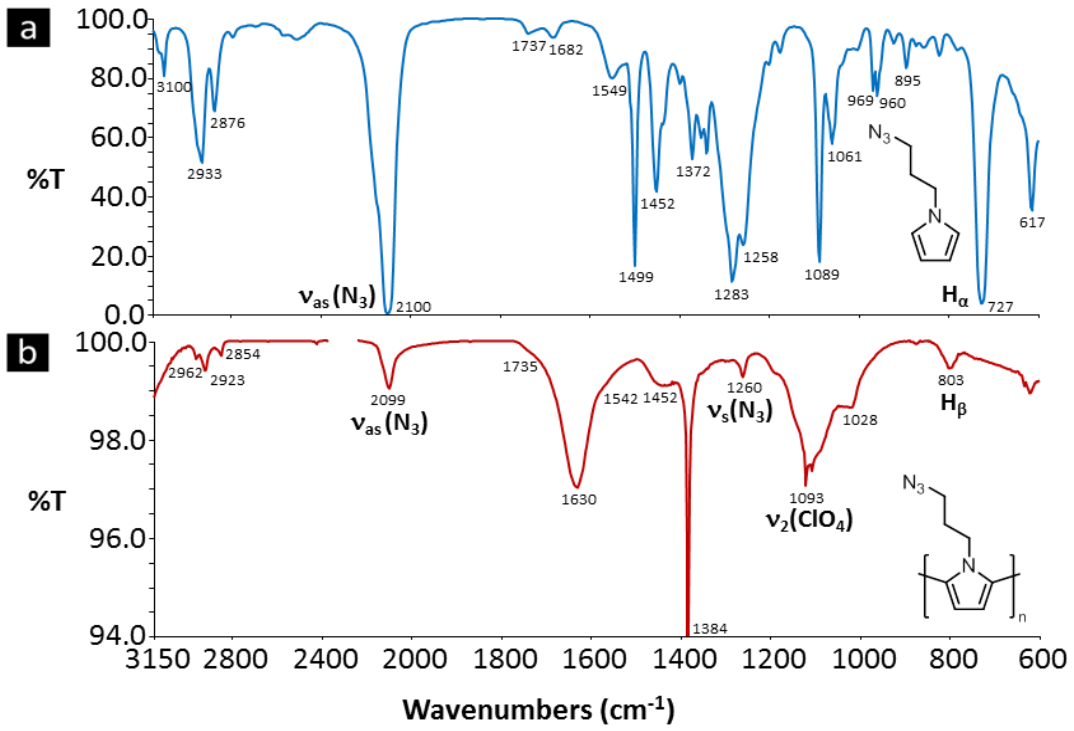

Figure 3.7: FTIR spectra of (a) $PyPrN_3$ (—) and (b) $PPyPrN_3$ grown in MeCN with $LiClO_4$ (100 mM) (—) at ±2 cm^{-1} resolution in KBr. The band at 1384 cm^{-1} observed in the polymer spectrum (Figure 3.19 (b) (—)) was due to an impurity present in the KBr powder.[25]

The SEM micrographs recorded of the $PPyPrN_3$ film are shown in Figure 3.8. As can be seen from the micrographs, the polymer forms a homogeneous film across the electrode surface and has developed the 'cauliflower' morphology, which has been seen to occur with PPy.[26,27]

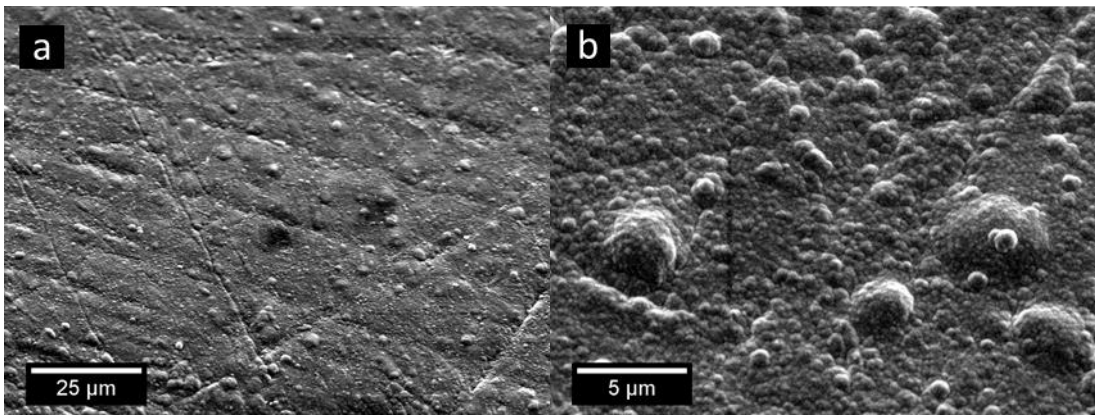

Figure 3.8: SEM micrographs of $PPyPrN_3$ grown in MeCN with $LiClO_4$ (100 mM) displaying the 'cauliflower' morphology.

The EDX spectrum of the $PPyPrN_3$ film (Figure 3.9) displayed carbon, nitrogen, chlorine and oxygen peaks due to their presence with the polymer film. The carbon and nitrogen signals appeared at 0.277 and 0.392 keV respectively, as they were present within the structure of the monomer before polymerisation was initiated. The chlorine signals appeared at 0.182, 2.622 and 2.816 keV, while the oxygen signal appeared at 0.525 keV. As the polymer film was doped with the electrolytic salt, $LiClO_4$, during the electrochemical deposition process, both signals were expected in the spectrum for the $PPyPrN_3$ film. As discussed previously in Section 3.2.1.1, it cannot be confirmed that lithium cations were trapped in the polymer. It must be considered that the ions are free to diffuse in or out of the polymer, as it is cycled through its redox states, since this has been recorded for similar polymers.[21,33]

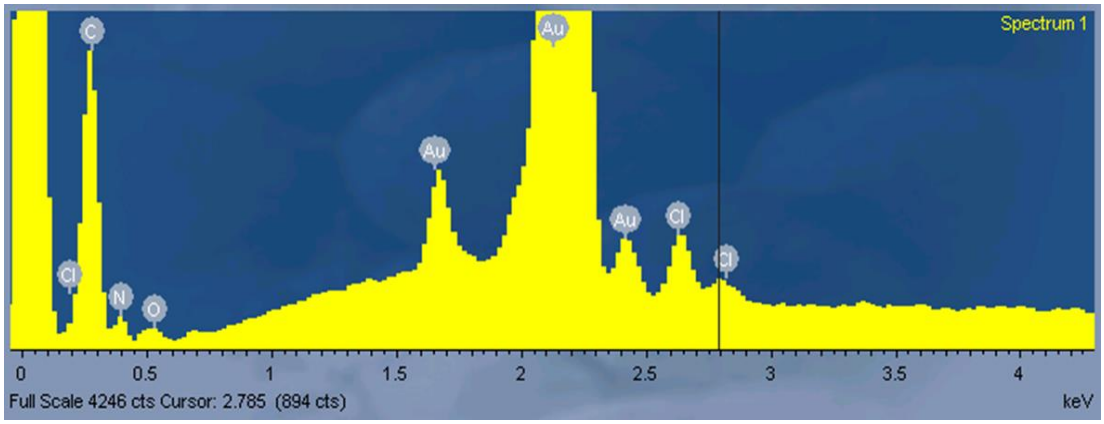

Figure 3.9: EDX spectrum of $PPyPrN_3$ grown in MeCN doped with $LiClO_4$. Intense Au peaks were a consequence of the gold substrate utilised for electrodeposition.

The electrochemical characterisation of $PPyPrN_3$ was executed by performing CV on the polymer film in MeCN containing $LiClO_4$ (100 mM), between 0.000 - 1.000 V vs. Ag/AgCl, recording the five different scan rates in reverse consecutive order from 25 - 125 mV s^{-1} (Figure 3.10). This produced stable cycles and only a small loss of electroactivity was observed during the first few cycles. The *quasi*-reversible redox couple was located between 0.610 - 0.790 V vs. Ag/AgCl and the j_c/j_a ratio varied from 1.58 - 2.37 over the applied scan rate range. During analysis of the CVs, difficulties were encountered determining an appropriate j_a value and also when determining the amount of capacitive current within the system. The inadequate

calculation of the two values could eschew the attained the j_c/j_a ratio, producing a result which does not fit to a one-electron oxidation system. The E_{pa} and E_{pc} shifted to progressively higher and lower potentials respectively, when the scan rate was increased; cycling at 25 mV s^{-1} produced a ΔE_p of 118 mV, while cycling at 125 mV s^{-1} yielded a ΔE_p of 174 mV. The increase in the applied scan rate also produced increases with regard to j_p. Both j_{pa} and j_{pc} (minus background current density) when plotted against the square root of scan rate, $v^{1/2}$ increased linearly, possessing r^2 of 0.9339 and 0.9515 respectively. This indicated that a diffusion controlled processes (diffusion of ions) was dominant in this system[35].

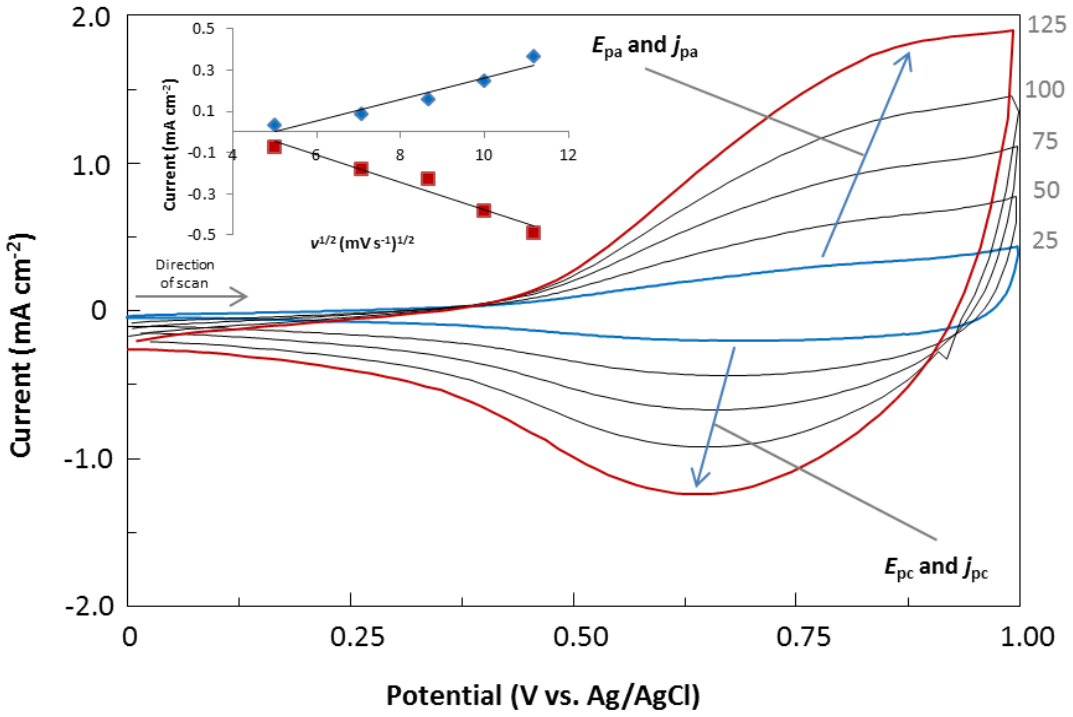

Figure 3.10: CVs of $PPyPrN_3$, grown in MeCN and doped with $LiClO_4$, showing the electroactivity of the polymer cycled in MeCN and $LiClO_4$ (100 mM) from 25 (—) to 125 (—) mV s^{-1} in 25 mV s^{-1} increments. (Inset) Plot of anodic and cathodic peak current, j_p vs. square root of potential scan rate, $v^{1/2}$.

3.2.1.3 Poly[*N*-(2-azidoethyl)pyrrole]

The $PyEtN_3$ monomer was synthesised utilising a method reported by Storey and co-workers.[2] First the E_{pox} of $PyEtN_3$ (2 mM) was determined to be 1.500 V vs. Ag/AgCl, in MeCN containing $LiClO_4$ (100 mM). $PyEtN_3$ (20 mM) was

then electrochemically deposited on to a gold substrate from the $LiClO_4$ (100 mM) in anhydrous MeCN solution by successive scanning (7 scans) in the potential window 0.000 - 1.400 V vs. Ag/AgCl at a scan rate of 100 mV s^{-1} (Figure 3.11). The onset potential of the $PyEtN_3$ oxidation was observed at approx. 1.100 V vs. Ag/AgCl and the current density steeply increased, until it reached the E_λ of 1.400 V vs. Ag/AgCl. The presence of and an oxidation peak shoulder was observed in this region due to the oxidation of the $PyEtN_3$ monomer[5] and the first cycle displayed the expected 'nucleation loop' due to polymer nucleation on the polished electrode surface.[17] As in Sections 3.2.1.1 and 3.2.1.2, during cycling a *quasi*-reversible redox couple developed over scans due to the doping/de-doping of the growing polymer. Both the j_p and E_p for the oxidation and reduction of this redox couple shifted to greater current densities and oxidative potentials, as the film thickness increased[15] during cycling. The increase in j_p is characteristic of polymer growth, while the increase in E_p was attributed to resistive properties developing with thickness.[18] For example the oxidation peak for the polymer occurred at 0.700 V vs. Ag/AgCl in cycle 2 and at 0.825 V vs. Ag/AgCl in cycle 7. Similar observations were made for the $PPyDeN_3$ and $PPyPrN_3$ films, which have the same type of substitution on the heteroatom.[4,15]

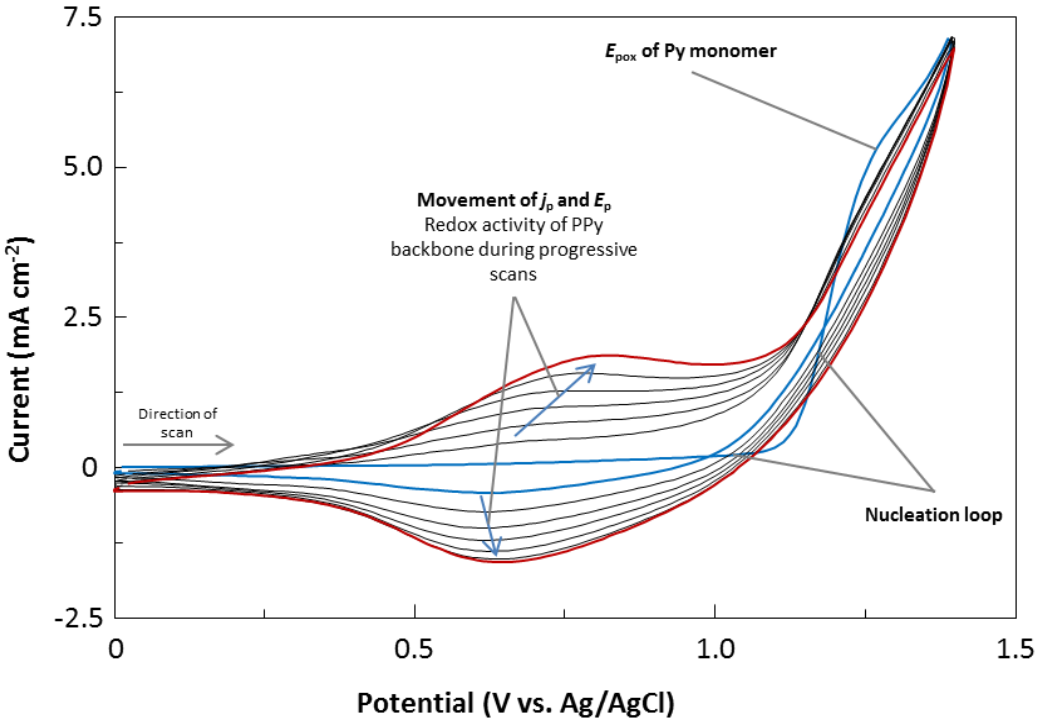

Figure 3.11: CVs recorded from a reaction medium involving $PyEtN_3$ (20 mM) and $LiClO_4$ (100 mM) in MeCN, utilising the Au substrate at a scan rate of 100 mV s^{-1}. The polymer was grown for 7 cycles (first (—) and last (—) cycle)).

After the electrochemical deposition process had taken place, a thin black film was visible on the surface of the electrode. In order to ensure that the polymer still contained the azide functionality, it was removed from the surface and mixed into a KBr pellet. The FTIR spectrum of $PPyEtN_3$ (Figure 3.12 (a) (—)), along with that for the monomer (Figure 3.12 (b) (—)), displayed a band at 2099 cm^{-1} allocated to the azide asymmetric stretch,[5] while the weak band at 1258 cm^{-1} was assigned to the symmetric stretch of the same moiety.[19] As for the decyl and propyl congeners, the existence of these two bands indicates that the azide functional group was still intact after polymerisation had concluded. As in Section 3.2.1.2 it can be seen for the $PPyEtN_3$ film (Figure 3.7 (b) (—)) that there was a band positioned at 2962 cm^{-1} due to the presence of MeCN as solvent impurity. MeCN was employed to wash the film after deposition, for the removal of any residual $PyEtN_3$ monomer. The bands at 2923 and 2874 cm^{-1} were assigned to the aliphatic CH stretch vibrations[20] of the alkyl chain and the heterocyclic ring. The band at 1628 cm^{-1} was assigned to the possible presence of residual H_2O.[21] The less intense bands at approx. 1600 -

1000 cm^{-1} were assigned to the polymer backbone modes and the sharp band at 1084 cm^{-1} was assigned to the ν_2 mode of the perchlorate anion dopant.[22,23] In the spectrum of the monomer (Figure 3.12 (a) (—)), there was the presence of a band at 728 cm^{-1}. This was assigned to the CH out of plane bending vibration for the H_α on the heterocyclic ring, which has been recorded for other *N*-substituted Py monomers.[24] This band was absent from the polymer film spectrum (Figure 3.12 (b) (—)), probably due to loss of these hydrogen atoms upon polymerisation.

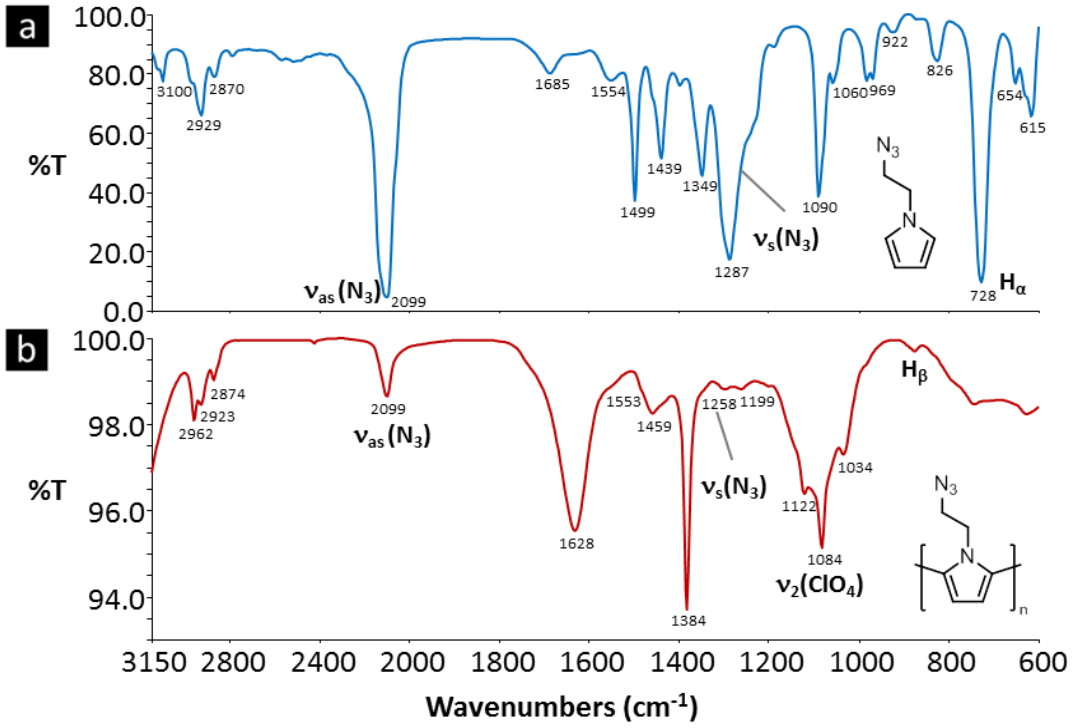

Figure 3.12: FTIR spectra of (a) $PyEtN_3$ (—) and (b) $PPyEtN_3$ grown in MeCN with $LiClO_4$ (100 mM) (—) at ±2 cm^{-1} resolution in KBr. The band at 1384 cm^{-1} observed in the polymer spectrum (Figure 3.19 (b) (—)) was due to an impurity present in the KBr powder.[25]

The $PPyEtN_3$ film, which was grown in MeCN with $LiClO_4$ (100 mM) was analysed by SEM (Figure 3.13) and it was apparent that the polymer deposited in homogeneous 'cauliflower' morphology on the substrate.[26,27]

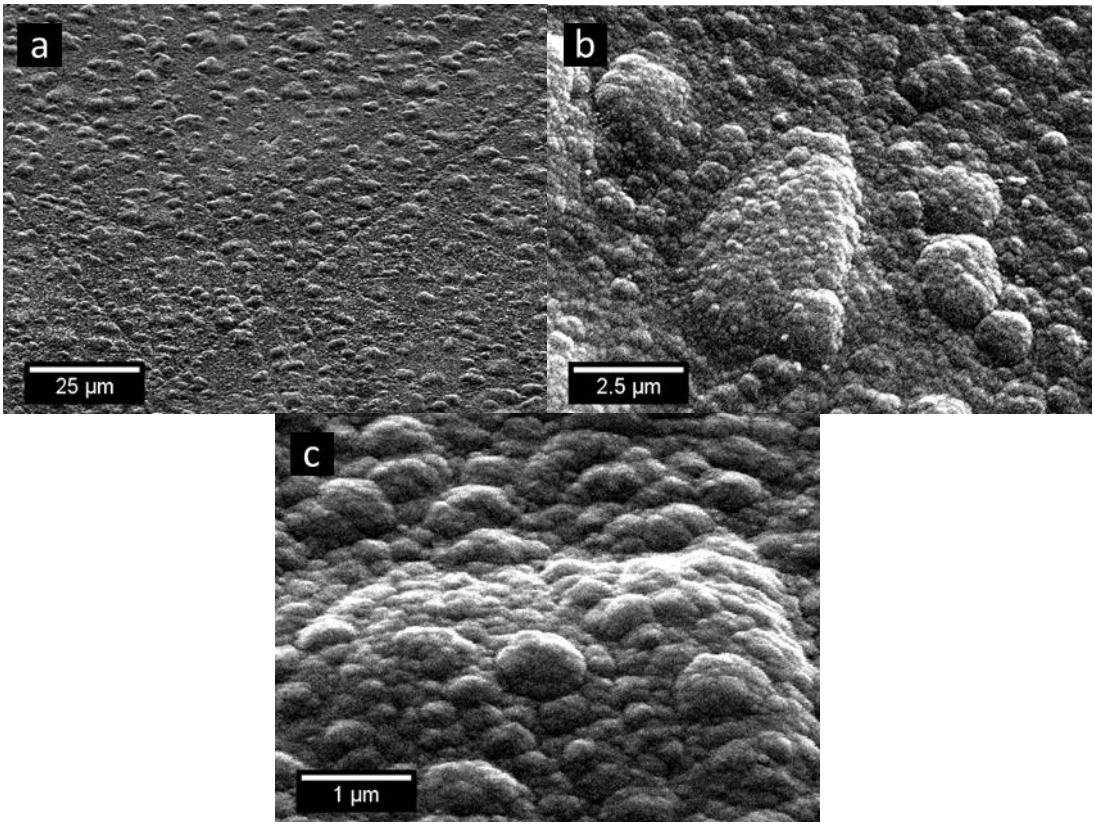

Figure 3.13: SEM micrographs of $PPyEtN_3$ grown in MeCN with $LiClO_4$ (100 mM) displaying the 'cauliflower' morphology.

The $PPyEtN_3$ film grown in MeCN with $LiClO_4$ (100 mM) had its composition investigated by EDX spectroscopy (Figure 3.14). Once again, the spectrum for the film contained signals for carbon and nitrogen at 0.277 and 0.392 keV respectively, due to the structure of the $PyEtN_3$ monomer. During electrochemical deposition of the polymer, the $LiClO_4$ acts as a counter anion and this was confirmed in the spectrum, due to the presence of chlorine peaks at 0.182, 2.622 and 2.816 keV and an oxygen peak at 0.525 keV. It was likely that the diffusion of ions was due to an anionic mechanism as has been reported for PPyMe[21] and *N*-substituted Py polymers.[33] By analysing the EDX spectral data for the three polymers, $PPyDeN_3$, $PPyPrN_3$ and $PPyEtN_3$, it was evident that the length of the alkyl chain substituent has no observable negative effects in relation to the doping of the polymer with perchlorate during polymerisation, as the presence of the perchlorate anion within the three polymers has been confirmed using this data.

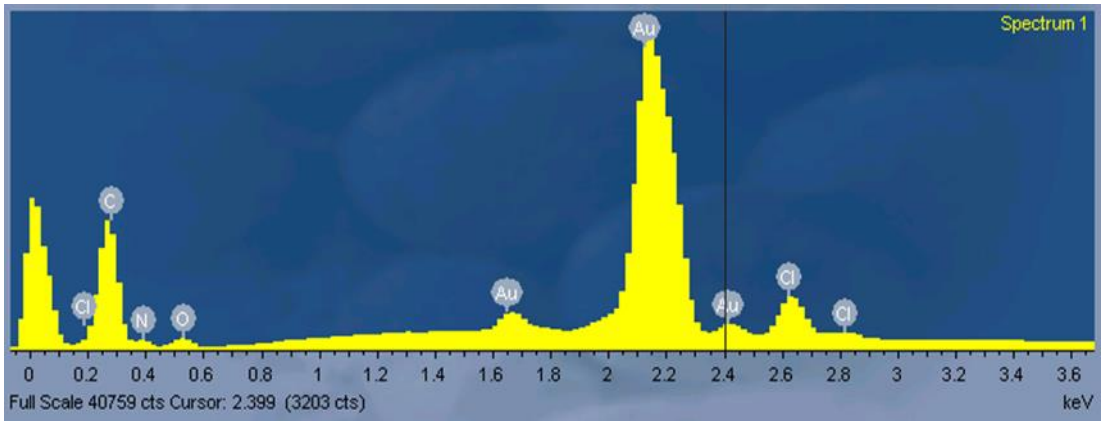

Figure 3.14: EDX spectrum of $PPyEtN_3$ grown in MeCN doped with $LiClO_4$. Intense Au peaks were a consequence of the gold substrate utilised for electrodeposition.

The $PPyEtN_3$ film was electrochemically characterised using CV in MeCN solution containing $LiClO_4$ (100 mM), between 0.000 - 0.950 V vs. Ag/AgCl at five different scan rates from 25 - 125 mV s^{-1} in reverse consecutive order (Figure 3.15). The film yielded stable CVs accompanied by slight loss of activity during the first cycles. The *quasi*-reversible redox couple for doping/de-doping of the polymer was located between 0.600 - 0.780 V vs. Ag/AgCl. The j_c/j_a ratio varied from 1.52 to 2.93 over the applied scan rate range, but this value was not accurate as it proved difficult to define a precise j_a and capacitive current values, which could cause an incorrect ratio to be attained. By scanning the polymer film at 25 mV s^{-1}, this produced a ΔE_p of 107 mV, which increased to 184 mV at 125 mV s^{-1}. The intensity of j_{pa} and j_{pc} increased linearly with $v^{1/2}$, (r^2 of 0.9620 and 0.9805 respectively), which was indicative of a diffusion controlled process.[35]

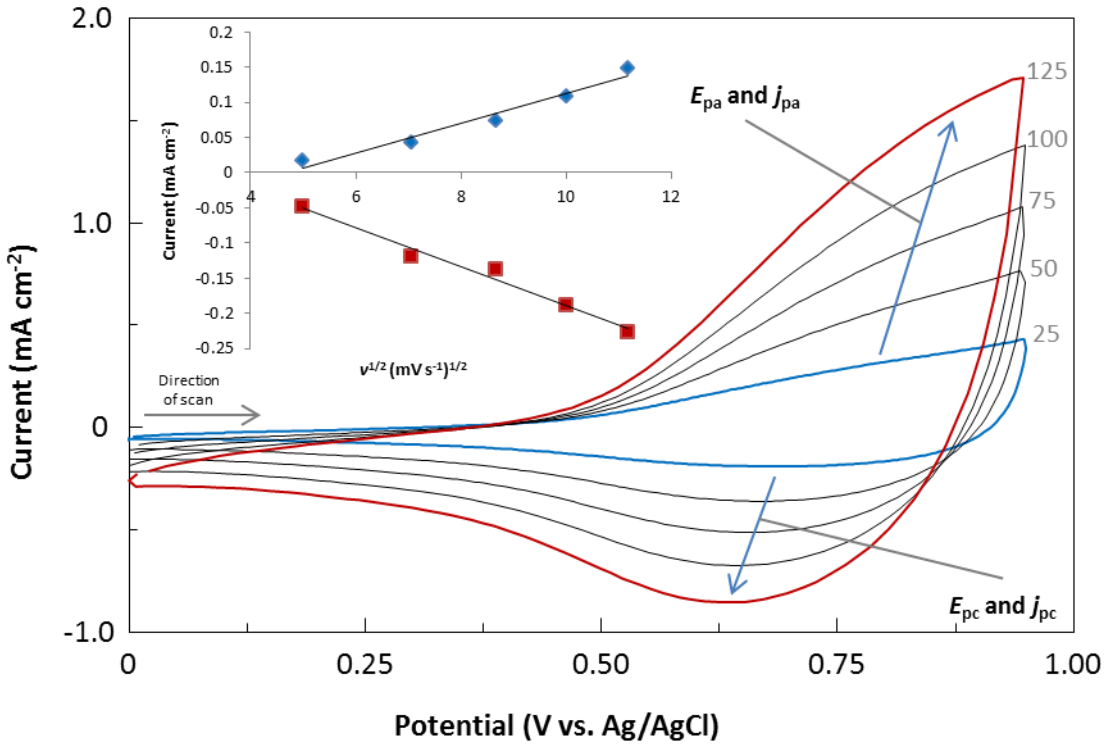

Figure 3.15: CVs of $PPyEtN_3$, grown in MeCN and doped with $LiClO_4$, showing the electroactivity of the polymer cycled in MeCN and $LiClO_4$ (100 mM) at 25 (—) to 125 (—) mV s^{-1} in 25 mV s^{-1} increments. (Inset) Plot of anodic and cathodic peak current, j_p vs. square root of potential scan rate, $v^{1/2}$.

Studies were then extended to grow a poly[(azidoalkyl)pyrrole] in the nanowire morphology. Considering the three monomers investigated, $PyEtN_3$ was deemed most suitable due to its short alkyl chain, resulting in a greater affinity for more polar solvents.[36] It has been reported that the electrodeposition of conducting PPy nanowires, when employing the template-free approach requires either carbonate[37,38] or phosphate[14] salts and yields nanowires of varied dimensions with excellent control.[14] These reported electrochemical depositions were performed in an aqueous system, which is problematic due to the insolubility of $PyEtN_3$ in the polar medium. Therefore, a novel organic/aqueous co-solvent system was employed to increase $PyEtN_3$ solubility. Also, as a carbonate or phosphate salt (≥200 mM) was required to obtain nanowire morphology,[14] the solvent system must be sufficiently polar for adequate solubility of these salts. Considering these parameters, a short chain alcohol

such as EtOH or MeOH was added to the solvent system, to ensure sufficient solubility of the phosphate salt and the monomer.

3.2.1.4 Poly[*N*-(2-azidoethyl)pyrrole] grown in a co-solvent medium

The employment of an EtOH/H_2O co-solvent system with regard to the growth of $PyEtN_3$, meant that investigation of the E_{pox} in this solvent system was required. The E_{pox} was positioned at 1.300 V vs. SCE and was first determined using a dilute monomer solution (2 mM). Then $PyEtN_3$ (20 mM) was electrochemically deposited on to the gold substrate using $LiClO_4$ (100 mM) in 3:4 EtOH/H_2O, by cycling between 0.000 - 1.000 V vs. SCE, at a scan rate of 100 mV s^{-1} (Figure 3.16). The onset potential of the $PyEtN_3$ oxidation in the co-solvent system was observed at approx. 0.800 V vs. SCE, from which the current density increased significantly, showing the presence of an oxidation peak shoulder until it reached the E_λ. Upon performing the reverse scan, this showed that the oxidation of $PyEtN_3$ was irreversible,[5] possessing a 'nucleation loop' due to the polymer nucleation process.[17] During cycling there was initially difficulty observing any oxidation of the polypyrrole backbone. Eventually a *quasi*-reversible redox couple developed but as the number of cycles increased, the current density did not increase significantly, even when an anodic E_λ of 1.100 - 1.300 V vs. SCE was applied and this resulted in a very thin film being deposited. This was probably due to attack by hydroxide anions at the H_α or H_β of the Py units in the growing polymer backbone during the oxidative scans. During deposition, these nucleophilic anions can neutralise the positive charges on the backbone with a greater tendency than the doping perchlorate counter ion, resulting with increased resistivity within the growing polymer, caused by disruption of conjugation in the sp^2 carbons. Also, this very thin film had its E_{ox} shift to a more anodic region during cycling and this increased difficulty to oxidise the polymer, indicated increasing film resistivity.[15,18]

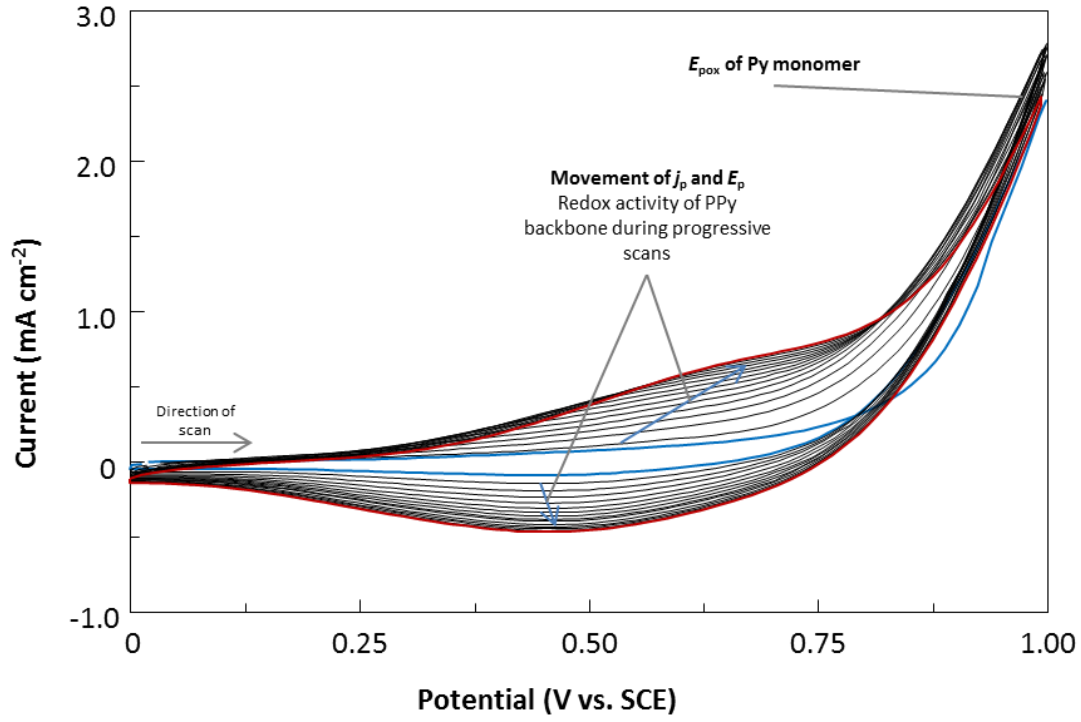

Figure 3.16: CVs recorded from a reaction medium involving $PyEtN_3$ (20 mM) and $LiClO_4$ (100 mM) in $EtOH/H_2O$ (3:4), utilising the Au substrate at a scan rate of 100 mV s^{-1}. The polymer was grown for 15 cycles (first (—) and last (—) cycle)).

The bulk $PPyEtN_3$ film grown in the aqueous/organic co-solvent system was characterised using CV in MeCN with $LiClO_4$ (100 mM), scanning between 0.000 - 0.900 V vs. Ag/AgCl in a non-consecutive order, at five different scan rates from 25 - 125 mV s^{-1} (Figure 3.17). CV of the $PPyEtN_3$ film yielded scans, which appeared to be stable over the course of the analysis. Along with this, there was a small loss of electroactivity, but this was isolated to the first cycles. The redox couple was observed between 0.670 - 0.710 V vs. Ag/AgCl and the j_c/j_a ratio varied from 1.02 - 1.10 over the various applied scan rates. This represented a one-electron transfer mechanism as the results were close to unity. The magnitude of j_p increased with scan rate and the intensity of j_{pa} and j_{pc} varied with $v^{1/2}$ (r^2 of 0.9762 and 0.9845), as was expected if diffusion controlled processes were dominant.[35]

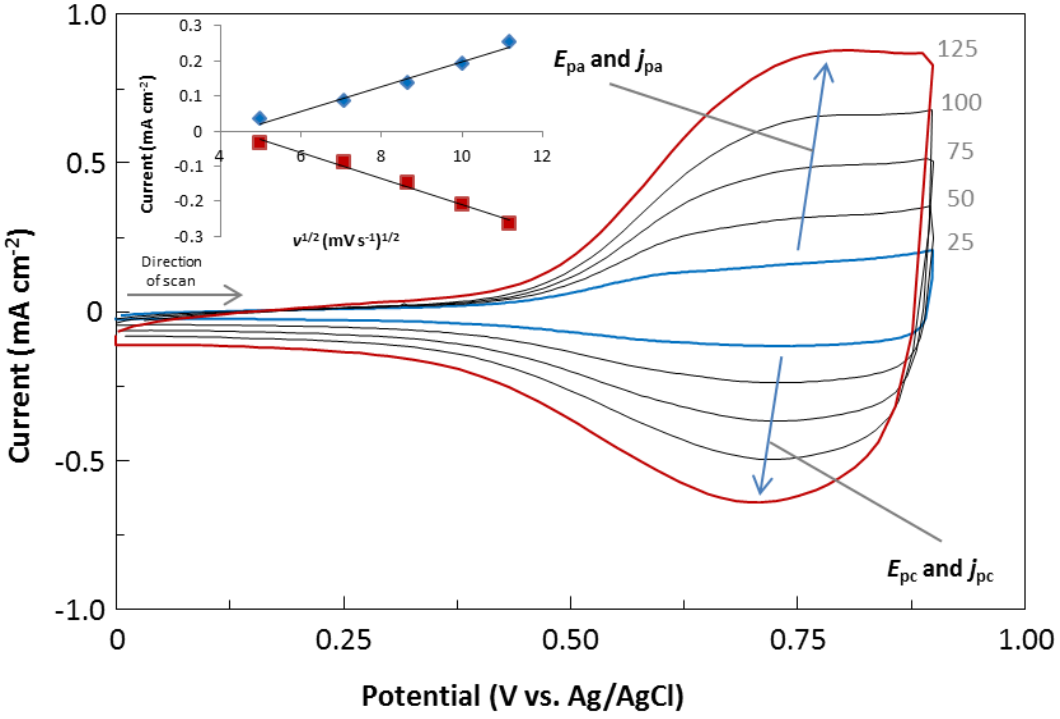

Figure 3.17: CVs of $PPyEtN_3$ (20 mM), grown in $EtOH/H_2O$ (3:4) and doped with $LiClO_4$, showing the electroactivity of the polymer cycled in MeCN and $LiClO_4$ (100 mM) from 25 (—) to 125 (—) mV s^{-1} in 25 mV s^{-1} increments. (Inset) Plot of anodic and cathodic peak current, j_p vs. square root of potential scan rate, $v^{1/2}$.

Polymer deposition employing $PyEtN_3$ (20 mM) yielded a thin film, which could not be characterised using FTIR spectroscopy, as there was insufficient material for analysis. Therefore, to promote polymerisation, the monomer concentration was increased and deposition was performed using $PyEtN_3$ (35 mM) with $LiClO_4$ (100 mM) in (3:4) $EtOH/H_2O$ (Figure 3.18). The scans were performed between 0.000 - 1.000 V vs. SCE at a scan rate of 100 mV s^{-1} and this produced j_{pox}; the oxidation of the monomer and also a slight redox couple; due to the activity of the polymer backbone. By increasing the concentration of the monomer (35 mM) to obtain a greater deposition of material, increased current densities were attained for j_{pox} and j_p for the redox couple, when compared to the deposition performed at the lower concentration (20 mM). By observing the electrode surface during deposition, it was apparent that at the higher monomer concentration, a thin film with sufficient material was deposited on the substrate for FTIR spectroscopic analysis.

As before, the current densities of the redox couple did not increase significantly between cycles.

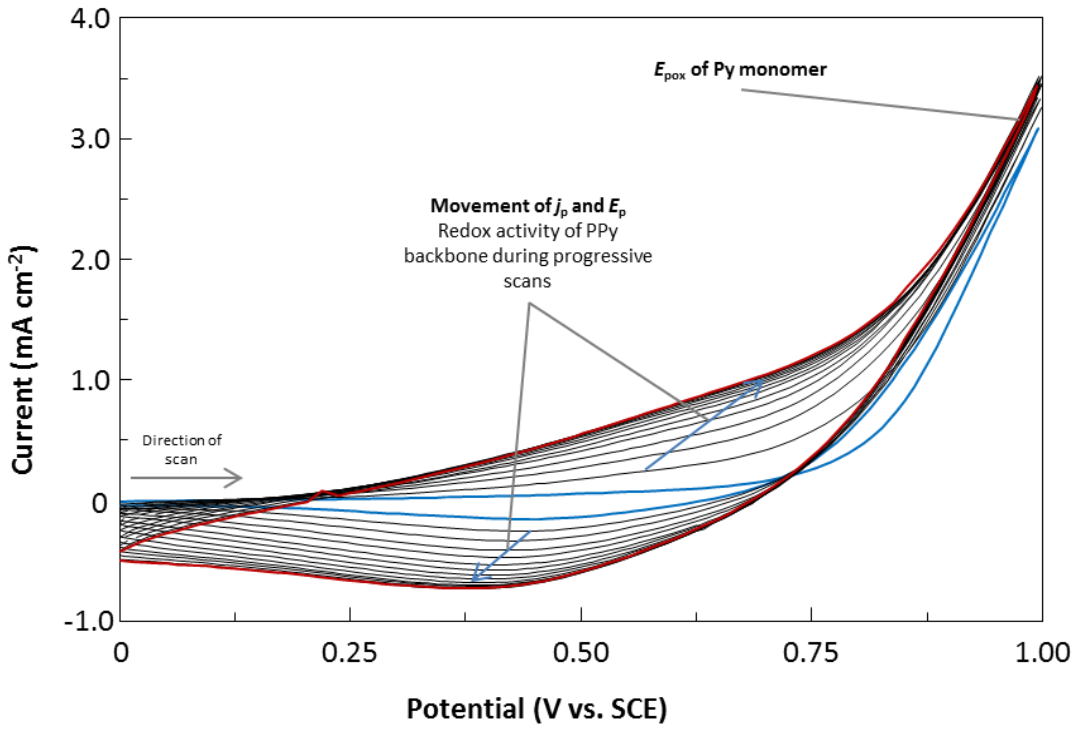

Figure 3.18: CVs recorded from a reaction medium involving $PyEtN_3$ (35 mM) and $LiClO_4$ (100 mM) in $EtOH/H_2O$ (3:4), utilising the Au substrate at a scan rate of 100 mV s^{-1} in the potential window 0.000 - 1.000 V vs. SCE. The polymer was grown for 15 cycles (first (—) and last (—) cycle)).

The $PPyEtN_3$ bulk film formed from $EtOH/H_2O$ was scrapped off the electrode, mixed with KBr and examined using FTIR spectroscopy. The FTIR spectra of the polymer (Figure 3.19 (b) (—)) and that of the monomer species (Figure 3.19 (a) (—)) possessed bands at approx. 2099 cm^{-1}, indicating retention of the azide moiety and were assigned to the asymmetric stretch,[5] while the band at 1258 cm^{-1} was assigned to the symmetric stretch.[19] The presence of these bands indicates that the azide group was not affected by the organic/aqueous medium during polymerisation. The bands at 2916 cm^{-1} and 2847 cm^{-1} were assigned to the aliphatic CH stretch vibrations.[20] The development of a medium intensity band at 1728 cm^{-1}, in the spectrum for the polymer (Figure 3.19 (b) (—)), was a consequence of the presence of carbonyl groups positioned at certain C_β positions on the Py ring backbone[39] and this is

indicative of attack from nucleophilic species as the polymer forms. In the EtOH/H_2O co-solvent system, the electrophilic C_β may be attacked during polymerisation by nucleophilic species such as hydroxide anions[39,40] and also bicarbonate anions[40] (present due to any dissolved CO_2 reacting with H_2O) as shown in Scheme 3.2.

1. Reversible oxidation: neutral species to polaron species

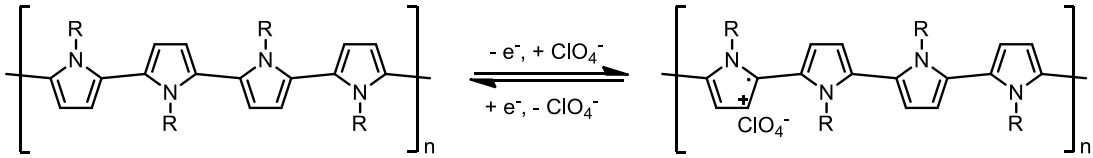

2. Reversible oxidation: polaron species to bipolaron species

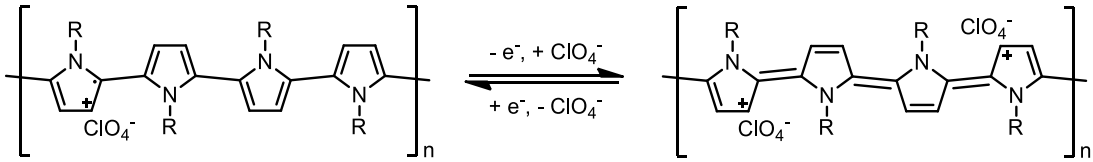

3. Irreversible overoxidation: bipolaron species to 3-hydroxypyrrole species

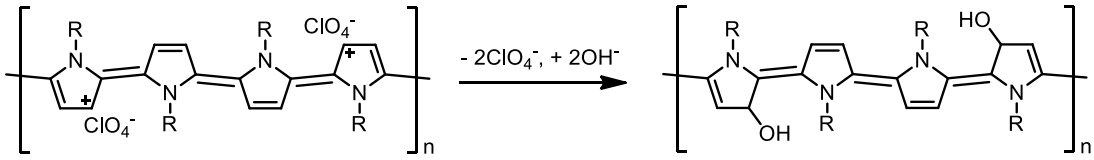

4. Irreversible overoxidation: 3-hydroxypyrrole species to pyrrolinone species

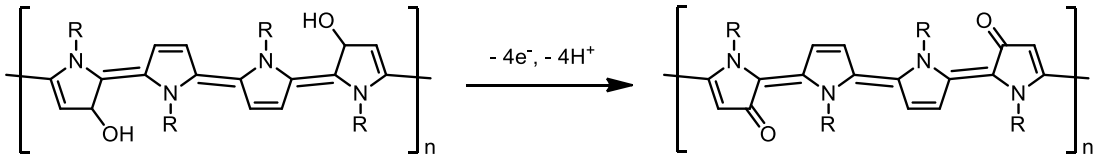

Scheme 3.2: Overoxidation of PPyR (R = EtN_3). The oxidation of the neutral polymer occurs through loss of two electrons yielding bipolarons in the polymer backbone, which are neutralised by counter anions such as perchlorate. When an excessive oxidising potential is applied to the polymer film, there is further loss of electrons. If this occurs in the presence of water, the film is irreversibly overoxidised, as the more mobile hydroxide anions attack the bipolaron species and sluggish perchlorate anions are excluded, resulting in loss of conductivity. This insulating 3-hydroxypyrrole species can then undergo further overoxidation to form the pyrrolinone species.

The nucleophilic attack of anions may also occur at the C_α position, if polymer branching occurs at the pyrrole C_β. This should result in an amide stretch vibration at 1670 cm^{-1} of medium intensity.[40] This band was not evident in any of the polymer spectra recorded here and it may therefore be indicative that polymer branching predominantly occurred as the α-α form. The broad band at approx. 1630 cm^{-1} was assigned to residual H_2O, a consequence of the incorporation of solvated perchlorate anions during oxidation, which has been recorded for PPyMe.[21] The less intense bands from 1600 - 1000 cm^{-1} were similar to the previous films, assigned to the polymer backbone modes and the sharp band at 1088 cm^{-1} was assigned to the doping perchlorate anion ν_2 mode.[22,23] The strong band present in the monomer spectrum (Figure 3.19 (a) (—)) positioned at 728 cm^{-1} was assigned to the CH out of plane bending vibration for the H_α on the heterocyclic ring.[24] Due to the expulsion of the hydrogen atoms from these positions during polymerisation, this band was not present in the spectrum of the polymer (Figure 3.2 (b) (—)).

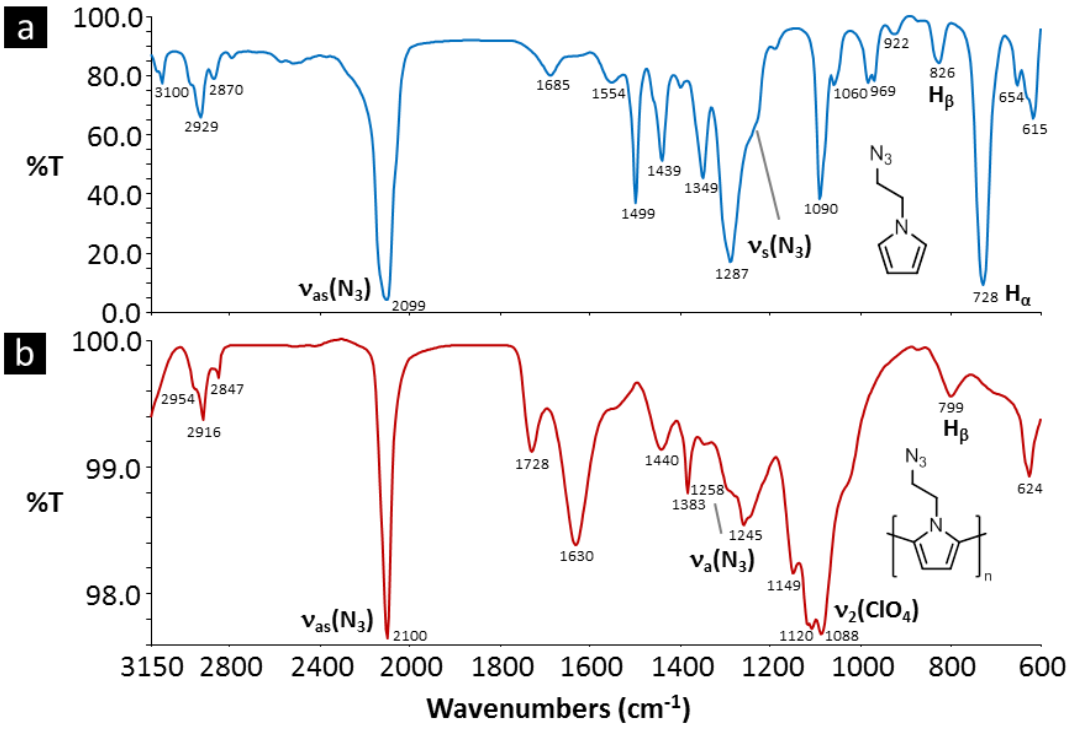

Figure 3.19: FTIR spectra of (a) $PyEtN_3$ (—) and $PPyEtN_3$ grown in $EtOH/H_2O$ (3:4) with $LiClO_4$ (100 mM) (—) at ±2 cm^{-1} resolution in KBr. The band at 1383 cm^{-1} observed in the polymer spectrum (Figure 3.19 (b) (—)) was due to an impurity present in the KBr powder.[25]

The $PPyEtN_3$ film grown in $EtOH/H_2O$ (3:4) with $LiClO_4$ (100 mM) and $PyEtN_3$ (35 mM) was investigated using SEM (Figure 3.20). Observing low and high magnification SEM micrographs it was apparent that this technique forms a $PPyEtN_3$ film, very similar to that previously grown in MeCN at a slightly lower concentration of monomer. The homogeneous film could be described as 'cauliflower' morphology, similar to that of PPy[10,11] grown under comparable conditions.[26,27]

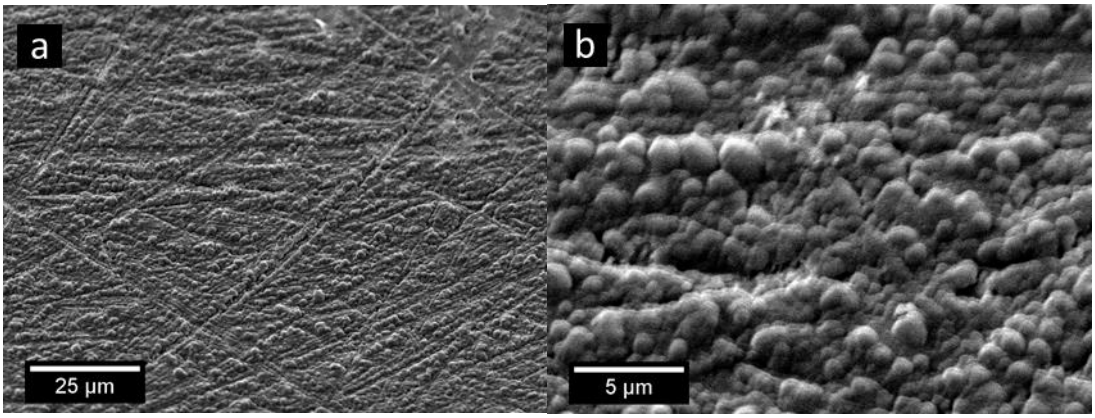

Figure 3.20: SEM micrographs of $PPyEtN_3$ grown in $EtOH/H_2O$ (3:4) with $LiClO_4$ (100 mM) displaying the 'cauliflower' morphology.

The composition of the $PPyEtN_3$ film grown in $EtOH/H_2O$ (3:4) with $LiClO_4$ (100 mM) and $PyEtN_3$ (35 mM) was examined using EDX spectroscopy (Figure 3.21). As observed previously for the other deposited polymer films, present in the spectrum and positioned at the expected values were carbon, nitrogen, oxygen and chlorine signals, due to the monomer structure and the dopant perchlorate.

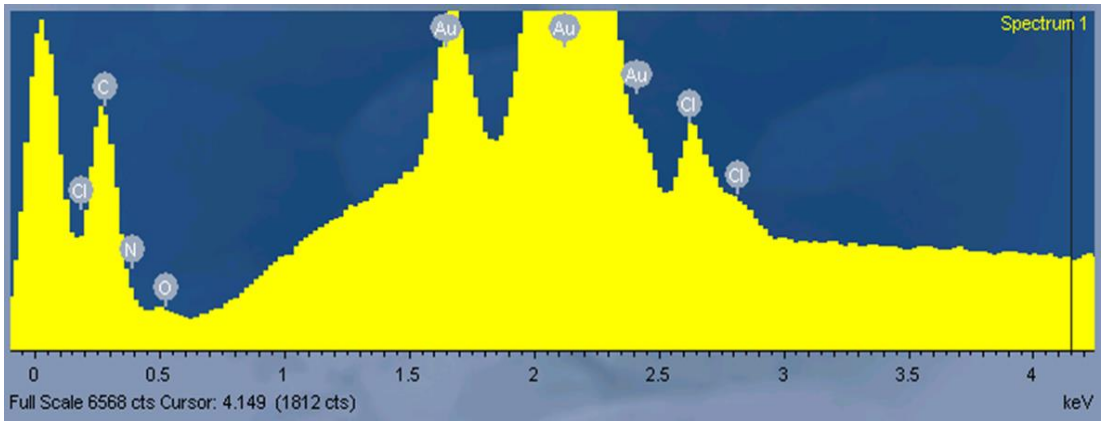

Figure 3.21: EDX spectrum of $PPyEtN_3$ grown in $EtOH/H_2O$ (3:4) doped with $LiClO_4$. Intense Au peaks were a consequence of the gold substrate utilised for electrodeposition.

The $PPyEtN_3$ film grown in $EtOH/H_2O$ (3:4) with $LiClO_4$ (100 mM) and $PyEtN_3$ (35 mM) was characterised using CV, to evaluate the impact of film growth in an aqueous/organic medium. The film was submerged in MeCN with $LiClO_4$ (100 mM) and scanning was performed between 0.000 - 0.900 V vs. Ag/AgCl with CVs recorded non-consecutively at different scan rates (Figure 3.22). This $PPyEtN_3$ film possessed good electrostability during the redox transition, with only a small loss of electroactivity during the first cycles and no discernible variations were observed in the successive scans. The reversible redox couple was located between 0.540 - 0.700 V vs. Ag/AgCl and as the scan rate was altered, the j_c/j_a ratio varied from 1.09 - 1.00, which represented the one-electron transfer mechanism. Upon increasing the scan rate from 25 to 125 mV s^{-1}, the ΔE_p increased from 76 mV to 158 mV. Also, the magnitude of j_{pa} and j_{pc} were observed to increase linearly with $v^{1/2}$ (r^2 of 0.9920 and 0.9845) respectively, supporting the proposal that the redox activity of this film was controlled by diffusion processes.[35]

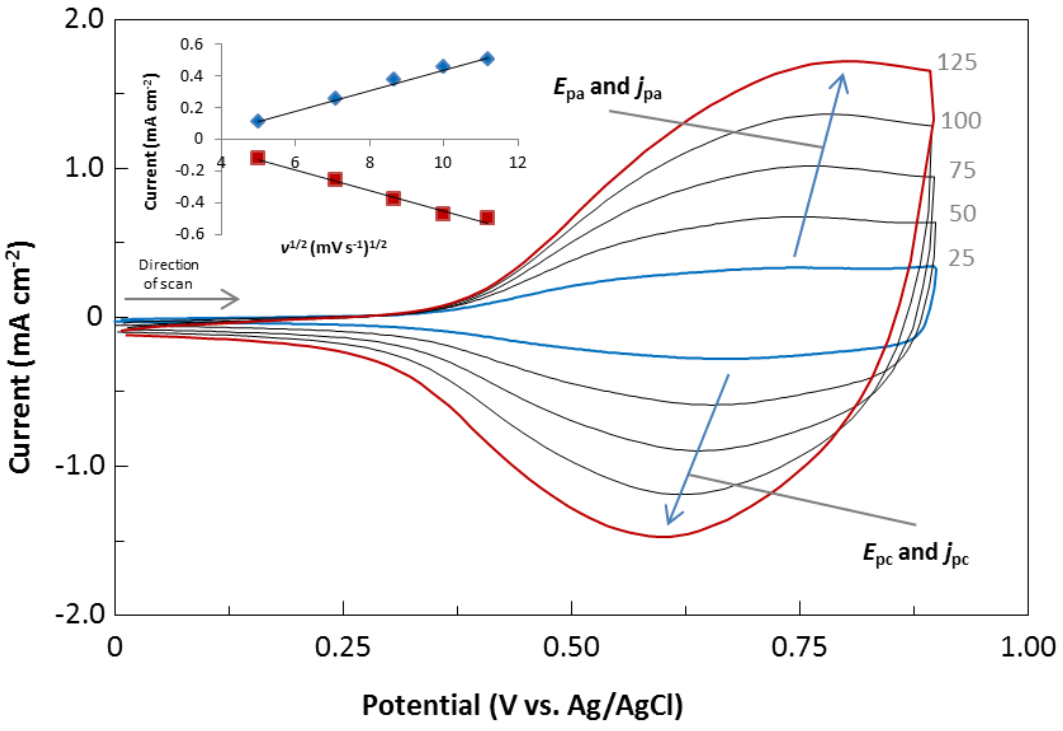

Figure 3.22: CVs of $PPyEtN_3$ (35 mM) grown in $EtOH/H_2O$ (3:4) and doped with $LiClO_4$ showing the electroactivity of the polymer cycled in MeCN and $LiClO_4$ (100 mM) from 25 (—) to 125 (—) mV s^{-1} in 25 mVs^{-1} increments. (Inset) Plot of anodic and cathodic peak current, j_p vs. square root of potential scan rate, $v^{1/2}$.

3.2.1.5 Poly[*N*-(2-azidoethyl)pyrrole] grown using potentiostatic method

It was decided to deposit the $PPyEtN_3$ film utilising constant potential amperometry (CPA) as polymer growth could be controlled to a greater extent, while the produced film would be less compact, when compared to that grown using CV.[41] Due to the incorporation of H_2O in the electrochemical system, this would result in increased polymer porosity.[42] This decrease in compactness and increased porosity should allow for increased mobility of ions during diffusion.[43] This is important as disadvantages from incorporating H_2O into the system are loss of electron transfer and conductivity, when compared to that of the MeCN solutions,[44] which were used previously in Section 3.2.1.1 - 3.2.1.4. It has been reported that CP nanowire films may be fabricated utilising CV as the deposition method, but these produced shorter nanowires when compared to that employing CPA.[45] With these factors in mind, growth *via* CV was perceived as a method, which would yield irreproducible growth with films of inferior quality, therefore reaffirming the choice of nanowire growth using CPA.

As we had chosen to attempt the deposition of $PPyEtN_3$ nanowire films utilising only CPA, investigation of the $PPyEtN_3$ bulk film deposition was also required and this was conducted by the characterisation methods used previously. It was decided that the deposition of bulk $PPyEtN_3$ films to different charge densities (1.9, 4.4, 6.3 and 12.6 mC cm^{-2}) using $PyEtN_3$ (35 mM) with $LiClO_4$ (100 mM) in an $EtOH/H_2O$ (3:4) co-solvent system at 0.850 V vs. SCE would be performed and the variation of polymer charge density yielded bulk films of increased thickness. The resulting polymer structures were analysed spectroscopically, electrochemically and morphologically.

The $PPyEtN_3$ bulk films of varied thickness, formed as semi-transparent or opaque polymers and the film structures were investigated using FTIR spectroscopy (Figure 3.26). It was observed that all films possessed a band at 2101 cm^{-1}, assigned to the asymmetric stretch of the azide moiety.[5] Due to this result, it was assumed that employment of CPA for electrodeposition did not affect the azide functional group, by attack from nucleophiles present in the organic/aqueous medium. The aliphatic CH stretch vibrations were observed at 2921 and 2852 cm^{-1} in the spectra.[20]

The medium intensity band at 1723 cm^{-1} (most prominent in Figure 3.23 (b) (—)) was due to the presence of carbonyl groups at certain C_β positions on the Py ring backbone,[39] caused by attack from hydroxyl and bicarbonate anions.[39,40] There was no evidence of amide formation (approx. 1670 cm^{-1} of medium intensity[40]), due to the possible development of carbonyl groups at the C_α position on the Py units in the polymer. Therefore, this may be indicative that α-α $PPyEtN_3$ branching predominantly occurs at the Py C_α. The weak bands from approx. 1600 - 1000 cm^{-1} were assigned to the modes of the polymer backbone, but the band at approx. 1085 cm^{-1} was assigned to the perchlorate dopant anion ν_2 mode[22,23] and this band can be seen to increase intensity, in relation to the increasing charge density (Figure 3.23 (c) (—) and (d) (—)). The broad band at approx. 1630 cm^{-1}, which can be observed in all four FTIR spectra, was assigned to residual H_2O, as reported for films of PPyMe.[21]

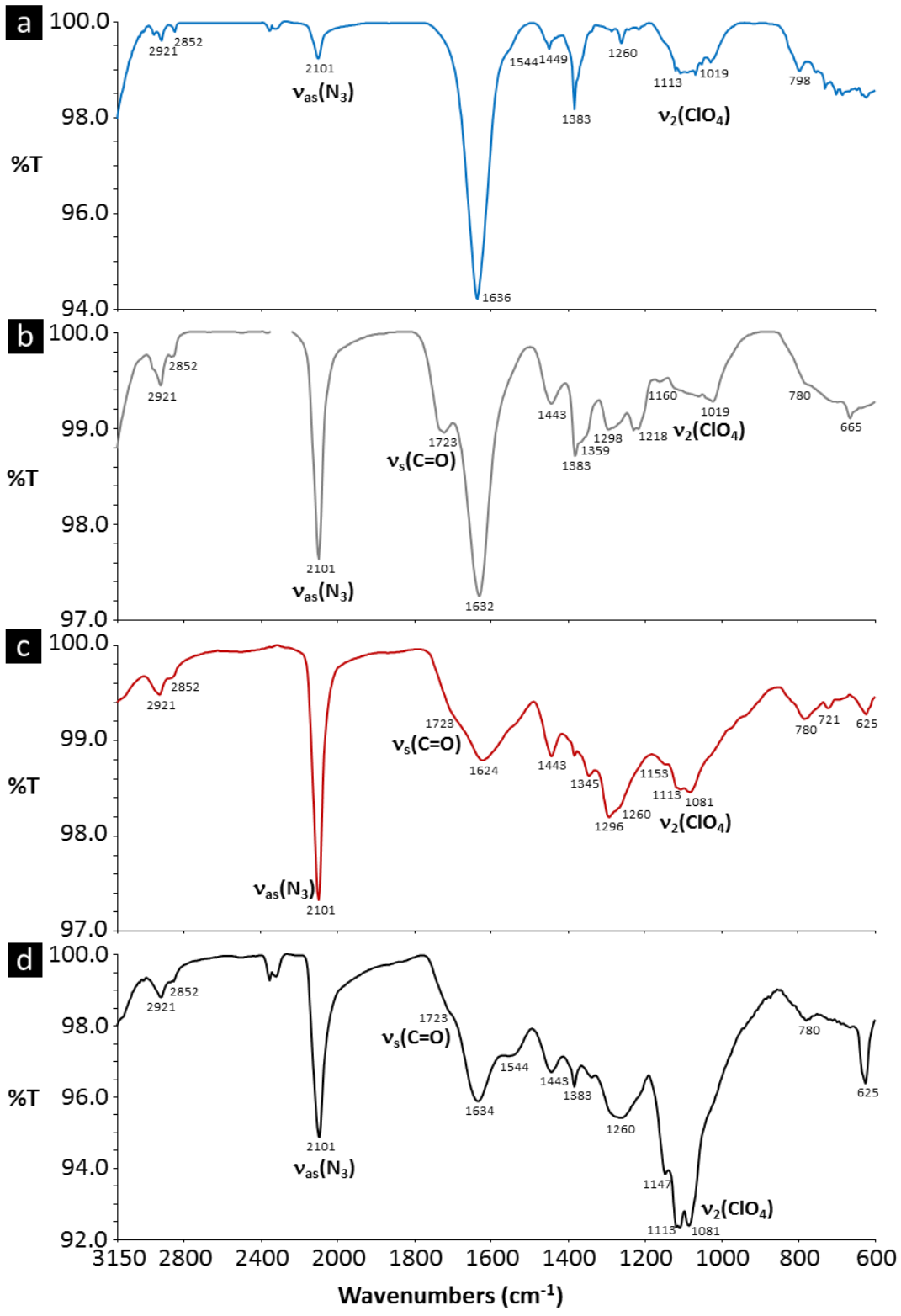

Figure 3.23: FTIR spectra of $PPyEtN_3$, grown in $EtOH/H_2O$ (3:4) with $LiClO_4$ (100 mM) to charge densities of (a) 1.9 (—), (b) 4.4 (—), (c) 6.3 (—) and (d) 12.6 (—) mC cm^{-2}, at ±2 cm^{-1} resolution in KBr. The band at approx. 1383 cm^{-1} was due to an impurity in the KBr powder.[25]

The $PPyEtN_3$ films, which were deposited to various charge densities, all formed homogeneous polymers (Figure 3.24), which could be described as 'cauliflower' morphology similar to that of PPy[10,11]. Interestingly, as the polymers increased in thickness with greater charge density, microstructures were seen to develop on top of the 'cauliflower' morphology (Figure 3.24 (i) and (l)).

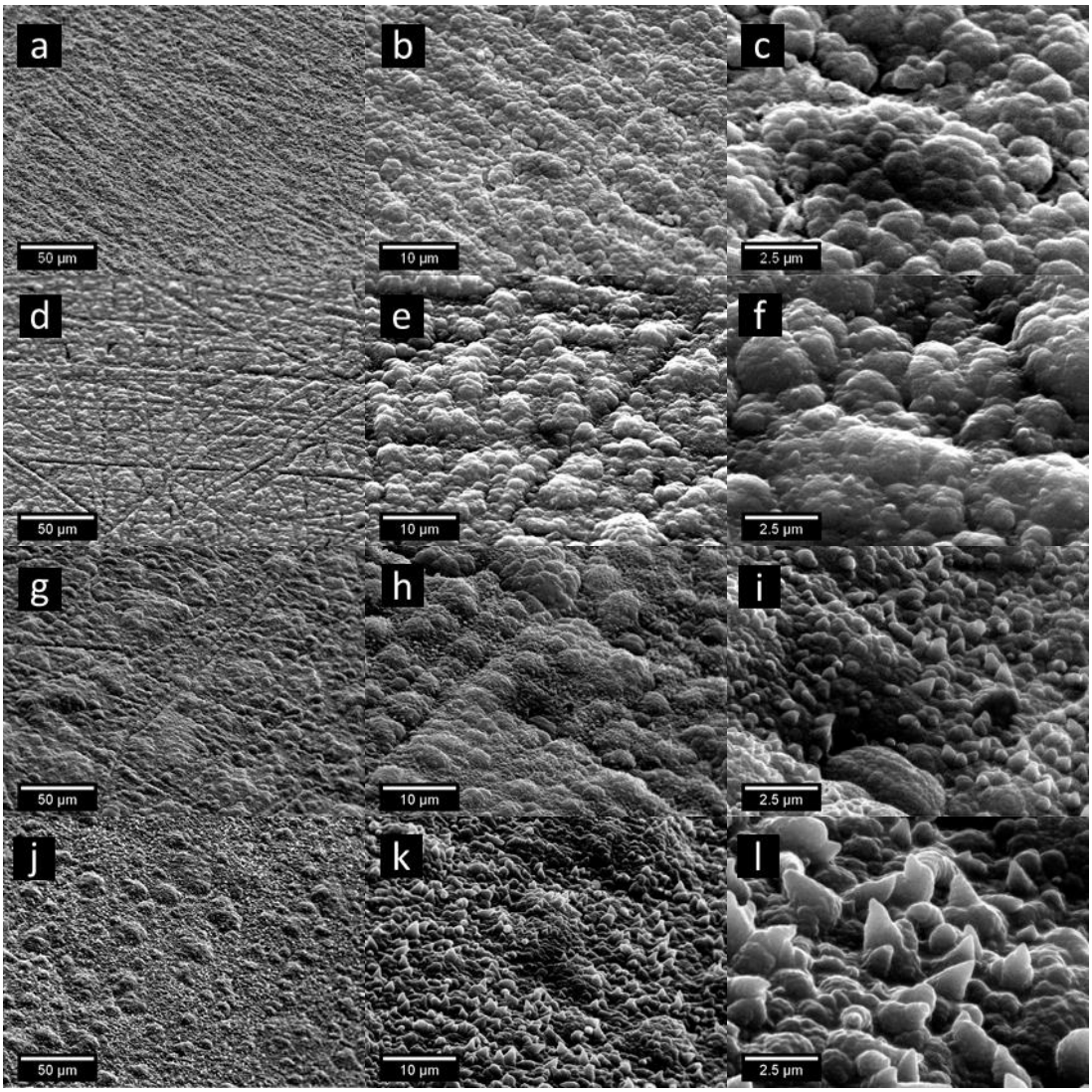

Figure 3.24: SEM micrographs of $PPyEtN_3$, grown in $EtOH/H_2O$ (3:4) with $LiClO_4$ (100 mM) to a charge density of (a - c) 1.9, (d - f) 4.4, (g - i) 6.3 and (j - l) 12.6 mC cm^{-2}, displaying the 'cauliflower' morphology.

The $PPyEtN_3$ films grown to varied charge densities in $EtOH/H_2O$ (3:4) with $LiClO_4$ (100 mM) were analysed using CV (Figure 3.25 (a) - (d)) by cycling non-consecutively at 25, 50, 75, 100 and 125 mV s^{-1} in MeCN with $LiClO_4$ (100 mM).

The $PPyEtN_3$ film grown to a charge density of 1.9 mC cm^{-2}, possessed a reversible redox couple located between 0.590 - 0.650 V vs. Ag/AgCl and the j_c/j_a ratio, which varied from 0.96 to 1.10, represented a one-electron transfer mechanism. j_{pa} and j_{pc} increased linearly with $v^{1/2}$ (0.9975 and 0.9836) indicating dominant diffusion controlled processes.[35] At 125 mV s^{-1}, this film possessed a j_{pa} of 1.64 mA cm^{-2}, while the film grown to 4.4 mC cm^{-2} possessed a j_{pa} of 2.20 mA cm^{-2}. It can be seen from these CVs that the E_{pa} of the film grown to 4.4 mC cm^{-2} (Figure 3.25 (b)) has shifted to a more positive potential (0.875 V vs. Ag/AgCl), if compared to the film grown to 1.9 mC cm^{-2}, which displayed a E_{pa} of 0.764 V vs. Ag/AgCl (Figure 3.25 (a)). This shift in potential represented the difficulty oxidising the polymer backbone. Reasons for this may include the increase in conjugation defects occurring, as the thickness of the films increased. Or that some areas of the polymer become electrochemically inactive during polymer growth.

The CVs of the polymer films grown to a charge density of 6.3 and 12.6 mC cm^{-2} are shown in Figure 3.25 (c) and (d) and it can be observed that the oxidation peak also became less prominent with increasing thickness of the polymer film. The $PPyEtN_3$ films grown to >4.4 mC cm^{-2} displayed decreased current densities, which were notable when compared to the current densities of the previous CVs for the film grown to 1.9 mC cm^{-2} (Figure 3.25 (a)). Further increasing the thickness of the films was shown to further decrease the current densities, as can be seen from the CVs of the films grown to 6.3 and 12.6 mC cm^{-2} (Figure 3.25 (c) and (d)). Decreases in current density were accompanied by increases in irreversibility for the polymers redox properties, as it changed from *quasi*-reversible to irreversible in Figure 3.25 (a) and (b). Also, j_{pc}/j_{pc} ratios and accurate peak currents could not be obtained for the thicker films, therefore no relationship to scan rate was reported. It has been recorded that overoxidation of electroactive polymers such as PPy, produces a loss of capacitance due to oxidation at positive potentials. This interrupts conjugation *via* formation of hydroxyl and carbonyl functional groups on the Py ring, finally resulting in loss of polymer material through formation of CO_2.[39] In basic aqueous solutions, nucleophilic attack facilitates this overoxidation of the polymer. With regards to PPy and its derivatives, hydroxide anions produce 3-hydroxypyrrole, which then converts to the pyrrolinone,[39] breaking down the electronic conjugation

of the polymer *via* overoxidation. These results illustrate how $PPyEtN_3$ polymer films must only be grown to a certain thickness, as growing the polymer to higher charge densities during electrochemical deposition results in loss of electrochemical activity and stability which has been reported for PPyEtCN by the Aleman group.[46]

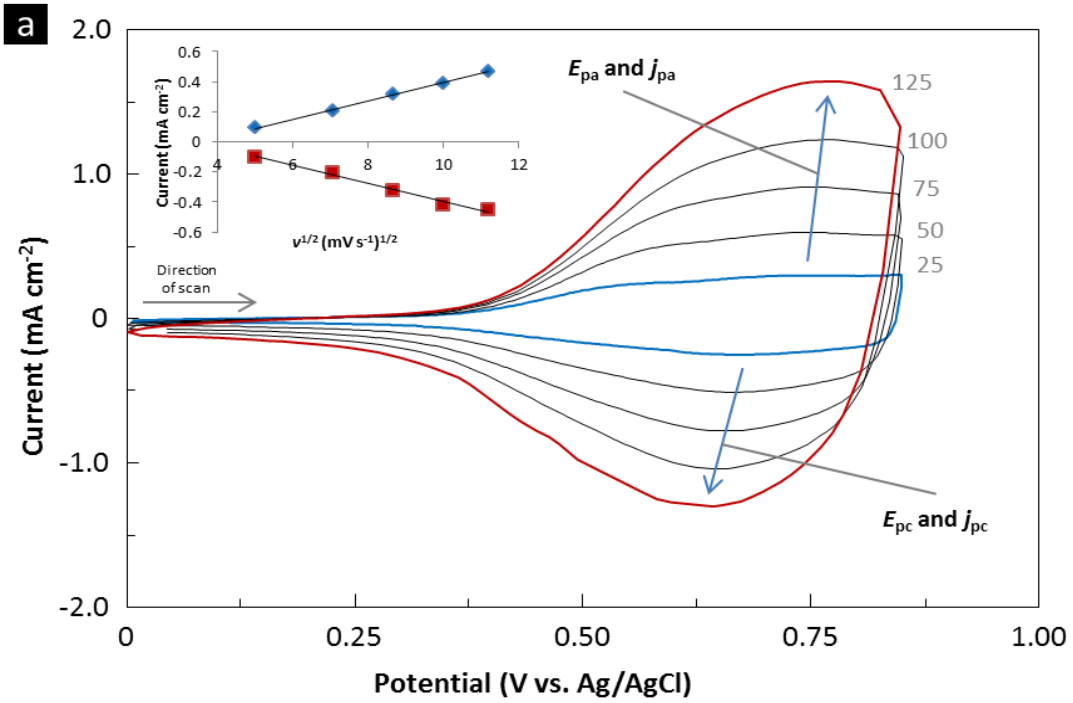

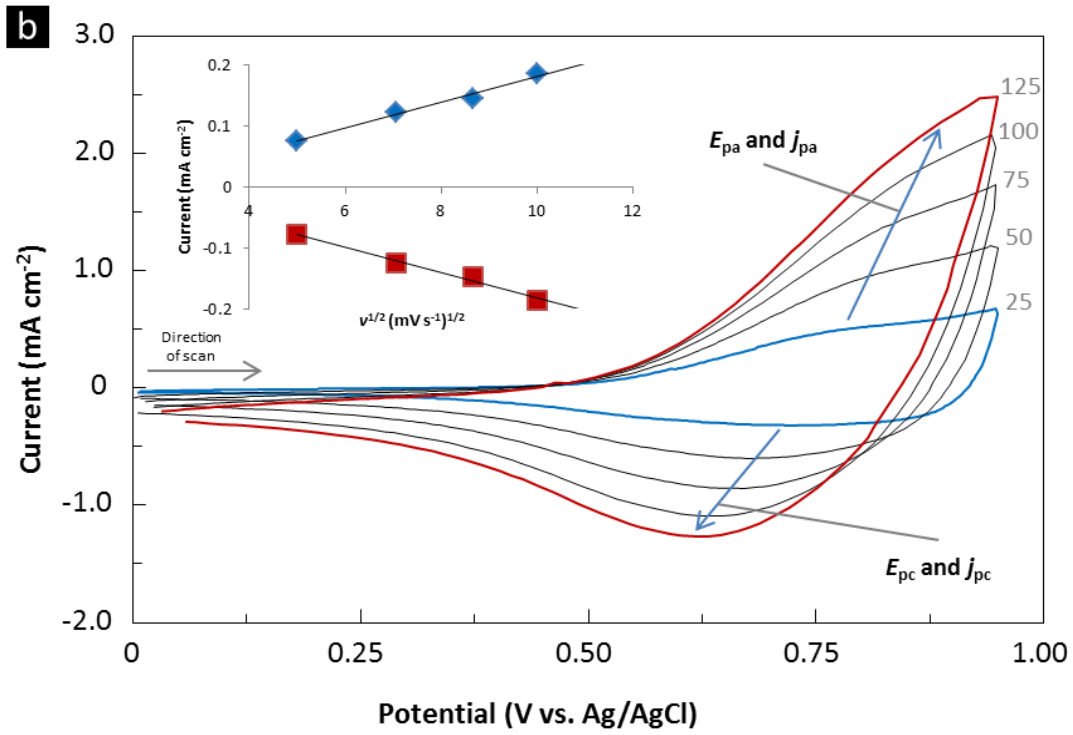

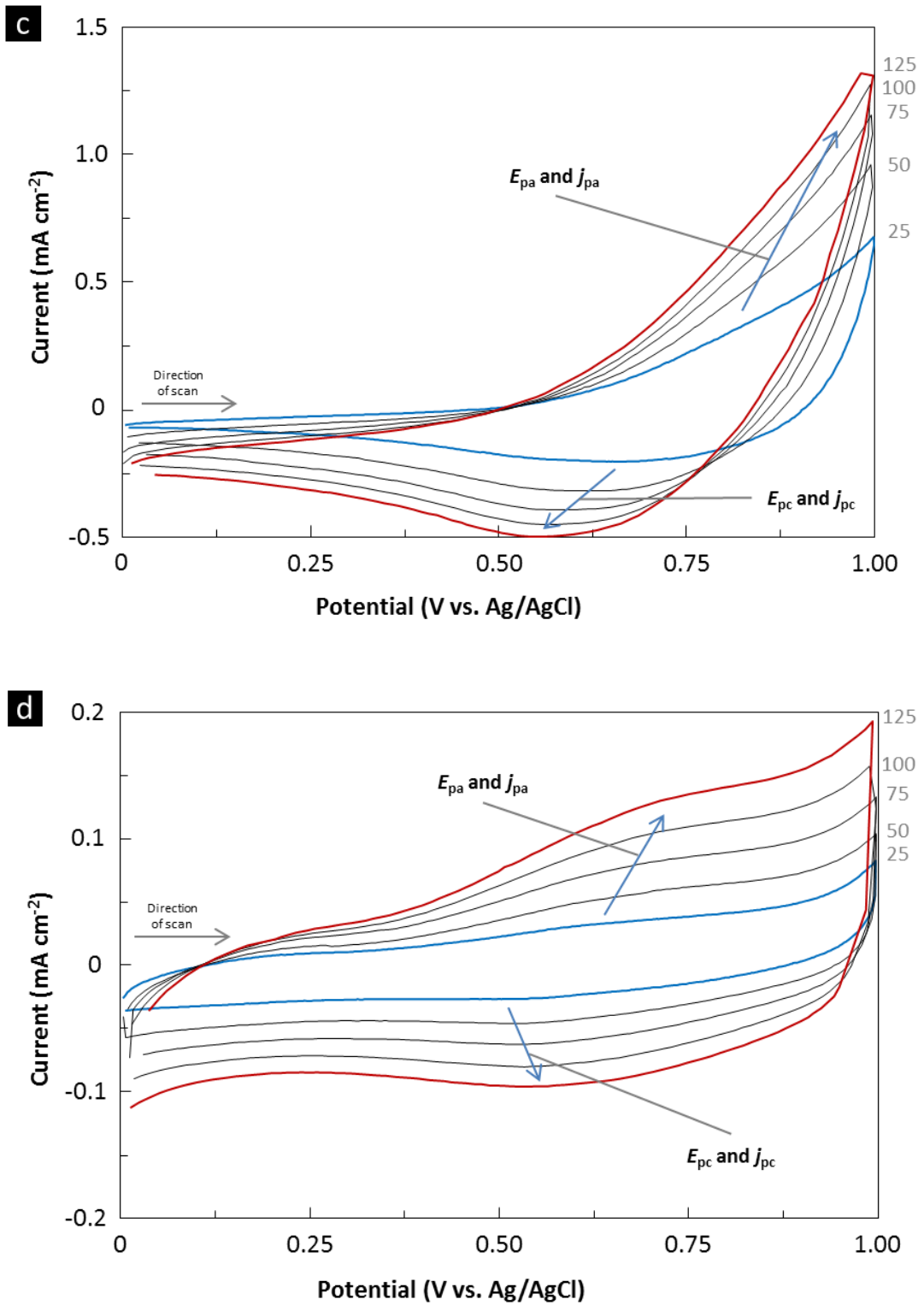

Figure 3.25: CVs of $PPyEtN_3$ grown in $EtOH/H_2O$ (3:4) with $LiClO_4$ (100 mM) to a charge density of (a) 1.9, (b) 4.4, (c) 6.3 and (d) 12.6 mC cm^{-2}, then cycled from 25 (—) to 125 (—) mV s^{-1} in 25 mV s^{-1} increments in MeCN and $LiClO_4$ (100 mM). (Inset) Plot of anodic and cathodic peak current, j_p vs. square root of potential scan rate, $v^{1/2}$.

It was determined from the preceding CVs that the electrochemical processes occurring in the films of various thicknesses, which were grown to charge densities ranging from 1.9 - 4.4 mC cm^{-2}, were similar to those in a thin layer cell. They clearly illustrated that electron transfer was more favourable for thinner films grown to 1.9 or 4.4 mC cm^{-2}. This was assumed as the j_{pa} values are proportional to the scan rate values and also the ΔE_p values are larger for films prepared to a greater charge density.[44] To corroborate these conclusions, the Log(j_{pa}) of the films grown to 1.9 and 4.4 mC cm^{-2} were plotted as a function of scan rate, Log(v), producing slopes of 1.01 and 0.63 respectively. It has been recorded by Park and co-workers,[44] that slopes of approx. 1.0 represent the electron transfer process for thin PPy films, (resembling thin layer cell). Thicker films produce slopes close to 0.5 representing the semi-infinite diffusion condition, which possesses an electron transfer process with mixed characteristics, where the diffusion of rate-limiting species is controlled by both thin layer cell and semi-infinite conditions. From the plot of Log(j_{pa}) vs. Log(v) it can be concluded that as the $PPyEtN_3$ films become thicker, the electron transfer eventually becomes controlled by a bulk-type diffusion of counter anions. The results here, for electron transfer processes and those for the previous CVs showing an increase in ΔE_p and decrease in j_{pa} with thickness, clearly illustrate that only thin films of $PPyEtN_3$ are viable in medical or industrial applications. In these situations a thin film which possessing a high amount of conjugation and displays *quasi*-reversible redox activity and stability are of the upmost importance.

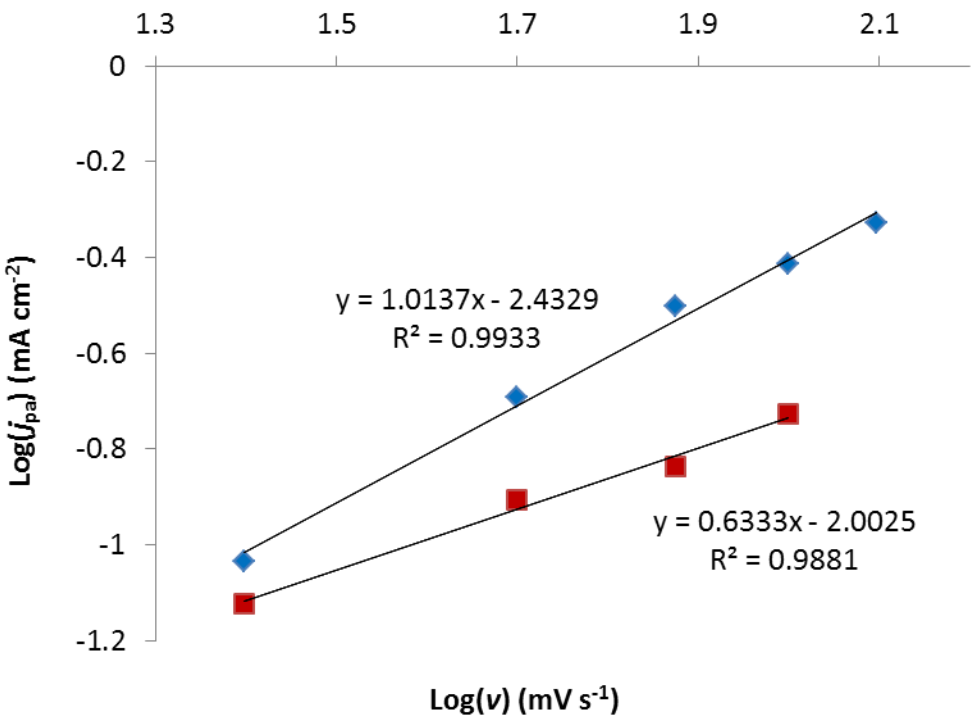

Figure 3.26: Plot of Log(j_{pa}) vs. Log(v) for CVs of $PPyEtN_3$, grown to charge densities of 1.9 (♦) and 4.4 (■) mC cm^{-2}, in $EtOH/H_2O$ (3:4) with $LiClO_4$ (100 mM), then cycled at 25, 50, 75, 100 and 125 mV s^{-1} in MeCN and $LiClO_4$ (100 mM).

Further structural investigation of the $PPyEtN_3$ films was deemed necessary at this point, as adequate knowledge had not been obtained for the polymers redox state after deposition had been performed. This cumulated with analysis of our electrodeposited $PPyEtN_3$ films using Raman spectroscopy. The Raman spectrum of a $PPyEtN_3$ film, deposited on a gold substrate at 0.850 V vs. SCE with $LiClO_4$ (100 mM) in $EtOH/H_2O$ (3:4) (Figure 3.27 (—)), was compared to a Raman spectrum of a PPy film, deposited on a gold substrate in $EtOH/H_2O$ (3:7) in the presence of $LiClO_4$ (100 mM) (Figure 3.27 (—)). The $PPyEtN_3$ film was grown to 6.3 mC cm^{-2} (as this produced a greater amount of polymer for analysis), scrapped off the electrode and finally embedded in a KBr pellet. The Raman spectra were attained using a laser line of 660 nm, as this wavelength produces spectra of the greatest clarity, when performing Raman spectroscopy on electroactive polymers such as PPy.[47]

In its open circuit state, a PPy film will be composed of neutral, polaron and bipolaron segments. In general, both polymers exhibited bands at similar wavenumbers in the spectra. The bands at approx. 1585 and 1520 cm^{-1} were assigned to the C=C stretch vibration for the PPy backbone for both polymers. In the $PPyEtN_3$ spectrum (Figure 3.27 (—)), the two bands were representative of C=C stretching for the charged oxidised quinoid species (1578 cm^{-1}) and the neutral reduced benzoid species (1523 cm^{-1}),[47] while in the PPy spectrum (Figure 3.27 (—)) these were positioned at 1593 cm^{-1} and 1515 cm^{-1}, respectively. The positioning of the band at 1578 cm^{-1} indicated that no bipolaron species and a moderate amount of polaron species were present within the $PPyEtN_3$ film,[48] while the PPy spectrum possesses this C=C stretching band at 1593 cm^{-1}, indicating the presence of bipolaron species. In the $PPyEtN_3$ spectrum, the double bands at 1362 cm^{-1} and 1332 cm^{-1} were assigned to the ring stretching mode. The other double bands at 1078 cm^{-1} and 1053 cm^{-1} were assigned to the CH in-plane deformation.[47] The band at 975 cm^{-1} was assigned to a ring deformation mode[48] representing the presence of polaron species[47] and it was noted that there was absence of a band at approx. 940 cm^{-1} for bipolaron species.[47] In the PPy spectrum it was clear that there was a significant band at 935 cm^{-1}, confirming the presence of bipolaron species. The absence of bipolaron species was expected in the $PPyEtN_3$ spectrum and it was attributed to the substitution of the PPy at the heteroatom. Substitution with bulky groups on the Py ring results in loss of coplanar formation due to steric effects,[49] which shortens conjugation length.[50] This factor negatively affects the concentration of charged defects, such as polarons and bipolarons, across the polymer backbone.[51]

The absence of bipolaron species in the $PPyEtN_3$ film was accentuated as the polymer films were grown in an aqueous based solvent system possessing nucleophilic species. It has been recorded in the literature that for the development of bipolaron species to occur in conducting polymers, the polymer film must acquire a critical concentration of polaron species during oxidation.[52] Nucleophilic species such as hydroxide interrupt the formation of these bipolaron species by decreasing the conjugation length of the electroactive polymer. The nucleophilic attack causes overoxidation to occur[53] resulting in carbonyl functional groups at the C_β on the

pyrrole ring[39] and the small band at approx.1705 cm^{-1} was confirmation of the presence of this group.

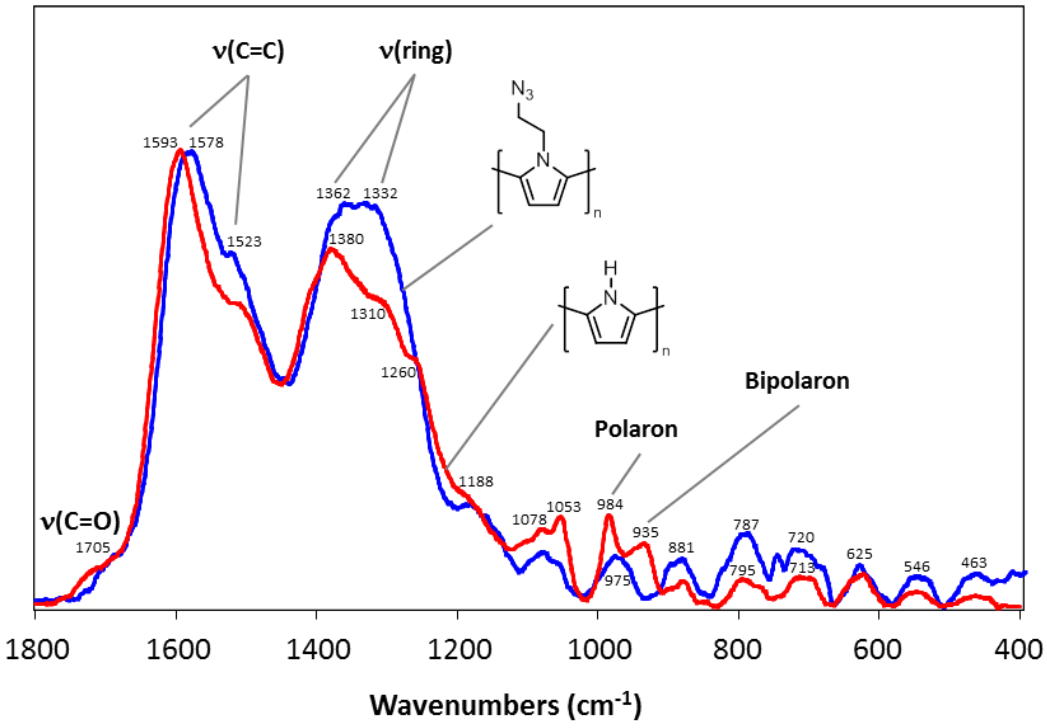

Figure 3.27: Raman spectra of $PPyEtN_3$ (35 mM) grown in $EtOH/H_2O$ (3:4) with $LiClO_4$ (100 mM) to a charge density of 6.3 mC cm^{-2} (—) and PPy (124 mM) grown in $EtOH/H_2O$ (3:7) with $LiClO_4$ (100 mM) to a charge density of 30.3 mC cm^{-2} (—). Both spectra were obtained using a laser line of 660 nm at ±1 cm^{-1} resolution in KBr.

3.2.2 Deposition of nanowire poly[*N*-(2-azidoethyl)pyrrole] films

The direct electrodeposition of nanowire films, consisting of a CP requires the utilisation of specific conditions to yield this desired morphology. During the electrodeposition of CP nanowire films on to substrates, phosphate[14] and carbonate[37,38] salts are usually required. These salts are capable of yielding nanowire films of varied dimensions with excellent control. It has been reported that the carbonate or phosphate salt require a critical concentration (≥200 mM) to yield a nanowire morphology.[14] Experiments performed by Li and co-workers, growing PPy nanowires illustrated that the phosphate salt concentration was the most important parameter affecting nanowire development. It was also determined that other variables in the system were significant and their work reported that there was a

monomer concentration ceiling value (≤100 mM). Also reported was the low concentration of the essential electrolytic salt, in this case $LiClO_4$ (≤70 mM). It was shown that nanowire fabrication was achieved only below a specific applied potential window (≤0.650 - 0.850 V vs. SCE) and drifting above this region yielded polymer microwires. Therefore, the observations made for these factors which control growth of PPy nanowires, were used as only guidelines when implementing the growth of poly[(azidoalkyl)pyrrole] nanowire films.

The nano-morphology of the $PPyEtN_3$ films can potentially diverge from wire to tube depending on substrate environment and the environment is known to be critical for optimal nanowire growth. As surface defects are known to be nucleation sites, producing aggressive uncontrolled structure development, they can potentially both accelerate and deviate growth from the desired nanostructure.[28,29] Using SEM the nanowire apex type can be observed to evolve (Figure 3.28). Due to variations on the surface of the gold substrate, the polymer morphology was shown to transform from pointed or flat-apex nanowires (foreground) into concave-apex nanowires (middle ground), eventually producing tubular microstructures (background) on a thin polymer base layer. From this evidence, it was clear that the gold substrate must be carefully polished before electrodeposition.

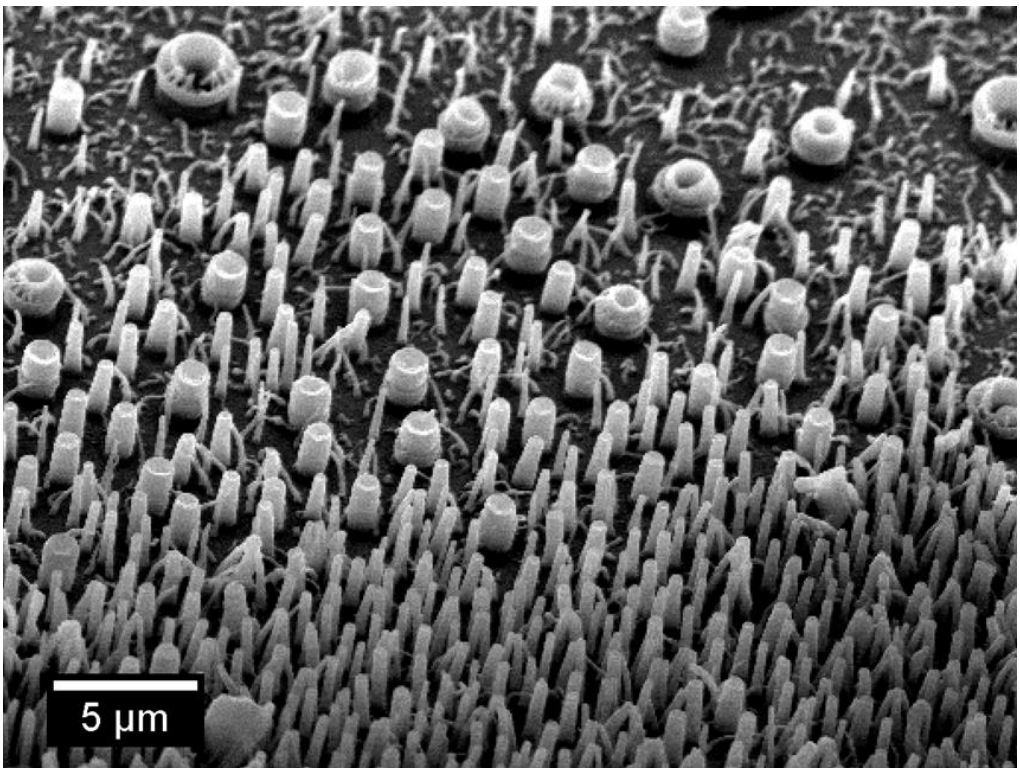

Figure 3.28: SEM micrograph of a $PPyEtN_3$ nanowire film grown, in $EtOH/H_2O$ (3:4) with ammonium dihydrogen phosphate ($(NH_4)H_2PO_4$) (300 mM) and $LiClO_4$ (20 mM), at 0.860 V vs. SCE for 5 min on the Au electrochemical quartz crystal microbalance (EQCM) electrode.

3.2.2.1 Effects of monomer concentration on poly[*N*-(2-azidoethyl)pyrrole] nanowire film morphology

Variation of the $PyEtN_3$ monomer concentration was investigated, as it has been reported in the literature that obtaining successful nanowire deposition can be greatly influenced by this growth parameter.[14,27] Therefore, polymer films of $PyEtN_3$ (65 mM) were deposited on to Au substrates, from a solution of $EtOH/H_2O$ (3:4) containing $LiClO_4$ (20 mM) and ammonium dihydrogen phosphate ($(NH_4)H_2PO_4$) (300 mM), whilst utilising CPA. The morphology of the resulting polymer film was determined using SEM (Figure 3.29 (a) - (f)). The variation of growth conditions and resulting observations from the corresponding SEM micrographs were summarised in Table 3.1. As can be seen from the table, under these conditions the most uniform wires possessing the smallest diameter were formed at an E_{app} of 0.770 V vs. SCE (Figure 3.29 (d)). When the E_{app} was below this, the beginning of wires (nodules) and 'shark tooth' structures were observed to form, while at higher E_{app} values more

irregular growth was produced, resulting in larger diameter nanowires of varied length and thickness.

Table 3.1: Electrodeposition conditions for films of $PyEtN_3$ (65 mM).[a]

E_{app} (V vs. SCE)[a]	Morphology	Mean diameter (nm)	SEM micrograph
0.700	Uniform shark tooth nodules	150	Fig. 3.29 (a)
0.730	Nodules and wires	140	Fig. 3.29 (b)
0.750	Uniform wires	110	Fig. 3.29 (c)
0.770	Uniform wires	135	Fig. 3.29 (d)
0.800	Mixed wires	180	Fig. 3.29 (e)
0.820	Mixed wires	160	Fig. 3.29 (f)

[a]For each above case, the polymer film was grown for 60 min on the Au substrate using $LiClO_4$ (20 mM) and $(NH_4)H_2PO_4$ (300 mM), while employing the stated parameters.

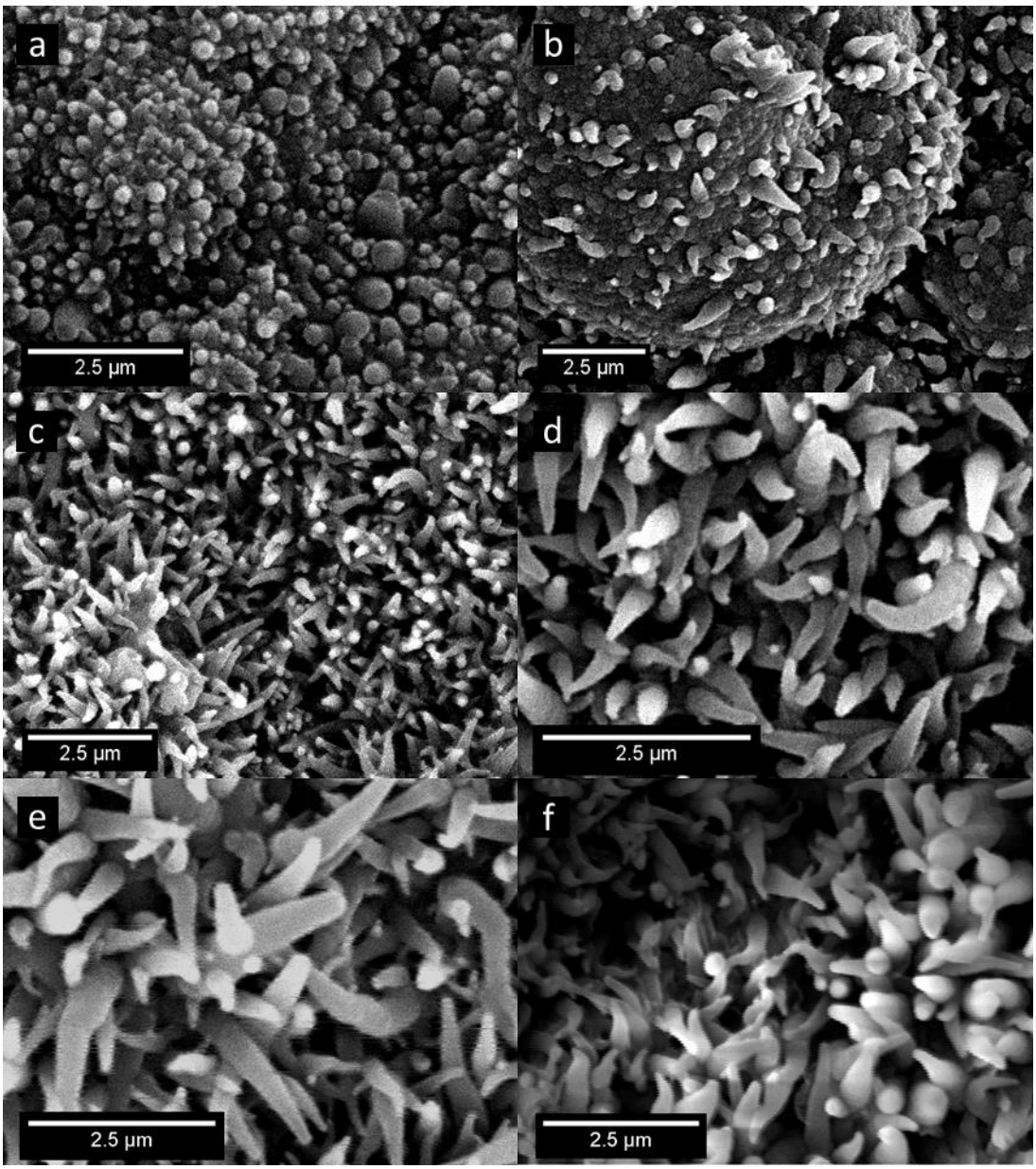

Figure 3.29: SEM micrographs of $PPyEtN_3$ films electrodeposited on the Au substrate using $PyEtN_3$ (65 mM), $LiClO_4$ (20 mM) and $(NH_4)H_2PO_4$ (300 mM), for 60 min at E_{app} values of (a) 0.700, (b) 0.730, (c) 0.750 (d) 0.770 (e) 0.800 and (f) 0.820 V vs. SCE.

It was desirable to attain wires, which possessed a diameter ≤100 nm, a similar set of experiments were performed, employing a lower monomer concentration (35 mM). This decrease of monomer concentration should slow down the rate of polymerisation at the substrate, as less monomer would be available to diffuse from the bulk solution to the surface during the polymerisation procedure. It has been

reported that lowering the monomer concentration inhibits the development of irregular PPy growth, during deposition of PPy nanowire films.[14]

The conditions of growth and the final morphology observed are presented in Table 3.2 with the associated SEM micrographs in Figure 3.30 (a) - (d). It was found that utilising a lower monomer concentration produced uniform nanowire films at all E_{app} values. However, at these conditions there were exceptional changes in nanowire length and width observed. At 0.770 V vs. SCE, which produced nanowires approx. 130 nm in diameter, the nanowires only grew very short (<1 μm) and were quite tapered. Upon increasing the E_{app} to 0.800 and 0.820 V vs. SCE, we were able to attain nanowires <100 nm in diameter, which grew in length considerably, to several microns. Upon application of 0.850 V vs. SCE, the nanowires did not develop in length but widened in diameter. The wires grown at the combined low monomer concentration (35 mM) and appropriate E_{app} (0.800 - 0.820 V vs. SCE) produced uniform non-tapered nanowires bound to a polymer film, which could be controlled easily in length and diameter.

Table 3.2: Electrodeposition conditions for films of $PyEtN_3$ (35 mM).[a]

E_{app} (V vs. SCE)[a]	$(NH_4)H_2PO_4$ conc. (mM)	Wire morphology	Mean Diameter (nm)	SEM micrograph
0.770	300	Uniform	130	Fig. 3.30 (a)
0.800	250	Uniform	80	Fig. 3.30 (b)
0.820	250	Uniform	75	Fig. 3.30 (c)
0.850	250	Uniform/contorted	100	Fig. 3.30 (d)

[a]For each above case, the polymer film was grown for 60 min on the Au substrate using $LiClO_4$ (20 mM), while employing the stated parameters.

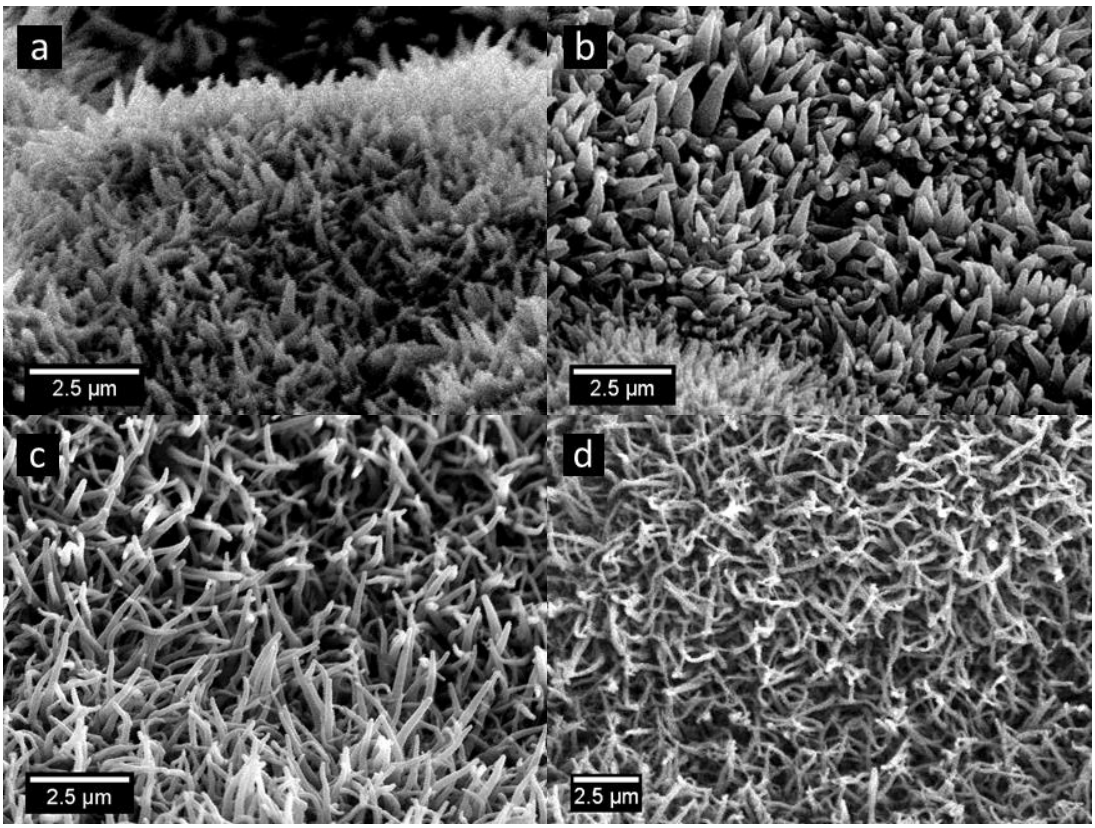

Figure 3.30: SEM micrographs of $PPyEtN_3$ films electrodeposited on the Au substrate using $PyEtN_3$ (35 mM) , $LiClO_4$ (20 mM) and $(NH_4)H_2PO_4$ (300 mM), for 60 min at E_{app} values of (a) 0.770, (b) 0.800, (c) 0.820 and (d) 0.850 V vs. SCE.

3.2.2.2 Effect of polymerisation time on poly[*N*-(2-azidoethyl)pyrrole] nanowire film morphology

In the preceding sections (Section 3.2.2.1 - 3.2.2.3), the polymer films that were grown for 60 min displayed a global film morphology consisting of highly uneven 'Hills and Valleys' type contours, as shown in Figure 3.31 (d). In order to circumvent the production of this morphology, the films were grown for substantially briefer time periods (5 and 10 min). The results of these experiments are given in Table 3.3 and the associated SEM micrographs in Figure 3.31. As the polymerisation time was decreased from 60 to 10 min, the 'Hills and Valleys' morphology completely disappeared and uniform oriented nanowires were produced (Figure 3.31 (b)). When the polymerisation time was further decreased to 5 min, it was observed that there was very little difference in the global film morphology, when compared to that grown for 10 min. While the overall film structure did not change, there was a

decrease in nanowire thickness, as the 5 min growth period produced nanowires approx. 100 nm in diameter (Figure 3.31 (c)). These results were significant, as it showed that the morphology and surface area of the nanowire film could be controlled further, simply by varying the polarisation time parameter. The ability to obtain reproducible nanowire films in 5 min is a beneficial attribute and makes this methodology much more user friendly and time efficient, when compared to the template approach.

After analyses of the film morphology were complete and wire dimensions were determined, a cross section of both films (5 and 60 min) was examined and can be observed in Figures 3.31 (e) and (f) respectively. The cross section of the nanowire polymer deposited for 5 min exhibits oriented homogeneous nanowires, approx. 2.5 µm in length and approx. 150 nm in diameter, growing away from a thin bulk layer of $PPyEtN_3$ ≤100 nm in thickness. The cross section of the nanowire polymer deposited for 60 min exhibits a thin outer film possessing nanowires, while beneath this outer film are multiple layers of thin bulk polymer, each spaced apart by an internal hollow chamber. These cavities which occur during the polymers growth yielded a decrease in polymer conductivity, due to the loss of connectivity between the polymer layers and the electrode surface.

Table 3.3: Electrodeposition conditions for films at varied time.[a]

Time (s)[a]	$(NH_4)H_2PO_4$ conc. (mM)	Wire morphology	Mean diameter (nm)	SEM micrograph
3600	250	Uniform/contorted	85	Fig. 3.31 (a)
600	300	Uniform/oriented	160	Fig. 3.31 (b)
300	300	Uniform/oriented	150	Fig. 3.31 (c)

[a]For each above case, the polymer film was grown for 60 min on the Au substrate using $PyEtN_3$ (35 mM) and $LiClO_4$ (20 mM), while employing the stated parameters.

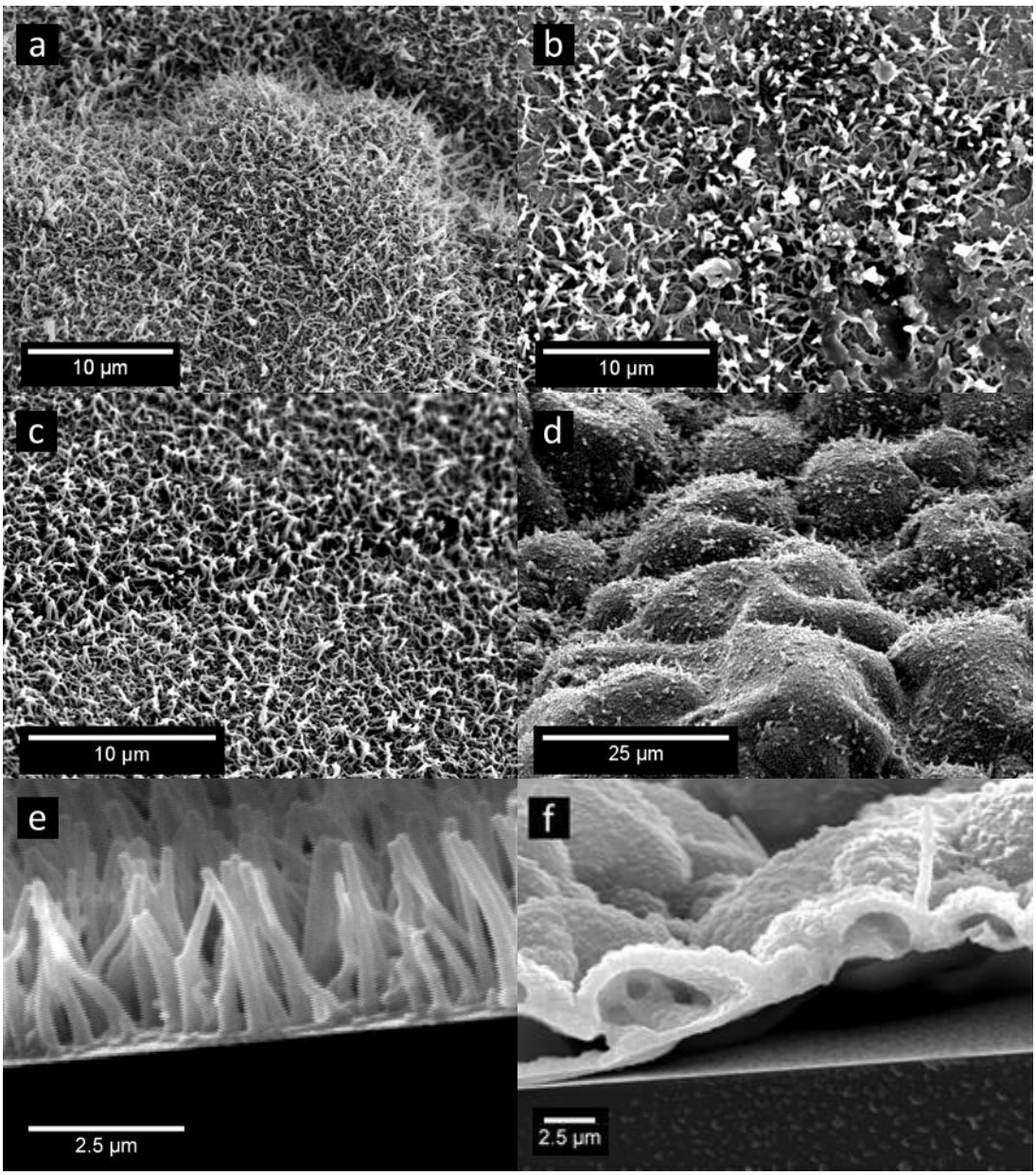

Figure 3.31: SEM micrographs of $PPyEtN_3$ films electrodeposited on Au substrates using $PyEtN_3$ (35 mM), $LiClO_4$ (20 mM) and $(NH_4)H_2PO_4$ (250/300 mM) for (a) (d) 60, (b) 10, (c) (e) 5 min.

3.2.2.3 Optimisation of the growth conditions for uniform poly[*N*-(2-azidoethyl)pyrrole] nanowire film formation

The preceding sections (Section 3.2.2.1 - 3.2.2.2) yielded an indication of the E_{app} necessary in the system for fabrication of homogeneous $PPyEtN_3$ nanowire films. A series of experiments were then executed for the purpose of probing some of the previously mentioned parameters more intensely, to confirm that effective

optimisation of the nanowire films had been attained. The results of these experiments are given in Table 3.4 and the associated SEM micrographs are displayed in Figure 3.32.

Beginning with a uniform nanowire film, a consequence of the growth conditions; $PyEtN_3$ (35 mM), $(NH_4)H_2PO_4$ (300 mM) and $LiClO_4$ (20 mM) at 0.850 V vs. SCE (Figure 3.32 (a)), the E_{app} was increased to 0.900 V vs. SCE and inhomogeneous wires were produced (Figure 3.32 (b)) due to the excess energy in the system. The monomer concentration (35 mM) was then reduced to 25 mM, while the $(NH_4)H_2PO_4$ concentration was unchanged (300 mM) and 0.850 V vs. SCE was applied to the cell. This yielded a very thin bulk film (Figure 3.32 (c)), but upon increasing the E_{app} to 0.900 V vs. SCE, this produced contorted wires displaced across the electrode (Figure 3.32 (d)). Further increase of E_{app} to 0.950 V vs. SCE yielded few isolated wires, but primarily nodules could be observed (Figure 3.32 (e)).

From this set of conditions, it can be determined that growth was not efficient enough to produce nanowires, due to the lower monomer concentration (25 mM) coupled with the high $(NH_4)H_2PO_4$ concentration (300 mM) even at higher E_{app} values (0.950 V vs. SCE). When the nanowires were produced, this was most probably due to substrate defects enhancing growth at these localities on the surface. It was found that the lower monomer concentration coupled with the high $(NH_4)H_2PO_4$ concentration was incapable of producing a homogeneous film of nanowires. Therefore, the $(NH_4)H_2PO_4$ concentration was slightly decreased (250 mM), while the monomer concentration (25 mM) was not altered. Then, 0.850 V vs. SCE was applied to the cell and some isolated wires and nodules were produced (Figure 3.32 (f)). By increasing the E_{app} to 0.900 V vs. SCE, some contorted wires were produced across the surface (Figure 3.32 (g)), but a further increase to 0.950 V vs. SCE produced uniform contorted wires (Figure 3.32 (h)). At these lower monomer and $(NH_4)H_2PO_4$ concentrations, it was possible to obtain homogeneous but non-oriented nanowires and it can be concluded that the appropriate $PyEtN_3/(NH_4)H_2PO_4$ concentration ratio was crucial to attain uniform nanowire film production.

Table 3.4: Electrodeposition conditions for optimisation of nanowire films.[a]

$PyEtN_3$ conc. (mM)[a]	**$(NH_4)H_2PO_4$ conc. (mM)**	**E_{app} (V vs. SCE)**	**Wire morphology**	**Mean diameter (nm)**	**SEM micrograph**
35	300	0.850	Uniform/oriented	125	Fig. 3.32 (a)
35	300	0.900	Inhomogeneous	150	Fig. 3.32 (b)
25	300	0.850	Thin bulk layer	N/A	Fig. 3.32 (c)
25	300	0.900	Sporadic contorted	125	Fig. 3.32 (d)
25	300	0.950	Nodules/isolated	200	Fig. 3.32 (e)
25	250	0.850	Nodules/isolated	140	Fig. 3.32 (f)
25	250	0.900	Sporadic/contorted	160	Fig. 3.32 (g)
25	250	0.950	Uniform/contorted	130	Fig. 3.32 (h)

[a]For each above case, the polymer film was grown for 5 min on the Au substrate using $LiClO_4$ (20 mM), while employing the stated parameters.

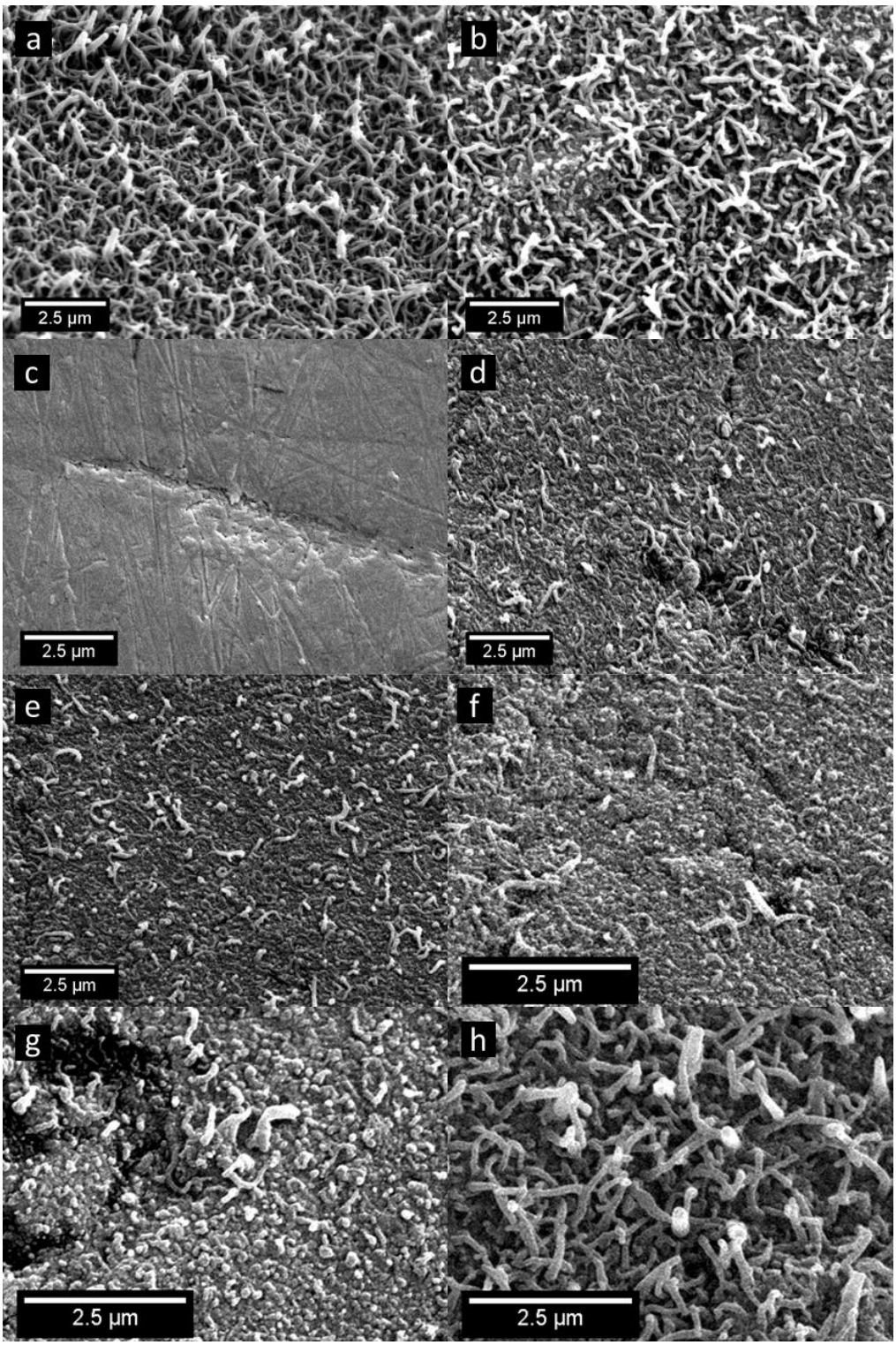

Figure 3.32: SEM micrographs of $PPyEtN_3$ films deposited using a variation of parameters: $PyEtN_3$ (mM)/$(NH_4)H_2PO_4$ (mM)/E_{app} (V vs. SCE). (a) 35/300/0.850, (b) 35/300/0.900, (c) 25/300/0.850 (d) 25/300/0.900, (e) 25/300/0.950, (f) 25/250/0.850, (g) 25/250/0.900 and (h) 25/250/0.950.

3.3 Conclusion

In this chapter, the depositions of three bulk polymer films ($PPyDeN_3$, $PPyPrN_3$ and $PPyEtN_3$) were performed using CV in an organic system. The films were characterised electrochemically using CV and structurally using SEM, EDX spectroscopy and FTIR spectroscopy. It was concluded from the data that with regard to the three bulk polymer films, the azide functional group remained tethered to the PPy backbone through the respective alkyl chain, the polymer was doped during polymerisation by the perchlorate counter anion and the polymer was deposited homogeneously in 'cauliflower' morphology across the substrate.

$PPyEtN_3$ was selected as the appropriate monomer for nanowire film deposition in an $EtOH/H_2O$ co-solvent system, as a consequence of its shorter alkyl chain length, yielding a greater affinity for more polar solvents. The $PPyEtN_3$ bulk films deposited in the organic/aqueous system were characterised electrochemically using CV and structurally using SEM, EDX spectroscopy and FTIR spectroscopy. Comparable results were obtained in relation to the preceding films deposited in purely organic aprotic solvent, except upon FTIR spectroscopy analysis, where the presence of a strong carbonyl band was observed at approx. 1725 cm^{-1}. Nucleophilic attack at the C_β of the PPy backbone, predominantly by hydroxide species, was accredited responsibility thus causing polymer overoxidation. This decrease in conjugation was reaffirmed by analysis of the CVs for these polymer films, where there is a decrease in current density, when compared to the films grown in a purely organic system.

The $PPyEtN_3$ films were also deposited using CPA, yielding more porous films with improved electrochemical activity and stability. Using this method permitted greater control as reproducibility was enhanced *via* the deposition of films to a predetermined charge density. This achieved precise film thickness control and a series of experiments were performed depositing films of increasing thickness. After analysis of the characterisation data, it was determined that only thin $PPyEtN_3$ films grown to a small charge density, exhibiting greater electron transfer are feasible for medical and industrial applications.

The utilisation of a novel template-free technique produced nanowire films consisting of $PPyEtN_3$, fabricated with great efficiency and control. Nanowire films were obtained on global morphologies of both a 'Hills and Valleys' and a flat monolayer type. Application of an appropriate E_{ox} for approx. 60 min achieves the 'Hills and Valleys' type morphology on the substrate. This consists of a thin-based outer film possessing nanowires, which grow out and away from the film, while beneath this outer film are multiple layers of thin bulk polymer, each spaced apart by an internal hollow chamber. These voids are likely to inhibit the conducting polymers desirable properties, due to the separation the voids create between the polymer layers and the electrode surface. At this stage of our research, the 'Hill and Valleys' type morphology was deemed an unattractive feature within our nanowire system and by reducing the polymerisation time, this feature could be diminished until no evidence of its presence was observed. The reduction of polymerisation time to 5 min furnished us with the ability to obtain reproducible nanowire films in a very short time period, producing a synthesis which is more time efficient, cost effective and much more user friendly.

3.4 References

1. Karsten, S.; Ameen, M. A.; Kallane, S. I.; Nan, A.; Turcu, R.; Liebscher, J. *Synthesis* **2010**, 3021-3028.
2. Martinez-Castro, N.; Magenau, A. J. D.; Storey, R. F. *J. Polym. Sci., Part A: Polym. Chem.* **2010**, *48*, 2533-2545.
3. Magenau, A. J. D.; Martinez-Castro, N.; Savin, D. A.; Storey, R. F. *Macromolecules* **2009**, *42*, 8044-8051.
4. Cernat, A.; Griveau, S.; Martin, P.; Lacroix, J. C.; Farcau, C.; Sandulescu, R.; Bedioui, F. *Electrochem. Commun.* **2012**, *23*, 141-144.
5. Li, Y.; Zhang, W.; Chang, J.; Chen, J.; Li, G.; Ju, Y. *Macromol. Chem. Phys.* **2008**, *209*, 322-329.
6. Jérôme, C.; Jérôme, R. *Angew. Chem., Int. Ed.* **1998**, *37*, 2488-2490.
7. Gao, M.; Huang, S.; Dai, L.; Wallace, G.; Gao, R.; Wang, Z. *Angew. Chem., Int. Ed.* **2000**, *39*, 3664-3667.
8. Tada, K.; Onoda, M. *Adv. Funct. Mater.* **2002**, *12*, 420-424.
9. Li, F.; He, J.; Zhou, W. L.; Wiley, J. B. *J. Am. Chem. Soc.* **2003**, *125*, 16166-16167.
10. Liang, L.; Liu, J.; Windisch Jr, C. F.; Exarhos, G. J.; Lin, Y. *Angew. Chem., Int. Ed.* **2002**, *41*, 3665-3668, 3520.
11. Wang, J. S.; Wang, J. X.; Wang, Z.; Wang, S. C. *Synth. Met.* **2006**, *156*, 610-613.
12. Yu, X.; Li, Y.; Kalantar-zadeh, K. *Sens. Actuators, B* **2009**, *136*, 1-7.
13. Debiemme-Chouvy, C. *Electrochem. Commun.* **2009**, *11*, 298-301.
14. Zang, J. F.; Li, C. M.; Bao, S. J.; Cui, X. Q.; Bao, Q. L.; Sun, C. Q. *Macromolecules* **2008**, *41*, 7053-7057.
15. West, R.; Josowicz, M.; Janata, J.; Minet, I.; Hevesi, L. *J. Electrochem. Soc.* **2009**, *156*, 55-59.
16. Kim, K. S.; Kato, T.; Uryu, T. *J. Polym. Sci., Part A: Polym. Chem.* **1999**, *37*, 3877-3887.
17. Li, Y.; Zhang, W. X.; Li, G. T.; Ju, Y. *Polymer* **2008**, *49*, 225-233.
18. Soto, J. P.; Diaz, F. R.; del Valle, M. A.; Velez, J. H.; East, G. A. *Appl. Surf. Sci.* **2008**, *254*, 3489-3496.
19. Chen, F.-F.; Wang, F. *Molecules* **2009**, *14*, 2656-2668.
20. Massoumi, B.; Lesani, H.; Saraei, M.; Entezami, A. A. *Iran. Polym. J.* **2011**, *20*, 747-756.
21. Lee, H.; Yang, H.; Kwak, J. *J. Electroanal. Chem.* **1999**, *468*, 104-109.
22. Roux, S.; Audebert, P.; Pagetti, J.; Roche, M. *Nouv. J. Chim.* **2000**, *24*, 877-884.
23. Sanchez De La Blanca, E.; Carrillo, I.; Gonzalez-Tejera, M. J.; Hernandez-Fuentes, I. *J. Polym. Sci., Part A: Polym. Chem.* **2000**, *38*, 291-298.
24. Diaw, A. K. D.; Yassar, A.; Gningue-Sall, D.; Aaron, J. J. *Arkivoc* **2008**, 122-144.
25. Goriletsky, V. I. M., A. I.; Belenko, L. E.; Rebrova, T. P. *Semi. Phys., Quant. Electron. Optoelectron.* **2001**, *4*, 139-141.
26. Annibaldi, V.; Rooney, A. D.; Breslin, C. B. *Corros. Sci.* **2012**, *59*, 179-185.
27. Zhang, X. L.; Wang, J. X.; Wang, Z.; Wang, S. C. *Sensors* **2005**, *5*, 580-593.

28. Nowicka, A. M.; Hasse, U.; Sievers, G.; Donten, M.; Stojek, Z.; Fletcher, S.; Scholz, F. *Angew. Chem., Int. Ed.* **2010**, *49*, 3006-3009.
29. Davies, A.; Audette, P.; Farrow, B.; Hassan, F.; Chen, Z. W.; Choi, J. Y.; Yu, A. P. *J. Phys. Chem. C* **2011**, *115*, 17612-17620.
30. Gandhi, M. R.; Murray, P.; Spinks, G. M.; Wallace, G. G. *Synth. Met.* **1995**, *73*, 247-256.
31. Thorne, N.; Dubus, A.; Lang, J. M.; Degreve, F.; Meyer, P. *J. Phys. Colloques* **1987**, *48*, 521-526.
32. Teng, F.; Santhanagopalan, S.; Asthana, A.; Geng, X.; Mho, S.-i.; Shahbazian-Yassar, R.; Meng, D. D. *J. Cryst. Growth* **2010**, *312*, 3493-3502.
33. Schiavon, G.; Zotti, G.; Comisso, N.; Berlin, A.; Pagani, G. *J. Phys. Chem.* **1994**, *98*, 4861-4864.
34. Oliveira Costa, S. D.; López Cascales, J. J. *J. Electroanal. Chem.* **2010**, *644*, 13-19.
35. Akinyeye, R.; Michira, I.; Sekota, M.; Al-Ahmed, A.; Baker, P.; Iwuoha, E. *Electroanal.* **2006**, *18*, 2441-2450.
36. Goosen, C.; Laing, T. J.; du, P. J.; Goosen, T. C.; Flynn, G. L. *Pharm. Res.* **2002**, *19*, 13-19.
37. Wang, J. X.; Mo, X. P.; Ge, D. T.; Tian, Y.; Wang, Z.; Wang, S. C. *Synth. Met.* **2006**, *156*, 514-518.
38. Li, J.; Lin, X. *J. Electrochem. Soc.* **2007**, *154*, B1074-B1079.
39. Rodríguez, I.; Scharifker, B. R.; Mostany, J. *J. Electroanal. Chem.* **2000**, *491*, 117-125.
40. Novák, P. *J. Electrochem. Soc.* **1991**, *138*, 3300.
41. Otero, T. F.; Delarreta, E. *Synth. Met.* **1988**, *26*, 79-88.
42. Carquigny, S.; Segut, O.; Lakard, B.; Lallemand, F.; Fievet, P. *Synth. Met.* **2008**, *158*, 453-461.
43. Garcia-Belmonte, G.; Bisquert, J. *Electrochim. Acta* **2002**, *47*, 4263-4272.
44. Ko, J. M.; Rhee, H. W.; Park, S. M.; Kim, C. Y. *J. Electrochem. Soc.* **1990**, *137*, 905-909.
45. Wang, Y.; Coti, K. K.; Wang, J.; Alam, M. M.; Shyue, J. J.; Lu, W.; Padture, N. P.; Tseng, H. R. *Nanotechnology* **2007**, *18*, 1-7.
46. Fabregat, G.; Cordova-Mateo, E.; Armelin, E.; Bertran, O.; Aleman, C. *J. Phys. Chem. C* **2011**, *115*, 14933-14941.
47. Chen, F.; Shi, G. Q.; Fu, M. X.; Qu, L. T.; Hong, X. Y. *Synth. Met.* **2003**, *132*, 125-132.
48. Santos, M. J. L.; Brolo, A. G.; Girotto, E. M. *Electrochim. Acta* **2007**, *52*, 6141-6145.
49. Ferraris, J. P.; Andrus, R. G.; Hrncir, D. C. *Chem. Commun.* **1989**, 1318-1320.
50. Liu, J.; Zhang, R.; Sauve, G.; Kowalewski, T.; McCullough, R. D. *J. Am. Chem. Soc.* **2008**, *130*, 13167-13176.
51. Street, G. B. *J. Phys. Colloques* **1983**, *186*, 599-606.
52. Christensen, P. A.; Hamnett, A. *Electrochim. Acta* **1991**, *36*, 1263-1286.
53. Redondo, M. I.; de la Blanca, E. S.; Garcia, M. V.; Raso, M. A.; Tortajada, J.; Gonzalez-Tejera, M. J. *Synth. Met.* **2001**, *122*, 431-435.

Chapter 4 Deposition mechanism and characterisation of nanowire poly[N-(2-azidoethyl)pyrrole] films and post-functionalisation of bulk and nanowire poly[N-(azidoalkyl)pyrrole] films

4.1 Introduction

There is current interest regarding the employment of template-free electrodeposition methodologies, during the fabrication of films consisting of CP nanowires/tubes on electrode substrates.[1-3] This methodology is facile and does not require the performance of additional steps for removal of a hard template. Recently, research has developed by extending this methodology to encompass substituted monomers. The presence of functional groups attached to the conducting polymer nanowire film may be utilised for the immobilisation of biomolecules, for development of biosensors or employed to alter the hydrophobic/hydrophilic properties of the coating.[4-6] A considerable proportion of the research described in this thesis concentrates on the fabrication of bulk and nanowire films composed of poly[*N*-(azidoalkyl)pyrrole]. This functional group has been previously incorporated into various CP monomers, succeeded by the electrodeposition of their respective bulk polymer coatings on electrode surfaces.[7-11] However, to the best of our knowledge, this is the first study focussed on the growth of poly[*N*-(azidoalkyl)pyrrole] in the nanowire morphology. The attractive feature of the azide functional group is that it yields the ability to exploit CuAAC chemistry. Previous studies have utilised this chemistry to covalently bind a vast array of chemical moieties, such as CNTs,[4,12,13] Fc,[14,15] polysulfobetaine[16] and polyethylene glycol[17] to the CP.

In Chapter 3, it was illustrated how a methodology was successfully developed to electrodeposit nanowires of $PPyEtN_3$ employing a template-free approach. In the current chapter, studies are performed to investigate the mechanism of nanowire formation and to characterise the nanowires using various surface analysis techniques. Investigations were also performed exploiting CuAAC chemistry to attach Fc to $PyEtN_3$, $PyDeN_3$ and to the $PPyEtN_3$ nanowire film.

4.2 Results and discussion

4.2.1 Investigation of the $PPyEtN_3$ nanowire films deposition mechanism

The efficient deposition of a nanowire polymer film is highly dependent on the processes of nucleation and growth, which are influenced greatly by polymerisation kinetics.[18,19] A number of studies have shown that a fast nucleation process, succeeded by a slow growth process, yields a nanostructured polymer morphology.[3,19] This is evident in work regarding the template-free fabrication of polyaniline (PANI) nanowires, performed utilising oxidative interfacial chemical polymerisation. During these studies an aqueous/organic biphasic system was employed, with oxidant dissolved in the aqueous phase and monomer dissolved in the organic phase. Employment of interfacial polymerisation suppressed secondary polymer growth; PANI leaves the interfacial zone terminating polymerisation, which circumvents the agglomeration of particles on the already formed nanowires.[18,20,21] In addition, studies exploiting interfacial chemical oxidative polymerisation have reported that small additions of the appropriate dimer (Py, aniline or thiophene) produce longer, less tangled nanowires. This occurs due to the increased rate of polymerisation during nucleation, as the dimer species exist as homogeneous nucleation sites.[22] Consumption of the dimers during nucleation induced a decreased rate of polymerisation thereafter, yielding a slower growth process. Exemplifying kinetic control of nanowire formation *via* an electrochemical technique is the template-free deposition of PANI nanowires. During these studies, researchers employed a stepwise decrease of current density, *j*, during the electrodeposition.[3,19] This methodology utilised a large *j* value to initially deposit PANI nanoparticles on the surface, which would act as nucleation sites to further develop oriented and uniform nanowires, fabricated at lower *j* values.[3,19] Significantly, it has been highlighted that homogeneous nucleation of the polymer on the substrate is essential for the one-dimensional (1D) development of nanowire morphology.[22] In this section, studies were performed to investigate how the polymerisation conditions, which were developed in Chapter 3, exert kinetic control over both the nucleation and subsequent propagation stages of polymer growth, permitting deposition of $PPyEtN_3$ nanowires.

4.2.1.1 Physical development of the $PPyEtN_3$ nanowire morphology

The deposition of a CP on a substrate can be monitored by recording the change in current density, *j*, of the system as a function of time, *t*. The current density-time (*j-t)* transient plot, attained during the electrodeposition of a $PPyEtN_3$ nanowire film at 0.850 V vs. SCE on a Pt substrate, in an $EtOH/H_2O$ (3:4) co-solvent system with $(NH_4)H_2PO_4$ (300 mM) and $LiClO_4$ (20 mM), is displayed in Figure 4.1. The points designated as t_0,j_0 and t_{max},j_{max} represent the onset of polymer nucleation and overlap of the diffusion zones, belonging to the growing nucleation sites, respectively. The significance of the shape of the *j-t* transient plot will be discussed in more detail in Section 4.2.1.2. Separate experiments were performed where discontinuation of the growth process was incited at approx. 25, 100 and 900 s (Figure 4.1 (1), (2) and (3)), precisely after the *j-t* minimum (t_0,j_0), at the approx. *j-t* maximum (t_{max},j_{max}) and at a time when nanowires have fully developed, respectively. This enabled the possibility of observing the progression of film morphology utilising scanning electron microscopy (SEM). The second *j-t* maximum (t'_{max},j'_{max}) at approx. 350 s was attributed to the Pt substrate. As Pt is a harder material in comparison to Au, it is not surprising that it is much more difficult to attain a smooth surface during polishing of the Pt substrates. Scratches remaining on the substrate after polishing may act as nucleation sites for the uncontrolled development of polymer, which could possibly contribute to unexpected features present in a *j-t* transient plot. CP nanowire films have been observed to grow on the substrate *via* the formation of a thin polymer layer covering the electrode surface, which thereafter, supports the perpendicular, 1D growth of nanowires away from the substrate.[23] Confirmation for this type of developmental process was necessary, as the utilisation of $PyEtN_3$ for the fabrication of nanowire morphology has not been attempted up until this point.

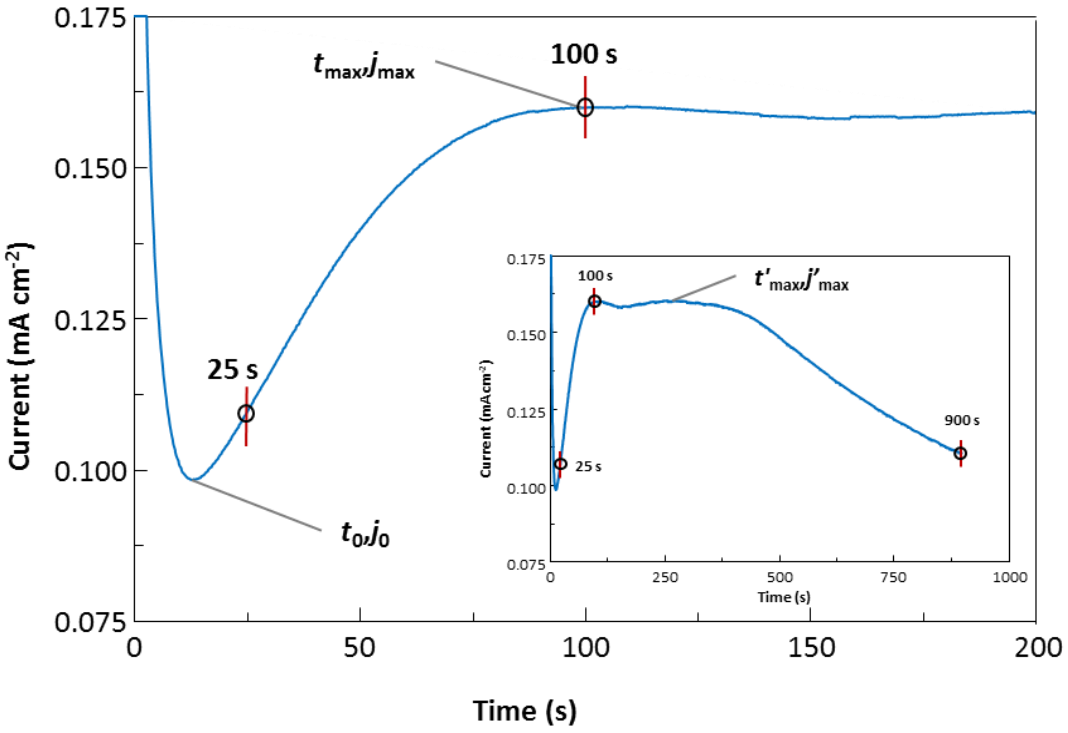

Figure 4.1: Current-density time (j-t) transients of $PPyEtN_3$ nanowire films deposited on the Pt substrate in $EtOH/H_2O$ (3:4) with $(NH_4)H_2PO_4$ (300 mM) and $LiClO_4$ (20 mM) at 0.850 V vs. SCE for 25, 100 and 900 s.

The SEM micrographs of a $PPyEtN_3$ nanowire film are displayed in both plan and oblique-angle-views (Figure 4.2) and it was determined from Figure 4.2 (a) and (b) that polymer growth in this system, begins with the deposition of a thin homogeneous layer of bulk $PPyEtN_3$ covering the substrate. A cross section of the $PPyEtN_3$ film is displayed in Figure 4.3, which illustrates that the $PPyEtN_3$ nanowires grow perpendicularly, away from a thin bulk base layer of polymer (Figure 4.3 (inset)). This thin layer of bulk $PPyEtN_3$ possesses little nodules protruding from the polymer surface, which are the beginning of nanowire development (25 s of growth, Figure 4.2 (a) and b)). Upon extension of the polymerisation time to 100 s, the nodules evolve into nanowires approx. 500 nm in length and approx. 100 nm in diameter (Figure 4.2 (c) and (d)). Further extension of the polymerisation time to 900 s produces longer and thicker nanowires, growing to approx. 1.5 µm in length and 200 nm in diameter. A slight tapering effect can be observed on the nanowires, grown for longer time periods (Figure 4.2 (e) and (f)). These results were consistent with work reported in the literature, in regards to the

prominence of nodules and the development of polymer nanowires from these sites over time.[3,24-26]

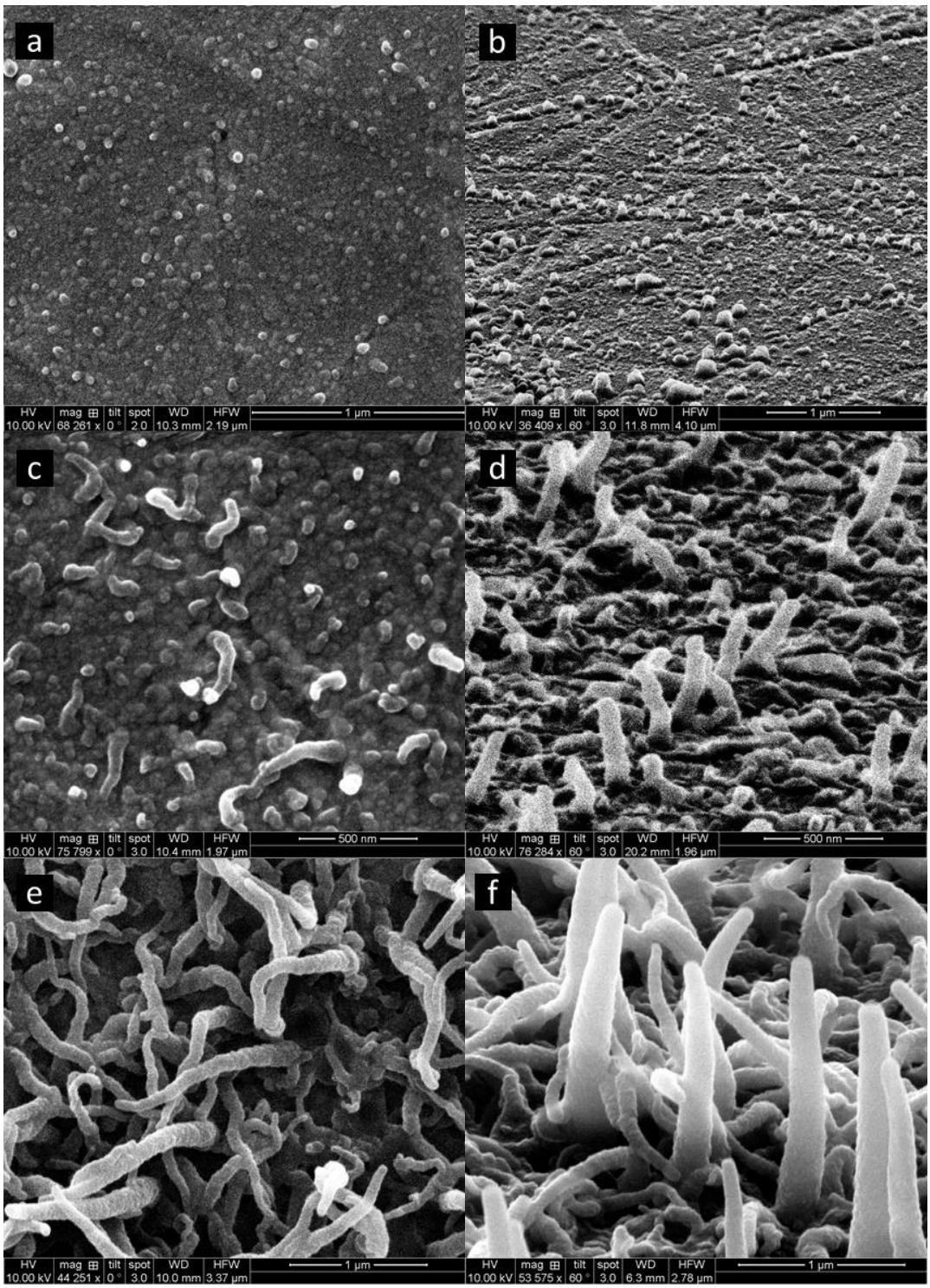

Figure 4.2: SEM micrographs (plan-view and oblique-angle-view) of $PPyEtN_3$ nanowire films deposited on the Pt substrate in $EtOH/H_2O$ (3:4) with $(NH_4)H_2PO_4$ (300 mM) and $LiClO_4$ (20 mM) at 0.850 V vs. SCE for (a - b) 25, (c - d) 100 and (e - f) 900 s.

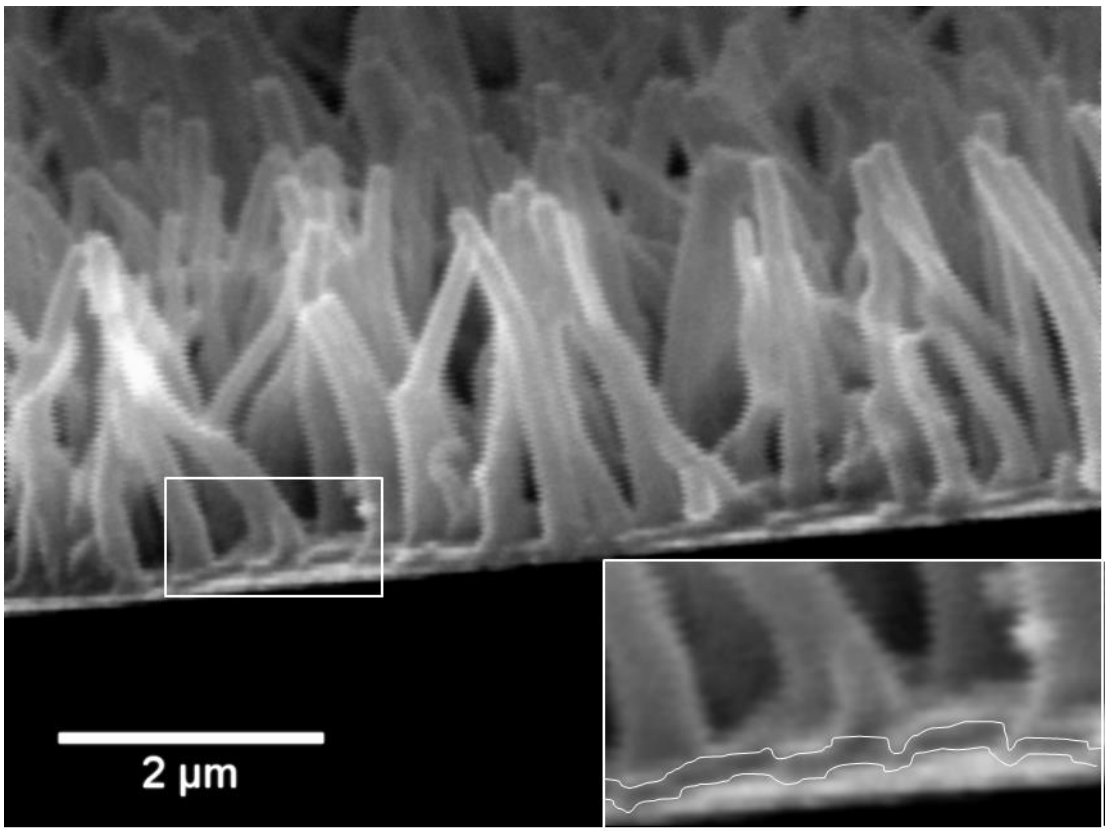

Figure 4.3: SEM micrograph of $PPyEtN_3$ nanowire film (cross section) deposited on the Au substrate in $EtOH/H_2O$ (3:4) with $(NH_4)H_2PO_4$ (300 mM) and $LiClO_4$ (20 mM) at 0.850 V vs. SCE, illustrating the thin bulk base layer approx. 100 nm in thickness. Inset: Magnified $PPyEtN_3$ base layer.

4.2.1.2 Modelling of experimental current density-time (*j*-*t*) transients

In the successive work, the very early stages of polymer nucleation were investigated. The substrate employed for electrodeposition was changed to Au, as preliminary studies revealed that a polished Au substrate yielded nanowire films of greater homogeneous character, in comparison to that of Pt. Also, the *j*-*t* transient for $PPyEtN_3$ nanowire deposition on Au, possessed a t_{max},j_{max} occurring earlier during CPA, while any t'_{max},j'_{max} processes occurred much later. In order to describe the type of nucleation and growth mechanism (NGM) occurring at the very early stages of polymer adhesion on the substrate, the equations developed by Harrison and Thirsk describing evolution of crystal nucleation and growth[27] were employed, as these equations have previously been applied to the nucleation and growth of bulk polymers films.[28-30] Our research group has performed the first study regarding the application of NGM modelling to the nanostructured deposition of a poly[*N*-

(substituted)pyrrole].[25] These NGM models describe polymer nucleation in two manners, as either an instantaneous nucleation (IN) or progressive nucleation (PN) process (Scheme 4.1). The IN mechanism involves simultaneous polymer nucleation on the substrate at specific sites, succeeded by polymer growth outwards from these nucleation sites, until a complete film covers the substrate. The PN mechanism involves isochronous polymer nucleation on the substrate, yielding nucleation sites at varied stages of growth.

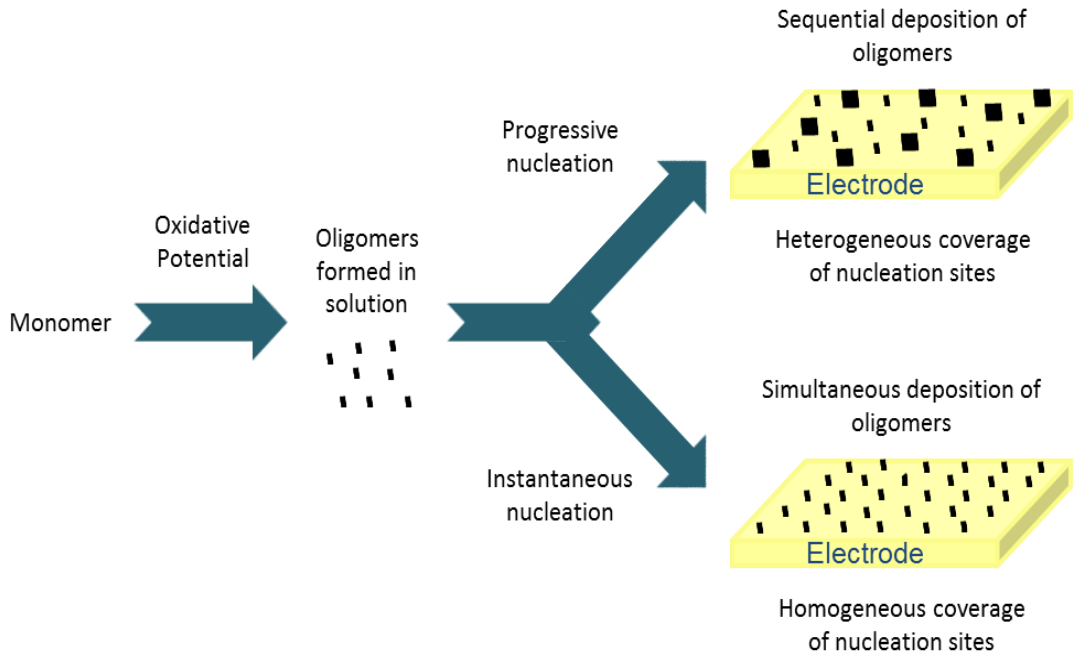

Scheme 4.1 Progressive nucleation and instantaneous nucleation processes for the deposition of polymers on a substrate.

Conspicuously, these two nucleation processes will produce respective films possessing dissimilar physical characteristics, as the IN process is a more controlled mechanism of polymer deposition. The NGM models also describe the subsequent growth of polymer occurring directly after nucleation in two manners (Scheme 4.2), as either a two-dimensional (2D) or a three-dimensional (3D) growth process.[31] The 2D growth process involves development of the polymer from the nucleation sites in the (x,y) plane, parallel to the substrate, yielding a very thin film that preferentially grows in only two dimensions of space. The 3D growth process involves polymer development in (x,y,z) space, growing equally in all directions away from the nucleation site, producing a thicker film growing in the three dimensions of space.

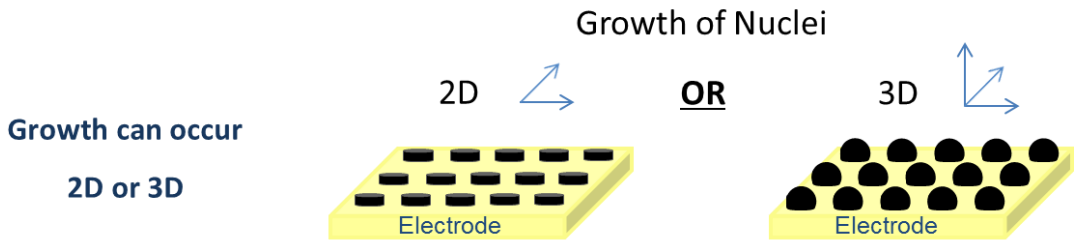

Scheme 4.2: 2D and 3D growth processes for the deposition of polymers on a substrate.

As stated previously, these processes occur at the first stage of polymer development (approx. 0 - 10 s for the nanowire deposition system) on the substrate and occur well before any 1D nanowire structure has been constructed.

Combination of the instantaneous and progressive nucleation processes with the 2D and 3D growth processes yields four NGMs, which describe the deposition process at the early stage of growth and can be expressed by the subsequent equations.[28]

Progressive nucleation and two-dimensional growth (PN2D):

$$\frac{J}{J_{\max}} = \left(\frac{t}{t_{\max}}\right)^2 \exp\left\{-\frac{2}{3}\left(\frac{t^3 - {t_{\max}}^3}{{t_{\max}}^3}\right)\right\} \tag{4.1}$$

Instantaneous nucleation and two-dimensional growth (IN2D):

$$\frac{J}{J_{\max}} = \left(\frac{t}{t_{\max}}\right) \exp\left\{-\frac{1}{2}\left(\frac{t^2 - {t_{\max}}^2}{{t_{\max}}^2}\right)\right\} \tag{4.2}$$

Progressive nucleation and three-dimensional growth (PN3D):

$$\left(\frac{J}{J_{\max}}\right)^2 = \frac{1.2254}{\left(\frac{t}{t_{\max}}\right)}\left\{1 - \exp\left[-2.3367\left(\frac{t}{t_{\max}}\right)^2\right]\right\}^2 \tag{4.3}$$

Instantaneous nucleation and three-dimensional growth (IN3D):

$$\left(\frac{J}{J_{\max}}\right)^2 = \frac{1.9542}{\left(\frac{t}{t_{\max}}\right)}\left\{1 - \exp\left[-1.2564\left(\frac{t}{t_{\max}}\right)\right]\right\}^2 \tag{4.4}$$

A *j-t* plot was recorded for the deposition of a $PPyEtN_3$ nanowire film at 0.850 V vs. SCE, utilising a $EtOH/H_2O$ (3:4) co-solvent system containing $(NH_4)H_2PO_4$ (300 mM) and $LiClO_4$ (20 mM) on the Au substrate. Analysis of the *j-t* plot attained after growth (Figure 4.4), yielded the experimental data necessary for insertion into the four NGM equations (Eq. 4.1, 4.2, 4.3, 4.4). The shape of the *j-t* transient (Figure 4.4) may be described in terms of a NGM and dissected into three specific regions relating to the steps of the deposition process given in Scheme 4.1 and 4.2.[31-35] Upon application of an oxidising potential (E_{ox}), the *j* value decreases (Figure 4.4 (**1**)) due to diffusion of bulk monomer to the substrate, which is succeeded by monomer oxidation to radical cation monomer species. These radical cation monomer species diffuse away from the substrate forming oligomers, producing an oligomeric high-density region (OHDR). This portion of the *j-t* transient can be referred to as the 'induction time', τ. At the point, t_0,j_0, oligomerisation has yielded long-chained oligomers, which are now insoluble and can precipitate on to the substrate as nuclei (*i.e.* nucleation occurs). The second region (Figure 4.4 (**2**)) involves an increase in the *j* value from t_0,j_0, attributed to successive nuclei growth on the substrate. The *j* value increases until the discrete diffusion zones of each growing *nuclei* begin to *overlap* at approx. t_{max},j_{max}. The final region (Figure 4.4 (**3**)) displays a slow decrease of *j*, which usually develops into a plateau due to the impeded diffusion of monomer from the bulk solution to polymer nucleation sites and the increased resistivity of the polymer, compared to that of the bare electrode.[31-35]

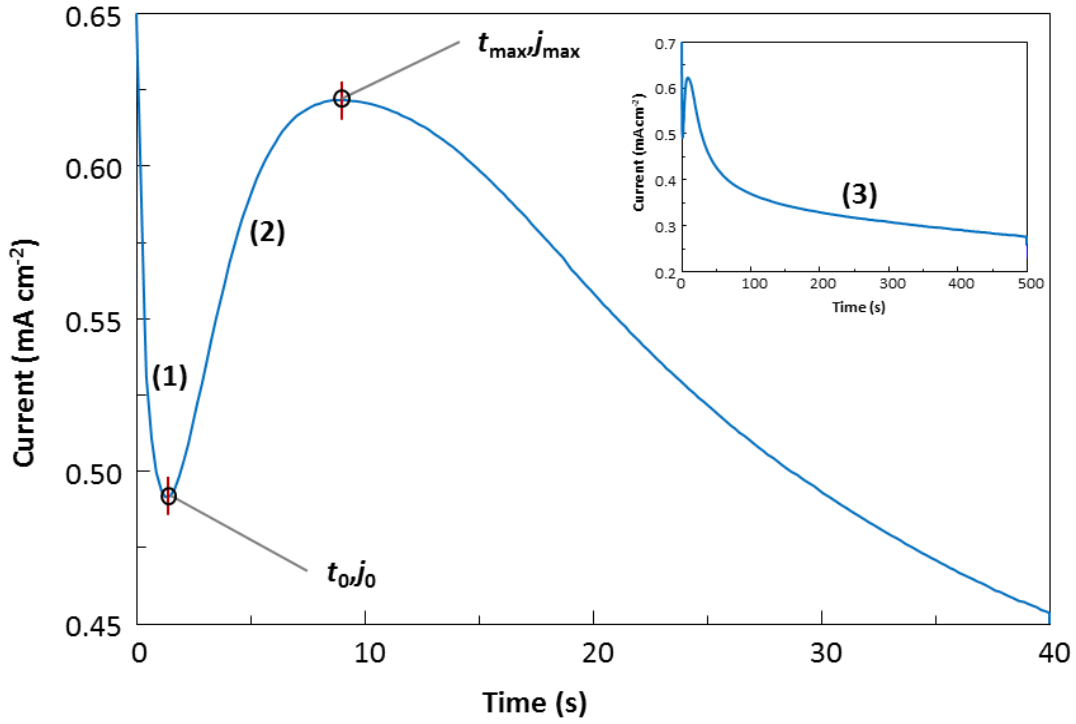

Figure 4.4: *j-t* transient of $PPyEtN_3$ nanowire film deposited on the Au substrate in EtOH/H_2O (3:4) with $(NH_4)H_2PO_4$ (300 mM) and $LiClO_4$ (20 mM) at 0.850 V vs. SCE.

The experimental *j-t* transients data were normalised using t_{max},j_{max} and compared to dimensionless theoretical models. It was observed upon production of nanowire films, that the attained nanowire experimental data produced an experimental data NGM model, which resembled the modelled IN3D (Figure 4.5 (b)) and did not resemble either of the 2D processes (Figure 4.5 (a)).

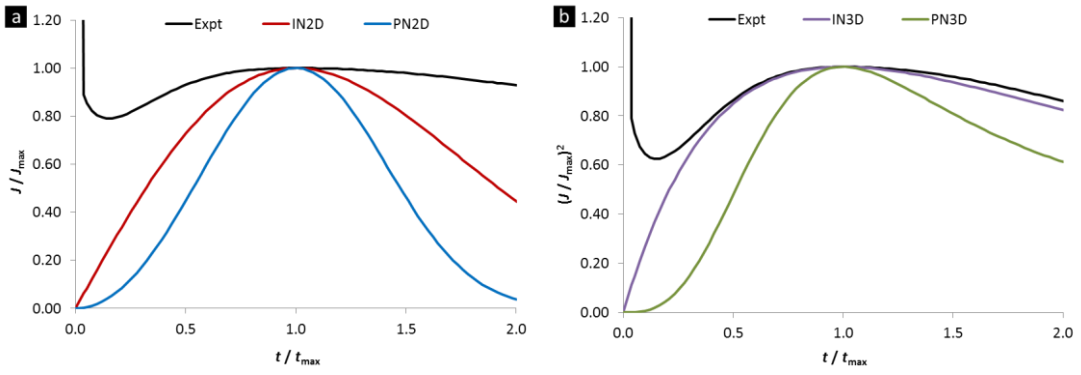

Figure 4.5: NGM plots of a $PPyEtN_3$ nanowire film deposited on the Au substrate in EtOH/H_2O (3:4) with $(NH_4)H_2PO_4$ (300 mM) and $LiClO_4$ (20 mM) at 0.850 V vs. SCE. Plot (a) curves are representative of experimental data (—), IN2D (—) and PN2D (—) mechanisms while plot (b) curves are representative of experimental data (—), IN3D (—) and PN3D (—) mechanisms.

Once the modelling analysis of the nanowire film was complete, deposition of a bulk film was performed, to permit the comparison of the NGM for $PPyEtN_3$ nanowire and bulk morphology films. The $PPyEtN_3$ bulk film was deposited on the Au substrate at 0.850 V vs. SCE, utilising an $EtOH/H_2O$ (3:4) co-solvent system containing $LiClO_4$ (100 mM). The *j-t* plot (Figure 4.6) yielded the experimental data necessary for insertion into the four NGM equations.

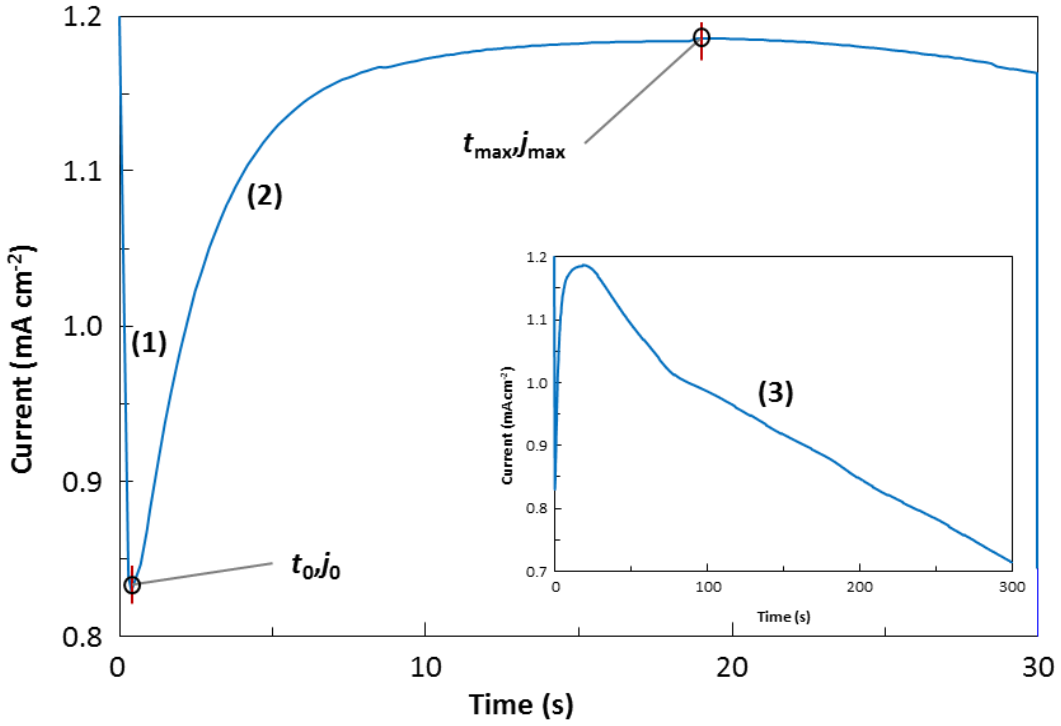

Figure 4.6: *j-t* transient of $PPyEtN_3$ bulk film deposited on the Au substrate in $EtOH/H_2O$ (3:4) with $LiClO_4$ (100 mM) at 0.850 V vs. SCE.

Observation of the growth models attained for the bulk morphology film (Figure 4.7 (a) and (b)) clearly illustrates the increased complexity for the NGM of $PPyEtN_3$ bulk film development in comparison to that of $PPyEtN_3$ nanowire films. Assessment of the data for both 2D and 3D processes evidently showed that more than one NGM is contributing to the development of the bulk film. This was not surprising, as the fabrication of bulk polymer films usually involve uncontrolled nucleation and growth.[28,29,36-38]

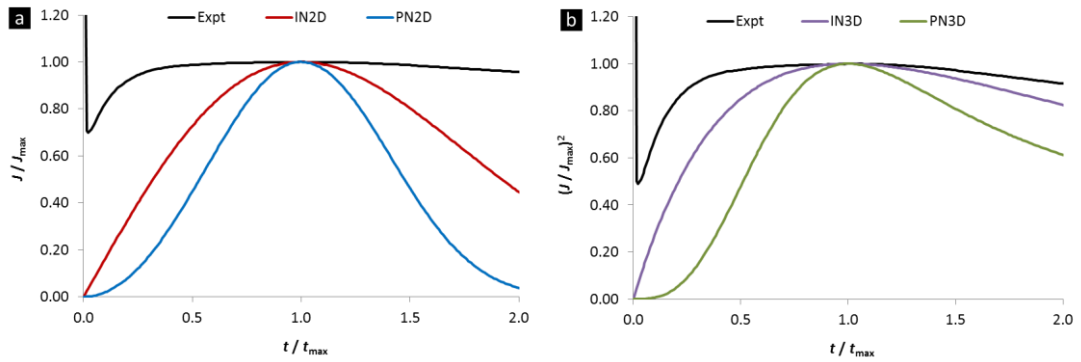

Figure 4.7: NGM plots of a $PPyEtN_3$ bulk film deposited on the Au substrate in $EtOH/H_2O$ (3:4) with $LiClO_4$ (100 mM) at 0.850 V vs. SCE. Plot (a) curves are representative of experimental data (—), IN2D (—) and PN2D (—) mechanisms while plot (b) curves are representative of experimental data (—), IN3D (—) and PN3D (—) mechanisms.

Observation showed that while employing the standard conditions of $PyEtN_3$ (35 mM) in an $EtOH/H_2O$ (3:4) co-solvent system accompanied by $(NH_4)H_2PO_4$ (300 mM) and $LiClO_4$ (20 mM), production of the nanowire films could only occur within a small specific E_{app} window (0.820 - 0.850 V vs. SCE) and upon application of an E_{ox} outside of this window, uncontrolled polymer deposition was prevalent. Drifting outside of this E_{app} window by increasing the E_{app} to 0.900 and 0.950 V vs. SCE produced films possessing an increasingly diminished presence of nanostructures, resembling bulk PPy upon SEM analysis. The *j-t* plots obtained from deposition at these E_{app} did not possess t_{max},j_{max} points, so the experimental data could not be inserted into the four NGM equations. This can clearly be seen in the *j-t* plot for the polymer deposited at 0.900 V vs. SCE (Figure 4.8). Moreover, deposition performed at potentials greater than 0.860 V vs. SCE (0.870 - 0.950 V vs. SCE) yielded erratic and irreproducible *j-t* transients due to an increase in the rate of overoxidation occurring within the polymer.[39] This meant investigation of the early stages of deposition could not be performed and compared to the results for analogous conditions at 0.850 V vs. SCE, but it was anticipated that there would be more than one process contributing to the fabrication of bulk-type films at 0.900 and 0.950 V vs. SCE.

Drifting outside of this E_{app} window by decreasing the E_{app} to 0.800 and 0.770 V vs. SCE produced films possessing nano/microstructured wires and tubes upon SEM

analysis and these structures shortened in length with decreasing E_{app}. The low charge density (q) values at t_0,j_0, indicated inefficient polymer deposition when compared to that of 0.850 V vs. SCE, which yielded the most reproducible *j-t* transient during investigation of the range, 0.770 - 0.950 V vs. SCE. Also, it was noted that experimental data attained from the *j-t* plots at 0.800 and 0.770 V vs. SCE possessed two *j-t* maximums each, termed t_{max},j_{max} and t'_{max},j'_{max} chronologically. The presence of the second *j-t* maximum, t'_{max},j'_{max}, has been previously reported by del Valle and co-workers during the electrodeposition of PT in MeCN, attributing t'_{max},j'_{max} to separate successive NG phenomena.[34] Visible in the *j-t* transient for the polymer grown at a potential of 0.770 V vs. SCE was the beginning of a t'_{max},j'_{max} (Figure 4.8 (—)), while in the *j-t* transient for the polymer grown at 0.800 V vs. SCE, the presence t'_{max},j'_{max} occurs earlier at 109 s, most likely a consequence of the increased E_{app}, permitting its earlier occurrence of this process.

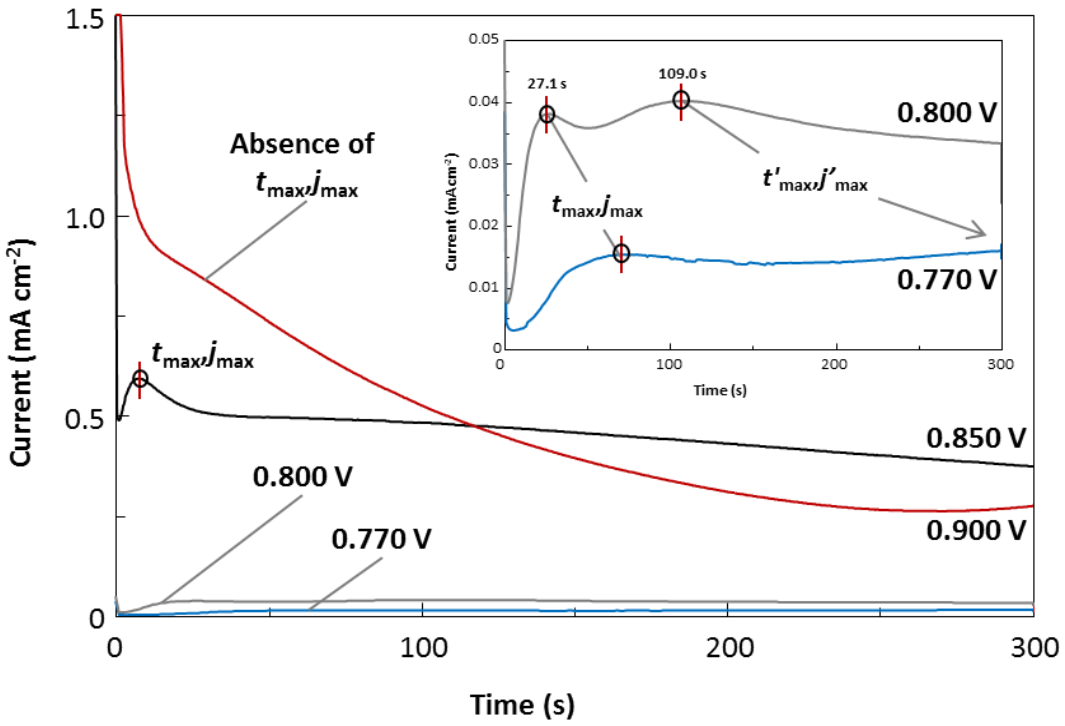

Figure 4.8: *j-t* plots of $PPyEtN_3$ films deposited on the Au substrate in $EtOH/H_2O$ (3:4) with $(NH_4)H_2PO_4$ (300 mM) and $LiClO_4$ (20 mM) at 0.900 (—), 0.850, (—), 0.800 (—) and 0.770 (—) V vs. SCE. Inset: Magnification of *j-t* plots for 0.800 (—) and 0.770 (—) V vs. SCE.

During investigation of the NGM processes at potentials below 0.850 V vs. SCE, specifically 0.770 V vs. SCE, it was difficult to discern which NGM was occurring

as the experimental data did not fit completely to any of the modelled data (Figure 4.9). Examining the shape of the modified experimental data for deposition at 0.770 V vs. SCE (Figure 4.9 (a) and (b) (—)), it would be wise to suggest that there was more than one process proceeding at the very early stages of nucleation.

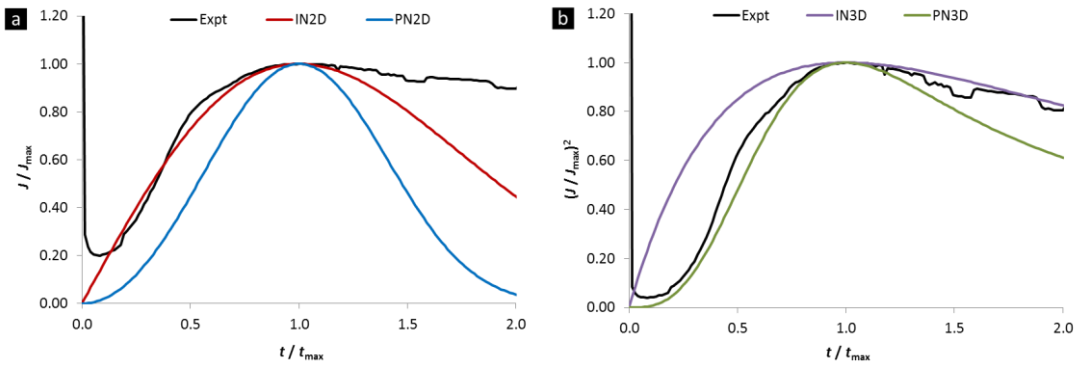

Figure 4.9: NGM plots of a $PPyEtN_3$ bulk film deposited on the Au substrate in $EtOH/H_2O$ (3:4) with $(NH_4)H_2PO_4$ (300 mM) and with $LiClO_4$ (20 mM) at 0.770 V vs. SCE. Plot (a) curves are representative of experimental data (—), IN2D (—) and PN2D (—) mechanisms while plot (b) curves are representative of experimental data (—), IN3D (—) and PN3D (—) mechanisms.

4.2.1.3 Investigation of the role played by the 'seed' electrolyte

In the literature, reports regarding the template-free electrodeposition of CP nanowires commonly state that the electrolyte system consists of a mixture of either phosphate or carbonate salts (bulk electrolyte), accompanied by a smaller concentration of generally, a perchlorate salt ('seed' electrolyte).[1,2,26,40-43] In the current section, the role of the 'seed' electrolyte during the deposition of $PPyEtN_3$ was investigated.

There is a substantial consensus that utilisation of the template-free approach for fabrication of a CP in a nanowire/tube morphology actually involves a soft template, which is consumed during the polymerisation process.[44] Significantly, in a study performed by Wei and co-workers, regarding the formation of polypyrrole (PPy) nanotubes on an electrode, it was shown that this 'transient soft template' was formed by nanodroplets of monomer, stabilised by the employed dopant, D-camphorsulfonic acid (D-CSA).[45] In this circumstance, the D-CSA dopant coated the droplets, inducing formation of monomer filled micelles, which could absorb on the

substrate yielding a monomer/dopant 'soft template' and upon application of an E_{ox}, a nanostructured polymer tube developed. We postulate the occurrence of an analogous process occurring during the electrodeposition process, leading to $PPyEtN_3$ nanowire formation. It is possible that the employment of the relatively nonpolar $PyEtN_3$ molecule in the polar $EtOH/H_2O$ (3:4) mixture permits the existence of nanodroplets, composed of $PyEtN_3$ monomer. Unfortunately, as nanoemulsions are stable and transparent, it is difficult to distinguish them from a solution using simple visual inspection. When produced, the nanodroplets must adhere homogeneously across the substrate, to form templates for nanowire formation. Support for this proposal comes from the work performed by Atobe and co-workers, who have reported that sequential low and high powered ultrasonication of insoluble EDOT monomer in an aqueous solution of $LiClO_4$ (1000 mM) yields a stable nanoemulsion.[46]

As discussed in Section 4.2.1.2, it was determined that attainment of nanowire morphology during $PPyEtN_3$ electrodeposition required an IN process *i.e.* all nuclei deposit simultaneously across the electrode. Occurrence of the monomer nanodroplet mechanism outlined above, suggests that some dopant must be soluble within the nanodroplets, inferring the coexistence of monomer and dopant at the substrate, upon application of an E_{ox}. Atobe and co-workers have performed significant work regarding acoustically formed emulsions (forming an emulsion using ultrasonication) of EDOT and not only reported the presence of $LiClO_4$ within the aqueous phase of the emulsion, but also within the submicrometre droplets themselves. It is this presence within the monomer droplet that is of the upmost importance for polymer deposition to occur[47] and upon application of an E_{ox}, only the monomer/dopant droplets within close proximity to the substrate polymerise. This is a consequence of the formation of an electric bilayer inside the droplet, occurring due to contributions from the soluble dopant and from the contact between the droplet and the substrate, thus permitting monomer polymerisation *via* direct electron transfer. In our system, it is believed that upon application of an $E_{ox,}$ initially the exclusive polymerisation of monomer/dopant nanodroplets on the substrate leads to instantaneous nucleation at the very early stages of the deposition process, succeeded by nanowire development thereafter.

Two known properties of perchlorate salts are their high solubility in many organic solvents,[48] coupled with their low tendency to ion pair.[49-51] A study was executed to investigate which electrolytic salts retained the potential to act as a 'seed' for $PPyEtN_3$ nanowire formation. In addition, we set out to correlate the findings obtained with the proposed mechanism for nanowire formation, which involves the 'seed' electrolyte dissolved in nanodroplets of monomer. Specifically in this study, $LiClO_4$, which has been previously utilised to successfully deposit nanowires, was exchanged for other supporting electrolytes, selected due to their different organic solvent solubilities, ion mobilities, dissociation constants in organic solvents and ionic sizes. These electrolytic salts are displayed in Table 4.1, accompanied by their respective physical property data, as determined from the literature.

Table 4.1: Ionic properties of salts employed during $PyEtN_3$ deposition.

Cationic data values				
Dopant	**Solubility (g 100 cm^{-3})[a]**	**Ionic size (pm)[b]**	**Relative ion mobility[c]**	**Dissociation constant**
$LiClO_4$	151.800	~68	0.5260[c]	5.11[d]
$NaClO_4$	14.700	~97	0.6820[c]	5.37[d]
$KClO_4$	0.012	~133	1.0000[c]	5.69[d]
Anionic data values				
Dopant	**Solubility (g 100 cm^{-3})[a]**	**Ionic size (pm)[b]**	**Relative ion mobility[c]**	**Dissociation constant**
LiCl	2.500	~181	1.0382[c]	-
$LiBF_4$	soluble	~218	-	8.40[e]
Li_2SO_4	0.000	~230	0.5440[c]	-
$LiClO_4$	151.800	~288	0.9160[c]	2.80[e]
LiTFSI	soluble	~325	-	1.50[e]

[a]Solubility in g 100 cm^{-3}EtOH. [b]Ionic size in picometers (pm). [c]Ionic mobility relative to K^+ in H_2O. [d]In acetic acid (ε = 6.15). [e]In propylene carbonate (ε = 64.00).

4.2.1.3a Investigation of the role played by the 'seed' electrolytes anion

Upon consideration of the physical properties displayed in Table 4.1, it would be anticipated that if the proposed mechanism for nanowire formation, involving the 'seed' electrolyte dissolving in monomer nanodroplets, is accurate, chloride and sulfate lithium salts should act poorly as electrolytes, demoting polymer formation, as they both possess low solubility in organic solvent,[52] while lithium chloride has a known propensity to ion pair in organic solvents.[53] Therefore, very little of the dissociated anion would be anticipated to be found within the $PyEtN_3$ nanodroplets. When $PyEtN_3$ polymerisation was attempted, employing an electrolytic solution containing either of these two lithium salts, it was observed that no $PPyEtN_3$ was deposited on the substrate (Table 4.2). The growth profile clearly illustrates the occurrence of very little electrochemical reaction (Figure 4.11 (—) and (—)). This finding was consistent with studies performed by Atobe and co-workers, who reported that by utilising acoustic emulsification, water insoluble EDOT monomer formed an emulsion in a $LiClO_4$ (1000 mM) aqueous solution and upon the application of an appropriate E_{app}, polymerisation occurred at the substrate. However, when the synonymous procedure was replicated, employing either lithium sulfate (Li_2SO_4) or lithium nitrate ($LiNO_3$) as the supporting electrolyte, no polymerisation was observed.[54,55] The authors proposed that the special behaviour exhibited by $LiClO_4$ arose as it was contained within the EDOT droplets. This was confirmed using inductively coupled plasma spectrometry, which confirmed the containment of lithium ions within the microdroplets when employing $LiClO_4$, but not upon the employment of Li_2SO_4 or $LiNO_3$.[54,55] A number of lithium salts are known to have significant solubility in organic solvents, with a reasonable proportion of the salt existing as dissociated ions. The two supporting electrolytes chosen for our study were lithium tetrafluoroborate ($LiBF_4$) and lithium bis(trifluoromethane)sulfonimide (LiTFSI) (Figure 4.10).

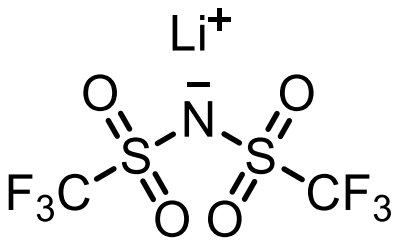

Figure 4.10: Structure of lithium bis(trifluoromethane)sulfonimide (LiTFSI).

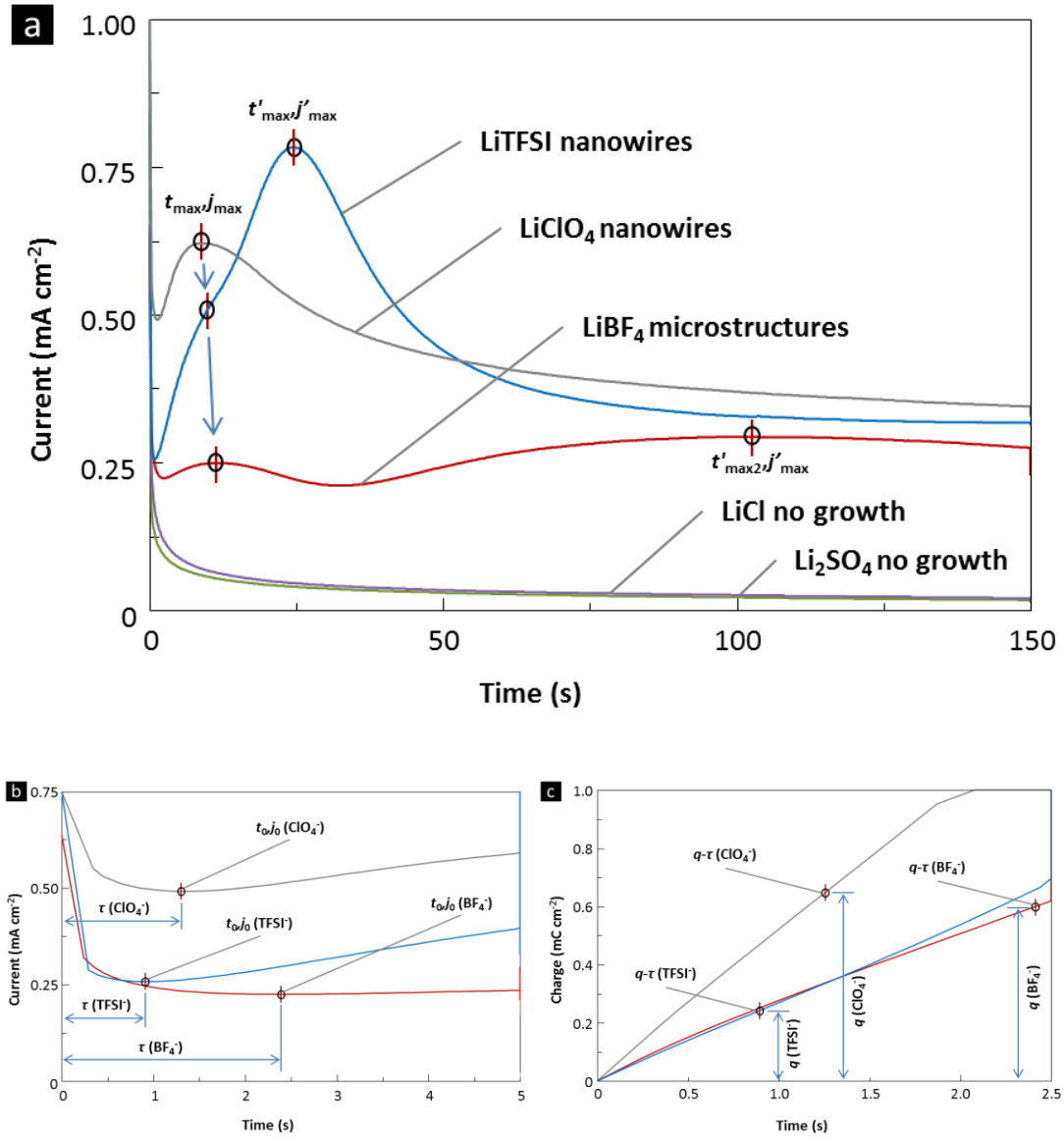

Figure 4.11: Plots of (a) *j-t* (150 s), (b) *j-t* (5 s) and (c) *q-t* (2.5 s) of $PPyEtN_3$ films deposited on the Au substrate at 0.850 V vs. SCE, until *q* value of 68 mC cm^{-2} or 400 s was achieved in $EtOH/H_2O$ (3:4) with $(NH_4)H_2PO_4$ (300 mM) and $LiClO_4$ (—), LiTFSI (—), $LiBF_4$ (—), LiCl (—) and Li_2SO_4 (—) (20 mM).

In this study, the substitution of $LiClO_4$ for $LiBF_4$ yielded cylindrical $PPyEtN_3$ microstructures, while utilisation of the LiTFSI salt resulted in the formation of uniform $PPyEtN_3$ nanowires (Table 4.2). The associated SEM micrographs of these polymer films are displayed in Figure 4.12 (d) - (f) and Figure 4.12 (g) - (i) respectively, while the growth profiles for polymerisation of the five lithium salts are displayed in Figure 4.11.

Table 4.2: Electrochemical growth results for $PyEtN_3$ varying dopant anion.[a]

Anion variation					
Dopant	**Growth**	**Wire morphology**	**Dia. (nm)**	**Length (nm)**	**SEM micrograph**
$LiClO_4$	Excellent	Uniform/oriented	100	1000	Fig. 4.9 (c)
$LiBF_4$	Good	Microtubes	2000	500	Fig. 4.9 (f)
LiTFSI	Good	Uniform/contorted	250	1000	Fig. 4.9 (i)
LiCl	None	N/A	N/A	N/A	N/A
Li_2SO_4	None	N/A	N/A	N/A	N/A

[a]For each above case an oxidation potential of 0.850 V vs. SCE was applied to the Au substrate in $EtOH/H_2O$ (3:4) using $(NH_4)H_2PO_4$ (300 mM) and the stated dopant (20 mM), until *q* value of 68 mC cm^{-2} or 400 s was achieved.

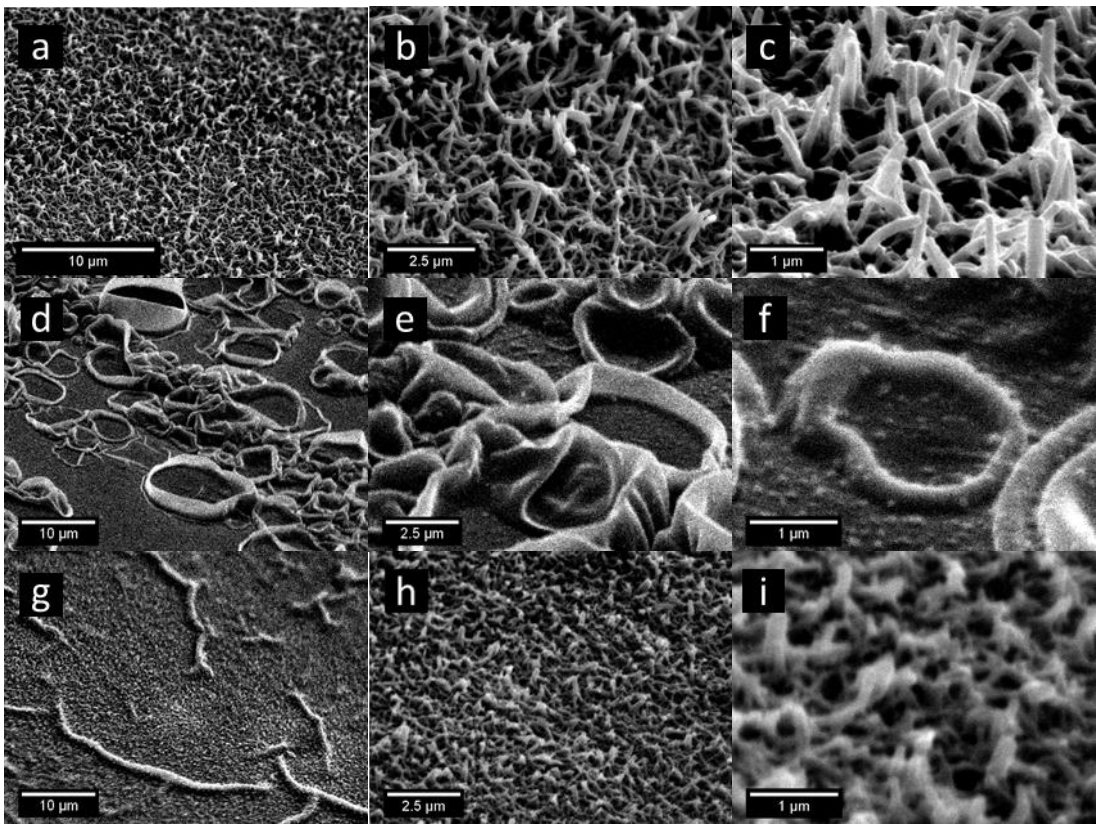

Figure 4.12: SEM micrographs (showing oblique-angle-view) of $PPyEtN_3$ nanowire films deposited on the Au substrate at 0.850 V vs. SCE, until q of 68 mC cm^{-2} or 400 s was achieved in $EtOH/H_2O$ (3:4) with $(NH_4)H_2PO_4$ (300 mM) and $LiClO_4$ (a) - (c), $LiBF_4$ (d) - (f) and LiTFSI (g) - (i) (20 mM).

Efficient polymerisation, which resulted in the deposition of a nanowire film, occurred from mixtures containing the supporting electrolytes, $LiClO_4$ (Figure 4.11 (—)) or LiTFSI (Figure 4.11 (—)), their t_{max},j_{max} both occurring at approx. 9 s. There was only a negligible difference for the t_{max},j_{max} values of the respective *j-t* transients, probably a consequence of a combination of factors, such as the solubility of these lithium salts in organic solvents, the larger size and therefore, lower mobility of the TFSI anion and also the degree of ion pairing occurring during polymerisation. However, the results clearly indicate that the choice of 'seed' electrolyte was extremely influential when determining the initial rate of polymerisation. The growth profile of the $PPyEtN_3$ microstructures, deposited utilising $LiBF_4$ as the 'seed' electrolyte (Figure 4.11 (—)), showed two stages of growth which may account for the different morphology observed (Figure 4.9 (d) - (f)).

Inspection of the growth profiles (Figure 4.11 (b) and (c)) show that variation of the anion in each supporting electrolyte differentiated the *j-t* transients by affecting the induction time, τ, which from the experimental data (Figure 4.11 (b)), may be sequenced as,

$$\tau(BF_4^-)\ 2.40\ s > \tau(ClO_4^-)\ 1.27\ s > \tau(TFSI^-)\ 0.90\ s$$

The induction time was observed to be below 2.5 s during the polymerisation experiments employing the three anion variations, therefore these were deemed to be low τ values, which indicate a nucleation process initiating very quickly at the substrate. A short induction time is reported to be promoted by the insolubility of oligomeric clusters in the oligomeric high-density region (OHDR) at the electrode (Figure 4.13).[35,56] Induction and nucleation can be explained by the process displayed in Figure 4.13. During induction, the monomer is firstly present both in the diffuse layer and in the bulk solution (Figure 4.13 (**1**)). An oxidising potential is applied to the substrate, generating oxidised radical cation monomer species in high concentration at the interface. The resulting concentration gradient causes these radical cation monomer species to diffuse away from the substrate, while neutral monomer species diffuse in towards the substrate (Figure 4.13 (**2**)). The radical cation monomer species generate neutral dimer species in the diffuse layer, while more radical cation monomer species are created by oxidation at the substrate (Figure 4.13 (**3**)). Radical cation dimer species are generated, which diffuse away from the substrate, while neutral monomer species diffuse in from the bulk solution to the diffuse layer (Figure 4.13 (**4**)). Neutral oligomeric species of various chain lengths are produced in the diffuse layer, termed the Oligomeric High Density Region (OHDR), while more radical cation dimer species are created by oxidation at the substrate. The radical cation dimer species diffuse away from the electrode, while more neutral monomer species diffuse in from the bulk solution towards the substrate (Figure 4.13 (**5**)). As the neutral oligomeric species become longer due to on-going electrode oxidation, the OHDR becomes supersaturated with oligomers of various chain lengths. Therefore, the solubility of the oligomer chains decrease, inducing precipitation of oligomeric clusters on the substrate, *i.e.* nucleation (Figure 4.13 (**6**)).

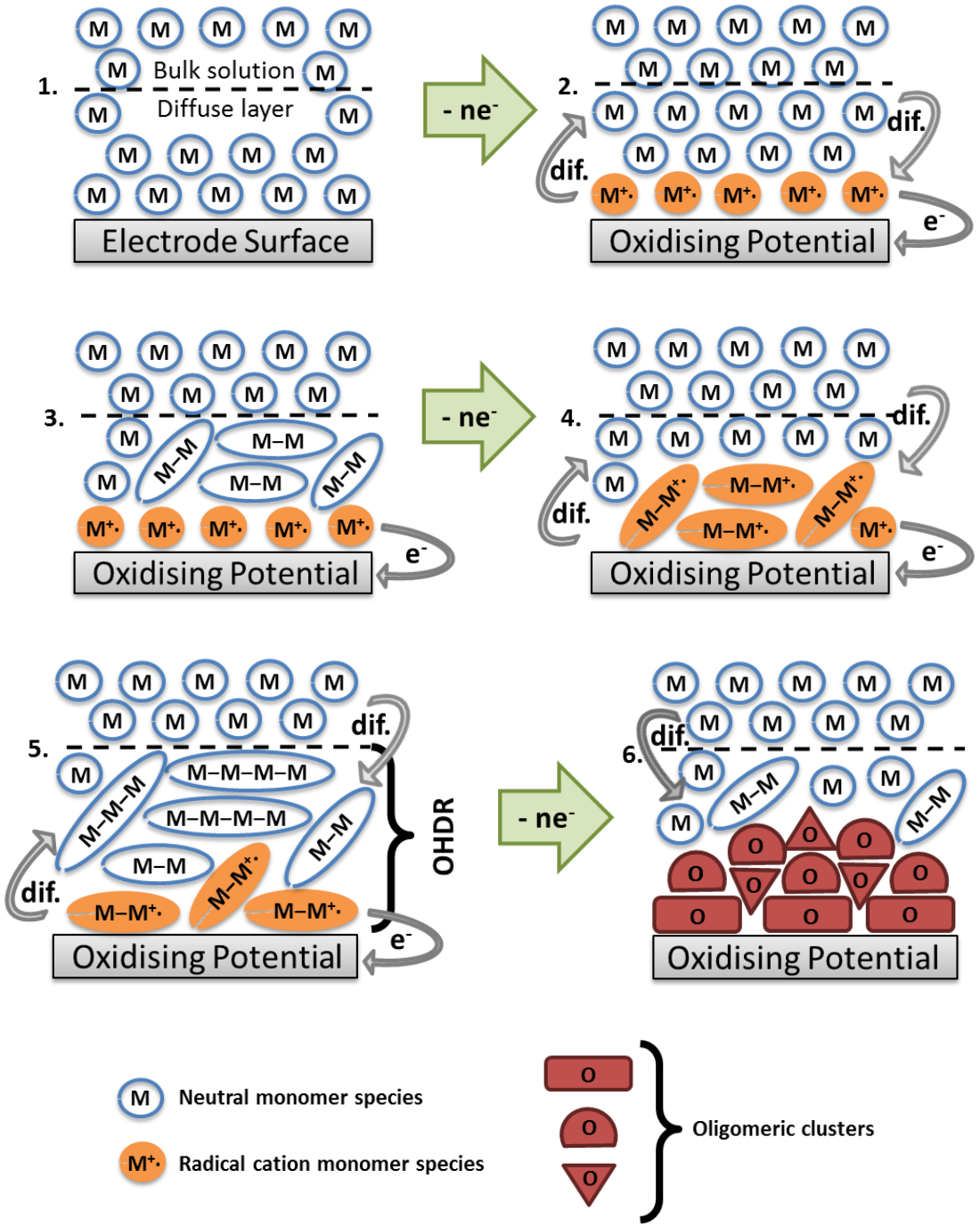

Figure 4.13: Precipitation of oligomeric clusters on to the substrate after the point of supersaturation in the oligomeric high-density region (OHDR).

The insolubility of the oligomeric clusters can be affected by many experimental parameters including temperature, application of ultrasonication irradiation and solvent medium,[35,56] albeit presently, the supporting electrolyte was the only variable. Therefore, it is justified to conclude that the employed supporting electrolyte determined the point of nucleation, t_0,j_0. This occurs as the time required

to attain OHDR supersaturation, can be determined by the type of electrolytic anion present, as the BF_4^-, ClO_4^- and $TFSI^-$ anion are capable of ion pairing with charged oligomers in the OHDR (Scheme 4.3). Therefore, oligomers paired with different anions can possess various solubilities, thus the concentration required to attain OHDR supersaturation will be anion dependent. In respect to the system here, this suggests the employment of the LiTFSI salt during electrodeposition produces a lower density of oligomeric clusters required for supersaturation in the OHDR, inducing a shorter induction time, which instigates the nucleation of shorter chain oligomers on the substrate.[34]

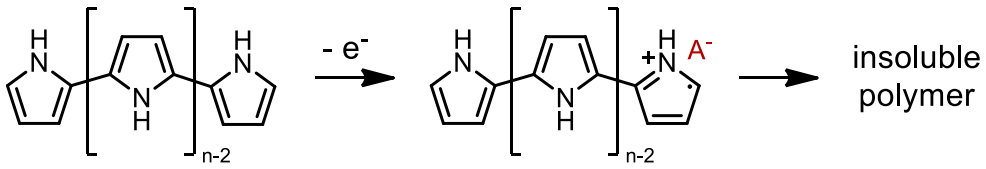

Scheme 4.3: Oligomerisation of Py displaying ion pairing of electrolytic anion, A^-, with the oligomeric radical cation during oxidation.

The deposition of CPs on the Au substrate can be analysed by observing the change in q of the system as a function of t, yielding a charge density-time (q-t) transient (Figure 4.11 (c)), which equates to the amount of polymer deposited on the electrode.[57] Procuring the q value at the end of the induction time, τ, produced values for the charge density-induction time point, q-τ, and it was observed that the following sequence was present,

$$q(ClO_4^-)\ 654.91\ \mu C\ cm^{-2} > q(BF_4^-)\ 596.27\ \mu C\ cm^{-2} > q(TFSI^-)\ 243.62\ \mu C\ cm^{-2}$$

This was consistent with that discussed regarding variation of induction times. The ion pairs formed between charged oligomer chains and $TFSI^-$ anions have the lowest solubility and precipitate out of solution as oligomeric clusters at an earlier time. Therefore, oligomer chains nucleating, after $TFSI^-$ ion pairing are the shortest (lowest q-τ value), while those paired with ClO_4^- are the longest (highest q-τ value).

The SEM micrographs of the $PPyEtN_3$ films deposited using various lithium salts (Figure 4.12) were observed to possess diverse morphologies, therefore it was deemed appropriate to investigate if the morphology of the respective films could be

related to the NGM processes occurring at the very early stages of deposition. The experimental *j-t* data was modified appropriately as discussed previously and the data were compared to the respective theoretical models obtained using the NGM equations. The NGM plots were procured by inserting the required *j-t* data into the four NGM equations. Examination of the NGM plots revealed the anticipated absence of any trend, as the various anions employed during polymerisation are known to possess diverse attributes, illustrated in Table 4.1. The experimental data representative of the $PPyEtN_3$ film deposited in the presence of $LiClO_4$ was observed to fit very soundly to an IN3D process (Figure 4.14 (f)). This produced a nanowire film, absent of inhomogeneity (Figure 4.12 (a) - (c)) with a *j-t* transient possessing one t_{max},j_{max} early in the deposition procedure (Figure 4.11 (a) (—)). Upon alteration of the salt to the $TFSI^-$ anion, the modified data did not fit to any of the NGM. This occurred due to the presence of second *j-t* maximum, t'_{max},j'_{max}, appearing in the *j-t* transient at approx. 25 s, which masked the first *j-t* maximum, t_{max},j_{max}, positioned at approx. 9 s (Figure 4.11 (a) (—)). As discussed in Section 4.2.1.2, del Valle and co-workers reported that the presence of a t'_{max},j'_{max} was attributed to a separate successive NG phenomena.[34] This would explain the observation of microstructures of varied length, approx. 1 μm in diameter growing parallel to the substrate, accompanied by a homogeneous distribution of short nanowires (Figure 4.12 (g)).

While utilising $LiBF_4$ as the supporting electrolyte, deposition of the $PPyEtN_3$ film yielded a *j-t* transient, that when modified using NG equations, most closely resembled an IN3D process (Figure 4.14 (b)), but interestingly, the respective SEM micrographs (Figure 4.12 (d) - (f)) depicted a film possessing only circular microstructures on the surface. This was confirmed by examining the film at high magnification (Figure 4.12 (f)), which showed only the beginning of irregular microtube development, accompanied by sporadic nodule formation. The presence of nodules may be attributed to the IN3D process, but it was obvious upon observation of the NGM plot (Figure 4.14 (b)), that more than one NGM process contributes to the deposition of the polymer. This was congruent with the presence of t'_{max},j'_{max} at 104.5 s in the *j-t* transient (Figure 4.11 (a) (—)). The morphologies and the NGM plots of the films were a good indication that the properties associated with each salt, determined by their respective anion (Table 4.1), control the very early stages of

nuclei deposition and growth thereafter, when the respective salt was employed during the polymerisation process.

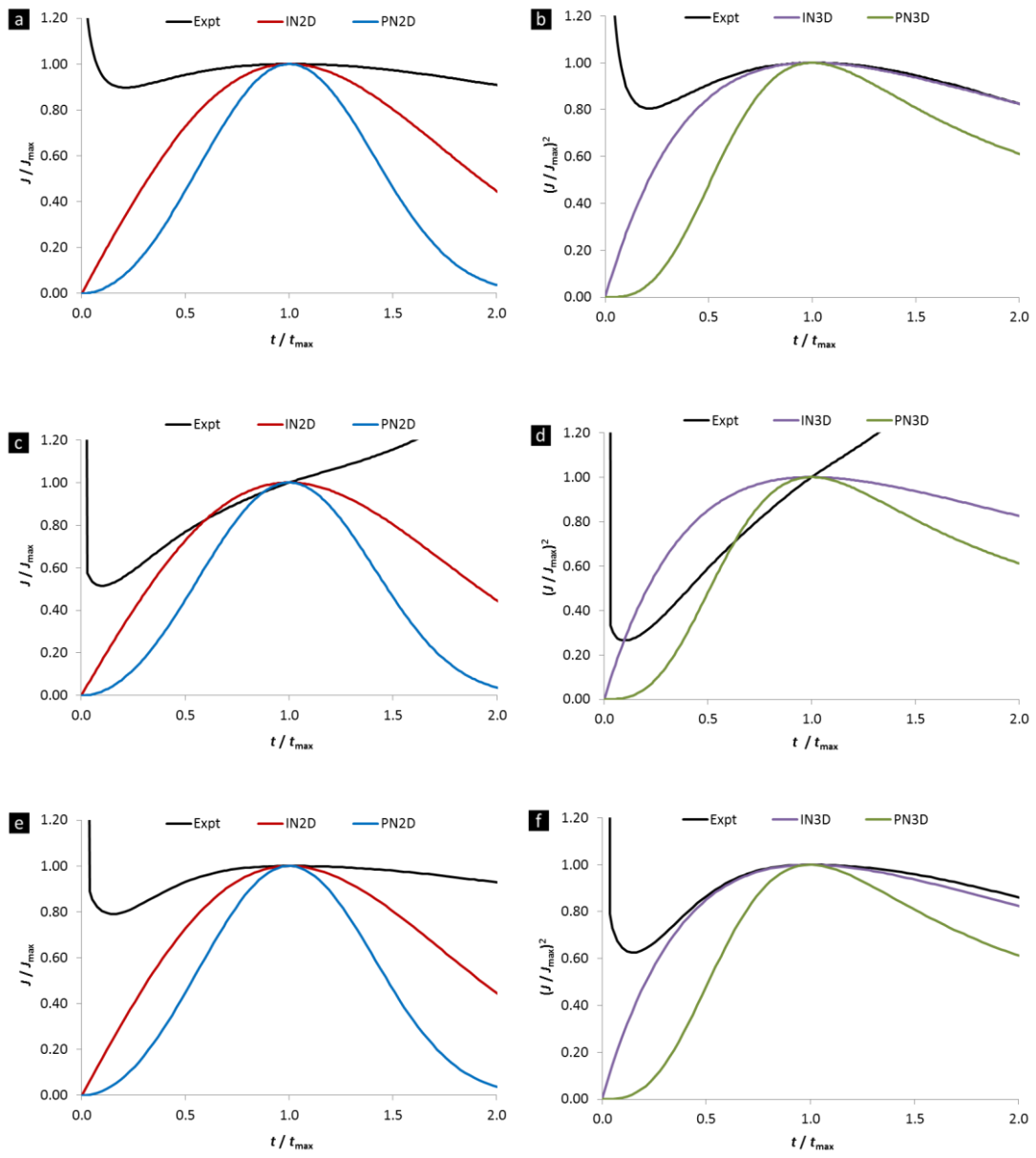

Figure 4.14: NGM plots of a PPyEtN$_3$ film deposited on the Au substrate in EtOH/H$_2$O (3:4) with (NH$_4$)H$_2$PO$_4$ (300 mM) and (a) - (b) LiBF$_4$ (20 mM), (c) - (d) LiTFSI or (e) - (f) LiClO$_4$ (20 mM) at 0.850 V vs. SCE. Plot (a), (c) and (e) curves are representative of experimental data (—), IN2D (—) and PN2D (—) mechanisms while plot (b), (d) and (f) curves are representative of experimental data (—), IN3D (—) and PN3D (—) mechanisms.

4.2.1.3b Investigation of the role played by the 'seed' electrolytes cation

In order to study the role of the electrolytic cation and its effect on the final morphology of the $PPyEtN_3$ film, studies were performed substituting $LiClO_4$ for either sodium perchlorate ($NaClO_4$) or potassium perchlorate ($KClO_4$). Upon inspection of the physical properties of these three salts (Table 4.3), it was anticipated that an electrolytic mixture containing $KClO_4$ would have the largest conductivity and would promote polymerisation if the monomer was dissolved in an aqueous solvent system. Alternatively, $KClO_4$ possesses the lowest solubility in organic solvents; therefore presence of this salt would be anticipated to demote nanowire formation, upon occurrence of the nanodroplet deposition mechanism.

Table 4.3: Electrochemical growth results for $PyEtN_3$ varying dopant cation.[a]

Cation variation					
Dopant	**Growth**	**Wire morphology**	**Dia. (nm)**	**Length (nm)**	**SEM micrograph**
$LiClO_4$	Excellent	Uniform oriented	100	1000	Fig. 4.12 (c)
$NaClO_4$	Good	Nodules/isolated	180	1200	Fig. 4.12 (f)
$KClO_4$	Poor	Isolated/sporadic	180	770	Fig. 4.12 (i)

[a]For each above case an E_{ox} of 0.850 V vs. SCE was applied to the Au substrate in $EtOH/H_2O$ (3:4) using $(NH_4)H_2PO_4$ (300 mM) and the stated dopant (20 mM), until q of 68 mC cm^{-2} or 400 s was achieved.

As seen from the results summarised in Table 4.3, with the respective SEM micrographs, the mixture containing $LiClO_4$ formed a superior $PPyEtN_3$ film consisting of uniform nanowires with complete surface coverage (Figure 4.15 (a) - (c)). The $NaClO_4$ mixture was also observed to produce a homogeneous nanowire film, *albeit* possessing a sparse distribution of nanowires (Figure 4.15 (d) - (f)), whereas that containing $KClO_4$ yielded a $PPyEtN_3$ base layer, displaying a sporadic distribution of uniform nanowire sites across the substrate (Figure 4.15 (g) - (i)).

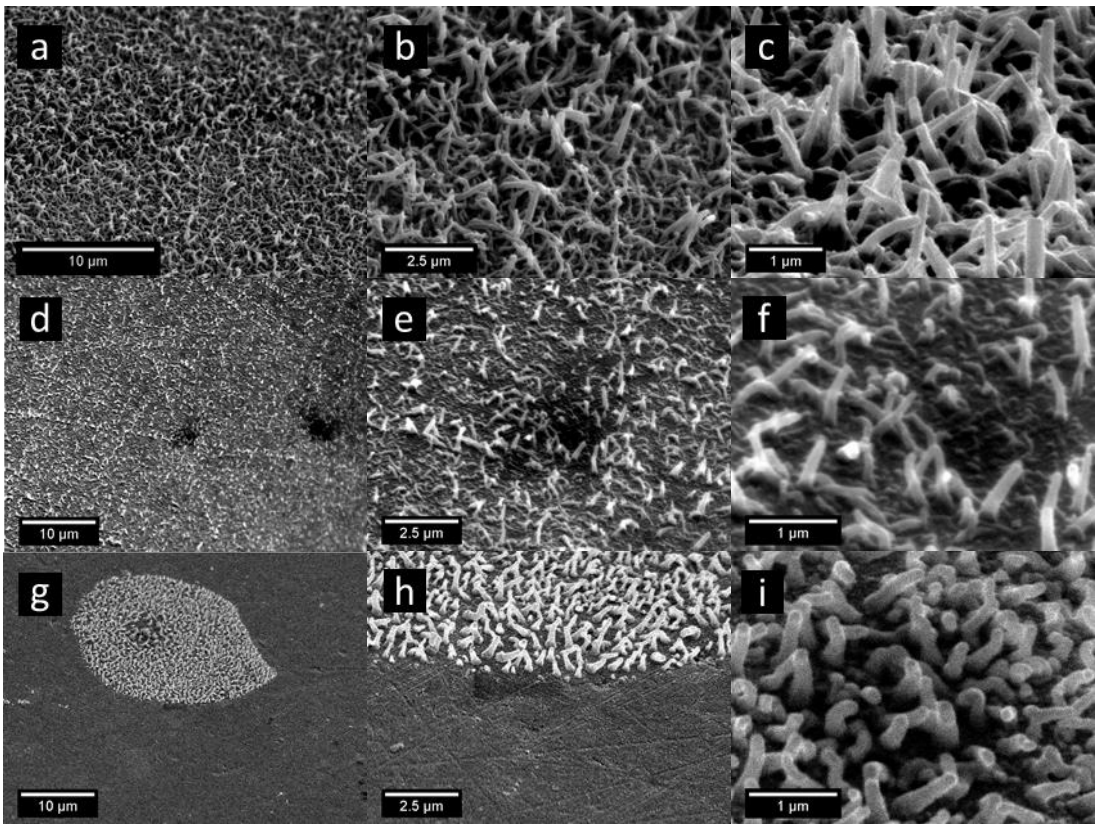

Figure 4.15: SEM micrographs (showing oblique-angle-view) of $PPyEtN_3$ nanowire films deposited on the Au substrate at 0.850 V vs. SCE, until q of 68 mC cm^{-2} or 400 s was achieved in $EtOH/H_2O$ (3:4) with $(NH_4)H_2PO_4$ (300 mM) and $LiClO_4$ (a) - (c), $NaClO_4$ (d) - (f) and $KClO_4$ (g) - (i).

The growth profiles of the films deposited using the three perchlorate salts (Figure 4.16 (a) and (b)) were examined and revealed that cation variation in each system significantly changed the *j-t* transients by affecting the induction time, τ. Using the experimental data (Figure 4.16 (b)), the order of decreasing induction time can be sequenced as,

$$\tau(Na^+)\ 5.37\ s > \tau(K^+)\ 2.17\ s > \tau(Li^+)\ 1.27\ s$$

Upon employing the lithium and potassium salt during polymerisation, the induction time was found to be below 2.5 s (low τ value), but this was not the case for that in the presence of the sodium salt, which possessed a slow nucleation process at the substrate. These induction times represent a significant variation with regard to the promotion of oligomeric cluster insolubility in the (OHDR) at the substrate (Figure 4.13).[35,56] In these cases, the only variable present was the employed

supporting electrolyte, which determined the time of nucleation and was related to the point at which the OHDR becomes supersaturated. Nevertheless, in this system the employment of the $LiClO_4$ salt produces a lower density of oligomeric clusters required for supersaturation in the OHDR, inducing a shorter induction time, which instigates the nucleation of shorter chain oligomers on the substrate.[34]

The *q-t* transient (Figure 4.16 (c)), which equates to the amount of polymer deposited on the electrode,[57] was examined. The *q* value at the end of the induction time was procured yielding values for the *q-τ*, present the proceeding sequence,

$$q(Na^+)\ 949.75\ \mu C\ cm^{-2} > q(K^+)\ 783.92\ \mu C\ cm^{-2} > q(Li^+)\ 654.91\ \mu C\ cm^{-2}$$

The findings attained for the induction time, describing point of nucleation, correlate well with that of the respective *q-τ* value, describing the density of the oligomeric clusters. During oxidation at the substrate, ion pairing between the charged oligomer chains and the perchlorate anion of the lithium salt possess the lowest solubility. This permits the subsequent oligomeric cluster to precipitate out of solution at an earlier time. Therefore, in the case of cation variation, the nucleation of charged oligomer chains occurs as short chains, after ion pairing with the perchlorate anion of the lithium salt (lowest *q-τ* value), while long chains manifested upon pairing with the perchlorate anion of the sodium salt (highest *q-τ* value).

If we observe the properties belonging to each salt (Table 4.1) it would suggest that this would not be the case. The great similarity in dissociation constant shared by the three perchlorates, accompanied by the very low solubility of the potassium salt in organic solvents could indicate that the potassium salt would have the longest induction time during application of an oxidising potential. Understandably, the system at hand is one of great complexity, which cannot then, be described by only one mechanism. This can be reaffirmed by observing the NGM models in Figure 4.6, which confirms that the mechanism controlling growth employing the potassium salt was undefined.

These findings strongly indicate that solubility of the perchlorate salts in organic media is a vitally important electrolytic property, necessary for homogeneous

nanowire deposition across the substrate, within a complex system of polymer deposition.

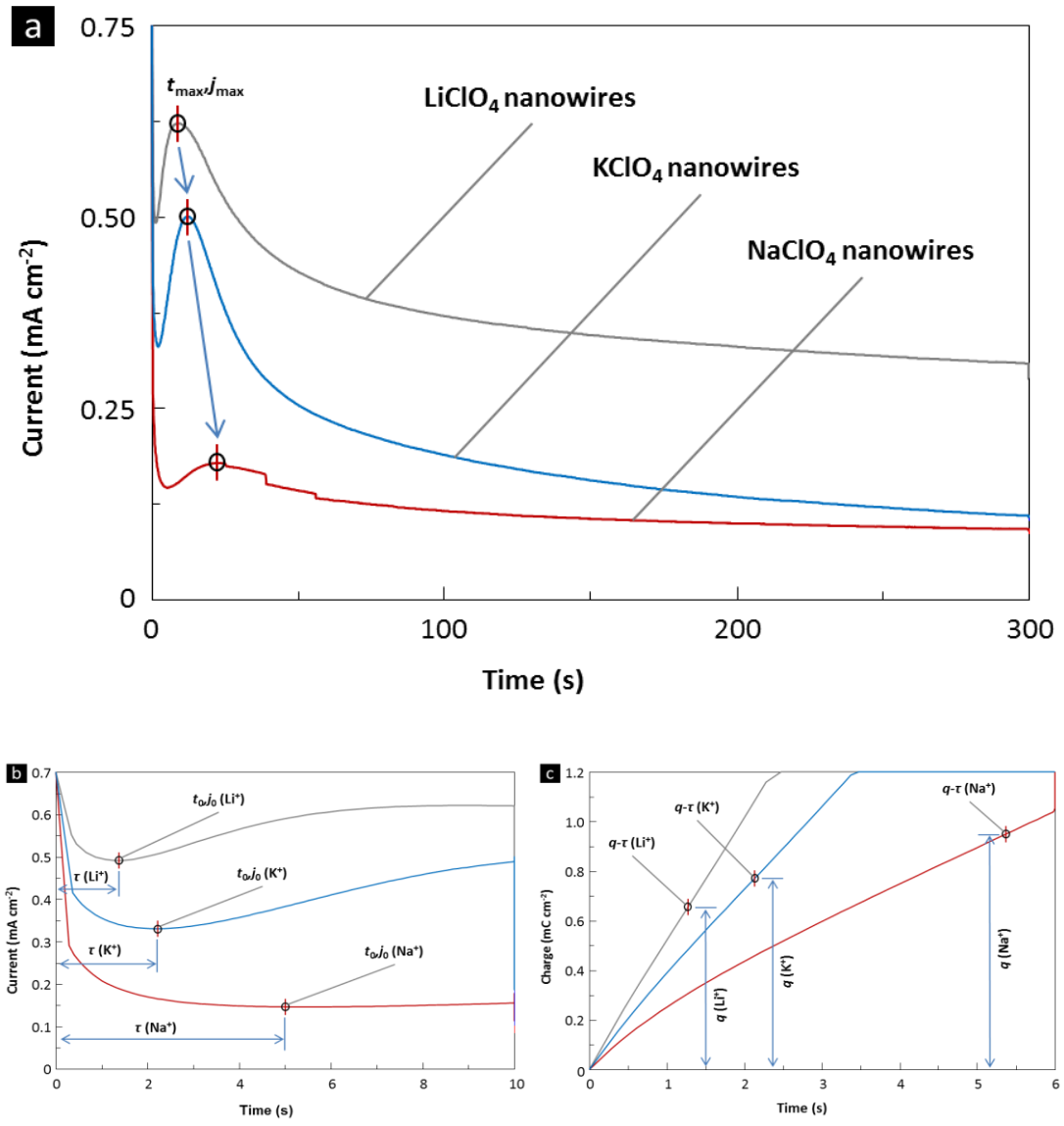

Figure 4.16: Plots of (a) *j-t* (300 s), (b) *j-t* (10 s) and (c) *q-t* (6 s) of $PPyEtN_3$ films deposited on the Au substrate at 0.850 V vs. SCE, until *q* of 68 mC cm^{-2} or 400 s was achieved in $EtOH/H_2O$ (3:4) with $(NH_4)H_2PO_4$ (300 mM) and $LiClO_4$ (—), $NaClO_4$ (—) and $KClO_4$ (—) (20 mM).

The NGM processes controlling the deposition of $PPyEtN_3$ in the presence of the three varied perchlorate salts were investigated, as it was observed from the SEM micrographs, that the nanowire films decreased in homogeneity from films grown in the presence of $LiClO_4$ down to that grown in $KClO_4$ (Figure 4.15). Therefore, the experimental data attained during the deposition procedures were normalised using

t_{max},j_{max} and the subsequent data were compared to dimensionless theoretical models obtained using the four NGM equations. Observing the produced NGM plots, it was apparent that a trend was present and could be related to the level of nanowire homogeneity in the films, deposited from the three perchlorate salts. The experimental data for the film deposited using $LiClO_4$, fitted very well to an IN3D process at the very early stages of growth (Figure 4.17 (b)) and this yielded a homogeneous film with an abundance of nanowires growing out from the substrate (Figure 4.15 (a) - (c)). Upon variation of the salt to the sodium cation, the experimental data veered towards a PN3D process, but still fitted reasonably to an IN3D process (Figure 4.17 (b)). The SEM micrographs revealed a film possessing short nodules, accompanied by a sporadic distribution of nanowires, shorter in length than that observed on the $LiClO_4$ nanowire film (Figure 4.15 (d) - (f)). Lastly, the modified experimental data of $KClO_4$ more closely resembled a PN3D mechanism (Figure 4.17 (f)), while yielding SEM micrographs depicting films with a sporadic distribution of nanostructures.

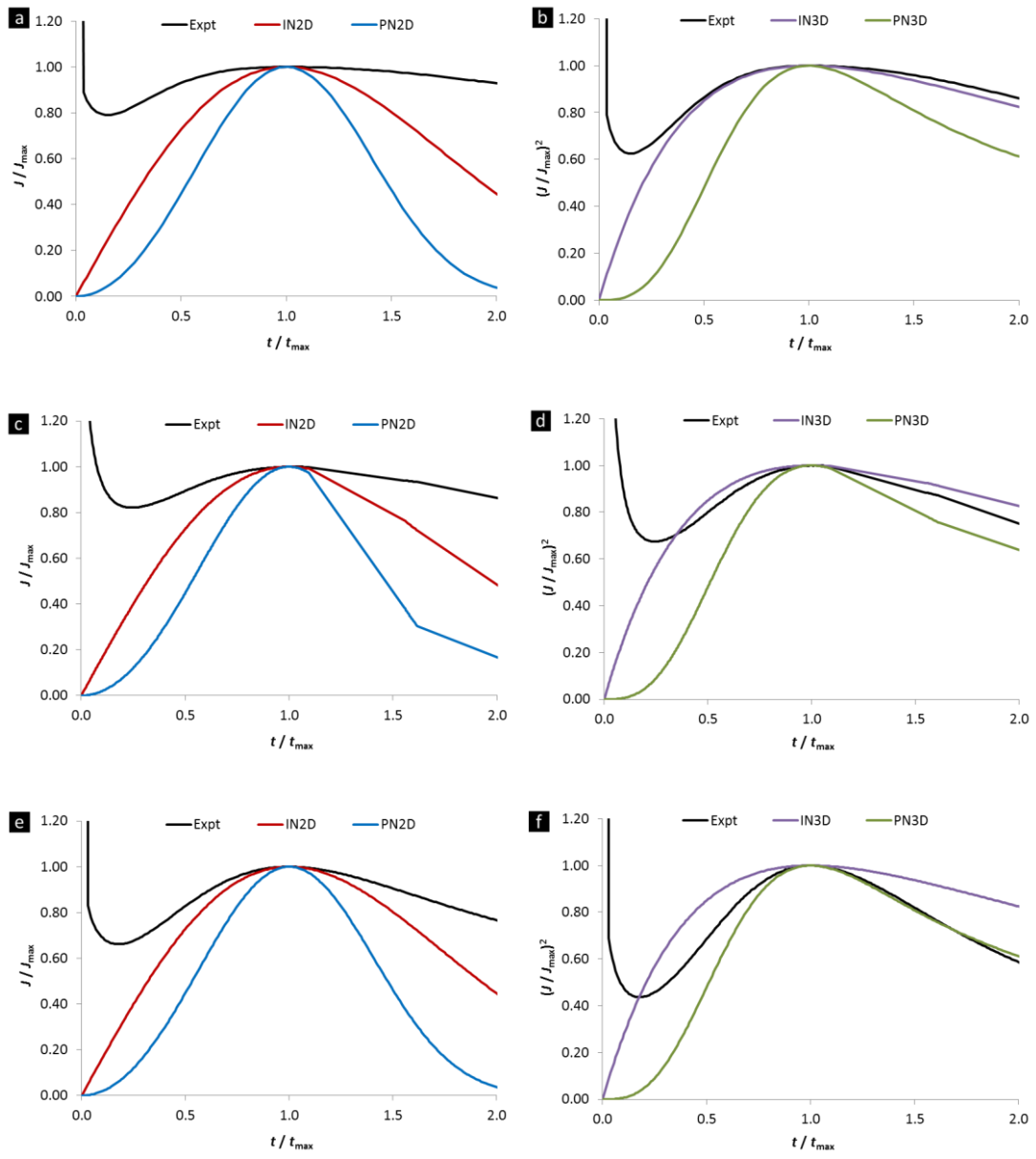

Figure 4.17: NGM plots of $PPyEtN_3$ nanowire films deposited on the Au substrate in $EtOH/H_2O$ (3:4) with $(NH_4)H_2PO_4$ (300 mM) and (a) - (b) $LiClO_4$ (20 mM), (c) - (d) $NaClO_4$ or (e) - (f) $KClO_4$ (20 mM) at 0.850 V vs. SCE. Plot (a) curves are representative of experimental data (—), IN2D (—) and PN2D (—) mechanisms while plot (b) curves are representative of experimental data (—), IN3D (—) and PN3D (—) mechanisms.

4.2.1.4 Investigation of the role played by the 'bulk' electrolyte

The template-free electrochemical deposition of $PPyEtN_3$ nanowire films performed in this research requires the utilisation of two electrolytic salts, $LiClO_4$ ('seed' electrolyte) and $(NH_4)H_2PO_4$ (bulk electrolyte), for film fabrication. The results in

Section 4.2.1.3 revealed that not all salts can act as an effective 'seed' electrolyte and those that act as a 'seed' electrolyte possess a reasonable solubility in organic solvents. Our studies and analyses were consistent with the proposal that it is the 'seed' electrolyte, which enables the necessary instantaneous nucleation of $PPyEtN_3$. As stated in Section 4.2.1.2, it is well established that the formation of CP nanowires, under a variety of conditions, are favoured by fast nucleation succeeded by slow propagation. Since it appears that the 'seed' electrolyte involvement ensures the fast nucleation of $PPyEtN_3$, it became judicious to postulate the role of $(NH_4)H_2PO_4$; ensuring slow propagation. In order to investigate this possibility, experiments were executed utilising the previously stated growth conditions, while excluding either $LiClO_4$ or $(NH_4)H_2PO_4$ from the electrolytic medium sequentially. Upon application of an oxidising potential to the system containing exclusively $LiClO_4$ (20 mM), a large *j-t* transient was produced possessing a t_0,j_0 with no t_{max},j_{max}, which increased thereafter, continuing until a plateau was attained (Figure 4.13 (—)). This system yielded the deposition of a bulk $PPyEtN_3$ film with no indication of nanostructured features.

Repeating this process with exclusively $(NH_4)H_2PO_4$ (300 mM) present as supporting electrolyte produced a *j-t* transient, which upon experiment commencement abruptly dropped towards zero and plateaued over time, yielding no visible growth on the substrate (Figure 4.18 (—)). This clearly supports the proposal that $LiClO_4$ plays a role in polymer nucleation. As observed in Section 4.2.1.2, application of E_{ox} = 0.850 V vs. SCE to a system, possessing both electrolytic salts at the appropriate concentration, permitted the development of the nanowire morphology. This *j-t* transient displays a moderate *j* value (Figure 4.18 (—)), when compared to the exclusively $LiClO_4$ (20 mM) containing system. However, instead of steadily increasing, as the *j* value does for the $LiClO_4$ system it was seen to reach a t_{max},j_{max} value and then decrease. This indicates over the time interval 30 - 150 s that polymer growth was slower in the mixed electrolyte system.

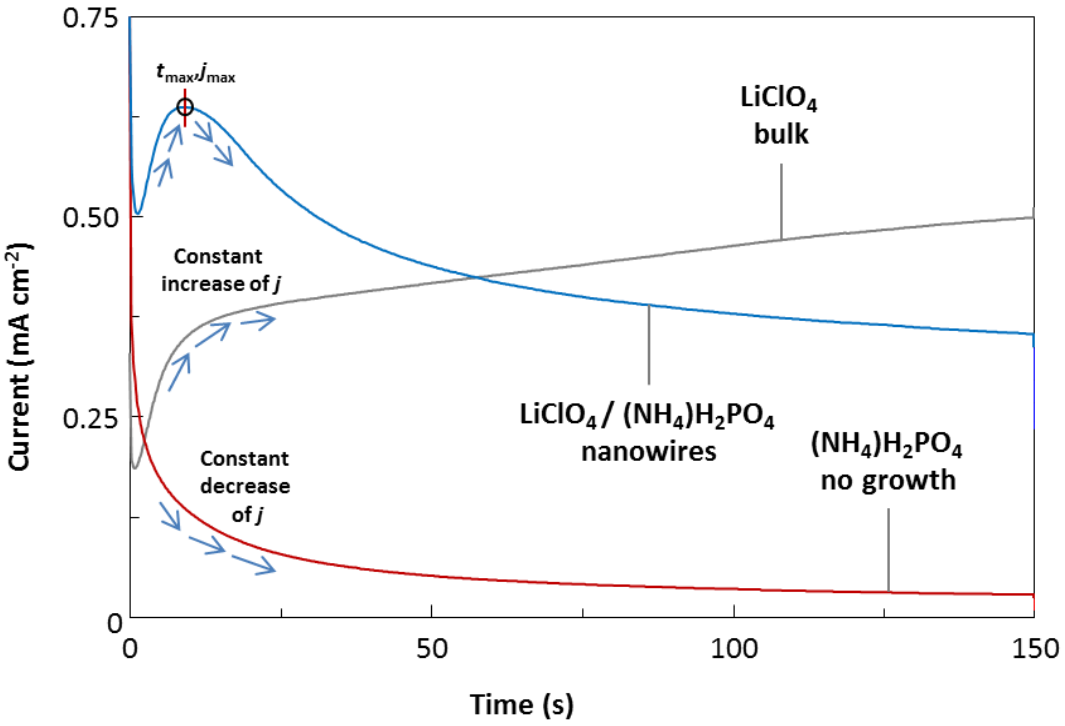

Figure 4.18: *j-t* transients of $PyEtN_3$ (35 mM) at 0.850 V vs. SCE on the Au substrate in EtOH/H_2O (3:4) with $LiClO_4$ (—) (20 mM), $(NH_4)H_2PO_4$ (—) (300 mM) and $LiClO_4$ (20 mM) with $(NH_4)H_2PO_4$ (—) (300 mM).

It has been proposed in the literature that the phosphate anion controls the vertical growth of polymer nanowires by acting as a scaffolding agent. Zang *et al.* suggested that non-covalent interactions[58,59] were primarily responsible for PPy nanowire formation, specifically due to the occurrence of electrostatic interactions between the phosphate anions and the electrooxidised positively charged Py/oligomers, combined also with the H-bonding of oxygen atoms on the phosphate anion and secondary amines in the Py rings.[1] Wang *et al.* proposed the PPy nanowire films formed in the presence of carbonate anions due to numerous reasons. Firstly, that the 1D deposition was due to exclusive growth at the polymer nanowire interface, which under certain conditions, were the only electroactive sites possessing the capability for polymer growth. They also stated that the low doping degree of PPy at certain E_{app} and the presence of structural defects throughout the polymer chain contribute to this morphology.[26] Debiemme-Chouvy has reported, during deposition of PPy nanowires in their Na_2HPO_4 (200 mM)/$NaClO_4$ (1 mM) and Na_2HPO_4 (200 mM)/$LiClO_4$ (1 mM) system, that the perchlorate anion was preferentially incorporated into the

nanowire matrix to neutralise the polymers bipolaron species.[43] She proposes that the pH at the polymer interface is lower than the bulk due to proton release during oxidation of Py monomer species. This excess of H^+ ions causes protonation of the amphoteric hydrogen phosphate anions, yielding their non-ionised form at the substrate. Evidence for this was illustrated in the XPS data, showing the absence of phosphorus due to the non-doping of the PPy nanowires with H_3PO_4 during oxidation.[2] It was proposed that a similar process occurs during the deposition of our $PPyEtN_3$ nanowire films; employment of dihydrogen phosphate anions, (pK_a of approx. 2),[60,61] during $PPyEtN_3$ nanowire deposition acts to slow down the kinetics of the system, raising the pH at the electrode surface by acting as a buffer, since it is well established that acidic pH values promote the rate of PPy formation.[62,63]

4.2.2 Characterisation of $PPyEtN_3$ nanowire films

The $PPyEtN_3$ nanowire films were characterised physically, electrochemically, and spectroscopically, utilising transmission electron microscopy (TEM), field emission SEM (FESEM), electron diffraction pattern-fast Fourier transform (ED-FFT), CV, FTIR spectroscopy, EDX spectroscopy, Raman spectroscopy and XPS. Comparison of $PPyEtN_3$ nanowire and bulk films were performed in respect to CV, focussing on the capacitance and redox activity of the polymer, while FTIR spectroscopy and Raman spectroscopy were utilised to investigate polymer conjugation and the occurrence of overoxidation, caused by the attack of nucleophilic species.

4.2.2.1 Physical characterisation of $PPyEtN_3$ nanowire morphology

The $PPyEtN_3$ nanowire films were deposited on a 4 mm diameter Au substrate at a range of E_{app} for various times in an $EtOH/H_2O$ (3:4) co-solvent system with $PyEtN_3$ (35 mM), $(NH_4)H_2PO_4$ (300 mM) and $LiClO_4$ (20 mM). A longer polymerisation time (30 - 60 min) was applied in comparison to the NGM studies so as to produce longer nanowires, for quicker location during TEM analyses. Firstly, the global morphology of the $PPyEtN_3$ nanowire film was investigated utilising FESEM. Analysis revealed the deposition of a networked $PPyEtN_3$ nanowire system possessing ‘spaghetti’ type morphology (Figure 4.19 (a)). The individual nanowires varied in diameter, ranging from approx. 80 - 150 nm and possessed some tapering

towards the tip. Investigation using TEM confirmed that the nanowires were connected *via* a layer of $PPyEtN_3$ at the base of each respective nanowire (Figure 4.19 (b)). The individual nanowires were several microns in length (approx. 2 - 3 μm) and were approx. 120 nm in diameter. Analysis of several individual nanowire structures, deposited at 0.860 V vs. SCE for 30 min, revealed attributes such as tapering towards the apex and 1D curvature effects, possessed predominantly by longer wires approx. ≥1 μm in length. Nanowires deposited at 0.820 V vs. SCE for 60 min exhibited a shorter length, while growing straight and experienced very little of these effects. Focussing on the nanowires apex, it was revealed that it could be quite varied in shape; convex, flat and concave tips were observed throughout the analysis. TEM was also performed to determine the elusive internal construction of the nanowire structure. Using the high magnification capabilities, the nanostructures in the micrograph were determined to be solid wires, not tubular structures (Figure 4.19 (c)). This was conclusive, as there were no internal cavities upon analysis of each wire from base to tip. The nanowire surface morphology was slightly rough or rugged, but with a uniform texture over the entire length. The ED-FFT pattern, (Figure 4.19 (d)) obtained for an individual $PPyEtN_3$ nanowire, displays the properties representative of a completely amorphous material, due to the long arc length produced by the non-crystalline orientation.

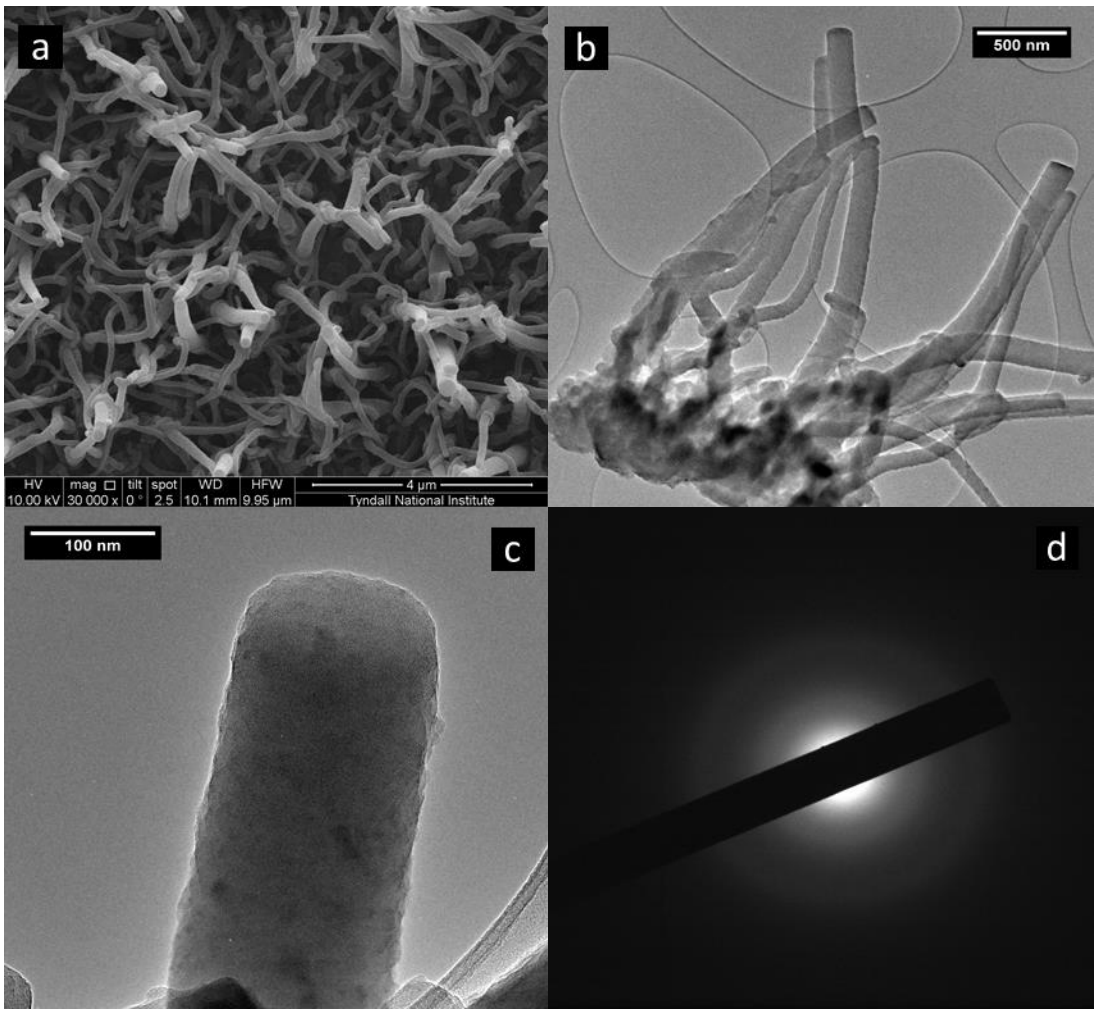

Figure 4.19: FESEM micrograph (plan-view) of (a) networked $PPyEtN_3$ nanowire film, TEM micrographs of (b) $PPyEtN_3$ nanowires connected to $PPyEtN_3$ base and (c) individual solid $PPyEtN_3$ nanowire. ED-FFT pattern of (d) individual solid $PPyEtN_3$ nanowire displaying non-crystalline orientation. $PPyEtN_3$ nanowire films were deposited on Au in $EtOH/H_2O$ (3:4) with $PyEtN_3$ (35 mM), $(NH_4)H_2PO_4$ (300 mM) and $LiClO_4$ (20 mM) at 0.820 - 0.860 V vs. SCE for 30 - 60 min.

4.2.2.2 Electrochemical characterisation of $PPyEtN_3$ nanowire morphology

The electrochemical activity and stability of the $PPyEtN_3$ nanowire films were compared to that of the bulk films fabricated during the work outlined in Chapter 3. CV was performed on the nanowire and bulk films in monomer-free, degassed, anhydrous MeCN, containing $LiClO_4$ (100 mM) and cycling was performed at 50 mV s^{-1}, while utilising a potential window of -0.150 - 0.950 V vs. $Ag/AgNO_3$. The $PPyEtN_3$ film possessed good electrochemical stability during the redox transition; only a small loss of electrochemical activity occurred during the first few cycles and

no discernible variations were observed in the successive scans. The bulk $PPyEtN_3$ film (Figure 4.20 (—)) possessed a *quasi*-reversible redox couple, attributed to the PPy backbone ($E_{1/2}$ = 0.639 V vs. $Ag/AgNO_3$, ΔE_p = 108 mV, j_a/j_c = 0.98), while the nanowire $PPyEtN_3$ film (Figure 4.20 (—)) possessed an analogous couple ($E_{1/2}$ = 0.666 V vs. $Ag/AgNO_3$, ΔE_p = 83 mV, j_a/j_c = 0.98). The bulk film displayed a greater electrochemical response when compared to the nanowire film, which was evident due to the greater j_{pa} and j_{pc} of the bulk film. This could possibly be attributed to the increased concentration (100 mM) of perchlorate dopant, present during deposition of the bulk film. The five-fold increase in this supporting electrolyte concentration, when compared to the nanowire film deposition concentration (20 mM), could incur more efficient neutralisation of charge carriers (predominantly polaron species) during film deposition. This should reduce the occurrence of overoxidation *via* attack by nucleophilic species (hydroxide) present in the electrolytic media, thus yielding a more electroactive bulk film. The nanowire film possessed both the E_{pa} and E_{pc} positioned at higher potentials, suggesting that the nanowire polymer film had greater difficultly undergoing oxidation and reduction, due to the more resistive nature of the nanowire film.[33,64]

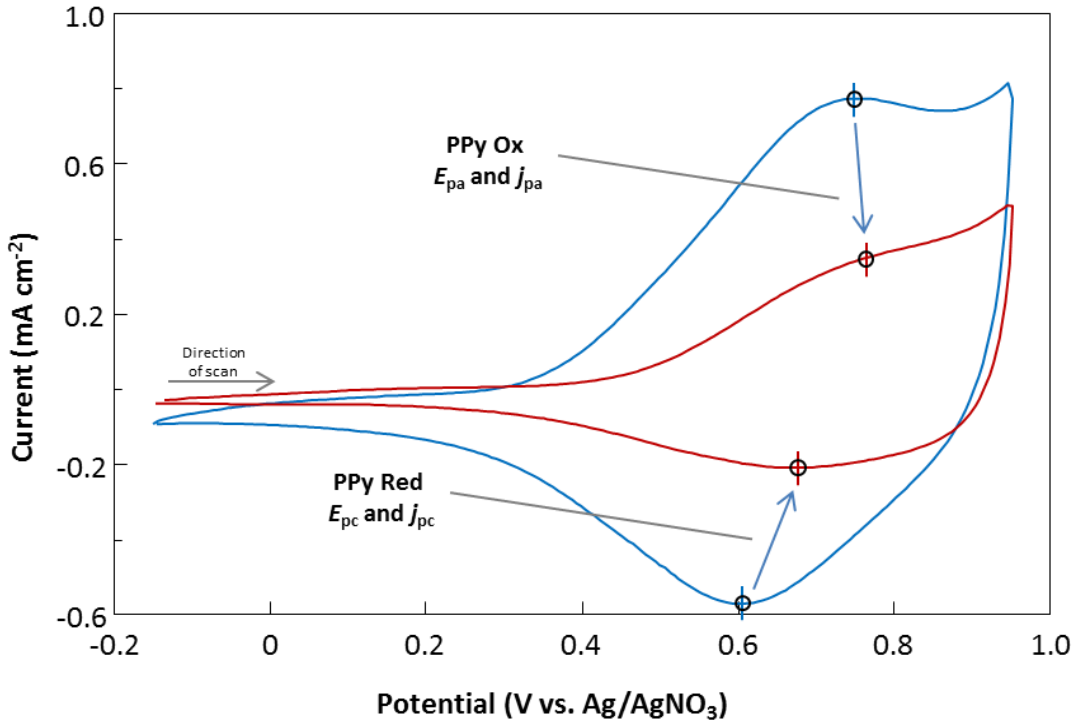

Figure 4.20: CVs of $PPyEtN_3$ bulk film (—) and $PPyEtN_3$ nanowire film (—) in MeCN with $LiClO_4$ (100 mM) at 50 mV s^{-1}. Both films were deposited from $PyEtN_3$ (35 mM) in $EtOH/H_2O$ (3:4) on the Au substrate at 0.850 V vs. SCE, until q of 119 mC cm^{-2} was achieved. The nanowire mixture contained $(NH_4)H_2PO_4$ (300 mM) and $LiClO_4$ (20 mM), while the bulk mixture contained $LiClO_4$ (100 mM).

4.2.2.3 Spectroscopic characterisation of $PPyEtN_3$ nanowire morphology

The $PPyEtN_3$ nanowire films were characterised using FTIR spectroscopy and comparison was made with bulk polymers, grown utilising the same deposition parameters. This was implemented to investigate differences in polymer conjugation and the occurrence of polymer overoxidation during deposition. The $PPyEtN_3$ nanowire films were deposited as transparent or opaque polymers on the Au substrate at 0.800 - 0.850 V vs. SCE, from an $EtOH/H_2O$ (3:4) co-solvent system containing $(NH_4)H_2PO_4$ (300 mM) and $LiClO_4$ (20 mM). This level of opacity was dependent of the q value achieved during the deposition process, as this influenced the eventual thickness of the film. The $PPyEtN_3$ nanowire and bulk films deposited at 0.850 V vs. SCE, until a q value of 481 mC cm^{-2} was attained are displayed in Figure 4.21.

The $PPyEtN_3$ nanowire film spectrum (Figure 4.21 (a)) possessed a band positioned at 2101 cm^{-1}, indicating retention of the azide functional group and was assigned specifically to the asymmetric stretch.[11] As for the bulk film (Figure 4.21 (b)), the bands at 2921 and 2854 cm^{-1} were assigned to aliphatic CH stretch vibrations.[65] The medium intensity band at 1701 cm^{-1}, in the spectrum for the nanowire film (Figure 4.21 (a)), was a result of carbonyl groups present at certain C_β positions on the Py ring backbone.[66] It can be seen upon comparison with the bulk film (Figure 4.21 (b)), that a band at 1723 cm^{-1}, representing the carbonyl stretch was present due to overoxidation, which occurred during deposition of the $PPyEtN_3$ bulk polymer. The shift in the position of the carbonyl band has been reported in the literature as a consequence of increased conjugation in proximity to the carbonyl on the PPy backbone. The absence of medium intensity amide stretch vibrations[67] at 1670 cm^{-1}, attributed to carbonyl groups at the C_α carbons, cannot be determined from the spectrum due to masking by other bands and therefore, it cannot be confirmed if branching during nanowire deposition occurs predominantly as the α-α form. However, the absence of a band at approx. 730 cm^{-1}, attributed to the CH out of plane bending vibration of the $Py–H_\alpha$, does suggest deposition in the α-α form.[68] The sharp band positioned at 1087 cm^{-1} was assigned to the perchlorate anion ν_2 mode.[69] Less intense bands from 1600 - 1000 cm^{-1} were assigned to the polymer backbone modes. The broad bands positioned at approx. 1630 cm^{-1} were assigned to residual H_2O, present due to the incorporation of solvated perchlorate anions during deposition, which has also been recorded for PPyMe.[70]

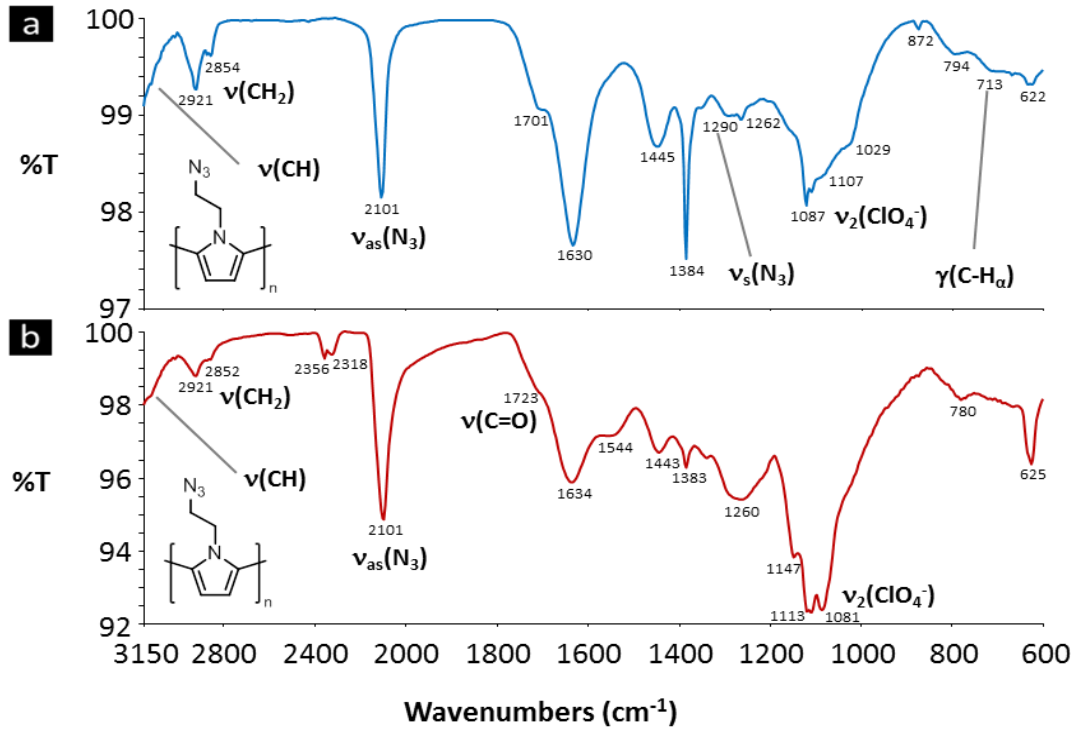

Figure 4.21: FTIR spectra of (a) $PPyEtN_3$ nanowire (—) and (b) bulk (—) films deposited on the Au substrate at 0.850 V vs. SCE, until q of 481 mC cm^{-2} was achieved in $EtOH/H_2O$ (3:4) with $(NH_4)H_2PO_4$ (300 mM) and $LiClO_4$ (20 mM) at ±2 cm^{-1} resolution in KBr. The sharp very intense band at approx. 1383 cm^{-1} is a consequence of an KBr powder impurity.[71]

The EDX spectral analysis of the $PPyEtN_3$ nanowire film (Figure 4.22) revealed carbon, nitrogen and oxygen signals positioned at 0.277, 0.392 and 0.526 keV respectively, due to the elemental composition of the $PPyEtN_3$ film. The presence of oxygen was likely due to the presence of the oxygen containing dopant anions or the occurrence of overoxidation during polymerisation. The elemental signal for chlorine was detected at 2.622 keV, confirming the presence of perchlorate anion as dopant within the nanowire film. Also, an elemental signal for phosphorus was observed at 2.014 keV. The presence of this phosphorus signal confirms the incorporation of an unspecified amount of dihydrogen phosphate within the nanowire matrix (most likely as a dopant counter ion) during the electrochemical deposition of the nanowire film. This was in contrast to the study carried out Debiemme-Chouvy, which determined that no phosphorus could be detected in her PPy nanowire film EDX spectrum.

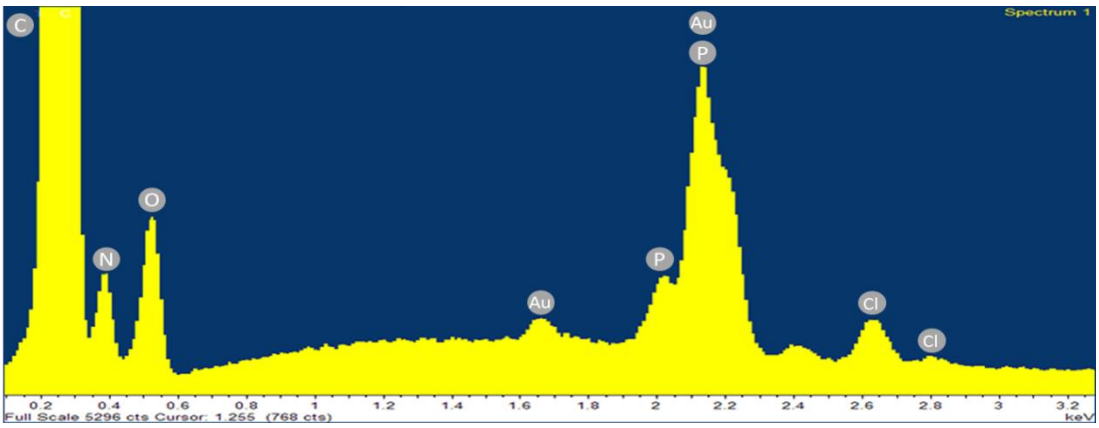

Figure 4.22: EDX spectrum of $PPyEtN_3$ nanowire film deposited on the Au substrate at 0.850 V vs. SCE, until q of 481 mC cm^{-2} was achieved, in $EtOH/H_2O$ (3:4) with $(NH_4)H_2PO_4$ (300 mM) and $LiClO_4$ (20 mM). Intense Au peaks are a consequence of the gold substrate utilised for electrodeposition.

Raman spectroscopy was performed on a $PPyEtN_3$ nanowire film, which had been deposited on a gold substrate at 0.850 V vs. SCE from a mixture of $EtOH/H_2O$ (3:4) containing $PyEtN_3$ (35 mM), $(NH_4)H_2PO_4$ (300 mM) and $LiClO_4$ (20 mM) (Figure 4.24 (—)). The spectrum of a $PPyEtN_3$ bulk film, deposited on to a gold substrate at 0.850 V vs. SCE from an $EtOH/H_2O$ (3:4) mixture containing $PyEtN_3$ (35 mM) and $LiClO_4$ (100 mM), was displayed for comparison (Figure 4.24 (—)). Both films were grown to comparable q values of 119 mC cm^{-2}, scrapped from the electrode surface and embedded within respective KBr pellets. Both the nanowire and bulk polymer films displayed bands at analogous wavenumbers. The Raman spectra of $(NH_4)H_2PO_4$ and $LiClO_4$ were recorded to ensure that bands from the electrolytic salts were not falsely attributed to the polymer films. Also, the Raman spectra of EtOH and H_2O were appropriated from the literature to guarantee accurate characterisation of the polymer films. In the $PPyEtN_3$ nanowire spectrum, the bands at 1590 cm^{-1} and 1531 cm^{-1} were assigned to the C=C stretch vibration for the PPy backbone, representative of the charged oxidised quinoid species and neutral reduced benzoid species respectively.[72] The double bands at 1366 cm^{-1} and 1341 cm^{-1} were assigned to the ring stretching mode.[72] The position of the band at 1590 cm^{-1} suggests the presence of bipolaron species within the $PPyEtN_3$ nanowire film,[73] but the absence of any band at approx. 940 cm^{-1} in the spectra would tend to indicate that there was no bipolaron species retained within the films.[72] Although the presence of

bipolaron species was not shown in the spectrum, the band at 979 cm^{-1} was assigned to a ring deformation mode,[73] representing the presence of polaron species.[72] As stated in Chapter 3, the absence of bipolaron species was anticipated in the nanowire and bulk $PPyEtN_3$ films. In the literature, it is stated that substitution of PPy at the ring heteroatom instigates a reduction in coplanarity of the PPy rings in the polymer backbone (Figure 4.23), which is a consequence of the steric effects, contributed from the substituted moiety.[74] These steric effects diminish the repeating conjugation lengths occurring throughout polymer backbone,[75] which reduces the polaron and bipolaron concentration across the polymer backbone.[76] Also, it has been reported that there is a necessity for the bipolaron species to acquire a critical concentration of polaron species during oxidation of the polymer,[77] but this process can be disturbed *via* nucleophilic attack by species in the deposition medium. This undesired process promotes overoxidation of the polymer,[78] yielding Py ring C_β carbonyl groups,[66] which can be seen in the spectrum as the band at 1705 cm^{-1}.

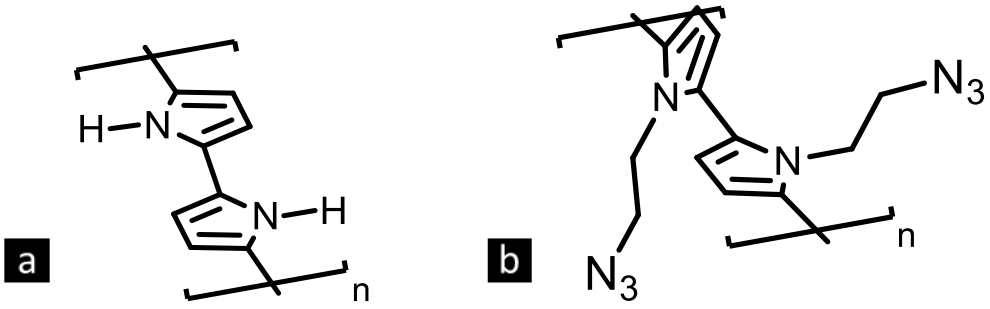

Figure 4.23: (a) PPy displaying a coplanar polymer backbone and (b) $PPyEtN_3$ displaying a non-planar polymer backbone, due to steric hindrance from the alkylazide substitution at the heteroatom.

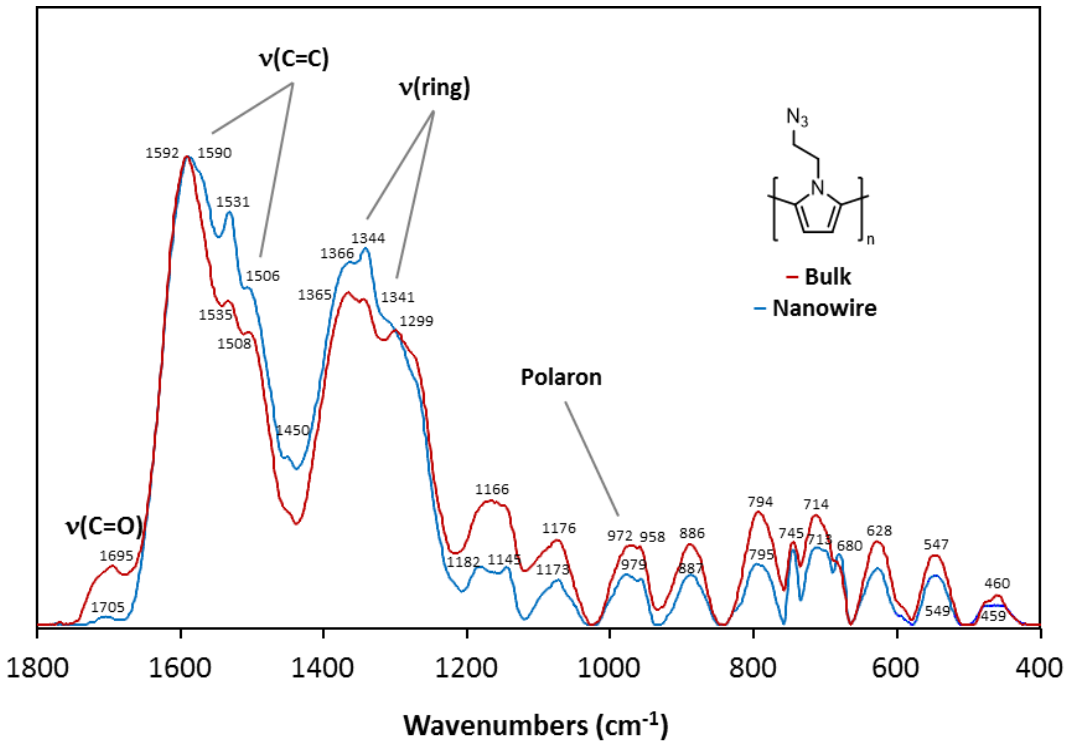

Figure 4.24: Raman spectra of $PPyEtN_3$ nanowire film (—) and $PPyEtN_3$ bulk film (—) deposited on Au substrates from $EtOH/H_2O$ (3:4) containing $PyEtN_3$ (35 mM) at 0.850 V vs. SCE until q of 119 mC cm^{-2} was achieved. Nanowire mixture contained $(NH_4)H_2PO_4$ (300 mM) and $LiClO_4$ (20 mM), while the bulk mixture contained $LiClO_4$ (20 mM) and the spectra were recorded utilising a laser line of 660 nm at ±1 cm^{-1} resolution in KBr.

XPS was performed on a $PPyEtN_3$ nanowire film, which had been deposited on the Au substrate from a $EtOH/H_2O$ (3:4) mixture containing $(NH_4)H_2PO_4$ (300 mM) and $LiClO_4$ (20 mM) at 0.850 vs. SCE until a q value of 119 mC cm^{-2} was achieved. The main peaks displayed in the survey scan were C 1s, N 1s and O 1s positioned at 285, 401 and 532 eV respectively (Figure 4.25 (a)). It was also noted that XPS is only capable of examining the outer layer of the film, as it is limited to a probing depth of approx. 10 nm.[79]

The narrow spectrum of the C 1s region (Figure 4.20 (b)) was decomposed into four functions with mean binding energies of 284.8, 286.4, 288.3 and 289.1 eV. The main contribution at 284.8 eV (E_{FWHM} of 1.2 eV) was attributed to carbon-bound carbons (C–C)[80,81] from within the PPy ring and from the *N*-substituted ethyl chain. The smaller peak positioned at 286.4 eV (E_{FWHM} of 1.7 eV) was accredited to nitrogen-bound carbons (N–C)[80-82] from the Py nitrogen and from the presence of the azide

moiety, which terminated the ethyl chain. The peak at 288.3 eV (E_{FWHM} of 1.2 eV) was suggested to be evident for the presence of ketone species (C=O) moieties,[82,83] a consequence of nucleophilic attack at the PPy ring C_β. The peak positioned at 289.1 eV (E_{FWHM} of 1.3 eV) was due to the presence of carboxyl groups within the polymer,[84,85] the product of overoxidation during film deposition.

The narrow spectrum of the N 1s region (Figure 4.25 (c)) was decomposed into four functions with mean binding energies of 398.6, 400.8, 404.6 and 408.1 eV. The contribution at 398.6 eV (E_{FWHM} of 1.6 eV) was ascribed to the azide moiety, specifically the ($C–N=N^+=\underline{N}^-$).[86] The main contribution at 400.8 eV (E_{FWHM} of 1.5 eV) was accredited to carbon-bound nitrogens of the tertiary amine (C–N)[80-82] and also, to the azide moiety, specifically the carbon bound nitrogen ($C–\underline{N}=N^+=N^-$).[86] Ammonium, present from $(NH_4)H_2PO_4$, was not detected within the polymer film, as a peak was not observed in the spectrum at the anticipated position of 401.5 eV.[87] Interestingly, the peak at 408.1 eV (E_{FWHM} of 1.1 eV) was indicative of nitrate presence,[88] which was presumed to be a consequence of ammonium electrooxidation, which has been reported to occur at approx. 0.900 V vs. SCE.[89,90] The contribution at 404.6 eV (E_{FWHM} of 1.0 eV) was credited to the azide moiety, specifically the ($C-N=\underline{N}^+=N^-$).[86]

The narrow spectrum of the O 1s region (Figure 4.25 (d)) was decomposed into three functions with mean binding energies of 530.7, 532.2 and 533.9 eV. The smallest peak at the lower binding energy of 530.7 eV (E_{FWHM} of 1.1 eV) was due to the dihydrogen phosphate oxygens ($H_2PO_4^-$),[91] resulting from the incorporation of dihydrogen phosphate anions as dopant during the deposition of the polymer film. The contribution at 532.2 eV (E_{FWHM} of 1.4 eV) was ascribed to PPy ring C_β ketones (pyrrolinone),[92] caused by overoxidation of the $PPyEtN_3$ nanowire film during deposition. The contribution at 533.9 eV (E_{FWHM} of 1.8 eV) was an indication of nitrate present within the polymer. This was further confirmation regarding the possible electrooxidation of ammonium ($(NH_4)H_2PO_4$) to nitrate, occurring during deposition of the $PPyEtN_3$ polymer film. It is conceivable that this peak could also be assigned to an ether-type oxygen within an ester/alcohol,[92] or residual EtOH from the deposition solvent system. It was also observed in the survey scan that the peak for

the presence of oxygen species was the most prominent, indicating that the outer layer of the polymer film had become overoxidised during deposition,[42,93] as the probe depth was limited to approx. 10 nm.[79]

The narrow spectrum of the P 2p region (Figure 4.25 (e)) possesses one small peak at 134.0 eV (E_{FWHM} of 1.8 eV) indicating the presence of the dihydrogen phosphate anion,[91] which was a consequence of the minimal doping of the film with the anion during deposition. The absence of chlorine peaks in the spectra was not a concern as XPS possesses an approximate probe depth of approx. 10 nm,[79] in which the polymer surface may not possess ClO_4^- anions. However, the presence of perchlorate had been confirmed within the polymer using EDX spectroscopy (Figure 4.22), which can analyse both the film surface and deeper within the polymer film.[94]

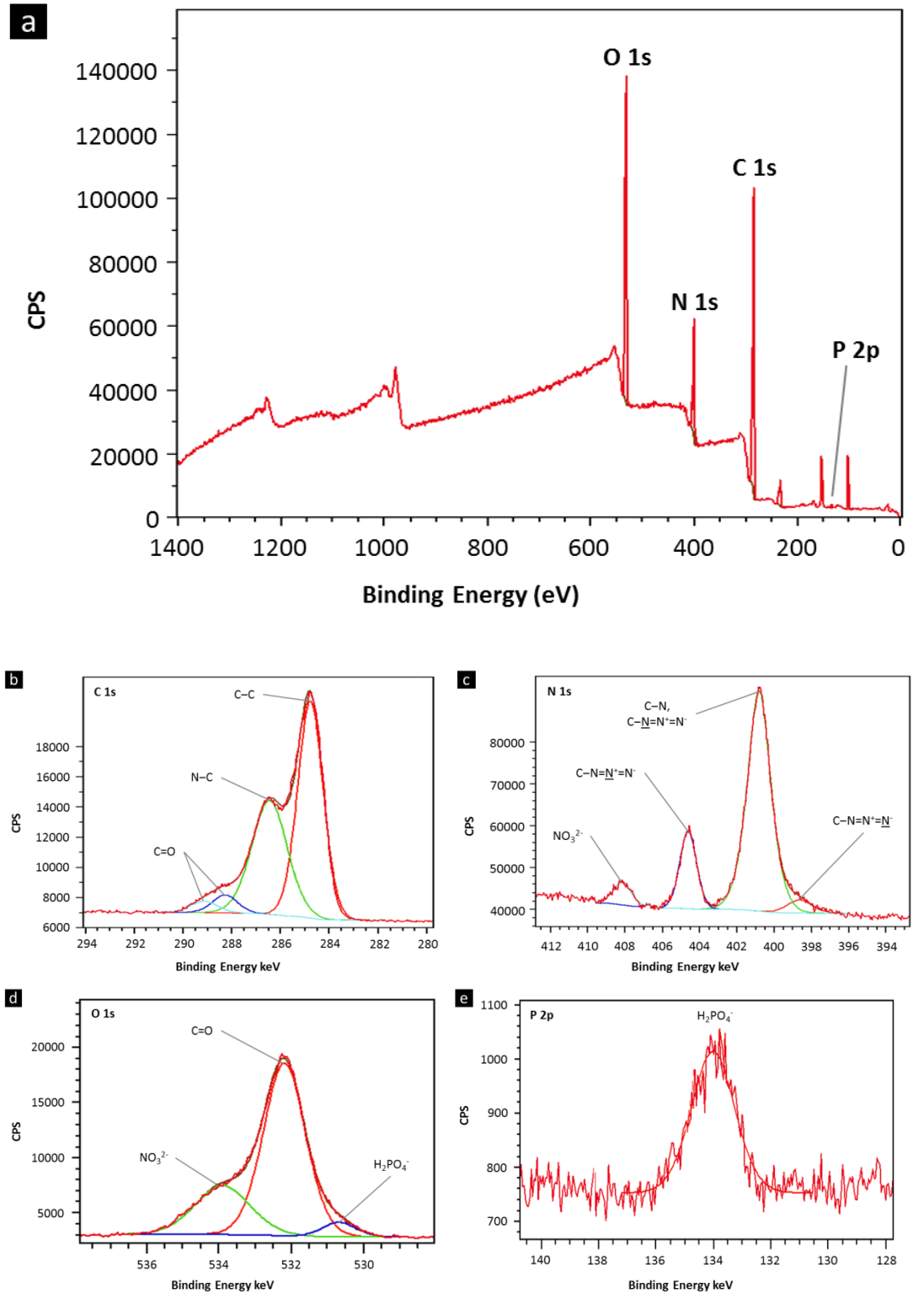

Figure 4.25: XPS spectra displaying (a) survey scan succeeded by narrow regions of (b) C 1s, (c) N 1s, (d) O 1s and (e) P 2p for a $PPyEtN_3$ nanowire film deposited on the Au substrate at 0.850 V vs. SCE until q of 119 mC cm^{-2} was achieved from EtOH/H_2O (3:4) containing $(NH_4)H_2PO_4$ (300 mM) and $LiClO_4$ (20 mM).

4.2.3 Post-functionalisation of $PPyEtN_3$ nanowire films

Once the successful deposition of $PPyEtN_3$ films in the bulk and nanowire morphologies were confirmed by utilising the previous characterisation methodologies in Section 4.2.3, post-functionalisation of the deposited films was attempted through modification of the azide functional group *via* CuAAC chemistry. This reaction was chosen as it is extremely versatile and its employment yields many benefits; the desired reaction may be performed at ambient temperature, in aqueous media, in the presence of oxygen and the overall reaction is usually high yielding, while producing negligible by-products. During the reaction (Scheme 4.4), the alkyne coordinates with the Cu^{I} catalyst to form a copper acetylide, which then coordinates with the azide. The charged azide functional group then attacks the alkyne to form a Cu^{III} metallocycle. This six-membered ring contracts to a triazolyl-copper derivative, which upon protonolysis produces the triazole product.

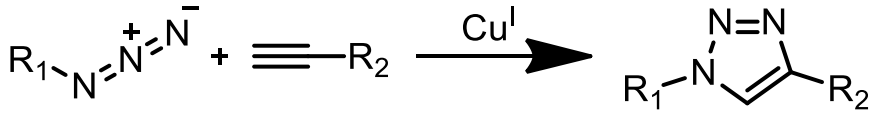

Scheme 4.4: CuAAC of an alkylazide and terminal alkyne to produce the triazole product.

The alkyne chosen for the CuAAC with the $PPyEtN_3$ films was FcCCH (Figure 4.26). FcCCH is an electrochemically active alkyne possessing a reversible redox couple, which can be controlled to produce the oxidised Fe^{III} ferricenium species and the reduced Fe^{II} ferrocene species, upon application of the appropriate potentials. The utilisation of a Fc analogue during post-functionalisation of our nanowire polymer films was encouraged by interest displayed with regards to the incorporation of Fc into CPs, or more specifically biosensors. Fc, in these cases, acts as an electron-transfer mediator and extensive studies have been reported.[95-99] An electron-transfer mediator is either a synthetic or biologically active charge carrier, possessing certain desirable properties, such as inducing negligible side reactions with the enzyme, e.g. GOx, displaying a fast reaction with the redox centre of the enzyme, while retaining reversible electrochemistry (fast rate constant).

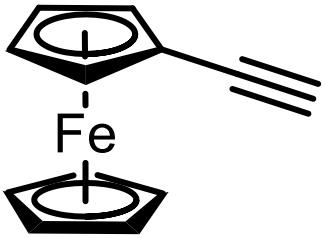

Figure 4.26: Structure of FcCCH.

The literature has shown that incorporating certain types of Fc or Fc derivatives into biosensors can have many negative effects on the system at hand. It has been reported that covalent binding of Fc to the biological enzyme, being incorporated into the CP, can reduce enzyme activity, while the non-covalent entrapment of Fc within the CP risks the possibility of leaching. Considering these factors, covalent attachment of the Fc derivative, to the CP, was selected. Therefore, upon deposition of $PPyEtN_3$ films, our chosen ligand, FcCCH, may be covalently bound to the nanowire and bulk $PPyEtN_3$ films *via* CuAAC. Before the bulk and nanowire $PPyEtN_3$ films underwent the CuAAC reaction on the electrode surface, analogous reactions were performed in solution. Employing the FcCCH reactant and the required reagents in MeCN, the $PyDeN_3$ monomer was reacted first, succeeded by the $PyEtN_3$ monomer. This was performed as formation of the both products could be easily analysed using characterisation techniques such as NMR spectroscopy, FTIR spectroscopy, mass spectrometry and CV.

4.2.3.1 CuAAC employing FcCCH

The CuAAC reaction was performed by adaption of the method outlined by Bauerle and co-workers.[14] As stated in the report, they utilised the Cu^I catalyst accompanied by elemental copper, as they attained better results when compared to the $CuSO_4/Cu^0$ procedure performed in an aqueous/organic co-solvent solution, as this yielded crystalline copper salts on the polymer surface.[14] General synthesis of the $PyDeN_3C_2HFc$ and $PyEtN_3C_2HFc$ monomers (Scheme 4.5) required an azide substituted Py and FcCCH dissolved in degassed, anhydrous MeCN, which was stirred in the presence of Cu^0 powder and the catalyst, tetrakisacetonitrilecopper(I) hexafluorophosphate ($[Cu^I(MeCN)_4]PF_6$). Synthesis of $PyEtN_3C_2HFc$ required the

use of base (diisopropylethylamine (DIPEA) or 2,6-lutidine). The mixture was stirred at ambient temperature under N_2 for a period of time between 8 and 72 hours, then diluted with DCM and filtered on a pad of Celite to remove elemental copper. The solvents were removed *in vacuo* to produce a yellow/orange solid, which was purified using column chromatography.

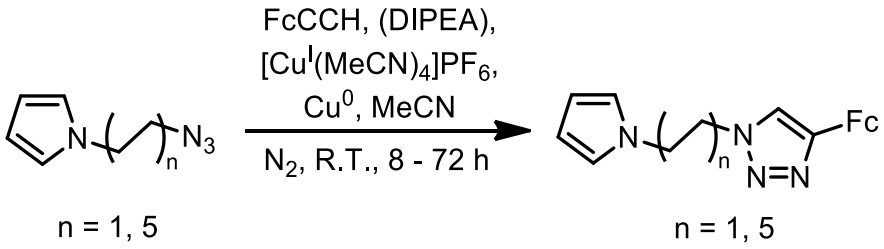

Scheme 4.5 CuAAC of the $PyDeN_3$ and $PyEtN_3$ monomer with FcCCH to produce the $PyDeN_3C_2HFc$ and $PyEtN_3C_2HFc$ products respectively.

General post-functionalisation of the $PPyEtN_3$ films (Scheme 4.6) *via* CuAAC required a $PPyEtN_3$ modified electrode, submerged in a mixture of FcCCH, DIPEA and $[Cu^I(MeCN)_4]PF_6$ (mol%) in degassed, anhydrous MeCN, to which freshly HNO_3 (dilute) washed Cu^0 powder was added. The electrode was submerged in this stirred mixture for approx. 30 hours at ambient temperature under N_2. The electrode was then removed, washed with MeCN, MeOH and Et_2O and dried *in vacuo* before commencement of polymer characterisation.

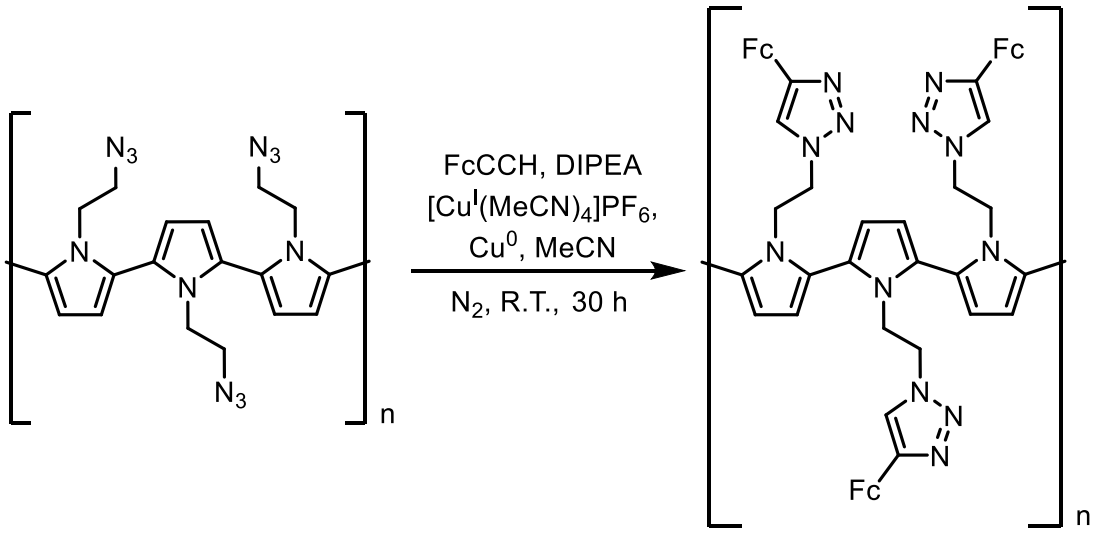

Scheme 4.6: CuAAC of the $PPyEtN_3$ film and FcCCH to produce the post-functionalised $PPyEtN_3C_2HFc$ film.

4.2.3.1a CuAAC of $PyDeN_3$ with FcCCH

The CuAAC of FcCCH with the $PyDeN_3$ monomer produced a sticky dark orange solid, which was characterised using FTIR spectroscopy, ^{1}H and ^{13}C NMR spectroscopy and mass spectrometry.

FTIR spectroscopy was performed on the $PyDeN_3C_2HFc$ product (Figure 4.27 (c)) in KBr at a resolution of 2 cm^{-1} and this was compared to spectra of the $PyDeN_3$ monomer (Figure 4.27 (a)) and the FcCCH reactant (Figure 4.27 (b)). The spectrum of the $PyDeN_3C_2HFc$ product (Figure 4.27 (c)) suggested the formation of a triazole moiety, as it displayed no indication for the presence of the $PyEtN_3$ asymmetric N_3 stretch band (2095 cm^{-1}), or the FcCCH alkyne CH stretch (3286 cm^{-1}) and C≡C stretch (2095 cm^{-1}), which could be observed in the reactant spectra.[100] Bands indicative of the Fc moiety were also observed in the spectrum. The CH stretch vibration on the Cp ring was present at 3117 cm^{-1}; in agreement with other substituted Fc derivatives reported in the literature, while the band associated with ring breathing was positioned at 1106 cm^{-1} in the spectra.[101] Also, the Fc CH out-of-plane parallel bend was positioned at 1000 cm^{-1}, while the out-of-plane perpendicular deformation was found at 819 cm^{-1}.[101] The band at 506 cm^{-1} represented the asymmetric metal ring stretch, while the band attributed to asymmetric ring tilt can be observed at 488 cm^{-1}. Both of these band positions were found to correspond well with the data reported for [Fe(η-C_5H_5)(η-C_5H_4Cl)] in the literature.[101] Bands, which could be attributed to an *N*-substituted Py monomer, were also present in the spectrum for the $PyDeN_3C_2HFc$ monomer. The aromatic CH stretch vibration band can be observed at 3078 cm^{-1}, accompanied by both the asymmetric and symmetric CH_2 stretch vibration bands at 2929 and 2854 cm^{-1} respectively.[64,102] Many bands attributed to the Py moiety and the triazole moiety can be observed from 1700 - 450 cm^{-1}. Quite noticeably, the strong band positioned at 720 cm^{-1} could be assigned to the both the CH bend at the Py-α position[103,104] and the CH_2 rock of the decyl tether.[102,104]

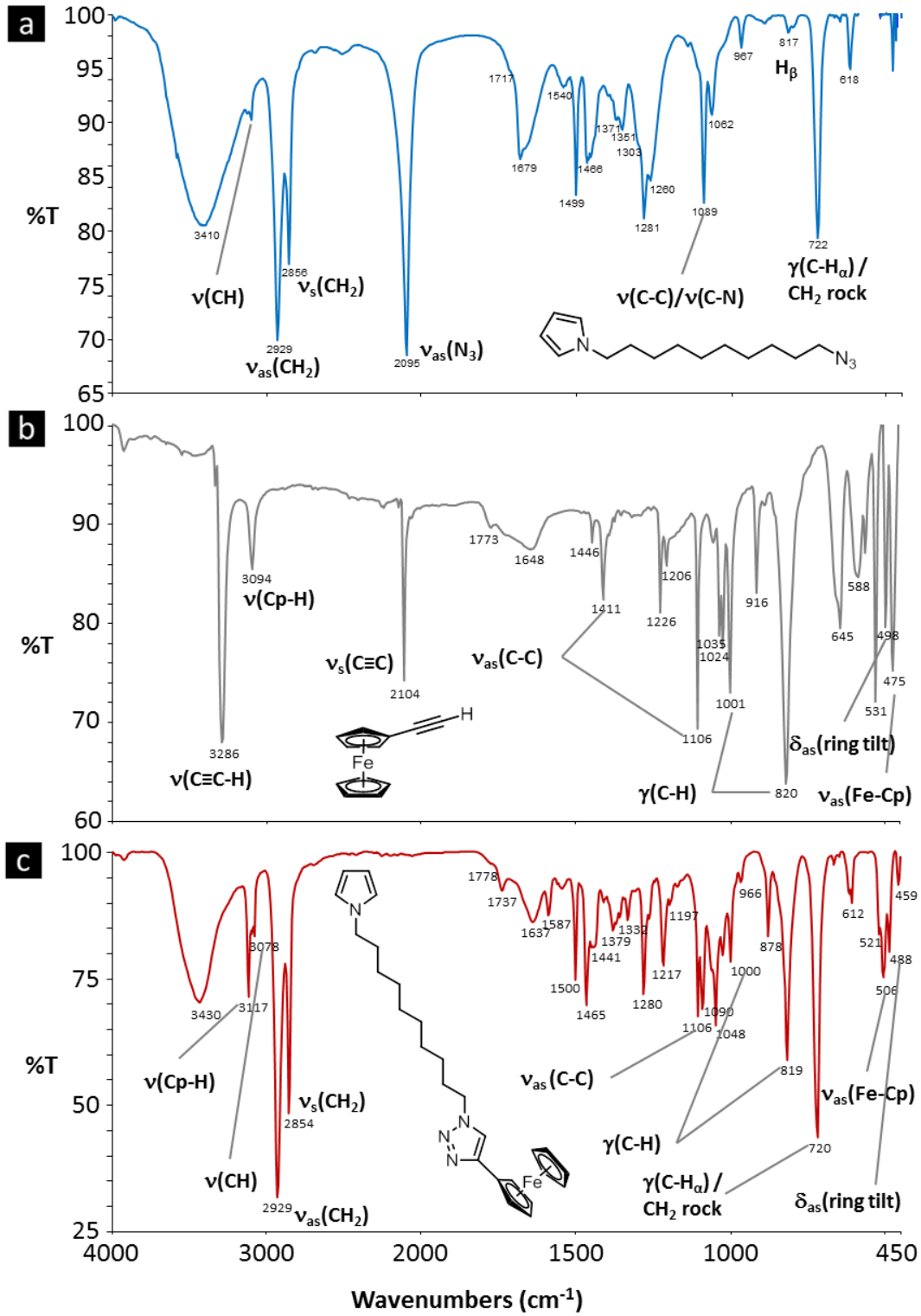

Figure 4.27: FTIR spectra of (a) $PyDeN_3$ monomer (—), (b) FcCCH (—) and (c) $PyDeN_3C_2HFc$ (—) at ±2 cm^{-1} resolution in KBr.

^{1}H and ^{13}C NMR spectroscopy was performed for characterisation of $PyDeN_3C_2HFc$ and the spectral assignments are displayed in Table 4.4.

^{1}H NMR spectroscopy of the $PyDeN_3C_2HFc$ monomer yielded a signal at 7.43 ppm that integrated to 1H. This singlet peak was attributed to the C=CH hydrogen of the triazole moiety, which has been observed in the literature when reported by Bauerle and co-workers for an EDOT monomer with a Fc unit bound covalently *via* a triazole moiety.[14,105] The proton was coupled to a carbon signal positioned in the alkene region of the spectrum at a chemical shift of 118.7 ppm. DEPT135 spectroscopy confirmed that this peak in the spectrum was a CH signal. Lacking in the spectrum was an alkyne CH peak at 2.72 ppm, confirming the absence of the FcCCH starting material. The ^{1}H NMR spectrum of the product showed that the Py–H_α and Py–H_β triplets, integrating to 2H each, shifted upfield slightly by 0.05 and 0.04 ppm to 6.59 and 6.08 ppm respectively, when compared to the $PyDeN_3$. The corresponding carbons signals resonated at 120.3 and 107.6 ppm respectively and appeared as CH signals in the DEPT135 spectrum. The triplet signals for the CH_2 protons adjacent to the triazole and Py moieties shifted downfield by 0.56 and 0.40 ppm to 3.80 and 4.30 ppm respectively and also integrated to 2H each. The signals for the analogous carbon atoms appeared at 49.6 and 50.1 ppm, as CH_2 signals in the DEPT135 spectrum. The large Fc singlet integrating to 5H, shifted upfield by 0.16 ppm to 4.03 ppm compared to that of FcCCH, while the two Fc triplets, Cp–H_α and Cp–H_β, integrated to 2H each and appeared at 4.68 and 4.25 ppm respectively. These proton signals were related to the CH resonances for the Fc moiety positioned at 69.5, 68.5 and 66.5 ppm, while that of the Fc quaternary carbon was positioned at 75.5 ppm. The triazole quaternary carbon resonance was present in the spectrum at 146.5 ppm.

Table 4.4: ^{13}C and ^{1}H NMR spectral data (δ in ppm) of $PyDeN_3C_2HFc$ in ($CDCl_3$) (75.5 and 300 MHz respectively).

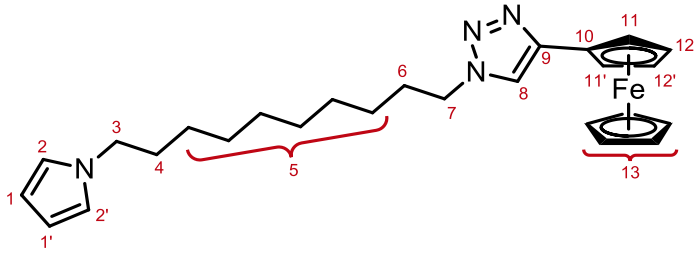

C / H	PyDeN$_3$C$_2$HFc (ppm)	
	δ ^{13}C	**δ ^{1}H (m); *J* Hz**
1,1’	107.6	6.08 (t); 2.1
2,2’	120.3	6.59 (t); 2.1
3	50.1	4.30 (t); 7.2
4	31.4	1.88 (m)
5	26.3 - 29.2	1.25 (m)
6	30.1	1.69 (m)
7	49.5	3.80 (t); 7.2
8	118.7	7.43 (s)
9	146.5	-
10	75.5	-
11,11’	68.5	4.68 (t); 1.5
12,12’	66.5	4.25 (t); 1.5
13	69.5	4.03 (s)

The calculated exact mass of protonated $PyDeN_3C_2HFc$ was determined to be 459.2206 g mol^{-1}, while mass spectrometry of the protonated monomer yielded a measured accurate mass of 459.2216 g mol^{-1}, producing a mass measurement error of 2.26 ppm.

4.2.3.1b CuAAC of $PyEtN_3$ with FcCCH

The CuAAC of $PyEtN_3$ with FcCCH produced an orange solid which was characterised using FTIR spectroscopy, ^{1}H and ^{13}C NMR spectroscopy and mass spectrometry.

The FTIR spectrum of the $PyEtN_3C_2HFc$ product in KBr at a resolution of 2 cm^{-1} can be observed in Figure 4.28 (c) accompanied by spectra for the $PyEtN_3$ monomer Figure 4.28 (a) and FcCCH reactant Figure 4.28 (b). The spectrum of the product yielded very similar results to that obtained for the decyl analogue. It can be seen that upon CuAAC of the two reactants there was a complete absence of the bands for the $PyEtN_3$ asymmetric N_3 stretch band (2101 cm^{-1}), the FcCCH alkyne CH stretch (3286 cm^{-1}) or C≡C stretch (2104 cm^{-1}) in the product (Figure 4.28 (c)),[100] confirming complete conversion of the azide and alkyne to the triazole functional group. It was suspected at this stage of the synthesis that FTIR spectroscopy would not be useful for confirmation of the successful post-functionalisation of $PPyEtN_3$ films, due to the overlap of the FcCCH alkyne band and the azide band at approx. 2102 cm^{-1}. The probability of FcCCH physisorption on to the polymer surface will produce a C≡C stretch in this region making confirmation for conversion of the azide functional group impossible. Bands indicative of the Fc moiety were present at 3109 and 1103 cm^{-1}, attributed to the Cp CH stretch vibration and ring breathing respectively.[101] The bands positioned at 1000 and 815 cm^{-1} were assigned to the Fc CH out-of-plane parallel bend and out-of-plane perpendicular deformation, respectively.[101] The bands associated with asymmetric metal ring stretch and asymmetric ring tilt were positioned at 513 cm^{-1} and 486 cm^{-1} respectively. The presence of an *N*-substituted Py monomer was confirmed by the bands positioned at 3095, 2928 and 2860 cm^{-1}, the Py aromatic CH stretch vibration band, succeeded by the asymmetric and symmetric CH_2 stretch vibration bands respectively.[64,102] The Py and triazole moieties have many bands associated with them present in the region 1700 - 450 cm^{-1}. In this case however, the strong band at 730 cm^{-1} was accredited only to the Py-α CH bend,[100,101] as a CH_2 rock vibration does not occur in the short ethyl tether.

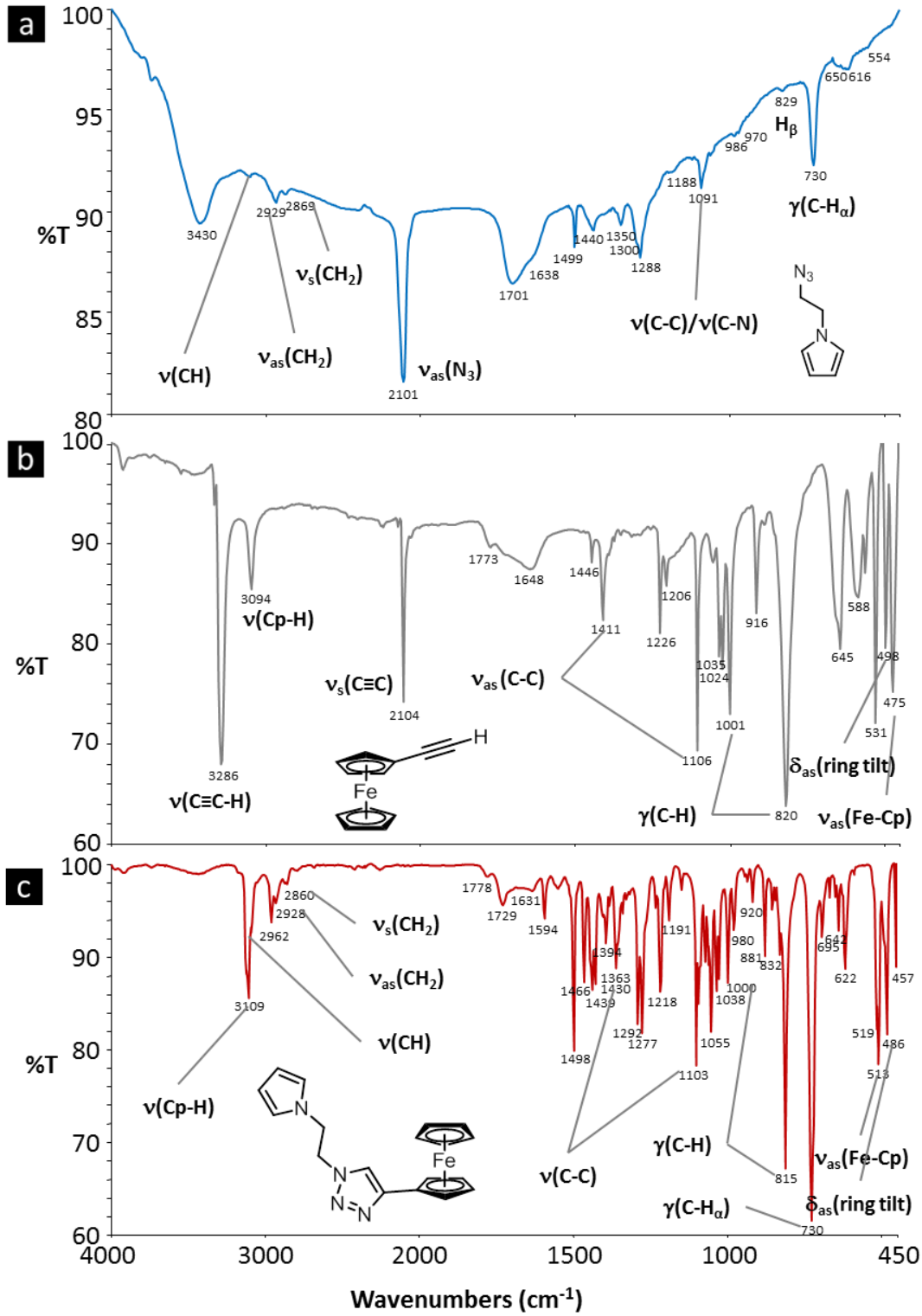

Figure 4.28: FTIR spectra of (a) $PyEtN_3$ monomer (—), (b) FcCCH (—) and (c) $PyEtN_3C_2HFc$ (—) at ±2 cm^{-1} resolution in KBr.

The ^{1}H and ^{13}C NMR spectroscopic assignments for $PyEtN_3C_2HFc$ are reported below in Table 4.5.

The ^{1}H NMR spectrum yielded a singlet peak positioned at 6.74 ppm, integrating for 1H. This resonance was attributed to the C=CH hydrogen, resulting from triazole formation upon CuAAC of $PyEtN_3$ with FcCCH and as anticipated, there was the absence of a singlet peak at 2.72 ppm for the alkyne CH. This triazole peak at 6.74 ppm was expected to resonate at a more downfield position of approx. 7.50 ppm, which had been observed for the decyl analogue and a similar EDOT compound.[14] The position of its more upfield chemical shift at 6.74 ppm was attributed to possible shielding by the Fc moiety.[106] 2D ^{1}H-^{1}H COSY was used to confirm the absence of coupling with hydrogen signals and 2D ^{1}H-^{13}C HSQC spectroscopy illustrated that the proton resonance was coupled to a carbon signal in the alkene region of the spectrum at 120.6 ppm. DEPTQ135 spectroscopy confirmed this peak as a CH signal. The Py–H_α and Py–H_β signals of the Py moiety integrated to 2H each and upon CuAAC of $PyEtN_3$ with FcCCH were observed to shift upfield by approx. 0.22 and 0.06 ppm to 6.50 and 6.18 ppm respectively. The corresponding carbons signals resonated at 120.6 and 109.6 ppm respectively, present in the DEPTQ135 spectrum as CH signals. The resonances assigned to the CH_2 protons adjacent to both the Py and triazole moieties shifted downfield by 0.58 and 0.79 ppm to 4.63 and 4.37 ppm respectively, while integrating to 2H. The corresponding carbon CH_2 signals were positioned at 51.6 and 49.6 ppm. The Fc singlet peak integrated to 5H as expected and this resonance shifted upfield by 0.17 ppm to 4.06 ppm. The two Fc triplet peaks, Cp–H_α and Cp–H_β, shifted downfield by 0.18 and 0.08 ppm to 4.65 and 4.28 ppm respectively and integrated to 2H each. The corresponding carbon signals were confirmed as CH resonances from DEPTQ135 spectroscopy and were positioned at 69.7, 68.8 and 66.7 ppm respectively. The Fc quaternary carbon signal was positioned at 75.5 ppm, while the triazole quaternary carbon resonance was present in the spectrum at 146.9 ppm.

Table 4.5: ^{13}C and ^{1}H NMR spectral data (δ in ppm) of $PyEtN_3C_2HFc$ in ($CDCl_3$) (75.5 and 300 MHz respectively).

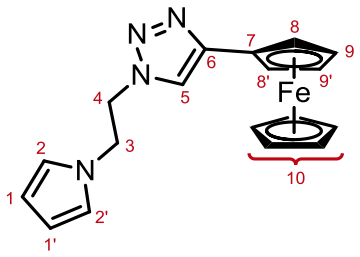

C / H	PyEtN$_3$C$_2$HFc (ppm)	
	δ ^{13}C	δ ^{1}H (m); *J* Hz
1,1’	109.6	6.18 (t); 2.1
2,2’	120.6	6.50 (t); 2.1
3	51.6	4.64 (t)
4	49.6	4.37 (t); 5.7
5	119.9	6.74 (s)
6	146.9	-
7	75.3	-
8,8’	66.7	4.64 (t)
9,9’	68.8	4.27 (t)
10	69.7	4.05 (s)

The calculated exact mass for protonated $PyEtN_3C_2HFc$ was found to be 347.0954 g mol^{-1}, while mass spectrometry of the sample produced a measured accurate mass of 347.0945 g mol^{-1}, yielding a mass measurement error of -2.48 ppm.

4.2.3.1c Electrochemical polymerisation of $PyEtN_3C_2HFc$

Once the $PyEtN_3C_2HFc$ monomer had been successfully synthesised and characterised, the electroactivity and electropolymerisation of the monomer was examined using CV in degassed, anhydrous MeCN containing $TBAPF_6$. Firstly, the electroactivity of the monomer was investigated in solution, using a low concentration (5 mM) of the monomer, while scanning at 200 mV s^{-1} within two

potential windows. The Fc redox couple for the $PyEtN_3C_2HFc$ monomer ($E_{1/2}$ = 0.142 V vs. $Ag/AgNO_3$, ΔE_p = 131 mV, j_c/j_a = 0.99) was determined to be *quasi*-reversible, using a potential window of -0.500 - 0.600 V vs. $Ag/AgNO_3$ (Figure 4.29 (—)). The irreversible oxidation of the Py moiety was identified at 1.316 V vs. $Ag/AgNO_3$, employing a potential window of -0.500 - 1.600 V vs. $Ag/AgNO_3$ (Figure 4.29 (—)). The reversibility of the Fc redox couple for the $PyEtN_3C_2HFc$ monomer in solution ($E_{1/2}$ = 0.142 V vs. $Ag/AgNO_3$, ΔE_p = 131 mV, j_c/j_a = 0.99) was observed to decrease upon application of a E_λ above 0.600 V vs. $Ag/AgNO_3$.

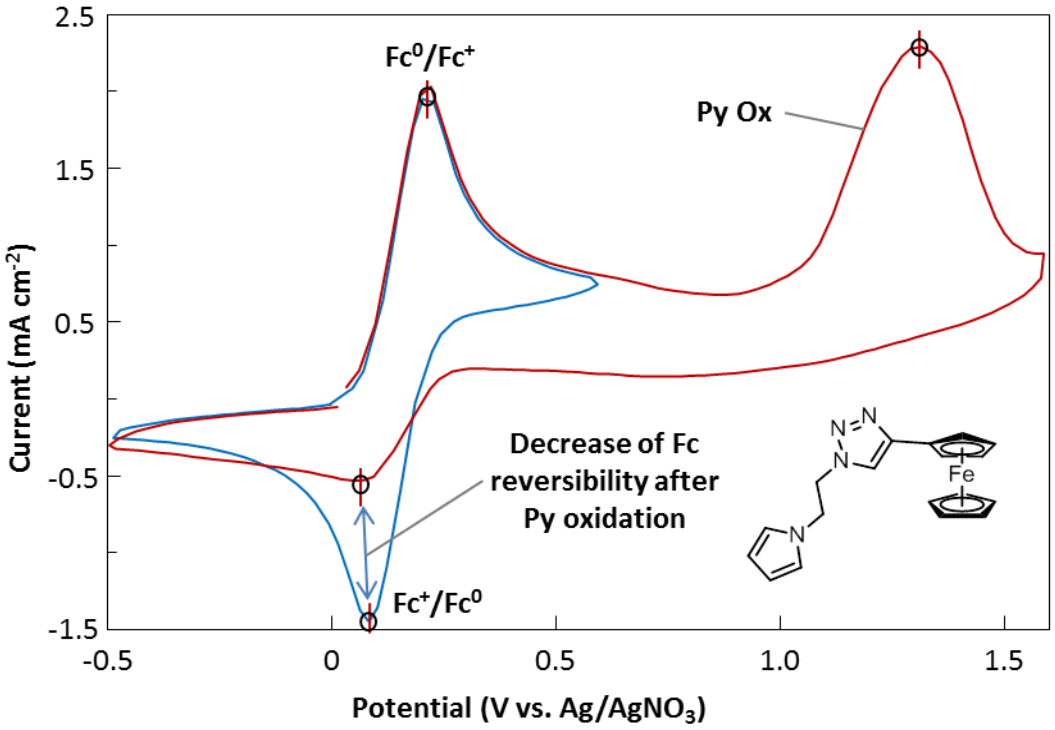

Figure 4.29: CVs of $PyEtN_3C_2HFc$ (5 mM) in MeCN with $TBAPF_6$ (100 mM) at 200 mV s^{-1} within two potential windows emphasising Fc (—) and Py electroactivity (—).

After the electroactivity of the monomer had been established, the concentration was increased to 50 mM (as polymerisation at 5 mM proved ineffective) and electrodeposition was attempted. The polymerisation of the monomer utilising CV, within a window of -0.500 to 1.600 V vs. $Ag/AgNO_3$ at 100 mV s^{-1} in anhydrous MeCN with $TBAPF_6$ (100 mM), did not produce an adherent film on the substrate after 30 cycles. Once again, it was observed that the reversibility of the Fc redox

couple decreased upon application of E_λ > 0.600 V vs. Ag/AgNO$_3$. Also, the j_{pa} of the Fc redox couple shifted to considerably greater oxidative potentials during cycling between -0.500 - 1.200 V vs. Ag/AgNO$_3$ (Figure 4.30). Due to this problem, CPA was employed to circumvent the issues present during deposition using CV. Therefore, an E_{ox} = 1.250 V vs. Ag/AgNO$_3$ was applied to the system for 5 minutes, attaining a q value of 1.19 C cm^{-2}, which was succeeded by characterisation of the attained film.

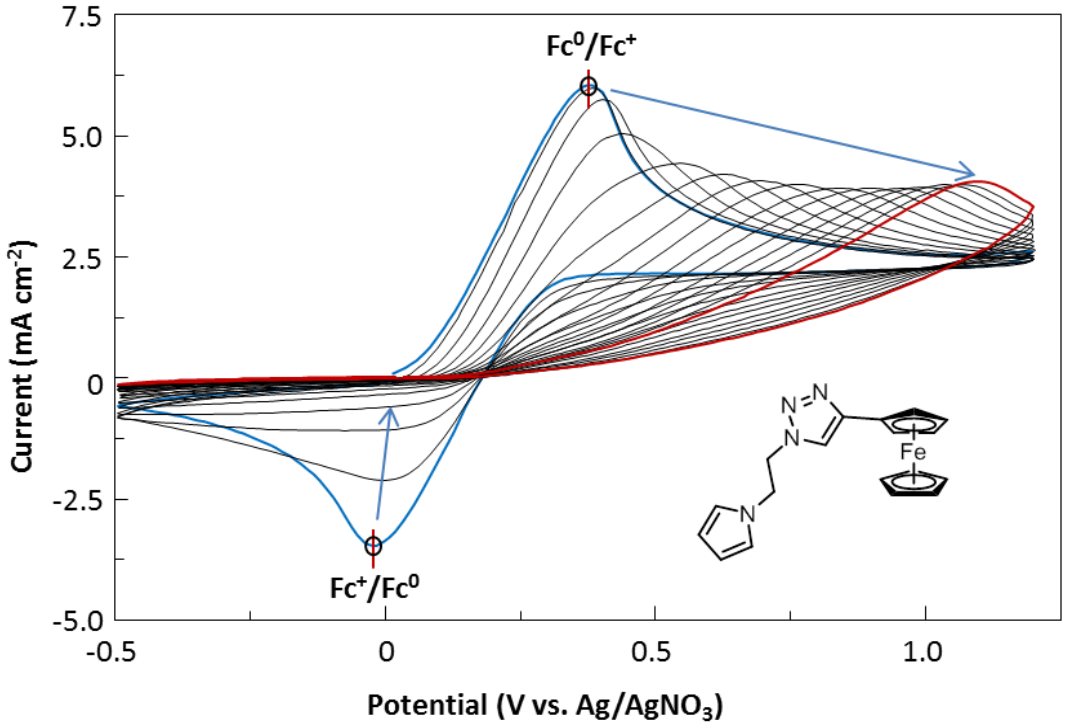

Figure 4.30: CVs of PyEtN$_3$C$_2$HFc (50 mM) in MeCN with TBAPF$_6$ (100 mM) at 100 mV s^{-1} using a potential window of -0.500 to 1.200 V vs. Ag/AgNO$_3$ showing the 1st (—) and 15th cycle (—).

The polymer electroactivity was next investigated using CV so the bulk PPyEtN$_3$C$_2$HFc film was submerged in an electrolytic solution of TBAPF$_6$ (100 mM) in anhydrous MeCN, which had been purged with argon gas for 15 minutes. Scanning was performed between -0.500 - 0.800 V vs. Ag/AgNO$_3$ at non-consecutive scan rates of 25, 50, 75 and 100 mV s^{-1}. The resulting cycles can be observed in Figure 4.31, accompanied by a plot representing j_p vs. v (Figure 4.31 (inset)), which illustrates that the peak currents vary linearly with scan rate. This characteristic can be attributed to thin layer electrochemistry with a surface confined process, deeming

it a system worthy of investigation, in relation to the use of mediator less (Fc covalently bound) biosensors.[99,107,108] The absence of defined j_p for the redox couple of PPy signifies the large steric effect of the covalently bound Fc moiety which induces non-planarity of the PPy backbone (Figure 4.23) and reduces polymer conjugation, obstructing the redox processes of PPy.[109]

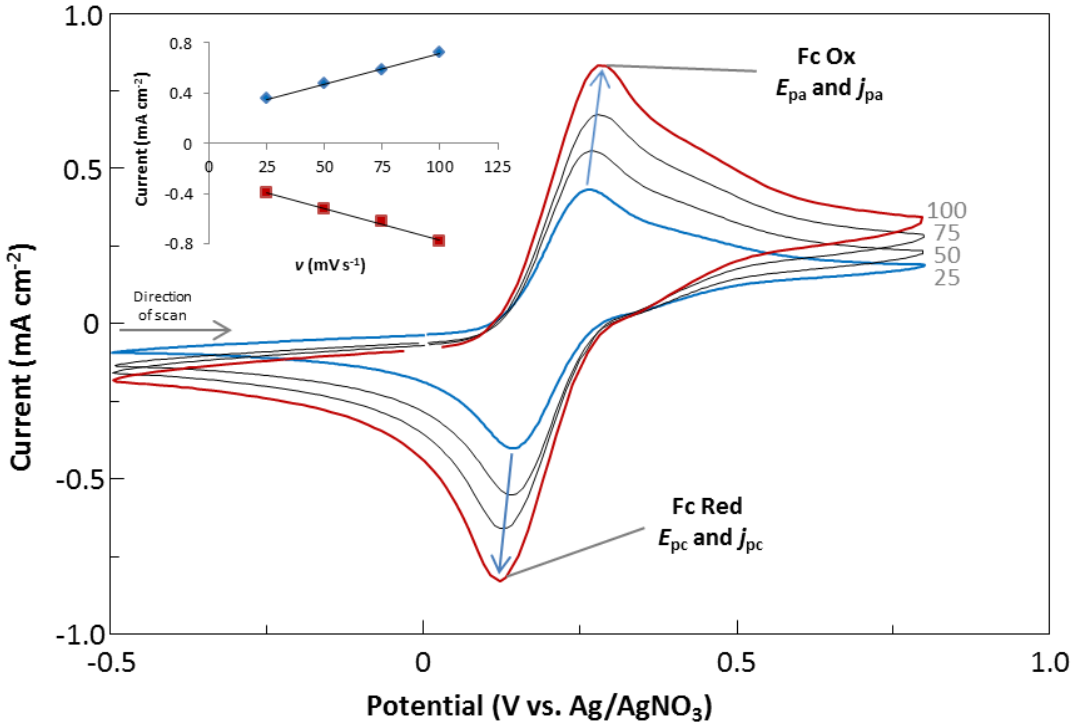

Figure 4.31: CVs of PPyEtN$_3$C$_2$HFc grown in MeCN and doped with TBAPF$_6$ showing the electroactivity of polymer cycled in MeCN and TBAPF$_6$ (100 mM) from 25 (—) to 100 (—) mV s^{-1} in 25 mV s^{-1} increments. Inset: Plot of anodic and cathodic peak current, j_p vs. potential scan rate, v.

EDX spectroscopy was performed on the PPyEtN$_3$C$_2$HFc bulk film (Figure 4.32). It must be stated now that the results obtained were only indications for the presence of elements and their respective atomic%. This was due to the very thin film being analysed when compared to the degree of the beam penetration, the nanowire film not being flat or polished and also the correct standards to deconvolute the Fe signals were not present. As anticipated, the spectrum yielded elemental signals attributed to the presence of iron at 0.705 and 6.404 keV. Phosphorus and fluorine signals were observed at 2.014 keV and 0.677 keV respectively, present due to the hexafluorophosphate anion dopant. Carbon, nitrogen and oxygen signals were also

detected at 0.277, 0.392 and 0.526 keV respectively. The ratio of carbon:nitrogen:iron (C:N:Fe) was calculated to be 18:4:1 in each $PyEtN_3C_2HFc$ unit and the approximate quantitative atomic% detected during analyses revealed a similar mean ratio of 22:3:1. This ratio may not be completely accurate due to residual MeCN in the polymer, although drying *in vacuo* preceded analyses. Also, deviation of this ratio could ensue as TBA^+ cations may be present, since ion pairing of $TBAPF_6$ during cycling of the film could occur, whilst performing CV. The approximate atomic% produced a carbon:nitrogen:oxygen (C:N:O) ratio of 22:3:1. As stated for the aforementioned reasons, this ratio may not be completely accurate, but it can be deduced that a significant degree of overoxidation has occurred during the electrodeposition process and this was valid as a high potential (E_{ox} = 1.250 V vs. $Ag/AgNO_3$) was employed during CPA. The approximate atomic% of fluorine:phosphorus:iron (F:P:Fe) yielded a ratio of 3:1/2:1, which infers that for every two $PyEtN_3C_2HFc$ units present in the polymer backbone, there was the possible presence of one PF_6^- dopant anion, which is greater than that reported for PPy reported in the literature (PPy/dopant 1:3).[76] Since CPA at the high oxidising potential was employed during electropolymerisation of $PyEtN_3C_2HFc$, this would induce one-electron oxidations of both Py and Fc, therefore, possibly attracting an increased number of dopant anions into the polymer, necessary for charge neutralisation.

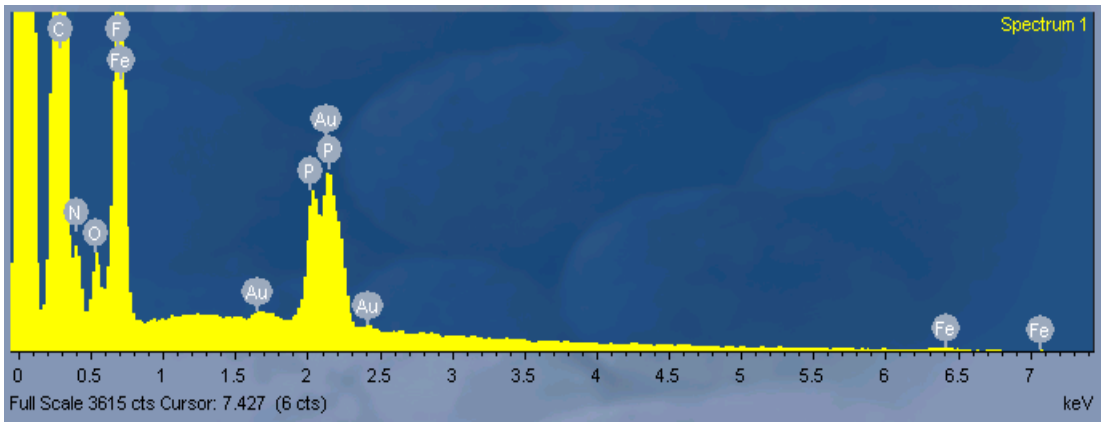

Figure 4.32: EDX spectrum of $PPyEtN_3C_2HFc$ bulk film deposited on the Au substrate, using CPA at 1.250 V vs. $Ag/AgNO_3$ for 5 min in a solution of $PyEtN_3C_2HFc$ (50 mM) with $TBAPF_6$ (100 mM) in MeCN until a q of 1.19 C cm^{-2} was achieved. Intense Au peaks are a consequence of the gold substrate utilised for electrodeposition.

CPA, which was employed during deposition, produced a thick, brown/black film on the electrode surface (Figure 4.33). Light microscopy was utilised to examine the substrate, producing the micrographs in Figure 4.34. It was apparent from these that a thick brown/black film adhered to the surface during application of the E_{ox}.

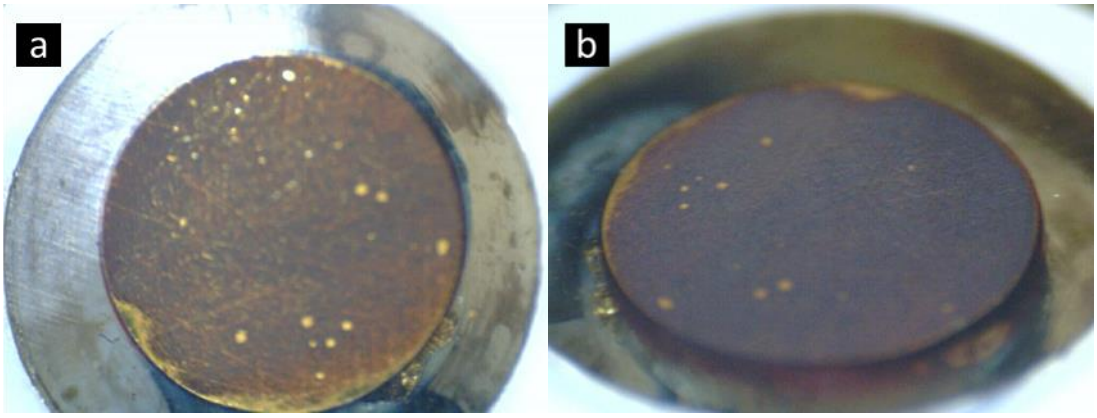

Figure 4.33: Magnified images of (a) plan and (b) oblique angle view for the PPyEtN_3C_2HFc bulk film.

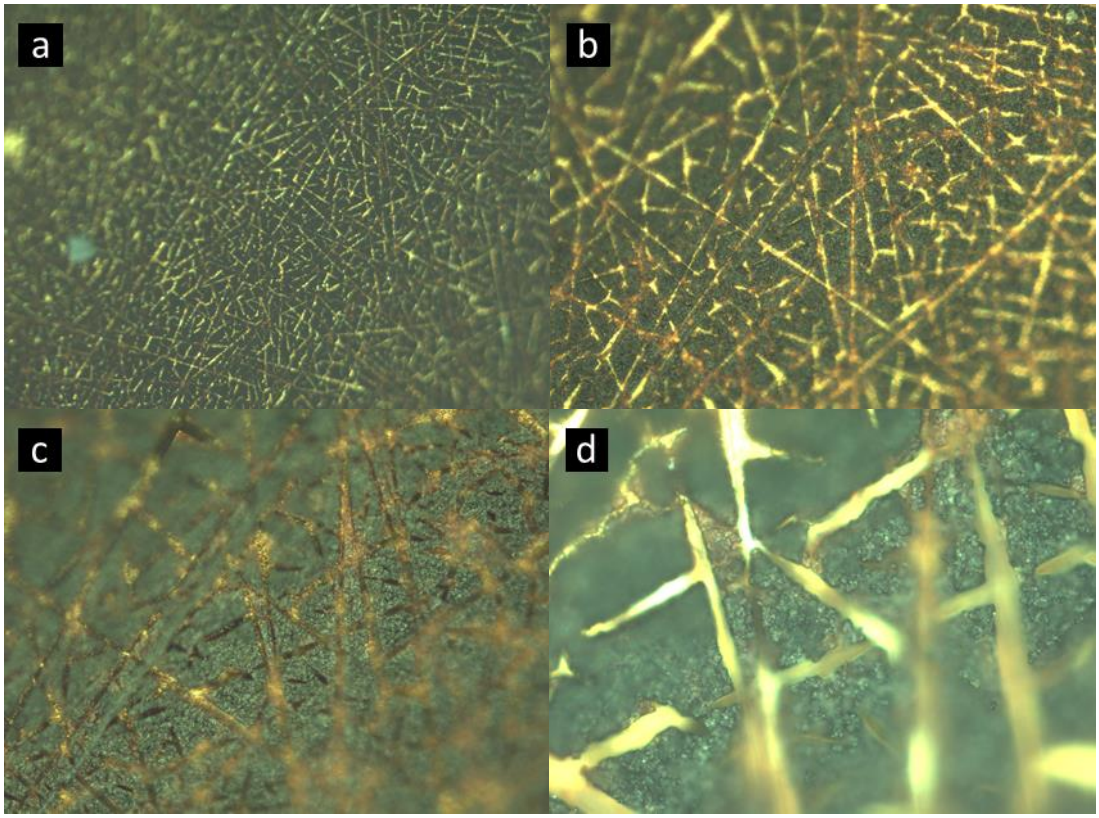

Figure 4.34: Light micrograph (plan-view) of PPyEtN_3C_2HFc bulk film at a magnification of (a) 50, (b) 100, (c) 200 and (d) 500.

The PPyEtN_3C_2HFc film was sputter coated with a thin film of Au/Pd and the morphology of the film was examined using SEM. CPA produced a film possessing good substrate coverage (Figure 4.35 (a) - (b)), possessing cracks throughout (Figure 4.35 (a) - (d)), which were most probably a consequence of the film thickness. Examining inside these cracks, a base layer was observed to adhere to the substrate, accompanied by subsequent multiple layers (Figure 4.35 (d) - (f)). Increasing magnification, it was apparent that PyEtN_3C_2HFc polymerisation yielded a film possessing the familiar PPy 'cauliflower' morphology (Figure 4.35 (e) - (f)).

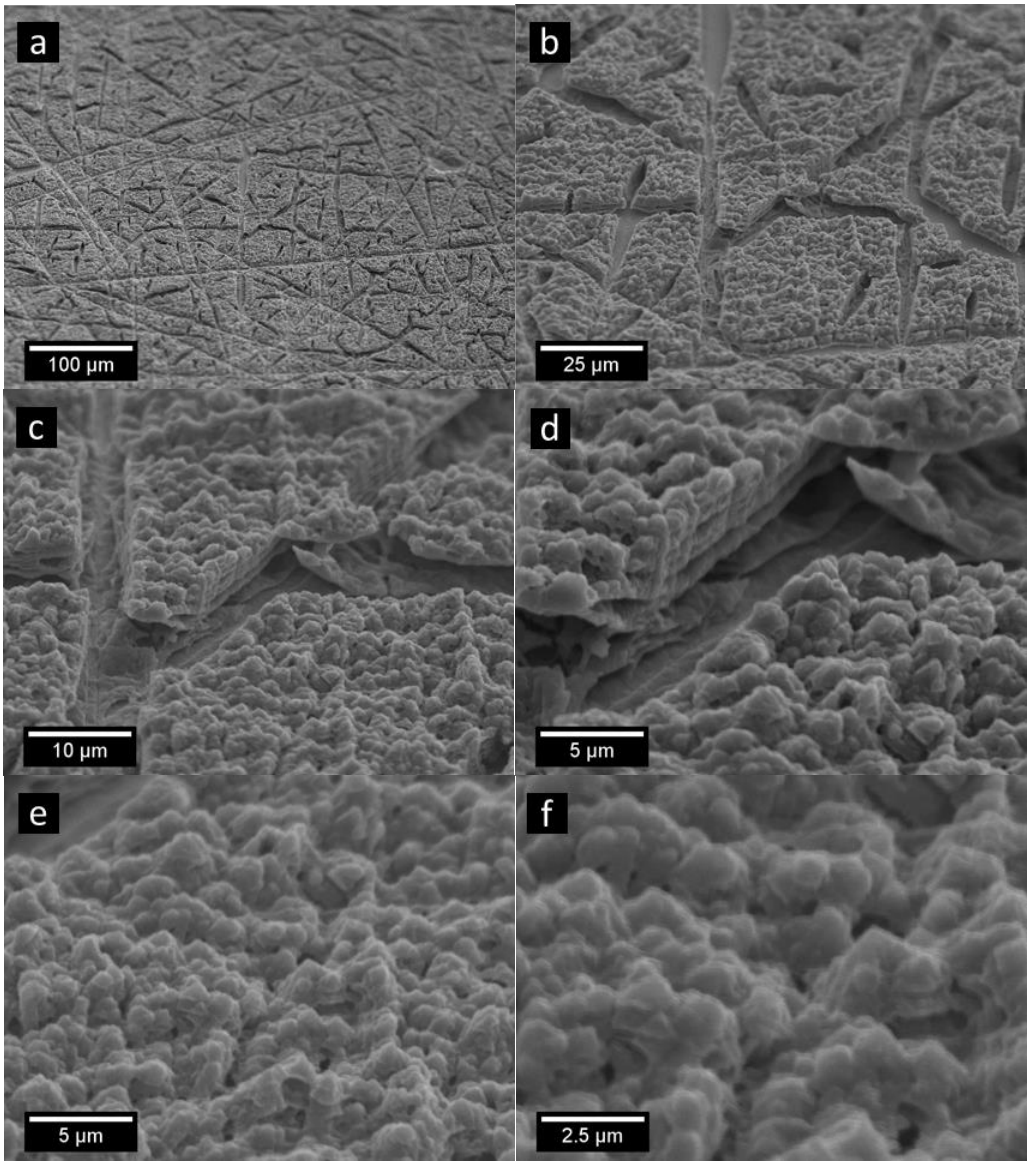

Figure 4.35: SEM micrographs of a PPyEtN_3C_2HFc bulk film electrodeposited on to the Au substrate, using CPA at 1.250 V vs. Ag/$AgNO_3$ for 5 min in a solution of PyEtN_3C_2HFc (50 mM) with $TBAPF_6$ (100 mM) in MeCN, until a *q* of 1.19 C cm^{-2} was achieved.

Once the $PPyEtN_3C_2HFc$ film had been characterised on the Au substrate it was then scrapped off the electrode surface and embedded in a KBr disk for characterisation using FTIR spectroscopy and Raman spectroscopy. The FTIR spectrum for the $PPyEtN_3C_2HFc$ bulk film, which can be observed in Figure 4.36 (c), was compared to that of $PyEtN_3C_2HFc$ monomer (Figure 4.36 (a)) and the $TBAPF_6$ dopant (Figure 4.36 (b)). By analysing the spectrum for the $PPyEtN_3C_2HFc$ bulk film, it is apparent that there is no azide or alkyne stretching vibration at approx. 2100 cm^{-1} as anticipated, but it was clear that it possessed features, which are recognisable within the $PyEtN_3C_2HFc$ monomer and the $TBAPF_6$ dopant. The bands positioned at 3125 and 1104 cm^{-1} were most likely attributed to the Cp–H and C–C stretch of the Fc moiety.[110] Also, the weak band at 489 cm^{-1} could be assigned to the asymmetric ring tilt of the same moiety, while the strong bands at 846 and 559 cm^{-1} are an indication of the presence of the free hexafluorophosphate anion.[111] The out-of-plane CH bend for the Fc moiety[110] can just barely be observed at 820 cm^{-1}, as it is being masked by the PF_6^- band at 846 cm^{-1}.

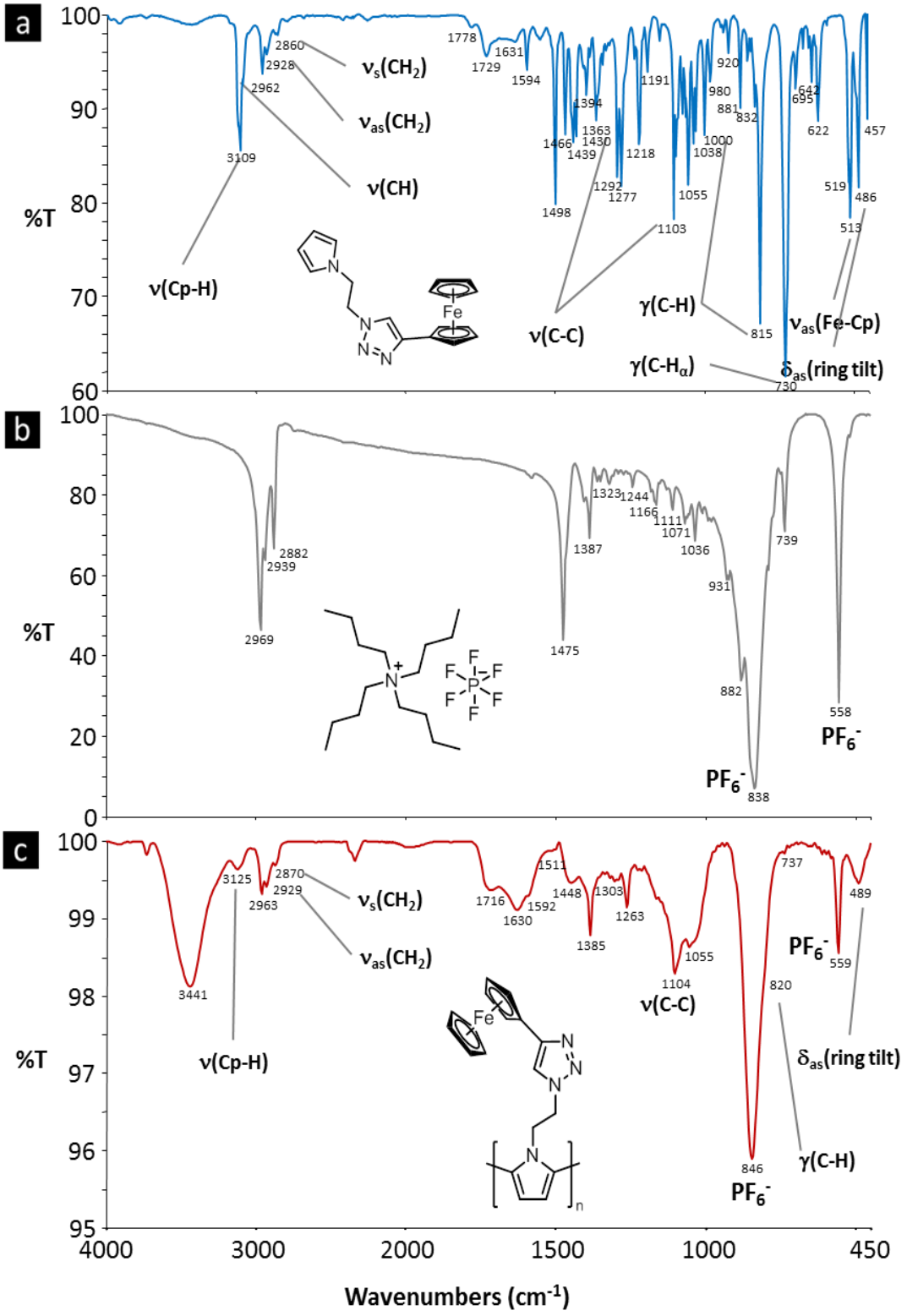

Figure 4.36: FTIR spectra of (a) $PyEtN_3C_2HFc$ (—), (b) $TBAPF_6$ (—) and (c) $PPyEtN_3C_2HFc$ (—) at ±2 cm^{-1} resolution in KBr.

Raman spectroscopy was performed on the PPyEtN_3C_2HFc bulk film grown from the PyEtN_3C_2HFc monomer (Figure 4.37 (—)) and a spectrum of a PPyEtN_3 bulk film was displayed for comparison (Figure 4.37 (—)). The PPyEtN_3C_2HFc nanowire film was grown to a *q* value of 1.19 C cm^{-2}, while the PPyEtN_3 bulk film was grown to a *q* value of 119 mC cm^{-2}, at 0.850 V vs. SCE, in a solution of PyEtN_3 (35 mM) with $LiClO_4$ (100 mM) in EtOH/H_2O (3:4). The films were then scrapped from their respective substrates and embedded within KBr pellets. The C=C stretch vibrations (representative of the charged oxidised quinoid species and neutral reduced benzoid species[72]) for the PPy backbone of the PPyEtN_3C_2HFc bulk film were found to be positioned at 1585 and 1517 cm^{-1}, while that for the PPyEtN_3 bulk film were positioned at 1591 and 1534 cm^{-1}. The position of the band at 1585 cm^{-1} indicates the absence of bipolaron species, while also representing of polaron species within the PPyEtN_3C_2HFc film.[73] The PPyEtN_3 bulk film possessed the C=C stretch vibration band at 1591 cm^{-1}, thus indicating the possibility of bipolaron species present, but as stated previously in Chapter 3 Section 3.3.5, it was likely that there was no bipolaron species present, due to the absence of any band at approx. 940 cm^{-1}; utilised to specifically identify bipolaron species.[72] The absence of a band at this position can be seen for both spectra, while bands from 970 - 990 cm^{-1} can be assigned to a ring deformation mode,[73] representing the presence of polaron species.[72] The nucleophilic attack of species from within the deposition medium encourages polymer overoxidation,[78] yielding Py ring C_β carbonyl groups.[66] This process manifests itself as C=O stretching vibration at 1712 cm^{-1}. The band positioned at 1350 cm^{-1} was assignable to the ring stretching mode,[72] while the band at 991 cm^{-1} indicated triazole ring formation.[112] The band at 1108 cm^{-1} represents the presence of the Fc moiety,[110,113,114] specifically attributed to symmetrical ring breathing.[110,114-116] Therefore, the band at 814 cm^{-1} could be assigned to the symmetric CH bend of the Fc moiety.[110,115,117] The band positioned at 733 cm^{-1} was assigned to C–H deformation.[118] Bands anticipated to be observed for PPyEtN_3C_2HFc forming during CuAAC, attributed to the C–N asymmetric stretch,[119] N–N symmetric stretch[120] and N=N symmetric stretch[121] (1230 to 1370 cm^{-1}) could not be assigned. This was caused by the broad intense band positioned at 1307 cm^{-1}, which inconveniently masked these bands. Evaluation of both spectra undoubtedly indicated that the

polymerisation of the $PyEtN_3C_2HFc$ and $PyEtN_3$ monomers produce similar spectra, as they both possess characteristics making them comparable, due to their common PPy backbone. In contrast, both spectra also both retain individualities, due to the presence of the triazole ring and the Fc moiety. It may also be probable that the $PPyEtN_3C_2HFc$ bulk film retains less oxidised species, due to the position of the C=C stretch vibration and this characteristic relates well to the inefficient deposition of this bulk polymer.

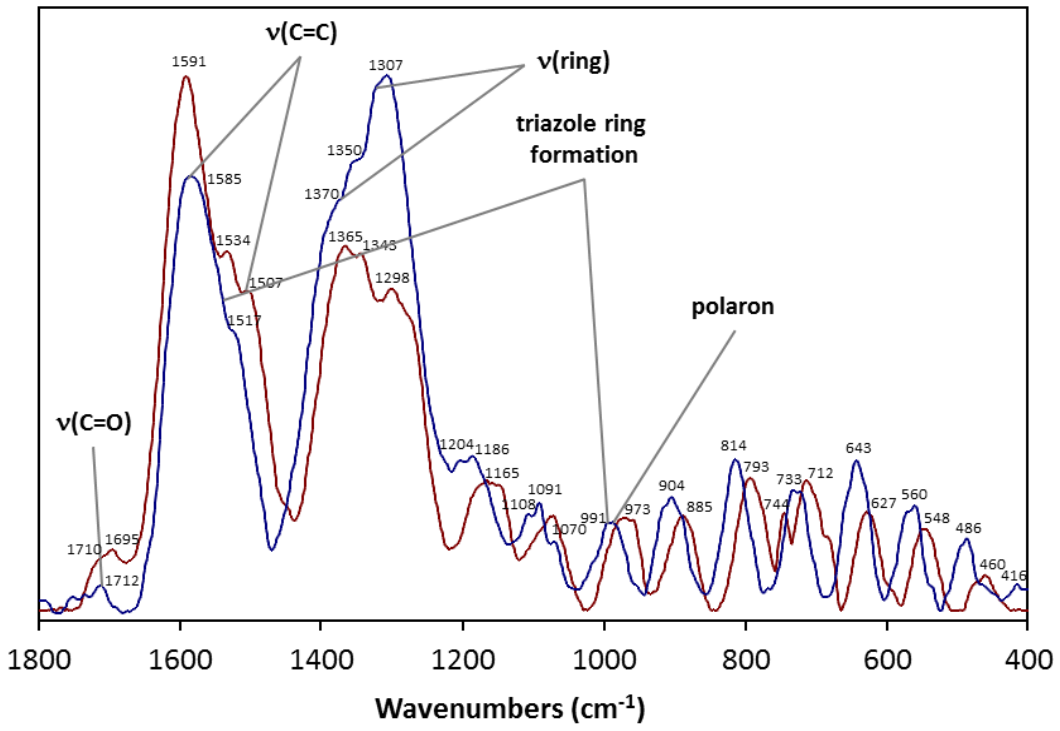

Figure 4.37: Raman spectra of $PPyEtN_3C_2HFc$ bulk film (—) and $PPyEtN_3$ bulk film (—) deposited on the Au substrates. The spectra were recorded utilising a laser line of 660 nm at ±1 cm^{-1} resolution in KBr.

4.2.3.1d CuAAC of $PPyEtN_3$ nanowire films with FcCCH

To begin the post-functionalisation process of a $PPyEtN_3$ nanowire film, a polymer was firstly electrodeposited on to the Au substrate, while employing the parameters depicted in Chapter 3. Specifically in this case, the $PPyEtN_3$ nanowire film was grown *via* electrochemical deposition at 0.840 V vs. SCE, from a mixture of $EtOH/H_2O$ (3:4) containing $PyEtN_3$ (35 mM), $(NH_4)H_2PO_4$ (300 mM) and $LiClO_4$ (20 mM), until a *q* value of 119 mC cm^{-2} was achieved. This film was submerged in

a suspension of FcCCH (5 mM), Cu^0 (5 mM), $[Cu^I(MeCN)_4]PF_6$ (10 mol%) and DIPEA (100 mM) in degassed, anhydrous MeCN and stirred for 30 hours to facilitate the CuAAC (Figure 4.38). The electrode was then removed from the solution and washed with copious amounts of MeCN, MeOH and Et_2O, yielding the post-functionalised nanowire polymer, $PPyEtN_3C_2HFc$, and dried for 12 h *in vacuo*.

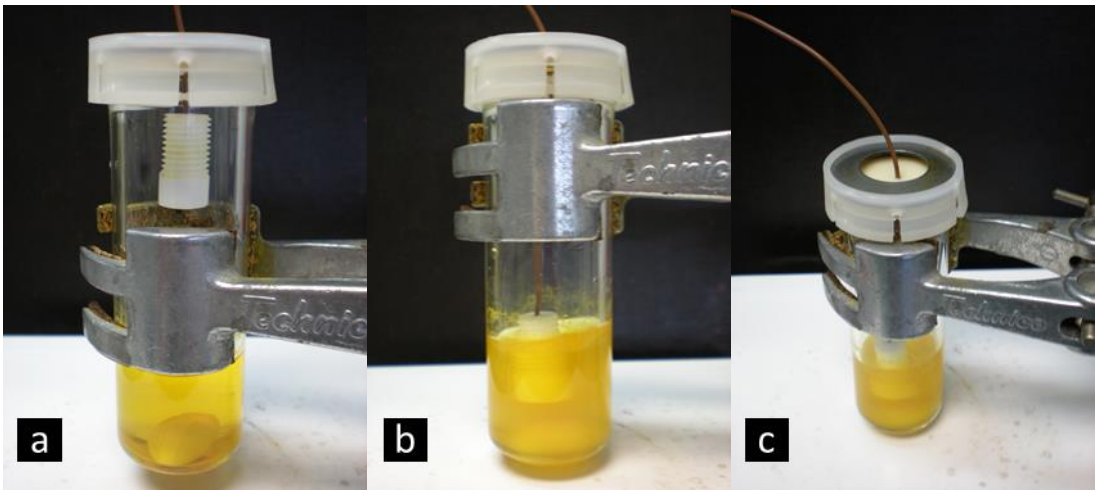

Figure 4.38: Images taken during the synthesis of post-functionalised $PPyEtN_3C_2HFc$ nanowire film performed on the substrate, employing a Pyrex microwave vessel combined with Teflon liner.

To appropriately examine the post-functionalised film, EDX spectroscopy (Figure 4.39) was employed and examination of the resulting data revealed elemental signals for iron positioned at 0.705 and 6.404 keV in the spectrum, due to the attachment of FcCCH *via* CuAAC. The chlorine signal observed at 2.622 keV represented the presence of the ClO_4^- anion, functioning as dopant within the film. A phosphorus signal was also present at 2.014 keV, due to the $H_2PO_4^-$ anion dopant. The presence of this signal could have been attributed to the hexafluorophosphate salt, which was employed as electrolyte during CV, but this was improbable due to the absence of fluorine in the spectrum at 0.677 keV. The presence of a copper signal at 0.930 keV in the spectrum was caused by utilisation of copper(0) and tetrakisacetonitrilecopper(I) hexafluorophosphate during CuAAC. Although thorough washing of the electrode was performed, the retention of copper was anticipated, as it has been reported in the literature that the PPy backbones conjugated π-system and nitrogen lone pair have an affinity for copper species.[122] Signals for carbon, nitrogen and oxygen were located at 0.277, 0.392 and 0.526 keV

respectively and the calculated ratio of C:N:Fe in each $PyEtN_3C_2HFc$ unit was determined to be 18:4:1 at 100% conversion. Upon analyses of the film, the approximate quantitative atomic% yielded a mean ratio of 20:4:2/3, or a conversion of approx. 68%. Once again, due to residual MeCN and the ion pairing of $TBAPF_6$ or TBAP during cycling of the film, this ratio may not be completely accurate and was only an approximation of the conversion occurring during CuAAC. The C:N:O ratio attained from the approximate atomic% was found to be 20:4:2. The substantial amount of oxygen detected was not surprising, as not only were both EtOH and H_2O utilised as the co-solvent system, but the employed supporting electrolytes, $LiClO_4$ and $(NH_4)H_2PO_4$, were oxygen-containing species. It was therefore impossible to determine if any overoxidation had occurred within the polymer using the EDX spectral data. The approximate atomic% of $PyEtN_3C_2HFc$ and supporting electrolytes in the polymer, yielded a ratio for carbon:nitrogen:phosphorus:chlorine (C:N:P:Cl) of 20:4:1/7:1/36. This ratio infers that for every seven $PyEtN_3C_2HFc$ units present in the polymer backbone there was one ClO_4^- dopant anion present and for every thirty-six $PyEtN_3C_2HFc$ units there was one $H_2PO_4^-$ dopant anion. This agrees well with the theory that, in this system, $LiClO_4$ acts as the primary dopant species, although it was employed at the lower concentration (20 mM), while $(NH_4)H_2PO_4$ (300 mM) acts as a buffer at the substrate during electrodeposition.

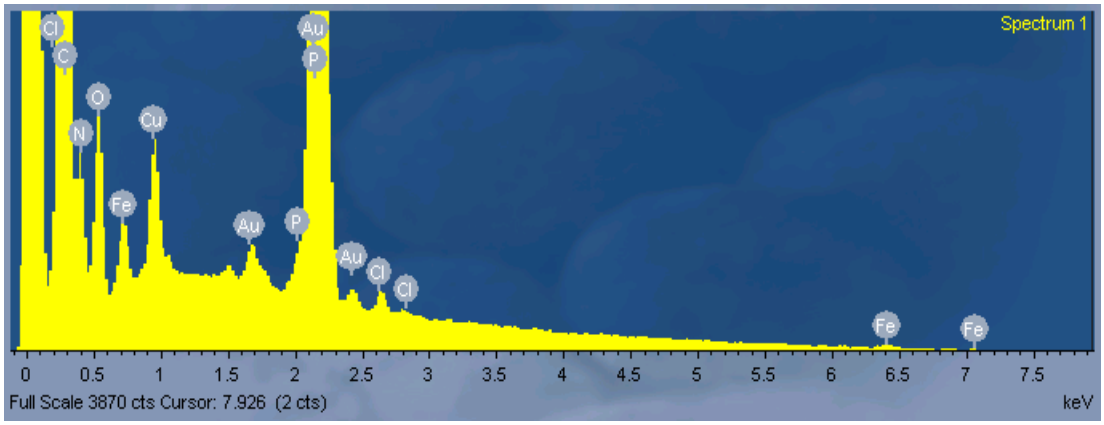

Figure 4.39: EDX spectrum of post-functionalised $PPyEtN_3C_2HFc$ nanowire film, deposited on the Au substrate at 0.840 V vs. SCE until *q* of 119 mC cm^{-2} was achieved in $EtOH/H_2O$ (3:4) with $(NH_4)H_2PO_4$ (300 mM) and $LiClO_4$ (20 mM). The $PPyEtN_3$ nanowire film then underwent CuAAC with FcCCH to produce the post-functionalised $PPyEtN_3C_2HFc$ nanowire film. Intense Au peaks are a consequence of the gold substrate utilised for electrodeposition.

The film was also characterised using CV, by employing a solution of degassed, anhydrous MeCN containing $TBAPF_6$ (100 mM), to investigate the electroactivity of the film (Figure 4.40 (—)).The post-functionalised film was compared to a CV of the same film, before its submersion in the CuAAC suspension, namely the $PPyEtN_3$ nanowire film (Figure 4.40 (—)). It was apparent that the PPy redox activity had decreased within the post-functionalised $PPyEtN_3C_2HFc$ nanowire film, which has been reported to indicate the presence of the covalently bound Fc moiety, as its large steric effects obstruct PPy redox processes due to non-planarity of the polymer backbone (Figure 4.23).[109] CV also revealed a redox couple for Fc ($E_{1/2}$ = 0.229 V vs. $Ag/AgNO_3$, ΔE_p = 36 mV, j_a/j_c = 0.56), attributed to the covalent attachment of FcCCH with the polymer. The $E_{1/2}$ for the Fc redox couple of the post-functionalised $PPyEtN_3C_2HFc$ nanowire correlated well with that attained for the $PPyEtN_3C_2HFc$ bulk film (0.202 V vs. $Ag/AgNO_3$, ΔE_p = 123 mV, j_a/j_c = 0.91) grown from the $PyEtN_3C_2HFc$ monomer (Figure 4.40 (inset) (—)), thus suggesting that covalent attachment of FcCCH had proceeded.

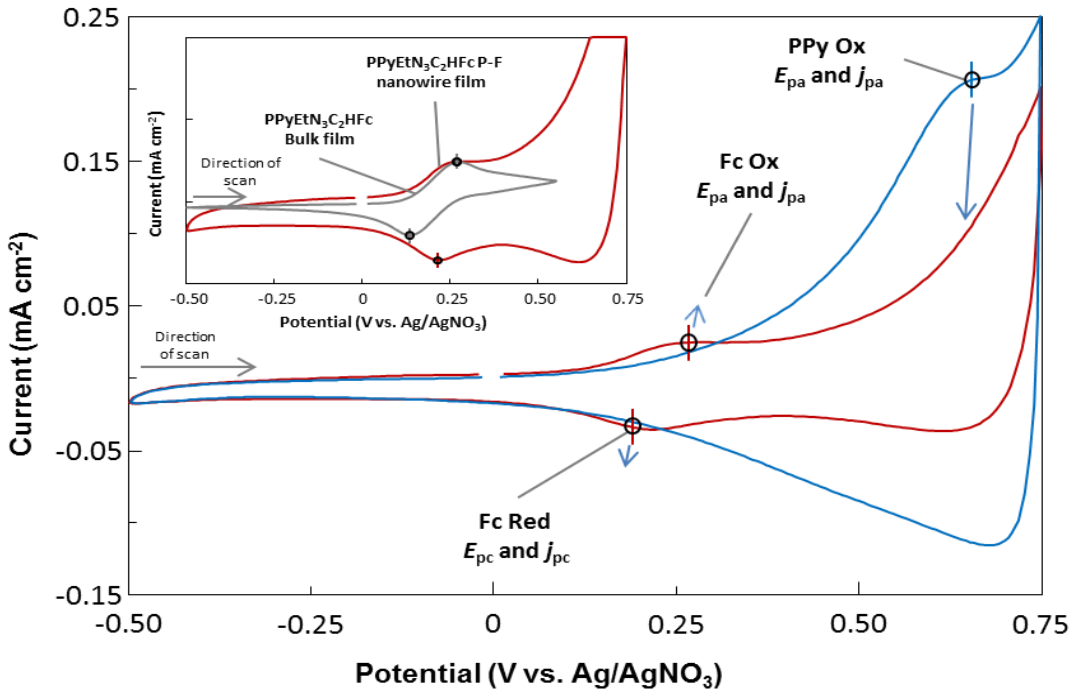

Figure 4.40: CVs of the post-functionalised $PPyEtN_3C_2HFc$ (—) and $PPyEtN_3$ (—) nanowire films in MeCN with $TBAPF_6$ (100 mM) at 50 mV s^{-1}. Inset: CVs of the post-functionalised $PPyEtN_3C_2HFc$ nanowire film (—) and $PPyEtN_3C_2HFc$ bulk film (—) in MeCN with $TBAPF_6$ (100 mM) at 50 mV s^{-1}.

Confirmation that the Fc moiety was actually bound to the polymer backbone was required, so a control experiment was performed whereby a $PPyEtN_3$ nanowire film was submerged in a solution of MeCN containing only FcCCH (5 mM) and this was stirred for 30 h. After washing the film with copious amounts of H_2O, MeCN and DCM, it was dried *in vacuo* and CV was performed on the $PPyEtN_3$/FcCCH control nanowire film (Figure 4.41 (—)). This was compared to the post-functionalised $PPyEtN_3C_2HFc$ nanowire film comprised of covalently bound Fc (Figure 4.41 (—)). Examining the CVs in Figure 4.41, it was clear that FcCCH did not covalently bind to the $PPyEtN_3$ nanowire polymer during the control experiment. This was evident as although the presence of a Fc redox couple was observed (Figure 4.41 (—)), it was attributed to FcCCH physisorbed on the surface of the film, *albeit* thorough washing was performed. Cycling of the $PPyEtN_3$/FcCCH control nanowire film at 50 mV s^{-1} in MeCN containing $TBAPF_6$ (100 mM) yielded a redox couple ($E_{1/2}$ = 0.349 V vs. $Ag/AgNO_3$, ΔE_p = 27 mV, j_a/j_c = 0.82), which was positioned in the area of FcCCH redox activity and this was proved true by determining the electroactivity of the FcCCH reactant (Figure 4.41 (inset) (—)) in the same electrolyte system at 50 mV s^{-1} ($E_{1/2}$ = 0.343 V vs. $Ag/AgNO_3$, ΔE_p = 114 mV, j_a/j_c = 1.27). The $PPyEtN_3$/FcCCH control nanowire film was also examined using EDX spectroscopy (Figure 4.42), which detected elemental signals for iron, positioned at 0.705 and 6.404 keV in the spectrum, due to physisorbed FcCCH. A chlorine signal was present at 2.622 keV due to the ClO_4^- dopant anion. Some phosphorus, due to the $H_2PO_4^-$ anion dopant, was also present at 2.014 keV. The presence of this signal could also be attributed to the hexafluorophosphate anion, employed as supporting electrolyte during CV, since the presence of fluorine can be seen at 0.677 keV in the spectrum. Carbon, nitrogen and oxygen peaks were positioned at 0.277, 0.392 and 0.526 keV respectively. Stated previously, the calculated ratio of C:N:Fe in each $PyEtN_3C_2HFc$ unit was determined to be 18:4:1 at 100% conversion. Upon analyses of the $PPyEtN_3$/FcCCH control nanowire film, the approximate quantitative atomic% yielded a mean ratio of 14:4:1/20. Therefore, this suggests that for every twenty $PPyEtN_3$ units present in the polymer backbone, there was one physisorbed FcCCH molecule on the film. Taking into consideration that the ion pairing of $TBAPF_6$ or TBAP during cycling of the film

and residual MeCN may be present, the ratio may not be entirely accurate but can be taken as an approximation.

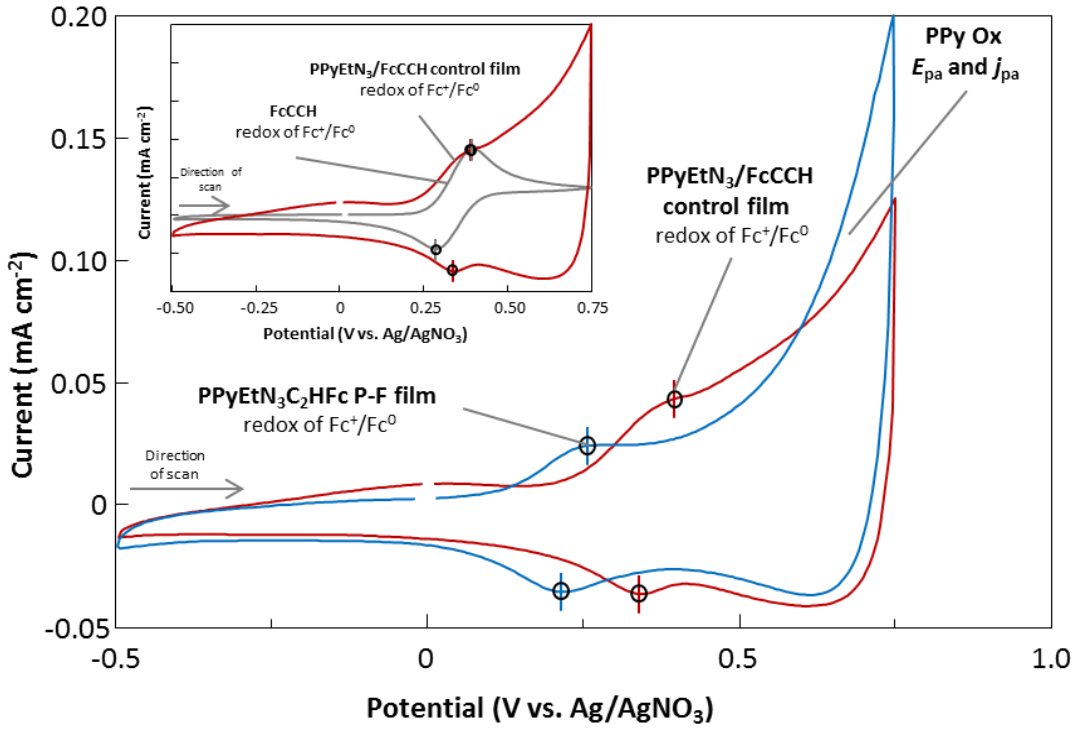

Figure 4.41: CVs of the control PPyEtN$_3$/FcCCH (—) and post-functionalised PPyEtN$_3$C$_2$HFc (—) nanowire films in MeCN with TBAPF$_6$ (100 mM) at 50 mV s^{-1}. Inset: CVs of control PPyEtN$_3$/FcCCH nanowire film (—) and FcCCH (—) in MeCN with TBAPF$_6$ (100 mM) at 50 mV s^{-1}.

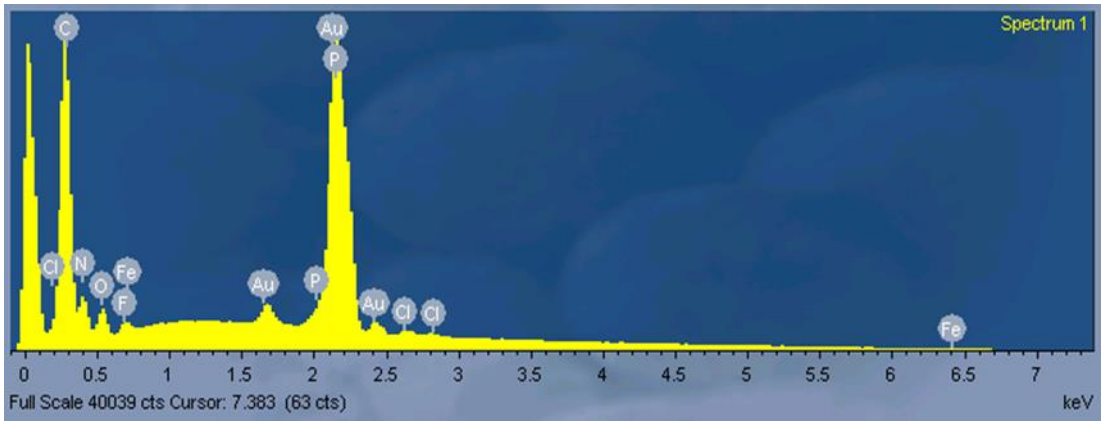

Figure 4.42: EDX spectrum of PPyEtN$_3$/FcCCH control nanowire film deposited on the Au substrate at 0.840 V vs. SCE, until q of 119 mC cm^{-2} was achieved in EtOH/H$_2$O (3:4) with (NH$_4$)H$_2$PO$_4$ (300 mM) and LiClO$_4$ (20 mM). The PPyEtN$_3$ nanowire film was submerged in a solution of FcCCH (5 mM) in MeCN for 30 h. Intense Au peaks are a consequence of the gold substrate utilised for electrodeposition.

The electroactivity of the post-functionalised PPyEtN$_3$C$_2$HFc nanowire film was investigated in degassed, anhydrous MeCN containing TBAPF$_6$ (100 mM) by performing cycles between -0.500 - 0.750 V vs. Ag/AgNO$_3$ at non-consecutive scan rates of 50, 75, 100 and 125 mV s^{-1} (Figure 4.43). The plot representing j_p vs. v (Figure 4.43 (inset)) illustrates how the magnitude of j_p increases linearly against v and this has been ascribed to thin layer electrochemistry with a surface confined process in the literature.[99,107,108] The diminished redox activity of PPy was attributed to the covalently bound Fc moiety, which induces large steric effects causing an increase of non-planarity in the PPy backbone (Figure 4.23). This in turn reduces polymer conjugation, thus hindering PPy redox.[109]

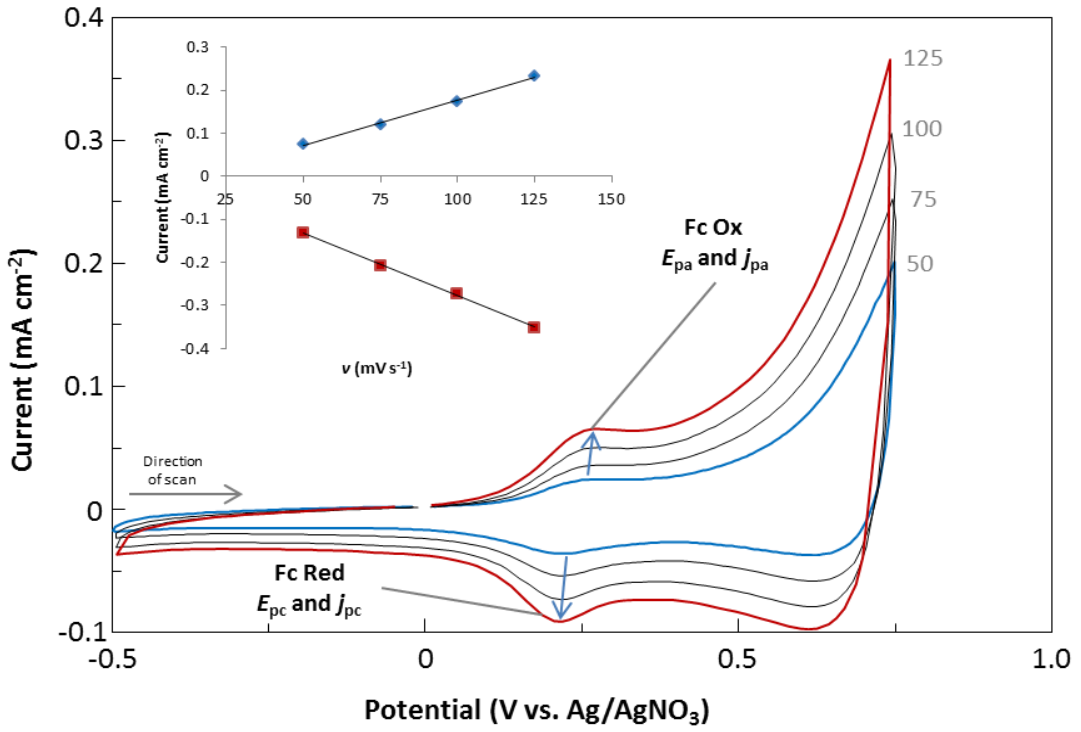

Figure 4.43: CVs of post-functionalised PPyEtN$_3$C$_2$HFc nanowire film in MeCN and TBAPF$_6$ (100 mM) from 50 (—) to 125 (—) mV s^{-1} in 25 mV s^{-1} increments. Inset: Plot of anodic and cathodic peak current, j_p vs. potential scan rate, v.

The electrode surface was examined using a light microscope and it was found that the film after post-functionalisation was an orange/brown colour. Observing the micrographs in Figure 4.44, good surface coverage and homogeneity was determined to be present across the substrate. The post-functionalised PPyEtN$_3$C$_2$HFc nanowire

film was sputter coated with a thin film of Au/Pd. Analysis of the SEM micrographs for the post-functionalised PPyEtN_3C_2HFc nanowire film (Figure 4.45), depicted a polymer film with nanowires remaining adhered to the base layer after post-functionalisation. The film possessed a homogeneous distribution of nanowires similar to films before functionalisation, but it was apparent that the nanowires were more contorted and appeared less oriented. This was probably a consequence of the chemical conditions and reaction time to which the nanowire film has been exposed.

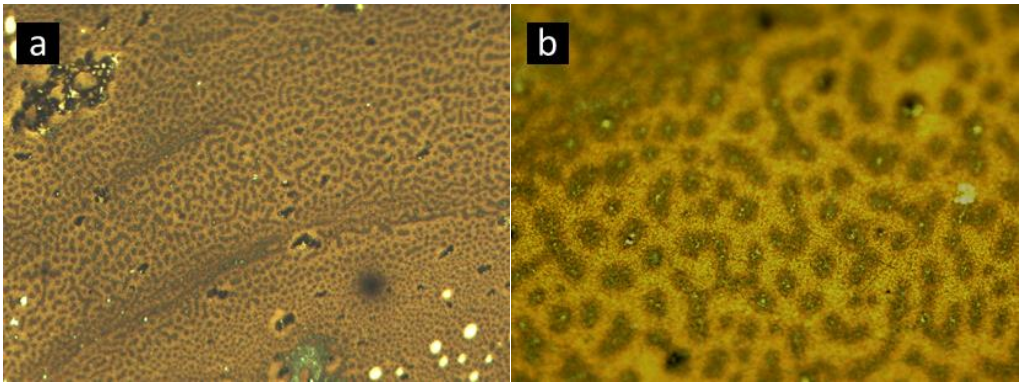

Figure 4.44: Light micrograph (plan-view) of post-functionalised PPyEtN_3C_2HFc nanowire film at a magnification of (a) 100 and (b) 500.

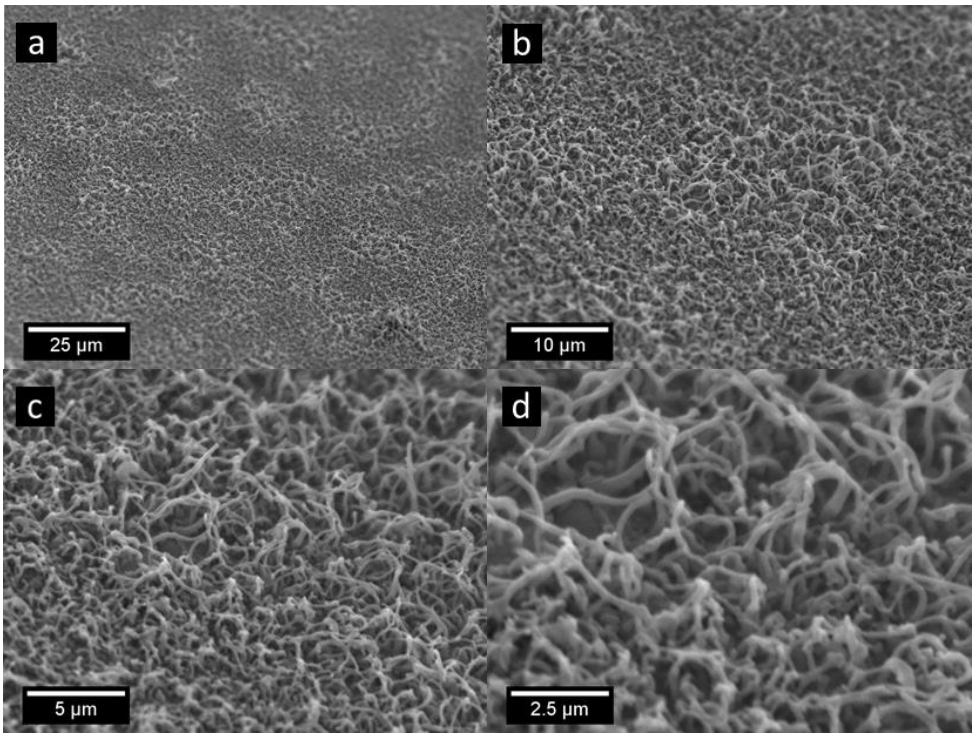

Figure 4.45: SEM micrograph of a networked post-functionalised PPyEtN_3C_2HFc nanowire film.

FTIR spectroscopy was used to determine that the azide functional group, which was bound to the PPy backbone, had converted to the triazole functional group upon submersion in the CuAAC reaction medium. Once all non-destructive characterisation techniques were performed, the post-functionalised $PPyEtN_3C_2HFc$ nanowire film was scrapped from the Au substrate and embedded in a KBr pellet. The resulting FTIR spectrum can be observed in Figure 4.46 (c). Accompanying the spectrum of the post-functionalised film are spectra of the FcCCH reactant (Figure 4.46 (b)) and a $PPyEtN_3$ nanowire film (Figure 4.46 (a)) grown to a *q* value of 119 mC cm^{-2}. It was apparent from Figure 4.46 (a) that the azide functional group band at 2101 cm^{-1} has depreciated significantly in intensity. This intensity transformation was a consequence of the CuAAC reaction with FcCCH proceeding successfully and forming triazole moieties within the polymer. Examining the spectrum of FcCCH (Figure 4.46 (b)) and the post-functionalised $PPyEtN_3C_2HFc$ nanowire film (Figure 4.46 (c)), it was clear that it was not possible to confirm complete azide conversion, due to the position of the band at 2104 cm^{-1}, which was assigned to the C≡C stretch vibration.[123] In this case, the ν(C≡C) band masked the absence or presence of the $\nu(N_3)$ band, due to the possible physisorption of FcCCH on the post-functionalised $PPyEtN_3C_2HFc$ nanowire film. The bands at approx. 1121 - 1087 cm^{-1} could be attributed to the presence of the perchlorate anion.[69,124]

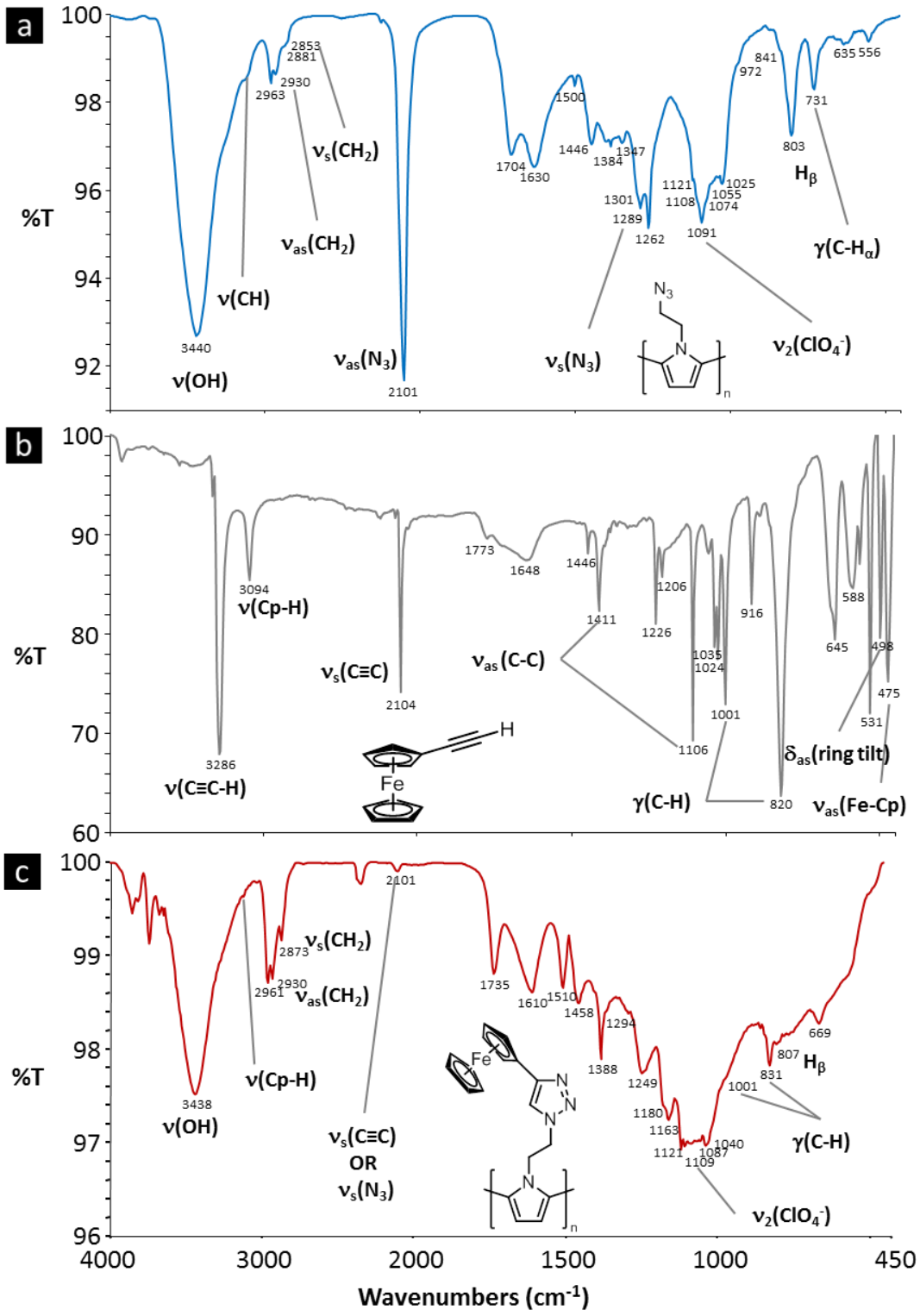

Figure 4.46: FTIR spectra of (a) $PPyEtN_3$ nanowire film (—), (b) FcCCH (—) and (c) post-functionalised $PPyEtN_3C_2HFc$ nanowire film (—) at ±2 cm^{-1} resolution in KBr.

Raman spectroscopy was performed on the post-functionalised $PPyEtN_3C_2HFc$ nanowire film (Figure 4.47 (—)). Displayed for comparison is a spectrum of a $PPyEtN_3C_2HFc$ bulk film (Figure 4.47 (—)), grown at 1.250 V vs. $Ag/AgNO_3$ from $PyEtN_3C_2HFc$ (50 mM) with $TBAPF_6$ (100 mM) in MeCN, until a *q* value of 1.19 C cm^{-2} was achieved. Once grown on their respective Au substrates, both film were scrapped off and embedded within KBr pellets. It was observed that both polymers films displayed bands at analogous wavenumbers in the spectra. The Raman spectra of $(NH_4)H_2PO_4$ and $LiClO_4$ were recorded to ensure that bands contributed from the electrolytic salts, were not falsely attributed to the polymer films. Also, the Raman spectra of EtOH and H_2O were appropriated from the literature to guarantee accurate characterisation of the polymer films. The bands at 1596 cm^{-1} and 1517 cm^{-1} were assigned to the C=C stretch vibration for the PPy backbone[72] and the band at 1364 cm^{-1} was assignable to the ring stretching mode.[72] The absence of any band at approx. 940 cm^{-1} in both spectra, provides evidence that there were no bipolaron species retained within either film,[72] while the band at 986 cm^{-1} was assigned to a ring deformation mode (polaron species).[72,73] Overoxidation of the Py ring C_β position can be seen as the band at 1712 cm^{-1} in the spectra.[66,78] The $PPyEtN_3C_2HFc$ nanowire film suggested triazole ring formation due to the bands positioned at 1537 and 996 cm^{-1}.[112] Also, the Fc ring breathing band could be present at approx. 1100 cm^{-1}, [110,113-116] accompanied by a band positioned at 806 cm^{-1} for the Fc CH bend.[102,106,108] It was clear from comparison of both spectra that polymerisation of the $PyEtN_3C_2HFc$ monomer and post-functionalisation of the $PPyEtN_3$ nanowire film with FcCCH produce very similar Raman spectral data. Also, when both spectra are compared to that of their starting materials (Figure 4.24), it is noted that significant changes occur upon exposure to the CuAAC medium. These results are a good indication that the post-functionalisation process is a viable method to produce a conducting nanowire film modified with the electron mediator, FcCCH.

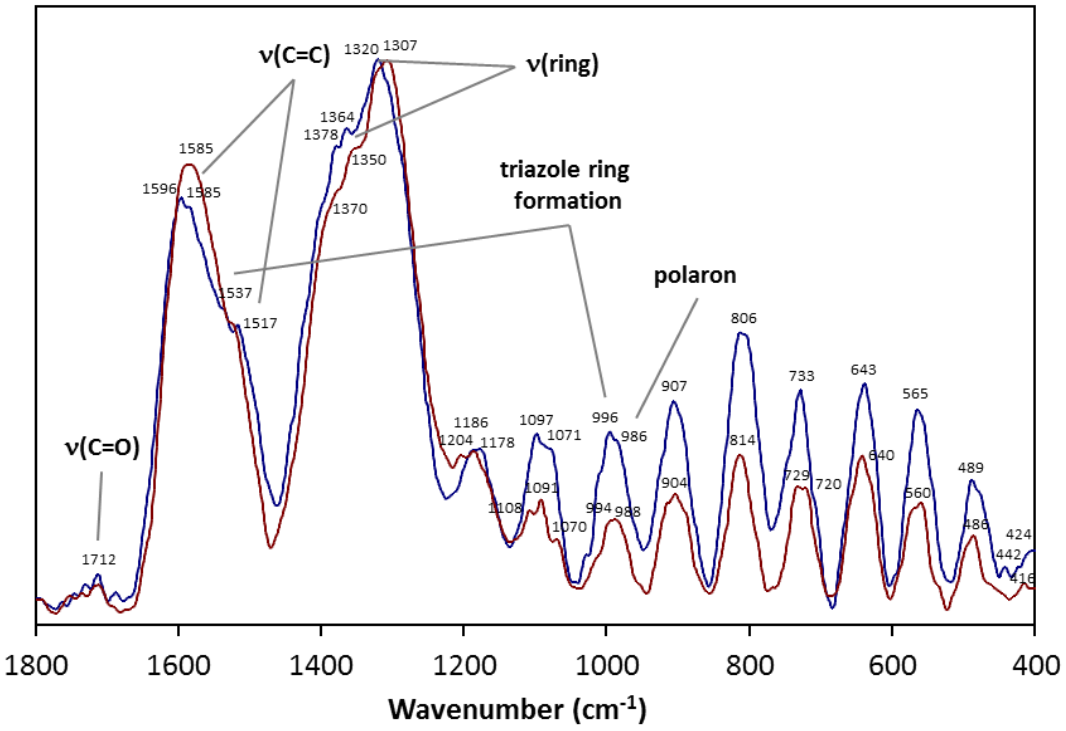

Figure 4.47: Raman spectra of $PPyEtN_3C_2HFc$ nanowire film (—) and $PPyEtN_3C_2HFc$ bulk film grown from $PyEtN_3C_2HFc$ monomer (—). The spectra were recorded utilising a laser line of 660 nm at ±1 cm^{-1} resolution in KBr.

4.3 Conclusion

This chapter begins with the investigation of the deposition mechanism for $PPyEtN_3$ nanowire films. The examination of the films morphology progression revealed that a thin bulk film was deposited, succeeded by $PPyEtN_3$ nodules, which developed into nanowires approx. 1.5 µm in length and >200 nm in diameter. Using NGM modelling, it was revealed that the very early stage of $PyEtN_3$ deposition proceeded *via* an IN3D process, which in this system was necessary for the homogeneous deposition of $PPyEtN_3$ nanowires, along with a specific E_{app} window of 0.820 - 0.860 V vs. SCE.

The role of the 'seed' electrolyte, $LiClO_4$, was investigated by varying the cation and anion sequentially during the deposition of $PPyEtN_3$ films. It was found that exchanging the lithium cation for other Group 1 metals yielded films of diminished nanowire homogeneity. The substitution of the perchlorate anion with other anions, possessing diverse solubilities in polar/nonpolar solvents, yielded films of various morphologies, which grew *via* a range of NGM processes. The role of the 'bulk' electrolyte, $(NH_4)H_2PO_4$, was investigated by performing CPA in the absence of both the 'seed' and 'bulk' electrolyte sequentially during $PPyEtN_3$ deposition. The absence of $(NH_4)H_2PO_4$ produced a $PPyEtN_3$ bulk film, while the absence of $LiClO_4$ in the medium did not support any $PPyEtN_3$ deposition. The results from these electrolyte investigations confirm the upmost importance of the 'seed' electrolytes properties, for the attainment of nanowire deposition and its function in polymer nucleation, while inferring that the 'bulk' electrolyte acts as a buffer, increasing pH at the electrode surface and in turn reducing the rate of polymer propagation.

In-depth characterisation of the $PPyEtN_3$ nanowire films determined that internal cavities were absent inside of the wires, which possessed a rough surface morphology of amorphous material. Bulk films, compared to nanowire films, showed a greater electrochemical response, but this could be attributed to the high perchlorate concentration used during bulk deposition, although the nanowire film did display E_{pa} and E_{pc} at greater potentials, inferring a resistive nature. FTIR spectroscopy of the nanowire film indicated the presence of overoxidation at the Py C_β and that polymerisation occurred *via* α-α branching. Chlorine and phosphorus

were detected in the film using EDX spectroscopy, confirming perchlorate anion as dopant counterion and the incorporation of some dihydrogen phosphate anion. Raman spectroscopy distinguished very little differences between bulk and nanowire films, while suggesting the absence of bipolaron (940 cm^{-1}) and presence of polaron (979 cm^{-1}) species; a consequence of polymer overoxidation.

Synthesis of the novel $PyDeN_3C_2HFc$ and $PyEtN_3C_2HFc$ monomers then commenced from $PyEtN_3$ and FcCCH in anhydrous MeCN, in the presence of Cu^0 powder and $[Cu^I(MeCN)_4]PF_6$, while DIPEA or 2,6-lutidine were required for $PyEtN_3C_2HFc$ synthesis. These reactions producing yellow/orange compounds, which when characterised displayed the absence of $\nu(N_3)$ and $\nu(C{\equiv}C)$ bands in the FTIR spectrum. The ^1H NMR spectrum of $PyDeN_3C_2HFc$ possessed a signal at 7.45 ppm, while that for $PyEtN_3C_2HFc$ displayed a peak at 6.74 ppm, both attributed to the C=CH hydrogen of the triazole moiety. This was confirmed using 2D ^1H-^1H COSY and 2D ^1H-^{13}C HSQC spectroscopy. CV of the $PyEtN_3C_2HFc$ monomer displayed a reversible Fc redox couple, until E_λ >0.600 V vs. $Ag/AgNO_3$ was applied, which produced the irreversible oxidation of the Py moiety, positioned at 1.316 V vs. $Ag/AgNO_3$, but this did not induce electrodeposition.

CPA of the $PyEtN_3C_2HFc$ monomer at an E_{ox} = 1.250 V vs. $Ag/AgNO_3$ for 5 minutes produced a thick, brown/black film, containing iron, phosphorus and fluorine, which were detected using EDX spectroscopy. The atomic% of F:P:Fe indicated one PF_6^- dopant anion for every two $PyEtN_3C_2HFc$ units present in the polymer. Using SEM, the bulk film was observed to deposit as multiple layers; in the 'cauliflower' type morphology. FTIR spectroscopy revealed that the film had characteristics, which were present in both the spectrum of the $PyEtN_3C_2HFc$ monomer and the $TBAPF_6$ dopant. As for the $PPyEtN_3$ films, Raman spectroscopy confirmed only the presence of polaron (970 - 990 cm^{-1}) species in the polymer, most likely due to overoxidation during electrodeposition.

The post-functionalisation of the $PPyEtN_3$ nanowire film was then performed, using a suspension of FcCCH, Cu^0, $[Cu^I(MeCN)_4]PF_6$ and DIPEA in MeCN. CV of the polymer after CuAAC displayed very little PPy redox activity but instead revealed a Fc redox couple, which was consistent with that of the $PPyEtN_3C_2HFc$ bulk film

grown from the $PyEtN_3C_2HFc$ monomer. This was further confirmed by examining the electroactivity of polymer-physisorbed-FcCCH and FcCCH in solution, both possessing $E_{1/2}$ at a much higher oxidative potentials. The polymer contained iron, chlorine and phosphorus and the atomic% of C:N:Fe indicated a conversion of approx. 68% for the CuAAC, while the atomic% for C:N:P:Cl indicated that there was one ClO_4^- dopant anion present for every seven $PyEtN_3C_2HFc$ units and one $H_2PO_4^-$ dopant anion for every thirty-six $PyEtN_3C_2HFc$ units. Interestingly, this data corroborated our proposal that during nanowire deposition, $LiClO_4$ acts as the 'seed', while $(NH_4)H_2PO_4$, acts as a buffer.

After CuAAC, it was found that the post-functionalised $PPyEtN_3C_2HFc$ nanowire film retained its homogeneous nanowire distribution and as anticipated the $\nu(N_3)$ band intensity had depreciated considerably in the FTIR spectrum. Employing Raman spectroscopy, the post-functionalised $PPyEtN_3C_2HFc$ nanowire film was then compared to the $PPyEtN_3C_2HFc$ bulk film previously electrodeposited from the novel $PyEtN_3C_2HFc$ monomer. The spectra were observed to be quite indistinguishable, possessing similar characteristics, such as the absence of bipolaron species; instead displaying bands representative of the presence of polaron species. Evidence present for the formation of a triazole ring could be found at 1537 and 996 cm^{-1}, while bands representing the covalently attached Fc were positioned at 1100 and 806 cm^{-1} in the spectrum.

4.4 References

1. Zang, J. F.; Li, C. M.; Bao, S. J.; Cui, X. Q.; Bao, Q. L.; Sun, C. Q. *Macromolecules* **2008**, *41*, 7053-7057.
2. Al-Mashat, L.; Debiemme-Chouvy, C.; Borensztajn, S.; Wlodarski, W. *J. Phys. Chem. C* **2012**, *116*, 13388-13394.
3. Liu, J.; Lin, Y.; Liang, L.; Voigt, J. A.; Huber, D. L.; Tian, Z. R.; Coker, E.; McKenzie, B.; McDermott, M. J. *Chemistry* **2003**, *9*, 604-611.
4. Rana, S.; Cho, J. W. *Nanotechnology* **2011**, *22*, 1-7.
5. Luo, S. C.; Sekine, J.; Zhu, B.; Zhao, H.; Nakao, A.; Yu, H. H. *ACS Nano* **2012**, *6*, 3018-3026.
6. Jiang, H. R.; Zhang, A. F.; Sun, Y. A.; Ru, X. N.; Ge, D. T.; Shi, W. *Electrochim. Acta* **2012**, *70*, 278-285.
7. Karsten, S.; Ameen, M. A.; Kallane, S. I.; Nan, A.; Turcu, R.; Liebscher, J. *Synthesis* **2010**, 3021-3028.
8. Martinez-Castro, N.; Magenau, A. J. D.; Storey, R. F. *J. Polym. Sci., Part A: Polym. Chem.* **2010**, *48*, 2533-2545.
9. Magenau, A. J. D.; Martinez-Castro, N.; Savin, D. A.; Storey, R. F. *Macromolecules* **2009**, *42*, 8044-8051.
10. Cernat, A.; Griveau, S.; Martin, P.; Lacroix, J. C.; Farcau, C.; Sandulescu, R.; Bedioui, F. *Electrochem. Commun.* **2012**, *23*, 141-144.
11. Li, Y.; Zhang, W.; Chang, J.; Chen, J.; Li, G.; Ju, Y. *Macromol. Chem. Phys.* **2008**, *209*, 322-329.
12. Li, H.; Cheng, F.; Duft, A. M.; Adronov, A. *J. Am. Chem. Soc.* **2005**, *127*, 14518-14524.
13. Rana, S.; Yoo, H. J.; Cho, J. W.; Chun, B. C.; Park, J. S. *J. Appl. Polym. Sci.* **2011**, *119*, 31-37.
14. Bu, H. B.; Gotz, G.; Reinold, E.; Vogt, A.; Schmid, S.; Blanco, R.; Segura, J. L.; Bauerle, P. *Chem. Commun.* **2008**, 1320-1322.
15. Xu, J. J.; Tian, Y.; Peng, R.; Xian, Y. Z.; Ran, Q.; Jin, L. T. *Electrochem. Commun.* **2009**, *11*, 1972-1975.
16. Li, M.; Neoh, K. G.; Xu, L. Q.; Wang, R.; Kang, E. T.; Lau, T.; Olszyna, D. P.; Chiong, E. *Langmuir* **2012**, *28*, 16408-16422.
17. Ostaci, R. V.; Damiron, D.; Al Akhrass, S.; Grohens, Y.; Drockenmuller, E. *Polym. Chem.* **2011**, *2*, 348-354.
18. Huang, J.; Kaner, R. B. *Chem. Commun.* **2006**, 367-376.
19. Liang, L.; Liu, J.; Windisch Jr, C. F.; Exarhos, G. J.; Lin, Y. *Angew. Chem., Int. Ed.* **2002**, *41*, 3665-3668.
20. Huang, J.; Kaner, R. B. *J. Am. Chem. Soc.* **2004**, *126*, 851-855.
21. Huang, J.; Kaner, R. B. *Angew. Chem., Int. Ed.* **2004**, *43*, 5817-5821.
22. Tran, H. D.; Wang, Y.; D'Arcy, J. M.; Kaner, R. B. *ACS Nano* **2008**, *2*, 1841-1848.
23. Kemp, N. T.; Cochrane, J. W.; Newbury, R. *Synth. Met.* **2009**, *159*, 435-444.
24. Shi, W.; Ge, D. T.; Wang, J. X.; Jiang, Z. Z.; Ren, L.; Zhang, Q. Q. *Macromol. Rapid Commun.* **2006**, *27*, 926-930.
25. McCarthy, C. P.; McGuinness, N. B.; Alcock-Earley, B. E.; Breslin, C. B.; Rooney, A. D. *Electrochem. Commun.* **2012**, *20*, 79-82.

26. Wang, J. X.; Mo, X. P.; Ge, D. T.; Tian, Y.; Wang, Z.; Wang, S. C. *Synth. Met.* **2006**, *156*, 514-518.
27. Harrison, J. A.; Thirsk, H. R. *Electroanal. Chem.* **1971**, *5*, 67-148.
28. Okner, R.; Domb, A. J.; Mandler, D. *Biomacromolecules* **2007**, *8*, 2928-2935.
29. Hwang, B. J.; Santhanam, R.; Lin, Y. L. *Electrochim. Acta* **2001**, *46*, 2843-2853.
30. Hwang, B. J.; Santhanam, R.; Lin, Y. L. *J. Electrochem. Soc.* **2000**, *147*, 2252-2257.
31. Raso, M. A.; Gonzalez-Tejera, M. J.; Carrillo, I.; de la Blanca, E. S.; Garcia, M. V.; Redondo, M. I. *Thin Solid Films* **2011**, *519*, 2387-2392.
32. Tamburri, E.; Orlanducci, S.; Toschi, F.; Terranova, M. L.; Passeri, D. *Synth. Met.* **2009**, *159*, 406-414.
33. Soto, J. P.; Diaz, F. R.; del Valle, M. A.; Velez, J. H.; East, G. A. *Appl. Surf. Sci.* **2008**, *254*, 3489-3496.
34. Del Valle, M. A.; Cury, P.; Schrebler, R. *Electrochim. Acta* **2002**, *48*, 397-405.
35. Schrebler, R.; Grez, P.; Cury, P.; Veas, C.; Merino, M.; Gomez, H.; Cordova, R.; del Valle, M. A. *J. Electroanal. Chem.* **1997**, *430*, 77-90.
36. Dai, L. Z.; Xu, Y. T.; He, Y. Y.; Gal, J. Y.; Wu, H. H. *Polym. Int.* **2005**, *54*, 1256-1261.
37. Lacaze, P. C.; Hara, S.; Soubiran, P.; Aeiyach, S. *Synth. Met.* **1995**, *75*, 111-118.
38. Rajagopalan, R.; Iroh, J. O. *Electrochim. Acta* **2001**, *46*, 2443-2455.
39. Arteaga, G. C.; del Valle, M. A.; Antilen, M.; Romero, M.; Ramos, A.; Hernandez, L.; Arevalo, M. C.; Pastor, E.; Louarn, G. *Int. J. Electrochem. Sci.* **2013**, *8*, 4120-4130.
40. Li, J.; Lin, X. Q. *J. Electrochem. Soc.* **2007**, *154*, 1074-1079.
41. Huang, J. Y.; Wang, K.; Wei, Z. X. *J. Mater. Chem.* **2010**, *20*, 1117-1121.
42. Debiemme-Chouvy, C. *Electrochem. Solid St.* **2007**, *10*, 24-26.
43. Debiemme-Chouvy, C. *Electrochem. Commun.* **2009**, *11*, 298-301.
44. Xia, L.; Wei, Z.; Wan, M. *J. Colloid Interface Sci.* **2010**, *341*, 1-11.
45. Huang, J. Y.; Quan, B. G.; Liu, M. J.; Wei, Z. X.; Jiang, L. *Macromol. Rapid Comm.* **2008**, *29*, 1335-1340.
46. Nakabayashi, K.; Amemiya, F.; Fuchigami, T.; Machida, K.; Takeda, S.; Tamamitsu, K.; Atobe, M. *Chem. Commun.* **2011**, *47*, 5765-5767.
47. Atobe, M.; Ikari, S.; Nakabayashi, K.; Amemiya, F.; Fuchigami, T. *Langmuir* **2010**, *26*, 9111-9115.
48. Markowitz, M. M.; Hawley, W. N.; Boryta, D. A.; Harris, R. F. *J. Chem. Eng. Data* **1961**, *6*, 325-327.
49. Tang, C. M.; Mclean, J. A. *Inorg. Chem.* **1981**, *20*, 2652-2655.
50. Kolling, O. W. *Anal. Chem.* **1968**, *40*, 956-959.
51. Barbosa, J.; Barron, D.; Bosch, E.; Roses, M. *Anal. Chim. Acta* **1992**, *264*, 229-239.
52. Burgess, J. *Metal Ions in Solution*; Wiley, 1978.
53. Weaver, W. M.; Hutchison, J. D. *J. Am. Chem. Soc.* **1964**, *86*, 261-265.
54. Asami, R.; Atobe, M.; Fuchigami, T. *J. Am. Chem. Soc.* **2005**, *127*, 13160-13161.
55. Asami, R.; Fuchigami, T.; Atobe, M. *Langmuir* **2006**, *22*, 10258-10263.

56. Romero, M.; del Valle, M. A.; del Rio, R.; Diaz, F. R.; Armijo, F. *Int. J. Electrochem. Sci.* **2012**, *7*, 10132-10141.
57. Abidian, M. R.; Martin, D. C. *Biomaterials* **2008**, *29*, 1273-1283.
58. Prins, L. J.; Reinhoudt, D. N.; Timmerman, P. *Angew. Chem., Int. Ed.* **2001**, *40*, 2382-2426.
59. Reinhoudt, D. N.; Crego-Calama, M. *Science* **2002**, *295*, 2403-2407.
60. Taube, F.; Andersson, I.; Angus-Dunne, S.; Bodor, A.; Toth, I.; Pettersson, L. *Dalton Trans.* **2003**, 2512-2518.
61. Andersson, I.; Gorzsas, A.; Kerezsi, C.; Toth, I.; Pettersson, L. *Dalton Trans.* **2005**, 3658-3666.
62. Hawkins, S. J.; Ratcliffe, N. M. *J. Mater. Chem.* **2000**, *10*, 2057-2062.
63. Reece, D. A.; Pringle, J. M.; Ralph, S. F.; Wallace, G. G. *Macromolecules* **2005**, *38*, 1616-1622.
64. West, R.; Josowicz, M.; Janata, J.; Minet, I.; Hevesi, L. *J. Electrochem. Soc.* **2009**, *156*, 55-59.
65. Massoumi, B.; Lesani, H.; Saraei, M.; Entezami, A. A. *Iran. Polym. J.* **2011**, *20*, 747-756.
66. Rodríguez, I.; Scharifker, B. R.; Mostany, J. *J. Electroanal. Chem.* **2000**, *491*, 117-125.
67. Novák, P. *J. Electrochem. Soc.* **1991**, *138*, 3300.
68. Diaw, A. K. D.; Yassar, A.; Gningue-Sall, D.; Aaron, J. J. *Arkivoc* **2008**, 122-144.
69. Roux, S.; Audebert, P.; Pagetti, J.; Roche, M. *Nouv. J. Chim.* **2000**, *24*, 877-884.
70. Lee, H.; Yang, H.; Kwak, J. *J. Electroanal. Chem.* **1999**, *468*, 104-109.
71. Goriletsky, V. I. M., A. I.; Belenko, L. E.; Rebrova, T. P. *Semi. Phys., Quant. Electron. Optoelectron.* **2001**, *4*, 139-141.
72. Chen, F.; Shi, G. Q.; Fu, M. X.; Qu, L. T.; Hong, X. Y. *Synth. Met.* **2003**, *132*, 125-132.
73. Santos, M. J. L.; Brolo, A. G.; Girotto, E. M. *Electrochim. Acta* **2007**, *52*, 6141-6145.
74. Ferraris, J. P.; Andrus, R. G.; Hrncir, D. C. *Chem. Commun.* **1989**, 1318-1320.
75. Liu, J.; Zhang, R.; Sauve, G.; Kowalewski, T.; McCullough, R. D. *J. Am. Chem. Soc.* **2008**, *130*, 13167-13176.
76. Street, G. B. *J. Phys. Colloques* **1983**, *186*, 599-606.
77. Christensen, P. A.; Hamnett, A. *Electrochim. Acta* **1991**, *36*, 1263-1286.
78. Redondo, M. I.; de la Blanca, E. S.; Garcia, M. V.; Raso, M. A.; Tortajada, J.; Gonzalez-Tejera, M. J. *Synth. Met.* **2001**, *122*, 431-435.
79. Materials & Surface Science Institute (MSSI) UL, L., XPS X-ray Photoelectron Spectroscopy, Date accessed, 2013.
80. Mangeney, C.; Bousalem, S.; Connan, C.; Vaulay, M. J.; Bernard, S.; Chehimi, M. M. *Langmuir* **2006**, *22*, 10163-10169.
81. Ciampi, S.; Le Saux, G.; Harper, J. B.; Gooding, J. J. *Electroanal.* **2008**, *20*, 1513-1519.
82. Thiébaut, J. M.; Belmonte, T.; Chaleix, D.; Choquet, P.; Baravian, G.; Puech, V.; Michel, H. *Surf. Coat. Technol.* **2003**, *169-170*, 186-189.

83. Plyuto, I. V.; Shpak, A. P.; Stoch, J.; Sharanda, L. F.; Plyuto, Y. V.; Babich, I. V.; Makkee, M.; Moulijn, J. A. *Surf. Interface Anal.* **2006**, *38*, 917-921.
84. Stevens, J. S.; Schroeder, S. L. M. *Surf. Interface Anal.* **2009**, *41*, 453-462.
85. Tyan, Y. C.; Liao, J. D.; Klauser, R.; Wu Ie, D.; Weng, C. C. *Biomaterials* **2002**, *23*, 65-76.
86. Liu, X.; Zheng, H. N.; Ma, Y. Z.; Yan, Q.; Xiao, S. J. *J. Colloid Interface Sci.* **2011**, *358*, 116-122.
87. Quan, D. T.; Le Bloa, A.; Hbib, H.; Bonnaud, O.; Meinnel, J.; Quemerais, A.; Marchand, R. *Rev. Phys. Appl.* **1989**, *24*, 545-551.
88. Baltrusaitis, J.; Jayaweera, P. M.; Grassian, V. H. *Phys. Chem. Chem. Phys.* **2009**, *11*, 8295-8305.
89. Song, M.; Xu, J. *ECS Solid State Lett.* **2013**, *2*, 24-27.
90. Halseid, R.; Wainright, J. S.; Savinell, R. F.; Tunold, R. *J. Electrochem. Soc.* **2007**, *154*, 263-270.
91. Diegle, R. B. *J. Electrochem. Soc.* **1988**, *135*, 1085-1092.
92. López, G. P.; Castner, D. G.; Ratner, B. D. *Surf. Interface Anal.* **1991**, *17*, 267-272.
93. Jaramillo, A.; Spurlock, L. D.; Young, V.; Brajter-Toth, A. *Analyst* **1999**, *124*, 1215-1221.
94. Instruments, O. "INCAEnergy Applications Training Course.," 2009.
95. Şenel, M. *Synth. Met.* **2011**, *161*, 1861-1868.
96. Foulds, N. C.; Lowe, C. R. *Anal. Chem.* **1988**, *60*, 2473-2478.
97. Eaves, J. G.; Mirrazaei, R.; Parker, D.; Munro, H. S. *J. Chem. Soc., Perk. T. 2* **1989**, *0*, 373-376.
98. Naji, A.; Cretin, M.; Persin, M.; Sarrazin, J. *J. Appl. Polym. Sci.* **2004**, *91*, 3947-3958.
99. Palomera, N.; Vera, J. L.; Melendez, E.; Ramirez-Vick, J. E.; Tomar, M. S.; Arya, S. K.; Singh, S. P. *J. Electroanal. Chem.* **2011**, *658*, 33-37.
100. Rodriguez, J. G.; Onate, A.; MartinVillamil, R. M.; Fonseca, I. *J. Organomet. Chem.* **1996**, *513*, 71-76.
101. Phillips, L.; Lacey, A. R.; Cooper, M. K. *J. Chem. Soc. Dalton* **1988**, 1383-1391.
102. Oberoi, S.; Jahne, E.; Adler, H. J. P.; Varma, I. K. *Des. Monomers Polym.* **2008**, *11*, 57-68.
103. Li, Y.; Zhang, W. X.; Li, G. T.; Ju, Y. *Polymer* **2008**, *49*, 225-233.
104. Guo, R.; Li, G.; Zhang, W.; Shen, G.; Shen, D. *Chemphyschem* **2005**, *6*, 2025-2028.
105. Bu, H. B.; Gotz, G.; Reinold, E.; Vogt, A.; Azumi, R.; Segura, J. L.; Bauerle, P. *Chem. Commun.* **2012**, *48*, 2677-2679.
106. Han, S. C.; Yoon, J.; Oh, J.; Lee, J. W. *Bull. Korean Chem. Soc.* **2011**, *32*, 3809-3812.
107. Rui, Q.; Komori, K.; Tian, Y.; Liu, H.; Luo, Y.; Sakai, Y. *Anal. Chim. Acta.* **2010**, *670*, 57-62.
108. Luo, Y.; Liu, H.; Rui, Q.; Tian, Y. *Anal. Chem.* **2009**, *81*, 3035-3041.
109. Su, C.; Wang, L. M.; Xu, L. H.; Zhang, C. *Electrochim. Acta* **2013**, *104*, 302-307.
110. Diana, E.; Rossetti, R.; Stanghellini, P. L.; Kettle, S. F. A. *Inorg. Chem.* **1997**, *36*, 382-391.

111. Aroca, R.; Nazri, R.; Nazri, G. A.; Camargo, A. J.; Trsic, M. *J. Solution Chem.* **2000**, *29*, 1047-1060.
112. Yoo, B. K.; Joo, S. W. *J. Colloid Interface Sci.* **2007**, *311*, 491-496.
113. Cuffe, L.; Hudson, R. D. A.; Gallagher, J. F.; Jennings, S.; McAdam, C. J.; Connelly, R. B. T.; Manning, A. R.; Robinson, B. H.; Simpson, J. *Organometallics* **2005**, *24*, 2051-2060.
114. Kažemekaite, M.; Bulovas, A.; Smirnovas, V.; Niaura, G.; Butkus, E.; Razumas, V. *Tetrahedron Lett.* **2001**, *42*, 7691-7694.
115. Long, T. V.; Huege, F. R. *Chem. Commun.* **1968**, 1239-1241.
116. Lippincott, E. R.; Nelson, R. D. *Spectrochim. Acta* **1958**, *10*, 307-329.
117. Fritz, H. P. *Advan. Organometal. Chem. (F. G. A. Stone and Robert West, editors. Academic)* **1964**, *1*, 239-316.
118. Nastase, F.; Mihaiescu, D.; Nastase, C.; Mirea, C.; Burzo, I.; Stamatin, I. *Compos. Part A-Appl. S.* **2005**, *36*, 503-507.
119. Davis, R. J.; Pemberton, J. E. *J. Phys. Chem. C* **2008**, *112*, 4364-4371.
120. Kabalan, L.; Matar, S. F. *Chem. Phys.* **2009**, *359*, 14-20.
121. Jbarah, A. A.; Ihle, A.; Banert, K.; Holze, R. *J. Raman Spectrosc.* **2006**, *37*, 123-131.
122. Liu, Y. C.; Hwang, B. J. *Thin Solid Films* **1999**, *339*, 233-239.
123. Luo, S. J.; Liu, Y. H.; Liu, C. M.; Liang, Y. M.; Ma, Y. X. *Synth. Commun.* **2000**, *30*, 1569-1572.
124. Sanchez De La Blanca, E.; Carrillo, I.; Gonzalez-Tejera, M. J.; Hernandez-Fuentes, I. *J. Polym. Sci., Part A: Polym. Chem.* **2000**, *38*, 291-298.

Chapter 5 Synthesis and characterisation of metal carbonyl complexes with the potential to be attached to polypyrrole films

5.1 Introduction

In the previous two chapters, the investigation of an *N*-substituted Py compound was performed. This compound possessed an azide moiety as a functional group, through which it was possible to covalently attach an organometallic compound, namely FcCCH. During the course of this research, two other methodologies involving two different types of functional groups were investigated, as a means of growing poly(*N*-substituted)pyrrole films through, which metal complexes could be bonded to the polymer surface. These were an *N*-substituted Py containing the 2,2'-bipyridyl moiety and an *N*-substituted Py containing the nitrile moiety.

5.1.1 *N*-substituted pyrrole containing the 2,2'-bipyridyl moiety

Py was bound to a 2,2'-bipyridine (Bipy), as this moiety is known for its versatile binding properties. Much research has been performed utilising Bipy as an organic group. The bidentate ligand is regarded for its versatile binding properties, as it possesses nucleophilic nitrogen atoms, which permit the formation of coordinate complexes, upon their bonding to one of the TMs.[1-6] It has been employed successfully as a chelating ligand to produce a wide variety of different metal complexes.[7] The ligands are in themselves electrochemically active, producing reversible one-electron redox waves, evident for heterocyclic ring systems at reductive potentials.[8-10] Bipy has the ability to be substituted at the 3,3', 4,4', 5,5' and 6,6' ring positions,[11,12] permitting functionalisation with different components. Functionalisation at the 4,4' position with short saturated alkyl chains terminating with *N*-substituted Py[3,6,7,13-15] yields a bidentate ligand, capable of undergoing irreversible oxidation of the Py unit at an E_{ox} greater than 1.000 V vs. SCE[7,16] to produce a polymer, while the Bipy unit undergoes a reversible or *quasi*-reversible one-electron reduction at a half-wave potential greater than -1.000 V vs. SCE.[7,10]

One series of metals this bidentate ligand can bind to are the Group 6 carbonyl s.[5,9,17,18] TM carbonyl species, $M(CO)_n$, when complexed with Bipy ligands in a coordinating solvent, such as MeCN or DMSO, have been reported to incur loss of CO accompanied by acquisition of a molecule of the coordinating solvent *via* CV at oxidative potentials.[1,2,18] This controlled electrochemical release of CO has potential,

as a means for the delivery of CO as a therapeutic agent, as it has been reported that within biological systems the release of small amounts of CO (20 - 500 ppm), using CORMs (Figure 5.1), has been shown to have many diverse beneficial effects. Administering small amounts of CO to animal models have shown effects, which include the prolongation of aortic graft survival, the improvement of liver and kidney function post-transplant, the prevention of sequela of sepsis, anti-inflammation, reduced joint inflammation and erosion, reduced injury from myocardial infarction, improvement in renal function, lowering intraocular pressure and hypertension, and cerebroprotection.[20]

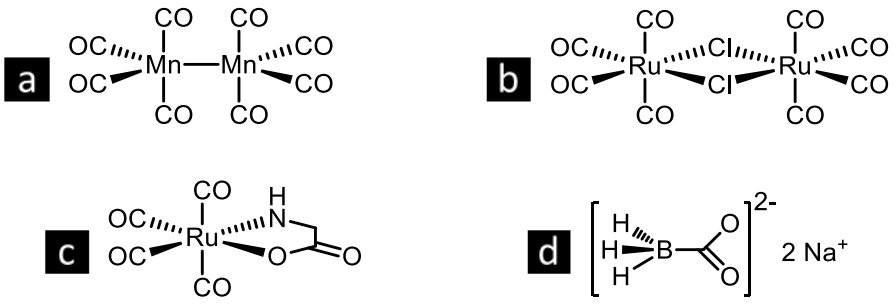

Figure 5.1: Structures of thermally/photochemically induced carbon monoxide releasing molecules (CORMs). (a) CORM-1, (b) CORM-2, (c) CORM-3 and (d) CORM-A1.

Moutet, Deronzier and Cosnier and co-workers have reported the electrochemical polymerisation of a number of Bipy *N*-substituted Py compounds (Figure 5.2), as free ligands and also, coordinated these ligands to various TMs, which undergo electrochemical polymerisation at oxidative potentials to produce thin adherent films.[3,4,6,7,13-16,35] In the research described in this chapter, we set out to produce similar films, possessing the potential to bind metal complexes, which could undergo loss of a CO ligand upon application of the appropriate E_{ox}.

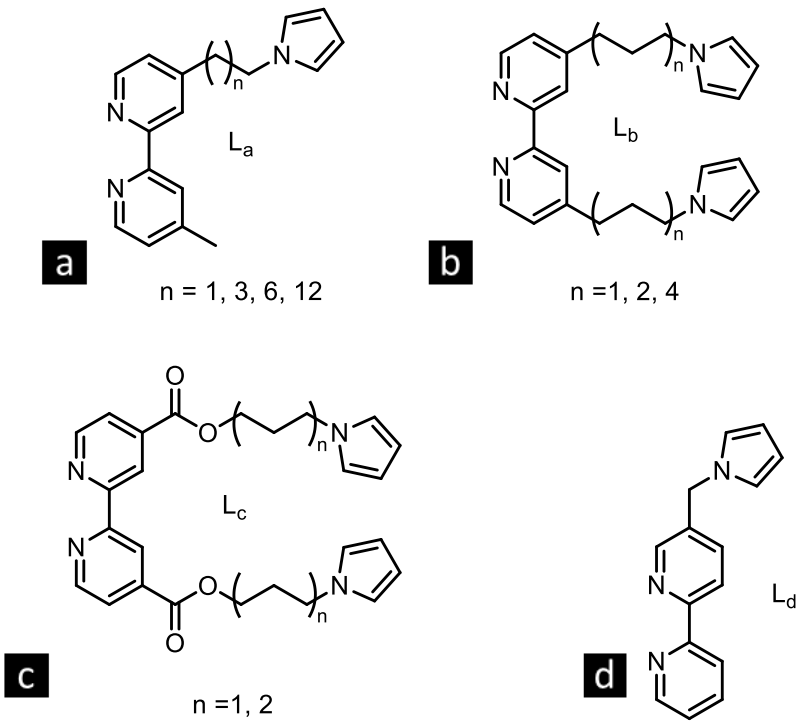

Figure 5.2: Structures of 2,2'-bipyridine ligands, capable of polymerisation *via* electrochemical oxidation of the Py moiety. (a) mono-substituted at the 4 position, L_a (b) di-substituted at the 4,4' positions, L_b (c) di-substituted at the 4,4' position with an carboxyl functional group within the tether, L_c, and (d) mono-substituted at the 5 position, L_d.

5.1.2 *N*-substituted pyrrole containing the nitrile moiety

Research regarding the compound *N*-(2-cyanoethyl)pyrrole (PyEtCN) has produced work examining its use as a polymer, poly[*N*-(2-cyanoethyl)pyrrole] (PPyEtCN), for the detection of organic vapours such as MeCN and triethylamine (TEA),[19] volatile alcohols and carbonyl compounds,[20] H_2O and a range of polar and nonpolar organic compounds,[21] as a sensor for oxidised dopamine,[22] as an impedimetric immunosensor[23] and for the immobilisation of antibodies to be used for enhanced target recognition and binding affinity.[24] We have previously published work regarding the controlled electrochemical deposition of PPyEtCN in the nanowire[25] and microtube[26] morphology, yielding polymer films with increased surface area and shorter diffusion lengths, when interacting with the species of interest.

Research, prominent in the literature due to its coordination chemistry, focussing on developing ligands containing the nitrile moiety, has yielded work regarding charged

complexes, composed of a variation of TMs such as the Group 6 metals,[27,28] iron,[29,30] ruthenium[31,32] and cobalt.[33] Such charged nitrile complexes are precursors to their respective neutral tetrazolate complexes, upon reaction with sodium azide.[29,30,34] Previous work performed within our research group has successfully synthesised and studied a variation of cyclopentadienyl molybdenum tricarbonyl cyanides in the tetrafluoroborate salt form.[35] The ability to coordinate a variation of cyanide ligands such as benzonitrile (NCPh), 2-thiophenecarbonitrile (NCT) and benzyl cyanide (NCBz) suggests that the binding of PyEtCN to the metal and its subsequent modification to the N_2-tetrazolate form, substituted at the C_5 position should be straightforward and produce a metal complex with electrochemical polymerisation capabilities, due to the Py moiety. The presence of CO ligands means it may be possible that the controlled electrochemical release of CO could be induced by oxidation of the metal complex.

5.2 Results and discussion

In this chapter, the aims of the work performed were to synthesise Group 6 metal carbonyl complexes and incorporate them into PPy, as it formed on an substrate and also, to synthesise Group 6 and 8 metal carbonyl complexes, which contain either (Bipy) or tetrazole (N_4CR) ligands, enabling attachment to the PPy surface, either by complexation to the monomer or *via* a post-polymerisation functionalisation method. This could permit the controlled electrochemical release of CO from a polymer film, which can be precisely controlled due to the potential applied to the modified electrode. This may yield the possibility of producing the precisely controlled electrochemical release of CO from the polymer film attached to a substrate, resulting in the fabrication of the first carbon monoxide releasing polymer (CORP).

5.2.1 Synthesis, electrochemical characterisation and attempted incorporation of $M^0(CO)_4$(Bipy) (M = Cr, Mo, W) into PPy

5.2.1.1 Synthesis of $M^0(CO)_4$(Bipy) (M = Cr, Mo, W)

Utilising the methods reported by Van Atta and co-workers and Paz and co-workers the $M^0(CO)_4$(Bipy) (M = Cr, Mo, W) complexes were prepared by ligand substitution of the respective hexavalent metal carbonyl, $M^0(CO)_6$ (M = Cr, Mo and W), with Bipy *via* microwave-assisted synthesis (MAS).[36,37] The metal complexes were also obtained using conventional synthesis *via* stirring of said reactants in toluene at reflux temperature, until evolution of gas had ceased.[38] However, this methodology produced significantly lower yields than anticipated, due to sublimation and condensation of the metal carbonyl reactant on the inside of the reflux condenser during the reaction. The products were characterised using ^{1}H and ^{13}C NMR spectroscopy and FTIR spectroscopy.

5.2.1.2 Electrochemical characterisation of $Mo^0(CO)_4$(Bipy)

Studies have shown that upon applying the appropriate E_{ox} to $Mo^0(CO)_4$(α-diimine) complexes, dissociation of CO ligands will occur when performed in a coordinating solvent.[1,2] Hanzlik *et al*. reported the substitution of CO during their CV study of $Mo^0(CO)_4$(Bipy) in a solution containing either MeCN or DMSO at -10 ºC. In the

study, it was reported that the electrochemically controlled ligand substitution produces the *fac*-$Mo^0(CO)_3$(Bipy)(MeCN) species in MeCN by the reaction shown in Scheme 5.1.[2] In addition, Bullock and co-workers completed a spectroelectrochemical study, entailing the application of an appropriate E_{ox} to a solution containing the $Mo^0(CO)_4$(Bipy) complex and confirming the release of CO *via* FTIR spectroscopy.[1] In the current work, a study was performed to confirm these findings.

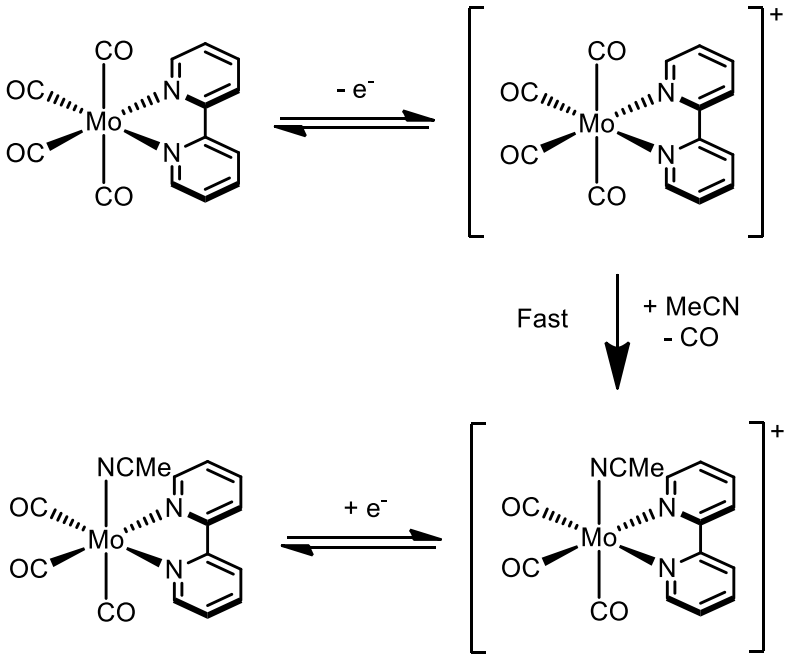

Scheme 5.1: Formation of *fac*-$Mo^0(CO)_3$(Bipy)(MeCN) due to electrochemical substitution of ligand, CO, by solvent molecule, MeCN.

During CV, cycling of the $Mo^0(CO)_4$(Bipy) (2 mM) species in a non-coordinating solvent, DCM, containing tetrabutylammonium hexafluorophosphate ($TBAPF_6$) (200 mM) at -77 °C, produced the expected *quasi*-reversible redox couple ($E_{1/2}$ = 0.848 V vs. bare Ag wire *quasi*-reference (Ag/Ag^+), ΔE_p = 0.130 V) (Figure 5.3 (—)). It was necessary to perform this experiment at temperatures below -44 °C, to obtain a reversible couple for the redox of $Mo^0(CO)_4$(Bipy), which was incongruent with the studies by Bullock and co-workers and Hanzlik *et al.*, who reported that temperatures of 20 and -10 °C were adequate respectively.

To confirm CO ligand substitution, a coordinating solvent, MeCN, was added to the electrolytic medium. Upon addition of 3 equivalents (in relation to the complex) of MeCN, the redox couple, **A**, became irreversible (Figure 5.3 (—)), due to production of $[Mo^{I}(CO)_3(Bipy)(MeCN)]^+$, a consequence of the 17-electron electrogenerated species undergoing rapid substitution of a ligand, CO, by a MeCN solvent molecule.[1,2] The formation of a second redox couple, **B**, ($E_{1/2}$ = 0.581 V vs. Ag/Ag^+, ΔE_p = 0.105 V) with a current ratio, j_c/j_a, of 1.02 has been attributed to a chemical reaction, which only occurs after several cycles have been performed and was not inhibited by the low temperature. This redox couple has been stated in the literature as representing the redox activity of the *fac*-$[Mo^{I}(CO)_3(Bipy)(MeCN)]^+$ species.[2] As an analogous redox couple was also present in the CV, illustrating the electroactivity of the $Mo^0(CO)_4(Bipy)$ species in DCM (Figure 5.3 (—)), we suggest that the formation of this redox couple may be due to residual H_2O in the system, which could produce the complex *fac*-$[Mo^{I}(CO)_3(Bipy)(H_2O)]^+$ upon oxidative cycling.

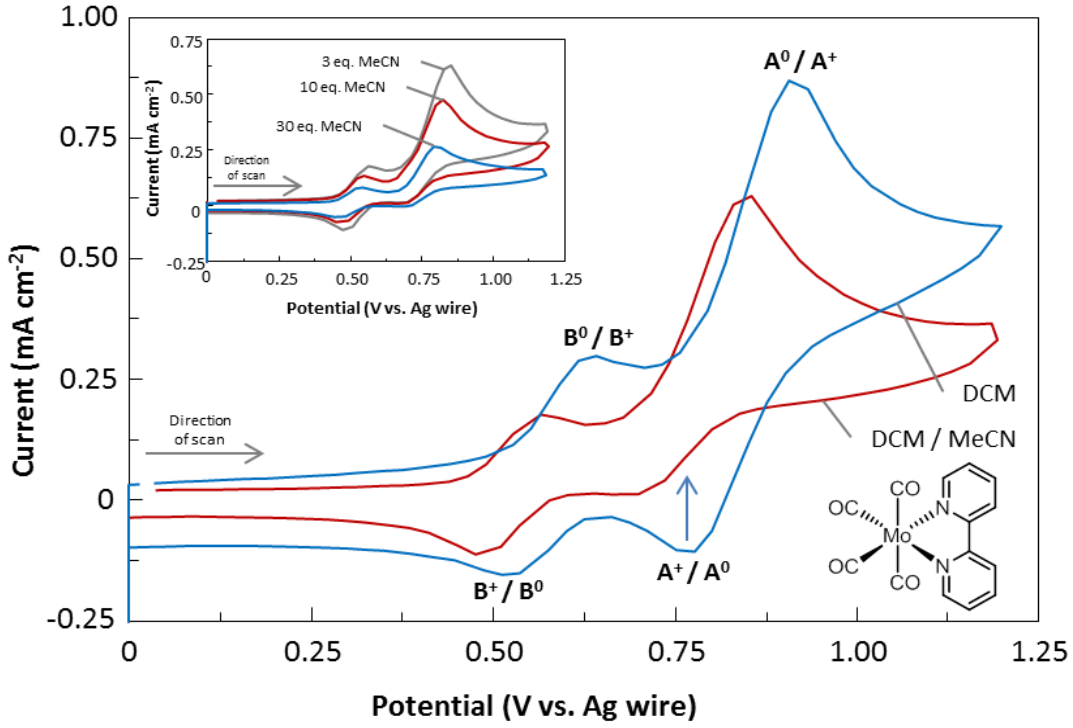

Figure 5.3: CVs of $Mo^0(CO)_4(Bipy)$ (2 mM) and $TBAPF_6$ (200 mM) in (a) DCM (—) and (b) DCM with 3 equivalents (in relation to the complex) of MeCN (—) between 0.000 - 1.200 V vs. Ag/Ag^+ at 250 mV s^{-1} (-77 °C). Inset: Analogous conditions with 3 (—), 10 (—) and 30 (—) equivalents of MeCN present in the electrochemical cell.

The spectroelectrochemical activity of $Mo^0(CO)_4(Bipy)$ was then replicated, using constant potential amperometry (CPA) with an optically transparent thin-layer electrochemical (OTTLe) cell, in conjunction with FTIR spectroscopic detection. A E_{ox} of 0.500 V vs. Ag/Ag^+ was applied for 15 minutes to the OTTLE cell containing $Mo^0(CO)_4(Bipy)$ (50 mM) with $TBAPF_6$ (100 mM) in DCM. The spectrum obtained during application of the E_{ox} (Figure 5.4 (a)) displayed an intensity decrease for the absorbance bands representative of $Mo^0(CO)_4(Bipy)$, indicating a reduction in its concentration, due to the oxidation of $Mo^0(CO)_4(Bipy)$ to the $[Mo^I(CO)_4(Bipy)]^+$ species. Also, observed in the spectra was an intensity increase for a band positioned at 2144 cm^{-1}. This band was indicative for the presence of CO dissolved in solution. The E_{ox} was applied for 30 minutes and no new bands were observed to develop in the metal-carbonyl stretching region of the FTIR spectrum, indicating that upon oxidation, decomposition occurred. As proposed by Bullock and co-workers, CO loss probably arises upon decomposition of the radical species by a number of pathways, such as substitution of CO by solvent/H_2O, or disproportionation.[1]

Following this procedure, an E_{app} of 0.500 V vs. Ag/Ag^+ was applied, for a total time of 480 seconds, to an OTTLE cell containing $Mo^0(CO)_4(Bipy)$ (50 mM) and $TBAPF_6$ (100 mM) in DCM, accompanied by 3 equivalents (in relation to the complex) of MeCN. An FTIR spectrum was firstly recorded before any E_{ox} was applied and then again after application of the E_{ox}, at time intervals of 40, 80, 120, 240, 360 and 480 seconds (Figure 5.4 (b)). The spectra recorded in the presence of MeCN possessed a significantly greater decrease in absorbance intensity for the bands attributed to the $Mo^0(CO)_4(Bipy)$ species (Figure 5.4 (b) **1.**), than that for the analogous species, upon application of an E_{ox} in the absence of MeCN (Figure 5.4 (a) **1.**). The absorbance intensity decrease for the band positioned at 1905 cm^{-1} was approx. 7% and 66% for oxidation of $Mo^0(CO)_4(Bipy)$ in DCM (0.500 V vs. Ag/Ag^+ for 15 minutes) and DCM/MeCN (0.500 V vs. Ag/Ag^+ for 8 minutes) respectively. Additionally, new bands were observed to form in the metal-carbonyl stretching region of the FTIR spectrum after the E_{ox} was applied and these bands increased in intensity during the course of the experiment. By comparison with literature values, the bands at 1990 and 1930 cm^{-1} are attributed to the $[Mo^{II}(CO)_2(Bipy)(MeCN)_3]^{2+}$ species (Figure 5.4 (b) **4.**) while the bands indicative of the two intermediate species,

$[Mo^{I}(CO)_3(Bipy)(MeCN)]^+$ (Figure 5.4 (b) **2.**) (2026 and 1905 (broad) cm^{-1}) and $[Mo^{II}(CO)_3(Bipy)(MeCN)_2]^{2+}$ (Figure 5.4 (b) **3.**) (2093, 2024 and 1990 cm^{-1}) were difficult to observe due to the intensity and position of the other absorbance bands present in the spectra. The formation of these products, which has been proposed by Bullock and co-workers, occurs *via* the reaction sequence displayed in Scheme 5.2.[1]

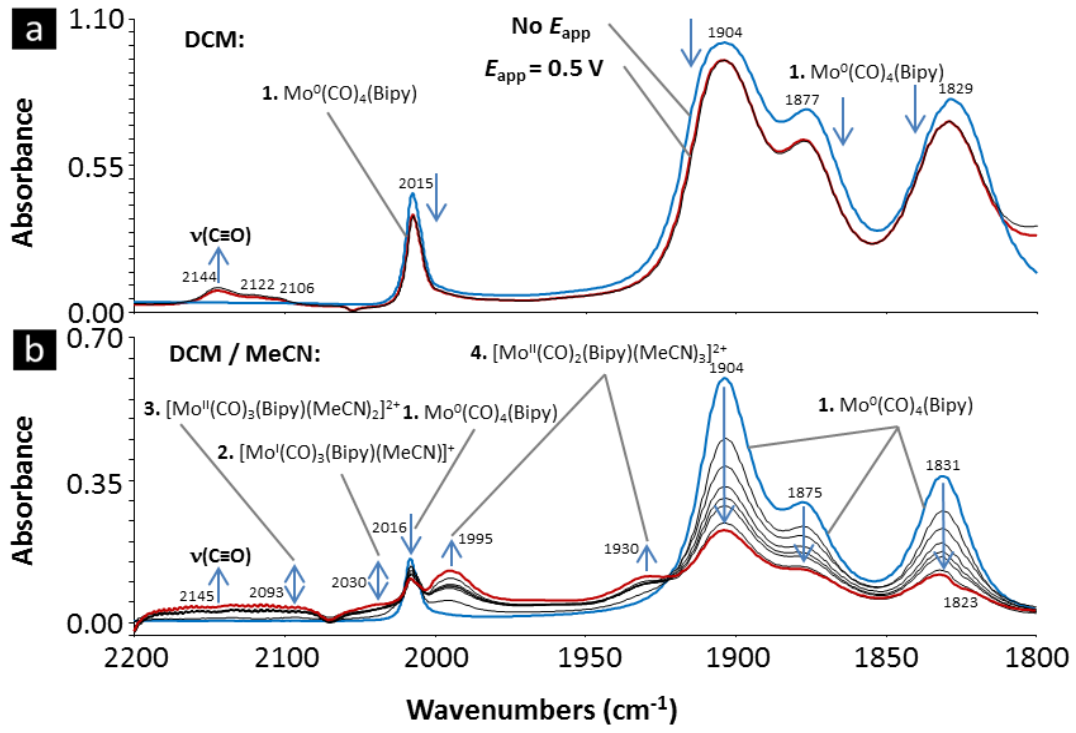

Figure 5.4: FTIR spectra of $Mo^0(CO)_4(Bipy)$ (50 mM) and $TBAPF_6$ (100 mM) in (a) DCM and (b) DCM with 3 equivalents (in relation to the complex) of MeCN, performed at ±2 cm^{-1} resolution when no E_{ox} was applied to the OTTLE cell (—) and when E_{app} = 0.500 V vs. Ag/Ag^+, for (a) 15 (—) and (b) 8 min (—).

The band centred at 2145 cm^{-1} (Figure 5.5), possessing the characteristic P and R branches, was assigned to the ν(CO) of CO gas.[39] Evidence to support the accumulation of CO gas was attained upon visual inspection of the OTTLE cell, where gas bubbles were visibly trapped within the Pt working electrode mesh. Also, control experiments were performed verifying the stability of the $Mo^0(CO)_4(Bipy)$ species in the OTTLE cell over 15 minutes and a check for CO in the background scan of the OTTLE cell was performed upon E_{ox} application.

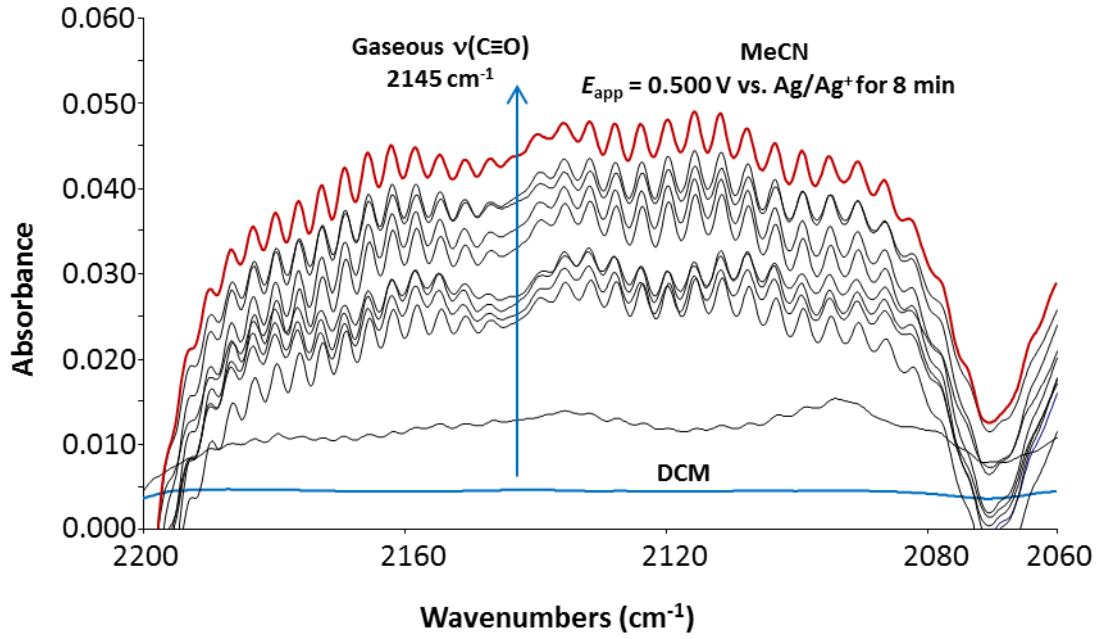

Figure 5.5: FTIR spectra of $Mo^0(CO)_4(Bipy)$ (50 mM) and $TBAPF_6$ (100 mM) in DCM with 3 equivalents (in relation to the complex) of MeCN performed at ±2 cm^{-1} resolution. No E_{ox} applied to the OTTLE cell (—) and E_{app} = 0.500 V vs. Ag/Ag^+ for 8 min (—).

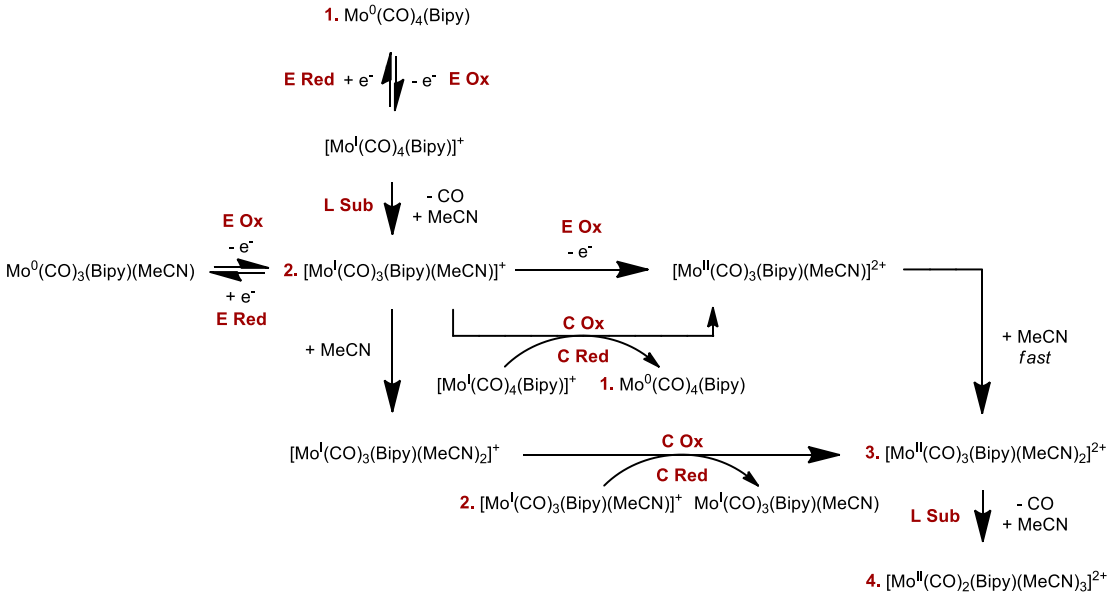

Scheme 5.2: Pathways for the electrochemical oxidation of $Mo^0(CO)4(Bipy)$. C = Chemical, E = Electrochemical, Ox = Oxidation, Red = Reduction, L = Ligand and Sub = Substitution.[1]

5.2.1.3 Attempted incorporation of $M^0(CO)_4(Bipy)$ (M = Mo, Cr) into polypyrrole modified electrode

A number of authors have claimed that it is possible to incorporate small neutral molecules such as Fc into PPy, as it forms on the substrate.[40] Therefore, the incorporation of $M^0(CO)_4(Bipy)$ (M = Cr, Mo) compounds into an electrochemically formed PPy matrix was attempted. PPy was deposited on a polished Au substrate from a solution containing Py (100 mM) with $LiClO_4$ (200 mM) and $Cr^0(CO)_4(Bipy)$ (50 mM) in MeCN at 0.850 V vs. SCE, until a q of 0.80 C cm^{-2} was attained. Upon analyses of the polymer films using EDX spectroscopy, a minuscule quantity of Cr (approx. 0.07 atomic%), positioned at 0.573 (Lα1,2) and 5.415 (Kα1) keV in the spectrum, was detected within the PPy films (Figure 5.6).

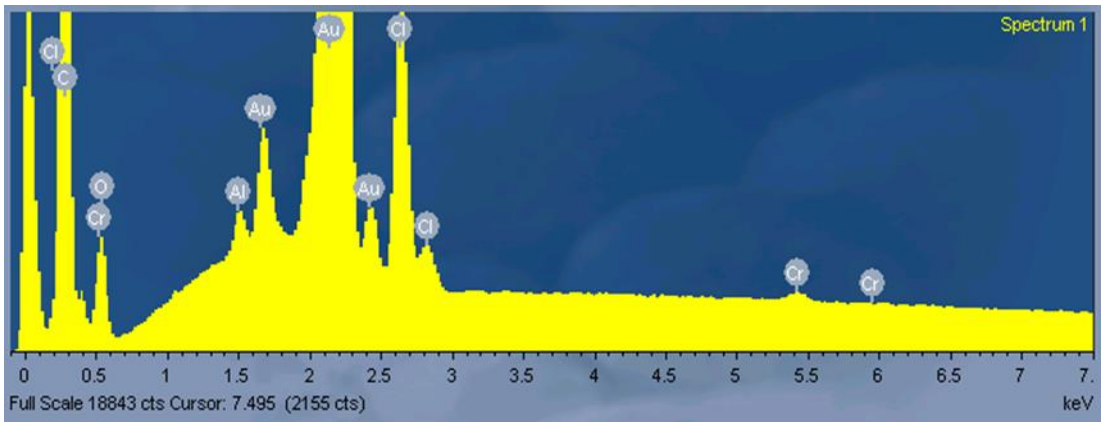

Figure 5.6: EDX spectrum of PPy grown in MeCN with $Cr(CO)_4(Bipy)$ and $LiClO_4$. Intense Au peaks are a consequence of the Au substrate utilised for electrodeposition.

The quantity of chromium detected, which was assumed to be entrapped within the polymer, was very low so another direction was pursued. The poor incorporation of the $Cr^0(CO)_4(Bipy)$ complex probably arose as it has essentially no electrostatic affinity for oxidised Py during polymerisation. It was probable that the small amount incorporated into the film was a consequence of the complexes proximity to the substrate, during the polymerisation process. In addition, there were concerns that the $M^0(CO)_4(Bipy)$ would become oxidised to $[M^I(CO)_4(Bipy)]^+$ upon application of the E_{ox}, which is necessary to electrochemically polymerise Py. Therefore, the use of a surfactant, sodium dodecyl sulfate (NaDS) (Figure 5.7), in H_2O was proposed. As this compound is amphiphilic and is known to form micelles in solution,[41] hopefully

anions would encapsulate some of the non-polar $M^0(CO)_4$(Bipy) species, since it is in H_2O, while simultaneously doping the oxidised Py during deposition, as it possesses a negatively charged sulfate group (Figure 5.7), thus entrapping the metal carbonyl within the polymer film. It was anticipated that by performing the polymerisation in an aqueous solvent a lower E_{app} could be employed, thus reducing the possibility of oxidising the metal carbonyl complex, before it was incorporated into the polymer.

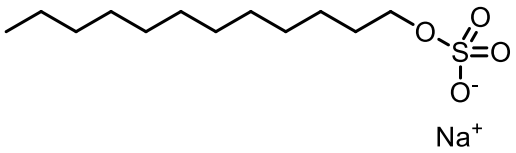

Figure 5.7: Structure of sodium dodecyl sulfate (NaDS).

Firstly, the solubilisation of the non-polar metal carbonyl by NaDS was determined in H_2O, *via* investigation using UV-Vis spectroscopy. Upon confirmation of the metal carbonyl species in solution, PPy was deposited on a polished Au substrate from a solution containing Py (100 mM) with NaDS (100 mM) and $Cr^0(CO)_4$(Bipy) (7 mM) in H_2O at 0.500 V vs. SCE, until a charge density of 0.10 C cm^{-2} was attained. The films were analysed once again using EDX spectroscopy (Figure 5.8) and displayed peaks representative of the NaDS dopant, positioned at 1.041 (Kα1,2) keV for the Na atom and at 2.308 (Kα1) keV for the S atom. The spectra did not display peaks representative of the $Cr^0(CO)_4$(Bipy) compound, which would be positioned at 0.573 (Lα1,2) and 5.415 (Kα1) keV for the Cr atom.

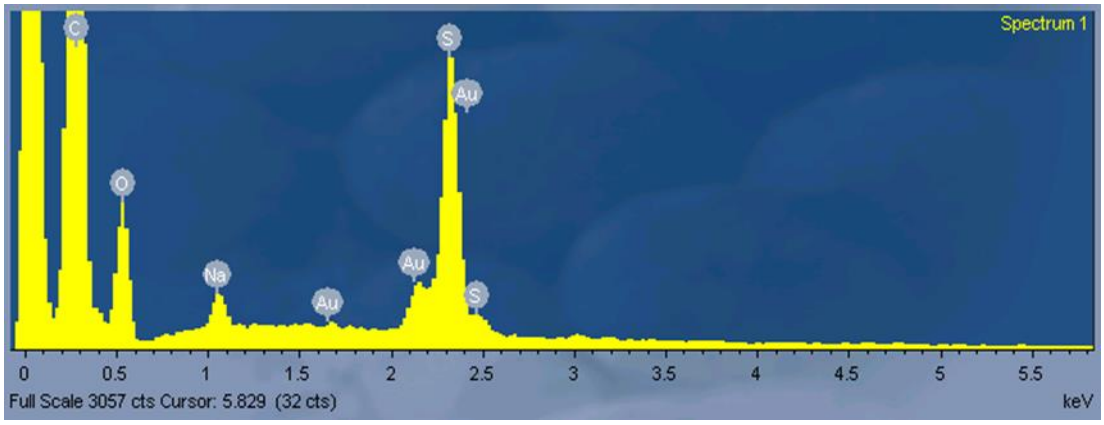

Figure 5.8: EDX spectrum of PPy grown in H_2O with $Cr^0(CO)_4$(Bipy) and NaDS. Intense Au peaks are a consequence of the Au substrate utilised for electrodeposition.

It was then decided to incorporate the Mo congener of the $Cr^0(CO)_4$(Bipy) species during deposition of PPy. This was performed using a GCE as it was found that the Mo peak, positioned at 2.293 (Lα1,2) keV, was masked in the EDX spectra by the Au peak at 2.123 (Mα1) keV, upon utilisation of the Au substrate. The EDX spectrum recorded of the polymer film (Figure 5.9) possessed peaks for Mo at 2.293 (Lα) and 17.480 (Kα) keV, but during analysis only a very small amount of Mo was detected (approx. 0.03 atomic%).

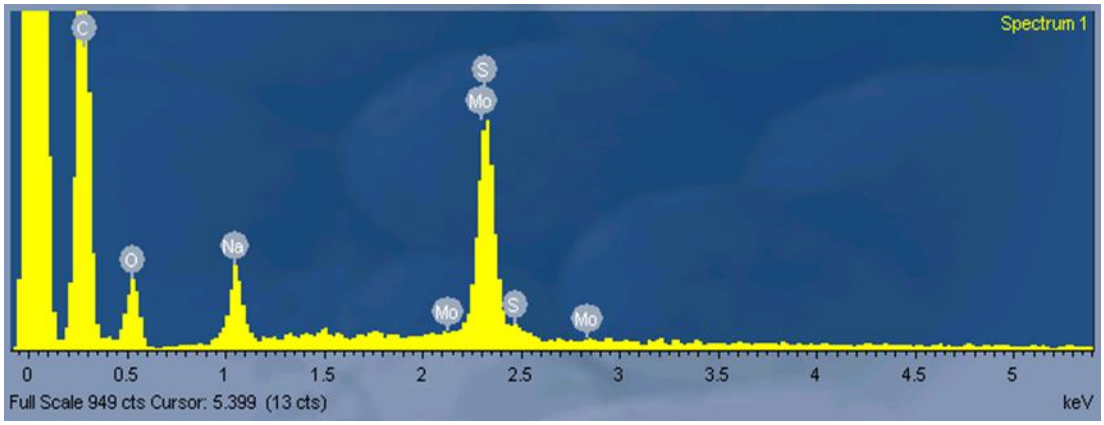

Figure 5.9: EDX spectrum of PPy grown in H_2O with $Mo^0(CO)_4$(Bipy) and NaDS.

Therefore, it appeared that the metal carbonyl species, $M^0(CO)_4$(Bipy) (M = Cr and Mo), could not be effectively entrapped within the PPy film by the methods employed. This evidence reaffirmed the opinion, that with regards to this study, a better approach would be to covalently bind the $M^0(CO)_4$(Bipy) species to the Py moiety for efficient incorporation within the polymer film.

5.2.2 Synthesis and characterisation of 4,4'-bis-(*N*-propyl-3-pyrrole-carbamoyl)-2,2'-bipyridine ($(PyPrNHCO)_2$Bipy)

5.2.2.1 Synthesis of $(PyPrNHCO)_2$Bipy

The product compound, 4,4'-bis-(*N*-propyl-3-pyrrole-carbamoyl)-2,2'-bipyridine ($(PyPrNHCO)_2$Bipy) was prepared in four steps. Firstly, reduction of PyEtCN to *N*-(3-aminopropyl)pyrrole ($PyPrNH_2$) was performed using lithium aluminium hydride ($LiAlH_4$) (Scheme 5.3 (i)).[42] Secondly, oxidation of 4'4'-dimethyl-2,2'-bipyridine to 2,2'-bipyridine-4,4'-dicarboxylic acid was performed using chromic acid (Scheme

5.3 (ii)),[43] which underwent chlorination to 2,2'-bipyridine-4,4'-diacyl chloride ($(ClCO)_2$Bipy) using thionyl chloride (Scheme 5.3 (iii)).[44] Finally, adapting a method reported by Vickers and co-workers,[45] condensation of $PyPrNH_2$ with 2,2'-bipyridine-4,4' diacyl chloride in the presence of TEA produced the final product, $(PyPrNHCO)_2$Bipy (Scheme 5.3 (iv)).

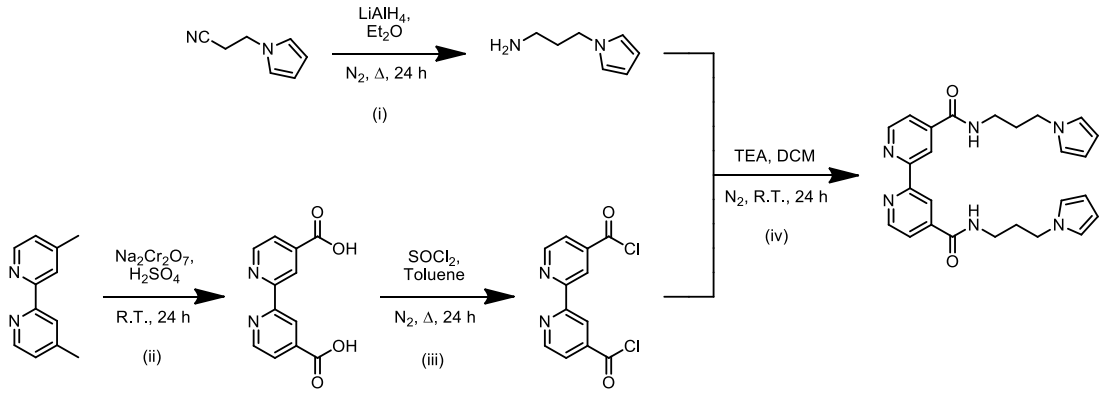

Scheme 5.3: Synthesis of $(PyPrNHCO)_2$Bipy.

The product of the reaction given in Scheme 5.3 was obtained as a pale pink solid at a fair yield of 62%. It was then characterised using FTIR spectroscopy in KBr, ^1H and ^{13}C NMR spectroscopy (COSY, DEPT spectroscopy and HSQC spectroscopy) in deuterated solvents and mass spectrometry.

The FTIR spectral assignments for $(PyPrNHCO)_2$Bipy are reported in Table 5.1 with that of the two reactants. The spectrum displayed a band at 3297 cm^{-1} attributed to the secondary amine N–H stretching mode of the amide functional group, produced during the condensation reaction.[42] The bands at 3063, 2939 and 2875 cm^{-1} were attributed to the C–H stretching modes of the Bipy ring CH, Py ring CH and aliphatic chain CH_2 respectively.[46] The amide (I) band present at 1638 cm^{-1} was assigned to the C=O stretching mode, while the amide (II) band at 1535 cm^{-1} was accredited to the N–H bending mode and the C–N stretching mode.[42] The bands representative of the N–H stretching mode and the amide (I) and (II) modes were indicative of successful condensation, resulting with formation of the amide functional group. The bands at 1592 and 1501 cm^{-1} were attributed to the Bipy and Py ring stretching vibrations[47] respectively, while the band at 1555 cm^{-1} could be a contribution from

both the ring stretching vibrations and the C=N stretching mode of the Bipy.[48] The bands at 1355 and 1088 cm^{-1} were assigned to the C–H in plane vibrations and the band at 1284 cm^{-1} was attributed to the C–N stretching mode of both the Bipy and Py rings.[48] The bands at 895 and 727 cm^{-1} correspond to the C_{β}–H and C_{α}–H out of plane bending modes on the Py ring respectively.[49]

Table 5.1: FTIR spectral data (cm^{-1}) for the product $(PyPrNHCO)_2Bipy$.

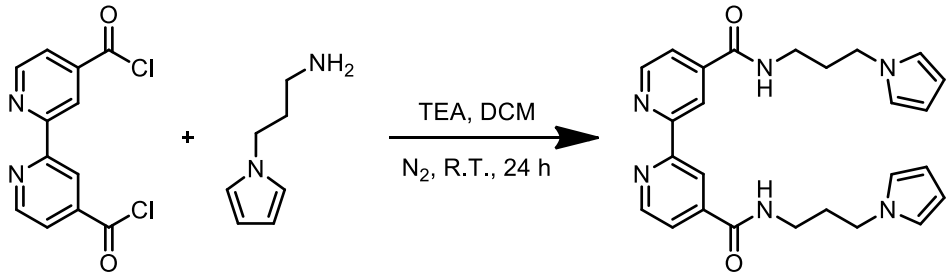

Vibration	Product / Reactant (cm^{-1})		
	$(PyPrNHCO)_2$ Bipy	**$PyPrNH_2$**	**$(ClCO)_2Bipy$**
ν_{as}(N–H)	-	3368	-
ν_{s}(N–H)	3297	3298	-
ν(C–H)	3063	3097	3067
ν_{as}(C–H)	2939	2930	-
ν_{s}(C–H)	2875	2869	-
ν(C=O)	1638	-	1754
ν(Bipy ring)	1592	-	1586
ν(C=N)	1555	-	1550
(N–H)/(C–N)	1535	-	
ν(Py ring)	1501	1554; 1501	-
C–H in plane	1355	1353	1356
ν(C–N)	1284	1280	1291
C–H in plane	1088	1090	1101
(C_{β}–H) out of plane	895	875	907
(C_{α}–H) out of plane	727	726	701

The ^{1}H and ^{13}C NMR spectroscopic assignments for $(PyPrNHCO)_2Bipy$ are reported in Table 5.2. It was found that the NMR spectral data was comparable to data reported by Beer and co-workers for the imidazole analogue.[45] The ^{1}H NMR spectrum displayed a peak positioned at 8.95 ppm integrating for 2H, which was representative of the nitrogen bound hydrogens of the amide functional groups. As the hydrogens were coupled to the adjacent alkyl chain CH_2, the N–H signal was split to give a triplet peak possessing a *J* value of 5.1 Hz. In $(CD_3)_2SO$, the strong H-bonding of the amide N–H to the sulfoxide oxygen deshields the amide proton, inducing a significant upfield shift (2.96 ppm) in $CDCl_3$ to 5.99 ppm.

The signals representative of the Bipy protons were observed in the expected aromatic region of the spectrum and integrated correctly.[45] The Bipy 6,6' protons were coupled to the Bipy 5,5' protons, thus producing a doublet peak observed at 8.87 ppm, which possessed a *J* value of 4.8 Hz. The Bipy 5,5' protons were coupled to both the Bipy 6,6' protons and the Bipy 3,3' protons and this splitting produced a doublet of doublets, observed at 7.85 ppm, which possessed *J* values of 0.9 and 4.8 Hz respectively. The *J* value of 0.9 Hz was expected for a ^{4}J aromatic meta coupling, while the *J* value of 4.8 Hz correlates correctly with that of the Bipy 6,6' protons. The signal representative of the Bipy 3,3' protons displayed no coupling with the 5,5' protons and was therefore observed as a singlet peak at 8.80 ppm.

The signals representative of the Py protons were observed in the expected vinylic region of the spectrum and integrated correctly with the other signals.[42,50] In the spectrum the Py C_α–H protons (12,12') were coupled to the Py C_β–H protons (13,13') producing a triplet peak observed at 6.79 ppm. The Py C_β–H protons (13,13') also displayed a triplet peak positioned at 5.99 ppm, with both signals possessing the correctly correlating *J* value of 1.8 Hz.

The signals representative of the CH_2 protons were observed at various positions between 1.99 - 3.96 ppm, due to the deshielding of certain CH_2 protons by their adjacent electronegative nitrogen atom containing moieties.[42,45,50] The CH_2 protons (9,9'), which integrated for 4H, were coupled to both the mid-chain CH_2 protons (10,10') and the amide N–H proton. In $(CD_3)_2SO$, the resulting signal was positioned at 3.29 ppm, but the splitting was indiscernible due to obstruction by a signal for

$(CD_3)_2SO$, nevertheless, upon analysis in $CDCl_3$ a quartet peak, which integrated for 4H was confirmed. The couplings of the proton signals were confirmed *via* ^1H 2D COSY.

The ^{13}C NMR spectrum displayed a downfield signal representative of the amide carbonyl carbon observed in the amide region of the spectrum at 164.7 ppm. The signals representative of the Bipy carbons were observed in the expected aromatic region of the spectrum.[45] The Bipy 3,3', 5,5' and 6,6' carbons were assigned to the signals at 118.2, 121.9 and 150.0 ppm respectively, using 2D HSQC spectroscopy to clarify the ^1H-^{13}C couplings. The downfield shift of the Bipy 6,6' carbons compared to the Bipy 3,3' and 5,5' carbons occurred due to the presence of the adjacent nitrogen atom within the ring system. Using DEPTQ135 spectroscopy, the signals at 142.9 and 155.5 ppm were observed to correlate to the Bipy quaternary carbons. These signals were assigned to the 4,4' and 2,2' position respectively, due to the greater deshielding of the Bipy nitrogen at the 1,1' position, compared to that of the amide substituent at the 4,4' position.

The signals representative of the Py carbons were observed in the expected vinylic region of the spectrum.[36,43] More specifically, the Py C_α–H carbon (12,12') peak was observed at 120.5 ppm, due to deshielding by the nitrogen on the Py ring, while the Py C_β–H carbon (13,13') peak was positioned more upfield, at a chemical shift of 107.5 ppm. The 2D HSQC spectrum was analysed to confirm the ^1H-^{13}C couplings. The signals representative of the CH_2 carbons were all observed in the sp^3 alkane region of the spectrum,[42,45,50] resonating at 31.0, 37.0 and 46.4 ppm and once again, analysis of the 2D HSQC spectrum was utilised to confirm the ^1H-^{13}C couplings.

Table 5.2: ^{13}C and ^{1}H NMR spectral data (δ in ppm) of $(PyPrNHCO)_2Bipy$ in $(CD_3)_2SO$ (75.5 MHz and 300 MHz respectively).

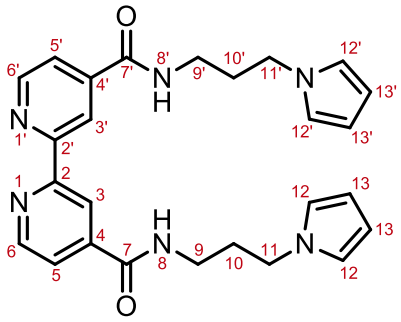

C / H	(PyPrNHCO)₂Bipy (ppm)	
	δ ^{13}C	δ ^{1}H (m); *J* Hz
2,2’	155.5	-
3,3’	118.2	8.80 (s)
4,4’	142.9	-
5,5’	121.9	7.85 (dd); 0.9, 4.8
6,6’	150.0	8.87 (d); 4.8
7,7’	164.7	-
8,8’	-	8.95 (t); 5.1
9,9’	37.0	3.29 (pt); 6.0
10,10’	31.0	1.99 (m)
11,11’	46.4	3.96 (pt); 6.9
12,12’	120.5	6.79 (pt); 1.8
13,13’	107.5	5.99 (pt); 1.8

The calculated exact mass for protonated $(PyPrNHCO)_2Bipy$ was found to be 457.2347 g mol^{-1}, while mass spectrometry of the sample produced a measured accurate mass of 457.2326 g mol^{-1}, yielding a mass measurement error of -4.48 ppm.

5.2.2.2 Polymerisation of (PyPrNHCO)₂Bipy

Upon completion of chemical characterisation, the $(PyPrNHCO)_2Bipy$ monomer was first polymerised using chemical oxidation. Polymerisation was carried out on a glass substrate, which had been roughened with sand paper (400 grit) to increase surface

area and improve adhesion.[51] Once the substrate had been cleaned, $(PyPrNHCO)_2Bipy$ (15 mM) was applied to the surface as a thin layer. The glass substrate modified with the monomer was submerged in DCM containing iron trichloride hexahydrate (25 mM) as oxidant/dopant, and 60% perchloric acid ($HClO_4$) (100 mM) in a Teflon beaker. Upon addition of $(PyPrNHCO)_2Bipy$ to the reaction mixture, polymerisation proceeded and a black film was formed on the glass substrate. After 18 hours the slide was removed from the mixture and extensively washed with DCM, H_2O, MeOH and DCM and dried *in vacuo*. The polymer film was characterised using Attenuated Total Reflectance (ATR)-FTIR spectroscopy. The ATR-FTIR spectrum of the chemically oxidised poly[$(PyPrNHCO)_2Bipy$] (Figure 5.10 (a)) was compared to that of the FTIR spectrum obtained for the $(PyPrNHCO)_2Bipy$ monomer in KBr (Figure 5.10 (b)). The poly[$(PyPrNHCO)_2Bipy$] spectrum possessed a broad band at 3393 cm^{-1}, which was attributed to residual water and the small bands (2960 cm^{-1} and 2869 cm^{-1}), partially masked by this band, were attributed to CH aliphatic stretching vibrations.[46] The small band observable at 1707 cm^{-1} was accredited to overoxidation of the PPy backbone during polymerisation, induced by hydroxide ions, contributed from H_2O in the system.[52,53] The broad band at 1631 cm^{-1} was attributed to the amide (I) carbonyl stretch,[42] which possibly masked the stretching vibration of the Bipy ring.[47] The band at 1554 cm^{-1} was representative of the stretching vibration of Py,[48] while it was possible that the amide (II) secondary amide bend was masked by this band.[42] The presence of a band for the perchlorate doping anion was observed at approx. 1109 cm^{-1}.[54,55]

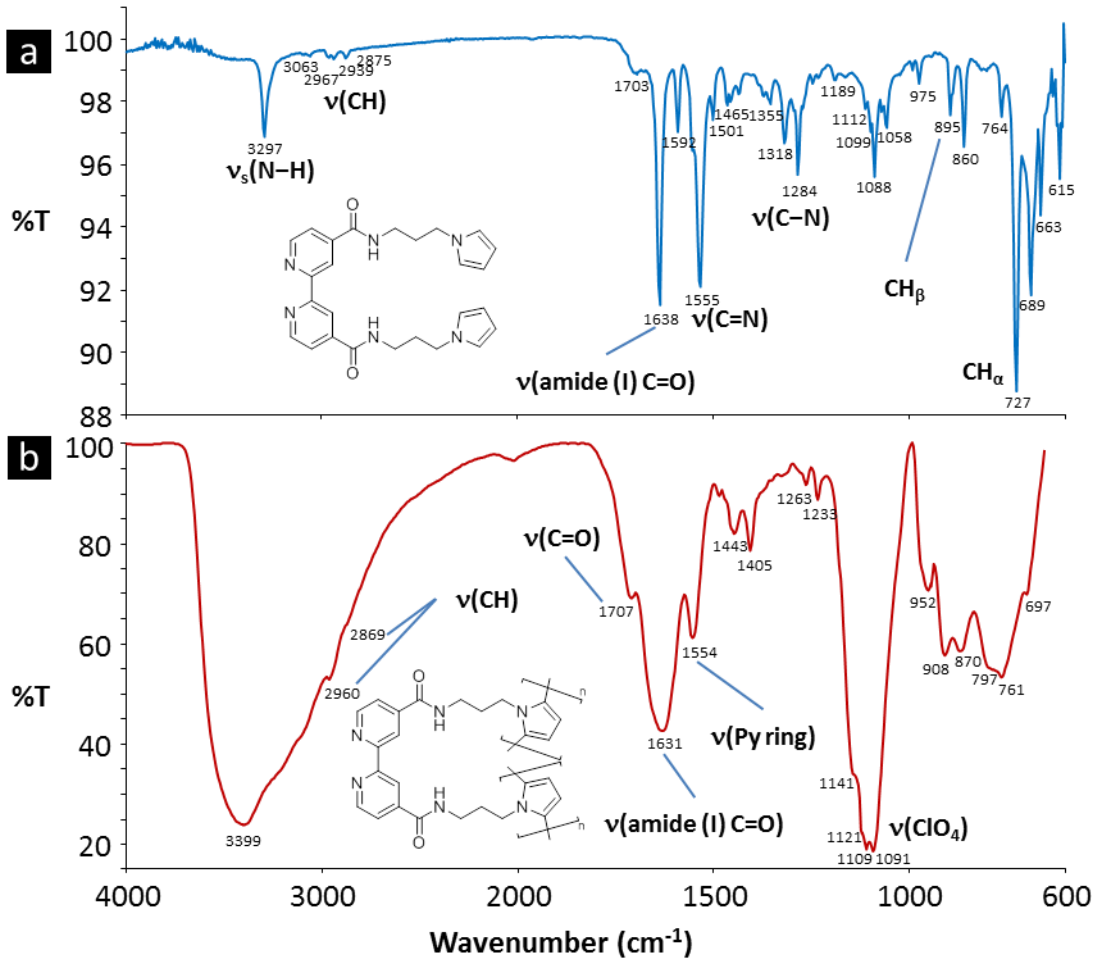

Figure 5.10: FTIR spectra of (a) chemically oxidised poly[$(PyPrNHCO)_2Bipy$] film obtained using ATR-FTIR spectroscopy (—) and (b) $(PyPrNHCO)_2Bipy$ monomer (—) performed at 2 cm^{-1} resolution.

Once it was confirmed that the monomer could undergo chemical oxidation, the monomer was then subjected to electrochemical deposition on a polished Au substrate. This deposition of $(PyPrNHCO)_2Bipy$ (100 mM) was performed in a solution of MeCN containing $LiClO_4$ (200 mM). It was essential that $HClO_4$ (550 mM) was added to the polymerisation medium in order to protonate the basic Bipy nitrogen atoms yielding the soluble $[(PyPrNHCO)_2BipyH_2]^{2+}$ species. Work reported by Moutet and co-workers has shown that electrochemical deposition of a similar compound consisting of a Bipy unit bound to Py would not polymerise in a basic polymerisation medium, but upon addition of $HClO_4$, underwent efficient deposition.[47,56,57]

The polymer was deposited using a range of E_{app}; 1.000 - 1.150 V vs. SCE in 0.050 V increments, as polymerisation below these values was observed to be very slow from *j-t* and *q-t* transients. The formation of a visible film on the substrate did not occur below 0.900 V vs. SCE but above this E_{ox}, black films were observed to adhere to the electrode surface. Once the E_{app} was above 1.050 V vs. SCE, there was a large increase in current density and charge density over time, due to the rate of deposition (Figure 5.11 (—) 1.100 and (—) 1.150 V vs. SCE) that was occurring at the electrode surface.[58-63] This was accompanied by adhesion of a black film on the substrate, which increased in opaqueness with E_{app}.

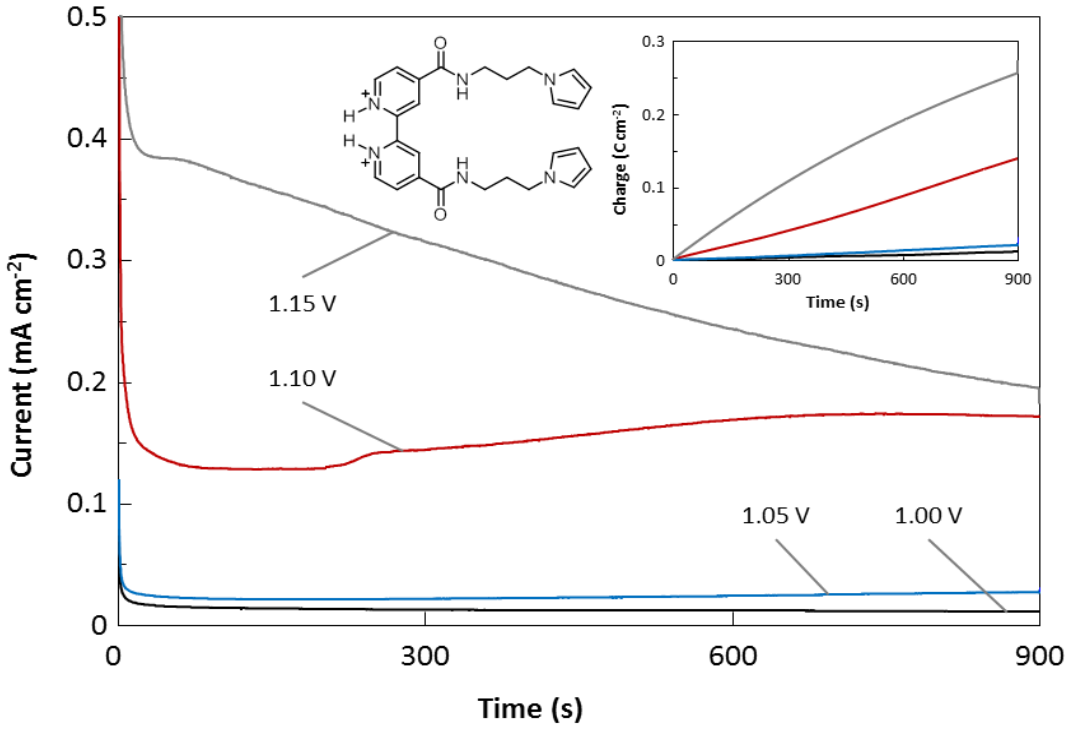

Figure 5.11: *j-t* transients of $[(PyPrNHCO)_2BipyH_2]^{2+}$ during deposition on the Au substrate at 1.000 (—), 1.050 (—), 1.100 (—) and 1.150 (—) V vs. SCE in MeCN with tetrabutylammonium perchlorate (TBAP) (100 mM) and $HClO_4$ (550 mM). Inset: *q-t* transients of synonymous experiment.

The electrochemical characterisation of the poly$[(PyPrNHCO)_2BipyH_2]^{2+}$ consisted of performing CV between 0.000 - 0.900 V vs. Ag/Ag^+, with the polymer modified electrode submerged in monomer free MeCN containing $TBAClO_4$ (200 mM). The CVs, performed over 20 cycles at 100 mV s^{-1} (Figure 5.12), showed quite good stability of the polymer, as the current density only slightly increases during

scanning. The redox couple, ($E_{1/2}$ = 0.441 V vs. Ag/Ag^+, ΔE_p = 0.118 V) with j_c/j_a = 0.85, was attributed to the one-electron, *quasi*-reversible oxidation and reduction of the PPy backbone present in the poly[$(PyPrNHCO)_2BipyH_2]^{2+}$ film.[56] This couple was assigned to be arising from the redox activity of the PPy backbone, as was previously observed for the *N*-substituted PPy systems studied in Chapter 3 (Section 3.3.1 - 3.3.5) and Chapter 4 (Section 4.2.2.2). Within the window studied, no redox activity was observed for the Bipy moiety, which has been observed in the literature.[64] During CV, when the polymer was cycled to more reductive potentials (>-1.000 V vs. Ag/Ag^+), no redox couple was observed, which could be assigned to the Bipy redox couple, anticipated to be positioned between -3.000 - (-1.000) V vs. Ag/Ag^+.[47,56,57] However, previous studies have shown that the presence of a Bipy redox couple will be impaired by even the most miniscule amounts of water present in the electrochemical media.[9]

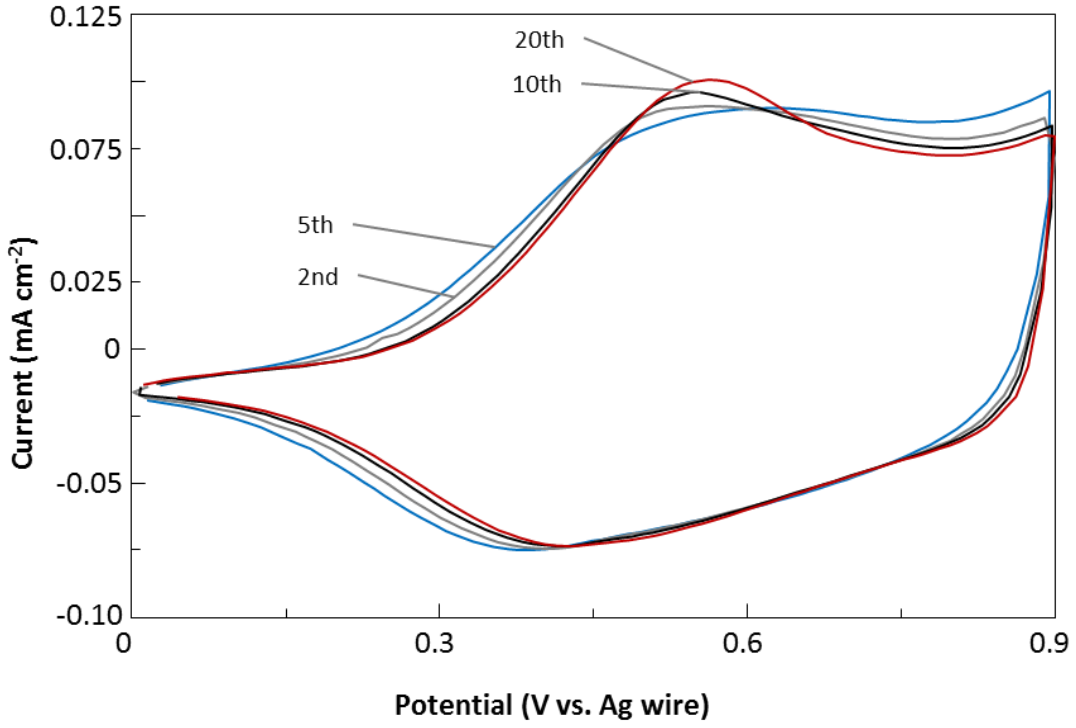

Figure 5.12: CVs of poly[$(PyPrNHCO)_2Bipy$] on a GCE in MeCN with $LiClO_4$ (200 mM), at the 2nd (—), 5th (—), 10th (—) and 20th (—) cycle, within a potential window of 0.000 - 0.900 V vs. Ag/Ag^+ at 100 mV s^{-1}.

It was observed that the $[(PyPrNHCO)_2BipyH_2]^{2+}$ monomer would only deposit efficiently on the substrate at a E_{app} of approx. 1.000 V vs. SCE, which is typical for *N*-substituted Py monomers,[56,57] and it was anticipated that the metal carbonyl analogue would require a similar E_{app} for effective polymerisation. Therefore, a study was performed to investigate the possibility of successfully lowering the E_{ox} required for the polymerisation of $(PyPrNHCO)_2Bipy$. This was extremely important, as it has been already reported (Section 5.2.1.1) that the E_{app} required to electrochemically release CO from the $Mo^0(CO)_4(Bipy)$ species was approx. 0.500 V vs. Ag/Ag^+. By lowering the E_{ox} required for $(PyPrNHCO)_2Bipy$ polymerisation, the unintentional release of CO from the metal carbonyl monomer analogue could be circumvented, during polymerisation. Block co-polymerisation can be utilised to decrease the E_{ox} required for the polymerisation of successive monomer species in a system.[65] It has also been reported that PPy films already adhered to the surface of the electrode encourages the polymerisation of *N*-substituted Py monomers.[66] Therefore in our diblock co-polymer system, the substrate (Figure 5.13 (a)) would have an E_{ox} applied to it in the presence of Py monomer (Figure 5.13 (b)); yielding a film of PPy adhered to the substrate (**A**-block) (Figure 5.13 (c)). This procedure would be succeeded by the electrodeposition of $[(PyPrNHCO)_2BipyH_2]^{2+}$ monomer on to the PPy-modified electrode (Figure 5.13 (d)), producing a film of poly$[(PyPrNHCO)_2Bipy]$ (**B**-block) covalently bound to the PPy film (**A**-block) (Figure 5.13 (e)).

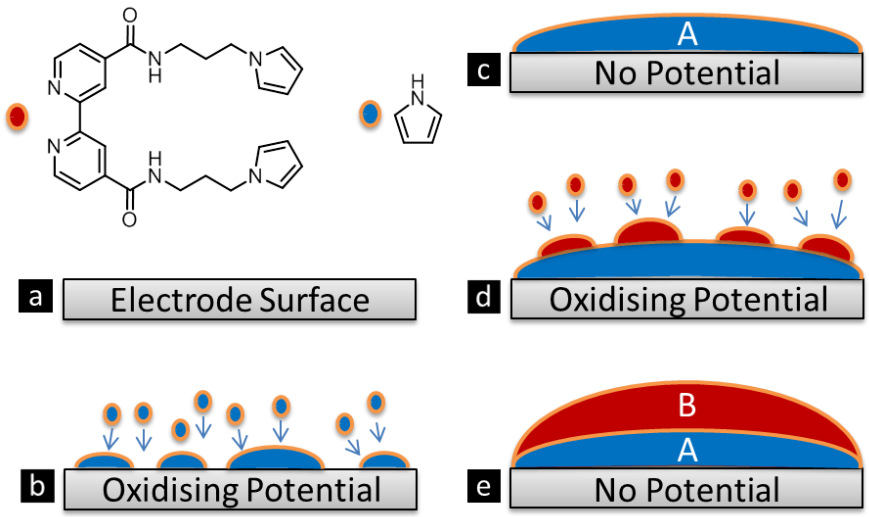

Figure 5.13: Electrochemical co-polymerisation of (b) Py (A-block monomer) and (d) $[(PyPrNHCO)_2BipyH_2]^{2+}$ (B-block monomer) producing (e) diblock co-polymer (AB) film.

Deposition of the Py (100 mM) monomer was performed in a solution of H_2O containing $LiClO_4$ (200 mM), applying an E_{ox} of 0.650 V vs. SCE until a q of 0.80 C cm^{-2} was attained. The efficient deposition of Py monomer was confirmed by the deposition of thin black film on the substrate, an increase in the *j-t* transient from a *j-t* minimum (t_0,j_0) of 0.661 mA cm^{-2} at 21 s (Figure 5.13 (—)), representing nucleation on the substrate[58-62] and the increase in *q-t* transients ((Figure 5.14 (—) inset), representing the amount of polymer depositing on the surface.[63] The polymer was then removed from the solution and washed with MeCN and transferred to a fresh solution, which contained the next monomer in our diblock co-polymer system, $(PyPrNHCO)_2Bipy$ (55 mM), accompanied by $LiClO_4$ (200 mM) and $HClO_4$ (550 mM) in MeCN.

A range of E_{app} were investigated (0.650 - 0.900 V vs. SCE in 50 mV increments) and it was found that oxidation of the $(PyPrNHCO)_2Bipy$ monomer could occur at quite low potentials (E_{app} of 0.650 V vs. SCE), when compared to the familiar oxidation (approx. 1.000 V vs. SCE) of *N*-substituted Py monomers.[67] During investigation, the application of 0.750 V vs. SCE produced the most efficient deposition of the $(PyPrNHCO)_2Bipy$ monomer, as the *j-t* transient possessed a *j-t* maximum (t_{max},j_{max}) of 3.584 mA cm^{-2} at 58 s (Figure 5.14 (—)), while a q of 1.90 C cm^{-2} was attained. Comparison was made between the *j-t* transients obtained, with that representing the regular electrodeposition process of poly$[(PyPrNHCO)_2BipyH_2]^{2+}$; $(PyPrNHCO)_2Bipy$ (55 mM) in MeCN with $LiClO_4$ (200 mM) and $HClO_4$ (550 mM) at 1.150 V vs. SCE, which was applied until 0.25 C cm^{-2} was attained (Figure 5.14 (—)). The *j-t* transient produced from the regular deposition process possessed a t_{max},j_{max} of 0.383 mA cm^{-2} at 48 s, which is approx. 10 times smaller than that occurring during the electrodeposition of poly$[(PyPrNHCO)_2Bipy]$ using block co-polymerisation.

The increased t_{max},j_{max} possessed by the *j-t* transient for the block co-polymerisation of poly$[(PyPrNHCO)_2BipyH_2]^{2+}$ on to the PPy film (Figure 5.14 (—)), when compared to that produced during regular poly$[(PyPrNHCO)_2BipyH_2]^{2+}$ deposition (Figure 5.14 (—)) could be attributed to a number of factors. It would be fair to anticipate that an increase in current density would occur due to the assumption that

the surface area has increased, upon electrodeposition of PPy (**A**-block film) on to the electrode (Figure 5.14 (—)). Also, the already modified PPy film would possess sites of polymerisation that contribute to the increased current density value upon application of the E_{ox}, which has also been increased to 0.750 V vs. SCE, further promoting Py polymerisation, but this should be negligible due to the presence of $HClO_4$, which could chemically polymerise these sites before the E_{ox} was applied, as it is known that Py oxidation is acid catalysed.[68,69]

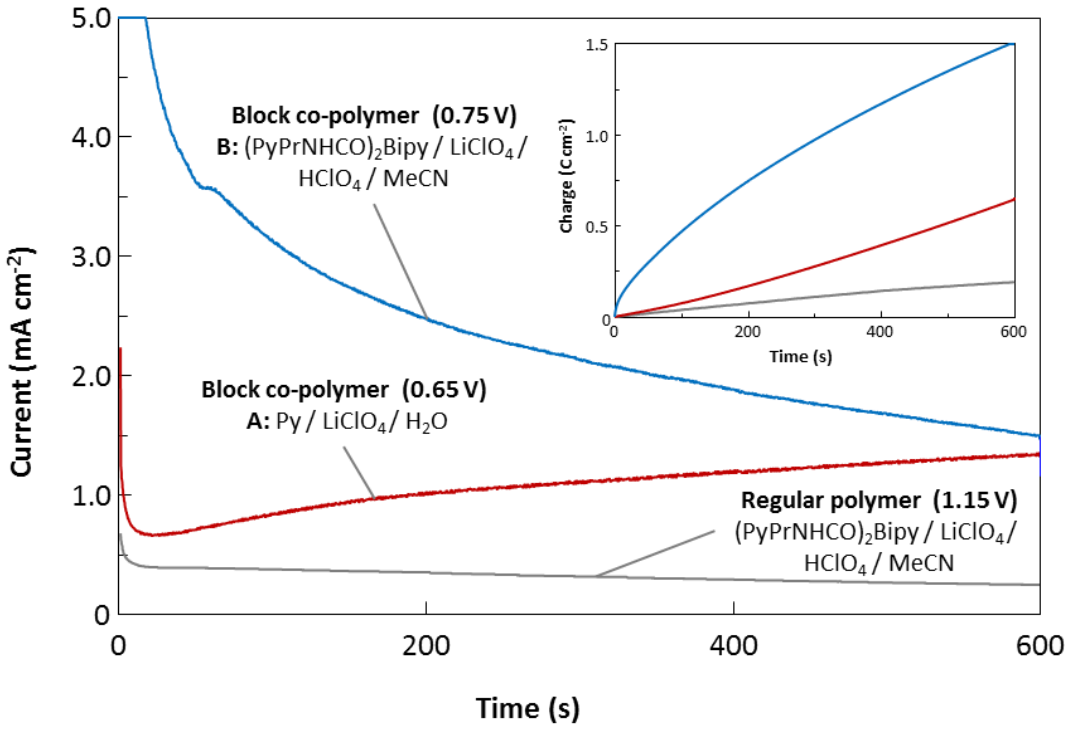

Figure 5.14: Diblock co-polymerisation (vs. SCE) beginning with electrodeposition of A-block film: Py (100 mM) in H_2O with $LiClO_4$ (200 mM) at 0.650 V until 0.80 C cm^{-2} was attained (—), succeeded by electrodeposition of B-block film: $(PyPrNHCO)_2Bipy$ (55 mM) in MeCN with $LiClO_4$ (200 mM) and $HClO_4$ (550 mM) at 0.750 V until 1.90 C cm^{-2} was attained (—). Regular polymerisation of $(PyPrNHCO)_2Bipy$ (55 mM) in MeCN with $LiClO_4$ (200 mM) and $HClO_4$ (550 mM) at 1.150 V until 0.25 C cm^{-2} was attained (—).

Although there are factors, which could contribute to the increased current density t_{max},j_{max} possessed by the *j-t* transient for the block co-polymerisation of poly$[(PyPrNHCO)_2BipyH_2]^{2+}$ on to the PPy film (Figure 5.14 (—)), this does not negate the observation that poly$[(PyPrNHCO)_2BipyH_2]^{2+}$ could be deposited on to the PPy-modified electrode at the significantly decreased E_{ox} of 0.750 V vs. SCE,

therefore confirming that block co-polymerisation was an efficient method of depositing *N*-substituted PPy films at a decreased E_{app}. This result was important as this methodology could possess the potential, to be employed during deposition of the complexed, Group 6 TM form of the $(PyPrNHCO)_2Bipy$ monomer, which may be required if post-functionalisation of the poly[$(PyPrNHCO)_2Bipy$] modified electrode was not successful.

5.2.3 Synthesis, characterisation and electrochemical characterisation of $M^0(CO)_4((PyPrNHCO)_2Bipy)$ (M = Mo, Cr, W)

5.2.3.1 Synthesis and characterisation of $M^0(CO)_4((PyPrNHCO)_2Bipy)$ (M = Mo, Cr, W)

The $(PyPrNHCO)_2Bipy$ tetracarbonyl Group 6 complexes were prepared by ligand substitution of $Mo^0(CO)_6$, with the bidentate Py di-substituted ligand through MAS, using a method adapted from Green and co-workers[36] and Paz and co-workers[37] shown in Scheme 5.4.

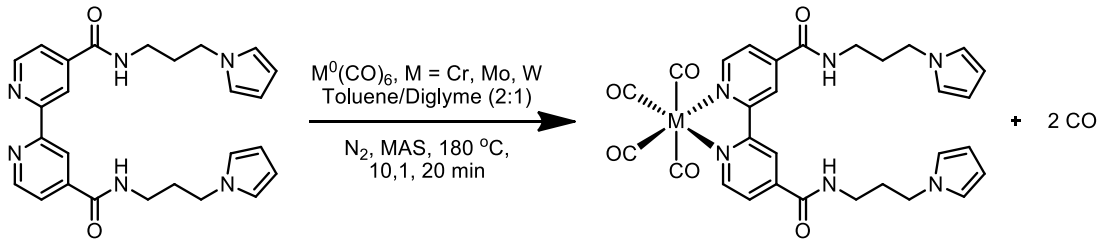

Scheme 5.4: Synthesis of $M^0(CO)_4((PyPrNHCO)_2Bipy)$ (M = Cr, Mo, W).

The $M^0(CO)_4((PyPrNHCO)_2Bipy)$ (M = Cr, Mo, W) complexes were obtained as red solids, but with impurities present in the form of the unreacted ligand, $(PyPrNHCO)_2Bipy$. Purification of the complexes proved difficult as upon separation on the column we obtained the polymerised form of the complex. The ratio of $(PyPrNHCO)_2Bipy$:product complex was estimated to be 36:64 and 45:55 for the chromium and tungsten complex respectively. The molybdenum complex was isolated in a 95% yield. The impure mixtures and the molybdenum complex were characterised using FTIR spectroscopy in KBr, ^1H and ^{13}C NMR spectroscopy

(COSY, DEPT spectroscopy and HSQC spectroscopy) in deuterated DMSO and mass spectrometry.

The ^{1}H NMR spectroscopic assignments for the three complexes, $M^{0}(CO)_4((PyPrNHCO)_2Bipy)$ (M = Cr, Mo, W) are reported in Table 5.3 and are displayed relative to the chemical shifts of the $(PyPrNHCO)_2Bipy$ ligand. It can be seen from the table that signals for the CH_2[42,45,50] and Py[42,50] protons do not appear to shift position in the spectrum, upon complexation with any of the three metal carbonyls. These proton signals, their chemical shifts and coupling constants have been described for the ligand, $(PyPrNHCO)_2Bipy$, previously in Section 5.2.2.1 and may be applied to that of the three complexes. The similar chemical shifts of the CH_2 and Py protons for the ligand and metal complexes were expected, as these protons are so far removed from the deshielding effect of the metal carbonyl that no change in chemical shift should be observed.

The Bipy and amide protons though were within close proximity of the chelating Bipy rings, so a deshielding effect was observed due to the coordinated metal carbonyl. It is well established that the withdrawing ability of Group 6 pentacarbonyl species increases in the order of $W(CO)_5 > Mo(CO)_5 > Cr(CO)_5$ and is due to a fractional charge influenc, it is likely that the same order holds true for the tetracarbonyl analogues.[70] The signals representative of the Bipy protons were observed in the expected aromatic region of the spectrum and integrated correctly.[37] Specifically, the Bipy 6,6' protons were adjacent to the chelating nitrogen atoms of the Bipy rings, so a downfield shift of 0.09 ppm, from 8.87 ppm to 8.96 ppm was observed, upon coordination of the ligand to the tetracarbonyl chromium. Coordination of the more withdrawing tetracarbonyl molybdenum and tungsten to the ligand, produced larger downfield shifts (especially tungsten), which increased from 9.13 to 9.23 ppm respectively. The adjacent ring position, Bipy 5,5', also displayed a downfield shift for its protons signal, upon coordination of the ligand to the tetracarbonyl chromium, increasing significantly from 7.85 to 7.95 ppm. Coordination with the molybdenum and tungsten carbonyls did not produce an increased deshielding effect, as only a small downfield shift, of 0.03 and 0.01 ppm from the chromium complex resonance position, was observed respectively. The

Bipy 3,3' signals displayed a shift in resonance position downfield, from 8.80 to 8.86, 8.96 and 9.02 ppm, for the chromium, molybdenum and tungsten congeners respectively.

Finally, the amide protons (7,7'), which had their signal positioned initially at 8.95 ppm for the ligand, were not affected by complexation with the chromium complex but were deshielded by the molybdenum and tungsten metal carbonyls, producing resonances at 8.94, 9.08 and 9.11 ppm respectively. All the peaks in the spectra integrated for their appropriate number of protons and the *J* values correlated correctly, while coupling was confirmed by ^{1}H-^{1}H COSY.

Table 5.3: ^{1}H NMR spectral data (δ in ppm) of $M^{0}(CO)_{4}((PyPrNHCO)_{2}Bipy)$ (M = Cr, Mo, W) in $(CD_{3})_{2}SO$ (2.54 ppm) (300 MHz).

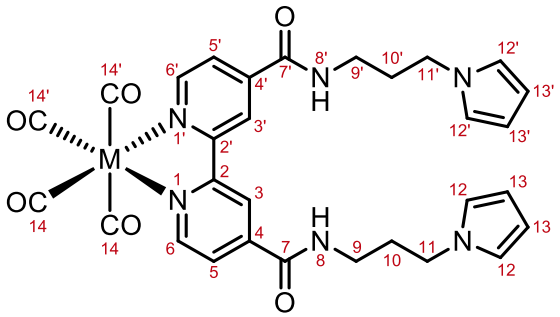

C / H	$M^{0}(CO)_{4}(PyPrNHCO)_{2}Bipy)$ (δ ^{1}H (m); *J* Hz)			
	$(PyPrNHCO)_{2}$ Bipy	**M = Cr**	**M = Mo**	**M = W**
3,3'	8.80 (s)	8.86 (s)	8.96 (s)	9.02 (s)
5,5'	7.85 (dd); 0.9, 4.8	7.95 (dd); 1.2, 4.8	7.98 (dd); 1.2, 5.1	7.99 (dd); 1.2, 5.7
6,6'	8.87 (d); 4.8	8.96 (d); 5.1	9.13 (d); 5.1	9.23 (d); 5.1
8,8'	8.95 (t); 5.1	8.94 (t): 5.1	9.08 (t); 5.1	9.11 (t); 5.1
9,9'	3.29 (q); 6.0	3.34 (q)	3.36 (q)	3.38 (q)
10,10'	1.99 (m)	1.98 (m)	2.00 (m)	2.00 (m)
11,11'	3.96 (t); 6.9	3.96 (t); 7.5	3.98 (t); 6.9	3.99 (t); 6.9
12,12'	6.79 (t); 1.8	6.79 (t); 1.8	6.79 (t); 1.8	6.79 (t); 1.8
13,13'	5.99 (t); 1.8	5.99 (t); 1.8	5.99 (t); 1.8	5.99 (t); 1.8

The ^{13}C NMR spectroscopic assignments for the three complexes, $M^0(CO)_4((PyPrNHCO)_2Bipy)$ (M = Cr, Mo, W) are reported in Table 5.4, accompanied by the resonance positions of the uncoordinated $(PyPrNHCO)_2Bipy$ ligand for comparison. It was clearly evident from observing the table below, upon coordination of any of the three Group 6 metal carbonyls to the $(PyPrNHCO)_2Bipy$ ligand that the carbon signals did not exhibit any effects from deshielding. It can be seen from the table that signals for the CH_2 and Py protons, do not appear to shift position in the spectrum, upon complexation of the ligand with any of the three metal carbonyls. These carbon signal assignments and their chemical shifts have been described for the ligand, $(PyPrNHCO)_2Bipy$, previously in Section 5.2.2.1 and those results may be applied to that of the three complexes. The ^{13}C NMR spectra of the complexes displayed a carbonyl signal at approx. 204 ppm. The downfield position was indicative of the presence of the metal bound C≡O groups.[37]

Table 5.4: ^{13}C NMR spectral data (δ in ppm) of $M^0(PyPrNHCO)_2Bipy$ (M = Cr, Mo, W) in $(CD_3)_2SO$ (75.5 MHz).

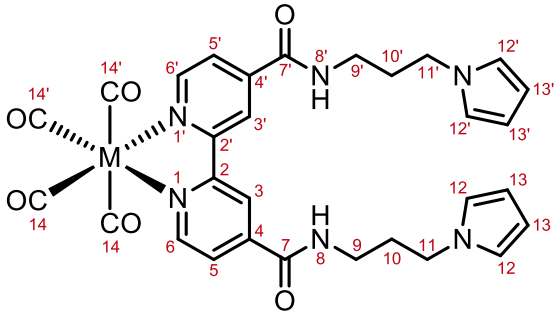

C / H	$M^0(CO)_4(LL)$ (LL = $(PyPrNHCO)_2Bipy$) (ppm)			
	δ ^{13}C			
	LL	M = Cr	M = Mo	M = W
2,2’	155.5	155.5	154.7	151.0
3,3’	118.2	119.3	118.2	122.0
4,4’	142.9	142.9	143.5	143.3
5,5’	121.9	123.4	123.9	124.9
6,6’	150.0	150.9	153.1	156.8
7,7’	164.7	165.0	163.5	163.5
9,9’	37.0	37.0	37.1	37.2
10,10’	31.0	31.0	31.0	31.0
11,11’	46.4	46.4	46.4	46.3
12,12’	120.5	120.6	120.6	120.6
13,13’	107.5	107.6	107.6	107.6
14,14’	-	206.5	204.8	201.4

The FTIR spectral data of the $M^0(CO)_4((PyPrNHCO)_2Bipy)$ (M = Cr, Mo, W) complexes are reported in Table 5.5, with that of $M^0(CO)_4(Bipy)$ (M = Cr, Mo, W). FTIR spectra for the high energy carbonyl region of each complex can be observed in Figure 5.15. The three complexes possessed intense bands at approx. 2015 - 1820 cm^{-1}, indicating successful reaction of the respective hexavalent metal carbonyls with the $(PyPrNHCO)_2Bipy$ ligand. The hexavalent metal carbonyls, $M^0(CO)_6$, (M = Cr, Mo, W), possess FTIR spectroscopic assignments at 1999, 2000

and 1999 cm^{-1} respectively,[71] which were not present in their respective spectra indicating that this starting material was not present as an impurity. The bands present in the spectra of the three $M^0(CO)_4((PyPrNHCO)_2Bipy)$ (M = Cr, Mo, W) complexes relate well to the reported FTIR spectral data of the structurally similar tetracarbonyl α-imine Group 6 complexes, $M^0(CO)_4(Bipy)$ (M = Cr, Mo, W).

Table 5.5: FTIR spectral data (cm^{-1}) for $M^0(CO)_4(LL)$ complexes (M = Cr, Mo, W; LL = $(PyPrNHCO)_2Bipy$, Bipy).

Vibration	**$M^0(CO)_4(LL)$ (cm^{-1})**					
	LL = $(PyPrNHCO)_2Bipy$[a]			**LL = Bipy[b,72]**		
	M = Cr	**M = Mo**	**M = W**	**M = Cr**	**M = Mo**	**M = W**
ν(C≡O)	2006	2011	2005	2010 (m)	2014 (m)	2008 (m)
ν(C≡O)	1899	1902	1890	1908 (vs)	1911 (vs)	1900 (vs)
ν(C≡O)	1878	1878	1872	1888 (sh)	1882 (sh)	1880 (sh)
ν(C≡O)	1826	1830	1825	1833 (s)	1830 (s)	1829 (s)

[a]Performed in KBr. [b]Performed in $CHCl_3$.[72]

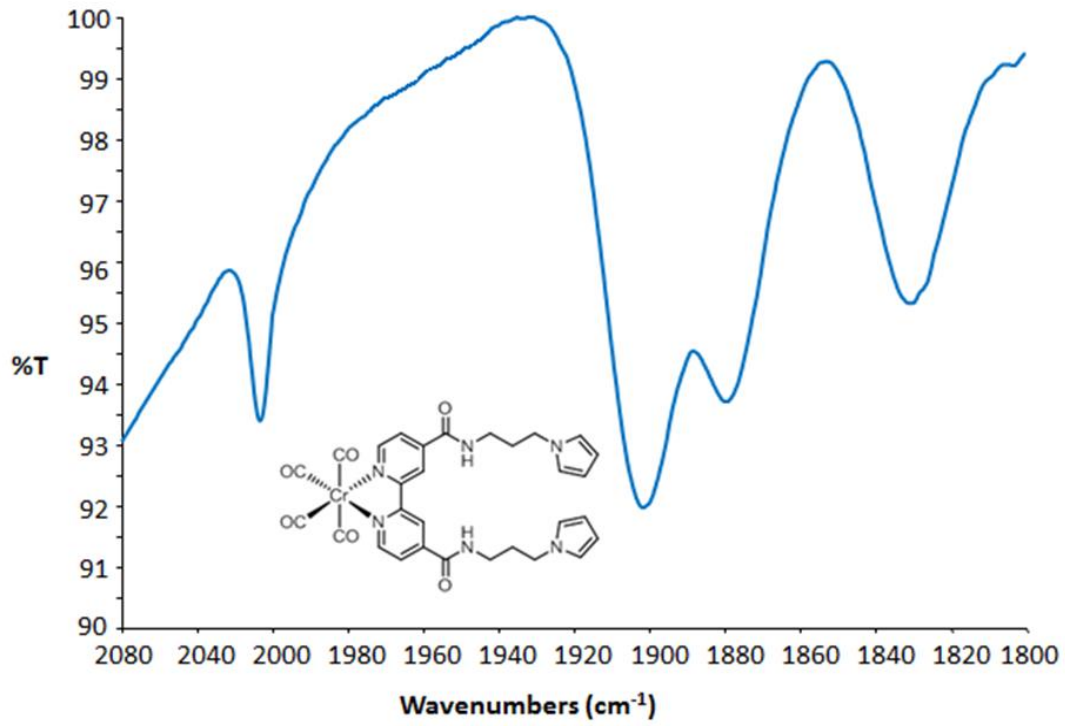

Figure 5.15: FTIR spectrum of $Cr^0(CO)_4((PyPrNHCO)_2Bipy)$ in CH_2Cl_2 performed at a resolution of 2 cm^{-1}.

The calculated exact mass for each complex was determined, while mass spectrometry of the complexes produced measured accurate masses, which were tabulated together and presented in Table 5.6. Using the respective values, the mass measurement error for each complex was also calculated. It can be seen from the table that both the chromium and molybdenum complexes defragment, upon analysis using mass spectrometry, which was also observed for the Bipy congeners.

Table 5.6: Mass spectrometry data for $M^0(CO)_4((PyPrNHCO)_2Bipy)$ complexes (M = Cr, Mo, W).

	$M^0(CO)_4((PyPrNHCO)_2Bipy)$		
	M = Cr	**M = Mo**	**M = W**
Calculated Exact Mass (g mol^{-1})	**M-(Cr(CO)$_4$+H)$^+$** 457.2347	**(M+H-(Mo(CO)$_4$))$^+$** 457.2347	**(M)$^+$** 752.1574
Measured Accurate Mass (g mol^{-1})	**M-(Cr(CO)$_4$+H)$^+$** 457.2355	**(M+H-(Mo(CO)$_4$))$^+$** 457.2383	**(M)$^+$** 752.1577
Mass Measurement Error (ppm)	1.86	7.99	-0.38

5.2.3.2 Electrochemical characterisation of $Mo^0(CO)_4((PyPrNHCO)_2Bipy)$

The oxidation processes of $Mo^0(CO)_4((PyPrNHCO)_2Bipy)$ were investigated using CV. Therefore, $Mo^0(CO)_4((PyPrNHCO)_2Bipy)$ (2 mM) was cycled between 0.000 - 1.200 V vs. Ag/Ag^+ at 250 mV s^{-1} in the non-coordinating solvent, DCM, containing $TBAPF_6$ (200 mM) at -77 ^oC (Figure 5.16 (—)). The oxidation of $Mo^0(CO)_4((PyPrNHCO)_2Bipy)$ produced the expected *quasi*-reversible redox couple ($E_{1/2}$ = 0.780 V vs. Ag/Ag^+, ΔE_p = 0.120 V) with a current ratio, j_c/j_a, of 0.70 attributed to the one-electron oxidation of the species.[1,2] To investigate the possibility of ligand substitution, a coordinating solvent, MeCN, was added to the electrolytic media, to instigate loss of CO. Upon addition of 3 equivalents (in relation to the complex) of MeCN, the redox couple became irreversible due to production of $[Mo^I(CO)_3(Bipy)(MeCN)]^+$. This was a consequence of the 17-electron electrogenerated species undergoing rapid substitution of the ligand, CO, by a MeCN solvent molecule (Figure 5.16 (—)). The formation of a second redox couple ($E_{1/2}$ = 0.547 V vs. Ag/Ag^+, ΔE_p = 0.110 V) with a current ratio, j_c/j_a, of 0.99 was attributed to a chemical reaction, which only occurred after the electrochemical formation of the $[Mo^I(CO)_4(PyPrNHCO)_2Bipy)]^+$ species. A similar reaction was

also observed during our studies of $Mo^0(CO)_4$Bipy (Section 5.2.1.2), displayed in Figure 5.16 (inset).

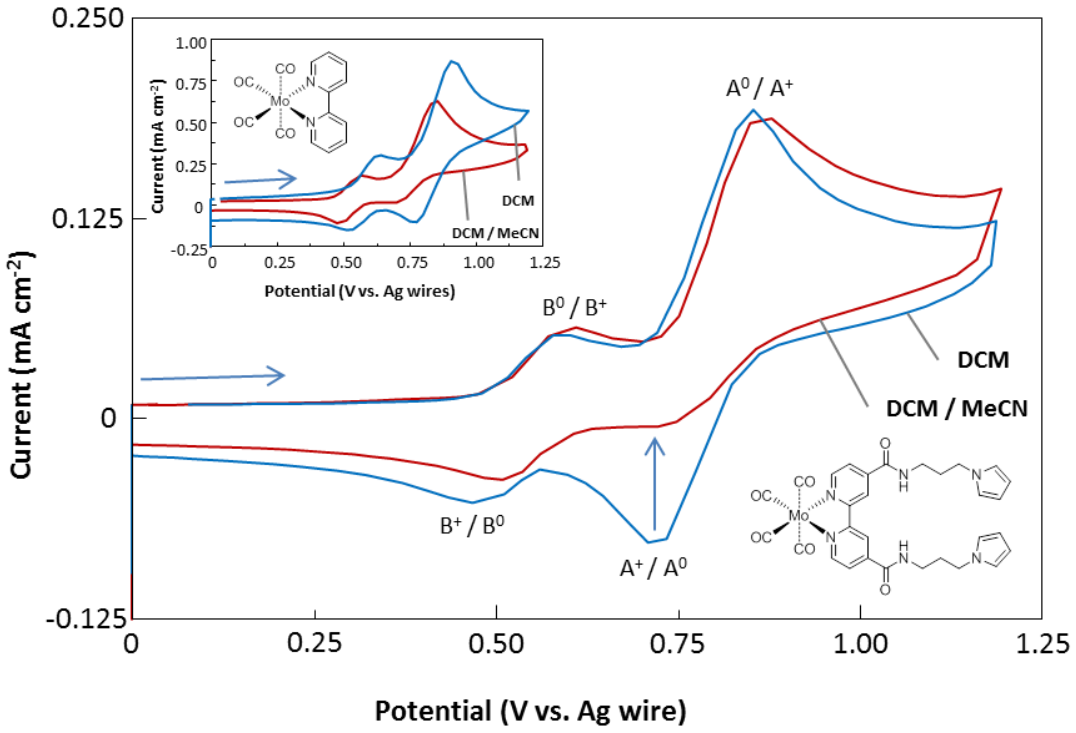

Figure 5.16: CVs of $Mo^0(CO)_4((PyPrNHCO)_2Bipy)$ (2 mM) and $TBAPF_6$ (200 mM) in degassed DCM (—) and DCM with 3 equivalents (in relation to the complex) of MeCN (—) between 0.000 - 1.200 V vs. Ag/Ag^+ at 250 mV s^{-1} (-77 °C). Inset: CVs of $Mo^0(CO)_4$(Bipy) using analogous conditions with DCM (—) and DCM with 3 equivalents (in relation to the complex) of MeCN (—) equivalents of MeCN present in the electrochemical cell.

The equivalents of MeCN were increased to induce an increase in the rate of substitution, which was described by Bullock and co-workers for the complex $Mo^0(CO)_4$(Bipy).[1] 3, 10 and 30 equivalents of MeCN (in relation to the complex) were added to the electrolytic system during cycling of $Mo^0(CO)_4((PyPrNHCO)_2Bipy)$ (2 mM) in DCM containing $TBAPF_6$ (200 mM). Upon introduction of the increased number of MeCN equivalents to the system, there was no observed increase of redox irreversibility (Figure 5.17) and this was replicated, when the experiment was performed using analogous conditions, in the presence of the $Mo^0(CO)_4$(Bipy) complex (Figure 5.17 (inset)).

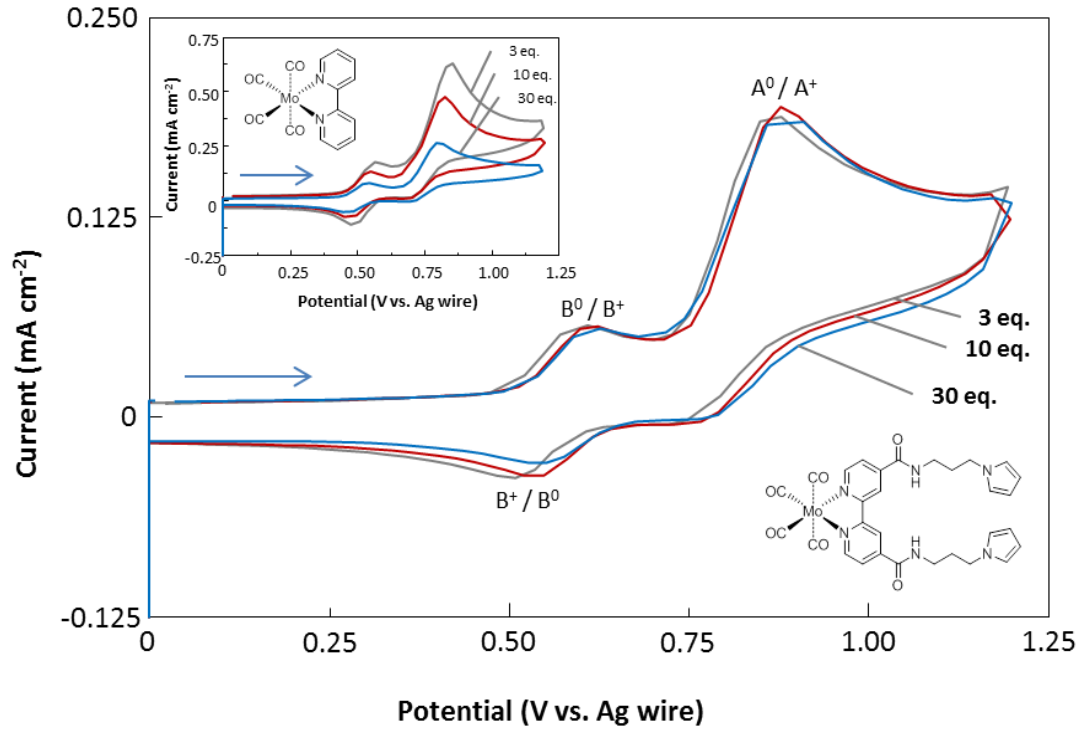

Figure 5.17: CVs of $Mo^0(CO)_4((PyPrNHCO)_2Bipy)$ (2 mM) and $TBAPF_6$ (200 mM) in DCM with (a) 3 equivalents (in relation to the complex) of MeCN (—), (b) 10 equivalents (in relation to the complex) of MeCN (—) and (c) 30 equivalents (in relation to the complex) of MeCN (—) between 0.000 - 1.200 V vs. Ag/Ag^+ at 250 mV s^{-1} (-77 °C). Inset: CVs of $Mo^0(CO)_4(Bipy)$ using analogous conditions with 3 (—), 10 (—) and 30 (—) equivalents of MeCN present in the electrochemical cell.

5.2.3.3 Chemical post-functionalisation of poly[(PyPrNHCO)$_2$Bipy]

The study carried out in Section 5.2.3.2, regarding the electrochemistry of $Mo^0(CO)_4((PyPrNHCO)_2Bipy)$, revealed that the complex underwent oxidatively induced CO loss, at a potential of approximately 0.875 V vs. Ag/Ag^+ in DCM with MeCN present. There was no indication from the CV studies, in which the complex was cycled up to 1.200 V vs. Ag/Ag^+, that the Py group was undergoing oxidation. Therefore, polymerisation of $(PyPrNHCO)_2Bipy$ would require applying potentials that would also result in CO loss, even if a block co-polymerisation approach was attempted, as illustrated in Section 2.2.2.2. Therefore, it was decided that deposition of the poly$[(PyPrNHCO)_2BipyH_2]^{2+}$ film would be executed first, succeed by the attachment of the $Mo^0(CO)_4$ moiety.

The chemical conditions employed for the direct synthesis of the complexes, $M^0(CO)_4((PyPrNHCO)_2Bipy)$ (M = Cr, Mo and W), from the $M(CO)_6$ starting material involved high temperatures in organic solvents, which could cause serious damage to the electrode casing and polymer itself. Therefore, a study was performed to investigate synthetic routes to the desired complex, which involved milder reaction conditions. In 2011, Frank and co-workers reported a method wherein they reacted dipiperidine tetracarbonyl molybdenum ($Mo^0(CO)_4(pip)_2$) with both spiro[azahomoadamantane-phenanthrolinoxazine] (ASPO) and spiro[indoline-phenanthrolinoxazine] (ISPO) at R.T. under N_2 in the absence of light, obtaining product yields of 90% and 84% respectively (Scheme 5.5 (a) and (b)).[73]

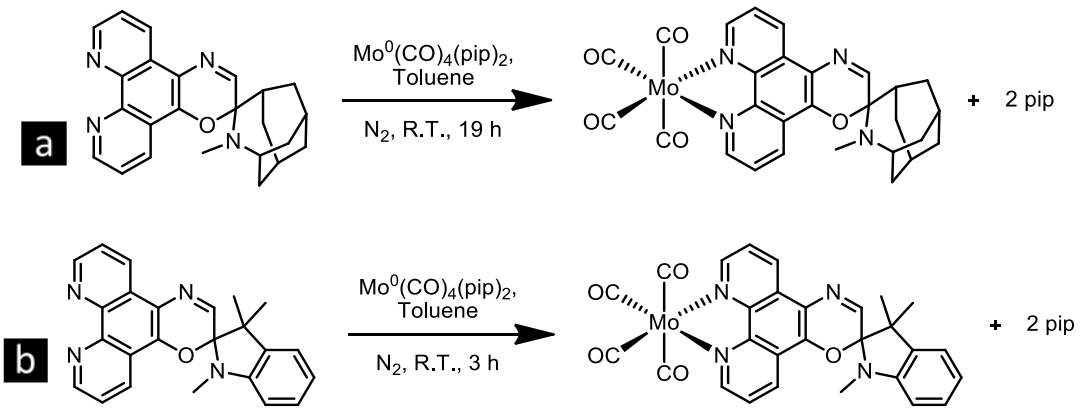

Scheme 5.5: Frank and co-workers coordination reaction of $Mo^0(CO)_4(pip)$ with (a) ASPO and (b) ISPO in toluene.[73]

In the first step $Mo(CO)_4(pip)_2$ was synthesised using the method reported by Darensbourg and Kump, producing a yellow solid in high yield.[38] The FTIR of the $Mo(CO)_4(pip)_2$ compound exhibited bands at 2012, 1914, 1888 and 1839 cm^{-1}, while those for $Mo(CO)_4(Bipy)$ in KBr exhibited bands at 2009, 1916, 1869 and 1812 cm^{-1}. In order to investigate the temperature required for $Mo(CO)_4(pip)_2$ to convert to $Mo(CO)_4(Bipy)$, two reactions were performed. Bipy was reacted with $Mo^0(CO)_4(pip)_2$ in DCM under N_2 at room temperature and an analogous reaction was also performed using reflux conditions (Scheme 5.6 (a) and (b)).

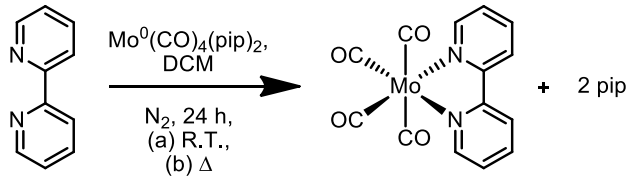

Scheme 5.6: Synthesis of $Mo^0(CO)_4$(Bipy) using Bipy and $Mo^0(CO)_4(pip)_2$ in anhydrous DCM in the absence of light for 24 hours at (a) ambient temperature and at (b) reflux temperature.

The experiments performed with varied temperature were stopped after 24 hours and FTIR spectra were recorded of the product mixtures. For the reaction, which was performed at ambient temperature, strong bands representative of the $Mo^0(CO)_4(pip)_2$ reactant were observed at 2012, 1914, 1888 and 1839 cm^{-1}. The product bands were not visible, possibly being masked by the $Mo^0(CO)_4(pip)_2$ reactant bands. In comparison, the FTIR recorded for the reaction performed at reflux temperature, clearly showed that $Mo^0(CO)_4$(Bipy) product had formed (Figure 5.18). Therefore, it would appear that quite forcing conditions were required to convert $Mo^0(CO)_4(pip)_2$ to $Mo^0(CO)_4$(Bipy) in high yield.

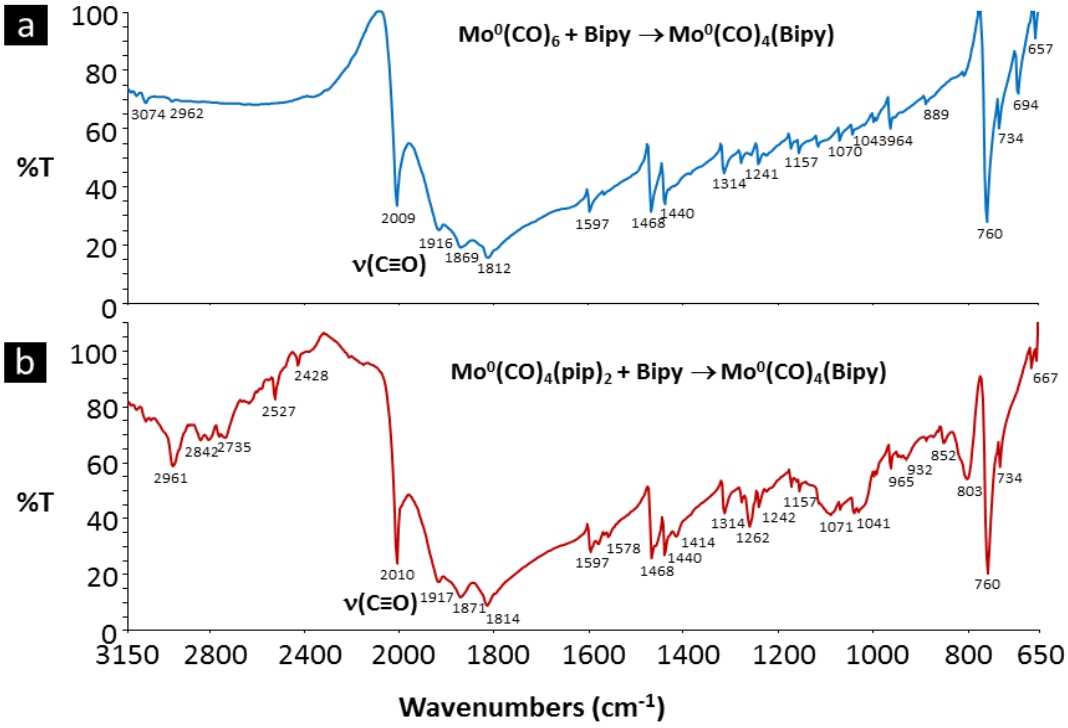

Figure 5.18: FTIR spectra of (a) $Mo^0(CO)_4$(Bipy) obtained from reaction of Bipy and $Mo^0(CO)_6$ using MAS (—) and (b) $Mo^0(CO)_4$(Bipy) obtained from reaction of Bipy and $Mo^0(CO)_4(pip)_2$ in DCM at reflux temperature in the absence of light for 24 h (—), performed at ±2 cm^{-1} resolution in KBr.

Although the results for the previous study were not encouraging, as it was unlikely that $Mo^0(CO)_4$(pip) would react with the poly[$(PyPrNHCO)_2$Bipy] film under mild conditions, one experiment was carried out to confirm if this was the case. Therefore, a poly[$(PyPrNHCO)_2$Bipy] film was electrodeposited on the substrate from the electrolytic solution using the appropriate E_{ox}, washed with DCM, MeOH, H_2O and MeOH and DCM and dried *in vacuo*. This washing procedure was employed for deprotonation of the Bipy nitrogen atoms, which were required to be protonated using $HClO_4$, during polymerisation of the monomer. Adapting the method reported by Frank and co-workers,[73] the poly[$(PyPrNHCO)_2$Bipy] modified electrode was submerged in a solution of anhydrous DCM containing $Mo^0(CO)_4(pip)_2$, under N_2 in the absence of light, at ambient temperature. The solution was swirled occasionally and after 24 hours the electrode was removed from the solution, washed with DCM and dried *in vacuo* (Scheme 5.7). It was anticipated that any residual, physisorbed $Mo^0(CO)_4(pip)_2$ could be washed off the polymer, potentially yielding the desired FTIR spectral bands attributed to the polymer coordinated tetracarbonyl molybdenum, even if the reaction had only proceeded in low yield.

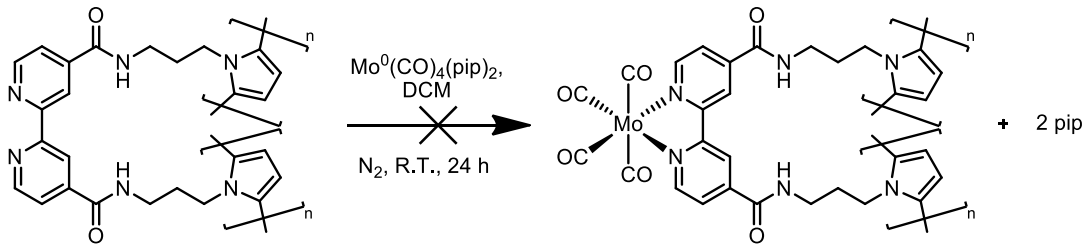

Scheme 5.7: Unsuccessful post-functionalisation reaction of poly[$(PyPrNHCO)_2$Bipy] with $Mo^0(CO)_4(pip)_2$.

The polymer film was scrapped from the substrate and ground into KBr so that an FTIR spectrum could be recorded (Figure 5.19 (—)). FTIR spectroscopy was also performed on an analogous polymer control film, which had not been exposed to the post-functionalisation reaction medium (Figure 5.19 (—)). It was apparent from the spectra that the tetracarbonyl molybdenum had not coordinated, due the absence of intense bands in the region, 2010 - 1800 cm^{-1}, previously attributed to ν(M–C≡O) of the $Mo^0(CO)_4$($(PyPrNHCO)_2$Bipy) ligand. The presence of molybdenum on the surface was also investigated using EDX spectroscopy, which yielded no peaks for

the metal in the spectra, further confirming that the coordination reaction did not proceed utilising these conditions

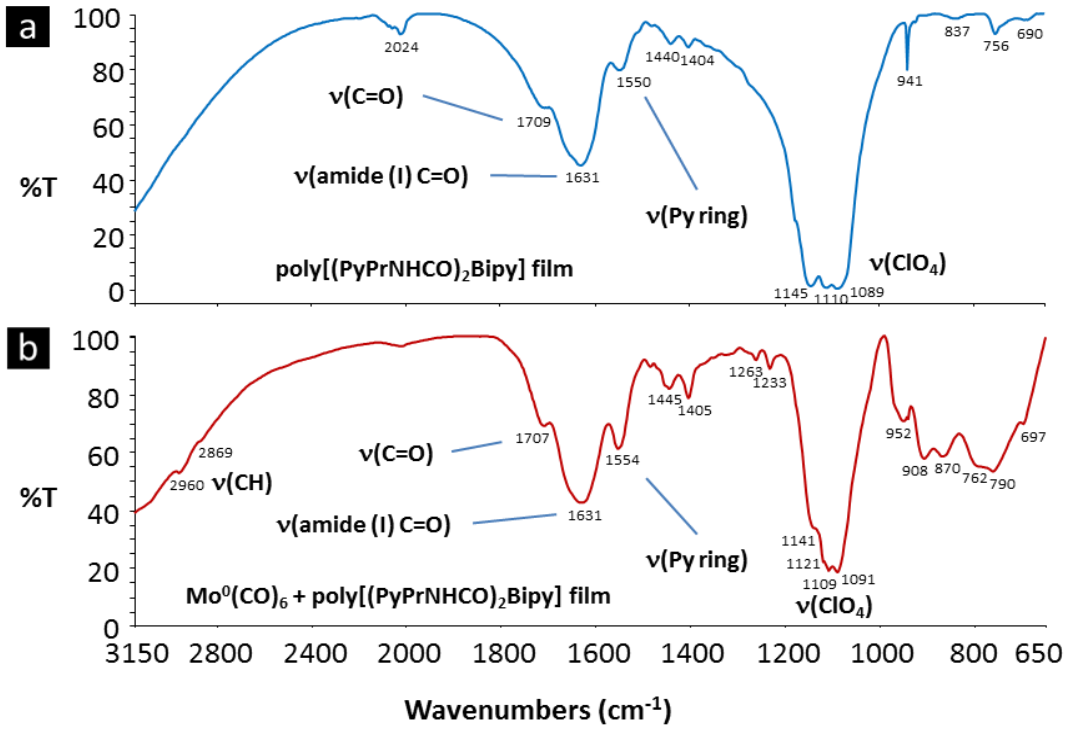

Figure 5.19: FTIR spectra of (a) poly[(PyPrNHCO)$_2$Bipy] film (—) and (b) chemically post-functionalised poly[(PyPrNHCO)$_2$Bipy)] film (—) performed at ±2 cm^{-1} resolution in KBr.

The studies executed above illustrated how Mo(CO)$_4$(pip)$_2$ was not a suitable precursor for the post-functionalisation of poly[(PyPrNHCO)$_2$Bipy] with Mo(CO)$_4$, as the reaction did not proceed at even a low efficiency, under conditions which would not damage the polymer and the electrode. Other possible avenues which could be investigated for post-functionalisation of the poly[(PyPrNHCO)$_2$Bipy] films include the employment of a chemical initiator. Hor and co-workers have shown that trimethylamine *N*-oxide (TMANO) can induce oxidative decarbonylation of M^0(CO)$_6$ (M = Cr, Mo, W) at ambient temperature, in the presence of stoichiometric quantities of Bipy to the metal tetracarbonyl complexes, producing yields of 81, 85 and 97% yield respectively.[74,75] Alternatively, Lang and co-workers and Lapinte and co-workers employed Mo^0(CO)$_4$(1,5-norbornadiene) in DCM based solutions to coordinate molybdenum tetracarbonyl to Bipy based structures, obtaining yields of 77% and 85% respectively,[76-78] while Chapman *et al.* have produced the

$W^0(CO)_4$(Bipy) complex *via* direct photolysis of $W^0(CO)_6$, using UV irradiation at 313 nm, attaining a yield of 57%. These methods are all viable contenders for the procurement of the post-functionalised poly[$Mo^0(CO)_4$((PyPrNHCO)$_2$Bipy)] film.

5.2.4 Synthesis of tetrazolate complexes

The coordination of Group 6 carbonyls to the poly[(PyPrNHCO)$_2$Bipy] film was unsuccessful, so it was decided that the employment of a less complicated ligand would be a more efficient route, to attain metal carbonyl coordinated polymer films. The ligand needed to be commercially available, easily purified using vacuum distillation, undergo facile electrochemically deposition on to a substrate and most importantly, possess a moiety with metal coordinating abilities. Such a moiety was the nitrile functional group, which has been extensively studied in regards of organometallic chemistry.[27-33] Therefore, PyEtCN was chosen as a suitable monomer. We have already published work involving the template-free electrodeposition of PPyEtCN nanowires[79] and the electrodeposition of hollow PPyEtCN microtubes from an acoustically formed emulsion[26].

A study was performed to co-ordinate a series of ligands containing the nitrile group to metal carbonyl moieties. This work built on research performed by a previous member of our group, who produced cyclopentadienyl molybdenum tricarbonyl nitrile tetrafluoroborate salts.[35] As these compounds were reported as being highly air-sensitive, further reaction of these complexes with sodium azide (NaN_3) would be advantageous, yielding more robust molecules in the form of uncharged tetrazolate complexes. This process could also be performed on the polymer after successful coordination of the metal carbonyl with the PPyEtCN film, as these types of cycloaddition reaction have a high success rate at solid substrates.[67,80,81]

5.2.4.1 Synthesis of [$CpMo^{II}(CO)_3$NCR]BF_4 (R = Ph, T, Bz) complexes

The family of cationic nitrile complexes, previously reported by our group, were produced by adaptation of the method outlined by Louattani and Suades.[82] The compounds, benzonitrile (NCPh), 2-thiophenecarbonitrile (NCT) and benzyl cyanide (NCBz), were reacted with cyclopentadienyl molybdenum(I) tricarbonyl dimer ([$Mo^I(CO_3)]_2$) in the presence of silver tetrafluoroborate ($AgBF_4$) yielding

cyclopentadienyl molybdenum tricarbonyl benzonitrile ([$CpMo^{II}(CO)_3NCPh$]BF_4), cyclopentadienyl molybdenum tricarbonyl 2-thiophencarbonitrile ([$CpMo^{II}(CO)_3NCT$]BF_4) and cyclopentadienyl molybdenum tricarbonyl benzyl cyanide ([$CpMo^{II}(CO)_3NCBz$]BF_4) respectively (Figure 5.20).

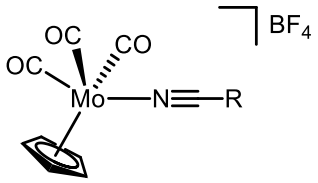

Figure 5.20: Structure of [$CpMo^{II}(CO)_3NCR$]BF_4 (R = Ph, T, Bz).

5.2.4.2 Synthesis of $CpMo^{II}(CO)_3N_4CR$ (R = Ph, T, Bz) complexes

The tetrazolate complexes were prepared from the nitrile BF_4^- precursors (Section 5.2.2.1) by adapting a method reported in the literature by Palazzi *et al.*.[29] The three nitrile BF_4^- salts, [$CpMo^{II}(CO)_3NCPh$]BF_4, [$CpMo^{II}(CO)_3NCT$]BF_4 and [$CpMo^{II}(CO)_3NCBz$]BF_4 were reacted with NaN_3 to produce the three tetrazolate complexes, cyclopentadienyl molybdenum(II) tricarbonyl phenyl 5-tetrazolate ($CpMo^{II}(CO)_3N_4CPh$), cyclopentadienyl molybdenum(II) tricarbonyl thiophene 5-tetrazolate ($CpMo^{II}(CO)_3N_4CT$) and cyclopentadienyl molybdenum(II) tricarbonyl benzyl 5-tetrazolate ($CpMo^{II}(CO)_3N_4CBz$) respectively (Scheme 5.8).

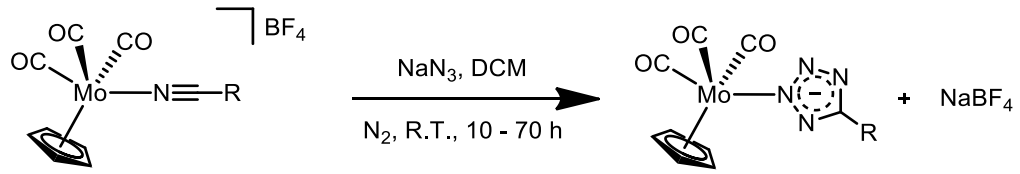

Scheme 5.8: Synthesis of $CpMo^{II}(CO)_3N_4CR$ (R = Ph, T, Bz).

The molybdenum atom in the nitrile BF_4^- salt complexes are coordinatively saturated so cyclisation to the tetrazolate occurs *via* an intermolecular mechanism in contrast to an intramolecular mechanism, which would involve the formation of an intermediate species. This intermediate species would display coordination of both the nitrile ligand and the azide anion simultaneously, but instead following an intermolecular mechanism here the nucleophilic azide anion attacks the electrophilic

carbon on the coordinated nitrile ligand. This is succeeded by the cyclisation reaction, yielding the N-1 tetrazolate complex (Scheme 5.9).

The molybdenum atom in the nitrile BF_4^- salt complexes are coordinatively saturated so cyclisation to the tetrazolate occurs *via* an intermolecular mechanism. The nucleophilic azide anion attacks the electrophilic carbon on the coordinated nitrile ligand. This is succeeded by the cyclisation reaction, yielding the N-1 tetrazolate complex (Scheme 5.9).

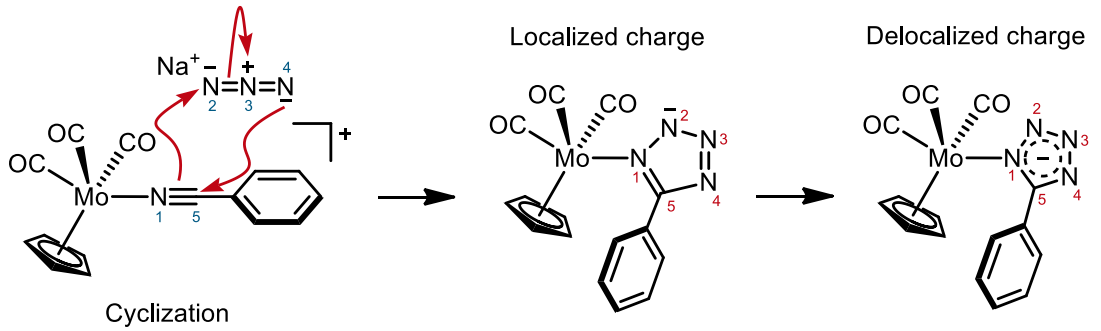

Scheme 5.9: Intermolecular cyclisation reaction involving NaN_3 and NCPh ligand producing the N-1 tetrazolate $CpMo^{II}(CO)_3N_4CPh$ species, possessing charge delocalisation around the ring.

Once synthesis of the tetrazolate family was complete characterisation was performed using FTIR spectroscopy in KBr, ^1H and ^{13}C NMR spectroscopy (COSY, DEPT spectroscopy and HMQC spectroscopy) in deuterated solvents and mass spectrometry.

The NMR spectral data, obtained for the three $CpMo^{II}(CO)_3N_4CR$ (R = Ph, T, Bz) complexes, are displayed in Table 5.7, 5.8 and 5.9 respectively. The C-5 resonance signals of the three $CpMo^{II}(CO)_3N_4CR$ (R = Ph, T, Bz) complexes, positioned at approx. 164 ppm in the ^{13}C data was observed to have shifted downfield approx. 20 ppm, when compared to the nitrile precursor. These derivatives all displayed signals at approx. 224 and 237 ppm in the ^{13}C spectral data, attributed to the resonance of the *cis* and *trans* metal carbonyls respectively,[83] which also compared well to their nitrile precursors. They also possessed signals positioned at approx. 94.5 ppm in the ^{13}C spectral data and at approx. 5.69 ppm as a singlet in the ^1H spectral data, representing the cyclopentadienyl ligand.[29,83,84] When compared to the nitrile analogues, the

tetrazolate signals for the Cp ligand were more shielded by approx. 4.2 ppm and 0.43 ppm in the ^{13}C and ^{1}H NMR data respectively.

Specifically the phenyl congener (Table 5.7) possessed other resonances in the ^{13}C data at 128.2 ppm attributed to the *ipso* carbon of the phenyl ring, at 127.5 ppm representative of the C-2',C-6' carbons, at 125.6 ppm signifying the C-3',C-5' carbons and at 128.1 ppm, assigned to the C-4' signal. The ^{1}H spectral data possessed a doublet of triplets at 8.10 ppm, accredited to the H_o signal, while a triplet of triplets were present at 7.43 ppm attributed to the H_p signal, followed by the H_m signal at 7.40 ppm.

Table 5.7: ^{1}H and ^{13}C NMR spectral data (δ in ppm) for $CpMo^{II}(CO)_3N_4CPh$.

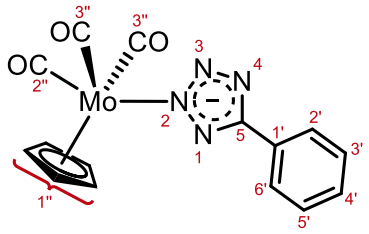

C / H	$CpMo^{II}(CO)_3N_4CPh$ (ppm)	
	δ ^{13}C	δ ^{1}H (m); *J* Hz
5	164.8	-
1'	128.2	-
2',6'	127.5	8.10 (dt); 1.8, 6.6
3',5'	125.6	7.40 (m)
4'	128.1	7.43 (tt); 1.8, 6.9
1''	94.4	5.70 (s)
2''cis	224.4	-
3''trans	237.4	-

The thiophene congener (Table 5.8) possessed other resonances in the ^{13}C data positioned at 130.3 ppm attributed to the *ipso* carbon of the thiophene ring, at 126.5 ppm representative of the C-4' carbon, and between 125.0 - 125.1 ppm for the C-3' and C-5' carbons. The ^{1}H NMR spectral data for this species possessed a doublet of

doublets at 7.09 ppm representing the H-4' signal. Another two doublet of doublets were positioned at 7.34 and 7.68 ppm for the H-5' and H-3' signals respectively.

Table 5.8: ^{1}H and ^{13}C NMR spectral data (δ in ppm) for $CpMo^{II}(CO)_3N_4CT$.

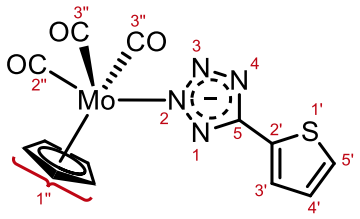

C / H	$CpMo^{II}(CO)_3N_4CT$ (ppm)	
	δ ^{13}C	**δ ^{1}H (m); *J* Hz**
5	160.7	-
2'	130.3	-
3'	125.1-125.0	7.68 (dd); 1.2, 3.6
4'	126.5	7.09 (dd); 3.6, 5.1
5'	125.1-125.0	7.34 (dd); 1.2, 5.1
1''	94.4	5.71 (s)
2''cis	224.2	-
3''trans	237.3	-

The benzyl congener (Table 5.9) possessed other resonances in the ^{13}C data; 138.5 ppm representative of the *ipso* carbon of the phenyl ring, at 129.0 ppm attributed to the C-2',C-6' carbons, 128.5 ppm signifying the C-3',C-5' carbons and at 126.4 ppm representative of the C-4' signal. The ^{1}H NMR spectral data for this derivative displayed multiplet peaks at 7.28 and 7.26 ppm signifying the phenyl ring signals. The CH_2 resonance was positioned at 4.18 ppm in the ^{1}H NMR spectral data, represented by a singlet peak and positioned at 31.8 ppm in the ^{13}C NMR spectral data. The downfield shifts for the CH_2 ^{1}H and ^{13}C NMR spectroscopic signals were anticipated due to the electron donating resonance effect of the adjacent tetrazolate.[85]

Table 5.9: ^{1}H and ^{13}C NMR spectral data (δ in ppm) for $CpMo^{II}(CO)_3N_4CBz$.

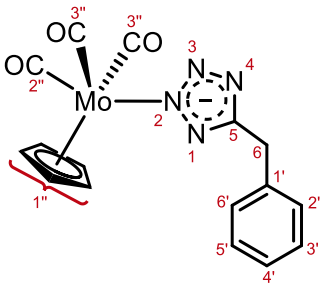

C / H	$CpMo^{II}(CO)_3N_4CBz$ (ppm)	
	δ ^{13}C	δ ^{1}H (m); *J* Hz
5	165.7	-
6	31.8	4.18 (s)
1’	138.5	-
2’,6’	129.0	7.26 (m)
3’,5’	128.5	7.28 (m)
4’	126.4	7.28 (m)
1’’	94.4	5.65 (s)
2’’cis	225.5	-
3’’trans	238.6	-

The full FTIR spectral data obtained for the three $CpMo^{II}(CO)_3N_4CR$ (R = Ph, T, Bz) complexes and that of the nitrile precursors are reported in Table 5.10. The FTIR spectral data for $CpMo^{II}(CO)_3N_4CR$ (R = Ph, T) showing the metal carbonyl bands are given in Figure 5.21. These metal carbonyl bands have shifted to lower wavenumbers, when compared to their nitrile precursors.[84] This has been ascribed to the back-bonding interaction of the metal atoms d-electrons with the tetrazolate ligand.[29,84] In the phenyl congener, there was the possible presence of an extended π-delocalised system, spanning from the metal atoms d-orbitals through the possibly coplanar tetrazolate and phenyl ring.[29]

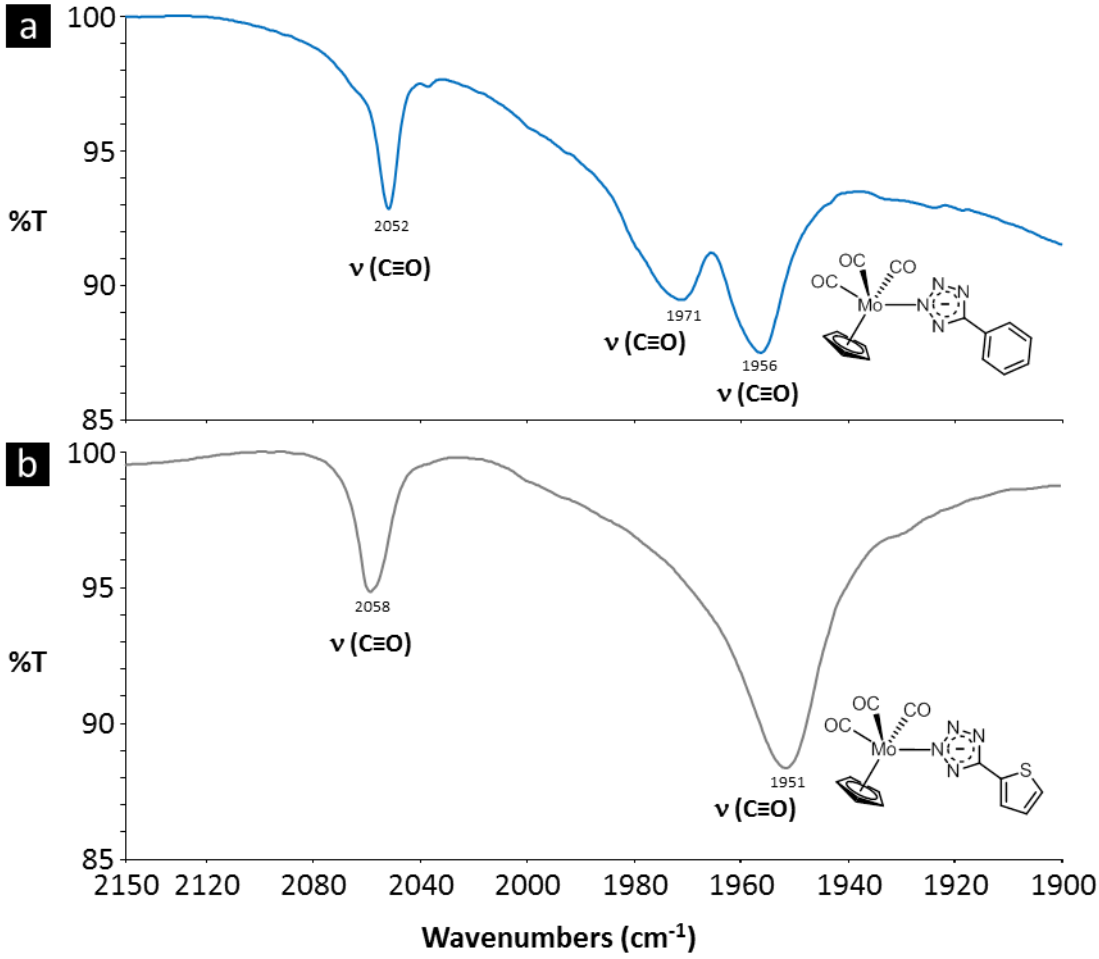

Figure 5.21: FTIR spectra of (a) $CpMo^{II}(CO)_3N_4CPh$ (—) and (b) $CpMo^{II}(CO)_3N_4CT$ (—) performed at ±2 cm^{-1} resolution in KBr.

Table 5.10: FTIR spectral data (cm^{-1}) for $CpMo^{II}(CO)_3L$ (L = NCR and N_4CR) (R = Ph, T, Bz) complexes in KBr.

Vibration	$CpMo^{II}(CO)_3L$ (cm^{-1})					
	L = NCR			L = N_4CR		
	R = Ph	R = T	R = Bz	R = Ph	R = T	R = Bz
ν(C≡N)	2272(w)	2253	2280	-	-	-
ν(C≡O)	2075	2073	2067(br)	2052	2058	2060
ν(C≡O)	2044	2040(w)		1971	-	1972(br)
ν(C≡O)	1975	1973	1972	1956	1951	-
ν(C=N)	-	-	-	1640(w)	1632(w)	1630(w)

The calculated exact mass for each tetrazolate complex was determined, while mass spectrometry of the complexes produced measured accurate masses, which were tabulated together and presented in Table 5.11. Using the respective values, the mass measurement error for each complex was also calculated. The values for the phenyl and benzyl species produced mass measurement errors which fell inside the 5 ppm bracket, while the thiophene species fell just outside at 7.49 ppm.

Table 5.11: Mass spectrometry data for $CpMo^{II}(CO)_3N_4CR$ (R = Ph, T, Bz) complexes.

	$CpMo^{II}(CO)_3N_4CR$		
	R = Ph	R = T	R = Bz
Calculated Exact Mass ($g\ mol^{-1}$)	**$(M)^+$** 391.9802	**$(M+H)^+$** 397.9371	**$(M+H)^+$** 407.0036
Measured Accurate Mass ($g\ mol^{-1}$)	**$(M)^+$** 391.9819	**$(M+H)^+$** 397.9409	**$(M+H)^+$** 407.0053
Mass Measurement Error (ppm)	4.47	-8.49	4.12

Tetrazole metal complexes have the potential to exist as either the N-1 or N-2 isomer as shown for the $CpMo^{II}(CO)_3N_4CPh$ complexes in Figure 5.22 (a) and (b), respectively. In the early 1980's, Purcell and co-workers performed analyses regarding tetrazolate tautomerisation employing the (5-substituted tetrazolato)pentaamminecobalt(III) complexes, where they were able to synthesis the N-1 derivative without observing conversion to the N-2 species. From their work, it was determined that the conversion to the N-2 derivative was due to steric factors and the rate of isomerism was seen to be affected by substituent electronic/steric properties and solvent. They also reported control of conversion upon change of pH and temperature.[34,86-88]

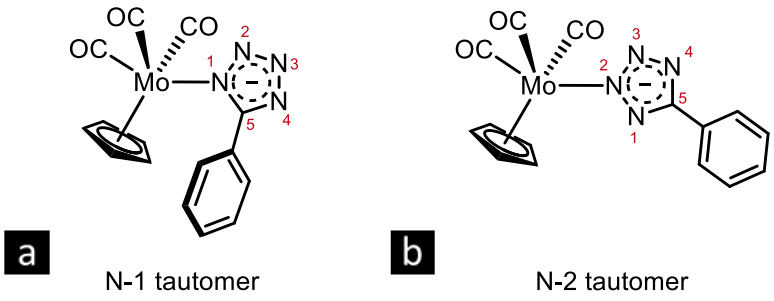

Figure 5.22: Structure of (a) cyclopentadienyl tricarbonyl molybdenum(II) N-1 tetrazolate isomer and (b) cyclopentadienyl tricarbonyl molybdenum(II) N-2 tetrazolate isomer species.

From the NMR data acquired, regarding the $CpMo^{II}(CO)_3N_4CR$ (R = Ph, T, Bz) family, it appeared that only one isomer was present in solution at ambient temperature. It is likely by considering the steric effects of the complex that this is the N-2 isomer. Each of the compounds possesses one Cp and three CO ligands coordinated to the metal. In the structure of the N-1 tautomer species these ligands produce steric crowding due to the presence of bulky aromatic substituents (phenyl, thiophene and benzyl) at the tetrazolate ring C-5 position (Scheme 5.10).

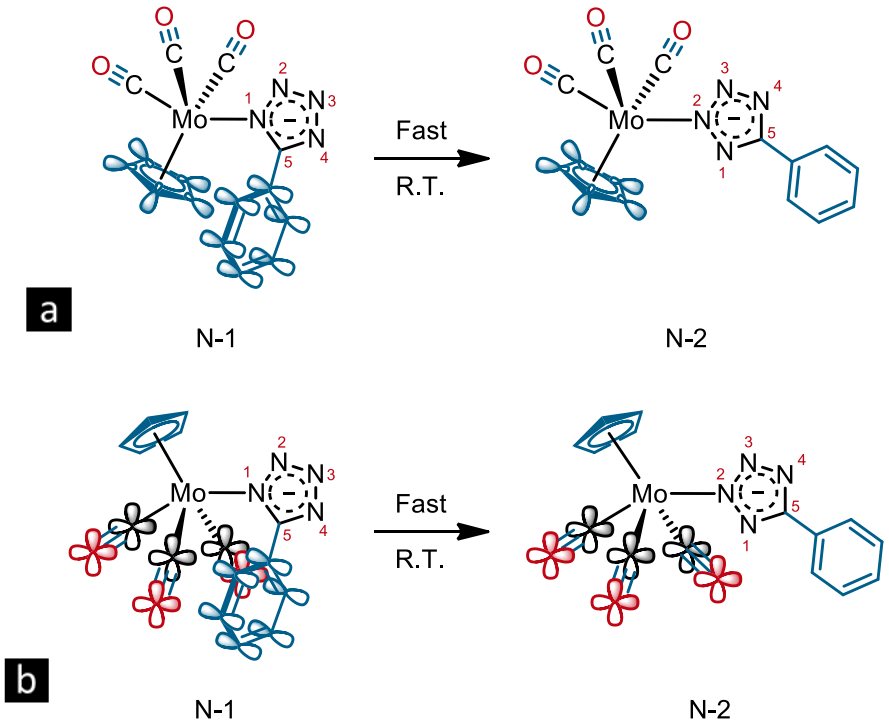

Scheme 5.10: Annular tautomerisation from the N-1 tetrazolate isomer to the N-2 isomer species at R.T. This is induced by steric crowding of the bulky aromatic substituents (phenyl shown) present at the C-5 position on the tetrazolate ring with the (a) cyclopentadienyl ligand or (b) CO ligands coordinated to the molybdenum centre.

Previous researchers have shown that it is possible to distinguish the N-1 from the N-2 isomer by analysis of the ^{13}C and ^{1}H NMR spectra. In the late 1970's, Butler and McEvoy employing a variation of organic aryltetrazoles (Scheme 5.11), reported that the ^{13}C chemical shift values of the tetrazole carbon (C-5) can determine the tetrazole annular tautomerism.[89,90] For 5-aryltetrazoles, they reported that the C-5 chemical shift of the N-1 isomer (δC-5 = 152 - 157 ppm) was positioned significantly more upfield than that of the compared to that of the N-2 isomer (δC-5 = 162 - 167 ppm),[89] and some have been shown to have a 8 - 13 ppm isomeric difference.[90]

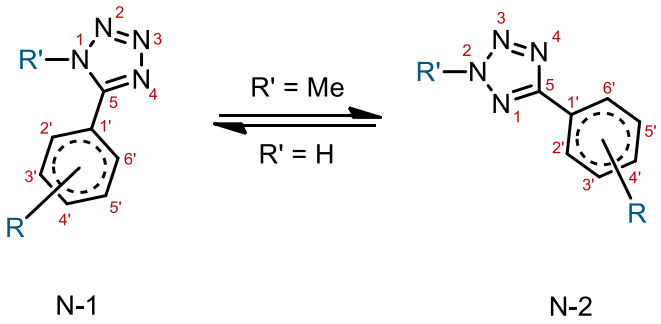

Scheme 5.11: Annular tautomerisation of organic aryltetrazoles, (Ph(R)CN_4(R')) N-1 isomer to N-2 isomer species (R = Me, H, NO_2. R' = Me, H) investigated by Butler and McEvoy.

For the $CpMo^{II}(CO)_3N_4CR$ (R = Ph, T, Bz) species, it was observed that the C-5 resonance signals were positioned at 164.8, 160.7 and 165.7 ppm for the phenyl,[29-31] thiophene[91] and benzyl derivatives respectively. The C-5 chemical shift for the thiophene and benzyl derivatives were slightly outside the window stated by Butler and McEvoy, but this was anticipated due to electron donation *via* the positive mesomeric effect of the sulfur atom in the thiophene ring and the positive inductive effect of the CH_2 in the benzyl derivative. Stagni and co-workers have produced work on thiophene congeners, employing them within ruthenium(II) complexes. The ^{13}C data for these N-2 tautomer compounds displayed a C-5 resonance signal at approx. 159 ppm and the structure was confirmed using X-ray crystallography.[91] Therefore, the ^{13}C NMR data are consistent with the complexes existing as the N-2 isomers.

Evidence that the $CpMo^{II}(CO)_3N_4CPh$ complex was formed as the N-2 tautomer, can also be deduced by inspection of the ^1H and the ^{13}C NMR spectral data. Studies have shown that sterically hindered ligands or substituents of the N-1 tetrazolate complex induce an out-of-plane rotation of the tetrazolate ring, in relation to the phenyl ring.[29,84] This loss of coplanarity between the two aromatic rings incites a decrease in interannular conjugation (Figure 5.23 (a)) and since the ligands/substituents possessed by the N-2 tautomer complex do not interact sterically, this tautomer attains increased interannular conjugation (Figure 5.23 (b)).

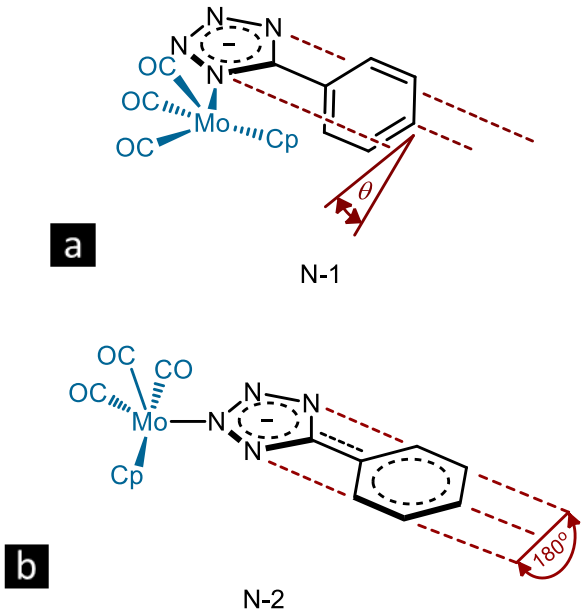

Figure 5.23: Structure of aryltetrazolate (a) N-1 tautomer displaying an absence of interannular conjugation and (b) N-2 tautomer displaying interannular conjugation between the tetrazolate and phenyl ring.

The increased interannular conjugation possessed by the N-2 tautomer can be determined by examining the ^{1}H and ^{13}C NMR spectral data, while also permitting distinction from the N-1 tautomer (Figure 5.24). The N-2 tautomer is represented in the ^{1}H spectral data by the *ortho* phenyl protons (H_o and H_o'), which are more deshielded. This is accompanied by more shielded *meta* (H_m and H_m') and *para* (H_p') phenyl protons, caused by the electron donating resonance effects of the tetrazole ring.[72] In work, reported by Palazzi and co-workers, the authors suggested that the large $\Delta(\delta C\text{-}3' - \delta C\text{-}2')$ (approx. 5.72 ppm) and $\Delta(\delta H_o - \delta H_m)$ (approx. 0.44 ppm) experienced by their cyclopendienyl dicarbonyl iron(II) derivatives could be a consequence of the metals d-electrons participating to the interannular conjugation of the delocalised system.[29] Analysis of the ^{1}H NMR spectral data in this work, showed that the N-2 tautomer of the $CpMo^{II}(CO)_3N_4CPh$ compound possessed a $\Delta(\delta H_o - \delta H_m)$ of 0.67 ppm. This value compares well for $\Delta(\delta H_o - \delta H_m)$ of the N-2 tautomers for organic compounds in the literature, which possess interannular conjugation.[29,30,84] The ^{13}C NMR data of the phenyl group of an N-2 tautomer would also be expected to be influenced by interannular conjugation with the tetrazole ring. Typically the variation for organic compounds in chemical shift of the *ortho* (C-2 and C-6) and

meta (C-3' and C-5') carbon signals (Δ(δC-3' – δC-2')) is approx. 2.9 - 3.7 ppm.[85,89,92] Upon examination of the ^{13}C NMR data for the $CpMo^{II}(CO)_3N_4CPh$ complex, it was observed that the (Δ(δC-3' – δC-2')) was 1.9 ppm, which was slightly lower than the values obtained for N-2 tautomers, exhibiting interannular conjugation in the literature.[29,30,74] Therefore, it is likely that interannular conjugation occurs within the $CpMo^{II}(CO)_3N_4CPh$ N-2 tautomer species and there is no clear evidence from the NMR spectral data that the d-electrons are participating in the interannular conjugation. However, these findings would need to be confirmed by obtaining a crystal structure of the complex.

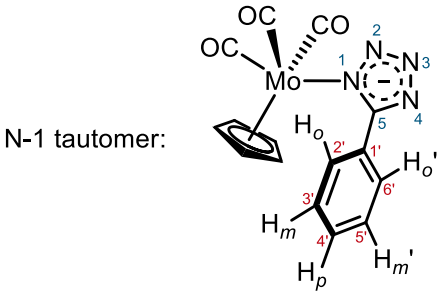

a

δC-5 = 152 - 157 ppm
Δ(C-3' - C-2') = 0.7- 1.4 ppm
Δ(H_o - H_m) = 0.6 - 0.7 ppm < N-2 Δ(H_o - H_m)

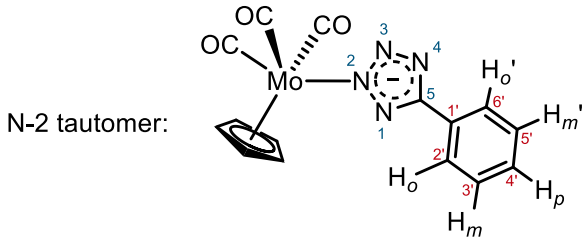

b

δC-5 = 162 -167 ppm
Δ(C-3' - C-2') = 2.9 - 3.7 ppm
Δ(H_o - H_m) = 0.6 - 0.7 ppm > N-1 Δ(H_o - H_m)

Figure 5.24: Structures of (a) N-1 and (b) N-2 tautomer $CpMo^{II}(CO)_3N_4CPh$ species with ^{13}C and ^{1}H NMR spectroscopic parameters, utilised for the determination of tautomer position.

As already stated, Palazzi and co-workers, proposed that the large Δ(δC-3'-δC-2') (approx. 5.72 ppm) and Δ(δH_o-δH_m) (approx. 0.44 ppm) experienced by their cyclopendienyl dicarbonyl iron(II) derivatives could be due to the TMs d-electrons, contributing to the delocalised systems interannular conjugation,[29] which was not

observed for the $CpMo^{II}(CO)_3N_4CR$ (R = Ph, T, Bz) compounds in this work. Although this may be the case, this increase of interannular conjugation for their iron(II) derivatives may instead be induced by the presence of an electron withdrawing nitrile moiety at the *para* position on the phenyl substituent.

5.2.4.3 Attempted synthesis of $CpFe^{II}(CO)_2N_4CEtPy$ complex

After successful characterisation of the series of $CpMo^{II}(CO)_3N_4CR$ (R = Ph, T, Bz) complexes, the coordination of the PyEtCN ligand to a metal carbonyl was attempted. $AgBF_4$ had been utilised as the oxidising agent to cleave the *cyclopentadienyl molybdenum*(II) *tricarbonyl dimer*, ($[CpMo^{I}(CO)_3]_2$), for coordination with the nitrile ligands, but this reagent could possibly react with the Py moiety of PyEtCN, as Ag salts are known to oxidise Py yielding PPy.[93] Therefore, a method was adapted from that reported in the literature by Palazzi *et al.* and Catheline and Astruc. The method involved using the reactive cyclopentadienyl iron(II) dicarbonyl tetrahydrofuran tetrafluoroborate salt ($[CpFe^{II}(CO)_2THF]BF_4$) as a source of the desired TM carbonyl fragment.[29,94] Due to the reactivity of the THF adduct, the sample was handled in a glove box under a positive pressure of N_2. This compound was reacted with distilled PyEtCN in degassed, anhydrous DCM under N_2 at R.T. in the absence of light (Scheme 5.12). After 17 hours, the reaction mixture had changed colour as anticipated from red to orange, so the solvent was removed *in vacuo* and no further workup of this mixture was performed. This was a consequence of the complications experienced during the filtration of the previous, very air sensitive $[CpMo^{II}(CO)_3NCR]BF_4$ (R = Ph, T, Bz) complexes in Section 5.2.4.1, so the $[CpFe^{II}(CO)_2NCEtPy]BF_4$ complex was not isolated or characterised.

Scheme 5.12 Synthesis of $[CpFe^{II}(CO)_2NCEtPy]BF_4$.

Adapting the method reported in the literature by Palazzi *et al.*, the orange residue obtained from the previous reaction step was dissolved in degassed anhydrous DCM and NaN_3 was added (Scheme 5.13).[29] This solution was stirred in the absence of light for 24 h, after which, the anticipated colour change was observed, yielding a yellow reaction mixture. This mixture was filtered on a Celite plug and the solvent was removed *in vacuo*, yielding a yellow residue, which was characterised using mass spectrometry and ^{1}H and ^{13}C NMR spectroscopy. The product was further purified in the glove box, using an Al_2O_3 preparative TLC. The mobile phase employed consisted of DCM/MeCN (4:1), which yielded a yellow spot at an R_f value of 0.55, but during this process no product was obtained.

Scheme 5.13: Synthesis of $CpFe^{II}(CO)_2N_4CEtPy$.

The calculated exact mass for $CpFe^{II}(CO)_2N_4CEtPy$ was determined, while mass spectrometry was performed on the impure $CpFe^{II}(CO)_2N_4CEtPy$ complex and the results obtained can be observed in Table 5.12. Using the respective values, the mass measurement error was obtained, which suggested that the reaction had proceeded successfully; the $CpFe^{II}(CO)_2N_4CEtPy$ complex present within the crude mixture.

Table 5.12: Mass spectrometry data for the $CpFe^{II}(CO)_2N_4CEtPy$ complexes.

	$CpFe^{II}(CO)_2N_4CEtPy$		
	Calculated Exact Mass (g mol^{-1})	**Measured Accurate Mass (g mol^{-1})**	**Mass Measurement Error (ppm)**
$(M+H)^+$	340.0491	340.0492	0.18

The ^{13}C and ^{1}H NMR spectral data for the $CpFe^{II}(CO)_2N_4CEtPy$ product is shown in Table 5.13. DEPTQ135 spectroscopy, COSY, and HSQC spectroscopy were also utilised to aid in the characterisation of the product. The ^{13}C NMR spectral data displayed a peak at an anticipated chemical shift of 210.0 ppm for the metal carbonyl signal.[29,84] The two CH_2 carbons signals were positioned at 29.5 and 48.5 ppm, which were assigned to the carbon atoms adjacent to the tetrazolate and Py moieties respectively. The resonances of the Py-α and Py-β carbons were observed at chemical shifts of 108.7 and 120.8 ppm respectively. The tetrazolate C-5 signal was not observed in the spectrum due to noise. The Cp signal was positioned at 86.0 ppm.

The product possessed signals in the ^{1}H NMR spectral data that were not split and all signals appeared as singlet peaks in the spectrum. The CH_2 protons resonated at chemical shifts of 4.49 and 3.20 ppm for the protons adjacent to the Py and tetrazolate moieties respectively and these integrated to two protons each. The singlet peak attributed to the Cp ligand was positioned at 4.86 ppm and integrated correctly to five protons. The Py-α and Py-β proton signals were represented by peaks positioned at 6.56 and 6.08 ppm respectively.

It would appear from the NMR spectroscopic characterisation that the reaction had proceeded successfully, although the compound was impure.

Table 5.13: ^{13}C and ^{1}H NMR spectral data (δ in ppm) of $CpFe^{II}(CO)_2N_4CEtPy$ in $CDCl_3$ (75.5 MHz and 300 MHz respectively).

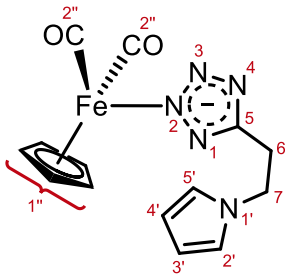

C / H	$CpFe^{II}(CO)_2N_4CEtPy$ (ppm)		PyEtCN (ppm)	
	δ ^{13}C	δ ^{1}H (m)	δ ^{13}C	δ ^{1}H (m)
5	-	-	117.7	-
6	29.5	3.20 (s)	19.7	2.60 (t)
7	48.5	4.49 (s)	44.0	4.01 (t)
2',5'	120.8	6.56 (s)	108.4	6.32 (t)
3',4'	108.7	6.08 (s)	120.0	6.78 (t)
1''	86.0	4.86 (s)	-	-
2''	211.1.0	-	-	-

5.3 Conclusion

In this chapter, CV and spectroelectrochemical techniques were employed to confirm the controlled electrochemically release of CO from the synthesised $Mo^0(CO)_4$(Bipy) complex, previously reported by Hanzlik *et al.*[2] and Bullock and co-workers.[1] The CV studies also indicted that CO loss could be electrochemically induced from $Mo^0(CO)_4$((PyPrNHCO)$_2$Bipy). Preliminary studies were executed to investigate if $M^0(CO)_4$(Bipy) (M = Cr, Mo) complexes could be incorporated into PPy, during film deposition. The electrodeposition was performed in MeCN with $LiClO_4$ and from an aqueous solution containing the anionic surfactant, NaDS. Analyses revealed that the two complexes could not be effectively entrapped with the films using these methodologies. It was then ascertained that covalent modification of PPy films with these metal complexes would be a superior approach, worthy of investigation.

The (PyPrNHCO)$_2$Bipy monomer was then synthesised, succeeded by its characterisation. Both chemical polymerisation and electrochemical deposition of poly[(PyPrNHCO)$_2$Bipy)] was completed and the resulting films were characterised using spectroscopic and electrochemical techniques. Electrodeposition of the polymer was investigated by analysing the *j-t* transients of the films at various E_{ox}. Using this data, it was determined that block co-polymerisation with PPy enabled the deposition of poly(PyPrNHCO)$_2$Bipy) at 0.750 V vs. SCE, a E_{ox} much lower than that expected for an *N*-substituted Py monomer.[50,51] This result indicated that deposition of a metal carbonyl (PyPrNHCO)$_2$Bipy complex may be possible at E_{ox} <1.000 V vs. SCE. Post-functionalisation with $Mo^0(CO)_4$(pip) was then attempted on the electrodeposited poly[(PyPrNHCO)$_2$Bipy] film using ambient conditions, but this did not produce the desired TM carbonyl modified poly[(PyPrNHCO)$_2$Bipy] film.

Syntheses were performed to produce three cyclopentadienyl tricarbonyl molybdenum tetrazolate complexes. Cycloaddition reactions were employed to convert the nitrile precursors to the tetrazolate form, which proved facile and yielded the N-2 tautomer in each case. Preliminary studies were also performed to investigate the formation of the $CpFe^{II}(CO)_2N_4$EtPy complex. Further work will be carried out to isolate and fully characterise this compound. Then, the next step would be to attempt the analogous reaction on a film of PPyEtCN, deposited on an electrode surface.

5.4 References

1. Johnson, R.; Madhani, H.; Bullock, J. P. *Inorg. Chim. Acta* **2007**, *360*, 3414-3423.
2. Hanzlík, J.; Pospíšil, L.; Vlček, A. A.; Krejčík, M. *J. Electroanal. Chem.* **1992**, *331*, 831-844.
3. Caix, C.; Chardon-Noblat, S.; Deronzier, A.; Moutet, J. C.; Tingry, S. *J. Organomet. Chem.* **1997**, *540*, 105-111.
4. Chardon-Noblat, S.; Pellissier, A.; Cripps, G.; Deronzier, A. *J. Electroanal. Chem.* **2006**, *597*, 28-38.
5. Miholová, D.; Vlček, A. A. *J. Organomet. Chem.* **1985**, *279*, 317-326.
6. Chardon-Noblat, S. *J. Mol. Catal. A: Chem.* **1995**, *99*, 13-21.
7. Cosnier, S.; Deronzier, A.; Moutet, J.-C. *J. Electroanal. Chem. Interfacial Electrochem.* **1986**, *207*, 315-321.
8. Weiner, M. A.; Basu, A. *Inorg. Chem.* **1980**, *19*, 2797-2800.
9. Miholová, D.; Gaš, B.; Záliš, S.; Klíma, J.; Vlček, A. A. *J. Organomet. Chem.* **1987**, *330*, 75-84.
10. Le Floch, P.; Carmichael, D.; Ricard, L.; Mathey, F.; Jutand, A.; Amatore, C. *Organometallics* **1992**, *11*, 2475-2479.
11. Case, F. H. *J. Am. Chem. Soc.* **1946**, *68*, 2574-2577.
12. Donnici, C. L.; Máximo Filho, D. H.; Moreira, L. L. C.; Reis, G. T. d.; Cordeiro, E. S.; Oliveira, I. M. F. d.; Carvalho, S.; Paniago, E. B. *J. Braz. Chem. Soc.* **1998**, *9*, 455-460.
13. Cosnier, S.; Deronzier, A.; Moutet, J. C. *J. Phys. Chem.* **1985**, *89*, 4895-4897.
14. De Oliveira, I. M. F.; Moutet, J.-C.; Vlachopoulos, N. *J. Electroanal. Chem. Interfacial Electrochem.* **1990**, *291*, 243-249.
15. Moutet, J. C.; Cho, L. Y.; Duboc-Toia, C.; Menage, S.; Riesgo, E. C.; Thummel, R. P. *Nouv. J. Chim.* **1999**, *23*, 939-944.
16. Deronzier, A.; Moutet, J. C. *Acc. Chem. Res.* **1989**, *22*, 249-255.
17. Lloyd, M. K.; Mcclever.Ja; Orchard, D. G.; Connor, J. A.; Hall, M. B.; Hillier, I. H.; Jones, E. M.; Mcewen, G. K. *J. Chem. Soc. Dalton* **1973**, *0*, 1743-1747.
18. Crutchley, R. J.; Lever, A. B. P. *Inorg. Chem.* **1982**, *21*, 2276-2282.
19. Deng, Z. P.; Stone, D. C.; Thompson, M. *Can. J. Chem.* **1995**, *73*, 1427-1435.
20. Deng, Z. P.; Stone, D. C.; Thompson, M. *Analyst* **1996**, *121*, 671-679.
21. Deng, Z.; Stone, D. C.; Thompson, M. *Analyst* **1997**, *122*, 1129-1138.
22. Fabregat, G.; Cordova-Mateo, E.; Armelin, E.; Bertran, O.; Aleman, C. *J. Phys. Chem. C* **2011**, *115*, 14933-14941.
23. Ouerghi, O.; Senillou, A.; Jaffrezic-Renault, N.; Martelet, C.; Ben Ouada, H.; Cosnier, S. *J. Electroanal. Chem.* **2001**, *501*, 62-69.
24. Um, H. J.; Kim, M.; Lee, S. H.; Min, J.; Kim, H.; Choi, Y. W.; Kim, Y. H. *Talanta* **2011**, *84*, 330-334.
25. McCarthy, C. P.; McGuinness, N. B.; Alcock-Earley, B. E.; Breslin, C. B.; Rooney, A. D. *Electrochem. Commun.* **2012**, *20*, 79-82.
26. McCarthy, C. P.; McGuinness, N. B.; Carolan, P. B.; Fox, C. M.; Alcock-Earley, B. E.; Breslin, C. B.; Rooney, A. D. *Macromolecules* **2013**, *46*, 1008-1016.

27. Palazzi, A.; Sabatino, P.; Stagni, S.; Bordoni, S.; Albano, V. G.; Castellari, C. *J. Organomet. Chem.* **2004**, *689*, 2324-2337.
28. Tate, D. P.; Knipple, W. R.; Augl, J. M. *Inorg. Chem.* **1962**, *1*, 433-&.
29. Palazzi, A.; Stagni, S.; Bordoni, S.; Monari, M.; Selva, S. *Organometallics* **2002**, *21*, 3774-3781.
30. Palazzi, A.; Stagni, S. *J. Organomet. Chem.* **2005**, *690*, 2052-2061.
31. Stagni, S.; Palazzi, A.; Zacchini, S.; Ballarin, B.; Bruno, C.; Marcaccio, M.; Paolucci, F.; Monari, M.; Carano, M.; Bard, A. J. *Inorg Chem* **2006**, *45*, 695-709.
32. Zanarini, S.; Bard, A. J.; Marcaccio, M.; Palazzi, A.; Paolucci, F.; Stagni, S. *J. Phys. Chem. B* **2006**, *110*, 22551-22556.
33. Balahura, R. J. *Can. J. Chem.* **1974**, *52*, 1762-1773.
34. Ellis, W. R.; Purcell, W. L. *Inorg. Chem.* **1982**, *21*, 834-837.
35. O'Brien, C. T., National University of Ireland Maynooth (NUIM), 2004.
36. VanAtta, S. L.; Duclos, B. A.; Green, D. B. *Organometallics* **2000**, *19*, 2397-2399.
37. Braga, S. S.; Coelho, A. C.; Gonçalves, I. S.; Almeida Paz, F. A. *Acta Crystallogr. E* **2007**, *63*, 780-782.
38. Darensbourg, D. J.; Kump, R. L. *Inorg. Chem.* **1978**, *17*, 2680-2682.
39. Ganske, J. A. *Chem. Educ.* **2003**, *8*, 353-357.
40. Arslan, F.; Yasar, A.; Kilic, E. *Russ. J. Electrochem.* **2006**, *42*, 137-140.
41. Flockhart, B. D. *J Coll. Sci. Imp. U. Tok.* **1957**, *12*, 557-565.
42. Abu-Rabeah, K.; Polyak, B.; Ionescu, R. E.; Cosnier, S.; Marks, R. S. *Biomacromolecules* **2005**, *6*, 3313-3318.
43. Hoertz, P. G.; Staniszewski, A.; Marton, A.; Higgins, G. T.; Incarvito, C. D.; Rheingold, A. L.; Meyer, G. J. *J. Am. Chem. Soc.* **2006**, *128*, 8234-8245.
44. Kim, Y.; Vanhelmont, F. W. M.; Stern, C. L.; Hupp, J. T. *Inorg. Chim. Acta* **2001**, *318*, 53-60.
45. Vickers, M. S.; Martindale, K. S.; Beer, P. D. *J. Mater. Chem.* **2005**, *15*, 2784-2790.
46. Massoumi, B.; Lesani, H.; Saraei, M.; Entezami, A. A. *Iran. Polym. J.* **2011**, *20*, 747-756.
47. Moutet, J. C.; Cho, L. Y. *Inorg. Chem. Commun.* **2000**, *3*, 620-623.
48. Garelli, N.; Vierling, P. *J. Org. Chem.* **1992**, *57*, 3046-3051.
49. Diaw, A. K. D.; Yassar, A.; Gningue-Sall, D.; Aaron, J. J. *Arkivoc* **2008**, 122-144.
50. Martinez-Castro, N.; Magenau, A. J. D.; Storey, R. F. *J. Polym. Sci., Part A: Polym. Chem.* **2010**, *48*, 2533-2545.
51. Bansal, L.; El-Sherif, M. *Proc. SPIE-Int. Soc. Opt. Eng.* **2004**, *5527*, 105-115.
52. Rodríguez, I.; Scharifker, B. R.; Mostany, J. *J. Electroanal. Chem.* **2000**, *491*, 117-125.
53. Novák, P. *J. Electrochem. Soc.* **1991**, *138*, 3300.
54. Sanchez De La Blanca, E.; Carrillo, I.; Gonzalez-Tejera, M. J.; Hernandez-Fuentes, I. *J. Polym. Sci., Part A: Polym. Chem.* **2000**, *38*, 291-298.
55. Roux, S.; Audebert, P.; Pagetti, J.; Roche, M. *Nouv. J. Chim.* **2000**, *24*, 877-884.
56. Dunand-Sauthier, M.-N. C.; Deronzier, A.; Moutet, J.-C.; Tingry, S. *J. Chem. Soc., Dalton Trans.* **1996**, *0*, 2503.

57. Hamar-Thibault, S.; Moutet, J.-C.; Tingry, S. *J. Organomet. Chem.* **1997**, *532*, 31-37.
58. Raso, M. A.; Gonzalez-Tejera, M. J.; Carrillo, I.; de la Blanca, E. S.; Garcia, M. V.; Redondo, M. I. *Thin Solid Films* **2011**, *519*, 2387-2392.
59. Tamburri, E.; Orlanducci, S.; Toschi, F.; Terranova, M. L.; Passeri, D. *Synth. Met.* **2009**, *159*, 406-414.
60. Soto, J. P.; Diaz, F. R.; del Valle, M. A.; Velez, J. H.; East, G. A. *Appl. Surf. Sci.* **2008**, *254*, 3489-3496.
61. Del Valle, M. A.; Cury, P.; Schrebler, R. *Electrochim. Acta* **2002**, *48*, 397-405.
62. Schrebler, R.; Grez, P.; Cury, P.; Veas, C.; Merino, M.; Gomez, H.; Cordova, R.; del Valle, M. A. *J. Electroanal. Chem.* **1997**, *430*, 77-90.
63. Abidian, M. R.; Martin, D. C. *Biomaterials* **2008**, *29*, 1273-1283.
64. Haddad, P. S.; Miranda, G.; Ananias, S. R.; Mauro, A. E.; Nogueira, V. M. *J. Braz. Chem. Soc.* **2000**, *11*, 419-423.
65. Jin, S.; Liu, X. R.; Zhang, W.; Lu, Y.; Xue, G. *Macromolecules* **2000**, *33*, 4805-4808.
66. Aradilla, D.; Estrany, F.; Armelin, E.; Oliver, R.; Iribarren, J. I.; Aleman, C. *Macromol. Chem. Phys.* **2010**, *211*, 1663-1672.
67. Li, Y.; Zhang, W.; Chang, J.; Chen, J.; Li, G.; Ju, Y. *Macromol. Chem. Phys.* **2008**, *209*, 322-329.
68. Hawkins, S. J.; Ratcliffe, N. M. *J. Mater. Chem.* **2000**, *10*, 2057-2062.
69. Reece, D. A.; Pringle, J. M.; Ralph, S. F.; Wallace, G. G. *Macromolecules* **2005**, *38*, 1616-1622.
70. Stringfield, T. W.; Chen, Y.; Shepherd, R. E. *Inorg. Chim. Acta* **1999**, *285*, 157-169.
71. Ishikawa, Y.; Kawakami, K. *J. Phys. Chem. A* **2007**, *111*, 9940-9944.
72. Stiddard, M. H. B. *J. Chem. Soc.* **1962**, 4712-4715.
73. Paquette, M. M.; Patrick, B. O.; Frank, N. L. *J. Am. Chem. Soc.* **2011**, *133*, 10081-10093.
74. Hor, T. S. A.; Chee, S.-M. *J. Organomet. Chem.* **1987**, *331*, 23-28.
75. Hor, T. S. A. *Inorg. Chim. Acta* **1987**, *128*, 3-4.
76. Packheiser, R.; Jakob, A.; Ecorchard, P.; Walfort, B.; Lang, H. *Organometallics* **2008**, *27*, 1214-1226.
77. Paul, F.; Goeb, S.; Justaud, F.; Argouarch, G.; Toupet, L.; Ziessel, R. F.; Lapinte, C. *Inorg. Chem.* **2007**, *46*, 9036-9038.
78. Packheiser, R.; Walfort, B.; Lang, H. *Organometallics* **2006**, *25*, 4579-4587.
79. McCarthy, C. P.; McGuinness, N. B.; Alcock-Earley, B. E.; Breslin, C. B.; Rooney, A. D. *Electrochem. Commun.* **2012**, *20*, 79-82.
80. Bu, H.-B.; Götz, G.; Reinold, E.; Vogt, A.; Schmid, S.; Segura, J. L.; Blanco, R.; Gómez, R.; Bäuerle, P. *Tetrahedron* **2011**, *67*, 1114-1125.
81. Bu, H. B.; Gotz, G.; Reinold, E.; Vogt, A.; Schmid, S.; Blanco, R.; Segura, J. L.; Bauerle, P. *Chem. Commun.* **2008**, 1320-1322.
82. Louattani, E.; Suades, J. *J. Organomet. Chem.* **2000**, *604*, 234-240.
83. Gomes, A. C.; Bruno, S. M.; Tomé, C.; Valente, A. A.; Pillinger, M.; Abrantes, M.; Gonçalves, I. S. *J. Organomet. Chem.* **2013**, *730*, 116-122.
84. Palazzi, A.; Stagni, S.; Selva, S.; Monari, M. *J. Organomet. Chem.* **2003**, *669*, 135-140.

85. Fraser, R. R.; Haque, K. E. *Can. J. Chem.* **1968**, *46*, 2855-2858.
86. Purcell, W. L. *Inorg. Chem.* **1983**, *22*, 1205-1208.
87. Hall, J. H.; Purcell, W. L. *Inorg. Chem.* **1990**, *29*, 3806-3811.
88. Hubinger, S.; Purcell, W. L. *Inorg. Chem.* **1991**, *30*, 3707-3710.
89. Butler, R. N.; McEvoy, T. M. *J. Chem. Soc., Perkin Trans. 2* **1978**, 1087-1090.
90. Butler, R. N.; McEvoy, T. M. *Proceedings of the Royal Irish Academy. Section B: Biological, Geological, and Chemical Science* **1977**, *77*, 359-364.
91. Stagni, S.; Palazzi, A.; Brulatti, P.; Salmi, M.; Muzzioli, S.; Zacchini, S.; Marcaccio, M.; Paolucci, F. *Eur. J. Inorg. Chem.* **2010**, *2010*, 4643-4657.
92. Begtrup, M.; Malmström, F.; Wennström, U.; Wennberg, I.; Norbury, A. H.; Swahn, C.-G. *Acta Chem. Scand.* **1973**, *27*, 3101-3110.
93. Fujii, S.; Aichi, A.; Akamatsu, K.; Nawafune, H.; Nakamura, Y. *J. Mater. Chem.* **2007**, *17*, 3777-3779.
94. Catheline, D.; Astruc, D. *Organometallics* **1984**, *3*, 1094-1100.

Publication List

McCarthy, C. P., McGuinness, N. B.; Carolan, P. B.; Fox, C. M. ; Alcock-Earley, B. E. ; Breslin, C. B., Rooney, A. D. 2013, Electrochemical Deposition of Hollow *N*-Substituted Polypyrrole Microtubes from an Acoustically Formed Emulsion, *Macromolecules* Vol: 46, ISSN:0024-9297, Pages: 1008-1016.

McCarthy, Conor P.; McGuinness, Niall B.; Alcock-Earley, Bernadette E; Breslin, Carmel B.; Rooney; A. D. 2012, Facile template-free electrochemical preparation of poly[*N*-(2-cyanoethyl)pyrrole] nanowires., *Electrochem. Commun.* Vol: 20, ISSN:1388-2481, Pages: 79-82.

Oral Presentations

McCarthy, C. P.; McGuinness, N. B.; Breslin, C. B.; Rooney, A. D. 2013, *Characterization of Functionalized Polypyrrole Nanowire/Tubule Modified Electrodes,* 8th Annual Scientific Workshop of the National Access Programme (NAP), Tyndall National Institute, UCC, Cork, Ireland.

McGuinness, N. B.; Breslin, C. B.; Rooney, A. D. 2012, *Novel Template-Free Electrochemical Growth and Post-functionalization of N-substituted Polypyrrole Nanowires***,** 64th Irish Universities Chemistry Research Colloquium, UL, Limerick, Ireland, Pages: 31-31.

McGuinness, N. B., McCarthy, C. P., Breslin, C. B., Rooney, A. D., 2011, *Novel N-substituted Polypyrrole Carbon Monoxide Releasing Molecules (CO-RMs) and Transition Metal Functionalized Polypyrrole Nanowire Films*, 4th Annual Meeting for the Irish Institute of Metal-Based Drugs (IIMBD), NUIM, Kildare, Ireland.

Poster Presentations

McGuinness, N. B.; Breslin, C. B., Rooney, A. D.; 2010, *Novel Polypyrrole Substituted Carbon Monoxide Releasing Molecules (CO-RMs); New Delivery System for Carbon Monoxide,* 64th Annual Meeting of the International Society of Electrochemistry (ISE), Nice, France, Pages 130-130.

McGuinness, N. B.; Breslin, C. B., Rooney, A. D. 2010, *Novel Polypyrrole Substituted Carbon Monoxide Releasing Molecules (CO-RMs); New Delivery System for Carbon Monoxide* 5th International Symposium on Bioorganometallic Chemistry (ISBOMC), Ruhr-Universitat Bochum (RUB), Bochum, Germany, Pages: 94-94.

McGuinness, N. B.; Breslin, C. B.; Rooney, A. D. 2009, *Novel Polypyrrole Substituted Carbon Monoxide Releasing Molecules (CO-RMs); New Delivery System for Carbon Monoxide,* 1st International Symposium on Functional Nanomaterials, NCSR, DCU, Dublin, Ireland.